
BLOOD PLATELETS IN THE MICROCIRCULATION
- A THEORETICAL AND COMPUTATIONAL STUDY

Von der Universität Bayreuth
zur Erlangung des Grades eines
Doktors der Naturwissenschaften (Dr. rer. nat.)
genehmigte Abhandlung

von

Christian Bächer
aus Marktredwitz

1. Gutachter: Prof. Dr. Stephan Gekle
2. Gutachter: Prof. Dr. Walter Zimmermann
3. Gutachter: Prof. Dr. Jens Harting

Tag der Einreichung: 28.08.2020

Tag des Kolloquiums: 19.01.2021

Abstract

The blood cells called blood platelets play a crucial role in keeping the blood circulatory system intact. Circulating through the human body within the flowing blood, platelets are responsible for the quick stop of a bleeding. A prime property of the platelets is the margination, i.e., the adaptation of a near-wall location in the flowing blood. However, the blood flow does not only facilitate their main function, but also contributes significantly to their highly efficient formation. The large number of 10^{11} blood platelets forms daily in the bone marrow in a strongly flow-accelerated process. In addition to the external fluid forces, actively generated stresses in the cell cortex, a thin layer of cytoskeletal filaments and motor proteins tethered to the cell membrane, are important for the development of blood platelets.

While simulations of passive elastic cells in flow are abundant, a combination with active cortex mechanics has so far not been addressed. In the present thesis, a simulation tool is developed, which allows such a combination. In a fully three-dimensional manner, the computational tool combines an arbitrarily deforming, elastic active cell cortex plus membrane with a dynamic coupling to a flowing liquid. By utilizing active gel and thin shell theory, the force balance equations are expressed on a triangulated membrane and forces resulting from active stresses are calculated using a parabolic fitting procedure. Suspending fluid flow dynamics as well as a two-way coupling of flow and membrane mechanics are achieved using a lattice-Boltzmann/immersed boundary scheme or the boundary integral method. On the same footing including the parabolic fitting procedure, a second three-dimensional simulation method is developed which considers an active cortex in the long time, i.e., viscous, limit. Here, a heterogeneous active stress distribution triggers flow inside the cell cortex. We numerically determine the flow velocity by globally solving the force balance equations by means of a minimization ansatz. Both simulation methods are extensively validated.

A particular interesting feature of a cell cortex is the occurrence of anisotropic active stress. Based on the mathematical description it becomes clear that a cortical active stress is analogous to the surface tension of a liquid despite their fundamentally different origin. Therefore, the Rayleigh-Plateau instability, which is known to describe the break-up of a cylindrical liquid jet into droplets, has also been predicted to occur in the presence of a cortical active stress. However, the question arises how an anisotropic active stress, in contrast to the isotropic surface tension, alters this instability. We analytically derive dispersion relations for a fluid-fluid interface as well as a shear and/or bending elastic membrane under the influence of an anisotropic interfacial tension. Our theoretical analysis accompanied by numerical simulations uncovers a strong impact of the anisotropy on the instability, where fragment size decreases and instability dynamics becomes faster for dominating azimuthal tension. Most remarkably, the interplay of elasticity and tension anisotropy can restrict the instability and can render the interface stable.

In blood platelet formation, progenitor cells trapped in the bone marrow develop long, finger-like membrane protrusions into blood vessels. These protrusions fragment into numerous platelets in the presence of blood flow. Using our developed simulation tool, we identify a biological Rayleigh-Plateau instability as the fundamental biophysical origin of the highly efficient formation of the blood platelets. We confirm the cortical activity as key ingredient for this fragmentation. In addition, we systematically study the influence of external blood flow, where we find a significant acceleration of the formation with increasing flow velocity in agreement with experiments. Simulations show that this acceleration is especially pronounced in a homogeneous flow field, which sheds light onto an efficient design of microfluidic devices for *in vitro* platelet production. In the presence of shear, we find an explanation for the formation of larger preplatelets, which are intermediate progenitors of blood platelets.

While it is well known that released blood platelets are expelled towards the vessel wall in a process called margination in blood flowing through straight channels, their behavior in vessel networks is hardly understood. In this thesis, we investigate their flow behavior passing through a vessel bifurcation as well as a vessel confluence. While our simulations show that their distinct near-wall position is robust along a bifurcation, we observe platelets located within an additional (red blood) cell-free layer in the vessel center behind a confluence. By determining the shear induced diffusion coefficient, we are able to draw conclusions on platelet dynamics in a vessel network, where succeeding confluences would lead to a more continuous distribution of blood platelets across the vessel diameter. Therefore, the observed antimargination behind a confluence can explain differences in platelet distribution between the arterial part with abundant bifurcations and the venous part of the microcirculation with a lot of confluences previously found *in vivo*.

Key words

Active membranes · Rayleigh-Plateau instability · anisotropic tension · blood platelets · blood platelet biogenesis · blood flow · (anti)margination · cell mechanics · fluid-particle interaction · computational fluid dynamics · biological physics

Zusammenfassung

Die als Blutplättchen bezeichneten Blutkörperchen sind für ein intaktes Kreislaufsystem von großer Bedeutung. Sie oszillieren mit dem Blut durch den menschlichen Körper und sorgen für einen schnellen Stopp von Blutungen. Eine wichtige Eigenschaft von Blutplättchen ist dabei die Margination, welche ihre Lokalisierung nahe von Gefäßwänden in fließendem Blut beschreibt. Jedoch begünstigt der Blutfluss die Blutplättchen nicht nur in ihrer Funktion, er spielt auch eine große Rolle in deren hocheffizienter Erzeugung. Ein unter Strömung stark beschleunigter Prozess im Knochenmark sorgt für die tägliche Produktion von 10^{11} Blutplättchen. Zusätzlich zu den Kräften aufgrund des äußeren Blutflusses sind aktiv generierte Spannungen im Zellkortex, einer dünnen Schicht von Filamenten des Zytoskeletts und Motorproteinen verknüpft mit der Zellmembran, essentiell für den Entstehungsprozess der Blutplättchen.

Während Computersimulationen von passiv elastischen Zellen im Fluss weite Verbreitung finden, wurde deren Kombination mit der aktiven Mechanik des Zellkortex bisher nicht berücksichtigt. In dieser Arbeit wird eine Simulationsmethode entwickelt, welche diese Kombination ermöglicht. Die komplett dreidimensionale Simulationsmethode koppelt einen beliebig deformierten, elastischen und aktiven Zellkortex zusammen mit der Zellmembran an ein äußeres Fluid. Unter Zuhilfenahme der Theorie aktiver Gele und der Theorie dünner Membranen wird das Kräftegleichgewicht auf dem triangulierten Zellkortex formuliert und die Kräfte, welche aus der aktiven Spannung resultieren, werden mittels einer parabolischen Anpassung berechnet. Die Gitter-Boltzmann-/Immersed-Boundary- oder die Randwertintegral-Methode ermöglichen die Berechnung von Fluiddynamik und eine dynamische beiderseitige Kopplung von Fluid und Membranmechanik. Auf selbiger Basis der parabolischen Anpassung wird darüber hinaus eine weitere dreidimensionale Simulationsmethode für den Zellkortex im Langzeitlimit, d.h. für einen viskosen Kortex, entwickelt. Hier sorgt die aktive Spannung für einen Fluss innerhalb des Zellkortex. Durch das globale Lösen des Kräftegleichgewichts durch einen Minimierungsansatz wird die Flussgeschwindigkeit numerisch bestimmt. Beide Simulationsmethoden werden ausgiebig validiert.

Ein besonders interessanter Aspekt des Zellkortex ist das Auftreten anisotroper aktiver Spannung. Aufgrund einer ähnlichen mathematischen Beschreibung ist die aktive Kortexspannung analog zur Oberflächenspannung einer Flüssigkeit. Daran erkennt man, dass die Rayleigh-Plateau-Instabilität, welche das Auseinanderbrechen eines zylindrischen Wasserstrahls in Tröpfchen beschreibt, auch in Folge einer aktiven Kortexspannung auftreten kann. Wie eine anisotrope Spannung im Gegensatz zur isotropen Oberflächenspannung diese Instabilität beeinflusst, ist bisher ungeklärt. In dieser Arbeit werden analytische Dispersionsrelationen sowohl für eine Fluid-Fluid-Grenzfläche als auch für eine scher- und biegeelastische Membran unter Einfluss anisotroper Spannung hergeleitet. Die theoretische Beschreibung im Zusammenspiel mit Simulationen zeigt einen starken Einfluss anisotroper Spannung, wobei mit dominierender azimuthaler Spannung die Fragmentgröße

abnimmt und die Dynamik schneller wird. Bemerkenswerterweise kann die Elastizität zusammen mit der aktiven Spannung zu einer Beschränkung und sogar zur Unterdrückung der Instabilität führen.

Die Blutplättchen entstehen aus langen, fingerartigen Membranfortsätzen, welche von den Vorläuferzellen im Knochenmark in die Blutbahn ausgebildet werden. Diese Fortsätze zerbrechen unter Einfluss des Blutflusses in zahlreiche Blutplättchen. Durch Computersimulationen mit der entwickelten Methode kann gezeigt werden, dass eine biologische Rayleigh-Plateau-Instabilität den biophysikalischen Mechanismus der hocheffizienten Blutplättchenbildung darstellt. Dabei wird die wichtige Rolle des aktiven Zellkortex bestätigt. Darüber hinaus zeigen die Simulationen eine systematische Beschleunigung des Entstehungsprozesses mit steigender äußerer Flussgeschwindigkeit im Einklang mit Experimenten. Im Hinblick auf eine effiziente Gestaltung von Mikrofluidikkanälen zur künstlichen Erzeugung von Blutplättchen, tritt die stärkste Beschleunigung in einem homogenen Flussfeld auf. Im Scherfluss wird eine Erklärung für die Bildung größerer Präplättchen gefunden, welche als eine Vorform von Blutplättchen auftreten können.

Während die Margination eine viel untersuchte Beschreibung der wand-nahen Lokalisierung der Blutplättchen in geraden Gefäßen darstellt, ist der Einfluss von verzweigten Gefäßen kaum verstanden. In dieser Arbeit werden Blutplättchen im Blutfluss innerhalb einer Bifurkation oder eines Zusammenflusses von Gefäßen untersucht. Computersimulationen zeigen, dass die Position nahe der Wand durch eine Bifurkation nicht beeinflusst wird, aber hinter einem Zusammenfluss von Gefäßen dazu führt, dass die Blutplättchen in die Kanalmitte migrieren. Durch die Bestimmung des scher-induzierten Diffusionskoeffizienten können Aussagen zum Verhalten in einem Netzwerk von Gefäßen getroffen werden. Hierbei führen mehrere Zusammenflüsse hintereinander zu einer kontinuierlichen Verteilung von Blutplättchen über den Gefäßdurchmesser. Somit kann die Antimargination experimentelle Unterschiede zwischen der Blutplättchenverteilung in arteriellen Gefäßen mit überwiegend Bifurkationen und venösen Gefäßen mit überwiegend Gefäßzusammenflüssen erklären.

Schlüsselwörter

Aktive Membranen · Rayleigh-Plateau-Instabilität · anisotrope Spannung · Blutplättchen · Blutplättchenbildung · Blutfluss · (Anti-)Margination · Zellmechanik · Fluid-Partikel-Wechselwirkung · Strömungssimulationen · biologische Physik

Publications for this thesis

- [pub1] C. Bächer and S. Gekle (2019). Computational Modeling of Active Deformable Membranes Embedded in Three-Dimensional Flows. *Physical Review E* **99** (6), p. 062418. DOI: [10.1103/PhysRevE.99.062418](https://doi.org/10.1103/PhysRevE.99.062418)
- [pub2] C. Bächer, D. Khoromskaia, G. Salbreux, and S. Gekle (2020). A Three-Dimensional Numerical Model of an Active Cell Cortex in the Viscous Limit. *Draft*
- [pub3] K. Graessel, C. Bächer, and S. Gekle (2021). Rayleigh–Plateau Instability of Anisotropic Interfaces. Part 1. An Analytical and Numerical Study of Fluid Interfaces. *Journal of Fluid Mechanics* **910**, A46. DOI: [10.1017/jfm.2020.947](https://doi.org/10.1017/jfm.2020.947)
- [pub4] C. Bächer, K. Graessel, and S. Gekle (2021). Rayleigh–Plateau Instability of Anisotropic Interfaces. Part 2. Limited Instability of Elastic Interfaces. *Journal of Fluid Mechanics* **910**, A47. DOI: [10.1017/jfm.2020.946](https://doi.org/10.1017/jfm.2020.946)
- [pub5] C. Bächer, M. Bender, and S. Gekle (2020). Flow-Accelerated Platelet Biogenesis Is Due to an Elasto-Hydrodynamic Instability. *Proceedings of the National Academy of Sciences* **117** (32), pp. 18969–18976. DOI: [10.1073/pnas.2002985117](https://doi.org/10.1073/pnas.2002985117)
- [pub6] C. Bächer, A. Kihm, L. Schrack, L. Kaestner, M. W. Laschke, C. Wagner, and S. Gekle (2018). Antimargination of Microparticles and Platelets in the Vicinity of Branching Vessels. *Biophysical Journal* **115** (2), pp. 411–425. DOI: [10.1016/j.bpj.2018.06.013](https://doi.org/10.1016/j.bpj.2018.06.013)

Contents

Abstract	III
Zusammenfassung	V
Publications for this thesis	VII
I Extended abstract	1
1 Introduction	3
2 Modeling of biological membranes in the context of blood flow	7
2.1 Biology of the cell membrane and cortex	7
2.2 Modeling a membrane in thin shell theory	8
2.2.1 Differential geometry	9
2.2.2 Mechanical properties	11
2.2.3 Passive elasticity and viscosity of a membrane	12
2.3 Active mechanics of the cell cortex	13
2.4 Blood flow mechanics	15
2.4.1 Blood flow	15
2.4.2 Theoretical fluid dynamics	16
2.4.3 Computational fluid dynamics	17
3 Numerical models for an active cell cortex	19
3.1 Numerical representation of the cortex	19
3.2 A numerical model for an elastic cell cortex coupled to a fluid	21
3.2.1 Active force calculation	21
3.2.2 Validation	22
3.2.3 Cell division in shear flow	23
3.3 A numerical model for a viscous cell cortex	24
3.3.1 Velocity field on the discrete cortex	24
3.3.2 Validation	27
4 Rayleigh-Plateau instability for anisotropic tension and blood platelet formation	31
4.1 Rayleigh-Plateau instability of anisotropic interfaces	32
4.1.1 Anisotropic interfacial tension	32
4.1.2 Linear stability analysis	32
4.1.3 Analytical and simulation results	35
4.1.4 Elastic interfaces	37

4.2	Blood platelet biogenesis as flow-accelerated instability	39
4.2.1	Motivation	39
4.2.2	Computational model of a proplatelet	39
4.2.3	Flow-accelerated biological Rayleigh-Plateau instability	40
5	Antimargination of platelets in vessel confluences	43
5.1	Motivation	43
5.2	Computational model of a vessel bifurcation and confluence	44
5.3	Main results	45
6	Conclusions and outlook	49
	References	53
II	Publications	77
	The author's contributions	79
	Contributions to the publications for this thesis	79
	Further publications	82
	Contributions to conferences and symposiums	82
	Publication 1: Computational Modeling of Active Deformable Membranes Embedded in Three-Dimensional Flows	85
	Publication 2: A Three-Dimensional Numerical Model of an Active Cell Cortex in the Viscous Limit	117
	Publication 3: Rayleigh–Plateau Instability of Anisotropic Interfaces. Part 1. An Analytical and Numerical Study of Fluid Interfaces	163
	Publication 4: Rayleigh–Plateau Instability of Anisotropic Interfaces. Part 2. Limited Instability of Elastic Interfaces	205
	Publication 5: Flow-Accelerated Platelet Biogenesis is due to an Elasto-Hydrodynamic Instability	241
	Publication 6: Antimargination of Microparticles and Platelets in the Vicinity of Branching Vessels	269
	About the author	297
	Acknowledgments	299
	Eidesstattliche Versicherung	301

Part I

Extended abstract

1 Introduction

An important aspect of the biological cell's ability to sustain life is the mechanical function including cellular shape regulation, which goes back to proteins acting in an orchestrated fashion [1, 2]. During polymerization and depolymerization of cytoskeletal protein filaments, e.g., actin, or movement of associated motor proteins such as myosin, chemically stored energy is constantly converted into mechanical work [1]. This drives cytoskeletal assemblies out of equilibrium and within the assembly mechanical stress is actively generated [3–6]. The non-equilibrium character of active stress [7–9] leads to new physical phenomena: the formation of protrusions on artificial vesicles [10], density and orientational instabilities [11, 12], the emergence of structures [13, 14], and spontaneous flows [15, 16]. In particular considering a biological cell, a thin layer of an active protein network made up of actin and myosin tethered to the plasma membrane, which is termed cell cortex, plays an important role. In turn, the biological composition and physical effects go hand in hand to determine cell behavior, among others leading to deformations and thus strongly regulating the cell shape [8, 17–21]. Often, cellular processes take place in aqueous environment such as blood flow, where cells constantly move and are exposed to external forces due to viscous stress. Therefore, not only active stress but also the flowing environment influences the cell shape [22, 23].

In the field of biological physics, the development of new tools [24, 25], such as the hydrodynamic theory of active gels [3, 26] covering the behavior of a cell cortex [27–29], is of great importance to describe and understand cellular processes [9, 29, 30]. Concerning a dynamically deforming shape, from the theoretical description often either predictions on instabilities are deduced [9, 13, 31–36] or equations are solved numerically to obtain the evolving cell shape [20, 37–41]. An analytical investigation of the flow field has been done inside a weakly deforming sphere subjected to active stress [42, 43]. Except the determination of the equilibrium shape of an elastic shell with a preferred curvature accounting for myosin activity [44] and the work by Torres-Sánchez et al. [45], who model a three-dimensional viscous cell cortex [45, 46], those methods are restricted to small deformations and/or axisymmetry. Furthermore, previous studies do not account for the full dynamics of a suspending fluid. Therefore, the framework of active gel theory could so far not been used to explore the combination of active stress in the cell cortex and external fluid dynamics in a three-dimensional fashion.

An important consequence of the presence of active stress is the occurrence of instabilities [11, 12, 47, 48]. Also an instability analogous to the Rayleigh-Plateau instability is predicted for a positive and isotropic active stress [32, 33, 49]. The Rayleigh-Plateau instability is well known for the break-up of a liquid jet driven by surface tension [50–54] and has been reported for vesicles in presence of an externally induced tension [55–58]. However, in contrast to a liquid jet or a vesicle, where an isotropic tension at the interface or membrane is present, the active stress in cytoskeletal assemblies can be anisotropic [59–62]. Therefore, the cell cortex, which together with the cell membrane represents the

interface between the interior and exterior of a cell, or a tissue layer can be subject to an anisotropic stress [20, 63–65]. The influence of an anisotropic interfacial tension on the Rayleigh-Plateau instability is unknown. Another property which has great impact on the mechanical behavior of a cell or tissue is its elasticity [23, 66–69]. While the influence of bending elasticity on the Rayleigh-Plateau instability of a vesicle has been addressed [56, 58, 70–73], the role of shear elasticity remains largely unknown [32, 33]. In addition, in cells or tissues both elasticity and anisotropic active stress often accompany each other.

By biomedical studies, a crucial role of active cortical mechanics has also been reported for the biogenesis, i.e., formation, of blood platelets [74–77]. Blood platelets, which are the cellular constituents of blood responsible for an intact circulatory system [78], are constantly produced in large numbers in the blood vessels of the bone marrow [79]. Their direct progenitor cells form long tubular extensions into the blood flow, which fragment into the later platelets [79]. In particular, it has been shown that a disturbed actin-myosin cortex in the extensions inhibits proper platelet formation [74, 80–83]. In addition, several experiments highlight a crucial role of external fluid flow, where a strong acceleration of the formation has been reported [84–89]. Therefore, the formation of blood platelets is a prime example of a biological process combining active cortex mechanics and external fluid flow. Despite these experimental observations, a fundamental understanding of the formation process on the one hand and the reason for the strong impact of fluid mechanics on the other hand is still absent.

Released blood platelets adopt a characteristic near-wall position in the flowing blood, which goes back to a mechanism called margination [90]. In the flowing blood, the deformable red blood cells migrate towards and enrich in the center of a blood vessel. This in turn triggers the expulsion of the platelets into the near-wall, (red blood) cell-free layer [90–93]. Whereas margination is well understood in straight channels [94–110], investigations of more complex vessel geometries are limited to an aneurysm [111, 112], a channel expansion [113], or a vessel constriction [114–117]. While experiments [118, 119] highlight a different distribution of platelets on the two sides of the microcirculatory vessel system, first studies of blood flow in branching vessels or networks focus on the red blood cell behavior [120–128]. How margination is affected by vessel branching in networks has so far not been addressed.

The aim of the present thesis is to go from the development of a three-dimensional computational method for cortical cell mechanics in interplay with external fluid flow to the investigation of physical and biological processes in the light of active cell mechanics and blood flow. It provides biophysical insight into and an explanation for blood platelet formation as well as platelet motion in vessel networks. In this course, which is illustrated in figure 1.1, the present thesis starts with the development of simulation tools. On the one hand, we cover three-dimensional deformations of an elastic cell cortex together with the cell membrane triggered by the presence of active stress. Here, the cell cortex with membrane is dynamically coupled to the internal fluid and the external blood flow. On the other hand, a cell cortex in the viscous limit is considered, where the flow velocity in the cell cortex due to active stress is dynamically obtained on the evolving cortex. Active stress is incorporated into a numerical thin shell model representing cortex and membrane embedded in a three-dimensional environment. Both methods have the same numerical basis for geometrical thin shell representation, but work with a fundamentally different solution scheme. These methods push the research forth towards a realistic cell

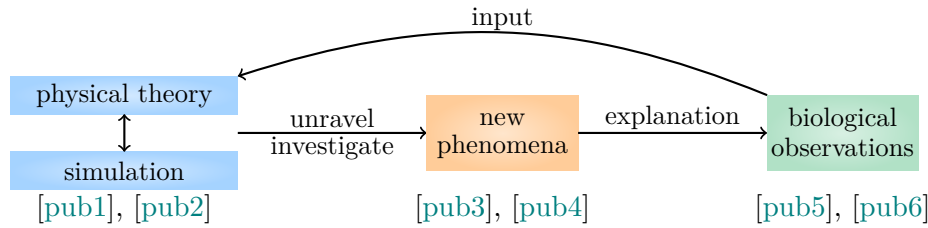


Fig. 1.1: **Scope of the present thesis.** In the course of the present thesis, two simulation methods are developed, one for an elastic [pub1] and one for a viscous cell cortex [pub2] subjected to active stress in three dimensions. Considering anisotropic active stresses often occurring in the cell cortex, the framework of the Rayleigh-Plateau instability is extended analytically and by means of simulations to include effects by anisotropic interfacial tension [pub3],[pub4]. Finally, a biological Rayleigh-Plateau instability, which is accelerated with increasing external flow velocity, is proposed as biophysical mechanism of blood platelet biogenesis [pub5]. Platelet behavior in blood flowing through a vessel bifurcation and confluence is investigated [pub6], where we report platelet antimargination triggered by a vessel confluence.

model covering the cortex. By its flexibility the model allows for application to the vast variety of different constitutive laws which account for the active cortex mechanics.

In a next step, physical processes with a new characteristic in the light of active mechanics are investigated. We extend the picture of the Rayleigh-Plateau instability, i.e., the pearling instability of jets, vesicles, and cellular tubes, to include anisotropic tension or active stress. We combine the theory describing this instability with active mechanics, where an anisotropic active stress is often observed in contrast to the classical instability with isotropic surface tension. The goal here is to provide an analytical extension to the general theory which is accompanied by simulations using the developed method focusing on anisotropic active stress. We explore the Rayleigh-Plateau instability of jets and vesicles or cells, highlighting the strong impact of anisotropic interfacial tension, both without and with interface elasticity. Blood platelet biogenesis is a beautiful example, where active cortical mechanics is strongly coupled to external blood flow and which therefore requires a coupled description for a detailed biophysical understanding. Using our developed three-dimensional simulation tool, we address the biophysical origin and the strong acceleration of platelet formation. Based on the Rayleigh-Plateau instability due to actin-myosin driven cortical active stress, we investigate blood platelet biogenesis from a numerical point of view. We thus provide the biological Rayleigh-Plateau instability as the biophysical mechanism underlying platelet formation and report a striking acceleration by the interplay of the instability and external fluid flow. Finally, released blood platelets are considered in blood flowing through a branching vessel. In the present thesis, we systematically shed light onto the margination of platelets in a vessel bifurcation and a vessel confluence, as they appear in the organism. This is a large step to an understanding of margination in realistic complex vessel networks as they become more and more subject of blood flow research [125, 127, 128].

This first part of this cumulative thesis provides the basics for and a summary of the publications that led to this thesis in a compact and coherent manner. The publications together with a list of the individual author contributions are attached to the thesis in part II. The remainder of the first part is structured as follows: in section 2, we first summarize the important aspects of cell biology, its realization in a physical membrane

model with special emphasis on the active mechanics, followed by a short introduction into fluid mechanics. The developed simulation methods are outlined in section 3. In section 3.1, we first introduce the numerical basis of the developed simulation methods for an active cell cortex in three dimensions. Next, we present the simulation method for an active elastic cell cortex and membrane in section 3.2 and afterwards for a viscous active cell cortex in section 3.3. In section 4, we discuss the Rayleigh-Plateau instability under the influence of anisotropic stress in section 4.1 and its application to blood platelet biogenesis under the influence of blood flow in section 4.2. In section 5, we summarize our results on the platelet distribution in flowing blood within a vessel bifurcation and confluence. We conclude in section 6 and give an outlook.

2 Modeling of biological membranes in the context of blood flow

In the following, necessary background information for the publications is presented. It starts with a biological introduction on the cell membrane and the cell cortex in section 2.1. Then, the modeling of cell membranes in thin shell theory is introduced in section 2.2 with a compact overview of differential geometry and the treatment of mechanical properties. Section 2.3 deals with the active mechanics with a special focus on the cell cortex. In section 2.4, first the fluid mechanics covering aspects of blood flow is addressed. Then, a short overview of theoretical fluid mechanics is given, followed by an introduction into the simulation methods used in this thesis.

2.1 Biology of the cell membrane and cortex

One key feature of a cell is its encapsulation, which is achieved by the plasma membrane [1]. However, the plasma membrane not only separates the cell interior from its environment, but also contributes to the cell's elastic behavior and thus to the cell shape. The membrane consists of two layers made of amphiphilic lipid molecules, which form a lipid bilayer with a height of a few nanometers [1]. The hydrophilic head groups of the lipid molecules are oriented towards the aqueous environment in the cell interior and exterior, the hydrophobic tails are oriented towards each other and form the core of the bilayer. While the bilayer behaves as a fluid in the plane of the layer [129] and consequently its resistance to shear deformation is zero [67], out-of-plane bending leads to exposure of the hydrophobic tails to water. As a consequence, the bilayer has a certain resistance to such bending deformations [67]. The preferred curvature of the membrane depends on the shape and sort of the lipid molecules the bilayer is composed of [130–132].

In addition, proteins that are linked to the interior side of the plasma membrane strongly influence cell mechanics [1]. A prominent example is the protein spectrin which forms long filaments that in turn form a triangulated [133] mesh-like, thin network that completely underlines the plasma membrane of red blood cells [1] and blood platelet progenitors [134]. Spectrin provides the membrane with an additional resistance to shear deformation [135] and thus is highly important for the cell shape [134, 136]. A eukaryotic cell further consists of complex networks of cross-linked, structural protein filaments, the cytoskeleton, which spans through the whole cell. The cytoskeleton consists of microtubules, actin, and intermediate filaments [1]. Microtubules form by polymerization of globular proteins into long tubes whereas polymerizing strings assemble into long filaments in case of actin and intermediate filaments [1].

The cytoskeleton is further responsible for a dynamic reorganization of the cell shape, another important factor of eukaryotic life. A highly dynamic reorganization and move-

ment in the cytoskeleton is among others crucial for transport processes, cell division, and cell movement [1]. Here, a network of actin located underneath and linked to the plasma membrane called cell cortex plays a special role [1, 137]. The cortex is responsible for the separation of two daughter cells during cell division, called cytokinesis, movement and the regulation of the cell shape [1, 19, 137–140]. On the one hand, cortex reorganization is driven by continuous polymerization and depolymerization of the actin filaments, on the other hand motor proteins can move the filaments relatively to each other [1]. The motor protein associated to actin is myosin. To microtubules both kinesin and dynein motor proteins can bind. The dynamic processes, polymerization and motor protein movement, are established by the presence of Adenosine triphosphate (ATP) and Guanosine triphosphate (GTP), the molecular storage units of chemical energy in the cell. Some types of proteins including the motor proteins are capable of converting ATP into Adenosine diphosphate (ADP) by hydrolysis and using the released energy for movement or other functions. Motor proteins in turn convert chemically stored energy into mechanical work. The dynamic processes taking place in the cell are constantly fueled by energy on the very small scale of single proteins [1, 3].

2.2 Modeling a membrane in thin shell theory

For red blood cells [23, 135, 141], blood platelets [142], their progenitors [143], but also for actin shells created in artificial vesicles [144] and cells in general [137] a cortex height in the order of hundred nanometers is reported. Therefore, the height of the plasma membrane and cortex together is small compared to a typical cell diameter in the order of several microns. As a consequence, the thin shell theory [145–147] has been established in membrane modeling, where membrane and cortex are represented by an infinitely thin shell.

In the following, we first start by introducing the important concepts of differential geometry, which is the framework of thin shell theory. Afterwards, we detail the treatment of membrane and cortex mechanics.

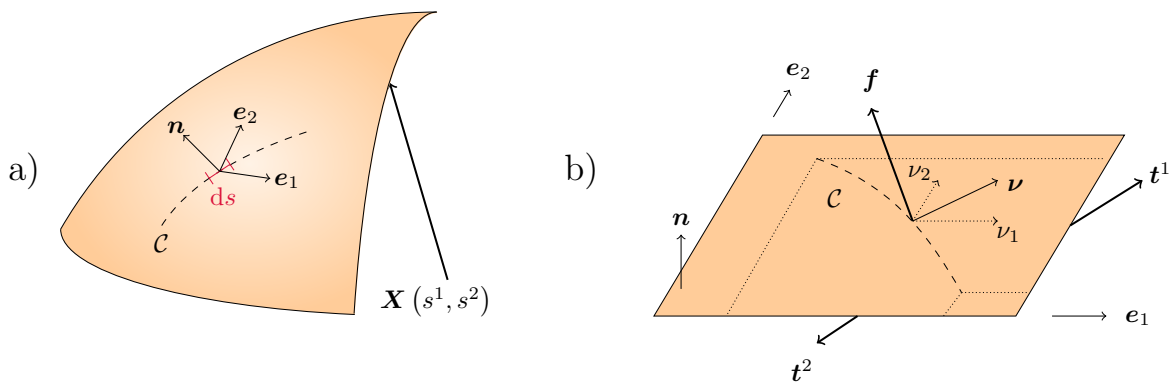


Fig. 2.1: **Membrane and cortex as thin shell.** a) The thin shell is parametrized by $\mathbf{X}(s^1, s^2)$ with in-plane coordinate vectors \mathbf{e}_α , where $\alpha = 1, 2$, and normal vector \mathbf{n} . \mathcal{C} represents a line along the thin shell with a line element ds . b) A force \mathbf{f} is acting on a line element of the thin shell with in-plane normal vector $\boldsymbol{\nu}$. The force is decomposed along the in-plane coordinate vectors in terms of the surface stress \mathbf{t}^α .

2.2.1 Differential geometry

Because of their relatively small thickness, the plasma membrane and cortex are treated as a thin shell, a two dimensional manifold in three-dimensional space [148]. The thin shell representing both the plasma membrane and cortex is sometimes called membrane [pub1]. Figure 2.1 a) provides a sketch. Mathematically, the thin shell is parametrized by a vector $\mathbf{X} = \mathbf{X}(s^1, s^2)$ depending on the two coordinates s^1, s^2 . In-plane coordinate vectors, which point along the interface, can be derived from the parametrization by a partial derivative

$$\mathbf{e}_\alpha = \frac{\partial}{\partial s^\alpha} \mathbf{X} =: \partial_\alpha \mathbf{X}, \quad (2.1)$$

where Greek letters refer to the thin shell coordinates and take the values $\alpha, \beta, \gamma, \delta = 1, 2$. The local unit normal vector on the membrane \mathbf{n} can be deduced from the two in-plane coordinate vectors by a cross product

$$\mathbf{n} = \frac{\mathbf{e}_1 \times \mathbf{e}_2}{|\mathbf{e}_1 \times \mathbf{e}_2|}. \quad (2.2)$$

The in-plane coordinate vectors and the normal vector build a coordinate system

$$(\mathbf{e}_1, \mathbf{e}_2, \mathbf{n}), \quad (2.3)$$

defined at each point located on the thin shell. Therefore, they provide a local coordinate system, where the three coordinate vectors themselves are vectors in the three-dimensional space. Each general vector can be decomposed into its components along these coordinate vectors

$$\mathbf{a} = a^\beta \mathbf{e}_\beta + a^n \mathbf{n}, \quad (2.4)$$

where the upper index refers to a contravariant component and a lower index correspondingly to a covariant component. Here and in the following, the Einstein sum convention is used, which implies a sum over an index occurring twice, as covariant as well as contravariant index. With Latin indices we refer to three-dimensional Cartesian coordinates, they take the values $i, j, k = 1, 2, 3$ and the Einstein sum convention simply applies to a double occurring index.

On the membrane, an arbitrary line \mathcal{C} can be considered with the line element ds pointing along $d\mathbf{X}$. From the first fundamental form

$$ds^2 = g_{11} ds^1 ds^1 + 2g_{12} ds^1 ds^2 + g_{22} ds^2 ds^2 = d\mathbf{X} \cdot d\mathbf{X}, \quad (2.5)$$

which allows for the measurement of length and area element on the membrane, the metric tensor can be derived

$$g_{\alpha\beta} = \mathbf{e}_\alpha \cdot \mathbf{e}_\beta. \quad (2.6)$$

The contravariant or inverse metric $g^{\alpha\beta}$ is defined by the relation $g_{\alpha\gamma} g^{\gamma\beta} = \delta_\alpha^\beta$ with δ_α^β being the Kronecker symbol. For a symmetric tensor, i.e., $t_\alpha^\beta = t_\beta^\alpha$, such as the Kronecker symbol, the order of covariant and contravariant indices can be changed and therefore no distinction of the order in the mathematical symbol is necessary. Using the metric tensor the index of a tensor component can be raised or lowered

$$a^\alpha = g^{\alpha\beta} a_\beta, \quad a_\alpha = g_{\alpha\beta} a^\beta, \quad (2.7)$$

$$t^{\alpha\beta} = g^{\beta\gamma} t_\gamma^\alpha, \quad t_{\alpha\beta} = g_{\alpha\gamma} t^\gamma_\beta. \quad (2.8)$$

Partial derivatives of the metric tensor components are given by a combination of the Christoffel symbols, which in turn are defined by

$$\Gamma_{\alpha\beta}^{\gamma} = \frac{1}{2}g^{\gamma\delta}(\partial_{\alpha}g_{\beta\delta} + \partial_{\beta}g_{\delta\alpha} - \partial_{\delta}g_{\alpha\beta}). \quad (2.9)$$

The Christoffel symbols further allow for a generalization of the derivative along the in-plane coordinates to the covariant derivative. The covariant derivative in contrast to the partial one transforms in a covariant manner [149] and is given for a scalar ϕ , a general vector a^{β} , and a general tensor $t^{\alpha\beta}$ by

$$\nabla_{\alpha}\phi = \partial_{\alpha}\phi, \quad \nabla_{\alpha}a^{\beta} = \partial_{\alpha}a^{\beta} + \Gamma_{\alpha\gamma}^{\beta}a^{\gamma}, \quad (2.10)$$

$$\nabla_{\alpha}t^{\beta\gamma} = \partial_{\alpha}t^{\beta\gamma} + \Gamma_{\alpha\delta}^{\beta}t^{\delta\gamma} + \Gamma_{\alpha\delta}^{\gamma}t^{\beta\delta}. \quad (2.11)$$

An important property, which strongly discriminates a deformed thin shell from the description of a three-dimensional body, is the curvature of the thin shell. It is characterized by the second fundamental form

$$c_{\alpha\beta} ds^{\alpha} ds^{\beta} = d\mathbf{X} \cdot d\mathbf{n}, \quad (2.12)$$

which is the variation of the normal vector projected onto a line element. Corresponding to the second fundamental form the (extrinsic) curvature tensor is defined by

$$c_{\alpha\beta} = \partial_{\alpha}\mathbf{X} \cdot \partial_{\beta}\mathbf{n} = -(\partial_{\alpha}\mathbf{e}_{\beta}) \cdot \mathbf{n}, \quad (2.13)$$

where the minus together with the second identity stems from the derivative of the identity $\mathbf{e}_{\alpha} \cdot \mathbf{n} = 0$ [149]. For the curvature tensor, two scalar invariants can be defined [149], the mean curvature

$$H = \frac{1}{2}g^{\alpha\beta}c_{\alpha\beta}, \quad (2.14)$$

and the Gaussian curvature

$$K = \det(c_{\alpha}^{\beta}). \quad (2.15)$$

The covariant derivative of an in-plane coordinate vector is given by the equation of Gauss [148, 149]

$$\nabla_{\alpha}\mathbf{e}_{\beta} = -c_{\alpha\beta}\mathbf{n}, \quad (2.16)$$

the covariant derivative of the normal vector by the equation of Weingarten [148, 149]

$$\nabla_{\alpha}\mathbf{n} = c_{\alpha}^{\beta}\mathbf{e}_{\beta}, \quad (2.17)$$

and the covariant derivative of the metric vanishes

$$\nabla_{\alpha}g^{\beta\gamma} = 0, \quad \nabla_{\alpha}g_{\beta\gamma} = 0. \quad (2.18)$$

Using equation (2.4), the covariant derivative of a general vector \mathbf{a} can be obtained

$$\nabla_{\alpha}\mathbf{a} = (\nabla_{\alpha}a_{\beta} + a^{\gamma}c_{\alpha\beta})\mathbf{e}^{\beta} + (\nabla_{\alpha}a^n - a_{\beta}c_{\alpha}^{\beta})\mathbf{n}. \quad (2.19)$$

2.2.2 Mechanical properties

The thin shell theory has to cover the mechanical properties of the membrane including the cortex. Both internal membrane mechanics and interaction with the environment result in forces on the membrane. In strong analogy to the well-known Cauchy stress tensor and Cauchy's law in three-dimensional continuum mechanics [150], the force on the membrane can be expressed in terms of stress vectors [145]

$$\mathbf{f} = \nu_\alpha \mathbf{t}^\alpha ds, \quad (2.20)$$

where \mathbf{f} is the force on a line \mathcal{C} , which is characterized by the in-plane normal vector $\boldsymbol{\nu}$ as sketched in figure 2.1 b). The force on a local area element on the membrane is calculated by the line integral over the force in equation (2.20) along the contour of the area element. We term \mathbf{t}^α as the surface stress [pub1]. It can be decomposed in analogy to equation (2.4)

$$\mathbf{t}^\alpha = t^{\alpha\beta} \mathbf{e}_\beta + t_n^\alpha \mathbf{n}, \quad (2.21)$$

with the components along the in-plane coordinates being the in-plane surface stress $t^{\alpha\beta}$ and the normal components named transverse shear stress t_n^α [69, 151, 152].

The surface stress \mathbf{t}^α covering internal mechanics is a sum of the different contributions from the different mechanical properties of the membrane [68]

$$\mathbf{t}^\alpha = \mathbf{t}_{\text{el}}^\alpha + \mathbf{t}_{\text{visc}}^\alpha + \mathbf{t}_{\text{act}}^\alpha, \quad (2.22)$$

where we here consider elastic surface stress $\mathbf{t}_{\text{el}}^\alpha$, viscous surface stress $\mathbf{t}_{\text{visc}}^\alpha$, and actively generated surface stress $\mathbf{t}_{\text{act}}^\alpha$. Furthermore, torques can arise which are described by moments such as active moments [9] or bending moments [69, 151].

In addition to the internal mechanical stresses, external forces are acting on the membrane, which are in equilibrium with the internal membrane forces [68, 145]. When the membrane is immersed in a fluid, forces from the fluid act onto the membrane. The fluid forces acting onto a membrane are given by the projection of the three-dimensional fluid stress tensor $\boldsymbol{\sigma}$ on the normal vector of the interface [150]

$$\hat{f}_i = \sigma_{ij} n_j. \quad (2.23)$$

A cell membrane is typically surrounded by an external medium (outer fluid) and encloses the cytoplasm (inner fluid). Considering the forces from both fluids $\hat{\mathbf{f}}^{\text{out}}$ and $\hat{\mathbf{f}}^{\text{in}}$, respectively, leads to the traction jump across the membrane $\Delta \mathbf{f}$ using equation (2.23)

$$\Delta \mathbf{f} = \hat{\mathbf{f}}^{\text{out}} - \hat{\mathbf{f}}^{\text{in}} = (\boldsymbol{\sigma}^{\text{out}} - \boldsymbol{\sigma}^{\text{in}}) \cdot \mathbf{n}. \quad (2.24)$$

The traction jump can again be decomposed into the components Δf^α along the in-plane coordinate vectors and the component Δf^n along the normal vector. For negligible inertia the traction jump is in equilibrium with the membrane forces \mathbf{f} , which are deduced from the surface stress in equation (2.22). This equilibrium results in the force balance equations

$$\nabla_\alpha t^{\alpha\beta} + c_\beta^\alpha t_n^\beta + \Delta f^\alpha = 0, \quad (2.25)$$

$$\nabla_\alpha t_n^\alpha - c_{\alpha\beta} t^{\alpha\beta} + \Delta f^n = 0, \quad (2.26)$$

which are the component-wise expression of (cf. equation (2.19))

$$\nabla_\alpha \mathbf{t}^\alpha + \Delta \mathbf{f} = 0, \quad (2.27)$$

and equivalent to the notation $\nabla_s \cdot \mathbf{T}$ with stress tensor \mathbf{T} and surface gradient ∇_s as used by Barthès-Biesel [68].

2.2.3 Passive elasticity and viscosity of a membrane

Under the action of forces a membrane (together with the cortex) can be deformed. The passive elasticity describes the force as response to a deformation, which drives the membrane back into an undeformed state (or towards the stress free shape). The elastic response is described in terms of a constitutive law accounting for a certain material or a certain class of materials.

For the elastic response of a red blood cell membrane towards shearing and area dilatation the Skalak law has been proposed [66]

$$W^{\text{SK}} = \frac{\kappa_S}{12} \left[(I_1^2 + 2I_1 - 2I_2) + CI_2^2 \right], \quad (2.28)$$

which gives the energy density W^{SK} in terms of the deformation invariants I_1 and I_2 , the shear modulus κ_S , and the area dilatation coefficient C . The deformation invariants can either be deduced from the deformation gradient [68, 153] or directly from the metric of the undeformed $G^{\alpha\beta}$ and deformed membrane $g^{\alpha\beta}$ [145, 154, 155] by

$$I_1 = G^{\alpha\beta} g_{\alpha\beta} - 2, \quad (2.29)$$

$$I_2 = \det(G^{\alpha\beta}) \det(g_{\alpha\beta}) - 1, \quad (2.30)$$

as explicitly performed in the publications [pub1] and [pub4]. The resistance towards shearing stems from the spectrin network in red blood cells which underlines the plasma membrane and the resistance towards area dilatation stems from the plasma membrane itself. We note that for $C = 1$ and small deformations the Skalak law is equivalent to the Neo-Hookean law for membrane elasticity [156–158].

For the elastic response to bending deformations of lipid membranes the Helfrich law [67] is widely used [68, 69, 159, 160] determining the bending energy density

$$W^{\text{HF}} = 2\kappa_B(H - H_0)^2 + \kappa_K K, \quad (2.31)$$

where κ_B is the bending modulus, κ_K the Gaussian curvature modulus and H_0 the reference curvature. The term including the Gaussian curvature K often can be neglected because of the Gauss-Bonnet theorem [149, 161]. Therefore, a finite elastic bending energy in equation (2.31) and a corresponding restoring force arise from deviations of the mean curvature H from the reference curvature H_0 .

From the energy density functional of the elastic constitutive law, e.g., equations (2.28) and (2.31), the force on the membrane can be deduced in two ways: the gradient of the energy with respect to the position on the membrane can be calculated [69, 153] or in the framework of thin shell theory the contribution to the surface stress \mathbf{t}_c^α is derived by derivatives with respect to the metric and curvature tensors [145]. The surface stress in

turn enters the force balance equations (2.25) and (2.26). The latter approach has been performed in the publications [pub1] and [pub4].

In the long-time limit the cell cortex behaves as a viscous fluid [20, 31, 37, 40, 162]. In analogy to the Newtonian stress tensor of a three-dimensional fluid (cf. equation (2.33) below), viscosity of the cortex enters as another contribution $\mathbf{t}_{\text{visc}}^\alpha$ to the surface stress in equation (2.22) [9, 163–166]. Similar to a three-dimensional compressible fluid [150] a planar shear viscosity η_s and a planar bulk viscosity η_b are introduced [9, 167, 168]. Viscous stresses, furthermore, depend on the surface velocity gradient, i.e., derivatives of the velocity along the thin shell. For a further discussion and explicit equations we refer to section 3.3 with equations (3.20) and (3.21) and publication [pub2].

2.3 Active mechanics of the cell cortex

Cytoskeletal networks such as the cell cortex are not only of great importance for cell functionality from the biological point of view [1], but are also part of a flourishing field of soft matter research as they represent a special class of material, namely active matter [3]. The constant conversion of chemically stored energy into mechanical work drives these kind of systems out of equilibrium on the scale of single molecules [3]. Kruse et al. [26] developed a hydrodynamic theory covering the non-equilibrium mechanics of cytoskeletal networks. The key quantity covering the actively induced forces is the active stress [169, 170]. Due to the general viscoelastic nature of cytoskeletal networks, the whole framework is called active gel theory [3, 4, 26, 29, 30, 171–175]. With its constant progress, active gel theory has been successfully used to describe the final stage of cell division, cytokinesis, where the cell locally contracts and separates into two daughter cells [31, 37, 38, 40, 176–178], remodulation of the cortex necessary for cell motility [162, 179–182], and cell shape regulation [18–20, 183, 184]. Salbreux et al. [9] presented a concise theory on thin shells made of active matter.

An active material is classified by a constitutive law for the active stress [9]. In case of an active thin shell, the in-plane component of the active contribution to the surface stress in equation (2.22) can be constituted

$$t_{\text{act}\alpha}{}^\beta = \begin{pmatrix} t_a^1 & 0 \\ 0 & t_a^2 \end{pmatrix}, \quad (2.32)$$

with components along the principal directions. From a distribution of active stress, e.g., across the height of a tissue, in addition active moments [9] can arise contributing to the normal component t_n^α , which, however, are beyond the scope of this thesis. In general, active stresses are classified as extensile or contractile [174]. The active stress nature is illustrated in figure 2.2 for a patch of active material. Further, it is classified as isotropic, i.e., being of equal strength in each direction, or anisotropic, i.e., with strength depending on the direction. The active stress strongly depends on the type of cytoskeletal filaments and motor proteins and the structure of their assembly [174]. By cross-linking or interaction of filaments by motor proteins different structures emerge, e.g., bundles, asters, or contractile stress fibers [185, 186]. The type of observed structures such as asters depends on the walking direction of the motor proteins [174, 187] and in turn affects active stress nature. Microtubule bundles with mixed polarity are mainly dipolar extensile [174,

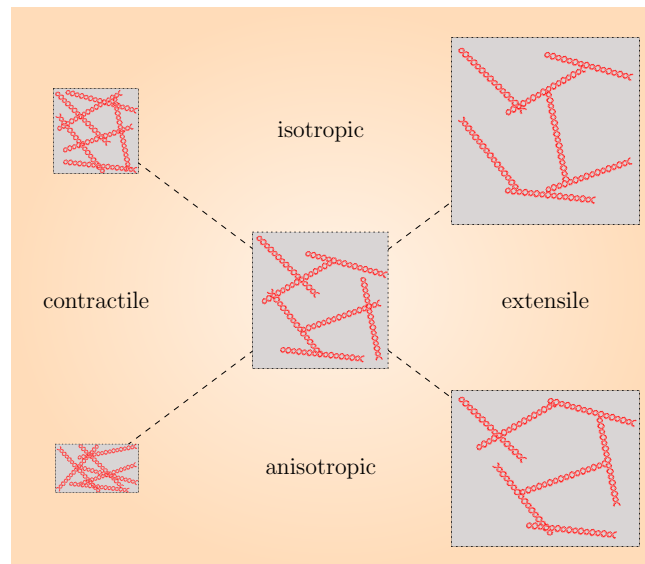


Fig. 2.2: **Active stress nature.** An active material (in the center) either tends to contract (contractile nature, left) or to expand itself (extensile nature, right) under the action of the actively induced stress, such as by motor protein movement. Depending on filament orientation and packing, contraction/expansion can be isotropic (top) or anisotropic (bottom). The illustration is based on figure 4 of ref. [174].

[188, 189]. Using a kinesin-driven filament gliding assay, Stanhope et al. [190] tuned the active stress of microtubule bundle networks from extensile to contractile by varying the concentration of microtubules and cross-linkers. Refs. [186, 191, 192] reported isotropic bulk contraction for a microtubule/dynein network composed of asters. Dynein motor proteins can induce aster formation in microtubule networks and furthermore can bridge between neighboring asters leading to contractile network formation [191, 193, 194]. Oriola et al. [195] refer to ref. [191] and state that contraction of dynein systems might drive contractile stresses in the spindle apparatus as well. Dynein mediated sliding of microtubule filaments is known to drive the extension of axon protrusions [196] and membrane protrusions of the blood platelet progenitors [87], which suggest an extensile nature in these situations. Actin-myosin networks including the cell cortex are known to be contractile, i.e., actin-myosin assemblies contract in each direction [21, 60, 137, 197–202]. In the cell cortex, actin-myosin often forms a disordered network [1, 60, 202]. Koenderink et al. [197] reported that for cross-linked actin filaments the contractile stress generated by myosin II is isotropic. Furthermore, the strength of cross-linking within a network triggers the contractility [200, 202–205]. Filament orientation can further lead to an anisotropic, active cortical stress [20, 31, 40, 59–65].

In order to incorporate the active stress into a continuum theory, such as the thin shell theory in section 2.2, a constitutive law has to be chosen representing the system of interest. The simplest approach is to consider a spatially constant and isotropic active stress with its magnitude depending on the chemical potential difference of ATP hydrolysis. In principal, the active stress can vary with the density of actin-myosin [20, 39, 206]. An advection-diffusion approach can be used to describe the density of actin, where further polymerization and depolymerization can be incorporated using reaction rates [13, 20, 31, 39]. Furthermore, the active stress depends on the orientation of cytoskeletal

filaments and formed structures such as stress bundles [1, 185]. As a consequence the active stress can become anisotropic [20, 31, 40, 59–65]. An explicit dynamic dependency can be modeled by the introduction of a vectorial polar orientation or a nematic tensor field [3, 26, 31, 40, 189]. Further variations include asymmetric membranes [9] and chiral active matter [30].

Due to the small length scale and the complexity of the systems of interest, precise values of quantities such as the active stress are scarce. Using cortical laser ablation in combination with active gel theory, the active stress relative to a friction coefficient has been measured to be on the order of $10 \mu\text{m}^2\text{s}^{-1}$ and the viscoelastic relaxation time to be on the order of 10 s in zebrafish cells and embryonic cells of the nematode *Caenorhabditis elegans* [207]. The latter value is in agreement with reported values of the relaxation time between 10 and 100 s for cortical actin [208, 209]. A cortical tension of $2 \times 10^{-5} \text{Nm}^{-1}$ has been reported for neutrophils [210]. In a zebrafish embryo, a cellular cortical tension of $2 \times 10^{-5} - 8 \times 10^{-5} \text{Nm}^{-1}$ has been found [211]. For fibroblasts, a typical cortical tension of 10^{-4}Nm^{-1} has been reported [212] and tensions in the same order of magnitude occur for macrophages [213] and for carcinoma cells [214]. The cortical tension predicted for blood platelets is about $1 \times 10^{-5} \text{Nm}^{-1}$ [142]. For activated blood platelets, an estimation [pub5] based on reported three-dimensional stresses [215, 216] gives an active surface stress of 10^{-3}Nm^{-1} . Finally, a tension on the order of 10^{-3}Nm^{-1} has been measured for HeLa cells in mitosis [200, 217].

2.4 Blood flow mechanics

2.4.1 Blood flow

Flowing blood may be the most important fluid for many complex living organisms. In a human body a wide network of vessels, the circulatory system, connects the different organs, limbs, and tissues. Both large vessels near the heart and very fine, structured vessels in the tissue occur. Blood represents a fluidic environment for many cells and is constantly in motion. The circulatory system continuously sustains the transport and supply of oxygen to all tissues of the organism. Furthermore, in the blood nutrients and other gases are transported.

Blood consists of cells which are immersed in the blood plasma. The blood plasma itself is a Newtonian fluid [218] of viscosity $\eta = 1.2 \times 10^{-3} \text{Pas}$ and density $\rho = 1000 \text{kg/m}^3$ [219, 220]. The oxygen is bound by the hemoglobin of anucleate blood cells, called erythrocytes or red blood cells. The red blood cells typically have a biconcave shape in rest with a diameter of $8 \mu\text{m}$ and a height of about $2 \mu\text{m}$ and form the main cellular constituent of blood [221]. Their volume fraction, approximately the hematocrit, ranges from 45% in large vessels towards 20% in small vessels [222–224]. Immune cells, the lymphocytes or white blood cells, either tackle infections in the blood stream or are enriched at sites of inflammation or infection of a tissue. In total, a healthy and functional organism requires a mechanism to keep the blood circulatory system intact. The blood cells responsible for an intact circulatory system are the anucleate thrombocytes or blood platelets. In case of an injury, the blood platelets are activated, quickly stop the bleeding, close the defect and therefore are of great importance for hemostasis [78].

All blood cells derive from a common progenitor in the bone marrow, the hematopoietic stem cell [225]. Following the hierarchy from the hematopoietic stem cell downwards, one precursor cell forms both red blood cells and blood platelets [226]. Further differentiation leads to the megakaryocyte which is the direct progenitor cell to the blood platelets. A megakaryocyte grows long membrane protrusions into the sinusoidal blood vessels of the bone marrow [75]. These protrusions form swellings [75] and eventually rupture releasing those swellings, which mature into functional blood platelets in the blood flow [227].

2.4.2 Theoretical fluid dynamics

The constitutive equation for a simple and incompressible liquid such as the blood plasma is expressed by the Newtonian stress tensor [150]

$$\boldsymbol{\sigma} = -p\mathbf{I} + \eta [(\nabla\mathbf{v} + (\nabla\mathbf{v})^T)], \quad (2.33)$$

with shear viscosity η , velocity vector field $\mathbf{v}(\mathbf{r}, t)$ and scalar pressure field $p(\mathbf{r}, t)$ both depending on position \mathbf{r} and time t and with \mathbf{I} being the unit matrix. The time evolution of the velocity field, i.e., fluid dynamics, is governed by the Navier-Stokes equation for an incompressible fluid

$$\frac{\partial\mathbf{v}}{\partial t} + (\mathbf{v} \cdot \nabla)\mathbf{v} = -\frac{1}{\rho}\nabla p + \nu\Delta\mathbf{v}, \quad (2.34)$$

where $\nu = \frac{\eta}{\rho}$ is the kinematic viscosity and ρ the density. Depending on the properties of the system of interest the non-linear left hand side of the Navier-Stokes equation (2.34) accounting for fluid inertia can exceed or is negligible compared to the viscous stress, the second term on the right hand side of equation (2.34). The relative strength of inertia and viscous stress is quantified by the dimensionless Reynolds number

$$Re = \frac{\rho L_0 V_0}{\eta}, \quad (2.35)$$

where L_0 is a typical length in the system and V_0 a typical velocity. In the limit of small Reynolds number, inertia effects are negligible and the linear Stokes equation becomes valid

$$-\nabla p + \eta\nabla^2\mathbf{v} = \mathbf{0}. \quad (2.36)$$

In the other limit of dominating inertia effects, the Euler equation can be used

$$\frac{\partial\mathbf{v}}{\partial t} + (\mathbf{v} \cdot \nabla)\mathbf{v} = -\frac{1}{\rho}\nabla p. \quad (2.37)$$

In addition to the Navier-Stokes equation (2.34), or in the discussed limits the Stokes equation (2.36) or Euler equation (2.37), the set of fluid equations is closed by the incompressibility condition or continuity equation

$$\nabla \cdot \mathbf{v} = 0. \quad (2.38)$$

The set of fluid equations is accompanied by boundary conditions. At a non-moving solid wall the fluid velocity has to vanish according to the no-slip boundary condition [150].

At a moving interface the no-slip condition implies the kinematic boundary condition [54, 152, 228, 229]

$$\frac{d}{dt}\mathbf{u} = \mathbf{v}|_{\mathbf{x}'}, \quad (2.39)$$

which relates the time derivative of the interface deformation \mathbf{u} to the fluid velocity \mathbf{v} at the position of the interface \mathbf{X}' .

2.4.3 Computational fluid dynamics

When systems become complex, maybe with an additional coupling to particle dynamics, an analytical solution of the Navier-Stokes equation (2.34) often cannot be achieved. Therefore, fluid dynamics is often solved numerically and therefore a variety of methods in the field of computational fluid dynamics has evolved. In the following, the methods used in this thesis, the lattice-Boltzmann/immersed boundary and the boundary integral method, are shortly outlined.

Lattice-Boltzmann method

In contrast to other common methods such as finite volume or finite element method, the lattice-Boltzmann method does not discretize and solve the Navier-Stokes equation directly. It is rather a mesoscopic approach which is based on the single particle distribution function $f(\mathbf{r}, \mathbf{p}, t)$ depending on position \mathbf{r} and momentum \mathbf{p} of a particle as well as time t [230–232]. The dynamics of the distribution function is determined by the Boltzmann equation. The Chapman-Enskog analysis proves that the Boltzmann equation leads to fluid behavior as governed by the Navier-Stokes equation [232, 233].

In the numerical realization, the lattice-Boltzmann method, a fluid is considered to be discretized on a regular Eulerian grid with nodes at position \mathbf{x}_j and discretized velocities \mathbf{c}_i . We use the D3Q19 scheme with $i = 0, \dots, 18$ in three dimensions. The Boltzmann equation becomes the lattice-Boltzmann equation

$$f_i(\mathbf{x}_j + \mathbf{c}_i\Delta t, t + \Delta t) = f_i(\mathbf{x}_j, t) + \Omega_i(\mathbf{x}_j, \mathbf{F}_j, t), \quad (2.40)$$

with Ω_i the collision operator and Δt a time increment. The collision operator Ω_i governs changes in the distribution function due to collisions and further contains forces \mathbf{F}_j , e.g., acting from a cell membrane onto the fluid. Those forces are transmitted to the fluid nodes by the immersed boundary method, as detailed below. We use a multiple relaxation time scheme [232] for the collision operator Ω_i . Equation (2.40) can be integrated numerically including an update of the discrete distribution function due to the collision operator and propagation. The multiple relaxation time scheme further allows for the incorporation of thermal fluctuations of the fluid [234, 235]. Solid boundaries can easily be implemented by the bounce back scheme [232], whereas for elastic, deformable, and moving boundaries the lattice-Boltzmann method is accompanied by the immersed boundary method.

Immersed boundary method

The immersed boundary method provides a fluid-interface coupling for a deformable, moving boundary such as the cell membrane [236, 237]. The interface is represented

by a Lagrangian grid of nodes immersed in the Eulerian fluid grid. In the present thesis, a discretization of the interface by nodes connected to triangles is used. From the corresponding constitutive equation the force per node \mathbf{f} is calculated as, e.g., detailed in section 3.2 and in publication [pub1]. This force serves as input for fluid dynamics at the position of the membrane \mathbf{X}'

$$\mathbf{F}_j = \int \mathbf{f}(\mathbf{X}', t) \delta(\mathbf{X}' - \mathbf{x}_j) d^2 X', \quad (2.41)$$

and is mapped from the Lagrangian membrane mesh to the Eulerian fluid mesh by extrapolation from each membrane node to the surrounding fluid nodes. With the interface force as input, fluid dynamics is solved by a lattice-Boltzmann time step. Afterwards, each interface node is advected with local fluid velocity, where the same interpolation scheme is used as for force spreading. All in all, the immersed boundary method provides a two-way, dynamic coupling of interface and fluid.

In the present thesis, the combined lattice-Boltzmann/immersed boundary method implemented in the software package ESPResSo [238, 239] has been used and extended.

Boundary integral method

In the limit of a small Reynolds number $Re \ll 1$, the boundary integral method can be used [110, 151, 240], which is directly based on the linearity of the Stokes equation (2.36) and as a consequence intrinsically neglects fluid inertia. Fluid dynamics is solved using the Green's functions of the Stokes equation. Elastic interfaces such as the cell membrane are discretized and at each node on the discrete interface the traction jump in equation (2.24) calculated from the membrane forces is prescribed. Using the Green's functions, the velocity in the simulation domain can be obtained for the current geometrical arrangement by the boundary integral equations. The interface nodes are then advected with the fluid velocity evaluated at the node position according to the kinematic boundary condition (2.39).

3 Numerical models for an active cell cortex

Following the thin shell theory from section 2.2, in section 3.1 the basics for the numerical representation of the cortex in a three-dimensional simulation is provided including the parabolic fitting procedure used to calculate geometrical properties and derivatives on the discrete cortex. In section 3.2, the computational method for an elastic, active cell cortex developed in publication [pub1] is introduced and in section 3.3 we summarize the method for a viscous cell cortex presented in publication [pub2].

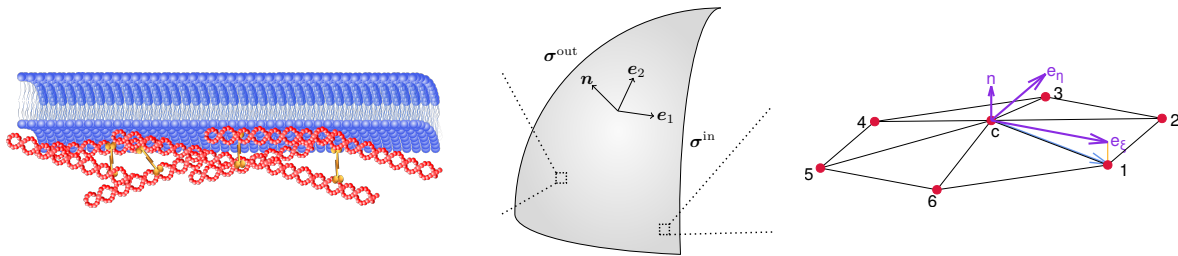


Fig. 3.1: **Numerical membrane representation.** Plasma membrane of the cell (blue) and cell cortex (red), as sketched on the left, are modeled together as thin shell (center) with the coordinate system (e_1, e_2, \mathbf{n}) defined on the thin shell. Constitutive equations for the thin shell recover the elastic, viscous, or active physical properties of the membrane and the cortex. The thin shell is surrounded by an outer fluid and encloses an inner fluid described by the stress tensor σ^{out} and σ^{in} , respectively. In numerical simulations the thin shell is discretized by nodes connected to triangles (right). Considering its neighbors, a local coordinate system $(e_\xi, e_\eta, \mathbf{n})$ can be constructed on each node. Adapted from publication [pub1] with permission from APS and the left image from publication [pub5] with permission from the National Academy of Sciences..

3.1 Numerical representation of the cortex

In the following, we outline our numerical model for the cell cortex, which is based on a parabolic fitting procedure. As described in section 2.2, plasma membrane and cell cortex sketched on the left hand side of figure 3.1 are condensed into a deformable thin shell (center of figure 3.1). For its representation in numerical simulations we use a discretization of the thin shell by N points that are connected to triangles. This is a common approach for vesicle or cell simulations [69, 151, 240–242]. On the thin shell each node can be considered together with its neighborhood defined by the triangles adjacent to the central node. A node with its neighborhood is illustrated on the right hand side of figure 3.1.

As discussed above, thin shell theory is based on a coordinate system defined on the shell, e.g., in equation (2.3). The first step in the numerical procedure is the construction

of the local coordinate system at the position of each node \mathbf{r}_c

$$(\mathbf{e}_\xi, \mathbf{e}_\eta, \mathbf{n}_c)_{\mathbf{r}_c}. \quad (3.1)$$

At first, the unit normal vector $\mathbf{n}_c = \mathbf{n}$ at the position of the central node is obtained by an average of the normal vectors \mathbf{n}_t on the adjacent triangles \mathcal{T}_c

$$\mathbf{n}_c = \sum_{t \in \mathcal{T}_c} \mathbf{n}_t \beta_t. \quad (3.2)$$

The normal vector on each triangle \mathbf{n}_t is obtained by the cross product of the two vectors connecting the central node and its two neighbors. In equation (3.2) each normal vector is weighted by the angle β_t of these two vectors. As the next step, for the first in-plane coordinate vector one neighbor node is chosen as reference, which is arbitrary but remains fixed during the simulation. The vector from the central node to the reference neighbor, e.g., \mathbf{x}_1 , can be converted to the first in-plane unit vector by Gram-Schmidt orthogonalization and the second one can be obtained by a cross-product

$$\mathbf{e}_\xi = \frac{\mathbf{x}_1 - (\mathbf{x}_1 \cdot \mathbf{n}_c) \mathbf{n}_c}{|\mathbf{x}_1 - (\mathbf{x}_1 \cdot \mathbf{n}_c) \mathbf{n}_c|}, \quad \mathbf{e}_\eta = \frac{\mathbf{n}_c \times \mathbf{e}_\xi}{|\mathbf{n}_c \times \mathbf{e}_\xi|}. \quad (3.3)$$

Now, each vector from the central node can be expressed in the local coordinate system in equation (3.1) with in-plane coordinates ξ, η .

Following thin shell theory in section 2.2 we have so far obtained the coordinate system on the discrete shell and we can decompose an arbitrary vector along those coordinates. This leaves us with the calculation of geometrical quantities, such as the metric tensor and the curvature tensor, but also the derivative of quantities defined on the shell. We achieve these using a parabolic fitting procedure such as used for calculation of bending forces [240]. The basic idea behind the parabolic fitting procedure is a Taylor expansion in the local coordinate system up to the second order around the central node. For an arbitrary function f the expansion in local in-plane coordinates (ξ, η) takes the form

$$f(\xi, \eta) = f_c + A\xi + B\eta + \frac{C}{2}\xi^2 + \frac{D}{2}\eta^2 + E\xi\eta, \quad (3.4)$$

where f_c is the function value at the central node. A to E represent the derivatives up to second order in the local coordinate system

$$\begin{aligned} A &= \nabla_\xi f|_{\mathbf{r}_c}, & B &= \nabla_\eta f|_{\mathbf{r}_c}, \\ C &= \nabla_\xi \nabla_\xi f|_{\mathbf{r}_c}, & D &= \nabla_\eta \nabla_\eta f|_{\mathbf{r}_c}, & E &= \nabla_\xi \nabla_\eta f|_{\mathbf{r}_c}, \end{aligned} \quad (3.5)$$

which are evaluated at the position of the central node. Considering the function value f_a at each of the \mathcal{N} neighboring nodes and the theoretical expansion in equation (3.4) evaluated at the corresponding position (ξ_a, η_a) the squared residuum is defined as

$$\chi^2 = \sum_{a \in \mathcal{N}} [f_a - f(\xi_a, \eta_a)]^2 = \sum_{a \in \mathcal{N}} \left[f_a - f_c - A\xi_a - B\eta_a - \frac{C}{2}\xi_a^2 - \frac{D}{2}\eta_a^2 - E\xi_a\eta_a \right]^2. \quad (3.6)$$

By minimization with respect to the parameter set (A, B, C, D, E)

$$\nabla_{(A, B, C, D, E)} \chi^2 = 0, \quad (3.7)$$

the derivatives along the local in-plane coordinates evaluated at the central node in equation (3.5) are obtained as fitting parameters. The minimization involves solving a linear system of equations (3.7) for A to E , which can be done either using numerical lower-upper (LU) decomposition or by analytically inverting the matrix.

Is the parabolic fitting applied to a vector field, e.g., a velocity field defined on the cortex or the position of the nodes, each spatial component of the vector can be fitted separately in the same way as detailed above. Using the positions of the neighboring nodes as input, the fitting leads to the first and second derivatives of the shell parametrization, which are used to compute the metric tensor in equation (2.6) as well as the curvature tensor in equation (2.13) on the discrete shell. Eventually, the area per node can be calculated using Meyer's mixed area [243].

The main quantity of interest in our numerical models is the active stress in the cell cortex. We start by prescribing the active stress from a constitutive law on the undeformed cortex, where typically an analytical expression is possible in a reference coordinate system (cf. equation (2.3)), such as cylindrical or spherical coordinates. Numerically, for each node of the undeformed discrete shell a coordinate system as given in equation (3.3) is constructed. The two coordinate systems share the normal vector, which means that both the analytical and numerical in-plane coordinate vectors are located in the same plane. Therefore, the in-plane coordinate vectors are tilted by an angle β . In order to project the active stress from the analytical in-plane coordinates to the numerical in-plane coordinates a rotation matrix $\mathfrak{D}(\beta)$ is applied to the in-plane surface stress tensor

$$\mathfrak{D} t_{\text{act}}^{\alpha\beta} \mathfrak{D}^{-1}. \quad (3.8)$$

During simulation the active stress expressed in the local coordinate system, which co-moves with the deforming thin shell, is used for active force calculation.

3.2 A numerical model for an elastic cell cortex coupled to a fluid

3.2.1 Active force calculation

On short time scales, where no reorganization of the cortex network takes place, it can be modeled as an elastic polymer network subjected to active stresses due to motor protein movement [9, 33]. Consequently, the surface stress in equation (2.22) consists of an elastic and an active part

$$\mathbf{t}^\alpha = \mathbf{t}_{\text{el}}^\alpha + \mathbf{t}_{\text{act}}^\alpha. \quad (3.9)$$

In simulations, the elastic stress $\mathbf{t}_{\text{el}}^\alpha$ is not explicitly computed, but rather an algorithm is used [153, 160] which directly calculates the elastic forces from the energy density given by the Helfrich constitutive law in equation (2.31) and the Skalak constitutive law in equation (2.28) for bending and shear elasticity, respectively. In contrast, the stress is the starting point of force calculation for the active contribution. For a given constitutive law the active stress can either be calculated on the discrete membrane, e.g., with a coupling to a concentration field of either ATP or actin-myosin, or can be prescribed in a reference coordinate system and converted into the local coordinate system as detailed

in the previous section. According to the force balance equations (2.25) and (2.26), the active forces acting from the membrane onto the fluid are given by

$$f_{\text{act}}^{\beta} = \nabla_{\alpha} t_{\text{act}}^{\alpha\beta}, \quad (3.10)$$

$$f_{\text{act}}^n = -c_{\alpha\beta} t_{\text{act}}^{\alpha\beta}. \quad (3.11)$$

In each time step of the simulation these forces are calculated for each node on the deformed thin shell. The gradient of the active stress is calculated on the deformed thin shell by a parabolic fitting procedure as detailed in section 3.1 with respect to the components of the active in-plane surface stress. The derivatives directly give the tangential active force at the position of the central node. By a parabolic fitting procedure with respect to the position vector of the nodes in local coordinates, as also detailed in section 3.1 the second derivatives of the position vector are obtained according to equation (3.5). In turn, the curvature tensor in equation (2.13) is obtained by the negative projection of the second derivatives in the local coordinate system onto the normal vector on the node. By contraction with the active in-plane surface stress in local coordinates the active normal force is computed. Eventually, the actual force per node in \mathbf{N} is obtained by multiplication with the local area per node.

Using, e.g., the lattice-Boltzmann/immersed boundary introduced in section 2.4, the active elastic cortex can be coupled to a suspending fluid. The actual force per node serves as input for the immersed boundary method and is spread to the surrounding fluid nodes according to equation (2.41). After solving fluid dynamics for one time step by the lattice-Boltzmann method, all membrane nodes are advected with the local fluid velocity. Alternatively, as done in publication [pub3], the force per node can be directly incorporated into the boundary integral method, which solves for the fluid velocity for given forces at the membrane (or respectively for given traction jump across the membrane being the inverse membrane force). All in all, the equations for force calculation together with the fluid equations of motion including the dynamic coupling are a closed set of equations.

3.2.2 Validation

Once constructed, each simulation method needs proper validation. For validation of the combined lattice-Boltzmann/immersed boundary method in case of passive elastic cells based on the Skalak Hamiltonian in equation (2.28) and the Helfrich Hamiltonian in equation (2.31) we refer to references [69, 160, 244, 245] and the Supplemental Information of publication [pub6]. In publication [pub1], an in-depth validation for active elastic membranes has been performed, which is outlined in the following.

Validation is based on analytical results for an axisymmetric active, elastic membrane in absence of a suspending fluid [33]. However, we note that the very good agreement between theoretical results and simulations including fluid dynamics in case of the Rayleigh-Plateau instability under the influence of anisotropic interfacial tension in section 4.1 and in publication [pub3] can also be seen as additional validation. Berthoumieux et al. [33] provide the Green's function, which describes the axial deformation $u_r(z)$ triggered by a small, local, δ -distributed perturbation to the homogeneous active stress T_a . The Green's function for a cylindrical membrane of radius R has in the Fourier space with coordinate

q associated to z the form

$$G(q) = \frac{1}{\frac{3\kappa_B}{2\kappa_S R^2} (Rq)^4 + \left(\frac{3T_a}{2\kappa_S} - \frac{3\kappa_B}{4\kappa_S R^2}\right) (Rq)^2 + \frac{3}{2} - \frac{3T_a}{2\kappa_S}}. \quad (3.12)$$

We utilized the Green's function G to analytically predict the deformation to a Gaussian distributed perturbation in the active stress with respect to the axial position z . One in-plane component of the active stress tensor is chosen to be

$$\mathbf{t}_{\text{act}}^\alpha = \left(T_a + \delta T_a^\alpha(z)\right) \mathbf{e}^\alpha, \quad (3.13)$$

where no summation applies to the index α and with

$$\delta T_a^\alpha(z) = T_a^\alpha \exp\left(-\frac{z^2}{R^2}\right). \quad (3.14)$$

The Gaussian distributed active stress leads to a smooth deformation, which can be reproduced in simulations. By means of linear response theory [246, 247], the resulting membrane deformation in the real space is given by the convolution of the Green's function in equation (3.12) [33] and the active stress perturbation in equation (3.14)

$$\frac{u_r(z)}{R} = -\frac{3}{2R\kappa_S} \int_{-\infty}^{\infty} G(z-z') \delta T_a^\phi(z') dz' + \frac{3}{4R\kappa_S} \int_{-\infty}^{\infty} G(z-z') \delta T_a^z(z') dz'. \quad (3.15)$$

This analytical result for the deformation of the membrane can directly be compared to simulations of a cylindrical membrane subject to an active stress perturbation according to equation (3.14). In publication [pub1] we report excellent agreement between the analytical and numerical solution together with proper convergence of the error with increasing resolution of the membrane mesh.

Furthermore, by analyzing the parameter combinations for which the Green's function diverges, Berthoumieux et al. [33] predict transitions to two instabilities giving an analytical formula of the corresponding thresholds, one to a buckling instability for negative active stress and one to a Rayleigh-Plateau like instability for a positive active stress. The threshold for the active stress is obtained depending on both shear and bending elasticity. Here, our three-dimensional algorithm can be again tested with respect to the instability threshold. It goes even one step further and provides the three-dimensional membrane shape while undergoing the predicted instability. To do so, we consider an initially cylindrical, elastic membrane and apply either a homogeneous negative (extensile) or a homogeneous positive (contractile) active stress. Our three-dimensional simulations show both types of instability with the threshold being in very good agreement with the analytical predictions. Analyzing the three-dimensional shapes of the membrane undergoing the buckling instability, we unravel an additional non-axisymmetric instability. For isotropic tension non-axisymmetric buckling occurs whereas for anisotropic tension with vanishing ϕ -component a pattern purely along the axis is obtained.

3.2.3 Cell division in shear flow

As a first model application of our elastic cortex model we consider a cell with a cortical ring of increased active stress, which resembles the situation of cytokinesis in cell division

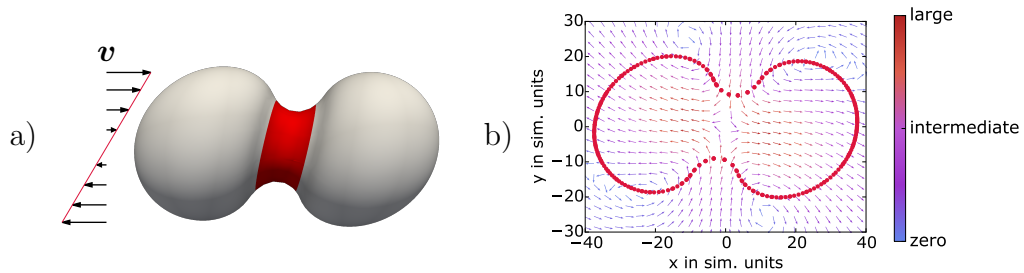


Fig. 3.2: **Active membrane in interplay with external fluid flow.** Cytokinesis during cell division in external shear flow is considered as first model application of the active elastic membrane method. a) An increase in active stress around the equator of the prolate ellipsoidal cell (red shaded area) in interplay with the external flow field leads to a combined deformation of the cell. b) The resulting flow field inside the dividing cell can be analyzed with arrows indicating flow direction and velocity magnitude color coded. Reprinted from publication [pub1] with permission from APS.

[31, 37, 38, 176–178, 248]. The generic two-way coupling of membrane mechanics and fluid flow allows us first to investigate the flow developing inside the cell and second to investigate the interplay of active cortex mechanics and external fluid flow. For passive and active elastic properties of the membrane plus cortex we use typical values reported for cells [23, 212, 213]. We consider an ellipsoidal cell membrane with a diameter of $7\ \mu\text{m}$ and a length of $14\ \mu\text{m}$ which is endowed with shear elasticity $\kappa_S = 5 \times 10^{-6}\ \text{N/m}$, $C = 1$, and bending elasticity $\kappa_B = 2 \times 10^{-19}\ \text{Nm}$. We further use a constant contractile active stress $T_a = 8 \times 10^{-5}\ \text{N/m}$ and a six-fold increased azimuthal active stress compared to T_a around the equator, as sketched in figure 3.2 a) by the red shaded area.

First, in a quiescent fluid our method allows us to analyze the membrane shape during equatorial contraction over time and in addition the developing flow field inside the dividing cell. While the contractile stress first leads to a rounding of the two daughter cells at the poles, a distinct flow from the equatorial plane towards the poles develops. Going one step further, we apply an external shear flow with a shear rate of about $1400\ \text{s}^{-1}$ which results in a non-axisymmetric membrane deformation as shown in figure 3.2 a). The total deformation arises according to the interplay of the active stress and the external flow, both leading to an intertwined separation of the daughter cells and shearing of the cell. Our method again allows us to analyze the flow field over time in this non-axisymmetric situation as shown in figure 3.2 b). In sum, this setup nicely illustrates the two-way coupling of active membrane mechanics and fluid flow.

3.3 A numerical model for a viscous cell cortex

3.3.1 Velocity field on the discrete cortex

In the following, we consider a cortex in the long-time limit, where reorganization processes and motion of filaments under the action of motor proteins in the cortex take place [1]. On time scales larger than the viscoelastic relaxation time the active gel theory can be formulated in the viscous limit [20, 31, 37, 40, 162]. The total surface stress in equation

(2.22) thus consists of a viscous and an active stress

$$\mathbf{t}^\alpha = \mathbf{t}_{\text{visc}}^\alpha + \mathbf{t}_{\text{act}}^\alpha. \quad (3.16)$$

The viscous surface stress consists of in-plane components $t_v^{\alpha\beta}$

$$\mathbf{t}_{\text{visc}}^\alpha = t_v^{\alpha\beta} \mathbf{e}_\beta, \quad (3.17)$$

and we consider an in-plane, isotropic active stress in the following

$$\mathbf{t}_{\text{act}}^\alpha = \zeta g^{\alpha\beta} \mathbf{e}_\beta = \zeta \delta_\beta^\alpha \mathbf{e}^\beta, \quad (3.18)$$

with its magnitude $\zeta = \zeta(s^1, s^2)$ depending on the position on the membrane.

In contrast to the deformation field, which enters the method for an elastic cortex implicitly in the Skalak law (2.28) and Helfrich law (2.31), the key quantity here is the velocity field \mathbf{v} of the cortex. The velocity field is a three-dimensional vector which can be expressed in local coordinates

$$\mathbf{v} = v^\alpha \mathbf{e}_\alpha + v^n \mathbf{n} \quad \text{with } v^\alpha = \mathbf{v} \cdot \mathbf{e}^\alpha \quad \text{and } v^n = \mathbf{v} \cdot \mathbf{n}. \quad (3.19)$$

Analogous to the stress tensor in three-dimensional fluid dynamics in equation (2.33), in-plane gradients in the cortical velocity will contribute to the viscous stress. Therefore, we consider the in-plane velocity gradient

$$v_{\alpha\beta} = \frac{1}{2} [(\nabla_\alpha \mathbf{v}) \cdot \mathbf{e}_\beta + (\nabla_\beta \mathbf{v}) \cdot \mathbf{e}_\alpha]. \quad (3.20)$$

A key difference to three-dimensional fluid dynamics is the contribution of the normal velocity itself, rather than its gradient, to the velocity gradient in equation (3.20) by a coupling to the curvature tensor as can be seen from equation (2.19).

We take into account an in-plane shear viscosity η_s as well as an in-plane bulk viscosity η_b . Therefore, the constitutive law for the viscous surface stress becomes [9]

$$\mathbf{t}_v^{\alpha\beta} = 2\eta_s \left(v^{\alpha\beta} - \frac{1}{2} v_\gamma^\gamma g^{\alpha\beta} \right) + \eta_b v_\gamma^\gamma g^{\alpha\beta}. \quad (3.21)$$

Combining the viscous surface stress in equation (3.21) and the active surface stress in equation (3.18) according to equation (3.16), the force balance equations (2.25) and (2.26) for a force free cell cortex become

$$2\eta_s \nabla_\alpha v^{\alpha\beta} + (\eta_b - \eta_s) \nabla_\alpha v_\gamma^\gamma g^{\alpha\beta} = -\nabla_\alpha \zeta^{\alpha\beta}, \quad (3.22)$$

$$-2\eta_s c_{\alpha\beta} v^{\alpha\beta} - (\eta_b - \eta_s) v_\gamma^\gamma c_{\alpha\beta} g^{\alpha\beta} = -P + c_{\alpha\beta} \zeta^{\alpha\beta}, \quad (3.23)$$

where P is the pressure difference between inner and outer fluid. The force balance equations are accompanied by several constraints. We consider an isolated cell and as a consequence the total velocity and angular momentum are zero. In addition, the cytoplasm is incompressible. These three constraints are expressed mathematically by the integrals

$$\begin{aligned} \int_S \mathbf{v} \, dS = \sum_{\nu=0}^{N-1} \mathbf{v}_\nu A_\nu = \mathbf{0}, \quad \int_S \mathbf{r} \times \mathbf{v} \, dS = \sum_{\nu=0}^{N-1} \mathbf{r}_\nu \times \mathbf{v}_\nu A_\nu = \mathbf{0}, \\ \int_S \mathbf{v} \cdot \mathbf{n} \, dS = \sum_{\nu=0}^{N-1} \mathbf{v}_\nu \cdot \mathbf{n} A_\nu = 0, \end{aligned} \quad (3.24)$$

where the first equality corresponds to the discretization of the cortex and A_ν is the area per node.

This leaves us with the force balance equations valid on the whole membrane, i.e., for each node on the discrete membrane, and with the constraints. Together, they form a closed system of equations, which can be solved for the velocity field \mathbf{v} and the pressure difference across the cortex P . The goal is to solve the viscous force balance equation for the velocity field \mathbf{v} on the discrete cortex numerically. This is again based on a parabolic fitting procedure as detailed in section 3.1. Corresponding to equation (3.4) we expand the velocity vector up to second order around each node ν with velocity \mathbf{v}_ν

$$\mathbf{v}(\xi, \eta) = \mathbf{v}_\nu + \underbrace{\nabla_\xi \mathbf{v}}_{\mathbf{A}_\nu} \xi + \underbrace{\nabla_\eta \mathbf{v}}_{\mathbf{B}_\nu} \eta + \frac{1}{2} \underbrace{\nabla_\xi \nabla_\xi \mathbf{v}}_{\mathbf{C}_\nu} \xi^2 + \frac{1}{2} \underbrace{\nabla_\eta \nabla_\eta \mathbf{v}}_{\mathbf{D}_\nu} \eta^2 + \underbrace{\nabla_\xi \nabla_\eta \mathbf{v}}_{\mathbf{E}_\nu} \xi \eta. \quad (3.25)$$

In contrast to before, the parabolic fitting procedure is not directly performed, because the actual velocity is now unknown. We rather invert the parabolic fitting procedure, i.e., the minimization of the theoretical expansion to the value at the neighboring nodes. We do so analytically to obtain the derivatives at node ν as a function of the velocity values of the node itself and its neighbors $a(\nu) = 1, \dots, N_\nu$

$$\mathbf{A}_\nu = \mathbf{A}_\nu(\mathbf{v}_\nu, \{\mathbf{v}_{a(\nu)}\}). \quad (3.26)$$

The second essential step is to define a squared difference for the force balance equations (3.22) and (3.23) evaluated in the local coordinate system (cf. equation 3.1) at each node. In the following, we abbreviate the left hand side as l.h.s. $_\rho$ and correspondingly the right hand side as r.h.s. $_\rho$ with the index $\rho = 1, 2, n$ enumerating the three force balance equations. Furthermore, the discretized constraints in equation (3.24) are considered with Lagrange multipliers λ_i and we define in total

$$\begin{aligned} \chi^2 = \sum_\rho \sum_\nu & \left(\text{l.h.s.}_\rho^\nu - \text{r.h.s.}_\rho^\nu \right)^2 + \lambda_1 \left(\sum_{\nu=0}^{N-1} v_\nu^x A_\nu - 0 \right) + \lambda_2 \left(\sum_{\nu=0}^{N-1} v_\nu^y A_\nu - 0 \right) \\ & + \lambda_3 \left(\sum_{\nu=0}^{N-1} v_\nu^z A_\nu - 0 \right). \end{aligned} \quad (3.27)$$

Here, the constraint of zero total velocity splitting up into its three spatial components is given for illustration. The χ^2 is then expressed in terms of the velocity derivatives, which in turn depend on the actual velocity evaluated at all nodes. Together with the derivatives analytically depending on the velocity values according to equation (3.26), the χ^2 can be minimized with respect to the velocity values

$$\arg \min_{\{\mathbf{v}_\nu\}} \chi^2 = \arg \min_{\{v_\nu^x\}, \{v_\nu^y\}, \{v_\nu^z\}} \chi^2. \quad (3.28)$$

In stark contrast to the elastic method in section 3.2 where forces are locally and independently calculated, the coupled system of equations cannot be solved locally. Rather the force balance equations, which are similar to a Poisson equation, have to be solved globally. The dimensions of the system of coupled equations excluding additional constraints is $(3N + 1) \times (3N + 1)$ for the 3 components of the velocity vector evaluated at the N nodes plus the pressure.

This system of equations we write in matrix form as

$$\begin{array}{l}
 \partial\chi^2/\partial v_0^x \rightarrow \\
 \partial\chi^2/\partial v_0^y \rightarrow \\
 \partial\chi^2/\partial v_0^z \rightarrow \\
 \vdots \quad \quad \quad \vdots \\
 \partial\chi^2/\partial v_{N-1}^x \rightarrow \\
 \partial\chi^2/\partial v_{N-1}^y \rightarrow \\
 \partial\chi^2/\partial v_{N-1}^z \rightarrow \\
 \partial\chi^2/\partial P \rightarrow
 \end{array}
 \begin{array}{c}
 \left(\begin{array}{ccc}
 \cdots & \cdots & \\
 \vdots & \ddots & \\
 \vdots & & \ddots
 \end{array} \right)
 \begin{array}{c}
 \left(\begin{array}{c}
 v_0^x \\
 v_0^y \\
 v_0^z \\
 \vdots \\
 v_{N-1}^x \\
 v_{N-1}^y \\
 v_{N-1}^z \\
 P
 \end{array} \right)
 =
 \begin{array}{c}
 \left(\begin{array}{c}
 \vdots \\
 \vdots \\
 \vdots
 \end{array} \right).
 \end{array}
 \quad (3.29)
 \end{array}$$

Numerically solving this system of equations (3.29), e.g., by LU decomposition, gives the velocity field \mathbf{v} on the cortex as set of the velocity values at the nodes $\{\mathbf{v}_\nu\}$.

3.3.2 Validation

In order to validate the numerical model of the cell cortex in the viscous limit we choose two different approaches: in the static case the velocity field obtained on a spherical cortex is compared to analytical solutions, which we obtain for an active stress distribution in terms of spherical harmonics. This further allows for a detailed comparison of the different quantities in simulations with the theoretical results. Next, we consider a dynamically deforming cell cortex with an active stress increasing around the equator, where we can compare the three-dimensional dynamic deformation and evolving flow field on the cortex to axisymmetric simulations [249, 250] performed by our collaboration partners in publication [pub2].

First, we apply an active stress expressed in spherical harmonics

$$\zeta(\theta, \phi) = \zeta_0 + \sum_{n,m} \zeta_{nm} Y_{nm}(\theta, \phi), \quad (3.30)$$

with a constant offset active stress ζ_0 , Y_{nm} being the spherical harmonics and ζ_{nm} the expansion coefficients. Expanding the velocity field on the cortex in terms of vector spherical harmonics, expressing the viscous surface stress tensor as function of tensorial spherical harmonics and applying identities of those, we are able to derive analytical conditions to the expansion coefficients from the viscous force balance equations. The analytical conditions then give an analytical expression for the velocity field for given active stress distribution.

The analytical procedure itself can be used for two different test setups: the full force balance equations which lead to a pure normal velocity on the cortex is tested on the one hand. On the other hand, the normal force balance can be replaced by a condition fixing the normal velocity to zero. The latter, somewhat artificial test setup allows us to obtain an analytical solution for a finite tangential velocity along the cortex. In both scenarios we can apply the algorithm described above and obtain numerical results in excellent agreement with the analytical solution. This is done for an axisymmetric as well as a non-axisymmetric active stress in terms of Y_{20} and Y_{21} , respectively. The three-dimensional velocity profile on the spherical cortex for the full system in case of the axisymmetric active stress in terms of Y_{20} with $\eta_s = 1$ and $\eta_b = 1$ in simulation units is

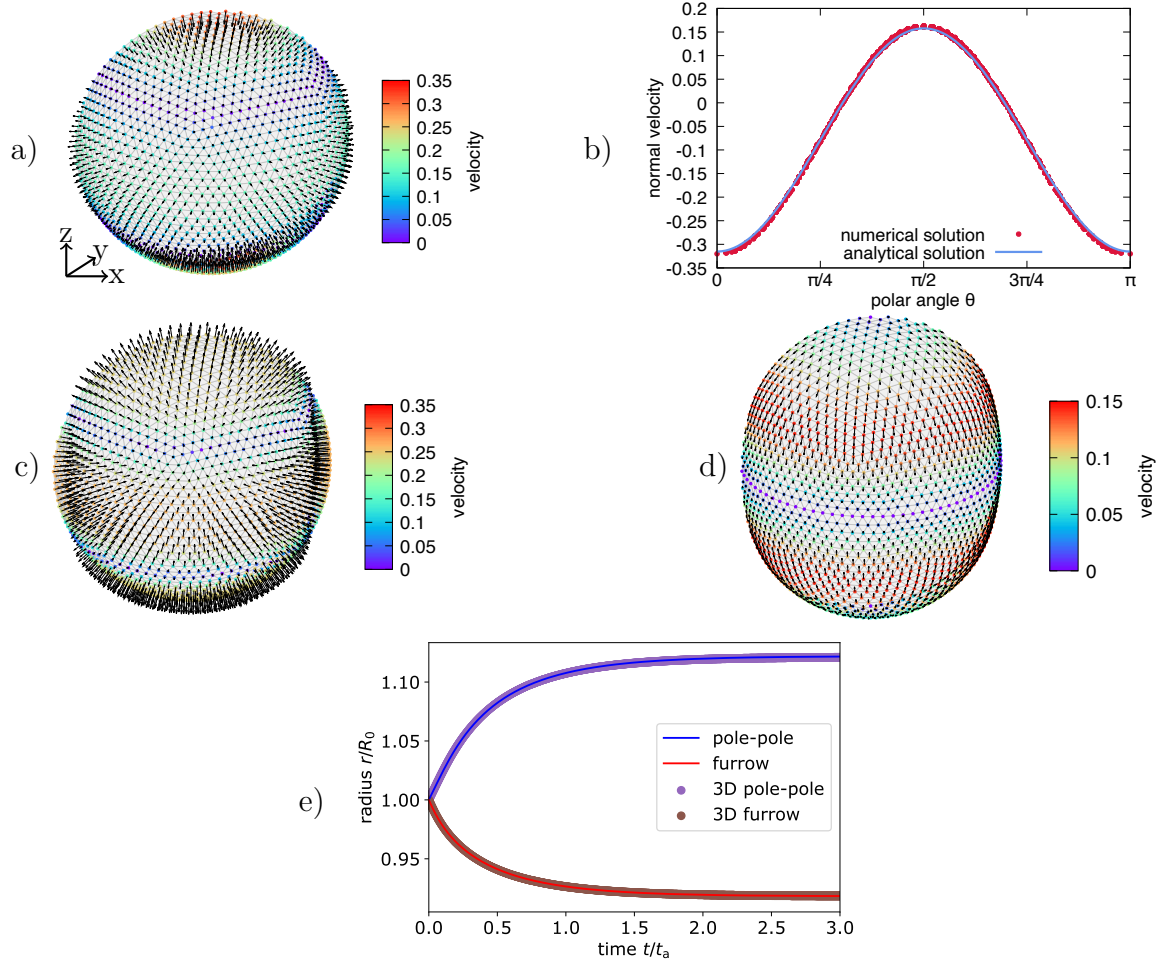


Fig. 3.3: **Validation for a viscous active cortex.** a) Three-dimensional velocity field numerically obtained on a static spherical cortex subjected to an axisymmetric active stress distribution in terms of the spherical harmonics Y_{20} with the arrows giving the velocity direction and the color coding for the velocity magnitude. b) The numerically obtained velocity with pure normal component depending on the polar angle θ is in very good agreement with the corresponding analytical solution. c) Initial and d) final velocity field on an evolving cortex with viscosities $\eta_s = 1$ and $\eta_b = 1$ subjected to an active stress distribution according to equation (3.31) with exponent $p = 4$, width $\sigma = 10$, offset $\zeta_0 = 1$, and magnitude $\hat{\zeta} = 1$. e) The dynamics in terms of the pole to pole and equatorial furrow radius (dots) agrees very well with results from axisymmetric simulations (lines). Time is considered relative to the time scale $t_a = \frac{\eta_s}{\zeta_0}$. Reprinted from publication [pub2].

shown in figure 3.3 a). The comparison of the numerically obtained normal velocity with the analytical solution over the polar angle is shown in figure b), where we obtain a very good agreement. These scenarios further show that the presented algorithm converges properly with the error decreasing systematically with increasing resolution.

In a second step, we consider an isotropic, axisymmetric active stress which increases around the equator according to

$$\zeta(\theta, \phi) = \zeta_0 + \hat{\zeta} \exp\left(-\sigma\left(\theta - \frac{\pi}{2}\right)^p\right), \quad (3.31)$$

with the exponent p being an even number, the magnitude $\hat{\zeta}$ and the width σ . For given active stress, we solve for the velocity field on the discrete cortex and use the normal velocity for an update of the cortex shape by applying the Euler algorithm. For an active stress distribution with exponent $p = 4$, offset active stress $\zeta_0 = 1$, and amplitude $\hat{\zeta} = 1$ with the viscosities $\eta_s = 1$ and $\eta_b = 1$ in simulation units, we show the velocity profile on the initial and the finally deformed cortex in figure 3.3 c) and d), respectively. The prescribed active stress leads to a contraction around the equator and, corresponding to the incompressibility of the cortex interior, to an extension at the poles. The dynamics of both the equatorial contraction and the pole extension is in very good agreement with results from the axisymmetric simulations of our collaborators as shown in figure 3.3 e). In addition, we compare the velocity field on the deformed, three-dimensional cortex to the one obtained by axisymmetric simulations at different times. Both tangential and normal velocity show very good agreement. In total, this successfully validates our three-dimensional model of a cell cortex in the viscous limit.

As a first test application of a deforming cell cortex in a non-axisymmetric situation, we apply our developed method to consider an initially spherical cortex with an active stress according to equation (3.31) and subjected to an initial shear deformation. In ref. [pub2], we analyze the cortex evolution and the velocity field on the deforming cortex over time.

4 Rayleigh-Plateau instability for anisotropic tension and blood platelet formation

The Rayleigh-Plateau instability is a well known phenomenon, which describes the instability leading to break-up of a liquid jet into droplets [54]. It is known to be driven by the surface tension γ of the jet interface [54, 251]. The surface tension leads to a pressure difference between the inner and outer fluid of the jet according to the Young-Laplace equation [54, 150]

$$p = \gamma \left(\frac{1}{R_\phi} + \frac{1}{R_z} \right), \quad (4.1)$$

where R_ϕ and R_z are the radius of curvature in azimuthal and axial direction, respectively. Initially, the jet is cylindrical with an unperturbed radius R_0 . A periodic undulation of the jet interface with wavelength λ along its axis leads to a spatial variation of the pressure p . Considering the first term of the Young-Laplace equation (4.1), at the site of a neck, the pressure contribution $\frac{\gamma}{R_\phi}$ increases due to a decrease of the local radius. Correspondingly, $\frac{\gamma}{R_\phi}$ decreases at the site of a bulge. This mechanism amplifies the undulation even further. In contrast, the second term $\frac{\gamma}{R_z}$ leads to an opposing effect: the curvature in axial direction leads to a positive pressure perturbation at a bulge and a negative one at a neck. This stabilizes the interface. The balance of both effects leads to a dominant perturbation mode, at which the interface becomes unstable and which grows fastest. For an ideal fluid jet with passive ambient fluid, the fastest growing wave number $k_m = \frac{2\pi}{\lambda_m}$ fulfills the condition [51, 54]

$$k_m R_0 = 0.697. \quad (4.2)$$

Based on the work of Plateau [50], a dispersion relation was first derived by Rayleigh [51], which yields the criterion in equation (4.2). For a viscous liquid jet in air again Rayleigh [252] and Chandrasekhar [253] derived a dispersion relation, which has been generalized to include an external fluid of arbitrary density and viscosity by Tomotika [52]. Experiments [55] have first shown that a Rayleigh-Plateau instability also occurs for tubular vesicles under externally induced tension [55–58, 164, 254]. Considering cell or tissue tubes, the active stress in the cortex has been proposed to trigger a Rayleigh-Plateau like instability [32, 33], which we confirmed by three-dimensional simulations [pub1]. Indeed, an active stress in the cell cortex bares a striking similarity to surface tension as it enters the in-plane component of the surface stress in equation (2.22) in the same way (cf. equation (2.32)) as surface tension does in case of a liquid jet

$$t_{\text{act}\alpha}^\beta = \begin{pmatrix} T_a & 0 \\ 0 & T_a \end{pmatrix}, \quad t_{\text{jet}\alpha}^\beta = \begin{pmatrix} \gamma & 0 \\ 0 & \gamma \end{pmatrix}, \quad (4.3)$$

for isotropic, contractile active stress $T_a > 0$. Therefore, despite their fundamental difference both isotropic active stress and surface tension lead to the same physical behavior. This analogy we use in the next section, where we refer to the term *interfacial tension* in general. Interestingly, there is a remarkable difference between cortical stress in cells or tissues and the classical scenario of a liquid jet with isotropic surface tension: cells often have an anisotropic, cortical active stress [20, 31, 40, 59–65].

In section 4.1, we summarize the effects which a stress anisotropy has on the Rayleigh-Plateau instability as investigated in detail in publications [pub3] and [pub4]. We combine analytical linear stability analyses with computer simulations based on our developed method [pub1]. The break-up of a liquid jet has a striking similarity to cell shapes occurring during blood platelet formation. Using our computational model [pub1], in section 4.2, we show that a biological Rayleigh-Plateau instability can explain the flow accelerated formation of blood platelets [pub5].

4.1 Rayleigh-Plateau instability of anisotropic interfaces

4.1.1 Anisotropic interfacial tension

In cells, often structures such as stress fibers [185] form, which can orientate in a regular fashion, e.g., under the influence of external flow [255, 256]. Therefore, anisotropic stress can occur in the cell cortex [20, 63–65]. A prominent example is the formation of the cortical ring [1] where anisotropic stress drives cell division [31, 37, 40, 257]. Furthermore, cortical anisotropic stress is important for the cell shape [20] and polarization of a cell [64]. Motivated by the occurrence of anisotropic active stress and its analogy to surface tension, the question arises how this anisotropy can alter the Rayleigh-Plateau instability. In the following, we consider an interface subjected to an anisotropic tension. Therefore, as one part of the total surface stress in equation (2.22), we consider an in-plane active stress $\mathbf{t}_{\text{act}}^\alpha = t_{\beta,\text{act}}^\alpha \mathbf{e}^\beta$ being anisotropic with

$$\mathbf{t}_{\text{act}}^\phi = \gamma^\phi \mathbf{e}^\phi, \quad \mathbf{t}_{\text{act}}^z = \gamma^z \mathbf{e}^z, \quad (4.4)$$

where γ^ϕ and γ^z represent a general anisotropic interfacial tension. The latter can also account for anisotropic surface tension, because of the analogy discussed above. Due to its generality and the broad range of parameters, our description covers a variety of systems. First, an interface with pure anisotropic interfacial tension is considered which encloses an inner fluid and is surrounded by an outer fluid. Afterwards, we combine the anisotropic interfacial tension with interface elasticity including bending and/or shear elasticity, which becomes important for vesicles, cells and tissues [23, 32, 68].

4.1.2 Linear stability analysis

In order to perform a linear stability analysis we perturb the radius of the initially cylindrical interface of radius R_0 in a periodic fashion

$$R(z, t) = R_0 + \delta R(z, t) = R_0 + R_0 \epsilon_0 e^{\omega t} \cos(kz), \quad (4.5)$$

with ϵ_0 being a small amplitude, $k = \frac{2\pi}{\lambda}$ the wave number, i.e., the magnitude of a wave vector pointing along the axis z of the interface, and ω the growth rate of the perturbation mode. The result of the linear stability analysis is a relation for the growth rate depending on the wave number, which allows to identify perturbations to which the interface is unstable (with positive growth rate) and the dominant mode that evolves fastest in time. The anisotropic interfacial tension, our key ingredient, modifies the Young-Laplace equation (4.1) in the way that both curvature components now are weighted differently by the two components of the interfacial tension in equation (4.4)

$$p = \frac{\gamma^\phi}{R_\phi} + \frac{\gamma^z}{R_z}. \quad (4.6)$$

This relation follows by contraction of the curvature tensor in equation (2.13) with $c_\phi^\phi = \frac{1}{R_\phi}$ and $c_z^z = \frac{1}{R_z}$ and the in-plane components of the surface stress in equation (4.4). This contraction equals the pressure difference according to the normal force balance equation (2.26) with the fluid force in equation (2.24) proportional to the pressure, cf. equation (2.33). In the modified Young-Laplace equation (4.6) the destabilizing and the stabilizing mechanism of the Rayleigh-Plateau instability as introduced at the beginning of this chapter are now weighted differently.

We first consider the suspending fluid in the limit of a small Reynolds number as often applicable to vesicles and cells [68, 151]. Therefore, we can solve the linear Stokes equation (2.36) which we modify to account for the presence of the interface

$$-\nabla p + \eta \nabla^2 \mathbf{v} + \delta(r - R_0) \frac{\gamma^\phi \epsilon_0}{R_0} \left(1 - \frac{\gamma^z}{\gamma^\phi} (R_0 k)^2 \right) \cos(kz) \mathbf{e}_r = \mathbf{0}, \quad (4.7)$$

where the interfacial force due to anisotropic interfacial tension enters via a ring force [53]. The system of equations is closed by the continuity equation (2.38). We solve this system of equations by introducing the Hankel transformation \mathcal{H}_ν and the inverse Hankel transformation \mathcal{H}_ν^{-1} of order ν of a general function f , which is defined by [258]

$$F(s) = \mathcal{H}_\nu[f] = \int_0^\infty f(r) r J_\nu(sr) dr, \quad f(r) = \mathcal{H}_\nu^{-1}[F] = \int_0^\infty F(s) s J_\nu(sr) ds, \quad (4.8)$$

with the Bessel function $J_\nu(x)$ of first kind and order ν . By introducing the Hankel transform of the velocity components and the pressure, we obtain the components of the modified Stokes equation (4.7) and the continuity equation (2.38) in the Hankel space. The equations in Hankel space can be solved analytically and the obtained velocity and pressure is transformed back into real space.

At the interface the no-slip boundary condition to the velocity field applies, which relates the radial motion of the interface to the radial fluid velocity v_r according to equation (2.39), which in linear order leads to

$$\frac{\partial R}{\partial t} = R_0 \epsilon_0 \omega e^{\omega t} \cos(kz) = v_r(r = R), \quad (4.9)$$

where the derivative of the interface perturbation given by equation (4.5) has been inserted. Evaluating the transform of the radial velocity from Hankel space to real space

at the interface, eventually leads to an equation which can be solved for the growth rate. This finally leads to the dispersion relation

$$\omega_{\text{Stokes}}(k) = \frac{\gamma^\phi}{R_0\eta} \left(1 - \frac{\gamma^z}{\gamma^\phi} (R_0 k)^2 \right) \left[I_1(kR_0)K_1(kR_0) + \frac{kR_0}{2} (I_1(kR_0)K_0(kR_0) - I_0(kR_0)K_1(kR_0)) \right], \quad (4.10)$$

with $I_\nu(x)$ the modified Bessel function of first kind and $K_\nu(x)$ of second kind and of order ν . Equation (4.10) is the dispersion relation for the Rayleigh-Plateau instability in the limit of the Stokes equation with the same viscosity of the inner and outer fluid. The dispersion relation gives the growth rate for each mode of wave number k . In case of a negative growth rate the interface is stable with respect to the corresponding mode, in case of a positive growth rate the interface is unstable and the corresponding mode grows.

Because the prefactor and the factor containing the Bessel functions are positive for positive wave number k , the root of the dispersion relation is determined by

$$1 - \frac{\gamma^z}{\gamma^\phi} (R_0 k)^2 = 0, \quad (4.11)$$

and therefore strongly influenced by the ratio $\frac{\gamma^z}{\gamma^\phi}$ that accounts for the anisotropy of the interfacial tension. This is in stark contrast to the classical Rayleigh-Plateau instability, which is covered as well by setting $\frac{\gamma^z}{\gamma^\phi} = 1$, where the root of the dispersion relation only depends on the radius of the fluid tube. For the axial tension γ^z exceeding the azimuthal tension γ^ϕ the range of unstable modes shrinks and vice versa. All in all, the axial tension dampens the dispersion relation and stabilizes the interface, while the azimuthal tension destabilizes the interface.

Utilizing the concept of the ring force and the Hankel transform, we further consider an interface enclosing an ideal fluid and surrounded by an ideal fluid with same density. Here, the Euler equation (2.37) in linear order of the velocity has to be solved, which can be done in a similar way as solving the Stokes equation. In this limit we end up with the dispersion relation

$$\omega_{\text{Euler}}^2(k) = \frac{\gamma^\phi}{\rho R_0^3} (kR_0)^2 \left(1 - \frac{\gamma^z}{\gamma^\phi} (kR_0)^2 \right) I_1(kR_0)K_1(kR_0). \quad (4.12)$$

Furthermore, we derived the dispersion relation for a liquid jet of an ideal fluid immersed in air [pub3], which is given by

$$\omega_{\text{jet}}^2(k) = \gamma^\phi \frac{kR_0}{\rho R_0^3} \left(1 - \frac{\gamma^z}{\gamma^\phi} (kR_0)^2 \right) \frac{I_1(kR_0)}{I_0(kR_0)}. \quad (4.13)$$

Both equations in the ideal fluid limit differ from the one in the Stokes regime by a different prefactor and distinctive combinations of the Bessel functions. However, the tension anisotropy enters in the same way. As a consequence, the discussion on unstable modes above holds for the limit of the Euler equation, as well.

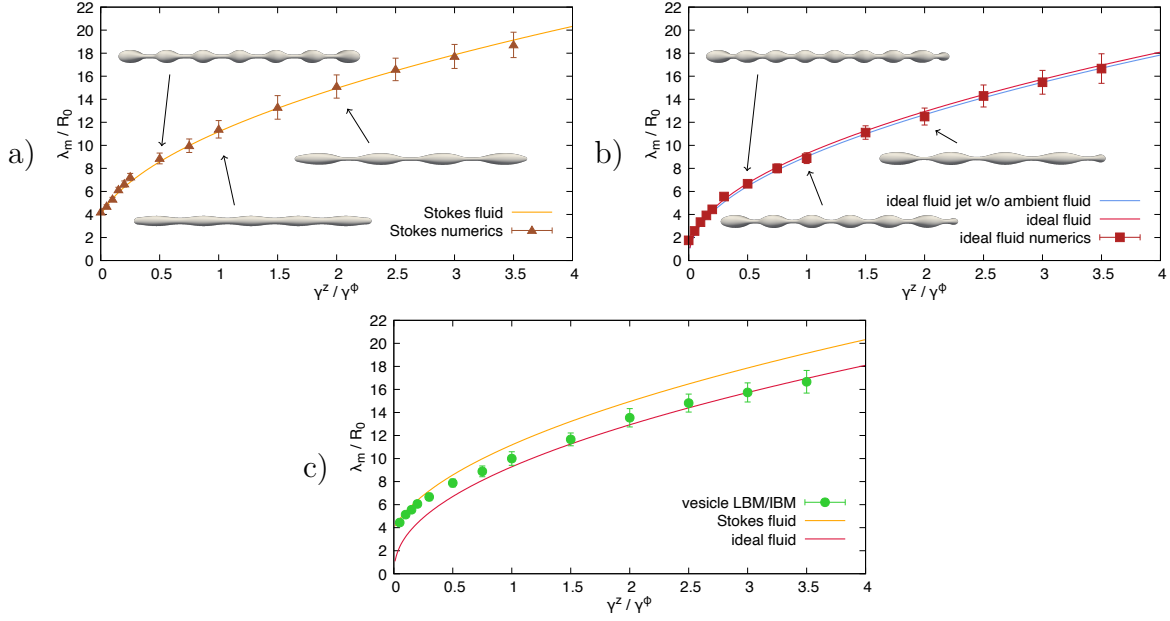


Fig. 4.1: **Tension anisotropy strongly alters the dominant wavelength of the Rayleigh-Plateau instability.** We compare the analytically obtained wavelength to simulation results both in the limit of a) the Stokes equation together with simulations using boundary integral method and in the limit of b) an ideal fluid governed by the Euler equation together with lattice-Boltzmann simulations. Analytical results for the ideal fluid limit with (red) and without (blue) an outer fluid differ only slightly. Simulation snapshots as insets show the interface shape for various tension anisotropies. c) Lattice-Boltzmann/immersed boundary (LBM/IBM) simulations covering fluid inertia show a transition in the dominant wavelength for typical vesicle parameters.

4.1.3 Analytical and simulation results

In addition to the change in the range of unstable modes, the fastest growing mode determined by the maximum of the dispersion relation is altered by the tension anisotropy. Both the value of the maximum growth rate and the corresponding dominant wavelength is altered, which determines the size of the droplets or vesicles pinching off. From the analytical results, the dispersion relations in equations (4.10), (4.12), (4.13), the maximum can be determined. In addition to the analytical linear stability analysis, we performed simulations of an anisotropic interface using the method developed in publication [pub1] combined with the boundary integral method as well as the lattice-Boltzmann/immersed boundary method. The combination of both methods enable simulations with a dimensionless Ohnesorge number $Oh = \frac{\eta}{\sqrt{\rho R_0 \gamma}}$ of infinity (boundary integral method) covering the Stokes limit and a very small Ohnesorge number (lattice-Boltzmann method) corresponding to the Euler limit. In both types of simulations the inner and outer fluid have the same density and/or viscosity and thus their results can directly be compared to the dispersion relations in equations (4.10) and (4.12). In one simulation, we apply a perturbation of fixed wavelength to the interface at the beginning and analyze its evolution over time. For fixed parameters, simulations with varying wavelength can be directly compared in order to extract the dominant mode. A simulation using an interface subjected to the dominant mode with reasonably small

initial amplitude allows for investigation of the corresponding growth rate.

In the Stokes as well as in the ideal fluid limit we obtain a growth rate strongly decreasing with increasing tension anisotropy with very good agreement between theory and simulations. In figure 4.1, we show the dominant wavelength λ_m depending on tension anisotropy in the limit of a Stokes fluid in a) and an ideal fluid in b). In both cases the wavelength decreases with dominating azimuthal tension, i.e. $\frac{\gamma^z}{\gamma^\phi} < 1$, and increases for $\frac{\gamma^z}{\gamma^\phi} > 1$ compared to the classical result for isotropic tension $kR_0 = 0.697$ (ideal fluid) and $kR_0 = 0.562$ (Stokes limit). This can be explained by the stabilizing nature of the axial tension, where a longer wavelength leads to less curvature contributing to the modified Young-Laplace equation. Weighted more for increasing anisotropy, the stabilizing axial tension dampens the growth rate and increases the dominant wavelength. Simulation results agree very well with the analytical solution and snapshots of the interface shape are shown as insets in figure 4.1. Compared to the ideal fluid the wavelength in the Stokes limit is larger, which may be attributed to the additional viscous stress stabilizing the interface.

This direct comparison of both simulation methods also shows the influence of inertia on interface dynamics. While in boundary integral simulations inertia is intrinsically absent, lattice-Boltzmann simulations cover the full fluid behavior governed by Navier-Stokes equation including inertia. Therefore, we perform Lattice-Boltzmann simulations with typical vesicle parameters, a diameter $2R_0 = 1 \mu\text{m}$, an interfacial tension of $\gamma^\phi = 10^{-4} \text{ Nm}^{-1}$ reported for neutrophils [212] within the range given by ref. [259], and for the surrounding fluid a density $\rho = 1000 \text{ kgm}^{-3}$ and a viscosity $\eta = 1.2 \times 10^{-3} \text{ Pas}$. The simulations as performed in publication [pub3] show a transition in the dominant wavelength in figure 4.1 c) between Stokes regime at anisotropy close to zero and ideal fluid regime at large anisotropy. This transition is accompanied and explained by a change in the Ohnesorge number Oh_z referring to the axial tension γ^z .

Using analytical calculations based on the Hankel transformation we further explored the influence of interface viscosity in the Stokes limit. We observe similar effects on the wavelength and growth rate under the influence of the tension anisotropy as described above for the Stokes regime. Except, for very large interface viscosity the instability is dampened and therefore the growth rate strongly decreases and the wavelength increases.

Our simulations allow us further to go beyond the linear stability analysis. The time till break-up obtained from simulations can be compared to an estimation based on the analytical growth rate from linear stability analysis. The difference of both gives the nonlinear correction to linear break-up time [260] which we obtain depending on the tension anisotropy. While this correction slightly increases with increasing tension anisotropy for an ideal fluid, we observe a stronger and reversed effect in the limit of Stokes flow, where the correction even changes sign. Solving fluid and interface equations of motion numerically in the limit of the long wavelength approximation [261–263], we were able to investigate the influence of tension anisotropy on the formation of a satellite droplet. The latter forms during jet break-up between the main droplets and is significantly smaller than the main droplets with typically 3 % of the volume [54, 260, 264]. A large tension anisotropy leads to a stabilization of the satellite droplet, which increases in length and volume and becomes cylindrical instead of spherical at intermediate Ohnesorge numbers.

4.1.4 Elastic interfaces

The next step is the consideration of interface elasticity as done in publication [pub4], which is of great importance in the context of vesicles, cells, or tissues. First, we include bending elasticity using the Helfrich constitutive law (2.31), which leads to contributions to the elastic part of the surface stress $\mathbf{t}_{\text{el}}^\alpha$ in equation (2.22). The additional elastic surface stress enters the force balance equations (2.25) and (2.26) and as a consequence the pressure perturbation in addition to the anisotropic interfacial tension. Therefore, the ring force in the Stokes equation (4.7) becomes

$$\delta(r - R_0) \frac{\gamma^\phi \epsilon}{R_0} \left(1 - \frac{\gamma^z}{\gamma^\phi} (kR_0)^2 - \frac{\kappa_B}{\gamma^\phi R_0^2} \left(1 - 2(kR_0)^2 + (kR_0)^4 \right) \right) \cos(kz) \mathbf{e}_r, \quad (4.14)$$

for a reference curvature of a cylinder $H_0 = \frac{1}{2R_0}$. The derivation of the dispersion relation can be performed as before and we eventually obtain the dispersion relation of the form

$$\omega_B(k) = \frac{\gamma^\phi}{R_0 \eta} \left(1 - \frac{\gamma^z}{\gamma^\phi} (R_0 k)^2 - \frac{\kappa_B}{\gamma^\phi R_0^2} \left(1 - 2(kR_0)^2 + (kR_0)^4 \right) \right) \left[I_1(kR_0) K_1(kR_0) + \frac{kR_0}{2} \left(I_1(kR_0) K_0(kR_0) - I_0(kR_0) K_1(kR_0) \right) \right]. \quad (4.15)$$

The bending contribution to the dispersion relation in equation (4.15), which enters with the bending modulus κ_B , is purely stabilizing, thus negative for positive wave number except its root at $kR_0 = 1$.

With increasing bending elasticity the root of the total dispersion relation shifts to smaller wave numbers as illustrated by figure 4.2 a). In figure 4.2 a) we show the root of the dispersion relation depending on $\frac{\gamma^z}{\gamma^\phi}$ with each curve for fixed bending modulus given by color code. For symmetry reasons, we only show the curves for positive wave numbers. Up to $\frac{\kappa_B}{\gamma^\phi R_0^2} = 1$ modes in the region $kR_0 \in]0; k_{\text{max}} R_0[$ are growing, where k_{max} is the maximum or cut-off wave number for which the growth rate becomes zero. The range of unstable modes becomes smaller with increasing bending resistance and increasing tension anisotropy. For larger bending modulus $\frac{\kappa_B}{\gamma^\phi R_0^2} > 1$ the dispersion relation develops a second root and the range of unstable modes is restricted towards both small and large wave numbers (blue curves). Most remarkably, parameter combinations of bending elasticity and tension anisotropy exist, for which the interface is stable to all wave numbers and therefore the cylindrical interface remains stable.

In figure 4.2 b) the threshold of the instability is systematically investigated in the phase space of tension anisotropy and bending resistance. Both increasing bending resistance and increasing tension anisotropy can lead to a transition across the threshold. Below the threshold, the interface undergoes a Rayleigh-Plateau instability with the fastest growing wavelength λ_m color coded. Beyond the threshold the interface is stable. In the top left region unstable modes are restricted towards both small and large wave numbers (cf. figure 4.2 a)). Around isotropic interfacial tension, i.e., $\frac{\gamma^z}{\gamma^\phi} = 1$, the wavelength is hardly affected by the bending resistance, whereas a strong alteration is observed at large anisotropy. In contrast to the wavelength, the growth rate is influenced mainly by the anisotropy rather than the bending resistance, except the region close to the instability threshold.

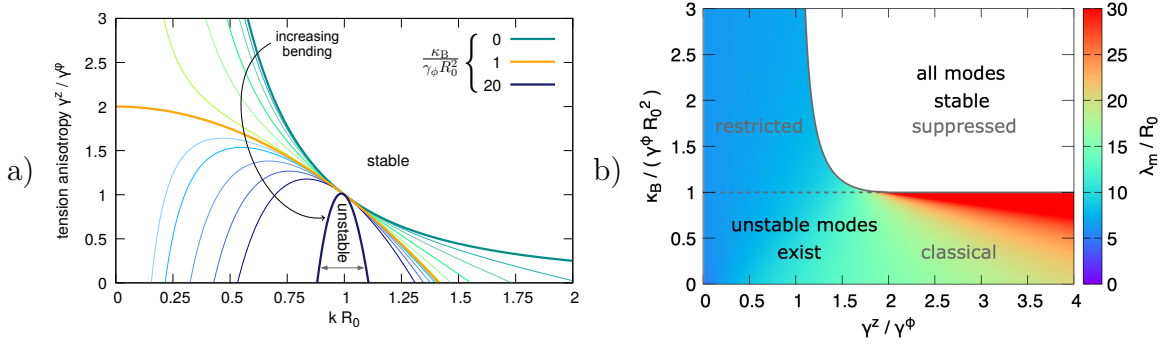


Fig. 4.2: **Interface stability under the influence of bending elasticity and tension anisotropy.** a) The root of the dispersion relation in terms of the wave number kR_0 is shown depending on tension anisotropy on the ordinate and bending resistance by color code (with the value increasing along the black arrow). Underneath the curves the interface undergoes a Rayleigh-Plateau instability. With increasing bending resistance a second root of the dispersion relation develops and towards large tension anisotropy the interface becomes stable. b) The phase diagram with respect to tension anisotropy and bending resistance shows the parameter region, where unstable modes exist. The dominant wavelength of the instability is given by color code.

Next, we consider an interface with shear elasticity and/or area dilatation governed by the Skalak constitutive law (2.28). Here, we first derive the elastic tensions and forces according to the force balance equations (2.25), (2.26) from the Skalak Hamiltonian depending on the deformation of the interface. Different to the situations of a pure anisotropic interface or including bending elasticity, we now obtain a non-vanishing tangential force. As a consequence the ring force in the modified Stokes equation (4.7) now has a component in axial direction. We again transform the equations of fluid motion into Hankel space and solve for the velocity components where the stresses at the interface in turn depend on the velocity components evaluated at the interface. The kinematic boundary condition again relates the radial velocity at the interface to the growth rate. Combining those equations and solving the resulting relation for the growth rate finally leads to the dispersion relation of a shear elastic interface. The whole procedure is detailed in publication [pub4]. This dispersion relation still contains integrals over Bessel functions which can be solved either analytically or numerically.

Shear elasticity is purely damping and has also a strong influence on the Rayleigh-Plateau instability triggered by anisotropic interfacial tension with the wavelength strongly increasing with anisotropy. We again observe a stable phase but now with the threshold due to shear elasticity not depending on tension anisotropy. However, the threshold systematically decreases with increasing resistance to area dilatation. Combining all three ingredients, tension anisotropy, bending as well as shear elasticity, eventually leads to a combination of the described effects. The stable phase extends due to the combination of bending and shear elasticity with the instability threshold again depending on tension anisotropy.

These findings allow us to conclude that a large variety of modifications of the Rayleigh-Plateau instability arise from anisotropic tension together with interface elasticity. Not only the dynamics of the instability is altered, but also the size of the fragments and the interface can remain stable.

4.2 Blood platelet biogenesis as flow-accelerated instability

4.2.1 Motivation

Because of their short life span of several days, the large number of 10^{11} blood platelets is produced per day in the bone marrow of the human body [77, 143, 265], which requires an efficient mechanism for platelet biogenesis. Their progenitor cell, the megakaryocyte, in a first step forms long, initially cylindrical membrane protrusions called proplatelets, as shown in the experimental micrograph in figure 4.3 a). In the bone marrow, the megakaryocytes are trapped at the wall of the sinusoidal blood vessels and extend the proplatelets into the blood stream [75]. In a second step, swellings form along the extended proplatelet as shown in b) and c), which eventually are released into the blood stream as premature platelets [75, 84]. In an additional route of platelet formation, larger structures are released from the megakaryocyte which are called preplatelets and which fracture into individual platelets in the blood stream.

Experiments have shown that the extension of the proplatelets is driven by cortical microtubule sliding [87] and attributed an important role in swelling formation to the actin-myosin cortex [74, 80–83, 266–269]. In the light of *in vitro* production of blood platelets for platelet transfusion [270, 271], intensive effort is under way to build efficient microfluidic devices for platelet production [85–89, 227, 270, 272–274]. In those devices a strong acceleration of the production under the influence of external fluid flow has been reported [84–89]. However, a detailed understanding of the swelling formation from a biophysical point of view and of the acceleration in fluid flow has so far been absent.

In the following, we utilize our method developed in publication [pub1] in order to propose the biological Rayleigh-Plateau instability due to anisotropic cortical stress, which is discussed in section 4.1, as the biophysical mechanism of blood platelet biogenesis [pub5]. Furthermore, we show that this mechanism leads to a pronounced acceleration of platelet biogenesis in the presence of an external fluid flow and that it can explain the occurrence of preplatelets, the intermediate progenitors in platelet biogenesis [275].

4.2.2 Computational model of a proplatelet

Starting point of our computational model is the already extended proplatelet in order to shed light onto the biophysical origin of swelling formation. The initial setup of the simulation is shown in figure 5.1 d). We model the proplatelet initially as a cylindrical membrane, which is fixed on one side (mimicking the fixed megakaryocyte) and possesses a free, capped end. The radius of the proplatelet is chosen as $R_0 = 1.5 \mu\text{m}$ [88], its length being 90 times the radius. The proplatelet is immersed in an external fluid with the properties of blood plasma with density $\rho = 1000 \text{ kgm}^{-3}$ and viscosity $\eta = 1.2 \times 10^{-3} \text{ Pas}$. The proplatelet can be confined, e.g., between two flat walls with a Poiseuille flow in-between, as shown in figure 4.3 d). For the channel diameter we use $23.5 \mu\text{m}$ as reported for sinusoidal blood vessels in the bone marrow [276].

Key entity of our model is the cortical active stress. The actin-myosin in the proplatelet cortex is modeled by an isotropic contractile active stress [277], as also discussed in section 2.3. In concert with the actin-myosin contractility, we consider the microtubules

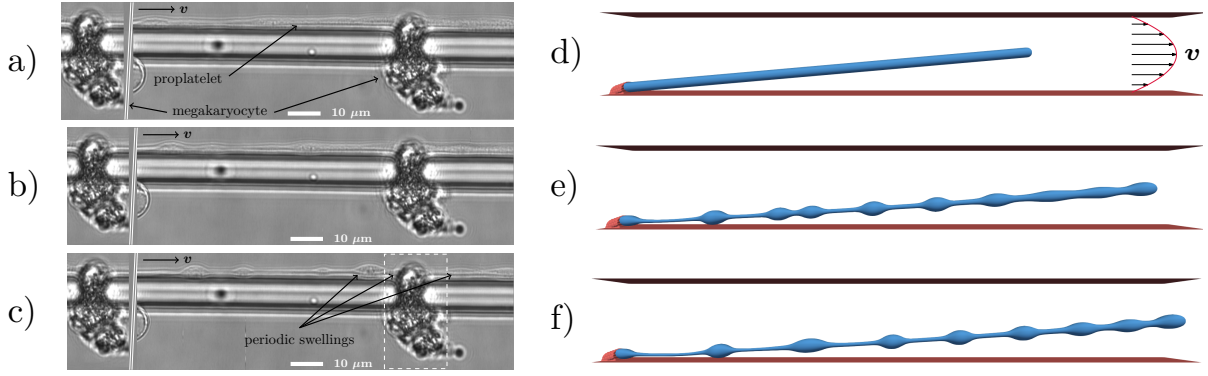


Fig. 4.3: **Blood platelet formation in experiments and simulations.** a), b), c) *In vitro* blood platelet formation in a microfluidic bioreactor. a) The trapped megakaryocytes form long membrane protrusions, the proplatelets. In order to illustrate the periodic arrangement of the megakaryocytes in the bioreactor the megakaryocyte shown in the white box in c) is reinserted on the left side of the figures. b), c) Along the proplatelet shaft swellings develop, which are eventually released as premature blood platelets. d), e), f) Blood platelet formation in Poiseuille flow with a maximum velocity of $v = 3.33$ mm/s using simulations. d) The initially cylindrical, elastic proplatelet is subject to anisotropic, contractile active stress accounting for actin-myosin contractility in concert with microtubule driven extension along the axis. e) The proplatelet undergoes a biological Rayleigh-Plateau instability, which leads to swellings along the proplatelet shaft in agreement with the experimental images. f) Two swellings fuse into a larger structure, which is attributed to shear-induced re-orientation and contractility of the proplatelet. Reprinted from publication [pub5] with permission from the National Academy of Sciences.

by an anisotropic active stress being extensile mainly along the proplatelet axis, because microtubule sliding is known as the origin of proplatelet extension [87]. Both contributions add up and in total we endow the proplatelet with an anisotropic, contractile in-plane active stress

$$t_{\text{act}\alpha}^{\beta} = \begin{pmatrix} T_a^z & 0 \\ 0 & T_a^{\phi} \end{pmatrix}, \quad (4.16)$$

with $T_a^z = 0.75T_a^{\phi}$ and $T_a^{\phi} = 2.5 \times 10^{-5} \text{ Nm}^{-1}$. This value of active stress is chosen with respect to the cortical tension reported for platelets [142] due to the lack of direct experimental data for the proplatelet cortex. The proplatelet membrane is further endowed with shear elasticity using the Skalak model in equation (2.28) with $\kappa_S = 5 \times 10^{-6} \text{ Nm}^{-1}$ and $C = 100$ and bending elasticity using the Helfrich model in equation (2.31) with $\kappa_B = 2 \times 10^{-19} \text{ Nm}$. The anisotropic contractility is well beyond the threshold discussed in section 4.1 [pub4] and the one for isotropic tension discussed in publication [pub1] and reference [33].

4.2.3 Flow-accelerated biological Rayleigh-Plateau instability

First, considering a quiescent surrounding fluid, the proplatelet starts to contract at its free tip and subsequently undergoes a biological Rayleigh-Plateau instability. This instability leads to periodic swellings along the proplatelet shaft which are connected by membrane strings. Swelling formation in simulations nicely resembles proplatelet shapes observed in experiments as shown in figure 4.3 a) - c). Those swellings will

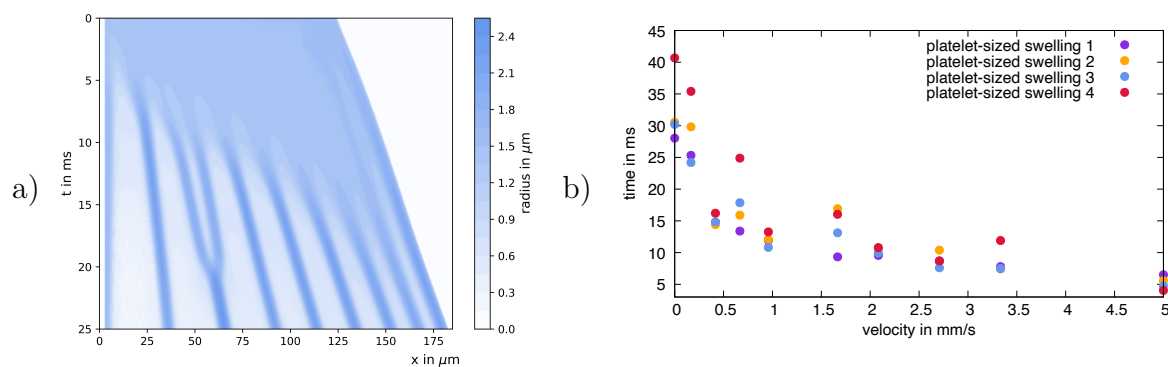


Fig. 4.4: **Acceleration of the platelet formation in Poiseuille flow.** a) Kymograph showing the dynamics of the biological Rayleigh-Plateau instability shown in figure 4.3 d), e), f) with respect to axial position x and time t . The proplatelet with constant initial radius (light blue) form swellings which are visible by the dark blue bands in the kymograph. b) Systematic variation of the external fluid flow velocity shows a strong acceleration of the swelling formation. Reprinted from publication [pub5] with permission from the National Academy of Sciences.

be finally released into the blood stream and each of the released swellings eventually matures into platelets in the blood stream. With the contractile active stress resembling actin-myosin as main input, our simulation results indeed support the experimental evidence that actin-myosin is crucial for proper platelet formation [74, 80–83, 266–269] and provide a detailed explanation on the biophysical level: if the actin-myosin system is perturbed by biochemical intervention [74, 80, 82, 83], the driving mechanism of the biological Rayleigh-Plateau instability is absent and accordingly no swellings will form. In addition, the instability determines the size of the blood platelets after formation by its intrinsic, dominant wavelength. Indeed, an estimation based on the criterion in equation (4.2) for the classical Rayleigh-Plateau instability leads to volumes of premature platelets in accordance with the reported platelet size distribution [278, 279], as detailed in publication [pub5].

Motivated by the natural flowing environment in the blood vessels of the bone marrow [276, 280] and by experimental evidence of accelerated platelet formation in presence of fluid flow in microfluidic devices [84–89], we next consider blood platelet formation in Poiseuille flow as shown in figure 4.3 d). As in the quiescent fluid, the proplatelet undergoes the biological Rayleigh-Plateau instability and forms swellings as shown in figure 4.3 e) in very good agreement with the experimentally observed shapes. Furthermore, we find that two separate swellings can fuse as shown by comparison of figure 4.3 e) and f). Such fusion events can explain the release of larger structures called preplatelets, which are frequently observed in the blood flow in addition to the platelets [275].

First, to investigate swelling fusion in more detail, we additionally consider a pure shear flow rather than a Poiseuille flow. In the shear flow swelling fusion occurs as well, which points to velocity gradients as reason for swelling fusion. Therefore, the interplay of proplatelet re-orientation together with the cortical contractility can explain the swelling fusion. Swelling fusion in Poiseuille flow is also shown by the kymograph in figure 4.4 a). Going one step further, the proposed biological Rayleigh-Plateau instability can further explain the break-up of a released, elongated preplatelet into two separate platelets due to actin-myosin contractility.

Next, we aim for a more detailed understanding of the influence of external fluid flow. Therefore, we consider the spatio-temporal evolution of the proplatelet shape in terms of a kymograph as shown in figure 4.4 a). By tracing the evolution from the constant initial radius to the final radius of each swelling, which is shown as a dark blue band in the kymograph, the duration of swelling formation can be determined: we consider the time difference between an initial deformation of 2% and the radius reaching a plateau value, the final swelling radius. This procedure is done for four swellings and for varying external fluid flow velocity. Figure 4.4 b) shows a strong acceleration of the swelling formation with increasing flow velocity. Comparing different flow conditions we report less pronounced acceleration in shear flow, but a systematic acceleration in a homogeneous flow. This points to the extension of the proplatelet under the influence of the pulling of the flow as the origin for the strong acceleration.

All in all, our simulations reproduce the features of both *in vivo* and *in vitro* blood platelet formation. While being strongly accelerated with increasing flow velocity, the biological Rayleigh-Plateau instability leads to platelets of nearly constant volume as shown in publication [pub5]. Therefore, we conclude that the platelet size after formation is determined by the dominant wavelength of the instability. Furthermore, the interplay of the elasto-hydrodynamic instability with fluid flow on the one hand explains the strong acceleration in agreement with experiments [84–89]. On the other hand, the presence of shear leading to swelling fusion accounts for the formation of preplatelets. Due to no/less preplatelet formation and an efficient acceleration, the homogeneous flow may be the most promising flow condition for *in vitro* bioreactors. In total, we are able to provide a biophysical mechanism which explains the efficient formation of blood platelets accelerated by fluid flow.

5 Antimargination of platelets in vessel confluences

5.1 Motivation

Once released into the blood stream, the blood platelets circulate through the vessel network and become activated by signaling processes in case of a vessel rupture [119]. Activated platelets form clots, which shall prevent a rapid and massive loss of blood [119]. For this task platelet location close to the vessel wall is advantageous, which is provided by a process called margination [104, 281]. In a cellular suspension, the deformable red blood cells are known to migrate to the channel center, both due to a lift force away from the wall [282, 283] and due to gradients in the flow velocity [92, 284]. The accumulation of red blood cells in the channel center leads to the formation of a cell-free layer next to the wall with vanishing red blood cell concentration [218, 285]. In contrast, a stiff particle alone does not migrate in inertia-less flows [150]. However, in suspension with the red blood cells a stiff particle is expelled into the cell-free layer due to heterogeneous collisions with the red blood cells [281, 286]. This process, termed margination, leads to a strong increase in platelet concentration next to the vessel wall.

Margination has been observed in straight channels with various types of cross-section both experimentally [95, 98, 104, 105] and in simulations [90, 94, 96, 97, 106, 107, 287]. It has been studied in constricted microchannels [116, 117], and also the effect of different particle shapes [100, 101, 103, 109, 110] and red blood cell concentration on the margination has been investigated in detail [99, 102, 108]. In the physiological blood network, the circulatory system, however, a multitude of vessel branching occurs. Larger vessels mainly split up into smaller ones in a cascade of bifurcations on the arterial side of the blood circulatory system until in the smallest vessels oxygen is transmitted to the tissue. Afterwards, the small vessels fuse into larger ones in a cascade of confluences towards the *vena cava* leading back to the heart. Experimental findings indeed indicate a strong difference in platelet distribution between the arterial side with more platelets near the wall [118] and a larger number of platelets integrated in clots [119] and the venous side with a more continuous distribution of platelets. While several studies have investigated the red blood cell distribution in bifurcations [120, 122–124, 288–290], microparticle behavior is scarcely addressed [291, 292]. Refs. [125–128] provide a first step towards simulations of more complex vessel networks.

Motivated by the reported difference in platelet concentration [118, 119] and to provide a deeper understanding of blood flow in vessel networks, margination in a vessel bifurcation as well as in a vessel confluence is investigated in publication [pub6] of the present thesis. Bifurcation and confluence are the main entities in a realistic vessel network and therefore our simulations provide a fundamental insight and basis for studies of networks. The

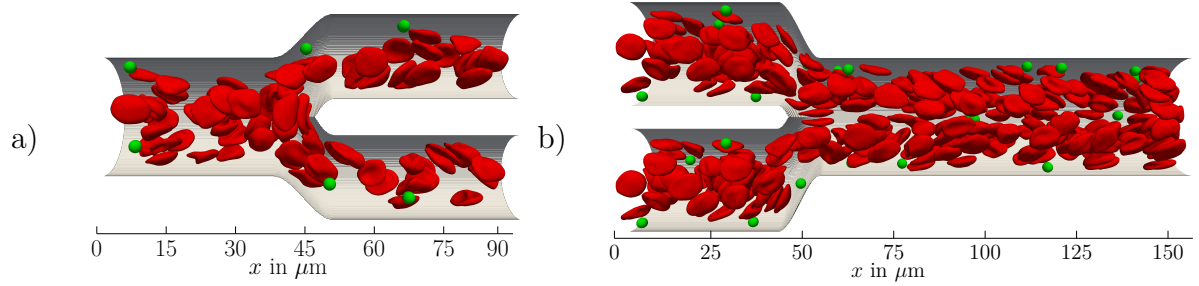


Fig. 5.1: **Vessel branching.** A suspension of microparticles (green), which mimic stiff particles such as drug carriers or blood platelets, and red blood cells (red) flowing through a vessel bifurcation in a) and a vessel confluence in b). The hematocrit, i.e., the volume fraction of red blood cells, is about 12%. Reprinted from publication [pub6] with permission from CellPress.

simulation setup and the main findings are outlined in the following.

5.2 Computational model of a vessel bifurcation and confluence

We simulate a suspension of stiff microparticles, which can either represent blood platelets or synthetic microparticles like drug carriers, and red blood cells in both a vessel bifurcation as shown in figure 5.1 a) as well as a vessel confluence in b). The microparticles are modeled as rigid spheres with a diameter of $3.2 \mu\text{m}$, but the shape is also varied to an oblate ellipsoid to mimic the typical shape of blood platelets. In case of the stiff particles a regular inner mesh is used in addition to the thin shell to ensure particle stiffness. The red blood cells are modeled with a diameter of $7.82 \mu\text{m}$ and using the Skalak constitutive law (2.28) accounting for shear elasticity with $\kappa_S = 5 \times 10^{-6} \text{ N/m}$ and area dilatation $C = 100$ together with the Helfrich law (2.31) accounting for bending elasticity with $\kappa_B = 2 \times 10^{-19} \text{ Nm}$. Fluid properties are chosen to mimic blood plasma behavior with a density $\rho = 1000 \text{ kg/m}^3$ and viscosity $1.2 \times 10^{-3} \text{ Pas}$.

In order to systematically investigate the influence of vessel bifurcation and vessel confluence separately, inflow and outflow boundary conditions have been implemented similar to ref. [293]. Therefore, a straight, cylindrical reference channel is simulated, where red blood cell and platelet concentration are obtained resembling what is known for margination in straight channels [90]. The temporal sequence of cell and particle positions is used to construct an inflow at the entrance of the bifurcation and at the entrance of both daughter channels of a confluence in figure 5.1 a) and b) on the left. Accordingly, further away from the bifurcation and the confluence red blood cells are located in the channel center and microparticles next to the wall. Cells or particles reaching the end of the bifurcation or confluence system are removed from the simulation. We use a small hematocrit, i.e., volume fraction of red blood cells, of $Ht = 12\%$ (shown here) and a large hematocrit of $Ht = 20\%$ covering the physiologically relevant range. A typical mean velocity at the channel entrance is 2.5 mm/s . In case of the bifurcation in figure 5.1 a) one main channel of radius $16 \mu\text{m}$ splits up into two daughter channels with radius $11.5 \mu\text{m}$ on a length of $13 \mu\text{m}$. The vessel confluence in figure 5.1 b) consists of two channels with radius $16 \mu\text{m}$ and separation of $39 \mu\text{m}$ between the center-lines merging in

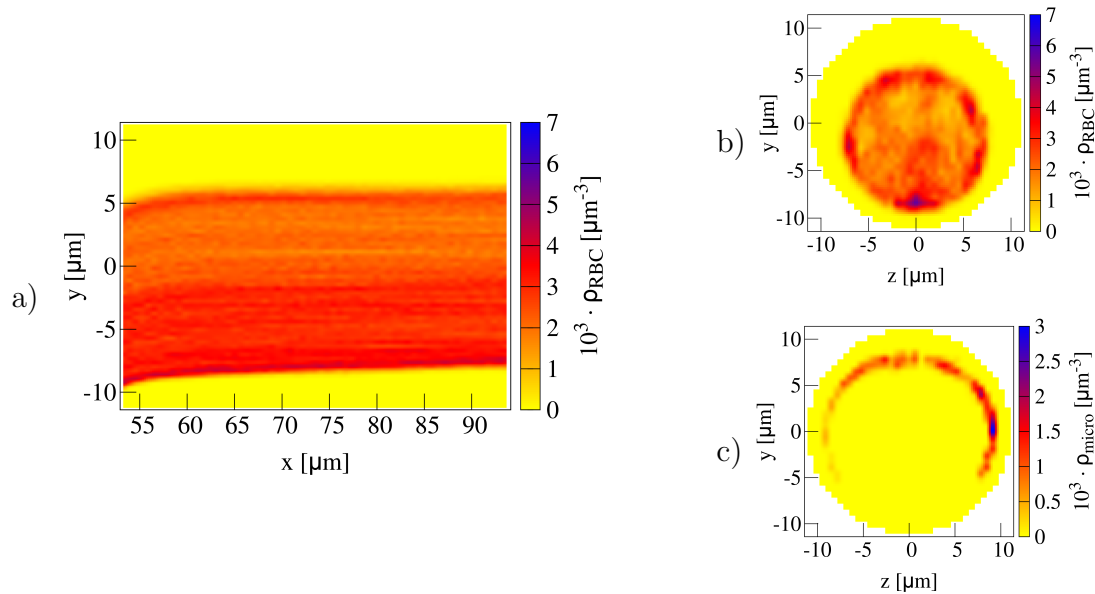


Fig. 5.2: **Cell distribution behind a vessel bifurcation.** a) Red blood cell (RBC) concentration in the (upper) daughter channel of the vessel bifurcation shown in figure 5.1 a). The cell-free layer with vanishing concentration becomes asymmetric. b), c) Cross-sectional concentration of b) red blood cells (RBC) and c) microparticles (micro) such as blood platelets at the beginning of the daughter channel behind a vessel bifurcation at $x = 57 \mu\text{m}$. Despite remaining margined, no blood platelets are located at the bottom of the daughter channel. Reprinted from publication [pub6] with permission from CellPress.

one larger channel with radius $17.5 \mu\text{m}$.

5.3 Main results

Vessel bifurcation

Up to a distance of about $10 \mu\text{m}$ before the vessel bifurcation (and also before the vessel confluence) the red blood cells gather around the channel center and accordingly next to the vessel wall a cell-free layer depleted of any cells is visible. Approaching the bifurcation, the cells start to flow into the two daughter channels and the cell-free layer decreases. As shown in figure 5.2 a), the cell-free layer in the daughter channel becomes asymmetric [123, 289] and the red blood cells are shifted towards the inner wall of the upper (or lower) channel. Remarkably, the asymmetry remains stable over the whole length of the daughter channel. As seen in the cross-sectional concentration profile in figure 5.2 b), a spot of increased red blood cell concentration is visible next to the inner wall. Related to this, an analysis of axial concentration as detailed in publication [pub6] shows a peak in red blood cell concentration at the apex of the bifurcation, where cells can get trapped and a lingering of cells is observable [125].

Arriving at a near-wall position, the margined state, the blood platelets remain next to the wall behind the bifurcation as seen in the cross-sectional concentration profile in figure 5.2 c). However, no platelets can reach the inner wall of the upper daughter channel (or lower daughter channel, correspondingly). Therefore, the region at the inner

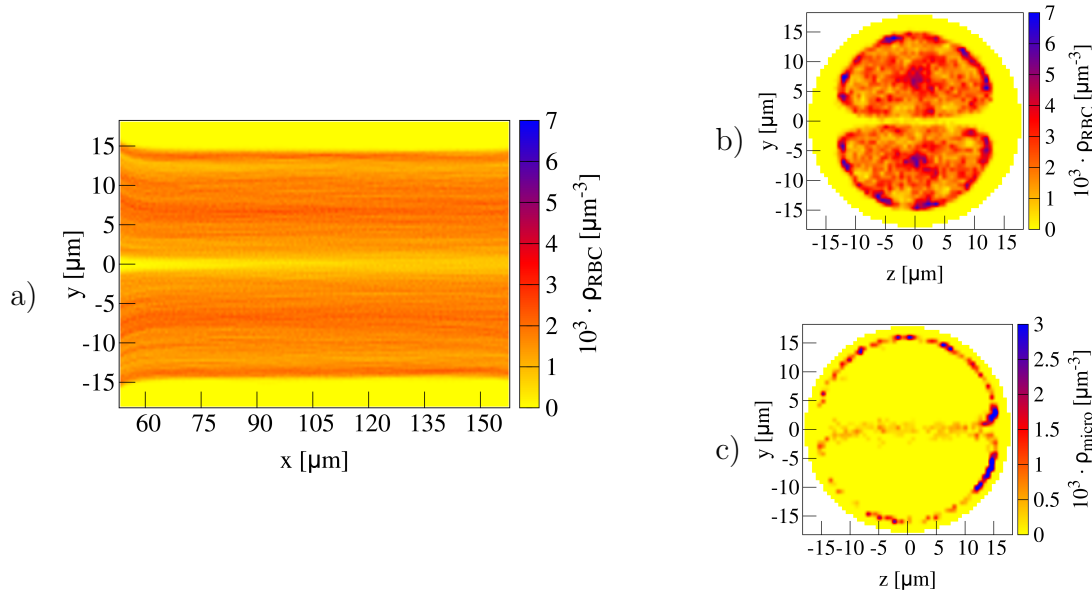


Fig. 5.3: **Cell distribution behind a vessel confluence.** a) Red blood cell (RBC) concentration in the larger channel behind the vessel confluence shown in figure 5.1 b). In the channel center an additional, robust cell-free layer develops. b), c) Cross-sectional concentration of b) red blood cells (RBC) and c) microparticles (micro) such as blood platelets at the beginning of the main channel behind a vessel confluence at $x = 55 \mu\text{m}$. A significant fraction of 16% of the blood platelets are located in the channel center, thus undergo antimargination. Reprinted from [pub6] with permission from CellPress.

wall with a larger amount of red blood cells lacks any blood platelets. All in all, the blood platelets retain their near-wall position, thus remain margined, throughout a vessel bifurcation.

Vessel confluence

Approaching a vessel confluence as shown in figure 5.1 b), the cell-free layer also becomes asymmetric at the end of the daughter channel due to the motion of the red blood cells towards the main channel. Entering the main channel at the confluence, red blood cells from both the upper and the bottom vessel compete for the channel center, where as a consequence an additional cell-free layer develops as seen in the concentration profile in figure 5.3 a). The central cell-free layer is also visible in the cross-sectional concentration profile in b) evaluated at the beginning of the main channel. This central cell-free layer, being especially pronounced left and right, remains robust over the total length of the main channel (cf. figure 5.3 a)).

In contrast to the vessel bifurcation, the blood platelets do not remain margined throughout the vessel confluence. A remarkable fraction of 15.8% of blood platelets undergoes antimargination and is located in the central cell-free layer behind the confluence as shown by figure 5.3 c). This antimargination is confirmed by *in vivo* experiments performed by our collaboration partners using synthetic microparticles. The platelets remain close to the center for the complete length of the main channel considered in our simulations. Calculating the shear-induced diffusion coefficient of the blood platelets, we

can estimate a length of 5 mm required for the blood platelets to be completely margined again. In addition, the axial concentration of blood platelets shows a pronounced peak at the vessel confluence, which we can attribute to the platelets arriving at the very top or, respectively, bottom of the confluence, which therefore have a larger residence time at the confluence.

Consequences

Thus, a network of bifurcations on the arterial side of the circulatory system can retain the demixing of the red blood cells and the blood platelets. The latter remain near the vessel wall. Considering a series of succeeding confluences this no longer holds. An estimation based on shear-induced diffusion as performed in publication [pub6] leads to a value of 5 mm required for complete margination of the blood platelets, whereas a succeeding vessel confluence appears typically after half to one millimeter [224, 294]. Therefore, the interplay of antimargination through confluences and margination in-between results in a stronger mixing of blood platelets and red blood cells and therefore a more continuous distribution of platelets across the vessel diameter is expected after several confluences. This is in very good agreement with experimental observations in the venous side of the circulatory system made up of numerous vessel confluences [118]. Furthermore, our proposed mechanism agrees with findings by Casa et al. [119] reporting more platelet-laden clots on the arterial side, where vessels consecutively bifurcate into smaller ones, compared to the venous side.

6 Conclusions and outlook

In this thesis, we developed an algorithm that dynamically computes active forces and the deformation of a cell membrane with underlying cortex in three dimensions. Its combination with a fluid solver such as the lattice-Boltzmann method by means of the immersed boundary method further allows for a dynamic coupling with an external fluid flow. An application of the algorithm to other fluid solvers is easily possible, as demonstrated with the boundary integral method in publication [pub3]. The parabolic fitting procedure used for force calculation on the deformed elastic active cortex has been further utilized for construction of a viscous cortex model, which extends the application towards processes involving reorganization of the cell cortex.

By combining the developed numerical tool with analytical theory, we were able to generalize the framework of the Rayleigh-Plateau instability to include anisotropic interfacial tension. This anisotropy strikingly influences the dynamics of the Rayleigh-Plateau instability as well as the size of the resulting droplets or vesicles after break-up. In combination with membrane and cortex elasticity, which is relevant for vesicles, cells, and tissues, cortical tension anisotropy leads to a broad spectrum of behavior. Depending on the anisotropy cell elasticity can even suppress the instability.

The concept of the biological Rayleigh-Plateau instability triggered by cortical active stress was further used to shed light onto the biophysical mechanism underlying blood platelet biogenesis. Considering one proplatelet immersed in blood flow explicitly, our simulations reproduce its fragmentation process into platelets with the actin-myosin contractility as basic entity. The combined lattice-Boltzmann/immersed boundary simulations allowed us to further study the influence of external flow systematically. We reported a strong acceleration due to fluid flow with increasing flow velocity. We therefore provided biophysical, fundamental and mechanical insight into blood platelet biogenesis.

For the released blood platelets we could show that their distinct near-wall position in the flowing blood is sustained by a vessel bifurcation. In stark contrast, our simulations uncover an antimargination of blood platelets in the confluence of two vessels, which has been supported by experimental measurements. Therefore, we were able to explain observed differences in platelet distribution between the arterial and venous side of the microcirculatory system.

On the methods developed and the results reported in this thesis various future research work can be based. The input for the numerical method in publications [pub1] and [pub2] is the constitutive law for the active stress. Up to now, we have considered isotropic or anisotropic active stress with spatial variation but being constant over time. Due to its generality, both methods can be extended to include a time-dependent active stress. Accordingly, different constitutive laws can be implemented. A prominent example would be a reaction-diffusion mechanism [49, 295] of either the actin, myosin or even the ATP concentration field. In particular, in the viscous cortex model in publication [pub2] a quantity on the cortex can be advected with local cortex velocity. Another

methodological direction would be to include dynamically evolving polar or nematic order of the cytoskeletal filaments in the cortex [26, 189]. Furthermore, active moments could be considered, which account for a variation in active stress across the membrane height [9]. A typical example is tissue mechanics, where active stress differs between the apical and basal interface [296, 297].

The investigation of the influence of anisotropic interfacial tension on the Rayleigh-Plateau instability can be extended to the consideration of anisotropic, passive elastic laws. An anisotropically structured cortical network may also lead to an elastic response to deformation depending on the direction of the deformation itself. Therefore, one can think of a constitutive law similar to the used Skalak Hamiltonian which in addition includes a dependency on the direction of the deformation. Rather than using a Hamiltonian for the constitutive law, one could also consider a formulation starting from the surface stress similar to what is done for the active stress in publication [pub1]. This easily allows for the incorporation of anisotropy by converting the elasticity modulus into a tensorial modulus. A first simple approach could include linear, anisotropic elasticity. Furthermore, the plasma membrane can exhibit anisotropic structure and one can consider the Helfrich Hamiltonian generalized to include an anisotropic membrane [298].

The presented theory on the anisotropic Rayleigh-Plateau instability in publications [pub3] and [pub4] can be furthermore generalized to describe a liquid jet neglecting the ambient medium for arbitrary Reynolds number by modifying the dispersion relation derived by Chandrasekhar [253]. In presence of an outer fluid, Tomotika [52] presents a general dispersion relation, where anisotropic interfacial tension can also be incorporated. This generalization can be done including the bending elasticity of the plasma membrane or a surfactant as well. The presence of a surfactant leads furthermore to tension gradients along the interface, which could also be considered [72]. Furthermore, the discussion could be extended to the buckling instability under the influence of tension anisotropy with focus on the orientation of the resulting pattern, as already seen in publication [pub1], maybe under additional influence of external fluid flow.

In the course of platelet biogenesis, also larger structures, the preplatelets, are released into the blood flow [275]. Extension of those preplatelets in concert with actin-myosin contractility leads to the break-up of a preplatelet into two separate platelets, as shown by simulations in the Supplemental Information of publication [pub5]. Here, the dynamics of such a preplatelet could be investigated in more detail under the influence of external flow. Furthermore, the explicit treatment of the cortical microtubule coil [275], the marginal band, would allow for mechanical and detailed insights into preplatelet conversion.

An additional application of the elastic cortex model in publication [pub1] could be the adhesion of cells. Smeets et al. [299] study the separation of two adhered cells and in addition micro-pipette aspiration in simulations. Our method can overcome one main limitation of this investigation [299], namely the linear elasticity. Our method has been extensively used with the strain hardening Skalak law (2.28), but can also be used with the strain softening Neo-Hookean law [156]. Furthermore, the coupling to an inner and outer fluid can be used to investigate cell-cell separation in external flow.

One ingredient of the presented methods is the consideration of the cell's interior as viscous fluid. The cell's interior can also behave in a viscoelastic fashion [300, 301]. The constant development of the lattice-Boltzmann method includes a lattice-Boltzmann method for viscoelastic fluids [302–304]. A combination of our cortex model and a

viscoelastic lattice-Boltzmann method together with a tracing algorithm detecting the cell's interior [305] could account for the viscoelastic properties of the cell cytoplasm. The presented method [pub1] to cope with forces resulting from cortical active stress can furthermore be coupled to an elastic cell model, where the interior of the cell is considered elastic [306]. The developed method in publication [pub1] can be easily used to further include an active cell cortex. In total, the present thesis can also contribute to the development of a more realistic and a possibly complete numerical model of a biological cell.

References

- [1] B. Alberts, A. Johnson, J. Lewis, M. Raff, K. Roberts, and P. Walter (2007). *Molecular Biology of the Cell*. 5th ed. New York: Garland Science (cited on pp. 3, 7, 8, 13–15, 24, 32).
- [2] N. Goldenfeld and C. Woese (2011). Life Is Physics: Evolution as a Collective Phenomenon Far From Equilibrium. *Annual Review of Condensed Matter Physics* **2** (1), pp. 375–399. DOI: [10.1146/annurev-conmatphys-062910-140509](https://doi.org/10.1146/annurev-conmatphys-062910-140509).
- [3] M. C. Marchetti, J. F. Joanny, S. Ramaswamy, T. B. Liverpool, J. Prost, M. Rao, and R. A. Simha (2013). Hydrodynamics of Soft Active Matter. *Reviews of Modern Physics* **85** (3), pp. 1143–1189. DOI: [10.1103/RevModPhys.85.1143](https://doi.org/10.1103/RevModPhys.85.1143).
- [4] E. Fodor, C. Nardini, M. E. Cates, J. Tailleur, P. Visco, and F. VAN Wijland (2016). How Far from Equilibrium Is Active Matter? *Physical Review Letters* **117** (3), p. 038103. DOI: [10.1103/PhysRevLett.117.038103](https://doi.org/10.1103/PhysRevLett.117.038103).
- [5] T. Hiraiwa and G. Salbreux (2016). Role of Turnover in Active Stress Generation in a Filament Network. *Physical Review Letters* **116** (18), p. 188101. DOI: [10.1103/PhysRevLett.116.188101](https://doi.org/10.1103/PhysRevLett.116.188101).
- [6] A. Ravichandran, G. A. Vliegenthart, G. Saggiorato, T. Auth, and G. Gompper (2017). Enhanced Dynamics of Confined Cytoskeletal Filaments Driven by Asymmetric Motors. *Biophysical Journal* **113** (5), pp. 1121–1132. DOI: [10.1016/j.bpj.2017.07.016](https://doi.org/10.1016/j.bpj.2017.07.016).
- [7] D. Mizuno, C. Tardin, C. F. Schmidt, and F. C. MacKintosh (2007). Nonequilibrium Mechanics of Active Cytoskeletal Networks. *Science* **315** (5810), pp. 370–373. DOI: [10.1126/science.1134404](https://doi.org/10.1126/science.1134404).
- [8] A. G. Clark, O. Wartlick, G. Salbreux, and E. K. Paluch (2014). Stresses at the Cell Surface during Animal Cell Morphogenesis. *Current Biology* **24** (10), R484–R494. DOI: [10.1016/j.cub.2014.03.059](https://doi.org/10.1016/j.cub.2014.03.059).
- [9] G. Salbreux and F. Jülicher (2017). Mechanics of Active Surfaces. *Physical Review E* **96** (3), p. 032404. DOI: [10.1103/PhysRevE.96.032404](https://doi.org/10.1103/PhysRevE.96.032404).
- [10] F. C. Keber, E. Loiseau, T. Sanchez, S. J. DeCamp, L. Giomi, M. J. Bowick, M. C. Marchetti, Z. Dogic, and A. R. Bausch (2014). Topology and Dynamics of Active Nematic Vesicles. *Science* **345** (6201), pp. 1135–1139. DOI: [10.1126/science.1254784](https://doi.org/10.1126/science.1254784).
- [11] T. B. Liverpool and M. C. Marchetti (2003). Instabilities of Isotropic Solutions of Active Polar Filaments. *Physical Review Letters* **90** (13), p. 138102. DOI: [10.1103/PhysRevLett.90.138102](https://doi.org/10.1103/PhysRevLett.90.138102).

- [12] N. Sarkar and A. Basu (2015). Role of Interfacial Friction for Flow Instabilities in a Thin Polar-Ordered Active Fluid Layer. *Physical Review E* **92** (5), p. 052306. DOI: [10.1103/PhysRevE.92.052306](https://doi.org/10.1103/PhysRevE.92.052306).
- [13] E. Hannezo, B. Dong, P. Recho, J.-F. Joanny, and S. Hayashi (2015). Cortical Instability Drives Periodic Supracellular Actin Pattern Formation in Epithelial Tubes. *Proceedings of the National Academy of Sciences* **112** (28), pp. 8620–8625. DOI: [10.1073/pnas.1504762112](https://doi.org/10.1073/pnas.1504762112).
- [14] K. Gowrishankar and M. Rao (2016). Nonequilibrium Phase Transitions, Fluctuations and Correlations in an Active Contractile Polar Fluid. *Soft Matter* **12** (7), pp. 2040–2046. DOI: [10.1039/C5SM02527C](https://doi.org/10.1039/C5SM02527C).
- [15] R. Voituriez, J. F. Joanny, and J. Prost (2005). Spontaneous Flow Transition in Active Polar Gels. *Europhysics Letters* **70** (3), pp. 404–410. DOI: [10.1209/epl/i2004-10501-2](https://doi.org/10.1209/epl/i2004-10501-2).
- [16] R. Ramaswamy and F. Jülicher (2016). Activity Induces Traveling Waves, Vortices and Spatiotemporal Chaos in a Model Actomyosin Layer. *Scientific Reports* **6**, p. 20838. DOI: [10.1038/srep20838](https://doi.org/10.1038/srep20838).
- [17] T. Lecuit and P.-F. Lenne (2007). Cell Surface Mechanics and the Control of Cell Shape, Tissue Patterns and Morphogenesis. *Nature Reviews Molecular Cell Biology* **8** (8), pp. 633–644. DOI: [10.1038/nrm2222](https://doi.org/10.1038/nrm2222).
- [18] S. W. Grill (2011). Growing up Is Stressful: Biophysical Laws of Morphogenesis. *Current Opinion in Genetics and Development* **21** (5), pp. 647–652. DOI: [10.1016/j.gde.2011.09.005](https://doi.org/10.1016/j.gde.2011.09.005).
- [19] G. Salbreux, G. Charras, and E. Paluch (2012). Actin Cortex Mechanics and Cellular Morphogenesis. *Trends in Cell Biology* **22** (10), pp. 536–545. DOI: [10.1016/j.tcb.2012.07.001](https://doi.org/10.1016/j.tcb.2012.07.001).
- [20] A. C. Callan-Jones, V. Ruprecht, S. Wieser, C. P. Heisenberg, and R. Voituriez (2016). Cortical Flow-Driven Shapes of Nonadherent Cells. *Physical Review Letters* **116** (2), p. 028102. DOI: [10.1103/PhysRevLett.116.028102](https://doi.org/10.1103/PhysRevLett.116.028102).
- [21] Y. Mulla, A. Aufderhorst-Roberts, and G. H. Koenderink (2018). Shaping up Synthetic Cells. *Physical Biology* **15** (4), p. 041001. DOI: [10.1088/1478-3975/aab923](https://doi.org/10.1088/1478-3975/aab923).
- [22] H. L. Goldsmith and J. C. Marlow (1979). Flow Behavior of Erythrocytes. II. Particle Motions in Concentrated Suspensions of Ghost Cells. *Journal of Colloid and Interface Science* **71** (2), pp. 383–407. DOI: [10.1016/0021-9797\(79\)90248-0](https://doi.org/10.1016/0021-9797(79)90248-0).
- [23] J. B. Freund (2014). Numerical Simulation of Flowing Blood Cells. *Annual Review of Fluid Mechanics* **46** (1), pp. 67–95. DOI: [10.1146/annurev-fluid-010313-141349](https://doi.org/10.1146/annurev-fluid-010313-141349).
- [24] G. Popkin (2016). The Physics of Life. *Nature* **529** (7584), pp. 16–18. DOI: [10.1038/529016a](https://doi.org/10.1038/529016a).
- [25] D. Saintillan (2020). Physical Mechanisms of Platelet Formation. *Proceedings of the National Academy of Sciences*, p. 202014390. DOI: [10.1073/pnas.2014390117](https://doi.org/10.1073/pnas.2014390117).

- [26] K. Kruse, J. F. Joanny, F. Jülicher, J. Prost, and K. Sekimoto (2005). Generic Theory of Active Polar Gels: A Paradigm for Cytoskeletal Dynamics. *The European Physical Journal E* **16** (1), pp. 5–16. DOI: [10.1140/epje/e2005-00002-5](https://doi.org/10.1140/epje/e2005-00002-5).
- [27] J.-F. Joanny and J. Prost (2009). Active Gels as a Description of the Actin-Myosin Cytoskeleton. *HFSP journal* **3** (2), pp. 94–104. DOI: [10.2976/1.3054712](https://doi.org/10.2976/1.3054712).
- [28] F. Huber, J. Schnauß, S. Rönicke, P. Rauch, K. Müller, C. Fütterer, and J. Käs (2013). Emergent Complexity of the Cytoskeleton: From Single Filaments to Tissue. *Advances in Physics* **62** (1), pp. 1–112. DOI: [10.1080/00018732.2013.771509](https://doi.org/10.1080/00018732.2013.771509).
- [29] J. Prost, F. Jülicher, and J.-F. Joanny (2015). Active Gel Physics. *Nature Physics* **11** (2), pp. 111–117. DOI: [10.1038/nphys3224](https://doi.org/10.1038/nphys3224).
- [30] F. Jülicher, S. W. Grill, and G. Salbreux (2018). Hydrodynamic Theory of Active Matter. *Reports on Progress in Physics* **81** (7), p. 076601. DOI: [10.1088/1361-6633/aab6bb](https://doi.org/10.1088/1361-6633/aab6bb).
- [31] G. Salbreux, J. Prost, and J. F. Joanny (2009). Hydrodynamics of Cellular Cortical Flows and the Formation of Contractile Rings. *Physical Review Letters* **103** (5), p. 058102. DOI: [10.1103/PhysRevLett.103.058102](https://doi.org/10.1103/PhysRevLett.103.058102).
- [32] E. Hannezo, J. Prost, and J.-F. Joanny (2012). Mechanical Instabilities of Biological Tubes. *Physical Review Letters* **109** (1), p. 018101. DOI: [10.1103/PhysRevLett.109.018101](https://doi.org/10.1103/PhysRevLett.109.018101).
- [33] H. Berthoumieux, J.-L. Maître, C.-P. Heisenberg, E. K. Paluch, F. Jülicher, and G. Salbreux (2014). Active Elastic Thin Shell Theory for Cellular Deformations. *New Journal of Physics* **16** (6), p. 065005. DOI: [10.1088/1367-2630/16/6/065005](https://doi.org/10.1088/1367-2630/16/6/065005).
- [34] R. Zhang, Y. Zhou, M. Rahimi, and J. J. DE Pablo (2016). Dynamic Structure of Active Nematic Shells. *Nature Communications* **7** (1), p. 13483. DOI: [10.1038/ncomms13483](https://doi.org/10.1038/ncomms13483).
- [35] T. B. Saw, A. Doostmohammadi, V. Nier, L. Kocgozlu, S. Thampi, Y. Toyama, P. Marcq, C. T. Lim, J. M. Yeomans, and B. Ladoux (2017). Topological Defects in Epithelia Govern Cell Death and Extrusion. *Nature* **544** (7649), pp. 212–216. DOI: [10.1038/nature21718](https://doi.org/10.1038/nature21718).
- [36] A. Maitra, P. Srivastava, M. Rao, and S. Ramaswamy (2014). Activating Membranes. *Physical Review Letters* **112** (25), p. 258101. DOI: [10.1103/PhysRevLett.112.258101](https://doi.org/10.1103/PhysRevLett.112.258101).
- [37] H. Turlier, B. Audoly, J. Prost, and J.-F. Joanny (2014). Furrow Constriction in Animal Cell Cytokinesis. *Biophysical Journal* **106** (1), pp. 114–123. DOI: [10.1016/j.bpj.2013.11.014](https://doi.org/10.1016/j.bpj.2013.11.014).
- [38] A. Sain, M. M. Inamdar, and F. Jülicher (2015). Dynamic Force Balances and Cell Shape Changes during Cytokinesis. *Physical Review Letters* **114** (4), p. 048102. DOI: [10.1103/PhysRevLett.114.048102](https://doi.org/10.1103/PhysRevLett.114.048102).
- [39] V. Ruprecht, S. Wieser, A. Callan-Jones, M. Smutny, H. Morita, K. Sako, V. Barone, M. Ritsch-Marte, M. Sixt, R. Voituriez, and C.-P. Heisenberg (2015). Cortical Contractility Triggers a Stochastic Switch to Fast Amoeboid Cell Motility. *Cell* **160** (4), pp. 673–685. DOI: [10.1016/j.cell.2015.01.008](https://doi.org/10.1016/j.cell.2015.01.008).

- [40] A.-C. Reymann, F. Staniscia, A. Erzberger, G. Salbreux, and S. W. Grill (2016). Cortical Flow Aligns Actin Filaments to Form a Furrow. *eLife* **5**, e17807. DOI: [10.7554/eLife.17807](https://doi.org/10.7554/eLife.17807).
- [41] C. A. Whitfield and R. J. Hawkins (2016). Immersed Boundary Simulations of Active Fluid Droplets. *PLOS ONE* **11** (9), e0162474. DOI: [10.1371/journal.pone.0162474](https://doi.org/10.1371/journal.pone.0162474).
- [42] N. Klughammer, J. Bischof, N. D. Schnellbacher, A. Callegari, P. Lénárt, and U. S. Schwarz (2018). Cytoplasmic Flows in Starfish Oocytes Are Fully Determined by Cortical Contractions. *PLOS Computational Biology* **14** (11), e1006588. DOI: [10.1371/journal.pcbi.1006588](https://doi.org/10.1371/journal.pcbi.1006588).
- [43] A. Farutin, J. Étienne, C. Misbah, and P. Recho (2019). Crawling in a Fluid. *Physical Review Letters* **123** (11), p. 118101. DOI: [10.1103/PhysRevLett.123.118101](https://doi.org/10.1103/PhysRevLett.123.118101).
- [44] N. C. Heer, P. W. Miller, S. Chanet, N. Stoop, J. Dunkel, and A. C. Martin (2017). Actomyosin-Based Tissue Folding Requires a Multicellular Myosin Gradient. *Development* **144** (10), pp. 1876–1886. DOI: [10.1242/dev.146761](https://doi.org/10.1242/dev.146761).
- [45] A. Torres-Sánchez, D. Millán, and M. Arroyo (2019). Modelling Fluid Deformable Surfaces with an Emphasis on Biological Interfaces. *Journal of Fluid Mechanics* **872**, pp. 218–271. DOI: [10.1017/jfm.2019.341](https://doi.org/10.1017/jfm.2019.341).
- [46] A. Torres-Sánchez, D. Santos-Oliván, and M. Arroyo (2020). Approximation of Tensor Fields on Surfaces of Arbitrary Topology Based on Local Monge Parametrizations. *Journal of Computational Physics* **405**, p. 109168. DOI: [10.1016/j.jcp.2019.109168](https://doi.org/10.1016/j.jcp.2019.109168).
- [47] J. J. Williamson and G. Salbreux (2018). Stability and Roughness of Interfaces in Mechanically Regulated Tissues. *Physical Review Letters* **121** (23), p. 238102. DOI: [10.1103/PhysRevLett.121.238102](https://doi.org/10.1103/PhysRevLett.121.238102).
- [48] H. Soni, W. Luo, R. A. Pelcovits, and T. R. Powers (2019). Stability of the Interface of an Isotropic Active Fluid. *Soft Matter* **15** (31), pp. 6318–6330. DOI: [10.1039/C9SM01216H](https://doi.org/10.1039/C9SM01216H).
- [49] A. Mietke, F. Jülicher, and I. F. Sbalzarini (2019). Self-Organized Shape Dynamics of Active Surfaces. *Proceedings of the National Academy of Sciences* **116** (1), pp. 29–34. DOI: [10.1073/pnas.1810896115](https://doi.org/10.1073/pnas.1810896115).
- [50] J. A. F. Plateau (1873). *Statique Expérimentale et Théorique Des Liquides Soumis Aux Seules Forces Moléculaires*. Vol. 2. Paris: Gauthier-Villars (cited on pp. 3, 31).
- [51] L. Rayleigh (1878). On the Instability of Jets. *Proceedings of the London mathematical society*. Wiley Online Library **1** (1), pp. 4–13. DOI: [10.1112/plms/s1-10.1.4](https://doi.org/10.1112/plms/s1-10.1.4).
- [52] S. Tomotika (1935). On the Instability of a Cylindrical Thread of a Viscous Liquid Surrounded by Another Viscous Fluid. *Proceedings of the Royal Society of London. Series A - Mathematical and Physical Sciences* **150** (870), pp. 322–337. DOI: [10.1098/rspa.1935.0104](https://doi.org/10.1098/rspa.1935.0104).

- [53] H. A. Stone and M. P. Brenner (1996). Note on the Capillary Thread Instability for Fluids of Equal Viscosities. *Journal of Fluid Mechanics* **318**, p. 373. DOI: [10.1017/S002211209600715X](https://doi.org/10.1017/S002211209600715X).
- [54] J. Eggers and E. Villermaux (2008). Physics of Liquid Jets. *Reports on Progress in Physics* **71** (3), p. 036601. DOI: [10.1088/0034-4885/71/3/036601](https://doi.org/10.1088/0034-4885/71/3/036601).
- [55] R. Bar-Ziv and E. Moses (1994). Instability and "Pearling" States Produced in Tubular Membranes by Competition of Curvature and Tension. *Physical Review Letters* **73** (10), pp. 1392–1395. DOI: [10.1103/PhysRevLett.73.1392](https://doi.org/10.1103/PhysRevLett.73.1392).
- [56] R. E. Goldstein, P. Nelson, T. Powers, and U. Seifert (1996). Front Propagation in the Pearling Instability of Tubular Vesicles. *Journal de Physique II* **6** (5), pp. 767–796. DOI: [10.1051/jp2:1996210](https://doi.org/10.1051/jp2:1996210).
- [57] V. Kantsler, E. Segre, and V. Steinberg (2008). Critical Dynamics of Vesicle Stretching Transition in Elongational Flow. *Physical Review Letters* **101** (4), p. 048101. DOI: [10.1103/PhysRevLett.101.048101](https://doi.org/10.1103/PhysRevLett.101.048101).
- [58] T. R. Powers (2010). Dynamics of Filaments and Membranes in a Viscous Fluid. *Reviews of Modern Physics* **82** (2), pp. 1607–1631. DOI: [10.1103/RevModPhys.82.1607](https://doi.org/10.1103/RevModPhys.82.1607).
- [59] A.-C. Reymann, R. Boujemaa-Paterski, J.-L. Martiel, C. Guerin, W. Cao, H. F. Chin, E. M. De La Cruz, M. Thery, and L. Blanchoin (2012). Actin Network Architecture Can Determine Myosin Motor Activity. *Science* **336** (6086), pp. 1310–1314. DOI: [10.1126/science.1221708](https://doi.org/10.1126/science.1221708).
- [60] M. Murrell, P. W. Oakes, M. Lenz, and M. L. Gardel (2015). Forcing Cells into Shape: The Mechanics of Actomyosin Contractility. *Nature Reviews Molecular Cell Biology* **16** (8), pp. 486–498. DOI: [10.1038/nrm4012](https://doi.org/10.1038/nrm4012).
- [61] R. Blackwell, O. Sweezy-Schindler, C. Baldwin, L. E. Hough, M. A. Glaser, and M. D. Betterton (2016). Microscopic Origins of Anisotropic Active Stress in Motor-Driven Nematic Liquid Crystals. *Soft Matter* **12** (10), pp. 2676–2687. DOI: [10.1039/C5SM02506K](https://doi.org/10.1039/C5SM02506K).
- [62] R. Zhang, N. Kumar, J. L. Ross, M. L. Gardel, and J. J. DE Pablo (2018). Interplay of Structure, Elasticity, and Dynamics in Actin-Based Nematic Materials. *Proceedings of the National Academy of Sciences* **115** (2), E124–E133. DOI: [10.1073/pnas.1713832115](https://doi.org/10.1073/pnas.1713832115).
- [63] M. Rauzi, P. Verant, T. Lecuit, and P.-F. Lenne (2008). Nature and Anisotropy of Cortical Forces Orienting Drosophila Tissue Morphogenesis. *Nature Cell Biology* **10** (12), pp. 1401–1410. DOI: [10.1038/ncb1798](https://doi.org/10.1038/ncb1798).
- [64] M. Mayer, M. Depken, J. S. Bois, F. Jülicher, and S. W. Grill (2010). Anisotropies in Cortical Tension Reveal the Physical Basis of Polarizing Cortical Flows. *Nature* **467** (7315), pp. 617–621. DOI: [10.1038/nature09376](https://doi.org/10.1038/nature09376).
- [65] M. Behrndt, G. Salbreux, P. Campinho, R. Hauschild, F. Oswald, J. Roensch, S. W. Grill, and C.-P. Heisenberg (2012). Forces Driving Epithelial Spreading in Zebrafish Gastrulation. *Science* **338** (6104), pp. 257–260. DOI: [10.1126/science.1224143](https://doi.org/10.1126/science.1224143).

- [66] R. Skalak, A. Tozeren, R. P. Zarda, and S. Chien (1973). Strain Energy Function of Red Blood Cell Membranes. *Biophysical Journal* **13** (3), p. 245. DOI: [10.1016/S0006-3495\(73\)85983-1](https://doi.org/10.1016/S0006-3495(73)85983-1).
- [67] W Helfrich (1973). Elastic Properties of Lipid Bilayers: Theory and Possible Experiments. *Zeitschrift für Naturforschung C* **28** (11-12), pp. 693–703. DOI: [10.1515/znc-1973-11-1209](https://doi.org/10.1515/znc-1973-11-1209).
- [68] D. Barthès-Biesel (2016). Motion and Deformation of Elastic Capsules and Vesicles in Flow. *Annual Review of Fluid Mechanics* **48** (1), pp. 25–52. DOI: [10.1146/annurev-fluid-122414-034345](https://doi.org/10.1146/annurev-fluid-122414-034345).
- [69] A. Guckenberger and S. Gekle (2017). Theory and Algorithms to Compute Helfrich Bending Forces: A Review. *Journal of Physics: Condensed Matter* **29** (20), p. 203001. DOI: [10.1088/1361-648X/aa6313](https://doi.org/10.1088/1361-648X/aa6313).
- [70] P. Nelson, T. Powers, and U. Seifert (1995). Dynamical Theory of the Pearling Instability in Cylindrical Vesicles. *Physical Review Letters* **74** (17), pp. 3384–3387. DOI: [10.1103/PhysRevLett.74.3384](https://doi.org/10.1103/PhysRevLett.74.3384).
- [71] F. Campelo and A. Hernández-Machado (2007). Model for Curvature-Driven Pearling Instability in Membranes. *Physical Review Letters* **99** (8), p. 088101. DOI: [10.1103/PhysRevLett.99.088101](https://doi.org/10.1103/PhysRevLett.99.088101).
- [72] G. Boedec, M. Jaeger, and M. Leonetti (2014). Pearling Instability of a Cylindrical Vesicle. *Journal of Fluid Mechanics* **743**, pp. 262–279. DOI: [10.1017/jfm.2014.34](https://doi.org/10.1017/jfm.2014.34).
- [73] C. Patrascu and C. Balan (2020). The Effect of Curvature Elasticity on Rayleigh–Plateau Instability. *European Journal of Mechanics - B/Fluids* **80**, pp. 167–173. DOI: [10.1016/j.euromechflu.2019.11.005](https://doi.org/10.1016/j.euromechflu.2019.11.005).
- [74] M. Bender, A. Eckly, J. H. Hartwig, M. Elvers, I. Pleines, S. Gupta, G. Krohne, E. Jeanclos, A. Gohla, C. Gurniak, C. Gachet, W. Witke, and B. Nieswandt (2010). ADF/n-Cofilin-Dependent Actin Turnover Determines Platelet Formation and Sizing. *Blood* **116** (10), pp. 1767–1775. DOI: [10.1182/blood-2010-03-274340](https://doi.org/10.1182/blood-2010-03-274340).
- [75] K. R. Machlus, J. N. Thon, and J. E. Italiano (2014). Interpreting the Developmental Dance of the Megakaryocyte: A Review of the Cellular and Molecular Processes Mediating Platelet Formation. *British Journal of Haematology* **165** (2), pp. 227–236. DOI: [10.1111/bjh.12758](https://doi.org/10.1111/bjh.12758).
- [76] M. Bender, S. Giannini, R. Grozovsky, T. Jonsson, H. Christensen, F. G. Pluthero, A. Ko, A. Mullally, W. H. A. Kahr, K. M. Hoffmeister, and H. Falet (2015). Dynamin 2-Dependent Endocytosis Is Required for Normal Megakaryocyte Development in Mice. *Blood* **125** (6), pp. 1014–1024. DOI: [10.1182/blood-2014-07-587857](https://doi.org/10.1182/blood-2014-07-587857).
- [77] J. Italiano and J. Hartwig. Production and Destruction of Platelets. In: *The Non-Thrombotic Role of Platelets in Health and Disease*. InTech, (2015). DOI: [10.5772/60678](https://doi.org/10.5772/60678) (cited on pp. 4, 39).
- [78] G. D. Boon (1993). An Overview of Hemostasis. *Toxicologic pathology* **21** (2), pp. 170–179. DOI: [10.1177/019262339302100209](https://doi.org/10.1177/019262339302100209).

- [79] K. R. Machlus and J. E. Italiano (2013). The Incredible Journey: From Megakaryocyte Development to Platelet Formation. *The Journal of Cell Biology* **201** (6), pp. 785–796. DOI: [10.1083/jcb.201304054](https://doi.org/10.1083/jcb.201304054).
- [80] J. E. Italiano, P. Lecine, R. A. Shivdasani, and J. H. Hartwig (1999). Blood Platelets Are Assembled Principally at the Ends of Proplatelet Processes Produced by Differentiated Megakaryocytes. *The Journal of Cell Biology* **147** (6), pp. 1299–1312. DOI: [10.1083/jcb.147.6.1299](https://doi.org/10.1083/jcb.147.6.1299).
- [81] A. Eckly, C. Strassel, M. Freund, J.-P. Cazenave, F. Lanza, C. Gachet, and C. Leon (2009). Abnormal Megakaryocyte Morphology and Proplatelet Formation in Mice with Megakaryocyte-Restricted MYH9 Inactivation. *Blood* **113** (14), pp. 3182–3189. DOI: [10.1182/blood-2008-06-164061](https://doi.org/10.1182/blood-2008-06-164061).
- [82] Z. Sui, R. B. Nowak, C. Sanada, S. Halene, D. S. Krause, and V. M. Fowler (2015). Regulation of Actin Polymerization by Tropomodulin-3 Controls Megakaryocyte Actin Organization and Platelet Biogenesis. *Blood* **126** (4), pp. 520–530. DOI: [10.1182/blood-2014-09-601484](https://doi.org/10.1182/blood-2014-09-601484).
- [83] I. Pleines, J. Woods, S. Chappaz, V. Kew, N. Foad, J. Ballester-Beltrán, K. Aurbach, C. Lincetto, R. M. Lane, G. Schevzov, W. S. Alexander, D. J. Hilton, W. J. Astle, K. Downes, P. Nurden, S. K. Westbury, A. D. Mumford, S. G. Obaji, P. W. Collins, NIHR BioResource, F. Delerue, L. M. Ittner, N. S. Bryce, M. Holliday, C. A. Lucas, E. C. Hardeman, W. H. Ouwehand, P. W. Gunning, E. Turro, M. R. Tijssen, and B. T. Kile (2017). Mutations in Tropomyosin 4 Underlie a Rare Form of Human Macrothrombocytopenia. *Journal of Clinical Investigation* **127** (3), pp. 814–829. DOI: [10.1172/JCI86154](https://doi.org/10.1172/JCI86154).
- [84] T. Junt, H. Schulze, Z. Chen, S. Massberg, T. Goerge, A. Krueger, D. D. Wagner, T. Graf, J. E. Italiano, R. A. Shivdasani, and U. H. von Andrian (2007). Dynamic Visualization of Thrombopoiesis Within Bone Marrow. *Science* **317** (5845), pp. 1767–1770. DOI: [10.1126/science.1146304](https://doi.org/10.1126/science.1146304).
- [85] C. Dunois-Larde, C. Capron, S. Fichelson, T. Bauer, E. Cramer-Borde, and D. Baruch (2009). Exposure of Human Megakaryocytes to High Shear Rates Accelerates Platelet Production. *Blood* **114** (9), pp. 1875–1883. DOI: [10.1182/blood-2009-03-209205](https://doi.org/10.1182/blood-2009-03-209205).
- [86] J. N. Thon, L. Mazutis, S. Wu, J. L. Sylman, A. Ehrlicher, K. R. Machlus, Q. Feng, S. Lu, R. Lanza, K. B. Neeves, D. A. Weitz, and J. E. Italiano (2014). Platelet Bioreactor-on-a-Chip. *Blood* **124** (12), pp. 1857–1867. DOI: [10.1182/blood-2014-05-574913](https://doi.org/10.1182/blood-2014-05-574913).
- [87] M. Bender, J. N. Thon, A. J. Ehrlicher, S. Wu, L. Mazutis, E. Deschmann, M. Sola-Visner, J. E. Italiano, and J. H. Hartwig (2015). Microtubule Sliding Drives Proplatelet Elongation and Is Dependent on Cytoplasmic Dynein. *Blood* **125** (5), pp. 860–868. DOI: [10.1182/blood-2014-09-600858](https://doi.org/10.1182/blood-2014-09-600858).
- [88] A. Blin, A. Le Goff, A. Magniez, S. Poirault-Chassac, B. Teste, G. Sicot, K. A. Nguyen, F. S. Hamdi, M. Reyssat, and D. Baruch (2016). Microfluidic Model of the Platelet-Generating Organ: Beyond Bone Marrow Biomimetics. *Scientific Reports* **6**, p. 21700. DOI: [10.1038/srep21700](https://doi.org/10.1038/srep21700).

- [89] Y. Ito, S. Nakamura, N. Sugimoto, T. Shigemori, Y. Kato, M. Ohno, S. Sakuma, K. Ito, H. Kumon, H. Hirose, H. Okamoto, M. Nogawa, M. Iwasaki, S. Kihara, K. Fujio, T. Matsumoto, N. Higashi, K. Hashimoto, A. Sawaguchi, K.-i. Harimoto, M. Nakagawa, T. Yamamoto, M. Handa, N. Watanabe, E. Nishi, F. Arai, S. Nishimura, and K. Eto (2018). Turbulence Activates Platelet Biogenesis to Enable Clinical Scale Ex Vivo Production. *Cell* **174**(3), 636–648.e18. DOI: [10.1016/j.cell.2018.06.011](https://doi.org/10.1016/j.cell.2018.06.011).
- [90] H. Zhao, E. S. G. Shaqfeh, and V. Narsimhan (2012). Shear-Induced Particle Migration and Margination in a Cellular Suspension. *Physics of Fluids* **24**(1), p. 011902. DOI: [10.1063/1.3677935](https://doi.org/10.1063/1.3677935).
- [91] G. W. Schmid-Schönbein, S. Usami, R. Skalak, and S. Chien (1980). The Interaction of Leukocytes and Erythrocytes in Capillary and Postcapillary Vessels. *Microvascular Research* **19**(1), pp. 45–70. DOI: [10.1016/0026-2862\(80\)90083-7](https://doi.org/10.1016/0026-2862(80)90083-7).
- [92] B. Kaoui, G. H. Ristow, I. Cantat, C. Misbah, and W. Zimmermann (2008). Lateral Migration of a Two-Dimensional Vesicle in Unbounded Poiseuille Flow. *Physical Review E* **77**(2), p. 021903. DOI: [10.1103/PhysRevE.77.021903](https://doi.org/10.1103/PhysRevE.77.021903).
- [93] B. Kaoui, G. Coupier, C. Misbah, and T. Podgorski (2009). Lateral Migration of Vesicles in Microchannels: Effects of Walls and Shear Gradient. *La Houille Blanche* (5), pp. 112–119. DOI: [10.1051/lhb/2009063](https://doi.org/10.1051/lhb/2009063).
- [94] J. B. Freund (2007). Leukocyte Margination in a Model Microvessel. *Physics of Fluids* **19**(2), p. 023301. DOI: [10.1063/1.2472479](https://doi.org/10.1063/1.2472479).
- [95] A. Jain and L. L. Munn (2009). Determinants of Leukocyte Margination in Rectangular Microchannels. *PLoS ONE* **4**(9), e7104. DOI: [10.1371/journal.pone.0007104](https://doi.org/10.1371/journal.pone.0007104).
- [96] A. Kumar and M. D. Graham (2011). Segregation by Membrane Rigidity in Flowing Binary Suspensions of Elastic Capsules. *Physical Review E* **84**(6), p. 066316. DOI: [10.1103/PhysRevE.84.066316](https://doi.org/10.1103/PhysRevE.84.066316).
- [97] J. Tan, A. Thomas, and Y. Liu (2012). Influence of Red Blood Cells on Nanoparticle Targeted Delivery in Microcirculation. *Soft Matter* **8**(6), pp. 1934–1946. DOI: [10.1039/C2SM06391C](https://doi.org/10.1039/C2SM06391C).
- [98] K. Namdee, A. J. Thompson, P. Charoenphol, and O. Eniola-Adefeso (2013). Margination Propensity of Vascular-Targeted Spheres from Blood Flow in a Microfluidic Model of Human Microvessels. *Langmuir* **29**(8), pp. 2530–2535. DOI: [10.1021/la304746p](https://doi.org/10.1021/la304746p).
- [99] D. A. Reasor, M. Mehrabadi, D. N. Ku, and C. K. Aidun (2013). Determination of Critical Parameters in Platelet Margination. *Annals of Biomedical Engineering* **41**(2), pp. 238–249. DOI: [10.1007/s10439-012-0648-7](https://doi.org/10.1007/s10439-012-0648-7).
- [100] K. Müller, D. A. Fedosov, and G. Gompper (2015). Margination of Micro- and Nano-Particles in Blood Flow and Its Effect on Drug Delivery. *Scientific Reports* **4**(1), p. 4871. DOI: [10.1038/srep04871](https://doi.org/10.1038/srep04871).

- [101] K. Vahidkhan and P. Bagchi (2015). Microparticle Shape Effects on Margination, near-Wall Dynamics and Adhesion in a Three-Dimensional Simulation of Red Blood Cell Suspension. *Soft Matter* **11** (11), pp. 2097–2109. DOI: [10.1039/C4SM02686A](https://doi.org/10.1039/C4SM02686A).
- [102] S. Fitzgibbon, A. P. Spann, Q. M. Qi, and E. S. Shaqfeh (2015). In Vitro Measurement of Particle Margination in the Microchannel Flow: Effect of Varying Hematocrit. *Biophysical Journal* **108** (10), pp. 2601–2608. DOI: [10.1016/j.bpj.2015.04.013](https://doi.org/10.1016/j.bpj.2015.04.013).
- [103] R. D’Apolito, G. Tomaiuolo, F. Taraballi, S. Minardi, D. Kirui, X. Liu, A. Cevenini, R. Palomba, M. Ferrari, F. Salvatore, E. Tasciotti, and S. Guido (2015). Red Blood Cells Affect the Margination of Microparticles in Synthetic Microcapillaries and Intravital Microcirculation as a Function of Their Size and Shape. *Journal of Controlled Release* **217**, pp. 263–272. DOI: [10.1016/j.jconrel.2015.09.013](https://doi.org/10.1016/j.jconrel.2015.09.013).
- [104] E. J. Carboni, B. H. Bognet, G. M. Bouchillon, A. L. Kadilak, L. M. Shor, M. D. Ward, and A. W. Ma (2016). Direct Tracking of Particles and Quantification of Margination in Blood Flow. *Biophysical Journal* **111** (7), pp. 1487–1495. DOI: [10.1016/j.bpj.2016.08.026](https://doi.org/10.1016/j.bpj.2016.08.026).
- [105] M. E. Fay, D. R. Myers, A. Kumar, C. T. Turbyfield, R. Byler, K. Crawford, R. G. Mannino, A. Laohapant, E. A. Tyburski, Y. Sakurai, M. J. Rosenbluth, N. A. Switz, T. A. Sulchek, M. D. Graham, and W. A. Lam (2016). Cellular Softening Mediates Leukocyte Demargination and Trafficking, Thereby Increasing Clinical Blood Counts. *Proceedings of the National Academy of Sciences* **113** (8), pp. 1987–1992. DOI: [10.1073/pnas.1508920113](https://doi.org/10.1073/pnas.1508920113).
- [106] T. Krüger (2016). Effect of Tube Diameter and Capillary Number on Platelet Margination and Near-Wall Dynamics. *Rheologica Acta* **55** (6), pp. 511–526. DOI: [10.1007/s00397-015-0891-6](https://doi.org/10.1007/s00397-015-0891-6).
- [107] K. Müller, D. A. Fedosov, and G. Gompper (2016). Understanding Particle Margination in Blood Flow – A Step toward Optimized Drug Delivery Systems. *Medical Engineering & Physics* **38** (1), pp. 2–10. DOI: [10.1016/j.medengphy.2015.08.009](https://doi.org/10.1016/j.medengphy.2015.08.009).
- [108] A. P. Spann, J. E. Campbell, S. R. Fitzgibbon, A. Rodriguez, A. P. Cap, L. H. Blackbourne, and E. S. Shaqfeh (2016). The Effect of Hematocrit on Platelet Adhesion: Experiments and Simulations. *Biophysical Journal* **111** (3), pp. 577–588. DOI: [10.1016/j.bpj.2016.06.024](https://doi.org/10.1016/j.bpj.2016.06.024).
- [109] M. Mehrabadi, D. N. Ku, and C. K. Aidun (2016). Effects of Shear Rate, Confinement, and Particle Parameters on Margination in Blood Flow. *Physical Review E* **93** (2), p. 023109. DOI: [10.1103/PhysRevE.93.023109](https://doi.org/10.1103/PhysRevE.93.023109).
- [110] A. Guckenberger and S. Gekle (2018). A Boundary Integral Method with Volume-Changing Objects for Ultrasound-Triggered Margination of Microbubbles. *Journal of Fluid Mechanics* **836**, pp. 952–997. DOI: [10.1017/jfm.2017.836](https://doi.org/10.1017/jfm.2017.836).
- [111] L. Mountrakis, E. Lorenz, and A. G. Hoekstra (2013). Where Do the Platelets Go? A Simulation Study of Fully Resolved Blood Flow through Aneurysmal Vessels. *Interface Focus* **3** (2), pp. 20120089–20120089. DOI: [10.1098/rsfs.2012.0089](https://doi.org/10.1098/rsfs.2012.0089).

- [112] W.-T. Wu, Y. Li, N. Aubry, M. Massoudi, and J. F. Antaki (2017). Numerical Simulation of Red Blood Cell-Induced Platelet Transport in Saccular Aneurysms. *Applied Sciences* **7** (5), p. 484. DOI: [10.3390/app7050484](https://doi.org/10.3390/app7050484).
- [113] R. Zhao, J. N. Marhefka, F. Shu, S. J. Hund, M. V. Kameneva, and J. F. Antaki (2008). Micro-Flow Visualization of Red Blood Cell-Enhanced Platelet Concentration at Sudden Expansion. *Annals of Biomedical Engineering* **36** (7), pp. 1130–1141. DOI: [10.1007/s10439-008-9494-z](https://doi.org/10.1007/s10439-008-9494-z).
- [114] W. Wang, T. G. Diacovo, J. Chen, J. B. Freund, and M. R. King (2013). Simulation of Platelet, Thrombus and Erythrocyte Hydrodynamic Interactions in a 3D Arteriole with In Vivo Comparison. *PLoS ONE* **8** (10), e76949. DOI: [10.1371/journal.pone.0076949](https://doi.org/10.1371/journal.pone.0076949).
- [115] T. Skorzewski, L. C. Erickson, and A. L. Fogelson (2013). Platelet Motion near a Vessel Wall or Thrombus Surface in Two-Dimensional Whole Blood Simulations. *Biophysical Journal* **104** (8), pp. 1764–1772. DOI: [10.1016/j.bpj.2013.01.061](https://doi.org/10.1016/j.bpj.2013.01.061).
- [116] A. Yazdani and G. E. Karniadakis (2016). Sub-Cellular Modeling of Platelet Transport in Blood Flow through Microchannels with Constriction. *Soft Matter* **12** (19), pp. 4339–4351. DOI: [10.1039/C6SM00154H](https://doi.org/10.1039/C6SM00154H).
- [117] C. Bächer, L. Schrack, and S. Gekle (2017). Clustering of Microscopic Particles in Constricted Blood Flow. *Physical Review Fluids* **2** (1), p. 013102. DOI: [10.1103/PhysRevFluids.2.013102](https://doi.org/10.1103/PhysRevFluids.2.013102).
- [118] B. Woldhuis, G. J. Tangelder, D. W. Slaaf, and R. S. Reneman (1992). Concentration Profile of Blood Platelets Differs in Arterioles and Venules. *American Journal of Physiology-Heart and Circulatory Physiology* **262** (4), H1217–H1223. DOI: [10.1152/ajpheart.1992.262.4.H1217](https://doi.org/10.1152/ajpheart.1992.262.4.H1217).
- [119] L. D. Casa, D. H. Deaton, and D. N. Ku (2015). Role of High Shear Rate in Thrombosis. *Journal of Vascular Surgery* **61** (4), pp. 1068–1080. DOI: [10.1016/j.jvs.2014.12.050](https://doi.org/10.1016/j.jvs.2014.12.050).
- [120] V. Leble, R. Lima, R. Dias, C. Fernandes, T. Ishikawa, Y. Imai, and T. Yamaguchi (2011). Asymmetry of Red Blood Cell Motions in a Microchannel with a Diverging and Converging Bifurcation. *Biomicrofluidics* **5** (4), p. 044120. DOI: [10.1063/1.3672689](https://doi.org/10.1063/1.3672689).
- [121] T. Wang, U. Rongin, and Z. Xing (2016). A Micro-Scale Simulation of Red Blood Cell Passage through Symmetric and Asymmetric Bifurcated Vessels. *Scientific reports* **6**, p. 20262. DOI: [10.1038/srep20262](https://doi.org/10.1038/srep20262).
- [122] J. O. Barber, J. P. Alberding, J. M. Restrepo, and T. W. Secomb (2008). Simulated Two-Dimensional Red Blood Cell Motion, Deformation, and Partitioning in Microvessel Bifurcations. *Annals of Biomedical Engineering* **36** (10), pp. 1690–1698. DOI: [10.1007/s10439-008-9546-4](https://doi.org/10.1007/s10439-008-9546-4).
- [123] Y. C. Ng, B. Namgung, S. L. Tien, H. L. Leo, and S. Kim (2016). Symmetry Recovery of Cell-Free Layer after Bifurcations of Small Arterioles in Reduced Flow Conditions: Effect of RBC Aggregation. *American Journal of Physiology-Heart and Circulatory Physiology* **311** (2), H487–H497. DOI: [10.1152/ajpheart.00223.2016](https://doi.org/10.1152/ajpheart.00223.2016).

- [124] B. Namgung, Y. C. Ng, H. L. Leo, J. M. Rifkind, and S. Kim (2017). Near-Wall Migration Dynamics of Erythrocytes in Vivo: Effects of Cell Deformability and Arteriolar Bifurcation. *Frontiers in Physiology* **8**, p. 963. DOI: [10.3389/fphys.2017.00963](https://doi.org/10.3389/fphys.2017.00963).
- [125] P. Balogh and P. Bagchi (2017). Direct Numerical Simulation of Cellular-Scale Blood Flow in 3D Microvascular Networks. *Biophysical Journal* **113** (12), pp. 2815–2826. DOI: [10.1016/j.bpj.2017.10.020](https://doi.org/10.1016/j.bpj.2017.10.020).
- [126] P. Balogh and P. Bagchi (2017). A Computational Approach to Modeling Cellular-Scale Blood Flow in Complex Geometry. *Journal of Computational Physics* **334**, pp. 280–307. DOI: [10.1016/j.jcp.2017.01.007](https://doi.org/10.1016/j.jcp.2017.01.007).
- [127] P. Balogh and P. Bagchi (2018). Analysis of Red Blood Cell Partitioning at Bifurcations in Simulated Microvascular Networks. *Physics of Fluids* **30** (5), p. 051902. DOI: [10.1063/1.5024783](https://doi.org/10.1063/1.5024783).
- [128] P. Balogh and P. Bagchi (2019). Three-dimensional Distribution of Wall Shear Stress and Its Gradient in Red Cell-resolved Computational Modeling of Blood Flow in in Vivo-like Microvascular Networks. *Physiological Reports* **7** (9), e14067. DOI: [10.14814/phy2.14067](https://doi.org/10.14814/phy2.14067).
- [129] S. J. Singer and G. L. Nicolson (1972). The Fluid Mosaic Model of the Structure of Cell Membranes. *Science* **175** (4023), pp. 720–731. DOI: [10.1126/science.175.4023.720](https://doi.org/10.1126/science.175.4023.720).
- [130] K. N. Burger (2000). Greasing Membrane Fusion and Fission Machineries. *Traffic* **1** (8), pp. 605–613. DOI: [10.1034/j.1600-0854.2000.010804.x](https://doi.org/10.1034/j.1600-0854.2000.010804.x).
- [131] N. Fuller and R. Rand (2001). The Influence of Lysolipids on the Spontaneous Curvature and Bending Elasticity of Phospholipid Membranes. *Biophysical Journal* **81** (1), pp. 243–254. DOI: [10.1016/S0006-3495\(01\)75695-0](https://doi.org/10.1016/S0006-3495(01)75695-0).
- [132] R. Dimova (2019). Giant Vesicles and Their Use in Assays for Assessing Membrane Phase State, Curvature, Mechanics, and Electrical Properties. *Annual Review of Biophysics* **48** (1), pp. 93–119. DOI: [10.1146/annurev-biophys-052118-115342](https://doi.org/10.1146/annurev-biophys-052118-115342).
- [133] D. A. Fedosov, B. Caswell, and G. E. Karniadakis (2010). A Multiscale Red Blood Cell Model with Accurate Mechanics, Rheology, and Dynamics. *Biophysical Journal* **98** (10), pp. 2215–2225. DOI: [10.1016/j.bpj.2010.02.002](https://doi.org/10.1016/j.bpj.2010.02.002).
- [134] S. Patel-Hett, H. Wang, A. J. Begonja, J. N. Thon, E. C. Alden, N. J. Wandersee, X. An, N. Mohandas, J. H. Hartwig, and J. E. Italiano (2011). The Spectrin-Based Membrane Skeleton Stabilizes Mouse Megakaryocyte Membrane Systems and Is Essential for Proplatelet and Platelet Formation. *Blood* **118** (6), pp. 1641–1652. DOI: [10.1182/blood-2011-01-330688](https://doi.org/10.1182/blood-2011-01-330688).
- [135] V. Heinrich, K. Ritchie, N. Mohandas, and E. Evans (2001). Elastic Thickness Compressibility of the Red Cell Membrane. *Biophysical Journal* **81** (3), pp. 1452–1463. DOI: [10.1016/S0006-3495\(01\)75800-6](https://doi.org/10.1016/S0006-3495(01)75800-6).

- [136] S. E. Lux, K. M. John, and T. E. Ukena (1978). Diminished Spectrin Extraction from ATP-Depleted Human Erythrocytes. Evidence Relating Spectrin to Changes in Erythrocyte Shape and Deformability. *Journal of Clinical Investigation* **61** (3), pp. 815–827. DOI: [10.1172/JCI108996](https://doi.org/10.1172/JCI108996).
- [137] P. Chugh and E. K. Paluch (2018). The Actin Cortex at a Glance. *Journal of Cell Science* **131** (14), jcs186254. DOI: [10.1242/jcs.186254](https://doi.org/10.1242/jcs.186254).
- [138] M. Herant and M. Dembo (2010). Form and Function in Cell Motility: From Fibroblasts to Keratocytes. *Biophysical Journal* **98** (8), pp. 1408–1417. DOI: [10.1016/j.bpj.2009.12.4303](https://doi.org/10.1016/j.bpj.2009.12.4303).
- [139] A. C. Callan-Jones and R. Voituriez (2013). Active Gel Model of Amoeboid Cell Motility. *New Journal of Physics* **15** (2), p. 025022. DOI: [10.1088/1367-2630/15/2/025022](https://doi.org/10.1088/1367-2630/15/2/025022).
- [140] W.-C. Lo, C. Madrak, D. P. Kiehart, and G. S. Edwards (2018). Unified Biophysical Mechanism for Cell-Shape Oscillations and Cell Ingression. *Physical Review E* **97** (6). DOI: [10.1103/PhysRevE.97.062414](https://doi.org/10.1103/PhysRevE.97.062414).
- [141] A. Nans, N. Mohandas, and D. L. Stokes (2011). Native Ultrastructure of the Red Cell Cytoskeleton by Cryo-Electron Tomography. *Biophysical Journal* **101** (10), pp. 2341–2350. DOI: [10.1016/j.bpj.2011.09.050](https://doi.org/10.1016/j.bpj.2011.09.050).
- [142] S. Dmitrieff, A. Alsina, A. Mathur, and F. J. Nédélec (2017). Balance of Microtubule Stiffness and Cortical Tension Determines the Size of Blood Cells with Marginal Band across Species. *Proceedings of the National Academy of Sciences* **114** (17), p. 201618041. DOI: [10.1073/pnas.1618041114](https://doi.org/10.1073/pnas.1618041114).
- [143] E. Brown, L. M. Carlin, C. Nerlov, C. Lo Celso, and A. W. Poole (2018). Multiple Membrane Extrusion Sites Drive Megakaryocyte Migration into Bone Marrow Blood Vessels. *Life Science Alliance* **1** (2), e201800061. DOI: [10.26508/lsa.201800061](https://doi.org/10.26508/lsa.201800061).
- [144] L.-L. Pontani, J. VAN DER Gucht, G. Salbreux, J. Heuvingh, J.-F. Joanny, and C. Sykes (2009). Reconstitution of an Actin Cortex Inside a Liposome. *Biophysical Journal* **96** (1), pp. 192–198. DOI: [10.1016/j.bpj.2008.09.029](https://doi.org/10.1016/j.bpj.2008.09.029).
- [145] A. E. Green and W. Zerna (1954). *Theoretical Elasticity*. Oxford: Clarendon Press (cited on pp. 8, 11, 12).
- [146] A. E. Green and J. E. Adkins (1960). *Large Elastic Deformations and Non-Linear Continuum Mechanics*. Oxford: Clarendon Press (cited on p. 8).
- [147] W. T. Koiter (1970). On the Mathematical Foundation of Shell Theory. In: vol. 3, pp. 123–130 (cited on p. 8).
- [148] E. Kreyszig (1968). *Introduction to Differential Geometry and Riemannian Geometry*. University of Toronto Press (cited on pp. 9, 10).
- [149] M. Deserno (2015). Fluid Lipid Membranes: From Differential Geometry to Curvature Stresses. *Chemistry and Physics of Lipids* **185**, pp. 11–45. DOI: [10.1016/j.chemphyslip.2014.05.001](https://doi.org/10.1016/j.chemphyslip.2014.05.001).
- [150] D. Chandrasekharaiah and L. Debnath (2014). *Continuum Mechanics*. Elsevier (cited on pp. 11, 13, 16, 31, 43).

- [151] C. Pozrikidis (2001). Interfacial Dynamics for Stokes Flow. *Journal of Computational Physics* **169** (2), pp. 250–301. DOI: [10.1006/jcph.2000.6582](https://doi.org/10.1006/jcph.2000.6582).
- [152] A. Daddi-Moussa-Ider, A. Guckenbergler, and S. Gekle (2016). Long-Lived Anomalous Thermal Diffusion Induced by Elastic Cell Membranes on Nearby Particles. *Physical Review E* **93** (1), p. 012612. DOI: [10.1103/PhysRevE.93.012612](https://doi.org/10.1103/PhysRevE.93.012612).
- [153] T. Krüger (2012). Computer Simulation Study of Collective Phenomena in Dense Suspensions of Red Blood Cells under Shear. Wiesbaden: Vieweg+Teubner Verlag. DOI: [10.1007/978-3-8348-2376-2](https://doi.org/10.1007/978-3-8348-2376-2) (cited on pp. 12, 21).
- [154] A. Daddi-Moussa-Ider and S. Gekle (2018). Brownian Motion near an Elastic Cell Membrane: A Theoretical Study. *The European Physical Journal E* **41** (2), pp. 1–13. DOI: [10.1140/epje/i2018-11627-6](https://doi.org/10.1140/epje/i2018-11627-6).
- [155] A. Daddi-Moussa-Ider, M. Lisicki, and S. Gekle (2018). Slow Rotation of a Spherical Particle inside an Elastic Tube. *Acta Mechanica* **229** (1), pp. 149–171. DOI: [10.1007/s00707-017-1965-6](https://doi.org/10.1007/s00707-017-1965-6).
- [156] D. Barthès-Biesel, A. Diaz, and E. Dhenin (2002). Effect of Constitutive Laws for Two-Dimensional Membranes on Flow-Induced Capsule Deformation. *Journal of Fluid Mechanics* **460**, p. 211. DOI: [10.1017/S0022112002008352](https://doi.org/10.1017/S0022112002008352).
- [157] E. Lac, D. Barthès-Biesel, N. A. Pelekasis, and J. Tsamopoulos (2004). Spherical Capsules in Three-Dimensional Unbounded Stokes Flows: Effect of the Membrane Constitutive Law and Onset of Buckling. *Journal of Fluid Mechanics* **516**, pp. 303–334. DOI: [10.1017/S002211200400062X](https://doi.org/10.1017/S002211200400062X).
- [158] A. Daddi-Moussa-Ider and S. Gekle (2017). Hydrodynamic Mobility of a Solid Particle near a Spherical Elastic Membrane: Axisymmetric Motion. *Physical Review E* **95** (1), p. 013108. DOI: [10.1103/PhysRevE.95.013108](https://doi.org/10.1103/PhysRevE.95.013108).
- [159] U. Seifert (1997). Configurations of Fluid Membranes and Vesicles. *Advances in Physics* **46** (1), pp. 13–137. DOI: [10.1080/00018739700101488](https://doi.org/10.1080/00018739700101488).
- [160] A. Guckenbergler, M. P. Schraml, P. G. Chen, M. Leonetti, and S. Gekle (2016). On the Bending Algorithms for Soft Objects in Flows. *Computer Physics Communications* **207**, pp. 1–23. DOI: [10.1016/j.cpc.2016.04.018](https://doi.org/10.1016/j.cpc.2016.04.018).
- [161] A. Daddi-Moussa-Ider, M. Lisicki, and S. Gekle (2017). Hydrodynamic Mobility of a Sphere Moving on the Centerline of an Elastic Tube. *Physics of Fluids* **29** (11), p. 111901. DOI: [10.1063/1.5002192](https://doi.org/10.1063/1.5002192).
- [162] A. E. Carlsson (2011). Mechanisms of Cell Propulsion by Active Stresses. *New Journal of Physics* **13** (7), p. 073009. DOI: [10.1088/1367-2630/13/7/073009](https://doi.org/10.1088/1367-2630/13/7/073009).
- [163] L. Scriven (1960). Dynamics of a Fluid Interface Equation of Motion for Newtonian Surface Fluids. *Chemical Engineering Science* **12** (2), pp. 98–108. DOI: [10.1016/0009-2509\(60\)87003-0](https://doi.org/10.1016/0009-2509(60)87003-0).
- [164] V. Narsimhan, A. P. Spann, and E. S. G. Shaqfeh (2015). Pearling, Wrinkling, and Buckling of Vesicles in Elongational Flows. *Journal of Fluid Mechanics* **777**, pp. 1–26. DOI: [10.1017/jfm.2015.345](https://doi.org/10.1017/jfm.2015.345).

- [165] A. R. Sprenger, V. A. Shaik, A. M. Ardekani, M. Lisicki, A. J.T. M. Mathijssen, F. Guzmán-Lastra, H. Löwen, A. M. Menzel, and A. Daddi-Moussa-Ider (2020). Towards an Analytical Description of Active Microswimmers in Clean and in Surfactant-Covered Drops. arXiv: [2005.14661](https://arxiv.org/abs/2005.14661) [[cond-mat](#), [physics:physics](#)].
- [166] F. Guglietta, M. Behr, L. Biferale, G. Falcucci, and M. Sbragaglia (2020). On the Effects of Membrane Viscosity on Transient Red Blood Cell Dynamics. *Soft Matter* **16** (26), pp. 6191–6205. DOI: [10.1039/D0SM00587H](https://doi.org/10.1039/D0SM00587H).
- [167] W. DEN Otter and S. Shkulipa (2007). Intermonolayer Friction and Surface Shear Viscosity of Lipid Bilayer Membranes. *Biophysical Journal* **93** (2), pp. 423–433. DOI: [10.1529/biophysj.107.105395](https://doi.org/10.1529/biophysj.107.105395).
- [168] A. Yazdani and P. Bagchi (2013). Influence of Membrane Viscosity on Capsule Dynamics in Shear Flow. *Journal of Fluid Mechanics* **718**, pp. 569–595. DOI: [10.1017/jfm.2012.637](https://doi.org/10.1017/jfm.2012.637).
- [169] Y. Hatwalne, S. Ramaswamy, M. Rao, and R. A. Simha (2004). Rheology of Active-Particle Suspensions. *Physical Review Letters* **92** (11), p. 118101. DOI: [10.1103/PhysRevLett.92.118101](https://doi.org/10.1103/PhysRevLett.92.118101).
- [170] K. Kruse, J. F. Joanny, F. Jülicher, J. Prost, and K. Sekimoto (2004). Asters, Vortices, and Rotating Spirals in Active Gels of Polar Filaments. *Physical Review Letters* **92** (7), p. 078101. DOI: [10.1103/PhysRevLett.92.078101](https://doi.org/10.1103/PhysRevLett.92.078101).
- [171] F. Jülicher, K. Kruse, J. Prost, and J. Joanny (2007). Active Behavior of the Cytoskeleton. *Physics Reports* **449** (1-3), pp. 3–28. DOI: [10.1016/j.physrep.2007.02.018](https://doi.org/10.1016/j.physrep.2007.02.018).
- [172] S. Ramaswamy (2010). The Mechanics and Statistics of Active Matter. *Annual Review of Condensed Matter Physics* **1** (1), pp. 323–345. DOI: [10.1146/annurev-conmatphys-070909-104101](https://doi.org/10.1146/annurev-conmatphys-070909-104101).
- [173] W. W. Ahmed, E. Fodor, and T. Betz (2015). Active Cell Mechanics: Measurement and Theory. *Biochimica et Biophysica Acta (BBA) - Molecular Cell Research* **1853** (11), pp. 3083–3094. DOI: [10.1016/j.bbamcr.2015.05.022](https://doi.org/10.1016/j.bbamcr.2015.05.022).
- [174] D. Needleman and Z. Dogic (2017). Active Matter at the Interface between Materials Science and Cell Biology. *Nature Reviews Materials* **2** (9), p. 17048. DOI: [10.1038/natrevmats.2017.48](https://doi.org/10.1038/natrevmats.2017.48).
- [175] J. M. Yeomans (2017). Nature’s Engines: Active Matter. *Europhysics News* **48** (2), pp. 21–25. DOI: [10.1051/e pn/2017204](https://doi.org/10.1051/e pn/2017204).
- [176] J. Sedzinski, M. Biro, A. Oswald, J.-Y. Tinevez, G. Salbreux, and E. Paluch (2011). Polar Actomyosin Contractility Destabilizes the Position of the Cytokinetic Furrow. *Nature* **476** (7361), pp. 462–466. DOI: [10.1038/nature10286](https://doi.org/10.1038/nature10286).
- [177] R. A. Green, E. Paluch, and K. Oegema (2012). Cytokinesis in Animal Cells. *Annual Review of Cell and Developmental Biology* **28** (1), pp. 29–58. DOI: [10.1146/annurev-cellbio-101011-155718](https://doi.org/10.1146/annurev-cellbio-101011-155718).
- [178] I. Mendes Pinto, B. Rubinstein, and R. Li (2013). Force to Divide: Structural and Mechanical Requirements for Actomyosin Ring Contraction. *Biophysical Journal* **105** (3), pp. 547–554. DOI: [10.1016/j.bpj.2013.06.033](https://doi.org/10.1016/j.bpj.2013.06.033).

- [179] D. Shao, H. Levine, and W.-J. Rappel (2012). Coupling Actin Flow, Adhesion, and Morphology in a Computational Cell Motility Model. *Proceedings of the National Academy of Sciences* **109** (18), pp. 6851–6856. DOI: [10.1073/pnas.1203252109](https://doi.org/10.1073/pnas.1203252109).
- [180] W. Marth, S. Praetorius, and A. Voigt (2015). A Mechanism for Cell Motility by Active Polar Gels. *Journal of The Royal Society Interface* **12** (107), p. 20150161. DOI: [10.1098/rsif.2015.0161](https://doi.org/10.1098/rsif.2015.0161).
- [181] A. C. Callan-Jones and R. Voituriez (2016). Actin Flows in Cell Migration: From Locomotion and Polarity to Trajectories. *Current Opinion in Cell Biology* **38**, pp. 12–17. DOI: [10.1016/j.j.ceb.2016.01.003](https://doi.org/10.1016/j.j.ceb.2016.01.003).
- [182] E. J. Campbell and P. Bagchi (2017). A Computational Model of Amoeboid Cell Swimming. *Physics of Fluids* **29** (10), p. 101902. DOI: [10.1063/1.4990543](https://doi.org/10.1063/1.4990543).
- [183] E. Fischer-Friedrich, Y. Toyoda, C. J. Cattin, D. J. Müller, A. A. Hyman, and F. Jülicher (2016). Rheology of the Active Cell Cortex in Mitosis. *Biophysical Journal* **111** (3), pp. 589–600. DOI: [10.1016/j.bpj.2016.06.008](https://doi.org/10.1016/j.bpj.2016.06.008).
- [184] E. Fischer-Friedrich (2018). Active Prestress Leads to an Apparent Stiffening of Cells through Geometrical Effects. *Biophysical Journal* **114** (2), pp. 419–424. DOI: [10.1016/j.bpj.2017.11.014](https://doi.org/10.1016/j.bpj.2017.11.014).
- [185] S. Tojkander, G. Gateva, and P. Lappalainen (2012). Actin Stress Fibers - Assembly, Dynamics and Biological Roles. *Journal of Cell Science* **125** (8), pp. 1855–1864. DOI: [10.1242/jcs.098087](https://doi.org/10.1242/jcs.098087).
- [186] P. J. Foster, S. Fürthauer, M. J. Shelley, and D. J. Needleman (2019). From Cytoskeletal Assemblies to Living Materials. *Current Opinion in Cell Biology* **56**, pp. 109–114. DOI: [10.1016/j.j.ceb.2018.10.010](https://doi.org/10.1016/j.j.ceb.2018.10.010).
- [187] M. P. N. Juniper, M. Weiss, I. Platzman, J. P. Spatz, and T. Surrey (2018). Spherical Network Contraction Forms Microtubule Asters in Confinement. *Soft Matter* **14** (6), pp. 901–909. DOI: [10.1039/C7SM01718A](https://doi.org/10.1039/C7SM01718A).
- [188] T. Sanchez, D. T. N. Chen, S. J. DeCamp, M. Heymann, and Z. Dogic (2012). Spontaneous Motion in Hierarchically Assembled Active Matter. *Nature* **491** (7424), pp. 431–434. DOI: [10.1038/nature11591](https://doi.org/10.1038/nature11591).
- [189] A. Doostmohammadi, J. Ignés-Mullol, J. M. Yeomans, and F. Sagués (2018). Active Nematics. *Nature Communications* **9** (1), pp. 1–13. DOI: [10.1038/s41467-018-05666-8](https://doi.org/10.1038/s41467-018-05666-8).
- [190] K. T. Stanhope, V. Yadav, C. D. Santangelo, and J. L. Ross (2017). Contractility in an Extensile System. *Soft Matter* **13** (23), pp. 4268–4277. DOI: [10.1039/C7SM00449D](https://doi.org/10.1039/C7SM00449D).
- [191] P. J. Foster, S. Fürthauer, M. J. Shelley, and D. J. Needleman (2015). Active Contraction of Microtubule Networks. *eLife* **4**, e10837. DOI: [10.7554/eLife.10837](https://doi.org/10.7554/eLife.10837).
- [192] R. Tan, P. J. Foster, D. J. Needleman, and R. J. McKenney (2018). Cooperative Accumulation of Dynein-Dynactin at Microtubule Minus-Ends Drives Microtubule Network Reorganization. *Developmental Cell* **44** (2), 233–247.e4. DOI: [10.1016/j.devcel.2017.12.023](https://doi.org/10.1016/j.devcel.2017.12.023).

- [193] F. Verde, J.-M. Berrez, C. Antony, and E. Karsenti (1991). Taxol-Induced Microtubule Asters in Mitotic Extracts of *Xenopus* Eggs: Requirement for Phosphorylated Factors and Cytoplasmic Dynein. *The Journal of Cell Biology* **112** (6), pp. 1177–1187. DOI: [10.1083/jcb.112.6.1177](https://doi.org/10.1083/jcb.112.6.1177).
- [194] T. Gaglio (1995). NuMA Is Required for the Organization of Microtubules into Aster-like Mitotic Arrays. *The Journal of Cell Biology* **131** (3), pp. 693–708. DOI: [10.1083/jcb.131.3.693](https://doi.org/10.1083/jcb.131.3.693).
- [195] D. Oriola, D. J. Needleman, and J. Brugués (2018). The Physics of the Metaphase Spindle. *Annual Review of Biophysics* **47** (1), pp. 655–673. DOI: [10.1146/annurev-biophys-060414-034107](https://doi.org/10.1146/annurev-biophys-060414-034107).
- [196] D. B. Oelz, U. DEL Castillo, V. I. Gelfand, and A. Mogilner (2018). Microtubule Dynamics, Kinesin-1 Sliding, and Dynein Action Drive Growth of Cell Processes. *Biophysical Journal* **115** (8), pp. 1614–1624. DOI: [10.1016/j.bpj.2018.08.046](https://doi.org/10.1016/j.bpj.2018.08.046).
- [197] G. H. Koenderink, Z. Dogic, F. Nakamura, P. M. Bendix, F. C. MacKintosh, J. H. Hartwig, T. P. Stossel, and D. A. Weitz (2009). An Active Biopolymer Network Controlled by Molecular Motors. *Proceedings of the National Academy of Sciences* **106** (36), pp. 15192–15197. DOI: doi.org/10.1073/pnas.0903974106.
- [198] M. R. Mofrad (2009). Rheology of the Cytoskeleton. *Annual Review of Fluid Mechanics* **41** (1), pp. 433–453. DOI: [10.1146/annurev.fluid.010908.165236](https://doi.org/10.1146/annurev.fluid.010908.165236).
- [199] D. V. Köster and S. Mayor (2016). Cortical Actin and the Plasma Membrane: Inextricably Intertwined. *Current Opinion in Cell Biology* **38**, pp. 81–89. DOI: [10.1016/j.ceb.2016.02.021](https://doi.org/10.1016/j.ceb.2016.02.021).
- [200] P. Chugh, A. G. Clark, M. B. Smith, D. A. D. Cassani, K. Dierkes, A. Ragab, P. P. Roux, G. Charras, G. Salbreux, and E. K. Paluch (2017). Actin Cortex Architecture Regulates Cell Surface Tension. *Nature Cell Biology* **19** (6), pp. 689–697. DOI: [10.1038/ncb3525](https://doi.org/10.1038/ncb3525).
- [201] C. J. Miller, D. Harris, R. Weaver, G. B. Ermentrout, and L. A. Davidson (2018). Emergent Mechanics of Actomyosin Drive Punctuated Contractions and Shape Network Morphology in the Cell Cortex. *PLOS Computational Biology* **14** (9), e1006344. DOI: [10.1371/journal.pcbi.1006344](https://doi.org/10.1371/journal.pcbi.1006344).
- [202] G. H. Koenderink and E. K. Paluch (2018). Architecture Shapes Contractility in Actomyosin Networks. *Current Opinion in Cell Biology* **50**, pp. 79–85. DOI: [10.1016/j.ceb.2018.01.015](https://doi.org/10.1016/j.ceb.2018.01.015).
- [203] P. M. Bendix, G. H. Koenderink, D. Cuvelier, Z. Dogic, B. N. Koeleman, W. M. Briehar, C. M. Field, L. Mahadevan, and D. A. Weitz (2008). A Quantitative Analysis of Contractility in Active Cytoskeletal Protein Networks. *Biophysical Journal* **94** (8), pp. 3126–3136. DOI: [10.1529/biophysj.107.117960](https://doi.org/10.1529/biophysj.107.117960).
- [204] H. Ennomani, G. Letort, C. Guérin, J.-L. Martiel, W. Cao, F. Nédélec, E. M. De La Cruz, M. Théry, and L. Blanchoin (2016). Architecture and Connectivity Govern Actin Network Contractility. *Current Biology* **26** (5), pp. 616–626. DOI: [10.1016/j.cub.2015.12.069](https://doi.org/10.1016/j.cub.2015.12.069).

- [205] J. M. Belmonte, M. Leptin, and F. Nédélec (2017). A Theory That Predicts Behaviors of Disordered Cytoskeletal Networks. *Molecular Systems Biology* **13** (9), p. 941. DOI: [10.15252/msb.20177796](https://doi.org/10.15252/msb.20177796).
- [206] G Salbreux, J. F. Joanny, J Prost, and P Pullarkat (2007). Shape Oscillations of Non-Adhering Fibroblast Cells. *Physical Biology* **4** (4), pp. 268–284. DOI: [10.1088/1478-3975/4/4/004](https://doi.org/10.1088/1478-3975/4/4/004).
- [207] A. Saha, M. Nishikawa, M. Behrndt, C.-P. Heisenberg, F. Jülicher, and S. W. Grill (2016). Determining Physical Properties of the Cell Cortex. *Biophysical Journal* **110** (6), pp. 1421–1429. DOI: [10.1016/j.bpj.2016.02.013](https://doi.org/10.1016/j.bpj.2016.02.013).
- [208] M. Fritzsche, A. Lewalle, T. Duke, K. Kruse, and G. Charras (2013). Analysis of Turnover Dynamics of the Submembranous Actin Cortex. *Molecular Biology of the Cell* **24** (6), pp. 757–767. DOI: [10.1091/mbc.e12-06-0485](https://doi.org/10.1091/mbc.e12-06-0485).
- [209] F. B. Robin, W. M. McFadden, B. Yao, and E. M. Munro (2014). Single-Molecule Analysis of Cell Surface Dynamics in *Caenorhabditis Elegans* Embryos. *Nature Methods* **11** (6), pp. 677–682. DOI: [10.1038/nmeth.2928](https://doi.org/10.1038/nmeth.2928).
- [210] E. Lomakina, C. Spillmann, M. King, and R. Waugh (2004). Rheological Analysis and Measurement of Neutrophil Indentation. *Biophysical Journal* **87** (6), pp. 4246–4258. DOI: [10.1529/biophysj.103.031765](https://doi.org/10.1529/biophysj.103.031765).
- [211] M. Krieg, Y. Arboleda-Estudillo, P.-H. Puech, J. Käfer, F. Graner, D. J. Müller, and C.-P. Heisenberg (2008). Tensile Forces Govern Germ-Layer Organization in Zebrafish. *Nature Cell Biology* **10** (4), pp. 429–436. DOI: [10.1038/ncb1705](https://doi.org/10.1038/ncb1705).
- [212] J.-Y. Tinevez, U. Schulze, G. Salbreux, J. Roensch, J.-F. Joanny, and E. Paluch (2009). Role of Cortical Tension in Bleb Growth. *Proceedings of the National Academy of Sciences* **106** (44), pp. 18581–18586. DOI: [10.1073/pnas.0903353106](https://doi.org/10.1073/pnas.0903353106).
- [213] J. Lam, M. Herant, M. Dembo, and V. Heinrich (2009). Baseline Mechanical Characterization of J774 Macrophages. *Biophysical Journal* **96** (1), pp. 248–254. DOI: [10.1529/biophysj.108.139154](https://doi.org/10.1529/biophysj.108.139154).
- [214] M. Bergert, S. D. Chandradoss, R. A. Desai, and E. Paluch (2012). Cell Mechanics Control Rapid Transitions between Blebs and Lamellipodia during Migration. *Proceedings of the National Academy of Sciences* **109** (36), pp. 14434–14439. DOI: [10.1073/pnas.1207968109](https://doi.org/10.1073/pnas.1207968109).
- [215] J. Hanke, D. Probst, A. Zemel, U. S. Schwarz, and S. Köster (2018). Dynamics of Force Generation by Spreading Platelets. *Soft Matter* **14** (31), pp. 6571–6581. DOI: [10.1039/C8SM00895G](https://doi.org/10.1039/C8SM00895G).
- [216] J. Hanke, C. Ranke, E. Perego, and S. Köster (2019). Human Blood Platelets Contract in Perpendicular Direction to Shear Flow. *Soft Matter* **15** (9), pp. 2009–2019. DOI: [10.1039/C8SM02136H](https://doi.org/10.1039/C8SM02136H).
- [217] E. Fischer-Friedrich, A. A. Hyman, F. Jülicher, D. J. Müller, and J. Helenius (2014). Quantification of Surface Tension and Internal Pressure Generated by Single Mitotic Cells. *Scientific Reports* **4**, p. 6213. DOI: [10.1038/srep06213](https://doi.org/10.1038/srep06213).

- [218] J. B. Freund and M. M. Orescanin (2011). Cellular Flow in a Small Blood Vessel. *Journal of Fluid Mechanics* **671**, pp. 466–490. DOI: [10.1017/S0022112010005835](https://doi.org/10.1017/S0022112010005835).
- [219] G. Késmárky, P. Kenyeres, M. Rábai, and K. Tóth (2008). Plasma Viscosity: A Forgotten Variable. *Clinical Hemorheology and Microcirculation* **39** (1–4), pp. 243–246. DOI: [10.3233/CH-2008-1088](https://doi.org/10.3233/CH-2008-1088).
- [220] T. W. Secomb (2017). Blood Flow in the Microcirculation. *Annual Review of Fluid Mechanics* **49** (1), pp. 443–461. DOI: [10.1146/annurev-fluid-010816-060302](https://doi.org/10.1146/annurev-fluid-010816-060302).
- [221] J.-O. Jost, H. Knoche, E. Fleischhacker, and M. Kribber (1977). Leitfaden der Hämatologie und Blutgruppenserologie für medizinisch-technische Assistentinnen und Studierende der Medizin: 19 Tabellen. Stuttgart: Fischer (cited on p. 15).
- [222] A. S. Popel and P. C. Johnson (2005). MICROCIRCULATION AND HEMORHEOLOGY. *Annual Review of Fluid Mechanics* **37** (1), pp. 43–69. DOI: [10.1146/annurev.fluid.37.042604.133933](https://doi.org/10.1146/annurev.fluid.37.042604.133933).
- [223] H. Lipowsky (2005). Microvascular Rheology and Hemodynamics. *Microcirculation* **12** (1), pp. 5–15. DOI: [10.1080/10739680590894966](https://doi.org/10.1080/10739680590894966).
- [224] G. Gompper and D. A. Fedosov (2016). Modeling Microcirculatory Blood Flow: Current State and Future Perspectives. *Wiley Interdisciplinary Reviews: Systems Biology and Medicine* **8** (2), pp. 157–168. DOI: [10.1002/wsbm.1326](https://doi.org/10.1002/wsbm.1326).
- [225] A. Birbrair and P. S. Frenette (2016). Niche Heterogeneity in the Bone Marrow: Cellular Complexity of the HSC Niche in the BM. *Annals of the New York Academy of Sciences* **1370** (1), pp. 82–96. DOI: [10.1111/nyas.13016](https://doi.org/10.1111/nyas.13016).
- [226] C. Bonifer and D. T. Bowen (2010). Epigenetic Mechanisms Regulating Normal and Malignant Haematopoiesis: New Therapeutic Targets for Clinical Medicine. *Expert Reviews in Molecular Medicine* **12**, e6. DOI: [10.1017/S1462399410001377](https://doi.org/10.1017/S1462399410001377).
- [227] S. R. Patel (2005). The Biogenesis of Platelets from Megakaryocyte Proplatelets. *Journal of Clinical Investigation* **115** (12), pp. 3348–3354. DOI: [10.1172/JCI26891](https://doi.org/10.1172/JCI26891).
- [228] S. E. Spagnolie, ed. (2015). Complex Fluids in Biological Systems: Experiment, Theory, and Computation. Biological and Medical Physics, Biomedical Engineering. New York: Springer (cited on p. 17).
- [229] A. Daddi-Moussa-Ider, B. Rallabandi, S. Gekle, and H. A. Stone (2018). Reciprocal Theorem for the Prediction of the Normal Force Induced on a Particle Translating Parallel to an Elastic Membrane. *Physical Review Fluids* **3** (8), p. 084101. DOI: [10.1103/PhysRevFluids.3.084101](https://doi.org/10.1103/PhysRevFluids.3.084101).
- [230] S. Succi (2001). The Lattice Boltzmann Equation: For Fluid Dynamics and Beyond. New York: Oxford university press (cited on p. 17).
- [231] C. K. Aidun and J. R. Clausen (2010). Lattice-Boltzmann Method for Complex Flows. *Annual Review of Fluid Mechanics* **42** (1), pp. 439–472. DOI: [10.1146/annurev-fluid-121108-145519](https://doi.org/10.1146/annurev-fluid-121108-145519).

- [232] T. Krüger, H. Kusumaatmaja, A. Kuzmin, O. Shardt, G. Silva, and E. M. Viggien (2016). *The Lattice Boltzmann Method: Principles and Practice*. Springer (cited on p. 17).
- [233] S. Harris (2004). *An Introduction to the Theory of the Boltzmann Equation*. Mineola, NY: Dover (cited on p. 17).
- [234] B. Dünweg, U. D. Schiller, and A. J. C. Ladd (2007). Statistical Mechanics of the Fluctuating Lattice Boltzmann Equation. *Physical Review E* **76** (3), p. 036704. DOI: [10.1103/PhysRevE.76.036704](https://doi.org/10.1103/PhysRevE.76.036704).
- [235] D. Roehm and A. Arnold (2012). Lattice Boltzmann Simulations on GPUs with ESPResSo. *The European Physical Journal Special Topics* **210** (1), pp. 89–100. DOI: [10.1140/epjst/e2012-01639-6](https://doi.org/10.1140/epjst/e2012-01639-6).
- [236] C. S. Peskin (2002). The Immersed Boundary Method. *Acta Numerica* **11**, pp. 479–517. DOI: [10.1017/S0962492902000077](https://doi.org/10.1017/S0962492902000077).
- [237] R. Mittal and G. Iaccarino (2005). Immersed Boundary Methods. *Annual Review of Fluid Mechanics* **37** (1), pp. 239–261. DOI: [10.1146/annurev.fluid.37.061903.175743](https://doi.org/10.1146/annurev.fluid.37.061903.175743).
- [238] H. Limbach, A. Arnold, B. Mann, and C. Holm (2006). ESPResSo—an Extensible Simulation Package for Research on Soft Matter Systems. *Computer Physics Communications* **174** (9), pp. 704–727. DOI: [10.1016/j.cpc.2005.10.005](https://doi.org/10.1016/j.cpc.2005.10.005).
- [239] F. Weik, R. Weeber, K. Szuttor, K. Breitsprecher, J. DE Graaf, M. Kuron, J. Landsgesell, H. Menke, D. Sean, and C. Holm (2019). ESPResSo 4.0 – an Extensible Software Package for Simulating Soft Matter Systems. *The European Physical Journal Special Topics* **227** (14), pp. 1789–1816. DOI: [10.1140/epjst/e2019-800186-9](https://doi.org/10.1140/epjst/e2019-800186-9).
- [240] A. Farutin, T. Biben, and C. Misbah (2014). 3D Numerical Simulations of Vesicle and Inextensible Capsule Dynamics. *Journal of Computational Physics* **275**, pp. 539–568. DOI: [10.1016/j.jcp.2014.07.008](https://doi.org/10.1016/j.jcp.2014.07.008).
- [241] A. Yazdani and P. Bagchi (2012). Three-Dimensional Numerical Simulation of Vesicle Dynamics Using a Front-Tracking Method. *Physical Review E* **85** (5), p. 056308. DOI: [10.1103/PhysRevE.85.056308](https://doi.org/10.1103/PhysRevE.85.056308).
- [242] Y. Seol, W.-F. Hu, Y. Kim, and M.-C. Lai (2016). An Immersed Boundary Method for Simulating Vesicle Dynamics in Three Dimensions. *Journal of Computational Physics* **322**, pp. 125–141. DOI: [10.1016/j.jcp.2016.06.035](https://doi.org/10.1016/j.jcp.2016.06.035).
- [243] M. Meyer, M. Desbrun, P. Schröder, and A. H. Barr. Discrete Differential-Geometry Operators for Triangulated 2-Manifolds. In: *Visualization and Mathematics III*. Springer, (2003), pp. 35–57 (cited on p. 21).
- [244] S. Gekle (2016). Strongly Accelerated Margination of Active Particles in Blood Flow. *Biophysical Journal* **110** (2), pp. 514–520. DOI: [10.1016/j.bpj.2015.12.005](https://doi.org/10.1016/j.bpj.2015.12.005).
- [245] A. Guckenberger, A. Kihm, T. John, C. Wagner, and S. Gekle (2018). Numerical–Experimental Observation of Shape Bistability of Red Blood Cells Flowing in a Microchannel. *Soft Matter* **14** (11), pp. 2032–2043. DOI: [10.1039/C7SM02272G](https://doi.org/10.1039/C7SM02272G).

- [246] Nonequilibrium Statistical Mechanics. In: *Nonequilibrium Statistical Mechanics*. Ed. by G. F. Mazenko. Weinheim, Germany: Wiley-VCH Verlag GmbH, (2006). DOI: [10.1002/9783527618958.ch1](https://doi.org/10.1002/9783527618958.ch1) (cited on p. 23).
- [247] M. L. Boas (2006). *Mathematical Methods in the Physical Sciences*. John Wiley & Sons, Inc (cited on p. 23).
- [248] T. D. Pollard (2017). Nine Unanswered Questions about Cytokinesis. *The Journal of Cell Biology* **216** (10), pp. 3007–3016. DOI: [10.1083/jcb.201612068](https://doi.org/10.1083/jcb.201612068).
- [249] D. Khoromskaia and G. Salbreux (2020). Active Morphogenesis of Epithelial Shells. *in preparation*.
- [250] D. Khoromskaia and G. Salbreux. (private communication).
- [251] P. G. Drazin and W. H. Reid (2004). *Hydrodynamic Stability*. Cambridge university press (cited on p. 31).
- [252] L. Rayleigh (1892). XVI. On the Instability of a Cylinder of Viscous Liquid under Capillary Force. *The London, Edinburgh, and Dublin Philosophical Magazine and Journal of Science* **34** (207), pp. 145–154. DOI: [10.1080/14786449208620301](https://doi.org/10.1080/14786449208620301).
- [253] S Chandrasekhar (1961). *Hydrodynamic and Hydromagnetic Stability*. Dover Publications (cited on pp. 31, 50).
- [254] C. Ménager, M. Meyer, V. Cabuil, A. Cebers, J.-C. Bacri, and R. Perzynski (2002). Magnetic Phospholipid Tubes Connected to Magnetoliposomes: Pearling Instability Induced by a Magnetic Field. *The European Physical Journal E* **7** (4), pp. 325–337. DOI: [10.1140/epje/i2001-10094-6](https://doi.org/10.1140/epje/i2001-10094-6).
- [255] M Sato, M. J. Levesque, and R. M. Nerem (1987). Micropipette Aspiration of Cultured Bovine Aortic Endothelial Cells Exposed to Shear Stress. *Arteriosclerosis: An Official Journal of the American Heart Association, Inc.* **7** (3), pp. 276–286. DOI: [10.1161/01.ATV.7.3.276](https://doi.org/10.1161/01.ATV.7.3.276).
- [256] D. A. Fletcher and R. D. Mullins (2010). Cell Mechanics and the Cytoskeleton. *Nature* **463** (7280), pp. 485–492. DOI: [10.1038/nature08908](https://doi.org/10.1038/nature08908).
- [257] J. White and G. Borisy (1983). On the Mechanisms of Cytokinesis in Animal Cells. *Journal of Theoretical Biology* **101** (2), pp. 289–316. DOI: [10.1016/0022-5193\(83\)90342-9](https://doi.org/10.1016/0022-5193(83)90342-9).
- [258] A. D. Poularikas, ed. (2000). *The Transforms and Applications Handbook*. 2nd ed. The Electrical Engineering Handbook Series. Boca Raton, Fla: CRC Press (cited on p. 33).
- [259] R. Winklbauer (2015). Cell Adhesion Strength from Cortical Tension - an Integration of Concepts. *Journal of Cell Science* **128** (20), pp. 3687–3693. DOI: [10.1242/jcs.174623](https://doi.org/10.1242/jcs.174623).
- [260] A. Martínez-Calvo, J. Rivero-Rodríguez, B. Scheid, and A. Sevilla (2020). Natural Break-up and Satellite Formation Regimes of Surfactant-Laden Liquid Threads. *Journal of Fluid Mechanics* **883**, A35. DOI: [10.1017/jfm.2019.874](https://doi.org/10.1017/jfm.2019.874).
- [261] C. Weber (1931). Zum Zerfall eines Flüssigkeitsstrahles. *ZAMM - Zeitschrift für Angewandte Mathematik und Mechanik* **11** (2), pp. 136–154. DOI: [10.1002/zamm.19310110207](https://doi.org/10.1002/zamm.19310110207).

- [262] J. Eggers and T. F. Dupont (1994). Drop Formation in a One-Dimensional Approximation of the Navier–Stokes Equation. *Journal of Fluid Mechanics* **262**, pp. 205–221. DOI: [10.1017/S0022112094000480](https://doi.org/10.1017/S0022112094000480).
- [263] J. Eggers (1997). Nonlinear Dynamics and Breakup of Free-Surface Flows. *Reviews of Modern Physics* **69** (3), pp. 865–930. DOI: [10.1103/RevModPhys.69.865](https://doi.org/10.1103/RevModPhys.69.865).
- [264] N. Ashgriz and F. Mashayek (1995). Temporal Analysis of Capillary Jet Breakup. *Journal of Fluid Mechanics* **291**, pp. 163–190. DOI: [10.1017/S0022112095002667](https://doi.org/10.1017/S0022112095002667).
- [265] L. A. Harker and C. A. Finch (1969). Thrombokinetics in Man. *Journal of Clinical Investigation* **48** (6), pp. 963–974. DOI: [10.1172/JCI106077](https://doi.org/10.1172/JCI106077).
- [266] T. Kanaji, J. Ware, T. Okamura, and P. J. Newman (2012). GPIb Regulates Platelet Size by Controlling the Subcellular Localization of Filamin. *Blood* **119** (12), pp. 2906–2913. DOI: [10.1182/blood-2011-08-376566](https://doi.org/10.1182/blood-2011-08-376566).
- [267] Y. Chen, S. Boukour, R. Milloud, R. Favier, B. Saposnik, N. Schlegel, A. Nurden, H. Raslova, W. Vainchenker, M. Balland, P. Nurden, and N. Debili (2013). The Abnormal Proplatelet Formation in MYH9-Related Macrothrombocytopenia Results from an Increased Actomyosin Contractility and Is Rescued by Myosin IIA Inhibition. *Journal of Thrombosis and Haemostasis* **11** (12), pp. 2163–2175. DOI: [10.1111/jth.12436](https://doi.org/10.1111/jth.12436).
- [268] J. Pan, L. Lordier, D. Meyran, P. Rameau, Y. Lecluse, S. Kitchen-Goosen, I. Badirou, H. Mokrani, S. Narumiya, A. S. Alberts, W. Vainchenker, and Y. Chang (2014). The Formin DIAPH1 (mDia1) Regulates Megakaryocyte Proplatelet Formation by Remodeling the Actin and Microtubule Cytoskeletons. *Blood* **124** (26), pp. 3967–3977. DOI: [10.1182/blood-2013-12-544924](https://doi.org/10.1182/blood-2013-12-544924).
- [269] K. R. Spinler, J.-W. Shin, M. P. Lambert, and D. E. Discher (2015). Myosin-II Repression Favors Pre/Proplatelets but Shear Activation Generates Platelets and Fails in Macrothrombocytopenia. *Blood* **125** (3), pp. 525–533. DOI: [10.1182/blood-2014-05-576462](https://doi.org/10.1182/blood-2014-05-576462).
- [270] D. F. Stroncek and P. Rebutta (2007). Platelet Transfusions. *The Lancet* **370** (9585), pp. 427–438. DOI: [10.1016/S0140-6736\(07\)61198-2](https://doi.org/10.1016/S0140-6736(07)61198-2).
- [271] Q. Feng, N. Shabrani, J. N. Thon, H. Huo, A. Thiel, K. R. Machlus, K. Kim, J. Brooks, F. Li, C. Luo, E. A. Kimbrel, J. Wang, K.-S. Kim, J. Italiano, J. Cho, S.-J. Lu, and R. Lanza (2014). Scalable Generation of Universal Platelets from Human Induced Pluripotent Stem Cells. *Stem Cell Reports* **3** (5), pp. 817–831. DOI: [10.1016/j.stemcr.2014.09.010](https://doi.org/10.1016/j.stemcr.2014.09.010).
- [272] J. N. Thon and J. E. Italiano (2010). Platelet Formation. *Seminars in Hematology* **47** (3), pp. 220–226. DOI: [10.1053/j.seminhematol.2010.03.005](https://doi.org/10.1053/j.seminhematol.2010.03.005).
- [273] J. N. Thon and J. E. Italiano. Platelets: Production, Morphology and Ultrastructure. In: *Antiplatelet Agents*. Ed. by P. Gesele, G. V. R. Born, C. Patrono, and C. P. Page. Vol. 210. Berlin, Heidelberg: Springer Berlin Heidelberg, (2012), pp. 3–22. DOI: [10.1007/978-3-642-29423-5_1](https://doi.org/10.1007/978-3-642-29423-5_1) (cited on p. 39).

- [274] J. N. Thon, B. J. Dykstra, and L. M. Beaulieu (2017). Platelet Bioreactor: Accelerated Evolution of Design and Manufacture. *Platelets* **28** (5), pp. 472–477. DOI: [10.1080/09537104.2016.1265922](https://doi.org/10.1080/09537104.2016.1265922).
- [275] J. N. Thon, A. Montalvo, S. Patel-Hett, M. T. Devine, J. L. Richardson, A. Ehrlicher, M. K. Larson, K. Hoffmeister, J. H. Hartwig, and J. E. Italiano (2010). Cytoskeletal Mechanics of Proplatelet Maturation and Platelet Release. *The Journal of Cell Biology* **191** (4), pp. 861–874. DOI: [10.1083/jcb.201006102](https://doi.org/10.1083/jcb.201006102).
- [276] M. G. Bixel, A. P. Kusumbe, S. K. Ramasamy, K. K. Sivaraj, S. Butz, D. Vestweber, and R. H. Adams (2017). Flow Dynamics and HSPC Homing in Bone Marrow Microvessels. *Cell Reports* **18** (7), pp. 1804–1816. DOI: [10.1016/j.celrep.2017.01.042](https://doi.org/10.1016/j.celrep.2017.01.042).
- [277] I. Pleines, S. Dutting, D. Cherpokova, A. Eckly, I. Meyer, M. Morowski, G. Krohne, H. Schulze, C. Gachet, N. Debili, C. Brakebusch, and B. Nieswandt (2013). Defective Tubulin Organization and Proplatelet Formation in Murine Megakaryocytes Lacking Rac1 and Cdc42. *Blood* **122** (18), pp. 3178–3187. DOI: [10.1182/blood-2013-03-487942](https://doi.org/10.1182/blood-2013-03-487942).
- [278] A. D. Michelson (2013). Platelets. Amsterdam: Elsevier (cited on p. 41).
- [279] A. K. Paknikar, B. Eltzner, and S. Köster (2019). Direct Characterization of Cytoskeletal Reorganization during Blood Platelet Spreading. *Progress in Biophysics and Molecular Biology* **144**, pp. 166–176. DOI: [10.1016/j.pbiomolbio.2018.05.001](https://doi.org/10.1016/j.pbiomolbio.2018.05.001).
- [280] O. Behnke and A. Forer (1998). From Megakaryocytes to Platelets: Platelet Morphogenesis Takes Place in the Bloodstream. *European Journal of Haematology* **60** (S61), pp. 3–23. DOI: [10.1111/j.1600-0609.1998.tb01052.x](https://doi.org/10.1111/j.1600-0609.1998.tb01052.x).
- [281] L. Crowl and A. L. Fogelson (2011). Analysis of Mechanisms for Platelet Near-Wall Excess under Arterial Blood Flow Conditions. *Journal of Fluid Mechanics* **676**, pp. 348–375. DOI: [10.1017/jfm.2011.54](https://doi.org/10.1017/jfm.2011.54).
- [282] G. Coupier, B. Kaoui, T. Podgorski, and C. Misbah (2008). Noninertial Lateral Migration of Vesicles in Bounded Poiseuille Flow. *Physics of Fluids* **20** (11), p. 111702. DOI: [10.1063/1.3023159](https://doi.org/10.1063/1.3023159).
- [283] T. M. Geislinger, B. Eggart, S. Braunmüller, L. Schmid, and T. Franke (2012). Separation of Blood Cells Using Hydrodynamic Lift. *Applied Physics Letters* **100** (18), p. 183701. DOI: [10.1063/1.4709614](https://doi.org/10.1063/1.4709614).
- [284] X. Grandchamp, G. Coupier, A. Srivastav, C. Minetti, and T. Podgorski (2013). Lift and Down-Gradient Shear-Induced Diffusion in Red Blood Cell Suspensions. *Physical Review Letters* **110** (10), p. 108101. DOI: [10.1103/PhysRevLett.110.108101](https://doi.org/10.1103/PhysRevLett.110.108101).
- [285] D. A. Fedosov, B. Caswell, A. S. Popel, and G. E. Karniadakis (2010). Blood Flow and Cell-Free Layer in Microvessels. *Microcirculation* **17** (8), pp. 615–628. DOI: [10.1111/j.1549-8719.2010.00056.x](https://doi.org/10.1111/j.1549-8719.2010.00056.x).

- [286] A. Kumar and M. D. Graham (2012). Mechanism of Margination in Confined Flows of Blood and Other Multicomponent Suspensions. *Physical Review Letters* **109** (10), p. 108102. DOI: [10.1103/PhysRevLett.109.108102](https://doi.org/10.1103/PhysRevLett.109.108102).
- [287] H. Zhao and E. S. G. Shaqfeh (2011). Shear-Induced Platelet Margination in a Microchannel. *Physical Review E* **83** (6), p. 061924. DOI: [10.1103/PhysRevE.83.061924](https://doi.org/10.1103/PhysRevE.83.061924).
- [288] K. Svanes and B. Zweifach (1968). Variations in Small Blood Vessel Hematocrits Produced in Hypothermic Rats by Micro-Occlusion. *Microvascular Research* **1** (2), pp. 210–220. DOI: [10.1016/0026-2862\(68\)90019-8](https://doi.org/10.1016/0026-2862(68)90019-8).
- [289] X. Li, A. S. Popel, and G. E. Karniadakis (2012). Blood–Plasma Separation in Y-Shaped Bifurcating Microfluidic Channels: A Dissipative Particle Dynamics Simulation Study. *Physical Biology* **9** (2), p. 026010. DOI: [10.1088/1478-3975/9/2/026010](https://doi.org/10.1088/1478-3975/9/2/026010).
- [290] S. Tripathi, Y. V. B. Varun Kumar, A. Prabhakar, S. S. Joshi, and A. Agrawal (2015). Passive Blood Plasma Separation at the Microscale: A Review of Design Principles and Microdevices. *Journal of Micromechanics and Microengineering* **25** (8), p. 083001. DOI: [10.1088/0960-1317/25/8/083001](https://doi.org/10.1088/0960-1317/25/8/083001).
- [291] C. Sun and L. L. Munn (2008). Lattice-Boltzmann Simulation of Blood Flow in Digitized Vessel Networks. *Computers & Mathematics with Applications* **55** (7), pp. 1594–1600. DOI: [10.1016/j.camwa.2007.08.019](https://doi.org/10.1016/j.camwa.2007.08.019).
- [292] X. Yang, O. Forouzan, J. M. Burns, and S. S. Shevkoplyas (2011). Traffic of Leukocytes in Microfluidic Channels with Rectangular and Rounded Cross-Sections. *Lab on a Chip* **11** (19), p. 3231. DOI: [10.1039/c1lc20293f](https://doi.org/10.1039/c1lc20293f).
- [293] K. Lykov, X. Li, H. Lei, I. V. Pivkin, and G. E. Karniadakis (2015). Inflow/Outflow Boundary Conditions for Particle-Based Blood Flow Simulations: Application to Arterial Bifurcations and Trees. *PLOS Computational Biology* **11** (8), e1004410. DOI: [10.1371/journal.pcbi.1004410](https://doi.org/10.1371/journal.pcbi.1004410).
- [294] A. R. Pries and T. W. Secomb. Blood Flow in Microvascular Networks. In: *Microcirculation*. Elsevier, (2008), pp. 3–36. DOI: [10.1016/B978-0-12-374530-9.00001-2](https://doi.org/10.1016/B978-0-12-374530-9.00001-2) (cited on p. 47).
- [295] A. Mietke, V. Jemseena, K. V. Kumar, I. F. Sbalzarini, and F. Jülicher (2019). Minimal Model of Cellular Symmetry Breaking. *Physical Review Letters* **123** (18), p. 188101. DOI: [10.1103/PhysRevLett.123.188101](https://doi.org/10.1103/PhysRevLett.123.188101).
- [296] L. Sui, S. Alt, M. Weigert, N. Dye, S. Eaton, F. Jug, E. W. Myers, F. Jülicher, G. Salbreux, and C. Dahmann (2018). Differential Lateral and Basal Tension Drive Folding of Drosophila Wing Discs through Two Distinct Mechanisms. *Nature Communications* **9** (1), p. 4620. DOI: [10.1038/s41467-018-06497-3](https://doi.org/10.1038/s41467-018-06497-3).
- [297] H. A. Messal, S. Alt, R. M. M. Ferreira, C. Gribben, V. M.-Y. Wang, C. G. Cotoi, G. Salbreux, and A. Behrens (2019). Tissue Curvature and Apicobasal Mechanical Tension Imbalance Instruct Cancer Morphogenesis. *Nature* **566** (7742), pp. 126–130. DOI: [10.1038/s41586-019-0891-2](https://doi.org/10.1038/s41586-019-0891-2).

- [298] A. Iglič, B. Babnik, U. Gimsa, and V. Kralj-Iglič (2005). On the Role of Membrane Anisotropy in the Beading Transition of Undulated Tubular Membrane Structures. *Journal of Physics A: Mathematical and General* **38** (40), pp. 8527–8536. DOI: [10.1088/0305-4470/38/40/004](https://doi.org/10.1088/0305-4470/38/40/004).
- [299] B. Smeets, M. Cuvelier, J. Pešek, and H. Ramon (2019). The Effect of Cortical Elasticity and Active Tension on Cell Adhesion Mechanics. *Biophysical Journal* **116** (5), pp. 930–937. DOI: [10.1016/j.bpj.2019.01.015](https://doi.org/10.1016/j.bpj.2019.01.015).
- [300] K. Luby-Phelps (2013). The Physical Chemistry of Cytoplasm and Its Influence on Cell Function: An Update. *Molecular Biology of the Cell* **24** (17), pp. 2593–2596. DOI: [10.1091/mbc.e12-08-0617](https://doi.org/10.1091/mbc.e12-08-0617).
- [301] A. Mogilner and A. Manhart (2018). Intracellular Fluid Mechanics: Coupling Cytoplasmic Flow with Active Cytoskeletal Gel. *Annual Review of Fluid Mechanics* **50** (1), pp. 347–370. DOI: [10.1146/annurev-fluid-010816-060238](https://doi.org/10.1146/annurev-fluid-010816-060238).
- [302] O. Malaspinas, N. Fiétier, and M. Deville (2010). Lattice Boltzmann Method for the Simulation of Viscoelastic Fluid Flows. *Journal of Non-Newtonian Fluid Mechanics* **165** (23-24), pp. 1637–1653. DOI: [10.1016/j.jnnfm.2010.09.001](https://doi.org/10.1016/j.jnnfm.2010.09.001).
- [303] S. Papenkort and T. Voigtmann (2014). Channel Flow of a Tensorial Shear-Thinning Maxwell Model: Lattice Boltzmann Simulations. *The Journal of Chemical Physics* **140** (16), p. 164507. DOI: [10.1063/1.4872219](https://doi.org/10.1063/1.4872219).
- [304] A. Gupta, M. Sbragaglia, and A. Scagliarini (2015). Hybrid Lattice Boltzmann/Finite Difference Simulations of Viscoelastic Multicomponent Flows in Confined Geometries. *Journal of Computational Physics* **291**, pp. 177–197. DOI: [10.1016/j.jcp.2015.03.006](https://doi.org/10.1016/j.jcp.2015.03.006).
- [305] M. Lehmann, S. J. Müller, and S. Gekle (2020). Efficient Viscosity Contrast Calculation for Blood Flow Simulations Using the Lattice Boltzmann Method: Efficient Viscosity Contrast Calculation for Blood Flow Simulations Using the Lattice Boltzmann Method. *International Journal for Numerical Methods in Fluids*. DOI: [10.1002/flid.4835](https://doi.org/10.1002/flid.4835).
- [306] S. J. Müller, F. Weigl, C. Bezold, C. Bächer, K. Albrecht, and S. Gekle (2020). A Hyperelastic Model for Simulating Cells in Flow. arXiv: [2003.03130](https://arxiv.org/abs/2003.03130) [[cond-mat](https://arxiv.org/archive/math), [physics:physics](https://arxiv.org/archive/physics)].
- [307] S. J. Müller, E. Mirzahosseini, E. N. Iftekhar, C. Bächer, S. Schrüfer, D. W. Schubert, B. Fabry, and S. Gekle (2020). Flow and Hydrodynamic Shear Stress inside a Printing Needle during Biofabrication. *PLOS ONE* **15** (7), e0236371. DOI: [10.1371/journal.pone.0236371](https://doi.org/10.1371/journal.pone.0236371).

Part II
Publications

The author's contributions

Contributions to the publications for this thesis

- [pub1] C. Bächer and S. Gekle (2019). Computational Modeling of Active Deformable Membranes Embedded in Three-Dimensional Flows. *Physical Review E* **99** (6), p. 062418. DOI: [10.1103/PhysRevE.99.062418](https://doi.org/10.1103/PhysRevE.99.062418)

Individual contributions:

Christian Bächer during this thesis

- designed the research
- designed, developed, and implemented the algorithm and the axisymmetric simulation method
- designed, performed, and analyzed the simulations
- wrote the article.

S. Gekle designed and supervised the research and helped writing the article.

- [pub2] C. Bächer, D. Khoromskaia, G. Salbreux, and S. Gekle (2020). A Three-Dimensional Numerical Model of an Active Cell Cortex in the Viscous Limit. *Draft*

Individual contributions:

Christian Bächer during this thesis

- designed the research
- designed and developed the algorithm and wrote the program
- designed, performed and analyzed the three dimensional simulations
- performed the analytical calculations used for validation
- wrote the manuscript.

D. Khoromskaia performed the axisymmetric simulations.

G. Salbreux supervised and designed the research and provided the mathematical basis of the analytical calculations.

S. Gekle supervised and designed the research and helped writing the article.

-
- [pub3] K. Graessel, C. Bächer, and S. Gekle (2021). Rayleigh–Plateau Instability of Anisotropic Interfaces. Part 1. An Analytical and Numerical Study of Fluid Interfaces. *Journal of Fluid Mechanics* **910**, A46. DOI: [10.1017/jfm.2020.947](https://doi.org/10.1017/jfm.2020.947)

Individual contributions:

Christian Bächer during this thesis

- designed the research
- did the analytical calculation and its evaluation in the Stokes limit as well as for the Euler equation in presence of an outer fluid
- wrote the method for, designed, performed and analyzed the numerical simulations using lattice-Boltzmann as well as boundary integral method
- performed the long wavelength approximation, developed and performed corresponding numerical simulations
- helped to supervise K. Graessel, especially regarding the membrane mechanics.

Together, Christian Bächer during this thesis and K. Graessel

- designed the figures
- wrote the manuscript
- discussed and interpreted the results.

K. Graessel did the analytical calculations and its evaluation for the ideal fluid jet in air and for an interface with surface viscosity. S. Gekle supervised and designed the research, discussed the results, and helped writing the article.

-
- [pub4] C. Bächer, K. Graessel, and S. Gekle (2021). Rayleigh–Plateau Instability of Anisotropic Interfaces. Part 2. Limited Instability of Elastic Interfaces. *Journal of Fluid Mechanics* **910**, A47. DOI: [10.1017/jfm.2020.946](https://doi.org/10.1017/jfm.2020.946)

Individual contributions:

Christian Bächer during this thesis

- designed the research
- did the analytical calculation and its evaluation considering bending elasticity in the Stokes limit
- analyzed the range of growing modes and performed the analysis and the construction of the phase diagram
- analyzed the influence of the reference curvature
- did the analytical calculation and its evaluation considering Skalak shear elasticity
- helped to supervise K. Graessel, especially regarding the membrane mechanics.

Together, Christian Bächer during this thesis and K. Graessel

- designed the figures
- wrote the manuscript
- discussed and interpreted the results.

K. Graessel did the analytical calculation with bending elasticity for the ideal fluid jet in air. S. Gekle supervised and designed the research, discussed the results, and helped writing the article.

- [pub5] C. Bächer, M. Bender, and S. Gekle (2020). Flow-Accelerated Platelet Biogenesis Is Due to an Elasto-Hydrodynamic Instability. *Proceedings of the National Academy of Sciences* **117** (32), pp. 18969–18976. DOI: [10.1073/pnas.2002985117](https://doi.org/10.1073/pnas.2002985117)

Individual contributions:

Christian Bächer during this thesis

- designed the research
- designed, performed and analyzed the simulations
- interpreted the results
- wrote the article.

M. Bender performed the in-vitro experiments and helped writing the article. S. Gekle supervised and designed the research, interpreted the results, and helped writing the article.

-
- [pub6] C. Bächer, A. Kihm, L. Schrack, L. Kaestner, M. W. Laschke, C. Wagner, and S. Gekle (2018). Antimargination of Microparticles and Platelets in the Vicinity of Branching Vessels. *Biophysical Journal* **115** (2), pp. 411–425. DOI: [10.1016/j.bpj.2018.06.013](https://doi.org/10.1016/j.bpj.2018.06.013)

Individual contributions:

Christian Bächer during this thesis

- extended the simulation tools (in- and outflow)
- designed, performed and analyzed the simulations
- interpreted the results
- wrote the article.

L. Schrack extended the simulation tools (branching geometry). A. Kihm, L. Kaestner, M.W. Laschke, C. Wagner designed, performed, analyzed, and interpreted the *in vivo* experiments. S. Gekle supervised and designed the research, interpreted the results, and helped writing the article.

Further publications

During his doctorate the author of the present thesis also contributed to the following publications

S. J. Müller, E. Mirzahassein, E. N. Iftekhar, C. Bächer, S. Schrüfer, D. W. Schubert, B. Fabry, and S. Gekle (2020). Flow and Hydrodynamic Shear Stress inside a Printing Needle during Biofabrication. *PLOS ONE* **15** (7), e0236371. DOI: [10.1371/journal.pone.0236371](https://doi.org/10.1371/journal.pone.0236371)

S. J. Müller, F. Weigl, C. Bezold, C. Bächer, K. Albrecht, and S. Gekle (2020). A Hyperelastic Model for Simulating Cells in Flow. arXiv: [2003.03130](https://arxiv.org/abs/2003.03130) [[cond-mat](#), [physics:physics](#)]

Contributions to conferences and symposiums

The different parts of the present thesis have been presented by the author during his doctorate at the following conferences, summer schools and symposiums:

Talks:

- Cell Physics 2019, Saarbrücken, Germany
- Living Fluids 2019, Bayreuth, Germany
- Elite Network of Bavaria Biological Physics Symposium 2019, Bayreuth, Germany
- DPG spring meeting 2019, Regensburg, Germany
- ENB Retreat Biological Physics 2018, Thurnau, Germany

-
- DPG spring meeting 2018, Berlin, Germany
 - Symposium Biofluid Simulation and Modeling 2017, Bayreuth, Germany
 - Summer School Complex Motion in Fluids 2017, Cambridge, Great Britain
 - Discrete Simulation of Fluid Dynamics 2017, Erlangen, Germany
 - DPG spring meeting 2017, Dresden, Germany

Poster contributions:

- Living Fluids 2019, Bayreuth, Germany
- CellMech meeting 2019, Milan, Italy
- DPG spring meeting 2019, Regensburg, Germany
- DPG spring meeting 2018, Berlin, Germany
- Symposium Biofluid Simulation and Modeling 2017, Bayreuth, Germany
- Blood Flow: Current State and Future Perspectives 2017, Paris, France

Publication 1

COMPUTATIONAL MODELING OF ACTIVE DEFORMABLE MEMBRANES EMBEDDED IN THREE-DIMENSIONAL FLOWS

C. Bächer and S. Gekle

Physical Review E **99** (6), 2019

Copyright by APS.

DOI: 10.1103/PhysRevE.99.062418

Computational modeling of active deformable membranes embedded in three-dimensional flows

Christian Bächer* and Stephan Gekle†

Biofluid Simulation and Modeling, Theoretische Physik VI, Universität Bayreuth, Universitätsstrasse 30, Bayreuth, Germany



(Received 27 March 2019; published 28 June 2019)

Active gel theory has recently been very successful in describing biologically active materials such as actin filaments or moving bacteria in temporally fixed and simple geometries such as cubes or spheres. Here we develop a computational algorithm to compute the dynamic evolution of an arbitrarily shaped, deformable thin membrane of active material embedded in a three-dimensional flowing liquid. For this, our algorithm combines active gel theory with the classical theory of thin elastic shells. To compute the actual forces resulting from active stresses, we apply a parabolic fitting procedure to the triangulated membrane surface. Active forces are then dynamically coupled via an immersed-boundary method to the surrounding fluid whose dynamics can be solved by any standard, e.g., Lattice-Boltzmann, flow solver. We validate our algorithm using the Green's functions of Berthoumieux *et al.* [New J. Phys. **16**, 065005 (2014)] for an active cylindrical membrane subjected (i) to a locally increased active stress and (ii) to a homogeneous active stress. For the latter scenario, we predict in addition a nonaxisymmetric instability. We highlight the versatility of our method by analyzing the flow field inside an actively deforming cell embedded in external shear flow. Further applications may be cytoplasmic streaming or active membranes in blood flows.

DOI: [10.1103/PhysRevE.99.062418](https://doi.org/10.1103/PhysRevE.99.062418)

I. INTRODUCTION

Many biological processes such as cell division or locomotion depend on the ability of living cells to convert chemical energy into mechanical work [1]. A prominent mechanism to achieve such a conversion are motor proteins which perform work through a relative movement of cross-linked cytoskeletal filaments. This movement induces active stresses in the cell cortex [2–7] which are transmitted via anchor proteins to the plasma membrane separating the interior of the cell from its surroundings. Active stresses have an inherent nonequilibrium character and are the basis of physically unique processes in active fluid layers such as instabilities [8,9], the emergence of spontaneous flows [10], or the creation of geometrical structures [11,12]. They are furthermore responsible for large shape deformations during cell morphogenesis [13–15], cell division [16–21], cell locomotion [22–26], cell rheology [27,28], or spike formation on artificial vesicles [29].

In recent years a theoretical framework has been developed describing cytoskeleton and motor proteins together as an active continuous gel [30–39]. This active gel theory in general treats the cell cortex as a viscoelastic medium with additional active contributions. On time scales short compared to the viscoelastic relaxation time active gel theory can be formulated in the elastic limit [3]. For thin active 2D membranes embedded in 3D space, active gel theory can be reformulated into force balance equations using the formalism of differential geometry [3,6]. Any active stress in the membrane is then balanced by a counterstress, usually due to viscous friction,

from the external medium. The force balance equations can be applied on fixed membrane geometries such as spheres, cylinders, or flat layers. This often results in the prediction of regions in parameter space where the prescribed shape is expected to become unstable [11,16,29,40–42]. Despite being a powerful qualitative tool, such calculations cannot make statements about the precise shape of the active membrane after the instability has set in.

To obtain actual shape predictions, a number of works start instead from a parametrized, free membrane shape which is adjusted so as to fulfill the force balance equations for a given set of parameters and boundary conditions. This procedure can be carried out either analytically [3,43] or numerically [15,20,21,44–46]. For example, Berthoumieux *et al.* [3] derived Green's functions to predict the deformation of an infinitely long cylindrical active, elastic membrane resulting from the application of a point active stress. For certain parameter ranges, these Green's functions exhibit divergences which have been interpreted as mechanical (buckling or Rayleigh-Plateau-like) instabilities of the cylindrical membrane. Sain *et al.* [21] investigated the axisymmetric dynamics of the furrow in cytokinesis. Turlier *et al.* [20] computed the time evolution of an axisymmetric membrane undergoing cytokinesis by advecting tracer points discretizing the membrane. Callan-Jones *et al.* [15] predicted a transition to a polarized cell shape because of an instability of the cell cortex. Reymann *et al.* [45] matched axisymmetric, theoretical results to observed cell shapes during cytokinesis using measured velocity and order parameter fields as input for the theory. Heer *et al.* [47] determined the equilibrium shape of an elastic tissue layer folded into a deformable ellipsoidal shell, where myosin activity is incorporated as a preferred curvature of the shell. Klughammer *et al.* [48] analytically calculated the flow inside a sphere that slightly deforms due to a traveling band

*christian.baecher@uni-bayreuth.de

†stephan.gekle@uni-bayreuth.de

of surface tension, which mimics cortical active tension, under the assumption of rotational symmetry. In all of these works the full dynamics of the external fluid was neglected and nearly all of them restricted themselves to deformations from simple rest shapes in the steady state. There currently exists no analytical or numerical method to compute the dynamical deformation of an arbitrarily shaped active membrane immersed in a three-dimensional (3D) moving Newtonian fluid.

In this work, we develop a computational algorithm to predict the dynamic deformation of arbitrarily shaped thin membranes discretized by a set of nodes connected via flat triangles. Starting from prescribed active stresses on the discretized membrane our algorithm computes the corresponding forces on every membrane node via a parabolic fitting procedure taking into account the full deformed surface geometry. Knowledge of the nodal forces then enables the dynamic coupling to a surrounding 3D fluid via the immersed-boundary method (IBM). The Navier-Stokes dynamics for the surrounding fluid is solved here by the Lattice-Boltzmann method (LBM), but other flow solvers can straightforwardly be incorporated. With this, our method allows the study of the dynamic evolution of active membranes in general external flows. It thus builds a bridge between the extensive literature on active fluids and the similarly extensive work on elastic cells, vesicles, and capsules in flows [49–56]. In biological situations often a flowing environment is present rendering the dynamic coupling of external fluid and membrane deformations necessary. Our proposed method allows such a coupling and thus the computation of dynamically evolving nonequilibrium shapes. Possible applications of our method include the study of active cell membranes inside the bloodstream or active cellular compartments in cytoplasmic streaming flows.

First in Sec. II, we extensively describe the LBM-IBM for a dynamic coupling of an elastic membrane and a suspending fluid. In Sec. III we start with the problem formulation in the framework of thin shell theory using differential geometry. Next, we describe our algorithm for three-dimensional active force calculation in Sec. IV. In Sec. V we provide an in-depth validation of our algorithm based on the analytical results for a cylindrical active membrane in the case of infinitesimal deformations by Berthoumieux *et al.* [3]. As an application, Sec. VIA presents the flow field inside a dividing elastic cell, where active stresses trigger membrane deformations that in turn lead to fluid flow. In Sec. VIB we analyze the same system in externally driven shear flow. Eventually, we conclude our work in Sec. VII.

II. DYNAMIC COUPLING OF MEMBRANE AND FLUID

A. Lattice-Boltzmann method for fluid dynamics

The Lattice-Boltzmann method (LBM) is an efficient and accurate flow solver which is well described in the literature [57–60]. In the following we therefore summarize only the basic concepts. In contrast to macroscopic, e.g., finite element, methods based directly on the discretized Navier-Stokes equation (NSE), LBM starts from the Boltzmann equation which is a common tool in statistical mechanics. Using Chapman-Enskog analysis the NSE are recovered from the Boltzmann equation [60,61].

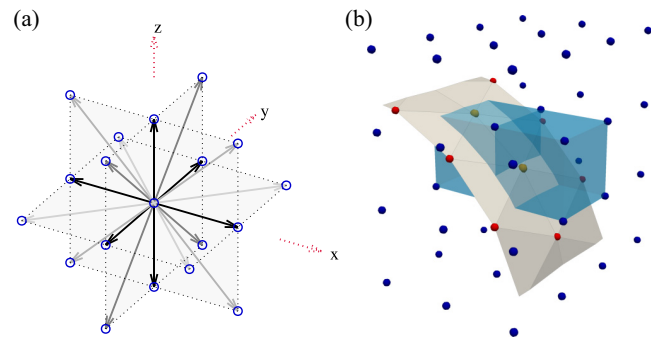


FIG. 1. (a) D3Q19 LBM scheme with the discrete velocity set (solid arrows) connecting nearest and next nearest neighboring fluid nodes (dots). (b) 3D illustration of the immersed-boundary method. A continuous membrane is discretized by Lagrangian nodes (red and orange dots) that are connected by triangles. The membrane is immersed in a Eulerian grid representing the fluid (blue dots). The velocity at a Lagrangian node is obtained by interpolation from the eight closest fluid nodes (illustrated for the two orange membrane nodes in the middle by the blue shaded cubes). The same stencil is used to transmit the forces from the membrane to the fluid.

The Boltzmann equation provides insight into a system on mesoscopic length scales by means of the continuous particle distribution function $f(\mathbf{r}, \mathbf{p}, t)$ where \mathbf{r} , \mathbf{p} , and t refer to position of the particles, momentum of the particles, and time, respectively. The expression $f(\mathbf{r}, \mathbf{p}, t) d\mathbf{r} d\mathbf{p} dt$ gives the probability to find a particle (fluid molecule) in the phase-space volume $d\mathbf{r} d\mathbf{p}$ at (\mathbf{r}, \mathbf{p}) in the time interval t to $t + dt$. The dynamic evolution of the particle distribution function $f(\mathbf{r}, \mathbf{p}, t)$ is given by

$$\frac{df}{dt} = \frac{\partial f}{\partial t} + \mathbf{v} \cdot \nabla_{\mathbf{r}} f + \mathbf{F} \cdot \nabla_{\mathbf{p}} f = \Omega \quad (1)$$

with Ω being the collision operator accounting for redistribution of molecules due to collisions.

Discretization of space, momentum space, and time leads from the Boltzmann equation (1) to the Lattice-Boltzmann equation. The discretization of the spatial domain is carried out using a cubic Eulerian grid. The distance between the fluid nodes is $\Delta x = 1$ in simulation units. In contrast to other methods, LBM also discretizes the momentum (velocity) space, i.e., $f = f(\mathbf{x}_j, \mathbf{p}_i, t)$ such that only a discrete set of velocities is allowed at each node. Here, we use the common D3Q19 scheme with 19 discrete velocity vectors, which is illustrated in Fig. 1(a). Thus, each node contains one population $f(\mathbf{x}_j, \mathbf{p}_i, t)$ for each momentum \mathbf{p}_i , which moves with the corresponding velocity \mathbf{c}_i away from the node \mathbf{x}_j within one time step. As an abbreviation the distribution functions are labeled by an index according to their discrete momentum (or velocity), i.e., $f(\mathbf{x}_j, \mathbf{p}_i, t) = f_i(\mathbf{x}_j, t)$. Finally, discrete time steps from t to $t + \Delta t$ are considered. Under discretization the Boltzmann equation in (1) becomes the Lattice-Boltzmann equation [60]

$$f_i(\mathbf{x}_j + \mathbf{c}_i \Delta t, t + \Delta t) = f_i(\mathbf{x}_j, t) + \Omega_i(\mathbf{x}_j, t) \Delta t. \quad (2)$$

The numerical integration of the Lattice-Boltzmann equation in time is split into two steps, collision and propagation. Collision is done by an approximation of the collision operator

in Eq. (2). The idea for the approximation of the collision operator is that the populations should relax towards the Maxwellian equilibrium distribution function in the absence of driving forces. Here, we use the multiple relaxation time scheme the relaxation is done in moment space of the populations with individual relaxation rates for the different moments [58,60]. Moments corresponding to conserved density and momentum do not have a relaxation time, while two relaxation rates related to bulk and shear viscosity, respectively, are chosen for moments corresponding to the stress tensor. For further discussion on the relaxation rates and moments used in our LBM implementation we refer to Refs. [58,62]. In the second step, the streaming, the populations after collision propagate according to the associated velocities.

We note that our LBM implementation supports adding thermal fluctuations to the fluid dynamics mimicking a given thermal energy $k_B T$ corresponding to fluctuating hydrodynamics [62]. Thermal fluctuations are taken into account by adding a random noise to those relaxed moments of the multiple relaxation time scheme which correspond to elements of the stress tensor [58,62]. We note that our approach using thermal fluctuations is different from considering a separate temperature field [63–65] as, e.g., required for convection flows [63]. Although they are not *per se* necessary, we employ thermal fluctuations in the present paper to speed up the onset of instabilities.

Although we do not consider solid walls in the present paper, we note that they can be realized by bounce back boundary conditions [60], where populations streaming towards nodes beyond a boundary are simply reflected. In the case of moving elastic objects (Sec. II B) having close contact to solid walls as it is considered, e.g., in Ref. [66], at least one fluid node between the object and the solid boundary is required in our method.

Typical LBM grids used in this work have dimensions of $126 \times 72 \times 72$ or $100 \times 100 \times 100$. Except in the case of the shear flow with moving boundaries in Sec. VI B, our LBM simulations use periodic boundary conditions for the fluid. A typical simulation run, e.g., in Fig. 6 consists of 10^7 time steps. Onset of Rayleigh-Plateau like instabilities in Fig. 7 typically appears after approximately 8×10^6 time steps. Simulations are performed with the simulation package ESPRESSO [67–69] which has been extended to include thin membranes using the immersed-boundary method described next.

B. Immersed-boundary method for membrane dynamics

The framework of the immersed-boundary method (IBM) [70–72] allows for the coupling of a cellular membrane to the suspending fluid, where the fluid is simulated using LBM as described in the previous section, Sec. II A. The IBM consists of two central steps: elastic forces acting on the membrane are transmitted to the fluid and due to no-slip boundary condition the massless membrane is advected with the local fluid velocity.

The membrane of a cell is represented by an infinitely thin elastic sheet in the framework of thin shell theory [73–75]. In our numerical simulations the membranes is discretized by a

set of nodes that are connected by flat triangles [51,76–78]. These represent the elastic membrane as a Lagrangian mesh immersed into the Eulerian fluid mesh as illustrated in Fig. 1(b).

Physical behavior of the membrane is characterized by appropriate constitutive laws which are described in Sec. III. The resulting forces are calculated on the deformed Lagrangian membrane mesh as described in Sec. IV. To transmit these forces into the fluid, the incompressible NSE for the fluid velocity $\mathbf{u}(\mathbf{x}, t)$ becomes [77]

$$\frac{\partial \mathbf{u}}{\partial t} + (\mathbf{u} \cdot \nabla) \mathbf{u} = -\frac{1}{\rho} \nabla p + \nu \Delta \mathbf{u} + \frac{1}{\rho} \int \mathbf{f}(X', t) \delta(X' - \mathbf{x}) d^2 X', \quad (3)$$

with p the pressure, ν the kinematic viscosity, ρ the density, and \mathbf{f} the membrane force per area acting on the membrane, which is parametrized by X' . The Dirac δ function ensures that the forces only act at the position of the actual membrane. Correspondingly, the Lattice-Boltzmann equation (2) changes to

$$\mathbf{F}_j = \int \mathbf{f}(X', t) \delta(X' - \mathbf{x}_j) d^2 X', \quad (4)$$

$$f_i(\mathbf{x}_j + \mathbf{c}_i \Delta t, t + \Delta t) = f_i(\mathbf{x}_j, t) + \Omega_i(\mathbf{x}_j, \mathbf{F}_j, t) \Delta t. \quad (5)$$

After an update of the fluid dynamics (LBM algorithm), which now include the forces from the membrane \mathbf{F}_j , the massless membrane nodes are advected with the local fluid velocity thus satisfying exactly the no-slip boundary condition [71]. Moving with the local fluid velocity is expressed for a membrane node $\mathbf{x}_n \in X'$ by [70,71]

$$\frac{d\mathbf{x}_n}{dt} = \mathbf{u}(\mathbf{x}_n(t), t) = \int \mathbf{u}(\mathbf{x}, t) \delta(\mathbf{x} - \mathbf{x}_n) d^3 x \quad (6)$$

with $\mathbf{u}(\mathbf{x}_n, t)$ being the fluid velocity at the position of the membrane node. In simulations Eq. (6) is integrated numerically using a Euler scheme in order to move each membrane node from time t to $t + \Delta t$.

The core of both steps, force transmission and movement with local fluid velocity, is the interpolation between the Eulerian fluid grid and the Lagrangian membrane grid. Considering the discretization and the resulting spatial mismatch of membrane nodes and fluid nodes, as illustrated in Fig. 1(b), it becomes clear that an interpolation is necessary. On the one hand the ideal point force at the site of a membrane node must be spread to the adjacent fluid nodes. On the other hand to obtain the local fluid velocity at the site of a membrane node the velocity of the adjacent fluid nodes is interpolated. This means the δ distributions in Eqs. (4) and (6) must be discretized. The interpolation between fluid and membrane is carried out by an eight-point stencil. As illustrated for two membrane nodes by the blue shaded cubes in Figs. 1(b), for each membrane node a cube containing the eight nearest fluid nodes is considered. A linear interpolation between the eight fluid points is performed [79].

A typical mesh for a cylinder in the present study contains 17 100 Lagrangian membrane nodes and 34 200 triangles. Simulating a cylindrical membrane, as it is partly shown in Fig. 4, is done using periodic boundary conditions for the fluid in all directions and for the membrane in the direction of the

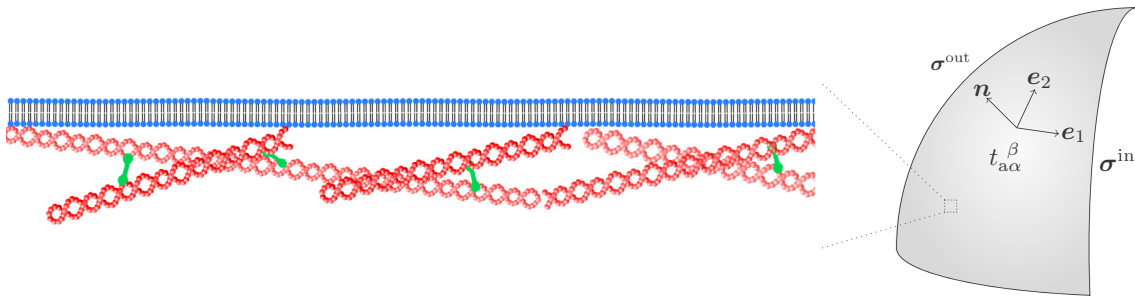


FIG. 2. Left: The cell cortex underlying the plasma membrane consists of cytoskeletal filaments and motor proteins. The latter constantly convert energy into mechanical work. Right: Membrane and cortex are condensed into a thin shell with normal vector \mathbf{n} and in-plane coordinates $\mathbf{e}_1, \mathbf{e}_2$. Mechanical work of motor proteins results in an active in-plane surface stress $t_{\alpha\beta}^{\beta}$. Forces from the cytoplasm inside the cell and from the extracellular medium onto the membrane can be treated by the 3D fluid stress tensors σ_{ij}^{in} and σ_{ij}^{out} .

cylinder axis. The latter is achieved by connecting membrane nodes at the end of the box to those at the beginning of the box.

C. Validation of LBM-IBM for passive, elastic membranes

Our implementation of the force calculation and the LBM-IBM have extensively been tested for passive, elastic membranes in previous publications [52,56,78,80–82].

The algorithm for the passive, elastic force calculation has been validated in Refs. [52,78] by comparison with exact results in static situations as well as for a capsule in shear flow. For red blood cells flowing through a rectangular channel very good agreement with *in vitro* experiments has been found [56,80].

The mixed LBM-IBM has been extensively validated for suspensions of red blood cells and rigid particles in complex geometries. In [81] the concentration profile of cells across the channel diameter (affected by cross streamline migration, which is triggered by the passive elasticity of the cells) has been successfully compared to well-established literature results. In Ref. [82] we have performed a validation based on the Zweifach-Fung effect for red blood cell suspension in branching channels. Furthermore, in the Supplementary Information of Ref. [82] we have shown red blood cell shapes for a single cell in tube flow and in a rectangular channel, respectively, that are in very good agreement with previous studies using dissipative particle dynamics [83] and the boundary integral method [56], respectively. The stability and behavior of stiff particles realized by IBM has been shown and validated in Refs. [81] and [82] for a spherical particle based on the Stokes relation (sphere pulled through a quiescent fluid as well as a fixed sphere in homogeneous flow) and an ellipsoidal particle rotating in shear flow.

In addition to the well-established passive elasticity, in this paper we introduce active elastic forces into simulations of membranes; see Sec. IV. We refer to Sec. V for the validation in the case of an active, elastic cell membrane.

III. FORCE BALANCE IN THIN SHELL FORMULATION INCLUDING ACTIVE STRESSES

A. Physical model

We consider the plasma membrane and the cytoskeletal filaments within the cell cortex, sketched in Fig. 2, as a

single physical entity which for simplicity we denote in the following as “the membrane.” Since this membrane is small in height compared to the cell diameter it is described as an infinitely thin shell. Thin shell theory treats the membrane as a two-dimensional manifold embedded in the three-dimensional environment, e.g., the intra- and extracellular fluid, thereby accounting for membrane curvature. For a condensed introduction into the required differential geometry on such manifolds as well as present conventions we refer the reader to Ref. [84] and Sec. 1 of the Appendix of this work, respectively. Here, we only note that Greek indices refer to coordinates on the membrane, i.e., $\alpha, \beta = 1, 2$, and Einstein summation convention is used. In this work, we consider the short-time limit of a purely elastic membrane noting that our algorithm can, without substantial difficulty, be extended to viscous or viscoelastic membranes.

The key quantity in the framework of thin shell theory are the in-plane surface stresses $t_{\alpha\beta}$ and moments $m_{\alpha\beta}$ [73,74,85]. The in-plane surface stress tensor or stress resultant [74] $t_{\alpha\beta}$ is the 3D elastic stress tensor for the material forming the membrane projected onto the membrane and integrated over the membrane thickness h [74] (dimensions of a force per length, i.e., N/m) [86]. It is a function of in-plane coordinates α, β and contains only in-plane components such that its matrix representation has dimensions 2×2 . Besides the in-plane surface stresses, we introduce the normal surface stress which is sometimes denoted as a shearing force [73] or transverse shear surface stress t_n^{α} [76,78]. The in-plane surface stresses $t_{\alpha\beta}$ contain a contribution from passive, elastic stresses as well as from active, force-generating mechanisms. Both contributions superpose linearly and thus can be treated separately [3,6]. Passive elastic stresses can be further split into different contributions such as, e.g., shear and bending resistances [50,78,88]. The moment tensor or stress couples [74] $m_{\alpha\beta}$ account for stress distribution across the membrane [74] (dimensions of a torque per unit length, i.e., N). We denote the corresponding normal surface moment by m_n . For explicit materials building up the membrane corresponding constitutive laws are required to derive explicit forms for in-plane surface stresses and moments.

Considering the passive, elastic properties of membranes in most cases constitutive laws are formulated in terms of a strain energy functional. For many biological membranes such

as red blood cells the passive, elastic forces arise from the resistance to shear deformation of the cortical, cytoskeletal network and the resistance to bending deformation and area dilatation of the plasma membrane. For shear resistance and area dilatation Skalak *et al.* [89] proposed an appropriate energy density functional,

$$w^{\text{SK}}(I_1, I_2) = \frac{\kappa_S}{12} [(I_1^2 + 2I_1 - 2I_2) + CI_2^2]. \quad (7)$$

The energy density depends on the invariants I_1, I_2 of the transformation between undeformed and deformed membranes [50,89]. Both invariants are defined in Eq. (A23) and (A24) of the Appendix. Resistance to shear is characterized by the shear modulus κ_S while resistance to area dilatation is characterized by $C\kappa_S$ with C much larger than unity for nearly area-incompressible membranes. For bending resistance the Helfrich model is used [78,90],

$$w^{\text{HF}} = 2\kappa_B(H - H_0)^2 + \kappa_K K, \quad (8)$$

with κ_B being the bending modulus, H denoting the local mean curvature, H_0 the spontaneous curvature, κ_K the Gaussian modulus, and K the Gaussian curvature. On the one hand, from a given energy functional, in-plane surface stresses and moments can be deduced by functional derivatives with respect to the strain tensor [74,91] and curvature tensor, respectively [78,92,93]. On the other hand, in numerical algorithms the explicit introduction of stresses is typically bypassed and forces on the nodes discretizing the membrane are often computed directly by deriving a discretized version of the energy functional, here equations (7) and (8), with respect to the node positions [50,78,94]. This approach is used here as well for the passive elastic forces. For bending force calculation we use the method denoted by B in Ref. [52].

For actively generated forces, however, this approach is not applicable since, due to their inherent nonequilibrium character, an energy functional cannot be defined in a strict sense. Instead, active contributions are usually given in terms of active stresses whose strength and direction can either be temporally constant or depend on additional quantities such a local concentration of motor proteins [6]. We will in the following construct a numerical method which explicitly applies these active stresses and derives the corresponding active forces on the discretized membrane nodes. These forces are then used to introduce a two-way coupling between active membrane dynamics and a surrounding hydrodynamic flow. For simplicity of demonstration and in order to connect to the analytical axisymmetric solutions of [3], we restrict ourselves to temporally constant active in-plane surface stresses. Time-dependent active stresses or active moments can be included without substantial modification of our numerical framework.

B. Force balance for deformable active membranes embedded in a 3D fluid

As sketched in Fig. 2, we consider a membrane immersed in an external fluid and enclosing an internal fluid, the cytosol. Coupling of the membrane to the internal and external fluid with the stress tensor σ_{ij}^{in} and σ_{ij}^{out} , respectively, is described

by the traction jump [51,76,88]

$$-f_j = (\sigma_{ij}^{\text{out}} - \sigma_{ij}^{\text{in}})n_i \quad (9)$$

with Latin subscripts denoting 3D coordinates and the components n_i of the local unit normal vector onto the membrane pointing towards the external fluid. Transforming to the in-plane coordinate system the traction jump can—as a vector on the membrane in general—be decomposed into tangential and normal components,

$$-f = -f^\alpha e_\alpha - f^n n. \quad (10)$$

Neglecting membrane inertia the traction jump between the internal and external fluid is balanced by membrane forces (per unit area). In the present situation, these arise from elastic and active contributions. Looking ahead, the numerical method, which we will construct in the following section, will compute elastic forces f_e^α and f_e^n via the classical discretized energy functional route, bypassing for simplicity the introduction of elastic stresses, while active forces need to be computed explicitly from active stresses and moments. It is thus convenient to write the force balance for a thin shell [3,6,73,88,91] as

$$\nabla'_\alpha t_a^{\alpha\beta} + C'_{\alpha\beta} t_{na}^\alpha + f_c^\beta = f^\beta, \quad (11)$$

$$\nabla'_\alpha t_{na}^\alpha - C'_{\alpha\beta} t_a^{\alpha\beta} + f_c^n = f^n, \quad (12)$$

$$\nabla'_\alpha m_a^{\alpha\beta} + C'_{\alpha\beta} m_{na}^\alpha = \epsilon'^{\beta\alpha} t_{na}^\alpha, \quad (13)$$

$$\nabla'_\alpha m_{na}^\alpha - C'_{\alpha\beta} m_a^{\alpha\beta} = -\epsilon'_{\alpha\beta} t_a^{\alpha\beta}, \quad (14)$$

with active contributions to the in-plane and normal surface stress $t_a^{\alpha\beta}, t_{na}^\alpha$ and active contributions to the moments $m_a^{\alpha\beta}, m_{na}^\alpha$. The geometrical quantities are the curvature tensor $C'_{\alpha\beta}$, the Levi-Civita tensor $\epsilon'_{\alpha\beta}$, and the covariant derivative ∇'_α taken on the deformed membrane as defined in the Appendix. On the basis of Eqs. (11) and (12) it becomes clear that the negative traction jump is the force exerted from the membrane on the fluid. We now consider the active contributions to the traction jump in the case of vanishing active moments ($m_a^{\alpha\beta} = m_{na}^\alpha = 0$) and vanishing active transverse shear surface stress ($t_{na}^\alpha = 0$),

$$f_a^\beta = \nabla'_\alpha t_a^{\alpha\beta} = t_{a,\alpha}^{\alpha\beta} + \Gamma_{\alpha\gamma}^{\prime\alpha} t_a^{\gamma\beta} + \Gamma_{\alpha\gamma}^{\prime\beta} t_a^{\alpha\gamma}, \quad (15)$$

$$f_a^n = -C'_{\alpha\beta} t_a^{\alpha\beta}, \quad (16)$$

where we have used the definition of the covariant derivative on the membrane [see Eq. (A20)] in the first line. To simulate the temporal dynamics and coupling to the external fluid of our discretized active membrane, we need to compute the forces on each membrane node corresponding to active in-plane surface stresses. According to Eqs. (15) and (16) the curvature tensor, the Christoffel symbols, and the active in-plane surface stresses together with their derivatives have to be known locally on each node on a deformed surface. In the next section we will develop an algorithm to compute these quantities numerically for the discretized thin shell embedded in a 3D environment.

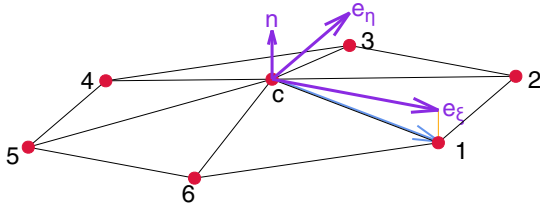


FIG. 3. The central node at \mathbf{r}_c is surrounded by N neighbors. The discretization is chosen such that all nodes on the cylindrical mesh in Fig. 4 have six neighbors. For the ellipsoid in Fig. 10, topology requires at least 12 triangles with $N = 5$ while all others have $N = 6$. From the surrounding triangles a local normal vector \mathbf{n} at \mathbf{r}_c can be computed. Together with the position of one neighbor local in-plane coordinate vectors \mathbf{e}_ξ , \mathbf{e}_η can be constructed. Applying the first step of Gram-Schmidt orthonormalization leads to \mathbf{e}_ξ and the cross product of \mathbf{n} and \mathbf{e}_ξ to \mathbf{e}_η .

IV. ALGORITHM FOR ACTIVE FORCE CALCULATION ON ARBITRARILY SHAPED DISCRETIZED MEMBRANES

Our algorithm starts from active in-plane surface stresses and computes the corresponding active forces on the discretized membrane. The key ingredient of the algorithm is the discrete computation of geometrical properties on the discretized, deformed membrane, such as the curvature tensor or Christoffel symbols. This is achieved by a parabolic fitting procedure and using the force balance equations (15) and (16) as described in Sec. IV B based on a local coordinate system which we introduce in Sec. IV A. With these forces the active membrane dynamics can be bidirectionally coupled to a surrounding fluid flow which is computed separately using either an overdamped dynamics or a Lattice-Boltzmann method.

A. Local coordinate system

As sketched in Fig. 3 each membrane node \mathbf{r}_c has a neighborhood consisting of N nodes, which are labeled in an ordered fashion around the central node. The choice of the starting node is arbitrary initially, but has to be retained through the simulation. In Fig. 12 we provide evidence that the choice of the starting node does not affect simulation results. At the site of the central node a local coordinate system (\mathbf{e}_ξ , \mathbf{e}_η , \mathbf{n}) can be defined, where we denote the in-plane coordinate vectors [\mathbf{e}_α ($\alpha = \xi, \eta$) in the Appendix] by \mathbf{e}_ξ and \mathbf{e}_η . We determine the local unit normal vector \mathbf{n} by the mean weight by angle of the normal vectors on the surrounding triangles [95]. The first in-plane vector \mathbf{e}_ξ is calculated using the vector from the central node to the first neighbor $\mathbf{x}_1 = \mathbf{r}_1 - \mathbf{r}_c$. The first step of the Gram-Schmidt orthogonalization is applied and the vector is normalized,

$$\mathbf{e}_\xi = \frac{\mathbf{x}_1 - (\mathbf{x}_1 \cdot \mathbf{n})\mathbf{n}}{|\mathbf{x}_1 - (\mathbf{x}_1 \cdot \mathbf{n})\mathbf{n}|}. \quad (17)$$

The second in-plane coordinate vector is calculated by the cross product

$$\mathbf{e}_\eta = \frac{\mathbf{n} \times \mathbf{e}_\xi}{|\mathbf{n} \times \mathbf{e}_\xi|}. \quad (18)$$

Using this method we can assign to every node at every time step a unique coordinate system which is adapted to the local deformed membrane geometry. We denote coordinates along \mathbf{e}_ξ and \mathbf{e}_η by ξ and η , respectively. In a figurative sense, we comove with a cytoskeletal filament initially positioned at \mathbf{r}_c pointing towards \mathbf{x}_1 .

B. Parabolic fitting

To obtain local geometrical quantities such as the curvature tensor on the deformed membrane we perform a parabolic fitting procedure based on the local coordinate system derived in the previous section. An arbitrary point $\bar{\mathbf{r}}$ in the neighborhood of the central node \mathbf{r}_c can be expressed by a Taylor expansion around \mathbf{r}_c up to the second order. For the i th component of the vector $\bar{\mathbf{r}}$ with $i = x, y, z$ we obtain

$$\bar{r}_i(\xi, \eta) \approx r_i^c + A_i\xi + B_i\eta + \frac{1}{2}(C_i\xi^2 + D_i\eta^2 + 2E_i\xi\eta), \quad (19)$$

with ξ, η being the coordinates along \mathbf{e}_ξ and \mathbf{e}_η , respectively. Using this expression we can apply a parabolic fitting procedure (see also [51,52] where a similar procedure has been used to compute passive bending forces) considering all N neighboring nodes with a squared deviation from the fitted surface,

$$\chi_i^2 = \sum_{v=1}^N (r_i^v - \bar{r}_i^v)^2, \quad (20)$$

with $i = x, y, z$. By minimizing the χ_i^2 we obtain the coefficients A_i – E_i . Using Eq. (19) we are able to analytically calculate the derivative of χ_i^2 with respect to the coefficients A_i – E_i . The derivative of χ_i^2 being zero in case of minimization then leads to a linear equation system for A_i – E_i . This linear equation system is solved numerically in the simulation using lower-upper decomposition. The paraboloid fitted to the neighborhood around \mathbf{r}_c provides a good approximation of the local curvature for typical cell shapes [52]. By construction, the fitting coefficients equal the derivatives of the membrane parametrization vector $\bar{\mathbf{r}}$ with respect to local coordinates at the site of the central node,

$$A_i = \bar{r}_{i,\xi}, \quad B_i = \bar{r}_{i,\eta}, \quad C_i = \bar{r}_{i,\xi\xi}, \quad D_i = \bar{r}_{i,\eta\eta}, \quad E_i = \bar{r}_{i,\xi\eta}, \quad (21)$$

or, equivalently,

$$\mathbf{A} = \bar{\mathbf{r}}_{,\xi}|_{\mathbf{r}_c}, \quad \mathbf{B} = \bar{\mathbf{r}}_{,\eta}|_{\mathbf{r}_c}, \quad \mathbf{C} = \bar{\mathbf{r}}_{,\xi\xi}|_{\mathbf{r}_c}, \\ \mathbf{D} = \bar{\mathbf{r}}_{,\eta\eta}|_{\mathbf{r}_c}, \quad \mathbf{E} = \bar{\mathbf{r}}_{,\xi\eta}|_{\mathbf{r}_c}. \quad (22)$$

Thus, we are able to calculate geometrical quantities, as defined in the Appendix, at the site of the central node in local coordinates with $\tilde{\alpha}, \tilde{\beta}, \tilde{\gamma} = \xi, \eta$, such as the metric tensor

$$g_{\tilde{\alpha}\tilde{\beta}} = \begin{pmatrix} \mathbf{A} \cdot \mathbf{A} & \mathbf{A} \cdot \mathbf{B} \\ \mathbf{B} \cdot \mathbf{A} & \mathbf{B} \cdot \mathbf{B} \end{pmatrix}, \quad (23)$$

the curvature tensor

$$C_{\tilde{\alpha}\tilde{\beta}} = \begin{pmatrix} -\mathbf{C} \cdot \mathbf{n} & -\mathbf{E} \cdot \mathbf{n} \\ -\mathbf{E} \cdot \mathbf{n} & -\mathbf{D} \cdot \mathbf{n} \end{pmatrix}, \quad (24)$$

and the derivatives of the metric tensor, e.g.,

$$g_{\xi\xi,\xi} = (\mathbf{A} \cdot \mathbf{A})_{,\xi} = 2\mathbf{A} \cdot \mathbf{C}, \quad (25)$$

which are necessary for the calculation of the Christoffel symbols. The tensor $g^{\tilde{\alpha}\tilde{\beta}}$ is obtained by inverting the metric $g_{\tilde{\alpha}\tilde{\beta}}$ since $g_{\tilde{\alpha}\tilde{\gamma}}g^{\tilde{\gamma}\tilde{\beta}} = \delta_{\tilde{\alpha}}^{\tilde{\beta}}$. Thus, we can further calculate $C_{\tilde{\alpha}}^{\tilde{\beta}} = C_{\tilde{\alpha}\tilde{\gamma}}g^{\tilde{\gamma}\tilde{\beta}}$ and $C^{\tilde{\alpha}\tilde{\beta}} = g^{\tilde{\alpha}\tilde{\gamma}}C_{\tilde{\gamma}}^{\tilde{\beta}}$. We note that this procedure can be used without any restriction on the deformed membrane as well. Correspondingly, we obtain the metric tensor $g'_{\tilde{\alpha}\tilde{\beta}}$, the curvature tensor $C'_{\tilde{\alpha}\tilde{\beta}}$, and the Christoffel symbols on the deformed surface.

Equation (15) for the in-plane, active force includes a partial derivative $t_{a,\alpha}^{\alpha\beta}$, which is calculated using another parabolic fitting procedure. As done in Eq. (19) for the position in local coordinates we can expand the active in-plane surface stress $t^{\alpha\beta}$ around the components of the central node $t_a^{c\alpha\beta}$,

$$\begin{aligned} \tilde{t}_a^{\alpha\beta}(\xi, \eta) &= t_a^{c\alpha\beta} + A_a^{\alpha\beta}\xi + B_a^{\alpha\beta}\eta \\ &+ \frac{1}{2}(C_a^{\alpha\beta}\xi^2 + D_a^{\alpha\beta}\eta^2 + 2E_a^{\alpha\beta}\xi\eta). \end{aligned} \quad (26)$$

Corresponding to Eq. (20) we consider here the squared deviation from the expanded active stress $\tilde{t}_a^{\tilde{\alpha}\tilde{\beta}}$,

$$\chi_a^2 = \sum_{\nu=1}^N (t_a^{\tilde{\alpha}\tilde{\beta}\nu} - \tilde{t}_a^{\tilde{\alpha}\tilde{\beta}\nu})^2, \quad (27)$$

with $t_a^{\tilde{\alpha}\tilde{\beta}\nu}$ being one component of the active in-plane surface stress of the ν th neighboring node in local coordinates. Thus, the corresponding fitting coefficients A_a and B_a represent the partial derivative of the active in-plane surface stress component with respect to the coordinate ξ and η , respectively, whereas the coefficients $C_a - E_a$ represent the second derivatives. We note that the matrix for the fit is the same as for the position. We perform one fitting procedure for each component, i.e., $\tilde{\alpha} = \xi, \eta$ and $\tilde{\beta} = \xi, \eta$.

With the method proposed here, we are able to calculate the covariant derivative, which consists of a partial derivative and Christoffel symbols, and perform the contraction of active in-plane surface stress tensor and curvature tensor in the local coordinate system to determine the traction jump given by Eqs. (15) and (16), which we repeat here for the deformed membrane in the local coordinate system

$$f_a^{\tilde{\beta}} = t_{a,\tilde{\alpha}}^{\tilde{\alpha}\tilde{\beta}} + \Gamma_{\tilde{\alpha}\tilde{\gamma}}^{\tilde{\alpha}} t_a^{\tilde{\gamma}\tilde{\beta}} + \Gamma_{\tilde{\alpha}\tilde{\gamma}}^{\tilde{\beta}} t_a^{\tilde{\alpha}\tilde{\gamma}}, \quad (28)$$

$$f_a^n = -C'_{\tilde{\alpha}\tilde{\beta}} t_a^{\tilde{\alpha}\tilde{\beta}}, \quad (29)$$

in the case of vanishing active moments and vanishing transverse shear stress. We note that the in-plane surface stress is the analog of the Cauchy stress tensor in three dimensions [3,88] and thus acting on the deformed membrane [96]. Equations (28) and (29) give the discrete forces (per area) on one membrane node. These forces then enter the fluid solver as illustrated in Sec. II B or are used for the relaxation dynamics in the overdamped limit (see Sec. 3 of the Appendix).

To convert the traction jump from Eqs. (28) and (29) into a nodal force we use Meyer's mixed area approach [78,95]: in the case of nonobtuse triangles the area is calculated using

Voronoi area A_{Voronoi} defined by

$$A_{\text{Voronoi}} = \frac{1}{8} \sum_{\nu=1}^N [\cot(\alpha_\nu) + \cot(\beta_\nu)] |\mathbf{x}_\nu| \quad (30)$$

with the angles α and β opposite to the edge connecting the central node and the ν th neighbor node within the adjacent triangles and in the case of obtuse triangles the midpoint of \mathbf{x}_ν that is opposite of the obtuse angle is chosen instead of the circumcenter point for each triangle.

C. Specification of active in-plane surface stress

Active stresses in membranes are often generated by ATP-fueled molecular motors “walking” along cross-linked rodlike structures such as actin filaments or microtubules. As a direct consequence, active stresses are often anisotropic with the direction of contractile or extensile stresses specified in a material frame moving and deforming along with the membrane itself. This naturally leads to a convenient specification of the active in-plane surface stress tensor $t_a^{\alpha\beta}$ in the local coordinate system introduced in Sec. IV A. Since the labeling of the neighbors around each node remains unchanged throughout the simulation, the distance vector $\mathbf{x}_1 = \mathbf{r}_1 - \mathbf{r}_c$ represents a material vector. Its normalized in-plane counterpart e_ξ , given in Eq. (17), together with e_η , given in Eq. (18), constitute the associated material frame. Imagining one cytoskeletal filament for an illustrative picture, the anchoring position of the filament is tracked by the node position \mathbf{r}_c , while the orientation of the filament is tracked by the fixed choice of the first neighbor \mathbf{r}_1 . We again note that the choice of the starting node for the labeling, here 1, does not affect simulation results, as shown in Fig. 12.

The active in-plane surface stress tensor $t_a^{\alpha\beta}$ itself is not computed by our method but needs to be specified as an input quantity according to a corresponding constitutive law for the surface stress [3,6]. Our algorithm allows for an arbitrary choice of active in-plane surface stress, subject to condition (14) for vanishing active moments, including spatially heterogeneous, anisotropic or time-dependent stresses. For the latter, coupling to a convection-diffusion model of active substances such as ATP or myosin (with the magnitude of $t_a^{\alpha\beta}$ proportional to local ATP or myosin concentration) is methodologically possible. Thus, if the concentration field of ATP or myosin is solved or prescribed on the membrane, e.g., by discretizing the convection-diffusion equation, the active stress can be calculated from the local concentration. The corresponding active forces and their coupling to the surrounding fluid dynamics are then straightforwardly achieved by the present algorithm, which allows for a spatially varying active stress. In the present work, we consider only temporally constant active stresses. Active stresses can thus conveniently be specified in the initial configuration of the membrane. For this, we first choose an intuitive coordinate system ($\mathbf{e}_1, \mathbf{e}_2$) appropriate for the initial shape of the undeformed cell membrane. The active in-plane surface stresses in this coordinate system are of the form

$$t_{a\alpha}^\beta = \begin{pmatrix} t_{a1}^1 & t_{a1}^2 \\ t_{a2}^1 & t_{a2}^2 \end{pmatrix}, \quad (31)$$

where the mixed form with upper and lower index is chosen such that the right-hand side contains physical material-specific constants with dimensions of N/m [3]. Because of the dynamical deformation of the membrane, the active in-plane surface stress of Eq. (31) needs to be mapped into the local coordinate system at each node. This can be achieved by mapping the coordinate system $(\mathbf{e}_1, \mathbf{e}_2)$ to the local coordinate system $(\mathbf{e}_\xi, \mathbf{e}_\eta)$.

In many situations, the intuitive coordinate system $(\mathbf{e}_1, \mathbf{e}_2)$ will correspond to cylindrical coordinates or spherical coordinates, e.g., for a rounded cell during mitosis [14]. By construction of the intuitive in-plane coordinate system and the local coordinate system both normal vectors, e.g., \mathbf{e}_r , for a cylinder or a sphere and the local \mathbf{n} are equal initially. Thus, the initial in-plane coordinate system $(\mathbf{e}_1, \mathbf{e}_2)$ can be converted directly into the local coordinate system $(\mathbf{e}_\xi, \mathbf{e}_\eta)$ on every node individually,

$$t_a^{\tilde{\alpha}\tilde{\beta}} = \mathcal{D} t_a^{\alpha\beta} \mathcal{D}^{-1}, \quad (32)$$

with \mathcal{D} being a rotation matrix around the local unit normal vector \mathbf{n} , with $\alpha = 1, 2$ and $\tilde{\alpha} = \xi, \eta$. We thus obtain the active in-plane surface stress along the local coordinate vectors \mathbf{e}_ξ and \mathbf{e}_η . The rotation in Eq. (32) is performed once at the beginning of a simulation. Since the local coordinate system $\mathbf{e}_\xi, \mathbf{e}_\eta$ is comoving with the membrane material, the active in-plane surface stress tensor $t_a^{\tilde{\alpha}\tilde{\beta}}$, expressed in these coordinates, does not change over time.

The parabolic fitting procedure in Eq. (27) requires the difference in active stress between neighboring nodes. The differences in active stress are calculated in the intuitive coordinate system, in which the active stresses are prescribed. Because active stresses do not change in time, calculation of the differences can be done also once at the beginning of the simulation. Projection into the local coordinate system for each node is done in the same way as for active stresses in Eq. (32).

Along a certain direction, the cytoskeletal filaments may tend to contract or to expand, respectively, resulting in a contractile or extensile active in-plane surface stress [37]. The contractile or extensile nature of the cytoskeletal filaments manifests itself in the sign of the active stress, namely a positive (negative) stress corresponds to a contractile (extensile) nature. In active matter consisting of cytoskeletal filaments, active stresses often possess different signs in different directions. Imagining two antiparallel polar filaments that are cross-linked by a motor protein walking in opposite directions on both filaments, a relative extensile shift of both filaments together with a lateral contraction occurs.

V. VALIDATION

In this section we provide an in-depth validation of our algorithm to compute the dynamics of active membranes embedded in a 3D fluid. For this, we first compute the deformation obtained when an initially unstressed cylindrical membrane is subjected to a localized perturbation due to active stresses. Our numerical results are in excellent agreement with analytical predictions by Berthoumieux *et al.* [3] which were obtained using a Green's-function approach in the limit of small deformations. Next, we apply homogeneous

active stresses again to an initially cylindrical membrane. In agreement with the analytical predictions of [3], we observe two kinds of axisymmetric instabilities. Going beyond the axisymmetric calculations of [3], our numerical method then predicts the existence of a third nonaxisymmetric instability.

To account for the dynamics of the surrounding fluid, we employ two qualitatively different approaches. In the first approach, we use simple overdamped dynamics such that the surrounding fluid acts purely as a viscous frictional damping; see Sec. 3 of the Appendix. In the second approach, we consider the full fluid dynamics of the surrounding liquid by solving the Navier-Stokes equations using a Lattice-Boltzmann method; see Sec. II A. Two-way coupling to the active membrane dynamics is provided by the immersed-boundary method, as detailed in Sec. II B.

A. Green's function formalism

We here briefly recall the central analytical results of [3] which will be used to validate our numerical computations in the subsequent paragraphs. In [3] the active in-plane surface stresses have the form

$$t_{a\alpha}^{\beta} = \begin{pmatrix} T_a + T_a^z \delta(z) & 0 \\ 0 & T_a + T_a^\phi \delta(z) \end{pmatrix} \quad (33)$$

on the initially unperturbed cylinder surface where the local coordinates α and β correspond to polar coordinates z and ϕ , respectively (cf. Sec. IV C). We note that the component t_{az}^z being positive represents a contractile stress along the cylinder axis and t_{az}^z being negative represents an extensile stress, as seen on the basis of the buckling instability reported for negative stress in Ref. [3]. A positive $t_{a\phi}^\phi$ represents a contractile stress in azimuthal direction, which causes a contraction of the cylinder. The latter becomes clear by considering the deformation caused by T_a^ϕ according to the Green's function. In Eq. (33) T_a represents an isotropic homogeneous background active stress while T_a^z and T_a^ϕ are the amplitudes of point active stresses along each of the two coordinate axes. $\delta(z)$ is the Dirac delta distribution.

As in Ref. [3], we focus on the radial deformation $u_r(z)$ of a cylinder with initial radius R resulting from an azimuthal in-plane surface stress T_a^ϕ . At the end of Sec. V C we perform a validation for an axial in-plane surface stress T_a^z . Berthoumieux *et al.* [3] consider a 3D elastic material and perform a projection onto the membrane resulting in the surface stretching modulus S and the bending modulus B as surface elastic parameters, together with the 3D Poisson ratio ν . The strength of the homogeneous active in-plane stress is measured by the dimensionless number $g = \frac{T_a}{S}$ and bending forces are quantified by the relative bending modulus $b = \frac{B}{SR^2}$. The radial deformation of a cylindrical shell with radius R is then given by the Green's function $G_{r\phi}(z)$ as

$$\frac{u_r(z)}{R} = -G_{r\phi}(z) T_a^\phi = -\frac{T_a^\phi}{RS} G(z). \quad (34)$$

An expression for $G(z)$ is given in Fourier space [3] by

$$G(q) = \frac{1}{2b(Rq)^4 + (g - 2\nu b)(Rq)^2 + 2(1 - \nu^2) - g} \quad (35)$$

with $G(z)$ being the inverse Fourier transform of $RG(q)$.



FIG. 4. (a) We consider a local increase in active in-plane surface stress of a cylindrical membrane. (b), (c) Membrane meshes as in main text with two different resolutions, (a) $\Delta z = 0.2$, $\Delta \phi = 0.2$ and (b) $\Delta z = 0.1$, $\Delta \phi = 0.15$, respectively.

In our numerical method, elastic forces are derived from the Skalak and Helfrich energy functionals as defined in Eqs. (7) and (8), respectively, which represent an accurate and widely used description of the elastic properties of biological cell membranes. In the limit of small deformations we show in Sec. 2 of the Appendix that the Skalak and Helfrich model, which we use in this study, and the elastic model used by Berthoumieux *et al.* [3] are related by $S = \frac{2}{3}\kappa_S$ and $B = \frac{1}{2}\kappa_B$. In the following these relations are used to calculate the Green's function in Eq. (35) and the corresponding deformation in Eq. (34) for comparison to our simulations. We furthermore set the bulk Poisson ratio $\nu = \frac{1}{2}$, corresponding to a 3D incompressible material, and the Skalak parameter $C = 1$. Then the Skalak law becomes equivalent to the Neo-Hookean membrane law which is built to model a membrane made of a 3D incompressible material [88]. For the shear modulus S we show in Sec. 2 of the Appendix that the shear related in-plane surface stresses determining the Green's function agree between the Skalak law and the model used by Ref. [3] in the limit of small deformation. Although we can relate the parameter of Helfrich model to the model used in Berthoumieux *et al.* [3] by $B = \frac{1}{2}\kappa_B$ as illustrated in the Appendix, the Helfrich model alters the in-plane surface stresses, which in turn alter the Green's function. However, since we consider the limit $B \rightarrow 0$ this has no effect for the Green's function used for validation of our simulations.

B. Singular active perturbation

We start by simulations of overdamped dynamics of an initially stress-free cylindrical shell subjected to a local increase in active in-plane surface stress. The active in-plane surface stress from Eq. (33) simplifies to

$$t_{a\alpha}^\beta = \begin{pmatrix} 0 & 0 \\ 0 & T_a^\phi \end{pmatrix} \delta(z), \quad (36)$$

as sketched in Fig. 4(a). Simulations are carried out with $R = 1$, $\kappa_S = 1$, $C = 1$, $\kappa_B = 0.001$, and $T_a^\phi = -0.01$ in simulation units. We employ two different triangulations of the cylindrical shape which are shown in Figs. 4(b) and 4(c). In the coarse mesh, the axial distance between rings of nodes is $\Delta z = 0.2$ and the azimuthal spacing is about $\Delta \phi = 0.2$ radians. The finer mesh uses an axial spacing of $\Delta z = 0.1$ and an azimuthal spacing of about $\Delta \phi = 0.15$ radians.

In Fig. 5 we compare the final shape of the shell as observed in 3D simulations for the two different resolutions and compare it to the prediction of the Green's function in Eq. (34). The analytical Green's function shows a peak in deformation of finite width centered at the site of active in-plane surface stress perturbation ($z = 0$) that decays with increasing distance, reaches a shallow minimum at around $z \approx \pm 0.7$,

and then approaches zero for $z \rightarrow \pm\infty$. Although for both resolutions the resulting amplitude of the peak in deformation from the simulation is close to the Green's function and both show a similar shape, we observe a significant deviation of the 3D simulation results from the theoretical expectation. Especially, the simulations cannot reproduce correctly the predicted shallow minima next to the main peak. We note that the deviations for singular perturbation also appear using the Lattice-Boltzmann-immersed-boundary method instead of overdamped dynamics (results not shown).

This observed deviation can be explained by the idealized singular nature of the active in-plane surface stress which is impossible to accurately reproduce on a discretized membrane shape. Along the cylinder axis, i.e., along the z direction, only one ring of nodes with $z = 0$ is attributed with finite active in-plane surface stress. Correspondingly, only these nodes are subjected to active forces and cause the neighboring nodes to move due to the elastic nature of the cylinder. We note that the central nodes—with active in-plane surface stress—experience a significantly larger deformation than their direct, adjacent neighbor nodes, as seen in Fig. 5. This steep gradient in deformation resulting in locally very large curvature cannot be completely resolved by the parabolic fit. Thus, the procedure fails to resolve the deformation caused by a point perturbation, although obtained deformations are similar in shape and nearly match the amplitude of the Green's function. Given that in real applications, all perturbations can be expected to be nonsingular, we proceed to investigate the behavior of our algorithm for spatially smooth active stresses.

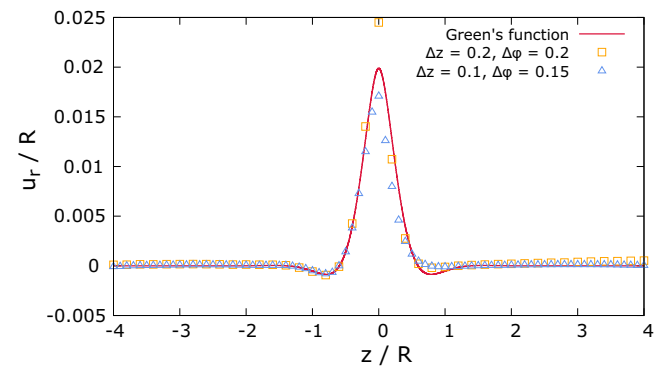


FIG. 5. The final deformation resulting from three-dimensional simulations of a singular active stress shows the same shape as the analytical prediction of the Green's function. However, peak height deviates from the theory. This can be attributed to the singular nature of the perturbation which is difficult to resolve numerically. Deformations are obtained for the parameter set $T_a^\phi = -0.01$, $\kappa_S = 1$, $C = 1$, and $\kappa_B = 10^{-3}$.

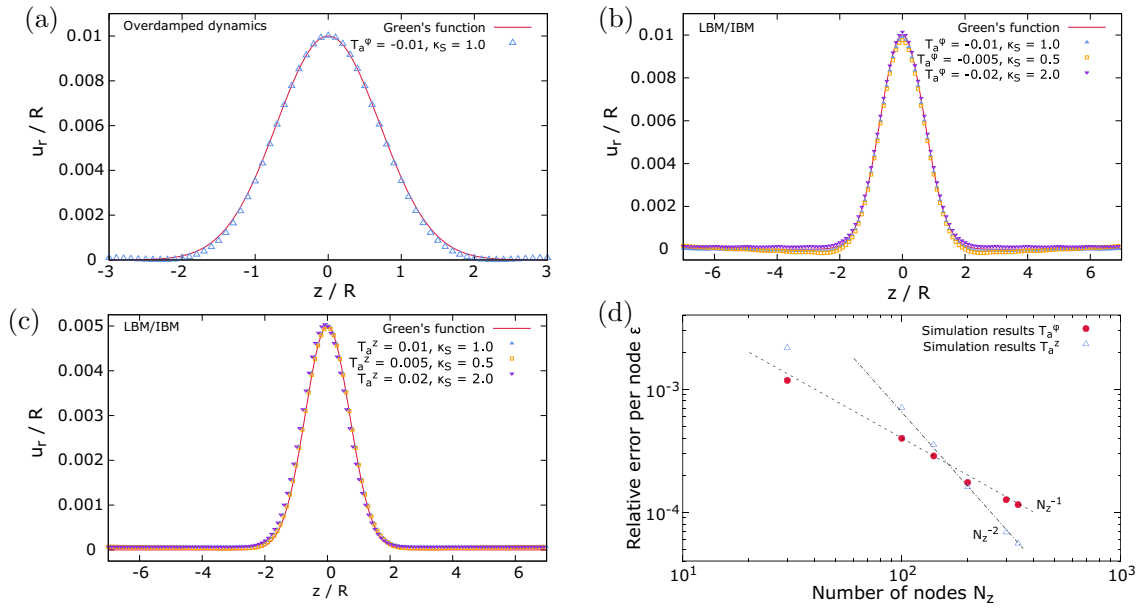


FIG. 6. (a) Comparison of the deformation obtained by the 3D overdamped dynamics with the theoretical expectation for a cylindrical shell with 160 nodes along z direction subjected to a Gaussian distributed active in-plane surface stress with $\kappa_S = 1$, $\kappa_B = 10^{-5}$, and $T_a^\phi = -0.01$. 3D simulations are in very good agreement with the theory. (b) Comparison of the deformation obtained with LBM-IBM simulations for $C = 1$ and $\kappa_B \approx 10^{-4}$ with the theoretical prediction for the same setup with perturbation in ϕ stress T_a^ϕ and (c) with perturbation in z stress T_a^z . (d) Increasing resolution of both membrane and fluid mesh show convergence of the relative error per node for the parameter set of (b) for a perturbation in T_a^ϕ (red dots) as well as for the parameter set of (c) for a perturbation in T_a^z (blue triangles). The error decreases proportional to N_z^{-1} and proportional to N_z^{-2} , respectively. In (b) and (c) simulations are done for 300 nodes in z direction.

C. Localized smooth perturbation

As a prototypical smooth distribution, we choose a Gaussian distributed active in-plane surface stress of the form

$$t_{\alpha\alpha}^\beta = \begin{pmatrix} 0 & 0 \\ 0 & T_a^\phi \end{pmatrix} \exp\left(-\frac{z^2}{R^2}\right), \quad (37)$$

where T_a^ϕ is again a constant amplitude. For this distribution, the predicted deformation can be obtained by superposing a distribution of Green's functions [Eq. (34)] leading to the deformation

$$\frac{u_r(z)}{R} = -\int_{-\infty}^{\infty} G_{r\phi}(z-z') T_a^\phi \exp(-z'^2/R^2) dz'. \quad (38)$$

We use the Green's function in Fourier space given in Eq. (35) and the Fourier transform of the Gaussian

$$\int_{-\infty}^{\infty} \exp(-z^2/R^2) \exp(-iqz) d\left(\frac{z}{R}\right) = \sqrt{\pi} \exp\left(-\frac{1}{4}(Rq)^2\right).$$

Using the convolution theorem in Fourier space and transforming back to real space leads to

$$\frac{u_r(z)}{R} = -\frac{1}{2\pi} \frac{R}{S} \int_{-\infty}^{\infty} \frac{\sqrt{\pi} T_a^\phi \exp\left[-\frac{1}{4}(Rq)^2\right]}{2b(Rq)^4 - 2vb(Rq)^2 + 2(1-\nu^2)} \times \exp(iqz) dq.$$

The integral can be solved analytically in the limit of small bending rigidity $b \ll 1$ (which corresponds well with the chosen simulation parameters) to obtain

$$\frac{u_r(z)}{R} = -\frac{T_a^\phi}{S} \frac{1}{2(1-\nu^2)} \exp\left(-\frac{z^2}{R^2}\right). \quad (39)$$

Alternatively, we can solve the integral in Eq. (38) numerically, which does not lead to any differences for small bending modulus (results not shown).

In Fig. 6(a) we compare the 3D simulation results using overdamped dynamics for parameters $R = 1$, $\kappa_S = 1$, $C = 1$, $\kappa_B = 10^{-5}$, and $T_a^\phi = -0.01$ to the analytical prediction of Eq. (39). The Gaussian distribution of active in-plane surface stress leads to a much smoother and broader peak of deformation than the singular perturbation of the previous subsection. Our simulation results are now in very good agreement with the theoretical prediction.

To go one step further, with applications in mind such as an active membrane in a flowing liquid, we now replace the simple overdamped fluid dynamics with a full Navier-Stokes dynamics solved by the Lattice-Boltzmann method and coupled to the active membrane via the immersed-boundary method as described in Sec. II. In Fig. 6(b) we compare simulation results obtained by the LBM-IBM to the theoretical Green's function. Again, our simulations are in very good agreement with the analytical theory. In Fig. 6(b) we include three sets of active in-plane surface stress and shear modulus with constant $\kappa_B = 0.00018$ which are chosen such that the ratio of active in-plane surface stress and shear modulus g remains constant. Thus, the Green's function predicts identical deformation in all three cases which is indeed observed in our simulations.

We now proceed to the validation for a perturbation in z stress, i.e., the active in-plane surface stress takes the form

$$t_{\alpha\alpha}^\beta = \begin{pmatrix} T_a^z & 0 \\ 0 & 0 \end{pmatrix} \exp\left(-\frac{z^2}{R^2}\right), \quad (40)$$

with the constant amplitude T_a^z . Corresponding to Eq. (38) the deformation can be obtained by [3]

$$\frac{u_r(z)}{R} = \int_{-\infty}^{\infty} G_{rz}(z-z') T_a^z \exp(-z'^2/R^2) dz', \quad (41)$$

with $G_{rz}(s) = \frac{\nu}{RS} G(z)$ and takes in analogy to Eq. (39) the form

$$\frac{u_r(z)}{R} = \frac{T_a^z}{S} \frac{\nu}{2(1-\nu^2)} \exp\left(-\frac{z^2}{R^2}\right). \quad (42)$$

In Fig. 6(c) we compare LBM-IBM simulation results for three different perturbations and shear moduli for $R = 1$, $C = 1$, and $\kappa_B = 0.00018$ to the theory. Our simulation results are in very good agreement with the theory and by comparing Figs. 6(b) and 6(c) we observe half the maximum deformation for $|T_a^\phi| = |T_a^z|$ which is indeed predicted by the theory for $\nu = \frac{1}{2}$.

As a further test of algorithm accuracy we now perform a convergence study based on the setup in Fig. 6(b) as well as in 6(c). We compare the deformation obtained by simulation u_r^{sim} and by Green's function u_r^{Green} by calculating the relative error per node defined as

$$\epsilon = \frac{1}{N_z} \sqrt{\sum_{z_i} \left\{ \left[\frac{u_r^{\text{sim}}(z_i) - u_r^{\text{Green}}(z_i)}{u_r^{\text{Green}}(0)} \right]^2 \right\}}, \quad (43)$$

where N_z denotes the number of nodes along the cylinder axis and the difference is in relation to the maximal deformation given by the Green's function. In Fig. 6(d) we show the relative error per node in dependency of the number of membrane nodes. With increasing resolution the error per node steadily decreases in both cases. The converge rate, however, is different for T_a^ϕ which decreases with slope N_z^{-1} and T_a^z which decreases more quickly with N_z^{-2} . This may be due to the fact that the Green's function is derived from linearized equations of motion [3], whereas simulations are also valid for larger deformations. A perturbation in T_a^ϕ shows half the maximal deformation as a perturbation in T_a^z as predicted in Eq. (42) and thus is in better agreement with the Green's function. The steady decrease in error demonstrates the accuracy of the presented algorithm for active force calculation.

From Fig. 6 we conclude that our algorithm presented in Sec. IV together with elastic force calculations gives reliable results for a reasonably smooth distribution of active in-plane surface stress. The very good accuracy of the predictions is achieved for the simple overdamped dynamics as well as for the substantially more complex and flexible combination of an active membrane with the Lattice-Boltzmann-immersed-boundary method.

D. Homogeneous perturbation: Instability diagram

To provide another test of our algorithm we perform simulations of a cylindrical membrane which now is subjected to a homogeneous active in-plane surface stress,

$$t_{\alpha\beta}^\beta = \begin{pmatrix} T_a & 0 \\ 0 & T_a \end{pmatrix}, \quad (44)$$

with $T_a = \text{const}$. This situation corresponds to a membrane with constant motor protein activity and isotropic cortex

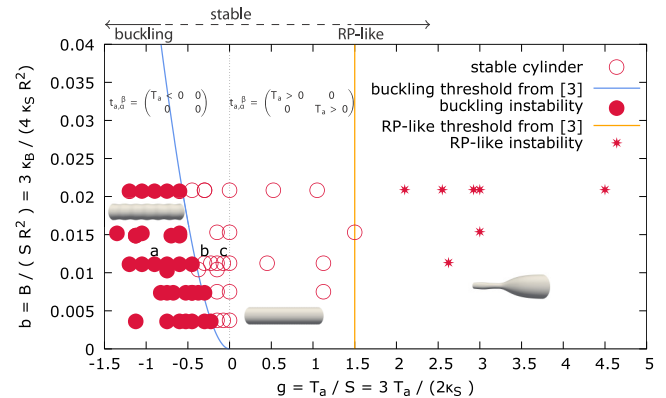


FIG. 7. Phase diagram of a cylindrical shell with relative, active in-plane surface stress $g = T_a/S = 3T_a/(2\kappa_S)$ and relative bending modulus $b = B/(SR^2) = 3\kappa_B/(4\kappa_S R^2)$ from 3D LBM-IBM simulations in comparison to the theoretically predicted thresholds [3]. On the left of the dotted line we apply a negative active stress, on the right of the dotted line we apply a positive active stress. For small negative or positive active stress (around the dotted line) the cylindrical membrane is stable. For large negative stresses, a buckling instability is observed. For large positive active in-plane surface stress a Rayleigh-Plateau like instability occurs. The theoretically predicted instability thresholds [3] and our 3D LBM-IBM simulations are in excellent agreement in both cases. Insets illustrate the shape of the shell corresponding to different values of active in-plane surface stress. The labels a, b, c refer to Fig. 8.

architecture. We note again that positive T_a represents contractile and negative T_a extensile stress in the z or ϕ direction. Although they did not explicitly compute the deformation for this situation, Ref. [3] predicts two unstable regions in g - b -parameter space for which the Green's function could be shown to diverge. The predicted instability thresholds serve us as a further validation of our simulation method.

By varying both the relative active in-plane surface stress $g = T_a/S = 3T_a/(2\kappa_S)$ and the relative bending modulus $b = B/(SR^2) = 3\kappa_B/(4\kappa_S R^2)$ we obtain the phase diagram in Fig. 7 and compare it to the predicted instability thresholds given by Berthoumieux *et al.* [3]. On the right, for large g , Berthoumieux *et al.* [3] predict an instability occurring for $T_a > \frac{4}{3}\kappa_S(1-\nu^2)$ shown by the vertical orange line in Fig. 7. Indeed, for simulations in this range we observe an instability with local contraction of the cylinder (see inset of Fig. 7 for a shape illustration). The threshold obtained by our simulations closely matches the analytically predicted threshold. This instability is analogous to a Rayleigh-Plateau instability of a liquid jet with the positive, contractile active in-plane surface stress playing the role of the surface tension. To the left of the threshold a fairly large region is observed in which the initial cylindrical shape remains stable. For negative g (extensile stress), [3] predicts a buckling instability when $T_a < -2\sqrt{\frac{\kappa_B \kappa_S}{R^2}}$. To compare to our simulations, we prescribe an active stress only along the cylinder axis, i.e., $t_{\alpha z}^z = T_a$ and $t_{\alpha\phi}^\phi = 0$. This corresponds to a contracting, cylindrical membrane and the resulting shape beyond the threshold is illustrated in Fig. 7 at the bottom left. Our simulations agree very well with the predicted instability onset depending on the

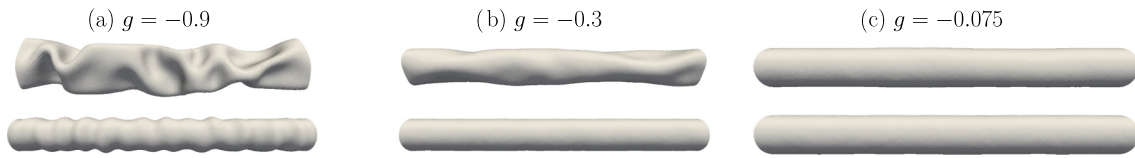


FIG. 8. Membrane shape for different values of negative active in-plane surface stress for fixed bending modulus $b = 0.01125$. In the upper row the membrane is subjected to both z and ϕ stress, while in the lower row the membrane is subjected to z stress only. For z stress only we observe a buckling instability in (a). However, for isotropic stress we observe an instability introducing nonaxisymmetric deformations at intermediate stresses in (b) where no buckling instability occurs. (c) For smaller active stress the cylindrical membrane remains stable in both cases. Corresponding points in the phase diagram in Fig. 7 are labeled a–c.

relative active in-plane surface stress and the relative bending modulus.

In addition, we investigate the transition to buckling in more detail and carry out simulations imposing an active tension in azimuthal and axial direction $t_{az}^z = t_{a\phi}^\phi = T_a$, which corresponds exactly to the scenario considered by [3]. In Fig. 8 we compare these simulations (top row) with the ones in Fig. 7 (bottom row), respectively. At large (negative) active stress in (a) we observe an instability in both simulations, however only the simulation with a purely axial stress clearly corresponds to a buckling instability. The instability in the top row exhibits a nonaxisymmetric character. For slightly smaller active stress in Fig. 8(b) the nonaxisymmetric instability remains for the isotropic stress, but the membrane becomes stable for z stress only. Decreasing the active stress further, we observe a stable cylindrical membrane in both cases, as shown in (c).

From Fig. 8 we conclude that an additional instability is present (not related to buckling) caused by a finite azimuthal stress $t_{a\phi}^\phi$. This additional instability induces nonaxisymmetric deformations and thus is not observed in the axisymmetric treatment of Ref. [3] nor in our axisymmetric simulations for which also the onset of the buckling instability is in exact agreement with the analytical prediction as shown in Fig. S2 of the Supplemental Material [97].

So far, we have validated our algorithm to agree with theoretical predictions on the basis of the Green's function. To obtain a validation in the nonlinear regime beyond the Green's function, we compare our 3D simulations to simulations of an axisymmetric membrane, as detailed in the Supplemental Material [97]. We do this by comparing the membrane shape in the case of a buckling instability. In Fig. 9 we show the deformation obtained from the axisymmetric simulation and compare it to three simulations using 3D LBM-IBM. The three 3D simulations are done for different resolutions $\Delta z/R$. We use the nondimensional parameters $g = -0.75$ and $b = 0.01125$. On the one hand all three 3D simulations show the same deformation and wavelength and on the other hand they agree in the wavelength with the axisymmetric simulation method. The wavelength of the buckling instability is about $1.75R$ for both very different simulation techniques. In the case of small bending elasticity Berthoumieux *et al.* [3] predict a wavelength at the threshold, where the denominator of the Green's function in Eq. (35) becomes zero for finite wave vector q . The predicted wavelength is $\lambda = 1.9R$ which is reasonably close to the value observed with simulations. The difference may arise from the periodicity of the shell in our

simulations and/or from finite bending together with being beyond the threshold. Nevertheless, the excellent agreement between the axisymmetric and 3D simulations provides strong evidence for the reliability of our algorithm also in the range of large deformations.

VI. MODEL APPLICATION: CELL DIVISION IN SUSPENDING FLUID

In the following we present a first application of our method including fluid flow. This illustrates the versatility and applicability of our combined LBM-IBM method for active cell membranes. For this, we consider a dividing ellipsoidal cell. Except the fact that we employ an elastic rather than a viscous cortex, our setup resembles the situation of cell cytokinesis [16,17,19–21]. Cell cytokinesis as part of cell division is a prominent subject of active matter research in biological physics [13,18,98]. Most previous studies, e.g., [20] or [21], investigated the dynamics of cell cytokinesis for an axisymmetric membrane without considering internal fluid flow. References [99] and [100] analyzed the flow field inside a dividing cell where the contractile ring is modeled as an additional force using the immersed-boundary method and phase field model, respectively. Ref. [101] analyzed the flow field by means of the phase field model as well, but considered the cortical ring as a shrinking elastic loop. Here,

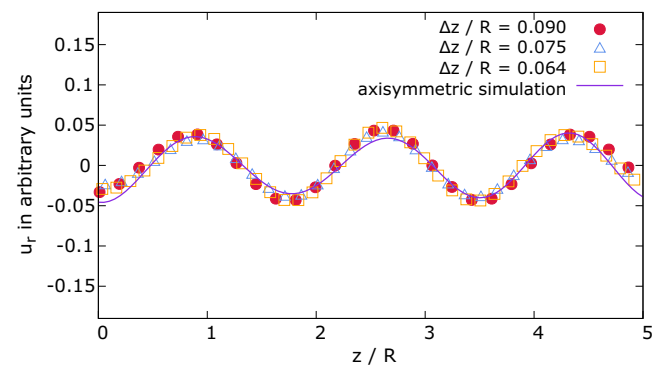


FIG. 9. Comparison of the deformation obtained for the buckling instability of an initially cylindrical membrane subjected to a homogeneous active in-plane surface stress with $g = -0.75$ and $b = 0.01125$. We compare the wavelength of the deformation obtained in 3D LBM-IBM simulations with different resolutions $\Delta z/R$ to one obtained by axisymmetric simulation. For a sample illustration of the 3D shape we refer to the inset on the left-hand side of Ref. 7. All simulations show the same wavelength for the buckling instability.

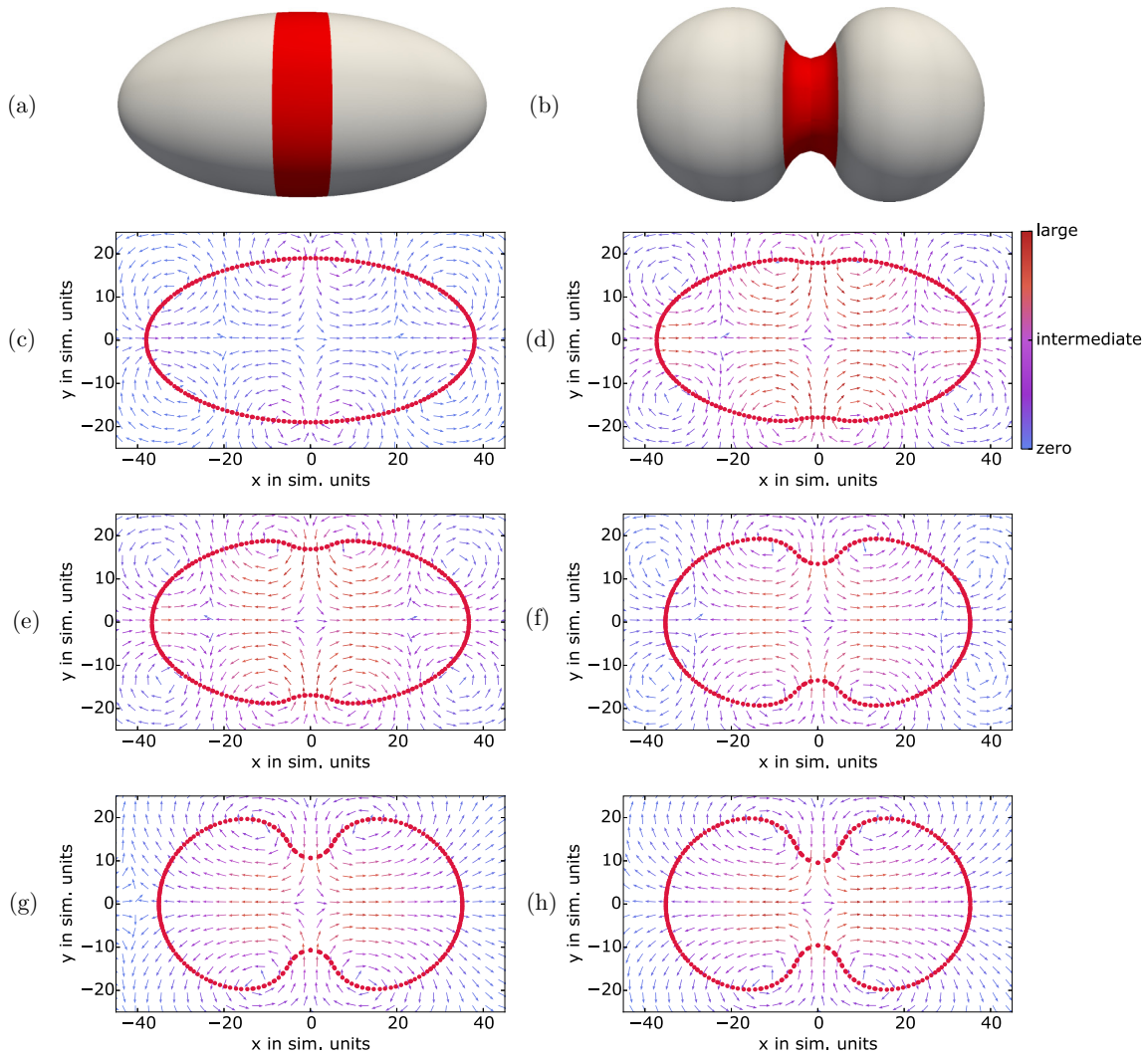


FIG. 10. (a) Similar to cell division an elastic cell membrane, which is subjected to homogeneous active stress and a local increase in azimuthal active stress in the red shaded area, contracts locally as shown in (b). Panels (c)–(h) show the outline of the deforming membrane (red nodes) in the central plane and the developing flow field (arrows) inside the cell over time. Eventually, a flow away from the contracting region towards the poles of the cell is observed. Arrows indicate the flow direction while the color indicates the flow velocity. Relative time is $t/t_{\max} =$ (a) 0, (b) 1, (c) 4×10^{-4} , (d) 0.08, (e) 0.16, (f) 0.51, (g) 0.86, (h) 1.0.

we consider cell division triggered by active stresses including an external flow leading to a fully 3D asymmetric membrane shape during the division. We first analyze the flow field dynamically evolving inside the dividing cell surrounded by a quiescent medium in Sec. VIA and then extend this setup by considering a dividing cell in an external shear flow in Sec. VIB.

A. Flow field inside a dividing cell

We consider a prolate ellipsoidal cell of diameter $7 \mu\text{m}$ and length $14 \mu\text{m}$ which is endowed with an isotropic active stress $T_a = 8 \times 10^{-5} \text{ N/m}$. In addition, in an interval of $\Delta\theta \approx \frac{\pi}{12}$ around the equator the active stress in the azimuthal direction is increased by a factor of 6 according to a step function. The membrane is endowed with shear

elasticity $\kappa_S = 5 \times 10^6 \text{ N/m}$, $C = 1$, and bending elasticity $\kappa_B = 2 \times 10^{-19} \text{ Nm}$ which are in the range of typical cell membranes.

We present the initial 3D membrane shape in Fig. 10(a) and a deformed 3D shape in Fig. 10(b). In both cases we illustrate the region with increased active stress along ϕ direction by the red shaded area. The shape and the developing flow field in the central plane, which includes the long axis of the ellipsoid, are shown over time in Figs. 10(c)–10(h). Here, the active stress triggers active deformation of the membrane which in turn triggers fluid flow inside the cell. We note that the fluid velocity at the position of the membrane corresponds to membrane motion, which moves with local fluid velocity due to no-slip condition as described in Sec. IIB. At the beginning the membrane contracts around the poles [left and right in Fig. 10(c)] due to the isotropic contractile active

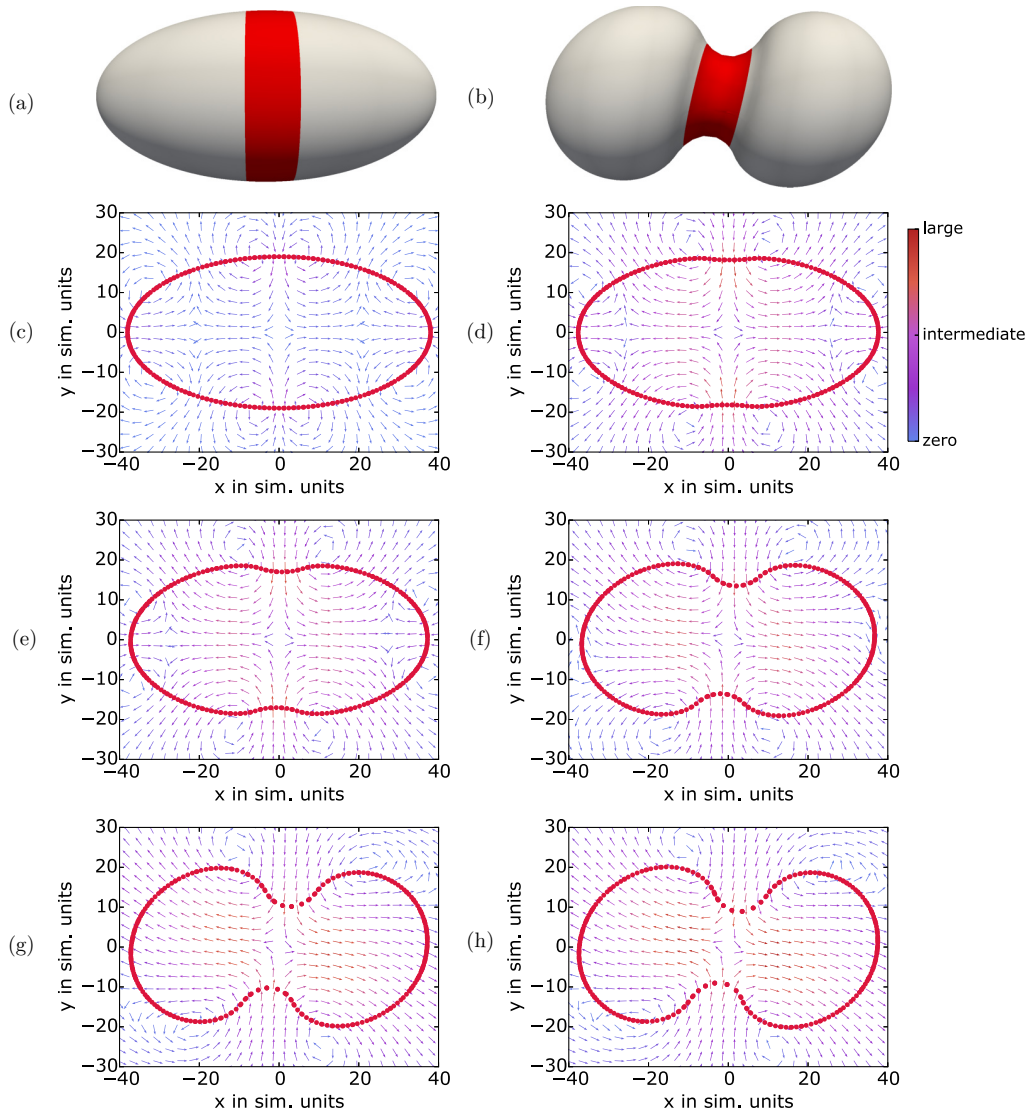


FIG. 11. An elastic dividing cell membrane in shear flow. (a) An increase in azimuthal active stress in the red shaded area of an ellipsoidal cell membrane triggers a local contraction as shown in (b) while the externally driven shear flow also deforms the membrane. Panels (c)–(h) show the outline of the deforming membrane (red nodes) in the central plane and the developing flow field (arrows) as perturbation to the shear flow over time. We here refer also to the Supplemental Material Video 1. The presence of the shear flow renders both the cell shape and the flow field asymmetric. Relative time is $t/t_{\max} =$ (a) 0, (b) 1, (c) 1.3×10^{-3} , (d) 0.07, (e) 0.17, (f) 0.52, (g) 0.88, (h) 1.0.

stress. The contraction at the poles causes a rounding which triggers a flow field pointing away from the poles at the beginning. Simultaneously, the membrane starts contracting around the equator; see Figs. 10(c) and 10(d). In Fig. 10(d) four vortices are present around the equator and four at the corners of the figure. After some time the contraction at the poles stops, see Figs. 10(e) and 10(f), and only the contraction at the equator proceeds. With progressive contraction a flow away from the midplane towards the poles develops. As it is visible in Figs. 10(g) and 10(h), the site of maximal velocity towards the poles is located at $x \approx \pm 10$. Thus, it does not coincide with the center of the two spheroids pinching off at $x \approx \pm 18$, but is rather shifted towards the equatorial plane at $x = 0$. Approaching the poles of the ellipsoid the velocity decreases.

B. Dividing cell in shear flow

In the previous section we considered an initially quiescent fluid. Here, we go one step further and include an externally driven flow interacting with the membrane. We apply a shear flow with a shear rate $\dot{\gamma} \approx 1400 \text{ s}^{-1}$. All other parameters are the same as in the previous section.

The cell membrane as illustrated in Fig. 11(a) deforms now due to the local increase in active stress [red shaded area in (a) and (b)] but also due to the external shear flow. This becomes visible by the nonsymmetrically deformed membrane in Fig. 11(b). Figures 11(c)–11(h) show the flow field relative to the shear flow, i.e., from each velocity vector the corresponding background flow is subtracted. The time evolution of the cell shape and the flow field is also illustrated in the Supplemental Material Video 1. In contrast to the previous

section, the shear flow triggers an asymmetric deformation and in turn an asymmetric flow inside the cell. The rounding together with the flow from the poles towards the equator is less pronounced [compare Fig. 11(d) to Fig. 10(d)].

The flow field inside a dividing cell suspended in a shear flow shows how the actively deforming membrane couples to a background flow and imposes perturbation on the shear flow. Both the active stress present in the cell cortex as well as the external flow trigger membrane deformation.

VII. CONCLUSION

We presented a computational algorithm to compute the dynamical deformation of arbitrarily shaped active biological (cell) membranes embedded in a 3D fluid. Active stresses in cells typically arise from the activity of motor proteins. Constitutive equations for active stresses in membranes have been developed recently [6,30] in the framework of differential geometry and form the theoretical basis for our computational method. The membranes are discretized by a set of nodes connected via flat triangles. The key ingredient of our algorithm is the computation of the active force acting on each node starting from prescribed active stresses via a parabolic fitting procedure on the deformed membrane. Besides active forces, the method also includes passive elastic forces derived from the well-established Skalak and Helfrich models for cell membranes. In simple cases, the surrounding fluid can be considered a purely frictional medium, such that the membrane nodes follow simple overdamped dynamics in time. For more realistic situations, we introduced a powerful and versatile coupling between the active membrane and the surrounding fluid via the immersed-boundary method. This technique incorporates the full Navier-Stokes dynamics for the surrounding liquid, solved here via the Lattice-Boltzmann method. Thus, our method allows us to go beyond the determination of equilibrium shapes of active elastic membranes and allows for simulations of dynamically deforming biological cells immersed in an external flow.

We successfully validated our algorithm for two distinct situations of an elastic, initially cylindrical membrane: (i) a local, Gaussian distributed active stress and (ii) a homogeneous active stress. For (i) our numerical results are in excellent agreement with the analytically predicted deformation of Berthoumieux *et al.* [3] and show convergence with increasing resolution. Overdamped dynamics and IBM-LBM dynamics are in good agreement. For (ii) we recovered both the buckling as well as the Rayleigh-Plateau-like instability predicted by [3]. Comparison to our own numerical solutions of the axisymmetric problem shows very good agreement with the full 3D algorithm also in the regime of large deformation not covered by [3]. In addition, our computations reveal the existence of a thus far unobserved nonaxisymmetric instability in the case of extensile axial and azimuthal stresses. In order to illustrate the versatility of our method, we analyzed the flow field inside an elastic, dividing cell membrane in shear flow. This represents the first investigation of the dynamic two-way coupling between active deformations and externally driven fluid flow. In this work, we considered temporally constant active stresses, but the inclusion of time-dependent active

stresses computed, e.g., by a convection-diffusion model of active substances is straightforwardly possible.

Our computational method significantly extends the range of physical problems to which existing active membrane theories can be applied. First, it is not restricted to simple shapes such as cylinders or spheres (or small deformations thereof) allowing efficient and accurate treatment of arbitrary membrane shapes and deformations. Second, our method couples the active membrane dynamics to the full Navier-Stokes dynamics of the surrounding fluid. In the described LBM-IBM scheme a viscosity contrast of the inner and outer fluid—as it is well known in the case of red blood cells [50]—can furthermore be incorporated, which allows for an even more realistic model of living cells. This opens up a wide range of applications in external flows such as active cells in the bloodstream or active cellular compartments in cytoplasmic streaming flows which currently remain largely unexplored. A particularly interesting application could be the formation of platelets from megakaryocytes which, according to a set of recent experiments [102,103], crucially depends on the interplay between active processes and external flows.

ACKNOWLEDGMENTS

C.B. thanks the Studienstiftung des deutschen Volkes for financial support and acknowledges support by the study program “Biological Physics” of the Elite Network of Bavaria. This project is part of the collaborative research center TRR225 (subproject B07) funded by the German Research Foundation (DFG). We gratefully acknowledge computing time provided by the SuperMUC system of the Leibniz Rechenzentrum, Garching, as well as by the Bavarian Polymer Institute and financial support from the Volkswagen Foundation.

APPENDIX

1. Membrane in thin shell formulation

In this Appendix, we summarize the necessary basics and conventions of differential geometry on thin shells used in this work. For a more detailed description we refer the reader to Refs. [73,84]. The 2D manifold in general is parametrized by two coordinates s^1, s^2 . We denote vector components on the manifold by Greek letters $\alpha, \beta = 1, 2$ and vector components in Euclidean space by latin letters $i, j, k = x, y, z$. Moreover, we use the Einstein summation convention, i.e., double occurrence of an index in sub- and superscript implies a sum over this index. A partial derivative with respect to s^β is denoted by a comma, i.e., for an arbitrary vector v this implies $v_{\alpha,\beta} = \partial v_\alpha / \partial s^\beta$.

The membrane in the undeformed state is parametrized by the vector

$$\mathbf{X}(s^1, s^2, t). \quad (\text{A1})$$

From the local in-plane coordinates

$$\mathbf{e}_\alpha = \mathbf{X}_{,\alpha} \quad (\text{A2})$$

the metric tensor is defined by

$$g_{\alpha\beta} = \mathbf{e}_\alpha \cdot \mathbf{e}_\beta, \quad (\text{A3})$$

with $g = \det(g_{\alpha\beta})$. The inverse metric $g^{\alpha\beta}$ can be obtained by the expression

$$g_{\alpha\gamma}g^{\gamma\beta} = \delta_{\alpha}^{\beta} \quad (\text{A4})$$

with δ_{α}^{β} denoting the Kronecker delta being 1 for $\alpha = \beta$ and 0 otherwise. For a general vector v_{α} , v^{α} or tensor $t_{\alpha\beta}$, t_{α}^{β} , t_{β}^{α} , $t^{\alpha\beta}$ subscript indices denote covariant components and superscript indices denote contravariant components. An index can be raised by

$$v^{\alpha} = v_{\beta}g^{\beta\alpha}, \quad t_{\alpha}^{\beta} = t_{\alpha\gamma}g^{\gamma\beta} \quad (\text{A5})$$

or lowered by

$$v_{\alpha} = v^{\beta}g_{\beta\alpha}, \quad t_{\alpha\beta} = t_{\alpha}^{\gamma}g_{\gamma\beta}. \quad (\text{A6})$$

A surface element is defined by $dS = \sqrt{g}ds^1ds^2$. The Christoffel symbols are given by

$$\Gamma_{\alpha\beta}^{\gamma} = \frac{1}{2}g^{\gamma\delta}[g_{\alpha\delta,\beta} + g_{\beta\delta,\alpha} - g_{\alpha\beta,\delta}]. \quad (\text{A7})$$

The in-plane coordinate vectors \mathbf{e}_{α} provide a local coordinate system together with the unit normal vector on the membrane

$$\mathbf{n} = \frac{\mathbf{e}_1 \times \mathbf{e}_2}{\|\mathbf{e}_1 \times \mathbf{e}_2\|}. \quad (\text{A8})$$

Considering the local unit normal vector allows for the definition of the curvature tensor

$$C_{\alpha\beta} = -\mathbf{e}_{\beta,\alpha} \cdot \mathbf{n}. \quad (\text{A9})$$

A covariant derivative of an arbitrary vector v^{α} or tensor $t^{\alpha\beta}$ defined on the membrane is given by

$$\nabla_{\alpha}v^{\beta} = v^{\beta}_{,\alpha} + \Gamma_{\alpha\gamma}^{\beta}v^{\gamma}, \quad (\text{A10})$$

$$\nabla_{\alpha}t^{\beta\gamma} = t^{\beta\gamma}_{,\alpha} + \Gamma_{\alpha\delta}^{\beta}t^{\delta\gamma} + \Gamma_{\alpha\delta}^{\gamma}t^{\beta\delta}. \quad (\text{A11})$$

On the membrane the Levi-Civita tensor is given by

$$\epsilon_{\alpha\beta} = \sqrt{g} \begin{pmatrix} 0 & 1 \\ -1 & 0 \end{pmatrix}, \quad \epsilon^{\alpha\beta} = \frac{1}{\sqrt{g}} \begin{pmatrix} 0 & 1 \\ -1 & 0 \end{pmatrix}. \quad (\text{A12})$$

An arbitrary vector \mathbf{v}^{α} defined on the manifold with respect to \mathbf{e}_{α} with $\alpha = 1, 2$ can be decomposed into an in-plane and a normal contribution

$$\mathbf{v}^{\alpha} = t^{\alpha\beta}\mathbf{e}_{\beta} + t_n^{\alpha}\mathbf{n} \quad (\text{A13})$$

with $t^{\alpha\beta}$ being the component of a tensor and t_n^{α} the component of a vector.

A connection from the in-plane coordinates to the Euclidean coordinates can be drawn by the expression

$$\mathbf{e}_{\alpha} = e_{\alpha}^i\mathbf{E}_i \quad (\text{A14})$$

with e_{α}^i being the i th component of \mathbf{e}_{α} and \mathbf{E}_i being the i th Euclidean unit vector. A three dimensional tensor t_{ij} can be projected onto the membrane via

$$t_{\alpha\beta} = t_{ij}e_{\alpha}^ie_{\beta}^j. \quad (\text{A15})$$

External or internal forces may lead to a deformation of the membrane characterized by the deformation field \mathbf{u} . The membrane in the deformed state is parametrized by

$$\mathbf{X}'(s^1, s^2) = \mathbf{X}(s^1, s^2) + \mathbf{u}(s^1, s^2). \quad (\text{A16})$$

We denote all vectors or tensors that are evaluated on the deformed surface by a prime. Corresponding to the change of local coordinate vectors $\mathbf{e}'_{\alpha} = \mathbf{X}'_{,\alpha}$ and normal vector \mathbf{n}' both the metric tensor and the curvature tensor changes to

$$g'_{\alpha\beta} = \mathbf{e}'_{\alpha} \cdot \mathbf{e}'_{\beta}, \quad (\text{A17})$$

$$C'_{\alpha\beta} = -\mathbf{e}'_{\beta,\alpha} \cdot \mathbf{n}'. \quad (\text{A18})$$

The Christoffel symbols have to be computed using $g'_{\alpha\beta}$ and the covariant derivative becomes

$$\nabla'_{\alpha}v^{\beta} = \partial'_{\alpha}v^{\beta} + \Gamma'^{\beta}_{\alpha\gamma}v^{\gamma}, \quad (\text{A19})$$

$$\nabla'_{\alpha}t^{\beta\gamma} = \partial'_{\alpha}t^{\beta\gamma} + \Gamma'^{\beta}_{\alpha\delta}t^{\delta\gamma} + \Gamma'^{\gamma}_{\alpha\delta}t^{\beta\delta}. \quad (\text{A20})$$

2. Elastic in-plane surface stresses

In the following we compare the elastic in-plane surface stresses used in Ref. [3] to those obtained for Skalak energy density in Eq. (7). We consider the displacement vector in Eq. (A16) decomposed into axial and normal deformation,

$$\mathbf{u} = u_z\mathbf{e}_z + u_n\mathbf{n}. \quad (\text{A21})$$

For the given energy density in Eq. (7) the in-plane surface stresses are obtained by [74,104,105]

$$t_{\text{SK}}^{\alpha\beta} = \frac{2}{J} \frac{\partial w^{\text{SK}}}{\partial I_1} g^{\alpha\beta} + 2J \frac{\partial w^{\text{SK}}}{\partial I_2} g'^{\alpha\beta} \quad (\text{A22})$$

with the invariants

$$I_1 = g^{\alpha\beta}g'_{\alpha\beta} - 2, \quad (\text{A23})$$

$$I_2 = \det(g^{\alpha\beta})\det(g'_{\alpha\beta}) - 1, \quad (\text{A24})$$

and with $J = \sqrt{I_2 + 1}$. Using Eqs. (A16) and (A17) and the deformation in Eq. (A21) we obtain for the metric on the deformed membrane in the limit of small deformations

$$g'_{\alpha\beta} = \begin{pmatrix} 1 + 2\partial_z u_z & 0 \\ 0 & 1 + 2\frac{u_r}{R} \end{pmatrix} \quad (\text{A25})$$

and for the in-plane surface stresses

$$t_{\text{SK}}^{zz} = \frac{2}{3}\kappa_S \left[(1 + C)\partial_z u_z + C\frac{u_r}{R} \right], \quad (\text{A26})$$

$$t_{\text{SK}}^{\phi\phi} = \frac{2}{3}\kappa_S \left[\frac{1}{R^2}C\partial_z u_z + (1 + C)\frac{u_r}{R^3} \right]. \quad (\text{A27})$$

These equations can be compared to the tensions in Eq. (11) of Ref. [3] for the elastic model used by Berthoumieux *et al.* [3]. The latter is based on Hooke's law in three dimensions which is projected onto the membrane. By comparing the stresses we find agreement in the limit of small deformations for the relation of the stretching modulus S to the shear modulus used in Eq. (7) of

$$S = \frac{2}{3}\kappa_S \quad (\text{A28})$$

and $C = 1$. This relation is used for the Green's function to match both elastic models.

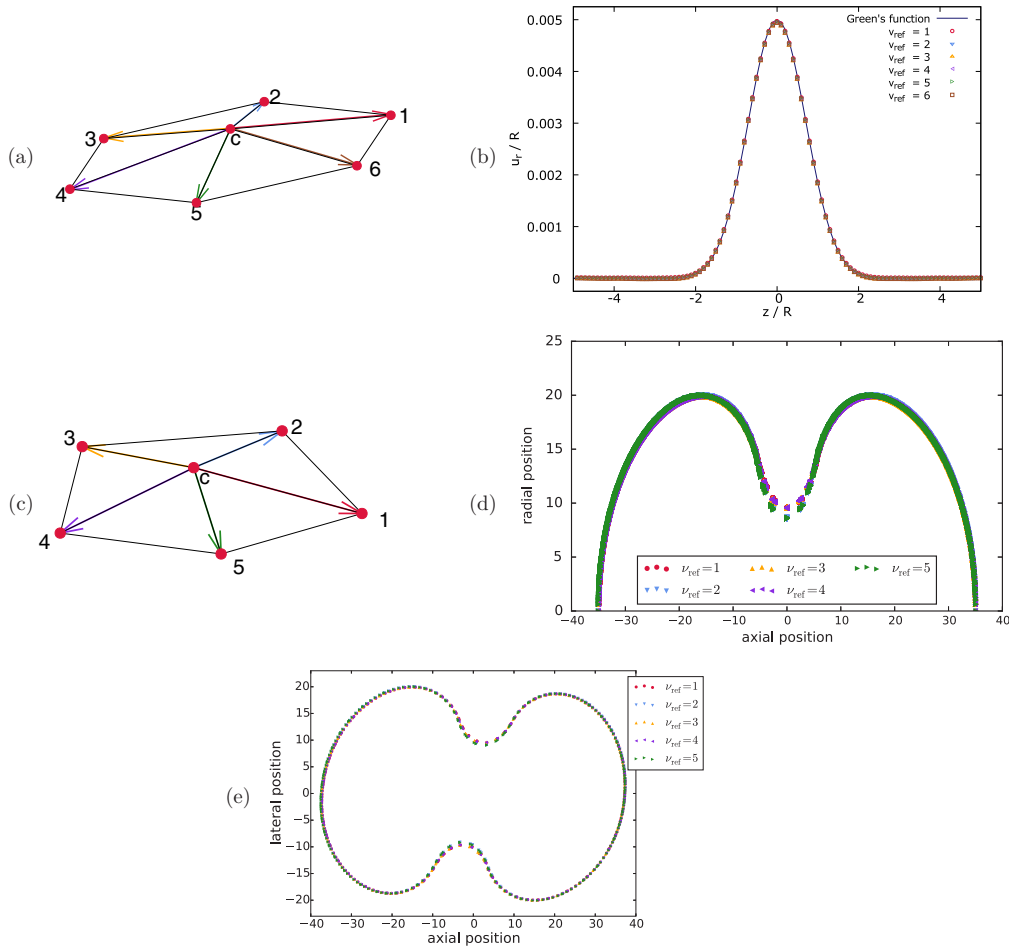


FIG. 12. (a) Color code for the neighbor node serving as reference to construct the local coordinate system on the cylindrical membrane at the site of the central node. (b) Deformation obtained for a cylindrical membrane subjected to a Gaussian perturbation in active in-plane surface stress along z direction for different reference neighbor nodes. The setup is identical to Fig. 6(c) with $T_{al}^z = 0.01$ and $\kappa_S = 1.0$. Obtained deformations are in very good agreement regardless of the choice of reference neighbor node. (c) Neighbor node serving as reference to construct the local coordinate system on the ellipsoidal membrane at the site of the central node. (d) Cell membrane shape for different reference neighboring node ν_{ref} at a given time corresponding to Fig. 10(g). Except for slight deviations in the region of largest curvature in case of neighboring nodes 2 and 5, all membrane shapes are in very good agreement. (e) Membrane shapes in shear flow for different reference neighboring node ν_{ref} at a given time corresponding to Fig. 11(g) are in very good agreement. Thus, we prove evidence that the choice of the reference neighboring node does not affect simulation results.

We furthermore can compare the bending modulus used in Berthoumieux *et al.* [3] to the one appearing in the Helfrich energy in Eq. (8) [78]. Berthoumieux *et al.* [3] defines $B = Eh^3/[24(1 - \nu^2)]$ with the Youngs modulus E and the thin shell height h . Comparing this to the expression $\kappa_B = Eh^3/[12(1 - \nu^2)]$ of Pozrikidis [106] we obtain the relation

$$B = \frac{1}{2}\kappa_B. \quad (\text{A29})$$

3. Overdamped dynamics method and simulation analysis

a. Overdamped dynamics

As a different approach than the LBM-IBM, we use a model program based on overdamped dynamics to solve for the final, equilibrium shape of the membrane in the case of validation. The resulting active and elastic forces \mathbf{F} calculated

for every node enter the equation of motion of the corresponding node \mathbf{r}_c which is given by

$$\mathbf{F} = \gamma \dot{\mathbf{r}}_c, \quad (\text{A30})$$

where γ is a friction coefficient. We solve the equations for all nodes using Euler integration scheme. We fix the nodes at the boundaries of the cylinder by harmonic springs of strength $1000\kappa_S$. This results in nearly vanishing deformation at the boundary of the cylinder.

b. Simulation analysis

To obtain the shape shown for example in Fig. 6(a) or Fig. 6(b) we average the final, radial deformation over all nodes at a certain z position. Due to the averaging and inherent errors in the bending algorithm [52] the deformation u_r does not reach exactly zero far away from the perturbation in active

stress, but shows a constant offset of 5×10^{-4} , which we eliminate in the figures.

4. Choice of reference neighbor does not influence simulation results

In Sec. IV A we explain how the local coordinate system is built using the first neighboring node as reference for the first in-plane coordinate vector e_ξ . This fact is also important for the projection of the active stress into the local coordinate system, as mentioned in Sec. IV C. In the following we show that the choice of the reference neighboring node is arbitrary and does not influence simulation results.

Therefore, we first consider the cylindrical membrane subjected to a homogeneous perturbation in active in-plane surface stress along the z direction T_a^z . We use exactly the setup analyzed in Fig. 6(c) with $T_a^z = 0.01$ and $\kappa_S = 1.0$. We systematically change the reference neighbor node serving for construction of the local coordinate system as illustrated in Fig. 12(a). Figure 12(b) shows that the deformation obtained in simulations is the same for every choice of reference neighbor node and agrees very well with the theoretically obtained Green's function. In the case of T_a^z perturbation the in-plane derivatives of the active in-plane surface stress are crucial and trigger the deformation. Thus, Fig. 12 provides evidence for the correct calculation of derivatives regardless of the choice of reference neighbor node and furthermore shows the choice is arbitrary.

Furthermore, in order to take into account a more complex membrane geometry, we use the setup in Fig. 10 and compare the dynamics for five different choices of reference

neighboring node. Choosing the sixth neighbor is not possible for the ellipsoidal geometry as the surface tiling requires at least 12 nodes with five neighbors only. We consider an initially ellipsoidal cell membrane endowed with active stress, which in azimuthal direction increases around the equator. The increased active stress triggers the cell membrane to contract. In Fig. 10 we show the dynamically evolving flow field inside the cell. Here, we redo the simulation and for each simulation we choose a different neighbor node to build the local coordinate system, which moves with the deforming membrane in time. In Fig. 12(c) we show the five different choices.

In Fig. 12(d) we consider the point in time corresponding to Fig. 10(g) and show the radial position of all membrane nodes as function of the position along the axis. All simulations with different reference neighbor show the same membrane shape and are in very good agreement. We note that slight deviations occur at the site of strongest indentation, which results also in the strongest curvature. At this position, the parabolic fit is not capable of covering the strongly deformed membrane shape completely and thus slight deviations occur. In Fig. 12(e) we do the same for a dividing cell in shear flow corresponding to Fig. 11(g). We show the node positions within the plane containing the long axis of the cell and the shear axis of the external flow. All simulations with different reference neighbor show the same membrane shape in shear flow and are in very good agreement. Thus, Figs. 12(d) and 12(e) provide evidence that the choice of reference neighbor is indeed arbitrary and does not alter the simulation in case of a dynamically deforming membrane coupled to a suspending fluid.

-
- [1] B. Alberts, A. Johnson, J. Lewis, M. Raff, K. Roberts, and P. Walter, *Molecular Biology of the Cell with CD*, 5th ed. (Garland Science, New York, 2007).
 - [2] A. G. Clark, O. Wartlick, G. Salbreux, and E. K. Paluch, *Curr. Biol.* **24**, R484 (2014).
 - [3] H. Berthoumieux, J.-L. Maître, C.-P. Heisenberg, E. K. Paluch, F. Jülicher, and G. Salbreux, *New J. Phys.* **16**, 065005 (2014).
 - [4] A. Saha, M. Nishikawa, M. Behrndt, C.-P. Heisenberg, F. Jülicher, and S. W. Grill, *Biophys. J.* **110**, 1421 (2016).
 - [5] T. Hiraiwa and G. Salbreux, *Phys. Rev. Lett.* **116**, 188101 (2016).
 - [6] G. Salbreux and F. Jülicher, *Phys. Rev. E* **96**, 032404 (2017).
 - [7] A. Ravichandran, G. A. Vliegthart, G. Saggiorato, T. Auth, and G. Gompper, *Biophys. J.* **113**, 1121 (2017).
 - [8] T. B. Liverpool and M. C. Marchetti, *Phys. Rev. Lett.* **90**, 138102 (2003).
 - [9] N. Sarkar and A. Basu, *Phys. Rev. E* **92**, 052306 (2015).
 - [10] R. Ramaswamy and F. Jülicher, *Sci. Rep.* **6**, 20838 (2016).
 - [11] E. Hannezo, B. Dong, P. Recho, J.-F. Joanny, and S. Hayashi, *Proc. Natl. Acad. Sci. USA* **112**, 8620 (2015).
 - [12] K. Gowrishankar and M. Rao, *Soft Matter* **12**, 2040 (2016).
 - [13] S. W. Grill, *Curr. Opin. Genet. Dev.* **21**, 647 (2011).
 - [14] G. Salbreux, G. Charras, and E. Paluch, *Trends Cell Biol.* **22**, 536 (2012).
 - [15] A. C. Callan-Jones, V. Ruprecht, S. Wieser, C. P. Heisenberg, and R. Voituriez, *Phys. Rev. Lett.* **116**, 028102 (2016).
 - [16] G. Salbreux, J. Prost, and J. F. Joanny, *Phys. Rev. Lett.* **103**, 058102 (2009).
 - [17] J. Sedzinski, M. Biro, A. Oswald, J.-Y. Tinevez, G. Salbreux, and E. Paluch, *Nature (London)* **476**, 462 (2011).
 - [18] R. A. Green, E. Paluch, and K. Oegema, *Annu. Rev. Cell Dev. Biol.* **28**, 29 (2012).
 - [19] I. Mendes Pinto, B. Rubinstein, and R. Li, *Biophys. J.* **105**, 547 (2013).
 - [20] H. Turlier, B. Audoly, J. Prost, and J.-F. Joanny, *Biophys. J.* **106**, 114 (2014).
 - [21] A. Sain, M. M. Inamdar, and F. Jülicher, *Phys. Rev. Lett.* **114**, 048102 (2015).
 - [22] A. E. Carlsson, *New J. Phys.* **13**, 073009 (2011).
 - [23] D. Shao, H. Levine, and W.-J. Rappel, *Proc. Natl. Acad. Sci. USA* **109**, 6851 (2012).
 - [24] W. Marth, S. Praetorius, and A. Voigt, *J. R. Soc., Interface* **12**, 20150161 (2015).
 - [25] A. C. Callan-Jones and R. Voituriez, *Curr. Opin. Cell Biol.* **38**, 12 (2016).
 - [26] E. J. Campbell and P. Bagchi, *Phys. Fluids* **29**, 101902 (2017).
 - [27] E. Fischer-Friedrich, Y. Toyoda, C. J. Cattin, D. J. Müller, A. A. Hyman, and F. Jülicher, *Biophys. J.* **111**, 589 (2016).

- [28] E. Fischer-Friedrich, *Biophys. J.* **114**, 419 (2018).
- [29] F. C. Keber, E. Loiseau, T. Sanchez, S. J. DeCamp, L. Giomi, M. J. Bowick, M. C. Marchetti, Z. Dogic, and A. R. Bausch, *Science* **345**, 1135 (2014).
- [30] K. Kruse, J. F. Joanny, F. Jülicher, J. Prost, and K. Sekimoto, *Eur. Phys. J. E* **16**, 5 (2005).
- [31] F. Jülicher, K. Kruse, J. Prost, and J. Joanny, *Phys. Rep.* **449**, 3 (2007).
- [32] S. Ramaswamy, *Annu. Rev. Condens. Matter Phys.* **1**, 323 (2010).
- [33] M. C. Marchetti, J. F. Joanny, S. Ramaswamy, T. B. Liverpool, J. Prost, M. Rao, and R. A. Simha, *Rev. Mod. Phys.* **85**, 1143 (2013).
- [34] J. Prost, F. Jülicher, and J.-F. Joanny, *Nat. Phys.* **11**, 111 (2015).
- [35] W. W. Ahmed, E. Fodor, and T. Betz, *Biochim. Biophys. Acta, Mol. Cell Res.* **1853**, 3083 (2015).
- [36] E. Fodor, C. Nardini, M. E. Cates, J. Tailleur, P. Visco, and F. van Wijland, *Phys. Rev. Lett.* **117**, 038103 (2016).
- [37] D. Needleman and Z. Dogic, *Nat. Rev. Mater.* **2**, 17048 (2017).
- [38] J. M. Yeomans, *Europhys. News* **48**, 21 (2017).
- [39] F. Jülicher, S. W. Grill, and G. Salbreux, *Rep. Prog. Phys.* **81**, 076601 (2018).
- [40] E. Hannezo, J. Prost, and J.-F. Joanny, *Phys. Rev. Lett.* **109**, 018101 (2012).
- [41] R. Zhang, Y. Zhou, M. Rahimi, and J. J. de Pablo, *Nat. Commun.* **7**, 13483 (2016).
- [42] T. B. Saw, A. Doostmohammadi, V. Nier, L. Kocgozlu, S. Thampi, Y. Toyama, P. Marcq, C. T. Lim, J. M. Yeomans, and B. Ladoux, *Nat. Publ. Group* **544**, 212 (2017).
- [43] A. Maitra, P. Srivastava, M. Rao, and S. Ramaswamy, *Phys. Rev. Lett.* **112**, 258101 (2014).
- [44] V. Ruprecht, S. Wieser, A. Callan-Jones, M. Smutny, H. Morita, K. Sako, V. Barone, M. Ritsch-Martel, M. Sixt, R. Voituriez *et al.*, *Cell* **160**, 673 (2015).
- [45] A.-C. Reymann, F. Staniscia, A. Erzberger, G. Salbreux, and S. W. Grill, *eLife* **5**, e17807 (2016).
- [46] C. A. Whitfield and R. J. Hawkins, *PLOS One* **11**, e0162474 (2016).
- [47] N. C. Heer, P. W. Miller, S. Chanet, N. Stoop, J. Dunkel, and A. C. Martin, *Development* **144**, 1876 (2017).
- [48] N. Klughammer, J. Bischof, N. D. Schnellbacher, A. Callegari, P. Lénárt, and U. S. Schwarz, *PLOS Comput. Biol.* **14**, e1006588 (2018).
- [49] D. Barthès-Biesel, *Curr. Opin. Colloid Interface Sci.* **16**, 3 (2011).
- [50] J. B. Freund, *Annu. Rev. Fluid Mech.* **46**, 67 (2014).
- [51] A. Farutin, T. Biben, and C. Misbah, *J. Comput. Phys.* **275**, 539 (2014).
- [52] A. Guckenberger, M. P. Schraml, P. G. Chen, M. Leonetti, and S. Gekle, *Comput. Phys. Commun.* **207**, 1 (2016).
- [53] T. W. Secomb, *Annu. Rev. Fluid Mech.* **49**, 443 (2017).
- [54] P. Balogh and P. Bagchi, *J. Comput. Phys.* **334**, 280 (2017).
- [55] C. Bächer, L. Schrack, and S. Gekle, *Phys. Rev. Fluids* **2**, 013102 (2017).
- [56] A. Guckenberger, A. Kihm, T. John, C. Wagner, and S. Gekle, *Soft Matter* **14**, 2032 (2018).
- [57] S. Succi, *The Lattice Boltzmann Equation: For Fluid Dynamics and Beyond* (Oxford University Press, New York, 2001).
- [58] B. Dünweg and A. J. Ladd, in *Advanced Computer Simulation Approaches for Soft Matter Sciences III* (Springer, New York, 2009), pp. 89–166.
- [59] C. K. Aidun and J. R. Clausen, *Annu. Rev. Fluid Mech.* **42**, 439 (2010).
- [60] T. Krüger, H. Kusumaatmaja, A. Kuzmin, O. Shardt, G. Silva, and E. M. Viggien, *The Lattice Boltzmann Method: Principles and Practice* (Springer, New York, 2016).
- [61] S. Harris, *An Introduction to the Theory of the Boltzmann Equation* (Dover, Mineola, NY, 2004).
- [62] B. Dünweg, U. D. Schiller, and A. J. C. Ladd, *Phys. Rev. E* **76**, 036704 (2007).
- [63] X. He, S. Chen, and G. D. Doolen, *J. Comput. Phys.* **146**, 282 (1998).
- [64] R. C. V. Coelho, A. Ilha, M. M. Doria, R. M. Pereira, and V. Y. Aibe, *Phys. Rev. E* **89**, 043302 (2014).
- [65] R. C. Coelho and M. M. Doria, *Comput. Fluids* **165**, 144 (2018).
- [66] Z. Zhang, W. Chien, E. Henry, D. A. Fedosov, and G. Gompper, *Phys. Rev. Fluids* **4**, 024201 (2019).
- [67] H. Limbach, A. Arnold, B. Mann, and C. Holm, *Comput. Phys. Commun.* **174**, 704 (2006).
- [68] D. Roehm and A. Arnold, *Eur. Phys. J.: Spec. Top.* **210**, 89 (2012).
- [69] A. Arnold, O. Lenz, S. Kesselheim, R. Weeber, F. Fahnenberger, D. Roehm, P. Košovan, and C. Holm, in *Mesh-free Methods for Partial Differential Equations VI* (Springer, Berlin, Heidelberg, 2013), pp. 1–23.
- [70] C. S. Peskin, *Acta Numerica* **11**, 479 (2002).
- [71] R. Mittal and G. Iaccarino, *Annu. Rev. Fluid Mech.* **37**, 239 (2005).
- [72] L. Mountrakis, E. Lorenz, and A. G. Hoekstra, *Phys. Rev. E* **96**, 013302 (2017).
- [73] A. E. Green and W. Zerna, *Theoretical Elasticity* (Clarendon, Oxford, 1954).
- [74] A. E. Green and J. E. Adkins, *Large Elastic Deformations and Non-Linear Continuum Mechanics* (Clarendon, Oxford, 1960).
- [75] W. T. Koiter, in *Proceedings of the International Congress of Mathematics Nice* (Gauthier-Villars, Paris, 1970), Vol. 3, pp. 123–130.
- [76] C. Pozrikidis, *J. Comput. Phys.* **169**, 250 (2001).
- [77] Y. Seol, W.-F. Hu, Y. Kim, and M.-C. Lai, *J. Comput. Phys.* **322**, 125 (2016).
- [78] A. Guckenberger and S. Gekle, *J. Phys.: Condens. Matter* **29**, 203001 (2017).
- [79] P. Ahlrichs and B. Dünweg, *J. Chem. Phys.* **111**, 8225 (1999).
- [80] S. Quint, A. F. Christ, A. Guckenberger, S. Himbert, L. Kaestner, S. Gekle, and C. Wagner, *Appl. Phys. Lett.* **111**, 103701 (2017).
- [81] S. Gekle, *Biophys. J.* **110**, 514 (2016).
- [82] C. Bächer, A. Kihm, L. Schrack, L. Kaestner, M. W. Laschke, C. Wagner, and S. Gekle, *Biophys. J.* **115**, 411 (2018).
- [83] D. A. Fedosov, M. Peltomäki, and G. Gompper, *Soft Matter* **10**, 4258 (2014).
- [84] M. Deserno, *Chem. Phys. Lipids* **185**, 11 (2015).
- [85] R. Vetter, N. Stoop, T. Jenni, F. K. Wittel, and H. J. Herrmann, *Int. J. Numer. Methods Eng.* **95**, 791 (2013).

- [86] The term in-plane surface stresses mainly follows the terminology of Deserno [84]. Guven [87] and Deserno [84] denote the corresponding force vector with its in-plane components being $t_{\alpha\beta}$ as surface stress. For the same quantity Berthoumieux *et al.* [3] and Salbreux and Jülicher [6] as well as Guckenberger and Gekle [78] use the term in-plane tension tensor. Daddi-Moussa-Ider *et al.* [91] call this quantity stress tensor. Finally, Green and Adkins [74] call it stress resultant.
- [87] J. Guven, *J. Phys. A: Math. Gen.* **37**, L313 (2004).
- [88] D. Barthès-Biesel, *Annu. Rev. Fluid Mech.* **48**, 25 (2016).
- [89] R. Skalak, A. Tozeren, R. P. Zarda, and S. Chien, *Biophys. J.* **13**, 245 (1973).
- [90] W. Helfrich, *Z. Naturforsch. C* **28**, 693 (1973).
- [91] A. Daddi-Moussa-Ider, A. Guckenberger, and S. Gekle, *Phys. Rev. E* **93**, 012612 (2016).
- [92] D. J. Steigmann, *Arch. Ration. Mech. Anal.* **150**, 127 (1999).
- [93] R. A. Sauer, T. X. Duong, K. K. Mandadapu, and D. J. Steigmann, *J. Comput. Phys.* **330**, 436 (2016).
- [94] M. Kraus, W. Wintz, U. Seifert, and R. Lipowsky, *Phys. Rev. Lett.* **77**, 3685 (1996).
- [95] M. Meyer, M. Desbrun, P. Schröder, and A. H. Barr, in *Visualization and Mathematics III* (Springer, New York, 2003), pp. 35–57.
- [96] D. Chandrasekharaiah and L. Debnath, *Continuum Mechanics* (Elsevier, New York, 2014).
- [97] See Supplemental Material at <http://link.aps.org/supplemental/10.1103/PhysRevE.99.062418> for an axisymmetric algorithm simulating an active cylindrical membrane and an additional video.
- [98] T. D. Pollard, *J. Cell Biol.* **216**, 3007 (2017).
- [99] Y. Li, A. Yun, and J. Kim, *J. Math. Biol.* **65**, 653 (2012).
- [100] J. Zhao and Q. Wang, *Int. J. Numer. Methods Biomed. Eng.* **32**, e02774 (2016).
- [101] S. Lee, *Bull. Math. Biol.* **80**, 583 (2018).
- [102] M. Bender, J. N. Thon, A. J. Ehrlicher, S. Wu, L. Mazutis, E. Deschmann, M. Sola-Visner, J. E. Italiano, and J. H. Hartwig, *Blood* **125**, 860 (2015).
- [103] A. Blin, A. Le Goff, A. Magniez, S. Poirault-Chassac, B. Teste, G. Sicot, K. A. Nguyen, F. S. Hamdi, M. Reyssat, and D. Baruch, *Sci. Rep.* **6**, 21700 (2016).
- [104] E. Lac, D. Barthès-Biesel, N. A. Pelekasis, and J. Tsamopoulos, *J. Fluid Mech.* **516**, 303 (2004).
- [105] A. Daddi-Moussa-Ider, M. Lisicki, and S. Gekle, *Phys. Fluids* **29**, 111901 (2017).
- [106] C. Pozrikidis, *J. Fluid Mech.* **440** 269 (2001).

Supplemental Material - Computational modeling of active deformable membranes embedded in 3D flows

Christian Bächer* and Stephan Gekle†

Biofluid Simulation and Modeling, Theoretische Physik VI,

Universität Bayreuth, Universitätsstr. 30, Bayreuth

(Dated: May 28, 2019)

I. NUMERICS FOR AN AXISYMMETRIC ACTIVE ELASTIC CYLINDER

Here we provide a detailed derivation of the numerical method used to obtain the axisymmetric shapes shown in figure 9 of the main text.

A. Axisymmetric, cylindrical shell

We consider a cylindrical shell under the assumption of axisymmetry. In the following we calculate the traction jump for the axisymmetric membrane for linear elasticity. The shell is parametrized using cylindrical coordinates with $s^1 = z$ and $s^2 = \phi$ so that

$$\mathbf{X}(z, \phi) = R \cos \phi \mathbf{e}_x + R \sin \phi \mathbf{e}_y + z \mathbf{e}_z. \quad (1)$$

We obtain for the in-plane coordinates $\mathbf{e}_z = (0, 0, 1)$, $\mathbf{e}_\phi = (-R \sin \phi, R \cos \phi, 0)$, and $\mathbf{n} = (-\cos \phi, -\sin \phi, 0)$. We follow Berthoumieux *et al.* [1] regarding conventions, thus the normal vector points inwards into the cylinder. The metric and curvature tensor become

$$g_{\alpha\beta} = \begin{pmatrix} 1 & 0 \\ 0 & R^2 \end{pmatrix} \quad C_{\alpha\beta} = \begin{pmatrix} 0 & 0 \\ 0 & R \end{pmatrix}. \quad (2)$$

Due to axisymmetry the deformation can be written as

$$\mathbf{u} = u^z(z) \mathbf{e}_z + u^n(z) \mathbf{n}. \quad (3)$$

and following equation (3) we obtain the metric on the deformed surface using $g'_{\alpha\beta} = \mathbf{e}'_\alpha \cdot \mathbf{e}'_\beta$

$$g'_{\alpha\beta} = \begin{pmatrix} 1 + 2\partial_z u^z & 0 \\ 0 & R^2 - 2Ru^n \end{pmatrix}. \quad (4)$$

Accordingly, the in-plane strain tensor can be calculated

$$u_{\alpha\beta} = \begin{pmatrix} \partial_z u^z & 0 \\ 0 & -Ru^n \end{pmatrix}. \quad (5)$$

With the expressions above we can calculate the curvature tensor

$$C'_{\alpha\beta} = (\partial_\alpha \partial_\beta \mathbf{X}') \cdot \mathbf{n}' \quad (6)$$

* christian.baecher@uni-bayreuth.de

† stephan.gekle@uni-bayreuth.de

on the deformed membrane to be

$$C'_{\alpha\beta} = \begin{pmatrix} \partial_z^2 u^n & 0 \\ 0 & R - u^n \end{pmatrix}. \quad (7)$$

The Levi-Civita tensor on the deformed surface for small deformations is

$$\epsilon'_{\alpha\beta} = (R + R\partial_z u^z - u^n) \begin{pmatrix} 0 & 1 \\ -1 & 0 \end{pmatrix}. \quad (8)$$

The Christoffel symbols on the deformed membrane are

$$\begin{aligned} \Gamma_{zz}^{z'} &\simeq \partial_z^2 u^z, & \Gamma_{\phi\phi}^{z'} &\simeq R\partial_z u^n, & \Gamma_{z\phi}^{\phi'} &\simeq -\frac{1}{R}\partial_z u^n, & \Gamma_{\phi z}^{\phi'} &\simeq -\frac{1}{R}\partial_z u^n, \\ \Gamma_{\phi\phi}^{\phi'} &= 0, & \Gamma_{zz}^{\phi'} &= 0, & \Gamma_{\phi z}^{z'} &= 0, & \Gamma_{z\phi}^{z'} &= 0. \end{aligned}$$

B. Force balance in axisymmetric formulation

In this section we consider the force balance equations in the case of an axisymmetric, cylindrical shell. The force balance (eqs. (11) - (12) in the main text) takes the following form in cylindrical coordinates

$$\nabla'_z t_a^{zz} + \nabla'_\phi t_a^{\phi z} - C'^z t_{na}^z - C'_\phi t_{na}^\phi + f_e^z = f^z \quad (9)$$

$$\nabla'_z t_a^{z\phi} + \nabla'_\phi t_a^{\phi\phi} - C'^\phi t_{na}^z - C'_\phi t_{na}^{\phi\phi} + f_e^\phi = f^\phi \quad (10)$$

$$\nabla'_z t_{na}^z + \nabla'_\phi t_{na}^\phi + C'_{zz} t_a^{zz} + C'_{z\phi} t_a^{z\phi} + C'_{\phi z} t_a^{\phi z} + C'_{\phi\phi} t_a^{\phi\phi} + f_e^n = f^n. \quad (11)$$

Elastic forces In the framework of our 3D simulations presented in the main text, elastic forces are computed by direct derivation of a discretized energy functional with respect to nodal positions. Here, we follow a different route and use elastic in-plane surface stresses in order to follow closely ref. [1]. Elastic properties of the shell are considered in the framework of Hooke's law for a three dimensional, elastic, isotropic solid with the stress tensor

$$\sigma_{ij} = \frac{E}{1+\nu} \left(e_{ij} + \frac{\nu}{1-2\nu} e_{kk} \delta_{ij} \right) \quad (12)$$

depending in a linear fashion on the strain tensor $e_{ij} = u_{i,j} + u_{j,i}$ with E being the Young's modulus and ν the Poisson ratio. From the bulk equation (12) expressions for the intrinsic

in-plane surface stress tensor and moments on the thin shell can be derived [1]

$$\bar{t}_{e\alpha\beta} = 2S \begin{pmatrix} \partial_z u^z - \nu \frac{u^n}{R} & 0 \\ 0 & \nu R^2 \partial_z u^z - u^n R \end{pmatrix} \quad (13)$$

$$\bar{m}_{e\alpha\beta} = 2BR \begin{pmatrix} 0 & -R^2 \partial_z^2 u^n - \nu u^n \\ \nu \partial_z^2 u^n + \frac{u^n}{R^2} & 0 \end{pmatrix}, \quad (14)$$

with S the stretching and B the bending modulus. Following [Salbreux and Jülicher](#) [2] by using eq. (16) and (17) of [2] we calculate the in-plane surface stress and moment tensor via

$$t_e^{\alpha\beta} = \bar{t}_e^{\alpha\beta} + \frac{1}{2} (m^{\gamma\alpha} C_\gamma^\beta + m^{\gamma\beta} C_\gamma^\alpha) \quad (15)$$

$$m_e^{\alpha\beta} = -\bar{m}_e^{\alpha\gamma} \epsilon_\gamma^\beta \quad (16)$$

and obtain

$$t_e^{zz} = \bar{t}_e^{zz} \quad (17)$$

$$t_e^{z\phi} = \bar{t}_e^{z\phi} \quad (18)$$

$$t_e^{\phi z} = \bar{t}_e^{\phi z} \quad (19)$$

$$t_e^{\phi\phi} = \bar{t}_e^{\phi\phi} - \frac{2B\nu}{R^3} \partial_z^2 u^n - \frac{2B}{R^5} u_n \quad (20)$$

and

$$m_e^{zz} = -2B \partial_z^2 u^n + \frac{2B\nu}{R^2} u^n \quad (21)$$

$$m_e^{z\phi} = 0 \quad (22)$$

$$m_e^{\phi z} = 0 \quad (23)$$

$$m_e^{\phi\phi} = -\frac{2B\nu}{R^2} \partial_z^2 u^n - \frac{2B}{R^4} u^n. \quad (24)$$

We obtain for the normal surface stress

$$t_{ne}^z = \partial_z m^{zz} + 2(\partial_z^2 u^z) m^{zz} + \left(-\frac{1}{R} \partial_z u^n\right) m^{zz} + (R \partial_z u^n) m^{\phi\phi} \quad (25)$$

$$t_{ne}^\phi = 0, \quad (26)$$

and by inserting the in-plane moments we eventually get

$$t_{ne}^z = -2B \partial_z^3 u^n + \frac{2B\nu}{R^2} \partial_z u^n. \quad (27)$$

Thus following

$$f_e^\beta = \nabla'_\alpha t_e^{\alpha\beta} + C'_\alpha{}^\beta t_{n,e}^\alpha \quad (28)$$

$$f_e^n = \nabla'_\alpha t_{n,e}^\alpha - C'_{\alpha\beta} t_e^{\alpha\beta} \quad (29)$$

we get for the elastic forces

$$f_e^z = 2S\partial_z^2 u^z - \frac{2S\nu}{R}\partial_z u^n \quad (30)$$

$$f_e^\phi = 0 \quad (31)$$

$$f_e^n = -2B\partial_z^4 u^n - \left(\frac{2B}{R^4} + \frac{2S}{R^2}\right)u^n + \frac{2S\nu}{R}\partial_z u^z \quad (32)$$

Active forces We neglect the contributions of active moments and normal stress and use the active in-plane surface stress in the general form

$$t_{a\alpha}^\beta = \begin{pmatrix} t_a^z(z) & 0 \\ 0 & t_a^\phi(z) \end{pmatrix}. \quad (33)$$

From the force balance in cylindrical coordinates we obtain the active force with components

$$f_a^z = \partial_z t_a^z - \frac{1}{R}t_a^z\partial_z u^n + \frac{1}{R}t_a^\phi\partial_z u^n \quad (34)$$

$$f_a^\phi = 0 \quad (35)$$

$$f_a^n = \partial_z^2 u^n t_a^z + \left(\frac{1}{R} + \frac{1}{R^2}u^n\right)t_a^\phi. \quad (36)$$

Both elastic force and active force together determine the traction jump, which is required for simulations.

C. Numerical method

In order to determine the shape of the membrane in the steady state for the axisymmetric problem we perform an overdamped relaxation. We discretize the contour of the membrane (which is a line in case of the axisymmetric formulation) by a series of marker points. According to the traction jump in equations (9) to (11) we calculate the forces of the membrane using quintic splines for the derivatives of the deformation. Once the forces are determined, we consider the equations of motion in the overdamped limit for each membrane node

$$\mathbf{F} = \gamma\dot{\mathbf{r}}. \quad (37)$$

This means we introduce a friction term in the equations of motion and neglect inertia. Equations of motion are solved by the Euler integration scheme. As boundary condition for the deformation we choose the first and second derivative to vanish on both ends.

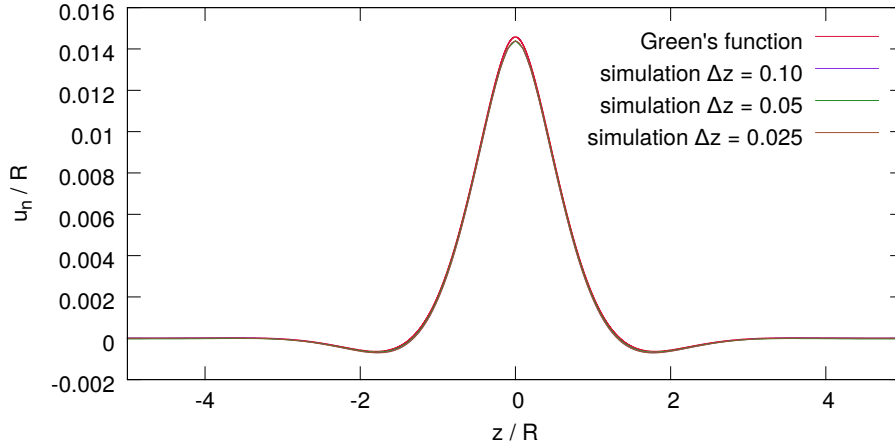


Figure 1. Comparison of the numerical solution of the axisymmetric problem for three different resolutions with the Green's function analytically predicted by Berthoumieux *et al.* [1]. Numerics and analytics agree very well in the case of a small, local, active in-plane surface stress $T_a^\phi = -0.025$. Shapes are obtained for $R = 1$, $S = 1$, $b = 0.02$, and $g = 0$.

D. Results

In order to validate our axisymmetric numerical method, we first compare the numerical results to the predicted Green's function of Berthoumieux *et al.* [1]. For the introduction of the Green's function we refer to the section V.A of the main text. As in section V.B of the main text we apply an active in-plane surface stress tensor of the form

$$t_{a\alpha}^\beta = \begin{pmatrix} 0 & 0 \\ 0 & T_a^\phi \end{pmatrix} \delta(z). \quad (38)$$

We compare axisymmetric simulations to the analytical Green's function in figure 1 for the parameter set $T_a^\phi = -0.025$, $T_a^z = 0$, $b = 0.02$, $g = 0$ for three different resolutions Δz . Figure 1 shows that our numerical method on the one hand does not depend on spatial discretization and on the other hand is in very good agreement with the theoretical expected deformation due to the Green's function given by ref. [1] including the shallow minima next to the main peak.

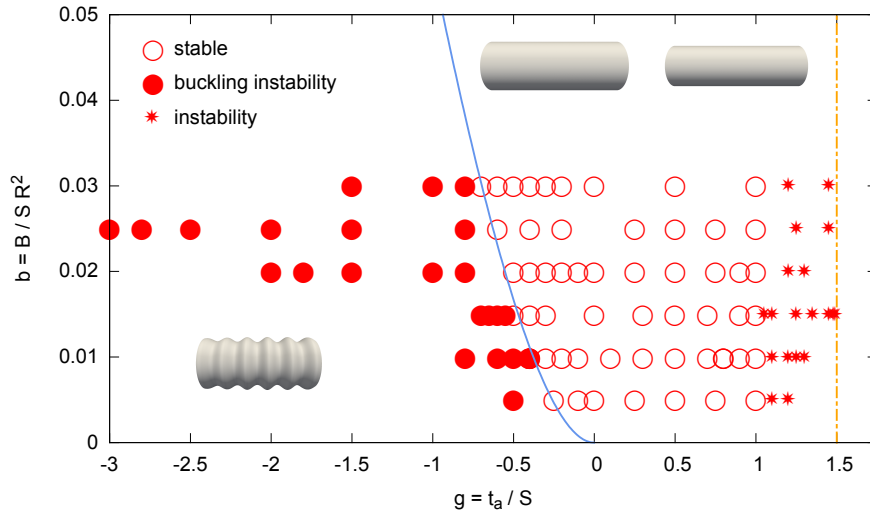


Figure 2. Phase diagram of a cylindrical shell with homogeneous, relative, active in-plane surface stress $g = t_a/S$ and relative bending modulus $b = B/(SR^2)$ for axisymmetric simulations. The Poisson ratio is $\nu = \frac{1}{2}$. For negative active in-plane surface stress a buckling instability occurs. The simulations match the predicted [1] critical active in-plane surface stress very well. For positive active in-plane surface stresses an instability occurs characterized by a deformation larger than the cylinder radius which happens even before the threshold predicted by [1] (orange dotted line). Insets show membrane shapes corresponding to the different phases.

As in section V.D of the main text for the full 3D method, we next consider a finite, homogeneous, active in-plane surface stress $t_a \neq 0$ without any singular perturbation, i.e., $T_a^z, T_a^\phi = 0$. In this case Berthoumieux *et al.* [1] predicts two kinds of instabilities depending on the magnitude of active in-plane surface stress: for negative active in-plane surface stress beyond $t_a < -2\sqrt{\frac{3BS}{R^2}}$ a buckling instability takes place and for positive active in-plane surface stress they predict an instability for $t_a > 2S(1 - \nu^2)$. This allows us to perform simulations for different parameter sets (g, b) and to construct a phase diagram classifying the final shape. The resulting phase diagram is shown in figure 2.

For negative, active in-plane surface stress $g < 0$ our axisymmetric numerics are in very good agreement with the predicted instability threshold for a broad range of relative bending moduli b . In the case of positive, active in-plane surface stress $g > 0$ the cylindrical shell contracts. Whereas the membrane in 3D shows an instability similar to a Rayleigh-Plateau instability of a liquid jet, in 2D the cylindrical membrane contracts homogeneously, since

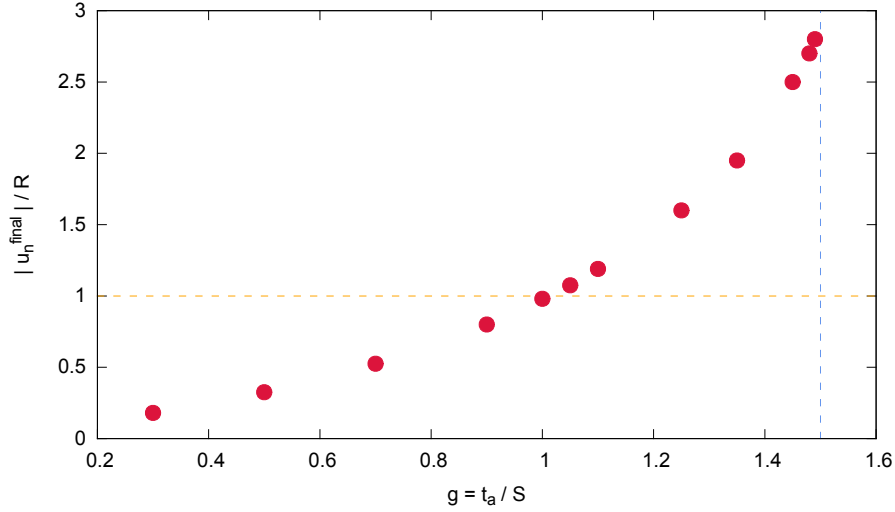


Figure 3. Final deformation of a cylinder with homogeneous active in-plane surface stress in the axisymmetric simulations for a bending modulus $b \approx 0.015$. Near the threshold $g = 1.5$ the deformation increases strongly and nearly diverges (divergence not completely covered by numerics).

volume conservation is not enforced in the axisymmetric case. Beyond a certain threshold, the deformation becomes larger than the cylinder radius R . This serves us as a criterion for an instability. The Green's function found by [Berthoumieux *et al.* \[1\]](#) diverges for $g = 1.5$, which is beyond our instability threshold. The discrepancy may be explained by the fact that our criterion is more realistic than that of [Berthoumieux *et al.*](#) which is based on the Green's function only. Nevertheless, we note that our instability threshold does not depend on the bending modulus, as predicted by ref. [1].

In order to discuss the latter issue in further detail we show in figure 3 the final deformation u_n^{final}/R depending on the relative, active in-plane surface stress g . We define the instability threshold by $|u_n^{\text{final}}| = R$. Beyond this threshold the deformation increases strongly, but our numerics do not cover the divergence predicted. However, we have to note that the behavior beyond the threshold is not physical in a strict sense.

In conclusion, this section proves that our axisymmetric numerical simulations are in very good agreement with the predicted theory and consequently can be used for validation of the three dimensional method as done in figure 8 of the main text.

-
- [1] H. Berthoumieux, J.-L. Maître, C.-P. Heisenberg, E. K. Paluch, F. Jülicher, and G. Salbreux, Active elastic thin shell theory for cellular deformations, *New Journal of Physics* **16**, 065005 (2014).
- [2] G. Salbreux and F. Jülicher, Mechanics of active surfaces, *Physical Review E* **96**, 10.1103/PhysRevE.96.032404 (2017).

Publication 2

A THREE-DIMENSIONAL NUMERICAL MODEL OF AN ACTIVE CELL CORTEX IN THE VISCOUS LIMIT

C. Bächer, D. Khoromskaia, G. Salbreux, and S.
Gekle

Draft, 2020

A three-dimensional numerical model of an active cell cortex in the viscous limit

Bächer, Christian¹ and Khoromskaia, Diana² and Salbreux, Guillaume² and Gekle, Stephan¹

¹Biofluid Simulation and Modeling, Theoretische Physik VI, University of Bayreuth, Universitätsstraße 30, 95448 Bayreuth, Germany

²The Francis Crick Institute, 1 Midland Road, London NW1 1AT, UK

Contents

1. Introduction	2
2. Thin shell formulation of a viscous active cortex	4
2.1. Differential geometry	4
2.2. Force balance for a viscous active cortex	5
2.3. The force balance in terms of the velocity	6
3. Computational model for a viscous active cortex	8
3.1. Discretization of the cortex	9
3.2. Minimization ansatz for the force balance	10
3.3. Constraints	11
3.4. Consideration of pressure	12
3.5. Bending viscosity for better stability	13
3.6. Velocity derivatives as a function of neighboring velocity vectors	15
3.7. Summary of the algorithm	19
4. Validation and application	22
4.1. Velocity profile by spherical harmonics on a static spherical cortex	22
4.2. Dynamics of a viscous active cortex	26
4.3. A first application	34
5. Conclusion	35
Appendices	38

Abstract

Dynamic cellular processes are often driven by the cell cortex, which is a highly dynamic network of cytoskeletal filaments where motor proteins actively induce stresses. In the present manuscript, we develop a simple three-dimensional computational model of a cell cortex in the viscous limit, where active stresses trigger flows within the cortex. Combining active gel and thin shell theory, we directly solve the force balance equations for the velocity field on a discrete and arbitrarily deforming cortex. We do so in two essential steps, where a minimization ansatz is used to fulfill the force balance equations and derivatives of the velocity field at each node are expressed in terms of an analytically inverted parabolic fitting procedure. Constraints on the velocity field are incorporated using the formalism of Lagrange multipliers. As validation in the static case we present an analytical test setup with an active stress distribution either resulting in a tangential or normal velocity in terms of spherical harmonics, where we successfully compare the numerical results to the derived analytical solution. Further, we test our algorithm in a dynamic situation of a viscous cortex with an active stress distribution resembling a cortical ring, where we successfully compare our three-dimensional results to simulations based on an axisymmetric description of the viscous active cell cortex. Going one step further we investigate the cell cortex subject to an initial shear deformation and analyze the dynamic evolution. Because our developed method is based on the general force balance equation, it can easily be extended to different constitutive laws or to include a dynamic coupling to a suspending fluid.

1. Introduction

Motor proteins in the cell are capable of converting chemically stored energy into movement and mechanical work [1] and therefore drive biophysical systems out of thermodynamic equilibrium [2]. Such motor proteins actively induce stresses [2–5], which lead to the formation of patterns [6–9] or spontaneous flows [10–18]. In particular in the cell cortex, which is a network of cytoskeletal actin filaments and myosin proteins [1], such an active material is confined to a thin layer. Together with the connected plasma membrane the cell cortex can strongly deform and therefore plays a crucial role in the regulation of the cell shape [19–23] and movement [24–29]. A prominent example is the cytokinesis in cell division, where a ring of actomyosin leads to furrow constriction and the separation of the two daughter cells [30–34].

The class of cytoskeletal filaments and motor proteins is successfully described in the framework of active gel theory [2, 35–37]. Key ingredient is the actively induced force from the motor proteins, which leads to an active stress in the material [38, 39]. In addition, polymerization and depolymerization leads to transient changes within the active gel [20, 35]. Focusing on the cell cortex of actomyosin or epithelial tissue, active gel theory has recently been formulated in the framework of thin shell theory [40]. The generic active gel theory [35] incorporates the viscoelastic nature of the cytoskeletal

assemblies, where the presence of an active stress triggers both elastic deformations and viscous flows. Starting from the viscoelastic theory two limits of the cortex behavior can be considered, the elastic limit [40–43] and the viscous limit [21, 28, 30, 33, 40, 44, 45], where flows arise. In the cell cortex, flows regulate cell morphogenesis with special impact on cell polarization [8, 19–21]. Here, a cell can undergo a transition from the spherical shape towards a pear-like shape depending on active stress and polymerization rate [20, 21]. In addition, a transition from spherical to oblate cell shape accompanied by concentration variations of the stress regulator has been reported [8]. An instability leading to a constant cortical flow has further been reported for cell movement [24, 46]. Marth et al. [27] analyzed the flow field inside and outside a moving cell in two dimensions. In addition, cell division has successfully been modeled [30, 31, 33, 34, 44, 47] including an threshold active stress needed to complete cytokinesis [33]. Furthermore, embryogenesis is regulated by active stress induced flows [48, 49], where anisotropy of the flows can lead to polarization [48].

Such investigations involving the cell cortex are often based on analytical calculations [21, 30, 41, 44], but also simulations get into the focus [9, 33, 42, 45, 46, 50, 51]. Farutin et al. [46] investigated cell crawling by coupling cortical mechanics to the boundary integral equation in axisymmetric treatment. Turlier et al. [33] used a numerical, axisymmetric formulation of cell cytokinesis advecting tracer points at the position of the membrane. Mietke et al. [9] developed another axisymmetric simulation method discretizing the arc length of the cellular membrane. Including myosin activity in terms of a preferred curvature, Heer et al. [50] determined the equilibrium of a tissue shell. Bächer and Gekle [42] have developed a three-dimensional simulation model of an active cell cortex in the elastic limit which is dynamically coupled to a fluid using the lattice-Boltzmann/immersed boundary method. Torres-Sánchez et al. [45] developed a fully three-dimensional computational model of a viscous active cell cortex based on finite element method. A generalization to arbitrary topology using local Monge parametrization method has been provided [51]. Despite the model developed in refs. [45, 51], investigations of a cortex in the viscous limit are restricted to axisymmetry.

In the present manuscript we develop a new and direct method, which numerically obtains the velocity profile in a three-dimensional, thin, and arbitrarily deformed active cell cortex in the viscous limit. We use the thin shell formulation combined with active gel theory [40] to obtain the force balance equations for the cortex involving active and viscous stresses. The force balance equations are discretized using a parabolic fitting procedure. Using an analytical inversion of the parabolic expansion and fitting of the cortical velocity field, we evaluate the force balance equation on the discrete nodes of the cortex depending on the velocity field. Solving the resulting system of coupled equations globally on the cortex by means of a minimization ansatz, we eventually solve for the cortical velocity field. Considering the normal component of the velocity, the cortex shape can be evolved in time in order to obtain the deforming cell shape. We provide an in-depth validation to analytical results on an undeformed, spherical cortex and to axisymmetric simulations for the evolving shape and cortical flow field. In addition, we apply an initial shear to the cortex and investigate the dynamic evolution. Due to its simplicity our proposed algorithm can be the basis for a dynamic coupling of a viscous active cortex or a tissue to a suspending fluid using, e.g., a coupled immersed boundary

and lattice-Boltzmann method.

We first introduce the force balance equations of the cell cortex treated as viscous thin shell in section 2. Afterwards, we present the discretization of the cortex based on a parabolic fitting procedure and the numerical solution procedure in section 3. In section 4, we validate our method to analytical calculations and axisymmetric simulations in a detailed manner and apply our algorithm to a dynamic non-axisymmetric situation. Eventually, we conclude in section 5.

2. Thin shell formulation of a viscous active cortex

In the following we consider a cell cortex in the viscous limit subject to active stress leading to reorganization of the cortex in terms of effective flows within the actomyosin network [37, 40]. Since the cortex is typically very small compared to the cell diameter [1], it is considered as thin shell [40, 52], i.e., as two dimensional manifold in three-dimensional space. The framework for the mathematical description of a thin shell is the differential geometry [53], which we introduce in section 2.1. Due to its viscous nature, forces from velocity gradients arise in the cell cortex in addition to the presence of the active stress. The goal of the presented method is to determine the velocity field in the cell cortex under consideration of viscous and active forces present in the cortex and expressed in terms of thin shell formulation. In section 2.2 we provide the analytical formulation of the force balance for the viscous active cortex, which we express in terms of the velocity and its derivatives in section 2.3.

2.1. Differential geometry

In general, the two dimensional thin shell representing the cell cortex is parametrized by the vector $\mathbf{X}(s^1, s^2)$ in three-dimensions which depends on two coordinates s^1, s^2 . The latter determine the in-plane position on the thin shell. From the parametrization \mathbf{X} two in-plane coordinate vectors pointing locally along the thin shell are derived

$$\mathbf{e}_1 = \frac{\partial \mathbf{X}}{\partial s^1}, \quad \mathbf{e}_2 = \frac{\partial \mathbf{X}}{\partial s^2}, \quad (1)$$

and using those a unit normal vector on the thin shell can be defined

$$\mathbf{n} = \frac{\mathbf{e}_1 \times \mathbf{e}_2}{|\mathbf{e}_1 \times \mathbf{e}_2|}. \quad (2)$$

The metric tensor of the thin shell is defined by

$$g_{\alpha\beta} = \mathbf{e}_\alpha \cdot \mathbf{e}_\beta, \quad (3)$$

and its curvature tensor by

$$C_{\alpha\beta} = -(\partial_\alpha \partial_\beta \mathbf{X}) \cdot \mathbf{n}, \quad (4)$$

with Greek indices $\alpha, \beta, \gamma = 1, 2$ referring to the in-plane coordinates s^1, s^2 . In the following, we use Einstein sum convention where a double occurrence of an upper (contravariant) and lower (covariant) index implies a sum. We denote the partial derivative

along the in-plane coordinates of a general function f by $\partial_\alpha f$ and the covariant derivative by $\nabla_\alpha f$ [53]. The covariant derivative of the in-plane and normal coordinate vector is given by the equation of Weingarten and Gauss

$$\nabla_\alpha \mathbf{n} = C_\alpha^\beta \mathbf{e}_\beta \quad \nabla_\alpha \mathbf{e}_\beta = -C_{\alpha\beta} \mathbf{n}. \quad (5)$$

The key quantity of interest for the viscous active cortex is the cortical velocity field \mathbf{v} . It is defined on the cortex, thus depending on (s^1, s^2) , but is a three-dimensional vector. Therefore, it can be decomposed in the local coordinate system on the thin shell by projection onto the in-plane and normal coordinate vector

$$v^\alpha = \mathbf{v} \cdot \mathbf{e}^\alpha \quad \text{and} \quad v^n = \mathbf{v} \cdot \mathbf{n}, \quad (6)$$

with its in-plane components v^α and its normal component v^n such that

$$\mathbf{v} = v^\alpha \mathbf{e}_\alpha + v^n \mathbf{n}. \quad (7)$$

The total in-plane vectorial component of the velocity field can further be determined by

$$\mathbf{v}_t = (\mathbf{1} - \mathbf{n}\mathbf{n}) \cdot \mathbf{v}, \quad (8)$$

with the projector $\mathbf{n}\mathbf{n}$ onto the normal vector, which is the outer product of the normal vector with itself, and with $\mathbf{1}$ the unit matrix. The velocity gradient on the thin shell is defined as [40]

$$v_{\alpha\beta} = \frac{1}{2} [\nabla_\alpha v_\beta + \nabla_\beta v_\alpha] + C_{\alpha\beta} v^n, \quad (9)$$

which is equivalent to the definition in vector notation

$$v_{\alpha\beta} = \frac{1}{2} [(\partial_\alpha \mathbf{v}) \cdot \mathbf{e}_\beta + (\partial_\beta \mathbf{v}) \cdot \mathbf{e}_\alpha] = \frac{1}{2} [(\nabla_\alpha \mathbf{v}) \cdot \mathbf{e}_\beta + (\nabla_\beta \mathbf{v}) \cdot \mathbf{e}_\alpha]. \quad (10)$$

2.2. Force balance for a viscous active cortex

Forces in the cortex, e.g., arising due to gradients in the velocity, are described by a stress tensor, as done in three-dimensional hydrodynamics [52, 54]. Here, the stress tensor is defined on the thin shell and therefore denoted as surface stress tensor [42, 52]. The stresses decomposed into in-plane and normal component are written as

$$\mathbf{t}^\alpha = t^{\alpha\beta} \mathbf{e}_\beta + t_n^\alpha \mathbf{n}. \quad (11)$$

For vanishing normal stresses t_n , the force balance for an external force free thin shell becomes

$$\nabla_\alpha t^{\alpha\beta} = 0 \quad (12)$$

$$-C_{\alpha\beta} t^{\alpha\beta} = 0. \quad (13)$$

We consider a viscous cortex with planar shear η_s and bulk viscosity η_b , which is subject to active forces described by the active surface stress tensor $\zeta^{\alpha\beta}$. Accordingly, the constitutive equation reads [40]

$$t^{\alpha\beta} = t_v^{\alpha\beta} + \zeta^{\alpha\beta}, \quad (14)$$

with the viscous surface stress tensor

$$t_v^{\alpha\beta} = 2\eta_s \tilde{v}^{\alpha\beta} + \eta_b v_\gamma^\gamma g^{\alpha\beta}, \quad (15)$$

where $\tilde{v}^{\alpha\beta} = v^{\alpha\beta} - \frac{1}{2}v_\gamma^\gamma g^{\alpha\beta}$. The active stress $\zeta^{\alpha\beta}$ describes internal forces in the cortex which stem from active processes, such as motor proteins walking along cytoskeletal filaments by conversion of chemically stored energy [35, 37, 40]. In the following, we assume that the distribution of active stress in the cortex is known, but our method allows for a potential coupling of active stress to a concentration field, e.g., myosin. Inserting the surface stress tensor (14) into the force balance equations (12) and (13) we obtain for the force free cortex

$$2\eta_s \nabla_\alpha v^{\alpha\beta} + (\eta_b - \eta_s) \nabla_\alpha v_\gamma^\gamma g^{\alpha\beta} = -\nabla_\alpha \zeta^{\alpha\beta} \quad (16)$$

$$-2\eta_s C_{\alpha\beta} v^{\alpha\beta} - (\eta_b - \eta_s) v_\gamma^\gamma C_{\alpha\beta} g^{\alpha\beta} = C_{\alpha\beta} \zeta^{\alpha\beta}. \quad (17)$$

Our goal is to solve the force balance equations (16) and (17) for the velocity field for a given active stress distribution $\zeta^{\alpha\beta}$.

2.3. The force balance in terms of the velocity

The aim of this section is a formulation of the force balance equations (16) and (17) in terms the velocity vector and its derivatives, which is directly used for the numerical algorithm in section 3. Motivated by the parabolic fitting procedure to determine curvature and derivatives on a discrete thin shell [42, 55], we start with a parabolic expansion of the velocity vector in in-plane coordinates (s^1, s^2) at given position \mathbf{r}_ν on the thin shell

$$\mathbf{v}(s^1, s^2) = \mathbf{v}_\nu + \underbrace{(\nabla_1 \mathbf{v})}_{\mathbf{A}_v} s^1 + \underbrace{(\nabla_2 \mathbf{v})}_{\mathbf{B}_v} s^2 + \frac{1}{2} \underbrace{(\nabla_1 \nabla_1 \mathbf{v})}_{\mathbf{C}_v} s^1 s^1 + \frac{1}{2} \underbrace{(\nabla_2 \nabla_2 \mathbf{v})}_{\mathbf{D}_v} s^2 s^2 + \underbrace{(\nabla_1 \nabla_2 \mathbf{v})}_{\mathbf{E}_v} s^1 s^2, \quad (18)$$

with $\mathbf{v}_\nu = \mathbf{v}(\mathbf{r}_\nu)$ and $\mathbf{A}_v - \mathbf{E}_v$ being the first and second derivative of the velocity field \mathbf{v} with respect to in-plane coordinates at position \mathbf{r}_ν . Using the parabolic expansion of the velocity field in equation (18), we can first directly express the velocity gradient (10) in terms of the velocity derivatives $\mathbf{A}_v - \mathbf{E}_v$

$$v_{11} = \mathbf{A}_v \cdot \mathbf{e}_1 \quad v_{22} = \mathbf{B}_v \cdot \mathbf{e}_2 \quad (19)$$

$$v_{12} = v_{21} = \frac{1}{2} (\mathbf{A}_v \cdot \mathbf{e}_2 + \mathbf{B}_v \cdot \mathbf{e}_1) \quad (20)$$

The trace of the velocity gradient is

$$\begin{aligned} v_\gamma^\gamma &= v_{\alpha\beta} g^{\alpha\beta} = g^{11} v_{11} + 2g^{12} v_{12} + g^{22} v_{22} \\ &= g^{11} \mathbf{A}_v \cdot \mathbf{e}_1 + g^{12} [\mathbf{A}_v \cdot \mathbf{e}_2 + \mathbf{B}_v \cdot \mathbf{e}_1] + g^{22} \mathbf{B}_v \cdot \mathbf{e}_2. \end{aligned} \quad (21)$$

Next, we can calculate the derivative of the velocity gradient tensor in equation (10), which becomes under use of the equations of Weingarten and Gauss (5)

$$\nabla_\alpha v_{\beta\gamma} = \frac{1}{2} (\nabla_\alpha \nabla_\beta \mathbf{v}) \cdot \mathbf{e}_\gamma - \frac{1}{2} C_{\alpha\gamma} (\nabla_\beta \mathbf{v}) \cdot \mathbf{n} + \frac{1}{2} (\nabla_\alpha \nabla_\gamma \mathbf{v}) \cdot \mathbf{e}_\beta - \frac{1}{2} C_{\alpha\beta} (\nabla_\gamma \mathbf{v}) \cdot \mathbf{n}. \quad (22)$$

Using the fact $\nabla_\alpha g^{\beta\gamma} = 0$, we can calculate the derivative of the contravariant components of the velocity gradient by

$$\nabla_\alpha v^{\beta\gamma} = g^{\beta\epsilon} g^{\delta\gamma} \nabla_\alpha v_{\epsilon\delta}. \quad (23)$$

Furthermore, we calculate the derivative of the velocity gradient's trace via

$$\begin{aligned} \nabla_\alpha v_\gamma^\gamma &= \nabla_\alpha (g^{\gamma\beta} v_{\beta\gamma}) = g^{\gamma\beta} \nabla_\alpha v_{\beta\gamma} \\ &= g^{11} \nabla_\alpha v_{11} + g^{12} \nabla_\alpha v_{12} + g^{21} \nabla_\alpha v_{21} + g^{22} \nabla_\alpha v_{22} \end{aligned}$$

using the formula for the gradient in equation (22). Writing down these equations for fixed indices $\alpha, \beta, \gamma = 1, 2$, they can be explicitly written in terms of $\mathbf{A}_v - \mathbf{E}_v$.

In the final step, we aim for a formulation of the force balance equations (16), (17) in terms of the velocity derivatives. Inserting the constitutive law for the viscous active cortex (14) and the definition of the viscous surface stress (15), the force balance equations have the form

$$2\eta_s g^{\gamma\alpha} \nabla_\alpha v_{\beta\gamma} + (\eta_b - \eta_s) (\nabla_\alpha v_\gamma^\gamma) \delta_\beta^\alpha = -\nabla_\alpha \zeta_\beta^\alpha \quad (24)$$

$$-2\eta_s C^{\alpha\beta} v_{\alpha\beta} - (\eta_b - \eta_s) v_\gamma^\gamma C_\delta^\delta = C_\beta^\alpha \zeta_\alpha^\beta, \quad (25)$$

where we used $v_\beta^\alpha = v_{\beta\gamma} g^{\gamma\alpha}$ and $g_{\alpha\beta} g^{\beta\gamma} = \delta_\alpha^\gamma$. The components of the force balance equation in this form can be explicitly expanded using the expressions derived above. Writing down each component on its own and collecting terms with respect to $\mathbf{A}_v - \mathbf{E}_v$ we end up with the first tangential force balance equation in the form

$$\begin{aligned} &(-2\eta_s g^{11} C_{11} \mathbf{n} - 3\eta_s g^{21} C_{12} \mathbf{n} - \eta_s g^{22} C_{22} \mathbf{n} - (\eta_b - \eta_s) g^{11} C_{11} \mathbf{n} - (\eta_b - \eta_s) g^{12} C_{12} \mathbf{n}) \cdot \mathbf{A}_v \\ &(-\eta_s g^{21} C_{11} \mathbf{n} - \eta_s g^{22} C_{21} \mathbf{n} - (\eta_b - \eta_s) g^{12} C_{11} \mathbf{n} - (\eta_b - \eta_s) g^{22} C_{12} \mathbf{n}) \cdot \mathbf{B}_v \\ &(+ 2\eta_s g^{11} \mathbf{e}_1 + \eta_s g^{21} \mathbf{e}_2 + (\eta_b - \eta_s) g^{11} \mathbf{e}_1 + (\eta_b - \eta_s) g^{12} \mathbf{e}_2) \cdot \mathbf{C}_v \\ &(+ \eta_s g^{22} \mathbf{e}_1) \cdot \mathbf{D}_v \\ &(+ 3\eta_s g^{21} \mathbf{e}_1 + \eta_s g^{22} \mathbf{e}_2 + (\eta_b - \eta_s) g^{12} \mathbf{e}_1 + (\eta_b - \eta_s) g^{22} \mathbf{e}_2) \cdot \mathbf{E}_v \\ &= -\nabla_1 \zeta_1^1 - \nabla_2 \zeta_1^2, \end{aligned} \quad (26)$$

the second tangential force balance equation

$$\begin{aligned} &(-\eta_s g^{11} C_{12} \mathbf{n} - (\eta_b - \eta_s) g^{12} C_{22} \mathbf{n} - \eta_s g^{12} C_{22} \mathbf{n} - (\eta_b - \eta_s) g^{11} C_{21} \mathbf{n}) \cdot \mathbf{A}_v \\ &(-\eta_s g^{11} C_{11} \mathbf{n} - 3\eta_s g^{12} C_{21} \mathbf{n} - 2\eta_s g^{22} C_{22} \mathbf{n} - (\eta_b - \eta_s) g^{12} C_{21} \mathbf{n} - (\eta_b - \eta_s) g^{22} C_{22} \mathbf{n}) \cdot \mathbf{B}_v \\ &(+ \eta_s g^{11} \mathbf{e}_2) \cdot \mathbf{C}_v \\ &(+ \eta_s g^{12} \mathbf{e}_1 + 2\eta_s g^{22} \mathbf{e}_2 + (\eta_b - \eta_s) g^{12} \mathbf{e}_1 + (\eta_b - \eta_s) g^{22} \mathbf{e}_2) \cdot \mathbf{D}_v \\ &(+ \eta_s g^{11} \mathbf{e}_1 + 3\eta_s g^{12} \mathbf{e}_2 + (\eta_b - \eta_s) g^{11} \mathbf{e}_1 + (\eta_b - \eta_s) g^{12} \mathbf{e}_2) \cdot \mathbf{E}_v \\ &= -\nabla_1 \zeta_2^1 - \nabla_2 \zeta_2^2, \end{aligned} \quad (27)$$

and the normal force balance equation

$$\begin{aligned} & \left(-2\eta_s C^{11} \mathbf{e}_1 - 2\eta_s C^{12} \mathbf{e}_2 - C(\eta_b - \eta_s) g^{11} \mathbf{e}_1 - C(\eta_b - \eta_s) g^{12} \mathbf{e}_2 \right) \cdot \mathbf{A}_v \\ & \left(-2\eta_s C^{12} \mathbf{e}_1 - 2\eta_s C^{22} \mathbf{e}_2 - C(\eta_b - \eta_s) g^{12} \mathbf{e}_1 - C(\eta_b - \eta_s) g^{22} \mathbf{e}_2 \right) \cdot \mathbf{B}_v \\ & = C_1^1 \zeta_1^1 + C_1^2 \zeta_2^1 + C_2^1 \zeta_1^2 + C_2^2 \zeta_2^2. \end{aligned} \quad (28)$$

On the right hand side of the tangential force balance the active stress appears which we consider symmetric and isotropic, i.e.,

$$\zeta_\alpha^\beta = \zeta(s^1, s^2) \delta_\alpha^\beta. \quad (29)$$

The derivatives of the active stress

$$\begin{aligned} \nabla_1 \zeta_1^1 &= \nabla_1 \zeta_2^2 = \nabla_1 \zeta(s^1, s^2), \\ \nabla_2 \zeta_1^1 &= \nabla_2 \zeta_2^2 = \nabla_2 \zeta(s^1, s^2), \end{aligned}$$

can be calculated from the given active stress distribution $\zeta(s^1, s^2)$ on the deforming thin shell. From equation (29) we can directly use

$$\begin{aligned} \nabla_1 \zeta_1^2 &= 0, & \nabla_1 \zeta_2^1 &= 0 \\ \nabla_2 \zeta_1^2 &= 0, & \nabla_2 \zeta_2^1 &= 0. \end{aligned}$$

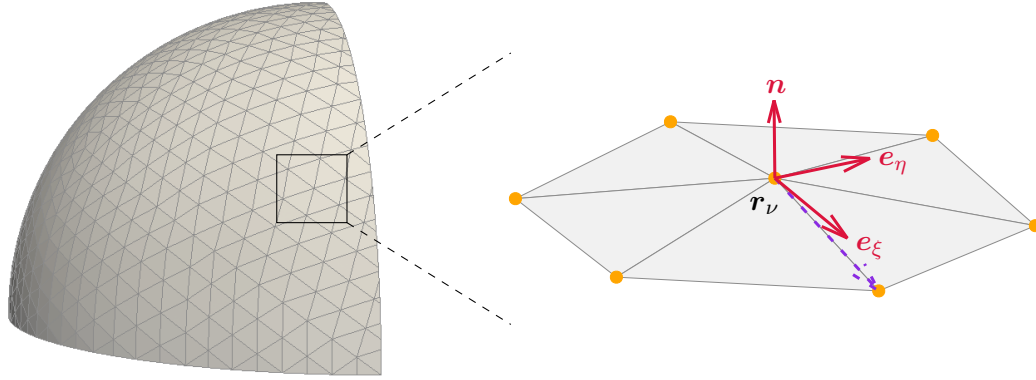


Figure 1: **Cortex discretization.** Discretization of a thin shell by nodes connected to triangles (left). For each node \mathbf{r}_ν a local coordinate system with in-plane coordinate vectors \mathbf{e}_ξ , \mathbf{e}_η and normal vector \mathbf{n} is constructed. The velocity field, its derivatives and the force balance equations can be expressed in this local coordinate system $(\mathbf{e}_\xi, \mathbf{e}_\eta, \mathbf{n})$ at the position \mathbf{r}_ν .

3. Computational model for a viscous active cortex

As introduced above, our aim is to calculate the corresponding velocity field for given active stress on a deforming cortex numerically. In the following, we illustrate the steps

of the numerical calculation of the velocity field. First, we discretize the thin shell representing a cell cortex and the velocity field in section 3.1. This allows us to write down the force balance equations (16) and (17) for each node of the discrete thin shell. The latter can be solved for the velocity field by a minimization ansatz as detailed in 3.2. We introduce constraints on the velocity field in section 3.3. Furthermore, the active stress in the cell cortex together with the incompressibility of the cell's interior, the cytosol, imposes a pressure difference inside the cell, which we treat in section 3.4. An additional contribution to the surface stress from a bending viscosity is introduced in section 3.5. In order to solve the system of equations we need the derivatives of the velocity field in equation (18) as functions of the velocity values at all discrete nodes, this step we illustrate in section 3.6. The final step to build a matrix for the equation system is detailed in section 3.7.

3.1. Discretization of the cortex

In our numerical implementation we discretize the thin shell representing the cortex plus membrane by nodes, which we refer to by their position \mathbf{r}_ν and/or index $\nu = 0, \dots, N-1$, where N is the total number of nodes. The nodes are connected to flat triangles [55–58], as sketched in figure 1. Here, the triangles serve us as a tool to determine the neighborhood of each node \mathbf{r}_ν . The numbering of neighbor nodes is arbitrary but in ordered fashion. For each node on the membrane we define a local coordinate system as done in ref. [42] and sketched on the right hand side of figure 1. First, by averaging all normal vectors of the adjacent triangles weighted by angle [59], we obtain the local normal vector \mathbf{n} on the node \mathbf{r}_ν . By connecting the ν -th node to one of its neighbors and subtracting the normal component of the resulting vector, we get the first in-plane coordinate vector \mathbf{e}_ξ . By a normalized cross-product of \mathbf{n} and \mathbf{e}_ξ the second in-plane coordinate vector \mathbf{e}_η is obtained. Thus, we have for each node a local coordinate system

$$(\mathbf{e}_\xi, \mathbf{e}_\eta, \mathbf{n})_\nu = (\mathbf{e}_\xi, \mathbf{e}_\eta, \mathbf{n}). \quad (30)$$

The local curvature tensor at the position of the central node and expressed in the local coordinate system in equation (30) can be obtained by a parabolic fitting procedure with respect to node position as detailed in ref. [42].

The key quantity of interest, the velocity \mathbf{v} , is a three-dimensional vector in the three-dimensional Cartesian space

$$\mathbf{v} = v^x \mathbf{e}_x + v^y \mathbf{e}_y + v^z \mathbf{e}_z, \quad (31)$$

with $\mathbf{e}_i, i = x, y, z$ the Cartesian unit coordinate vectors. Because the velocity field is defined on the thin shell, we can evaluate the velocity at each node ν giving $v_\nu^i = v^i(\mathbf{r}_\nu)$. In total, the velocity field consists of the velocity of each node

$$\begin{aligned} v^x &= \{v_\nu^x\}_{\nu \in \{0; \dots; N-1\}}, \\ v^y &= \{v_\nu^y\}_{\nu \in \{0; \dots; N-1\}}, \\ v^z &= \{v_\nu^z\}_{\nu \in \{0; \dots; N-1\}}. \end{aligned} \quad (32)$$

The velocity components in the local coordinate system (30) can easily be obtained by projection onto the corresponding local coordinate vectors according to equation (6)

$$v_\xi = \mathbf{v} \cdot \mathbf{e}_\xi, \quad v_\eta = \mathbf{v} \cdot \mathbf{e}_\eta, \quad v^n = \mathbf{v} \cdot \mathbf{n}. \quad (33)$$

With the derivatives of the velocity vector introduced in equation (18) evaluated in local coordinates, i.e., $\mathbf{A}_\nu = \nabla_\xi \mathbf{v} \dots \mathbf{E}_\nu = \nabla_\xi \nabla_\eta \mathbf{v}$, we can write down the velocity gradient (10) in the local coordinate system, e.g., the component

$$v_{\xi\eta} = \frac{1}{2} [\mathbf{A}_\nu \cdot \mathbf{e}_\eta + \mathbf{B}_\nu \cdot \mathbf{e}_\xi].$$

For the actual calculation of the derivatives of the velocity vector we refer to section 3.6. Using the derivatives of the velocity and the velocity gradient in local coordinates, we are able to write down the force balance equations (16) and (17) for each node ν in its local coordinate system. Considering the tangential force balance equations (26) and (27) together with the normal force balance equation (28), we end up with three equations of motion. These we refer to in the following by its left hand side, which depends on the velocity vectors \mathbf{v}_ν , and by the right hand side, which does not depend on the velocity vectors. Therefore we have three coupled equations of motions which the velocity field has to fulfill

$$\begin{aligned} \text{l.h.s.}_1^\nu &= \text{r.h.s.}_1^\nu, \\ \text{l.h.s.}_2^\nu &= \text{r.h.s.}_2^\nu, \\ \text{l.h.s.}_n^\nu &= \text{r.h.s.}_n^\nu, \end{aligned} \quad (34)$$

where the index 1,2 labels the two tangential force balance equations and the index n labels the normal force balance equation. By the superscript ν we refer to the equation in local coordinates of node ν , thus the force balance evaluated at position \mathbf{r}_ν of node ν .

3.2. Minimization ansatz for the force balance

The overall goal is to solve the force balance equations for the velocity field. The solution fulfills the force balance on the complete thin shell, i.e., the force balance equations must be fulfilled at every node \mathbf{r}_ν . With the evaluation of the force balance at a node in equation (34), as a consequence the difference between left hand side and right hand side has to vanish. Consequently, we can define

$$\chi^2 = \sum_\nu \left[(\text{l.h.s.}_1^\nu - \text{r.h.s.}_1^\nu)^2 + (\text{l.h.s.}_2^\nu - \text{r.h.s.}_2^\nu)^2 + (\text{l.h.s.}_n^\nu - \text{r.h.s.}_n^\nu)^2 \right], \quad (35)$$

with the sum \sum_ν over all nodes. For the exact solution the χ^2 would become zero, for the correct numerical solution the χ^2 becomes minimal. Thus, in simulations we have to solve for the set $v_\nu^x, v_\nu^y, v_\nu^z$ (32), which minimizes χ^2 in equation (35). We therefore have to calculate

$$\arg \min_{\{\mathbf{v}_\nu\}} \chi^2 = \arg \min_{\{v_\nu^x\}, \{v_\nu^y\}, \{v_\nu^z\}} \chi^2. \quad (36)$$

In order to perform this minimization, we calculate the derivatives of χ^2 in equation (35) with respect to the velocity components of each node v_ν^i . Due to minimization the derivatives equal zero and we can separate this equality for terms linear in v_ν^i and terms independent of the velocity under use of the parabolic expansion of the velocity field in equation (18). In total, this leads to a system of linear equations in matrix form, where we have $3N$ rows due to the derivatives w.r.t. to the N velocities with 3 components each and we have $3N$ columns due to the N velocities with 3 components each in the solution vector.

In order to calculate the corresponding matrix to the system of linear equations we have to evaluate the left hand side and right hand side of all three force balance equations on each node in the local coordinate system (30). This we do using the velocity derivatives in local coordinates as detailed in 3.1. For details on the dependency on the actual velocity values we refer to section 3.7. The system of equations can finally be solved numerically using LU-Decomposition.

3.3. Constraints

The algorithm described above solves the force balance equations, which are partial differential equations in the velocity. Because only derivatives of the velocity field occur, a constant velocity can be added without violating the force balance equations. Furthermore, these derivatives are directional and under certain circumstances, e.g., axisymmetry, a velocity in azimuthal direction can be added. Therefore, we need to specify certain constraints to the velocity field, which correspond to boundary conditions for the partial differential equations.

First, we use that the total velocity of the cortex has to vanish, i.e.,

$$\int_S \mathbf{v} dS = \sum_{\nu=0}^{N-1} \mathbf{v}_\nu A_\nu = \mathbf{0}, \quad (37)$$

where the second equality is the discretization to a sum over all nodes ν and A_ν being the local area of node ν . The local area is calculated using Meyer's mixed area [42, 59].

Second, we use the fact that the total angular momentum of the cortex must vanish, i.e.,

$$\int_S \mathbf{r} \times \mathbf{v} dS = \sum_{\nu=0}^{N-1} \mathbf{r}_\nu \times \mathbf{v}_\nu A_\nu = \mathbf{0}. \quad (38)$$

In addition, we use a vanishing total normal velocity v^n which corresponds to an incompressible liquid inside the cell, i.e.,

$$\int_S \mathbf{v} \cdot \mathbf{n} dS = \sum_{\nu=0}^{N-1} \mathbf{v}_\nu \cdot \mathbf{n} A_\nu = 0. \quad (39)$$

To incorporate the constraints into the solution procedure we use the concept of a Lagrange multiplier. The constraints (37) and (38) impose three conditions due to the three components of the velocity vector whereas constraint (39) imposes one condition.

This means we introduce three or respectively one Lagrange multiplier per constraint. The constraint times the Lagrange multiplier is added to the χ^2 in equation (35), e.g.,

$$\chi^2 = \sum_{\rho} \sum_{\nu} \left(\text{l.h.s.}_{\rho}^{\nu} - \text{r.h.s.}_{\rho}^{\nu} \right)^2 + \lambda_1 \left(\sum_{\nu=0}^{N-1} v_{\nu}^x A_{\nu} - 0 \right) + \lambda_2 \left(\sum_{\nu=0}^{N-1} v_{\nu}^y A_{\nu} - 0 \right) + \lambda_3 \left(\sum_{\nu=0}^{N-1} v_{\nu}^z A_{\nu} - 0 \right), \quad (40)$$

for the total velocity constraint (37) as illustration and with $\rho = 1, 2, n$. Concerning the minimization procedure in section 3.2, we add one row per Lagrange multiplier to the matrix, which corresponds to the derivative of χ^2 w.r.t. to the Lagrange multiplier, e.g., $\frac{\partial \chi^2}{\partial \lambda_1}$. In addition, the row corresponding to the derivative w.r.t. a certain velocity component now includes a contribution from the constraint including the Lagrange multiplier. Therefore, we extend the solution vector by the Lagrange multiplier and the matrix gets additional columns, so that it stays quadratic in the end. The additional right hand side component includes the velocity-independent terms of the constraint, which is zero for all constraints in equations (37) - (39).

3.4. Consideration of pressure

In the following, we detail the treatment of the pressure in addition with the incompressibility constraint of the enclosed fluid. First, the incompressibility constraint with an additional Lagrange multiplier (which is independent of the pressure) is discretized

$$\lambda_p \left(\int v^n \, dA \right) = \lambda_p \sum_{\nu} v_{\nu}^n A_{\nu} = \sum_{\nu} \underbrace{\lambda_p v_{\nu}^n A_{\nu}}_{=\hat{\chi}_p^c} = \sum_{\nu} \hat{\chi}_p^c, \quad (41)$$

where we introduce $\hat{\chi}_p^c$ representing the incompressibility constraint per node. In general, we use the notation that $\hat{\chi}^2$ denotes the force balance or $\hat{\chi}^c$ a constraint per node. The latter can be used to represent the general structure of the χ^2

$$\chi^2 = \sum_{\nu} \hat{\chi}^2 + \sum_{\nu} \hat{\chi}^c. \quad (42)$$

Next, the pressure can be deduced from the hydrodynamics traction jump, i.e., from the force acting from the fluid onto the membrane and cortex

$$\Delta \mathbf{f} = \left(\boldsymbol{\sigma}^{\text{out}} - \boldsymbol{\sigma}^{\text{in}} \right) \cdot \mathbf{n}, \quad (43)$$

where the three dimensional stress tensor of the incompressible inner fluid is proportional to the pressure [54], i.e., $\boldsymbol{\sigma} \propto -p$, and the normal component takes the form

$$\Delta f^n = -p^{\text{out}} + p^{\text{in}}. \quad (44)$$

As pressure P we identify the pressure difference between internal and external fluid

$$P = p^{\text{in}} - p^{\text{out}}. \quad (45)$$

The traction jump enters the normal force balance equation on the right hand side with a minus sign. Therefore, the normal force balance is extended by the pressure P

$$\text{l.h.s.}_n^\nu = -C_{\alpha\beta} t_v^{\alpha\beta} + P \stackrel{!}{=} C_\alpha^\beta \zeta_\beta^\alpha = \text{r.h.s.}_n^\nu. \quad (46)$$

We now define the adapted $\hat{\chi}_n^2$ for the normal force balance together with the incompressibility constraint $\hat{\chi}_p^c$ per node

$$\chi_n^2 + \chi_p^2 = (\text{l.h.s.}_n^\nu - \text{r.h.s.}_n^\nu)^2 + \lambda_p (v_\nu^x n_x + v_\nu^y n_y + v_\nu^z n_z) A_\nu. \quad (47)$$

Due to the additional pressure variable the matrix has an additional row

$$\frac{\partial \chi^2}{\partial P} = \frac{\partial \chi_n^2}{\partial P} = \sum_\nu \frac{\partial \hat{\chi}_n^2}{\partial P} \stackrel{!}{=} 0, \quad (48)$$

which leads to

$$\begin{aligned} \sum_\nu \left[(\text{l.h.s.}_n^\nu - \text{r.h.s.}_n^\nu) \frac{\partial \text{l.h.s.}_n^\nu}{\partial P} \right] &= 0 \\ \sum_\nu \left[\text{l.h.s.}_n^\nu \frac{\partial \text{l.h.s.}_n^\nu}{\partial P} \right] &= \sum_\nu \text{r.h.s.}_n^\nu \frac{\partial \text{l.h.s.}_n^\nu}{\partial P}, \end{aligned}$$

with $\frac{\partial \text{l.h.s.}_n^\nu}{\partial P} = +1$. Furthermore, the matrix has an additional column

$$\frac{\partial \chi^2}{\partial v_\nu^i} \propto \frac{\partial \text{l.h.s.}_n^\nu}{\partial v_\nu^i} \underbrace{\text{l.h.s.}_n^\nu(\{\mathbf{v}_\mu\}, P)}_{=\sum_{\mu,i} \frac{\partial \text{l.h.s.}_n^\nu}{\partial v_\mu^i} v_\mu^i + P} \quad (49)$$

for the node itself. For a neighboring node $\mu \neq \nu$

$$\frac{\partial \chi^2}{\partial v_\mu^i} \propto \frac{\partial \text{l.h.s.}_n^\nu}{\partial v_\mu^i} \underbrace{\text{l.h.s.}_n^\nu(\{\mathbf{v}_\sigma\}, P)}_{=\sum_{\sigma,i} \frac{\partial \text{l.h.s.}_n^\nu}{\partial v_\sigma^i} v_\sigma^i + P}. \quad (50)$$

3.5. Bending viscosity for better stability

For reasons of numerical stability, we consider an additional contribution to the surface stress tensor which corresponds to contributions due to a bending viscosity [40]. The aim of this additional bending contribution, which is chosen to be small, is to include a condition on the second derivative of the normal velocity. Therefore, we consider a parabolic expansion of the normal velocity in the same way as for the velocity vector in equation (18). Note, due to smallness and the limitations of the parabolic expansion we neglect the tangential contribution to the force balance equation. The normal components of the velocity are obtained from and related to the three-dimensional velocity by the the projection onto the normal vector (6). We consider the time derivative of the curvature tensor in the Eulerian frame according to Salbreux and Jülicher [40]

$$\partial_t C_\alpha^\beta = -\nabla_\alpha \nabla^\beta v^n - v^n C_{\alpha\gamma} C^{\beta\gamma}, \quad (51)$$

and the derivative of the trace

$$\partial_t C_\gamma^\gamma = -\nabla_\gamma \nabla^\gamma v^n - v^n C_{\gamma\delta} C^{\gamma\delta} = -\nabla_\gamma \nabla^\gamma v^n - v^n C_\gamma^\delta C_\delta^\gamma. \quad (52)$$

Further the derivative of the metric w.r.t. time is given by

$$\partial_t g^{\alpha\beta} = 2v^n C^{\alpha\beta}. \quad (53)$$

We extend the surface stress by bending viscosities $\bar{\eta}$ and $\bar{\eta}_b$ leading to the term

$$\begin{aligned} t_b^{\alpha\beta} &= 2\bar{\eta} \partial_t \left(C^{\alpha\beta} - \frac{1}{2} C_\gamma^\gamma g^{\alpha\beta} \right) + \bar{\eta}_b \partial_t C_\gamma^\gamma g^{\alpha\beta} \\ &= 2\bar{\eta} \left(-\nabla^\alpha \nabla^\beta v^n - v^n C_\gamma^\alpha C^{\beta\gamma} - C_\gamma^\gamma v_n C^{\alpha\beta} \right) + (\bar{\eta}_b - \bar{\eta}) \left(-\nabla_\gamma \nabla^\gamma v^n - v^n C_\gamma^\delta C_\delta^\gamma \right) g^{\alpha\beta}. \end{aligned}$$

The normal force balance contribution is calculated by the contraction with the curvature tensor

$$\begin{aligned} t_b^{\alpha\beta} C_{\alpha\beta} &= 2\bar{\eta} \left(-\nabla_\alpha \nabla_\beta v^n - v^n C_{\alpha\gamma} C_\beta^\gamma - C_\gamma^\gamma v_n C_{\alpha\beta} \right) C^{\alpha\beta} \\ &\quad + (\bar{\eta}_b - \bar{\eta}) \left(-\nabla_\gamma \nabla^\gamma v^n - v^n C_\gamma^\delta C_\delta^\gamma \right) g^{\alpha\beta} C_{\alpha\beta} \\ &= 2\bar{\eta} \left(-\nabla_\alpha \nabla_\beta v^n - v^n C_{\alpha\gamma} C_\beta^\gamma - C v_n C_{\alpha\beta} \right) C^{\alpha\beta} \\ &\quad + (\bar{\eta}_b - \bar{\eta}) \left(-\nabla_\gamma \nabla^\gamma v^n - v^n C_\gamma^\delta C_\delta^\gamma \right) C, \end{aligned}$$

with $C = g^{\alpha\beta} C_{\alpha\beta}$. With the derivatives of the normal velocity, the trace of the second derivative becomes

$$\nabla_\gamma \nabla^\gamma v^n = g^{\alpha\beta} \nabla_\alpha \nabla_\beta v^n = g^{11} C_{v^n} + g^{22} D_{v^n}. \quad (54)$$

We further use

$$C_{\alpha\beta} C^{\alpha\beta} = C_{11} C^{11} + 2C_{12} C^{12} + C_{22} C^{22} = \bar{C}, \quad (55)$$

and

$$C_{\alpha\gamma} C_\beta^\gamma C^{\alpha\beta} = \bar{C},$$

to obtain in total

$$\begin{aligned} t_b^{\alpha\beta} C_{\alpha\beta} &= \left(-2\bar{\eta} C^{11} - (\bar{\eta}_b - \bar{\eta}) C g^{11} \right) C_{v^n} + \left(-2\bar{\eta} C^{22} - (\bar{\eta}_b - \bar{\eta}) C g^{22} \right) D_{v^n} - 4\bar{\eta} C^{12} E_{v^n} \\ &\quad + \left(-2\bar{\eta} \bar{C} - 2\bar{\eta} C \bar{C} - (\bar{\eta}_b - \bar{\eta}) C \bar{C} \right) v^n. \end{aligned} \quad (56)$$

This contribution can be added to the normal force balance equation and can be incorporated to the solution procedure detailed above in a straightforward manner.

3.6. Velocity derivatives as a function of neighboring velocity vectors

Up to now, we have written the force balance equations (26), (27), (28) in terms of derivatives of the velocity vector in local coordinates $\mathbf{A}_v - \mathbf{E}_v$. What remains is to express these derivatives by means of the actual velocity vectors at all nodes. Therefore, we consider the neighborhood of a node, as sketched in figure 1. Considering all N_ν neighboring nodes $a(\nu)$ of node ν , the coefficients $\mathbf{A}_v - \mathbf{E}_v$ can be expressed by the velocity vector evaluated at the central node and at the sites of the neighboring nodes

$$\mathbf{A}_v = \mathbf{A}_v(\mathbf{v}_\nu, \{\mathbf{v}_{a(\nu)}\}) \quad \text{with } a(\nu) = 1, \dots, N_\nu. \quad (57)$$

In order to do so we write down the velocity at some distance around the (central) node ν in the local coordinates of the central node ξ, η

$$\bar{\mathbf{v}}(\xi, \eta) = \mathbf{v}_\nu + \mathbf{A}_v \xi + \mathbf{B}_v \eta + \frac{1}{2} \mathbf{C}_v \xi^2 + \frac{1}{2} \mathbf{D}_v \eta^2 + \mathbf{E}_v \xi \eta, \quad (58)$$

which is the parabolic expansion (18) evaluated in the local coordinate system (30). Plugging in the position of the neighbor nodes in the local coordinates of the central node, i.e., $\xi_{a(\nu)}, \eta_{a(\nu)}$, the expanded velocity has to equal the actual velocity \mathbf{v}_a of the neighbor node $a(\nu)$. Therefore, the squared difference of expanded and actual velocity has to be minimal

$$\chi_v^2 = \sum_{a=1}^{N_\nu} [\bar{\mathbf{v}}(\xi_{a(\nu)}, \eta_{a(\nu)}) - \mathbf{v}_a]^2. \quad (59)$$

With the differential form

$$d(\chi_v^2) = \sum_i \sum_{a=1}^{N_\nu} 2(\bar{\mathbf{v}} - \mathbf{v}_a)_i dv_i, \quad (60)$$

we are able to minimize χ_v^2 with respect to the components of the fitting coefficients, e.g., A_v^j

$$\frac{\partial(\chi_v^2)}{\partial A_v^j} = \sum_i \sum_a 2(\bar{\mathbf{v}} - \mathbf{v}_a)_i \underbrace{\frac{\partial \bar{v}_i}{\partial A_v^j}}_{\xi \delta_{ij}} = \sum_a 2(\bar{\mathbf{v}} - \mathbf{v}_a)_j \xi \stackrel{!}{=} 0. \quad (61)$$

Here, we clearly see that each component $j = x, y, z$ is minimized individually. Performing the minimization by calculating all derivatives with respect to $\mathbf{A}_v, \dots, \mathbf{E}_v$ we end up with a system of linear equations with $\mathbf{A}_v - \mathbf{E}_v$ building the solution vector. By solving this system we obtain $\mathbf{A}_v - \mathbf{E}_v$ in terms of the velocity evaluated at the central and neighbor nodes.

Analytic inversion of the parabolic fitting

We solve this system of linear equations analytically. Without restriction, we illustrate the procedure in the following for the fitting parameters not as vectors but as scalars. To go back to vectors the following can be done for all three components separately. We

consider a parabolic expansion of a quantity f around a central node and consider the equality with the value of f at the position of the neighbors a , as done in equation (59)

$$\bar{f}_\nu(\xi_a, \eta_a) = f_\nu + P_{\nu a} \stackrel{!}{=} f_{a(\nu)}, \quad (62)$$

with

$$P_{\nu a} = A\xi_a + B\eta_a + \frac{1}{2}C\xi_a^2 + \frac{1}{2}D\eta_a^2 + E\xi_a\eta_a. \quad (63)$$

We consider a χ_f^2 analogous to equation (59) and proceed as done in equation (61) with a minimization of χ_f^2 and obtain

$$\begin{aligned} \frac{\partial}{\partial A} (\chi_f^2) &= 2 \sum_i [f_{a(\nu)} - \bar{f}_\nu(\xi_a, \eta_a)] \xi_a = 0, \\ \frac{\partial}{\partial B} (\chi_f^2) &= 2 \sum_i [f_{a(\nu)} - \bar{f}_\nu(\xi_a, \eta_a)] \eta_a = 0, \\ \frac{\partial}{\partial C} (\chi_f^2) &= 2 \sum_i [f_{a(\nu)} - \bar{f}_\nu(\xi_a, \eta_a)] \frac{1}{2} \xi_a^2 = 0, \\ \frac{\partial}{\partial D} (\chi_f^2) &= 2 \sum_i [f_{a(\nu)} - \bar{f}_\nu(\xi_a, \eta_a)] \frac{1}{2} \eta_a^2 = 0, \\ \frac{\partial}{\partial E} (\chi_f^2) &= 2 \sum_i [f_{a(\nu)} - \bar{f}_\nu(\xi_a, \eta_a)] \xi_a \eta_a = 0, \end{aligned}$$

and re-writing these equations using equation (62) we get

$$\begin{aligned} \sum_a P_{\nu a} \xi_a &= \sum_a (f_{a(\nu)} - f_\nu) \xi_a, \\ \sum_a P_{\nu a} \eta_a &= \sum_a (f_{a(\nu)} - f_\nu) \eta_a, \\ \sum_a P_{\nu a} \frac{1}{2} \xi_a^2 &= \sum_a (f_{a(\nu)} - f_\nu) \frac{1}{2} \xi_a^2, \\ \sum_a P_{\nu a} \frac{1}{2} \eta_a^2 &= \sum_a (f_{a(\nu)} - f_\nu) \frac{1}{2} \eta_a^2, \\ \sum_a P_{\nu a} \xi_a \eta_a &= \sum_a (f_{a(\nu)} - f_\nu) \xi_a \eta_a. \end{aligned}$$

Inserting (63) we obtain for example for the first equation

$$\left(\sum_a \xi_a^2 \right) A + \left(\sum_a \eta_a \xi_a \right) B + \left(\sum_a \frac{1}{2} \xi_a^3 \right) C + \left(\sum_a \frac{1}{2} \eta_a^2 \xi_a \right) D + \left(\sum_a \eta_a \xi_a^2 \right) E = \sum_a (f_{a(\nu)} - f_\nu) \xi_a. \quad (64)$$

Taking all equations together and using the separation with respect to the fitting coefficients we obtain a system of linear equations

$$\boldsymbol{\alpha} \cdot \begin{pmatrix} A \\ B \\ C \\ D \\ E \end{pmatrix} = \begin{pmatrix} \sum_a (f_{a(\nu)} - f_\nu) \xi_a \\ \sum_a (f_{a(\nu)} - f_\nu) \eta_a \\ \sum_a (f_{a(\nu)} - f_\nu) \frac{1}{2} \xi_a^2 \\ \sum_a (f_{a(\nu)} - f_\nu) \frac{1}{2} \eta_a^2 \\ \sum_a (f_{a(\nu)} - f_\nu) \xi_a \eta_a \end{pmatrix} = \mathbf{r}_s, \quad (65)$$

with \mathbf{r}_s denoting the right hand side and the symmetric 5×5 matrix $\boldsymbol{\alpha}$, i.e., $\alpha_{mn} = \alpha_{nm}$ with $m, n = 1, \dots, 5$, being

$$\begin{pmatrix} \alpha_{11} = \sum_a \xi_a^2 & & & & \\ \alpha_{12} = \sum_a \xi_a \eta_a & \alpha_{22} = \sum_a \eta_a^2 & & & \\ \alpha_{13} = \sum_a \frac{1}{2} \xi_a^3 & \alpha_{23} = \sum_a \frac{1}{2} \xi_a^2 \eta_a & \alpha_{33} = \sum_a \frac{1}{4} \xi_a^4 & & \\ \alpha_{14} = \sum_a \frac{1}{2} \xi_a \eta_a^2 & \alpha_{24} = \sum_a \frac{1}{2} \eta_a^3 & \alpha_{34} = \sum_a \frac{1}{4} \xi_a^2 \eta_a^2 & \alpha_{44} = \sum_a \frac{1}{4} \eta_a^4 & \\ \alpha_{15} = \sum_a \xi_a^2 \eta_a & \alpha_{25} = \sum_a \xi_a \eta_a^2 & \alpha_{35} = \sum_a \frac{1}{2} \xi_a^3 \eta_a & \alpha_{45} = \sum_a \frac{1}{2} \xi_a \eta_a^3 & \alpha_{55} = \sum_a \xi_a^2 \eta_a^2 \end{pmatrix}. \quad (66)$$

By inverting the matrix $\boldsymbol{\alpha}$ to $\boldsymbol{\beta} = \boldsymbol{\alpha}^{-1}$ we can obtain the fitting parameters by

$$\begin{pmatrix} A \\ B \\ C \\ D \\ E \end{pmatrix} = \boldsymbol{\beta} \cdot \mathbf{r}_s. \quad (67)$$

Using Mathematica, we obtain the inverse of a general symmetric 5×5 matrix $\boldsymbol{\alpha}$ with entries α_{mn} , which we term β_{mn} . Inserting the actual values α_{mn} as given above, we calculate the numerical elements of the inverse matrix β_{mn} .

With the inverse matrix and using equation (67) we obtain the fitting coefficients

$$A = \sum_{n=1}^5 \beta_{1n} r_{sn} = A(\{f_\mu\}), \quad (68)$$

$$B = \sum_{n=1}^5 \beta_{2n} r_{sn} = B(\{f_\mu\}), \quad (69)$$

$$C = \sum_{n=1}^5 \beta_{3n} r_{sn} = C(\{f_\mu\}), \quad (70)$$

$$D = \sum_{n=1}^5 \beta_{4n} r_{sn} = D(\{f_\mu\}), \quad (71)$$

$$E = \sum_{n=1}^5 \beta_{5n} r_{sn} = E(\{f_\mu\}), \quad (72)$$

as functions of the set of quantity f evaluated at the nodes $\{f_\mu\}$. Thus, $A - E$ are linear combinations of the function values, in detail of the function evaluated at the central node ν and the corresponding neighbors. As a consequence the derivatives $\frac{\partial}{\partial f_\mu} A$ can easily be calculated.

In order to calculate the derivatives we re-write the expressions for the coefficients. Using the definition of \mathbf{r}_s in eq. (65) we obtain

$$A = \sum_a \underbrace{\left(\beta_{11}\xi_a + \beta_{12}\eta_a + \beta_{13}\frac{1}{2}\xi_a^2 + \beta_{14}\frac{1}{2}\eta_a^2 + \beta_{15}\xi_a\eta_a \right)}_{p_a^A} f_a + \underbrace{(-1) \left[\beta_{11} \left(\sum \xi_a \right) + \beta_{12} \left(\sum \eta_a \right) + \beta_{13} \left(\sum \frac{1}{2}\xi_a^2 \right) + \beta_{14} \left(\sum \frac{1}{2}\eta_a^2 \right) + \beta_{15} \left(\sum \xi_a\eta_a \right) \right]}_{p_\nu^A} f_\nu,$$

$$B = \sum_a \left(\beta_{12}\xi_a + \beta_{22}\eta_a + \beta_{23}\frac{1}{2}\xi_a^2 + \beta_{24}\frac{1}{2}\eta_a^2 + \beta_{25}\xi_a\eta_a \right) f_a + (-1) \left[\beta_{12} \left(\sum \xi_a \right) + \beta_{22} \left(\sum \eta_a \right) + \beta_{23} \left(\sum \frac{1}{2}\xi_a^2 \right) + \beta_{24} \left(\sum \frac{1}{2}\eta_a^2 \right) + \beta_{25} \left(\sum \xi_a\eta_a \right) \right] f_\nu,$$

$$C = \sum_a \left(\beta_{13}\xi_a + \beta_{23}\eta_a + \beta_{33}\frac{1}{2}\xi_a^2 + \beta_{34}\frac{1}{2}\eta_a^2 + \beta_{35}\xi_a\eta_a \right) f_a + (-1) \left[\beta_{13} \left(\sum \xi_a \right) + \beta_{23} \left(\sum \eta_a \right) + \beta_{33} \left(\sum \frac{1}{2}\xi_a^2 \right) + \beta_{34} \left(\sum \frac{1}{2}\eta_a^2 \right) + \beta_{35} \left(\sum \xi_a\eta_a \right) \right] f_\nu,$$

$$D = \sum_a \left(\beta_{14}\xi_a + \beta_{24}\eta_a + \beta_{34}\frac{1}{2}\xi_a^2 + \beta_{44}\frac{1}{2}\eta_a^2 + \beta_{45}\xi_a\eta_a \right) f_a + (-1) \left[\beta_{14} \left(\sum \xi_a \right) + \beta_{24} \left(\sum \eta_a \right) + \beta_{34} \left(\sum \frac{1}{2}\xi_a^2 \right) + \beta_{44} \left(\sum \frac{1}{2}\eta_a^2 \right) + \beta_{45} \left(\sum \xi_a\eta_a \right) \right] f_\nu,$$

$$E = \sum_a \left(\beta_{15}\xi_a + \beta_{25}\eta_a + \beta_{35}\frac{1}{2}\xi_a^2 + \beta_{45}\frac{1}{2}\eta_a^2 + \beta_{55}\xi_a\eta_a \right) f_a + (-1) \left[\beta_{15} \left(\sum \xi_a \right) + \beta_{25} \left(\sum \eta_a \right) + \beta_{35} \left(\sum \frac{1}{2}\xi_a^2 \right) + \beta_{45} \left(\sum \frac{1}{2}\eta_a^2 \right) + \beta_{55} \left(\sum \xi_a\eta_a \right) \right] f_\nu.$$

Using the notation indicated in the first line, we can write

$$\begin{aligned} A &= \sum_a p_a^A f_a + p_\nu^A f_\nu, \\ B &= \sum_a p_a^B f_a + p_\nu^B f_\nu, \\ C &= \sum_a p_a^C f_a + p_\nu^C f_\nu, \\ D &= \sum_a p_a^D f_a + p_\nu^D f_\nu, \\ E &= \sum_a p_a^E f_a + p_\nu^E f_\nu. \end{aligned} \tag{73}$$

The prefactors in front of f_ν and f_a , respectively, are the derivatives of the coefficients with respect to f_μ (in case of $\mu = \nu$ and $\mu = a(\nu)$, respectively).

3.7. Summary of the algorithm

Eventually, we put everything together to close the numerical algorithm. First, we prescribe an analytical expression for the active stress, which we evaluate on the discrete cortex. Its derivatives and the curvature tensor on the discrete and deforming cortex are calculated using a parabolic fitting procedure analogous to equation (18) but with respect to the active stress magnitude ζ or the position vector, respectively. We then use the inverse parabolic fitting (73) to obtain the derivatives up to second order of the velocity vector $\mathbf{A}_v - \mathbf{E}_v$ in local coordinates. We use the derivatives to express the force balance equations (34) or respectively (26), (27), (28) in terms of the velocity components of all nodes. This step allows us to build the matrix of the minimization method (36). In the following, we present the necessary steps in more detail.

As detailed in section 3.6, we obtain the derivatives as functions of the velocity at the central node ν and its neighbors $a = 1, \dots, N_\nu$

$$\mathbf{A}_v = \mathbf{A}_v(\mathbf{v}_\nu, \{\mathbf{v}_a\}). \quad (74)$$

This analogously holds for the derivatives $\mathbf{B}_v - \mathbf{E}_v$. To keep the notation clear in the following, we introduce the short-hand notation

$$\Delta = v_\nu^i \quad (75)$$

with $i = x, y, z$ the spatial component and ν a node. Thus, Δ represents one arbitrary velocity component and thus can take $3N$ values, but can without loss of generality be restricted to the central node and its neighbors (in case we just consider those dependencies, e.g., in derivatives). Furthermore, Δ can contain the pressure or a Lagrange multiplier. In addition, we abbreviate the components of the velocity derivatives by

$$\square_i \quad \text{with} \quad \square \in \{\mathbf{A}_v, \mathbf{B}_v, \mathbf{C}_v, \mathbf{D}_v, \mathbf{E}_v\}. \quad (76)$$

According to section 3.6 and equation (74) we can expand the derivatives as linear combination of the velocity components

$$\square_i = \sum_{\Delta} \frac{\partial \square_i}{\partial \Delta} \Delta. \quad (77)$$

In total, the minimization consists of derivatives of the force balance equations at each node with respect to the velocity components

$$\frac{\partial \text{l.h.s.}_\rho}{\partial \Delta} = \sum_{\square_i} \frac{\partial \text{l.h.s.}_\rho}{\partial \square_i} \frac{\partial \square_i}{\partial \Delta}. \quad (78)$$

For illustration, we write down the derivative for one force balance equation, e.g., with index 1 the derivative of χ_1^2 being part of χ^2 in equation (35), with respect to one velocity

component of one node $\Delta, \diamond = v_\mu^i$

$$\begin{aligned} \frac{\partial}{\partial \Delta} \sum_{\nu} (\text{l.h.s.}_1^{\nu} - \text{r.h.s.}_1^{\nu})^2 &= 2 \sum_{\nu} (\text{l.h.s.}_1^{\nu} - \text{r.h.s.}_1^{\nu}) \frac{\partial \text{l.h.s.}_1^{\nu}}{\partial \Delta} = \\ &2 \sum_{\nu} \text{l.h.s.}_1^{\nu} \frac{\partial \text{l.h.s.}_1^{\nu}}{\partial \Delta} - 2 \sum_{\nu} \text{r.h.s.}_1^{\nu} \frac{\partial \text{l.h.s.}_1^{\nu}}{\partial \Delta}. \end{aligned}$$

This corresponds to one line in the system of linear equations with the second term becoming the right hand side of the system and the first term to be sorted into columns using the expansion

$$\sum_{\nu} \text{l.h.s.}_1^{\nu} \frac{\partial \text{l.h.s.}_1^{\nu}}{\partial \Delta} = \sum_{\nu} \sum_{\diamond} \frac{\partial \text{l.h.s.}_1^{\nu}}{\partial \diamond} \frac{\partial \text{l.h.s.}_1^{\nu}}{\partial \Delta} \diamond,$$

where we further canceled out the factor 2. We note that to both derivatives $\frac{\partial \text{l.h.s.}_1^{\nu}}{\partial \diamond}$ and $\frac{\partial \text{l.h.s.}_1^{\nu}}{\partial \Delta}$ the chain rule with respect to \square_i applies

$$\frac{\partial \text{l.h.s.}_1^{\nu}}{\partial \diamond} = \sum_{\square_i} \frac{\text{l.h.s.}_1^{\nu}}{\partial \square_i} \frac{\partial \square_i}{\partial \diamond} \quad (79)$$

where we calculate the derivative $\frac{\partial \square_i}{\partial \diamond}$ using the results in section 3.6.

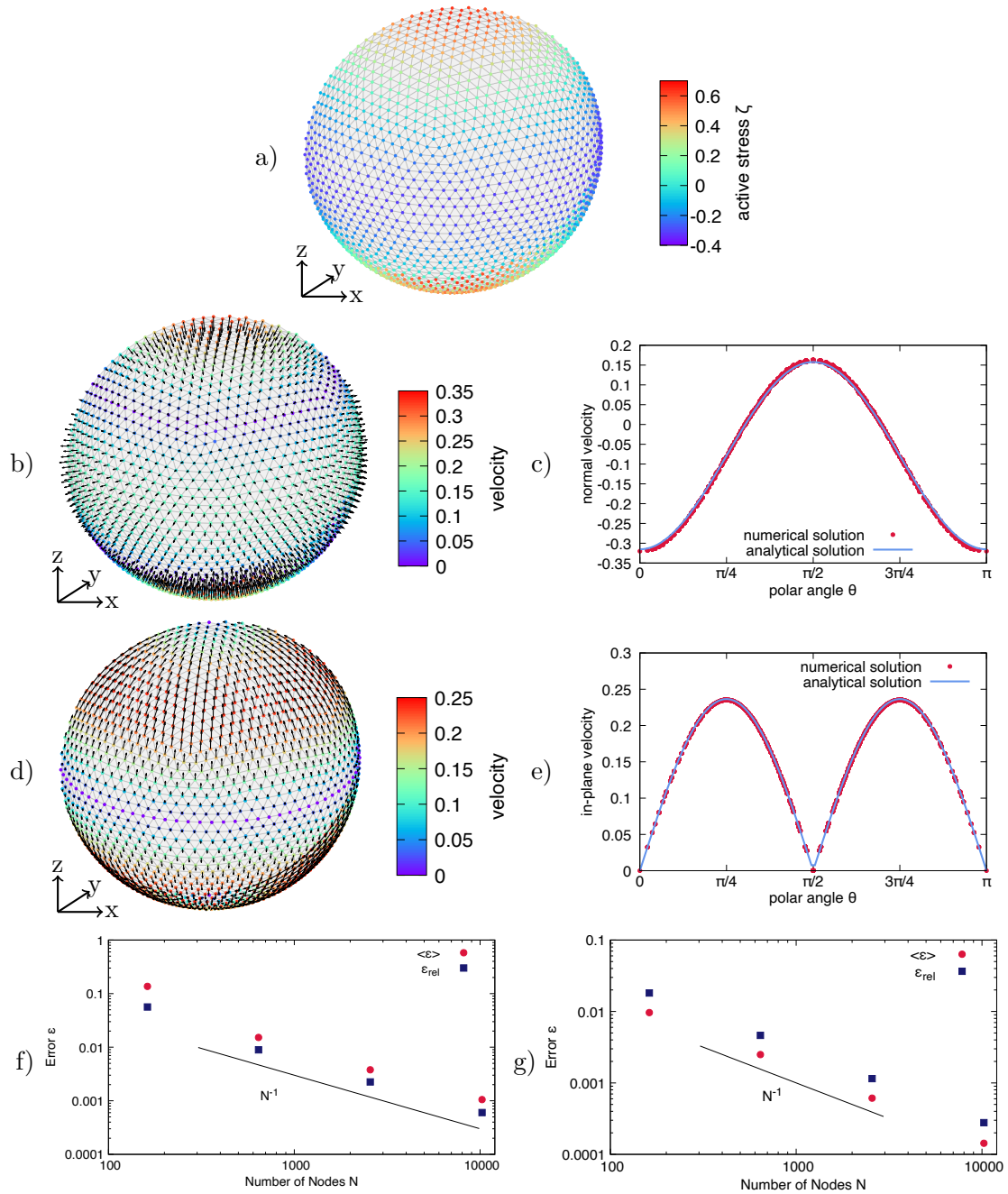


Figure 2: **Axisymmetric active stress on a spherical cortex.** a) An axisymmetric active stress distribution in terms of Y_{20} is considered on a spherical cortex. b), c) The full system i) is solved as well as d), e) the purely tangential system. b) The three-dimensional velocity field is shown as obtained by the numerical solution of the full system. c) While the tangential velocity is zero, the normal velocity depending on the polar angle θ agrees very well with the analytical prediction. d) The three-dimensional velocity field is shown as obtained by the numerical solution for solving the tangential force balance only. e) While the normal velocity is zero, the absolute value of the tangential velocity depending on the polar angle θ agrees very well with the analytical prediction. For both the full system i) in f) and the purely tangential system ii) in g), the error of the velocity converges with increasing resolution.

4. Validation and application

In the following, we intensively validate the developed algorithm for a viscous active cell cortex in three-dimensions. First, we consider in section 4.1 a static spherical cortex subjected to an active stress distribution in terms of spherical harmonics. We compare the resulting velocity field on the cortex to analytical solutions derived in the appendix A. Next, for a dynamically deforming cortex we compare our three-dimensional algorithm to simulations using an axisymmetric simulation method in section 4.2. Eventually, we consider a first test application in section 4.3.

4.1. Velocity profile by spherical harmonics on a static spherical cortex

As a first test setup, we compare three-dimensional numerical results on a static spherical cortex to corresponding analytical solutions. We consider an active stress distribution expanded in terms of spherical harmonics $Y_{nm}(\theta, \phi)$

$$\zeta^{\alpha\beta}(\theta, \phi) = \zeta(\theta, \phi)g^{\alpha\beta} = \left(\zeta_0 + \sum_{n,m} \zeta_{nm} Y_{nm}(\theta, \phi) \right) g^{\alpha\beta}, \quad (80)$$

where ζ_0 is a constant offset and ζ_{nm} are the expansion coefficients of the active stress distribution. For the given active stress profile in equation (80), we derive an analytical solution for the velocity field \mathbf{v} in appendix A. We expand the tangential velocity in terms of vector spherical harmonics $\mathbf{v}^t = \sum_{n,m} A_{nm} \partial_\alpha Y_{nm} \mathbf{e}^\alpha$ with coefficients A_{nm} and the normal velocity in terms of spherical harmonics $v^n = \sum_{n,m} N_{nm} Y_{nm}$ with coefficients N_{nm} . The force balance equations (16), (17) then lead to analytical relations for the velocity expansion coefficients A_{nm} and N_{nm} depending on ζ_{nm} . These relations are given in equations (A.9), (A.10) and determine the velocity field. In the following, we consider the quantities in units of the radius and the planer shear viscosity with $R = 1$ and $\eta_s = 1$. On the one hand, considering the full system of equations (case i)), the sum of the conditions (A.9) and (A.10) implies a vanishing in-plane velocity, i.e., the expansion coefficients of the in-plane velocity vanish

$$A_{nm}^i = 0. \quad (81)$$

In turn, the normal velocity has to fulfill

$$N_{nm}^i = -\frac{R}{2\eta_b} \zeta_{nm}. \quad (82)$$

In summary, the solution for the velocity field for given active stress ζ_{nm} is

$$\mathbf{v}^i = -\frac{R}{2\eta_b} \zeta_{nm} Y_{nm} \mathbf{n}, \quad (83)$$

with vanishing tangential component.

On the other hand, this system can be utilized to test the in-plane velocity separately (case ii)). For vanishing bulk viscosity $\eta_b = 0$ and fixing the normal velocity v^n to zero, i.e., implying

$$N_{nm}^{ii} = 0, \quad (84)$$

(instead of solving the normal force balance), the tangential force balance equations lead to a condition for the tangential velocity coefficients

$$A_{nm}^{ii)} = \frac{1}{[n(n+1) - 2]} \zeta_{nm}, \quad (85)$$

which is obtained from equation (A.9). Thus, for solving the tangential force balance equation only and for a vanishing normal velocity, we obtain an analytical solution for the velocity

$$\mathbf{v}^{ii)} = A_{nm} (\partial_\alpha Y_{nm}) \mathbf{e}^\alpha = \frac{1}{[n(n+1) - 2]} \zeta_{nm} (\partial_\alpha Y_{nm}) \mathbf{e}^\alpha, \quad (86)$$

for given active stress coefficient ζ_{nm} .

In both cases, the analytical solution in equation (83) for i) the full system and in equation (86) for ii) the pure tangential system allows us a direct comparison between the analytical and numerical solution. Using the three-dimensional algorithm developed above, we consider a discrete cortex with 2562 nodes and 5120 triangles without bending viscosity. After applying an active stress distribution in terms of spherical harmonics according to equation (80), we solve numerically for the three-dimensional velocity field. In the following, the comparison to the analytical solution is performed by considering two types of error measures. On the one hand, we consider the absolute value of the difference between numerical \mathbf{v} and analytical solution \mathbf{v}^{an} per node and average over all nodes

$$\langle \epsilon \rangle = \frac{1}{N} \sum_{\nu} |\mathbf{v} - \mathbf{v}^{\text{an}}|. \quad (87)$$

On the other hand, we calculate the sum of the squared difference of the velocities relative to the maximum velocity, average, and take the square root to obtain the relative error

$$\epsilon_{\text{rel}} = \sqrt{\frac{\frac{1}{N} \sum_{\nu} \left[(v_x - v_x^{\text{an}})^2 + (v_y - v_y^{\text{an}})^2 + (v_z - v_z^{\text{an}})^2 \right]}{\|\mathbf{v}^{\text{an,max}}\|}}. \quad (88)$$

We first consider an axisymmetric active stress distribution in terms of $\zeta_{20} Y_{20}$ with $\zeta_{20} = 1$ as shown in figure 2 a) on the discrete cortex. We further use $\eta_b = 1$ and an active stress offset of $\zeta_0 = 0$. A variation of the active stress offset leads to a finite pressure difference, but the velocity field is not altered. Figure 2 shows the full, three-dimensional velocity profile obtained numerically and the velocity depending on the polar angle θ in comparison to the analytical solution for both b), c) the full system i) and d), e) the purely tangential system ii). In the first case, the normal velocity is finite and points inward the cell around the equator and outward at both poles. In the second case, the tangential velocity is finite and directed from the equator towards the poles. Each three-dimensional simulation shows very good agreement with the analytical solution, as shown by the comparison over the polar angle. As a next step, we quantify the error $\langle \epsilon \rangle$ as well as ϵ_{rel} given in equation (87) and (88), respectively, and vary the resolution of the discrete spherical cortex. For both systems i) and ii) shown in figure 2 f) and g), respectively, we obtain a systematic decrease of both errors with increasing resolution. The error shows a scaling inverse proportional to the number of nodes.

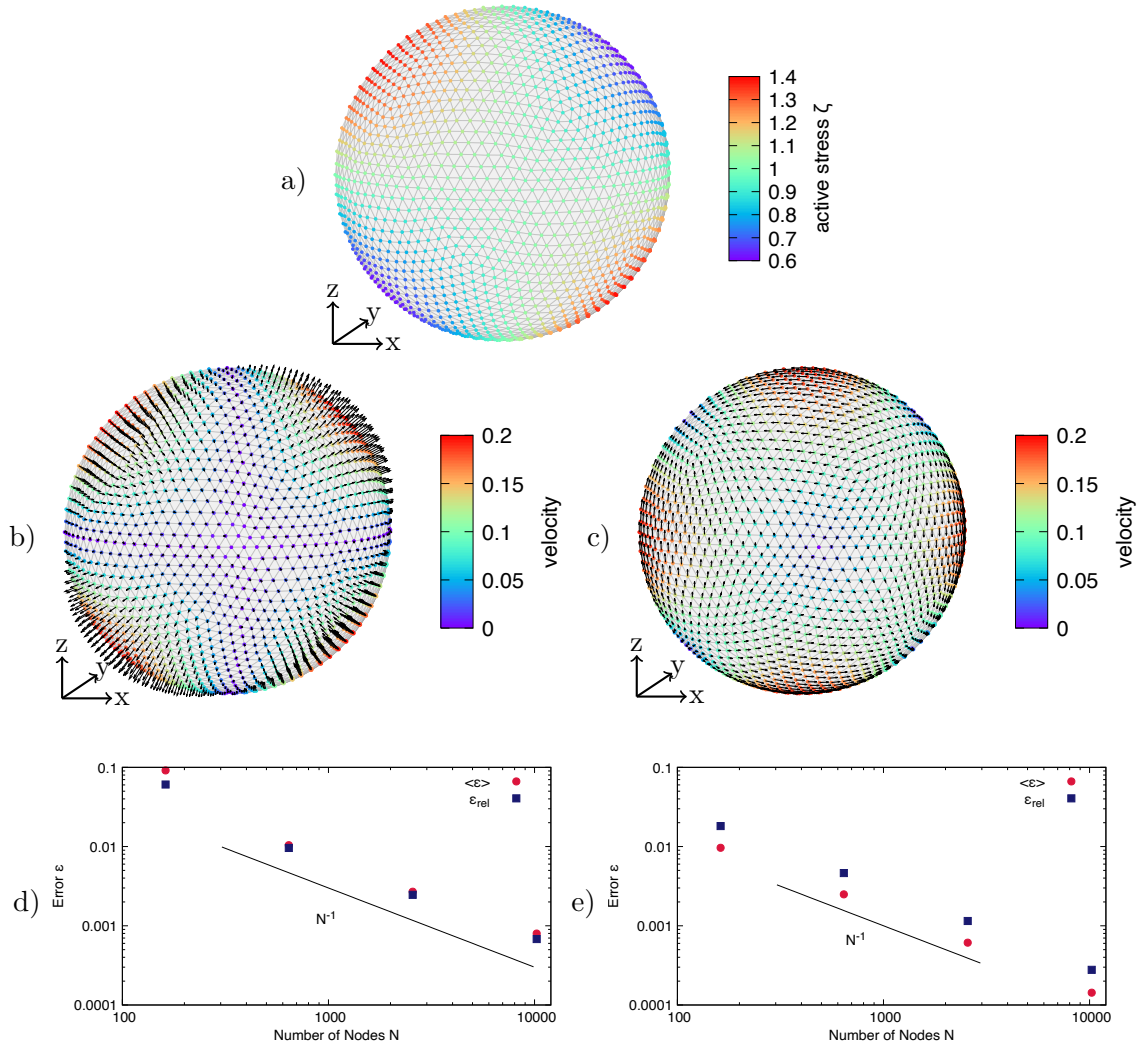


Figure 3: **Asymmetric active stress.** a) A non-axisymmetric active stress distribution in terms of Y_{21} is considered. b) The three-dimensional velocity field is shown as obtained by the numerical solution of the i) full system and c) by the numerical solution of the ii) tangential force balance only. The error d) of the normal velocity for the full system as well as e) the error of the tangential velocity for the reduced system of tangential force balance converges with increasing resolution.

We then proceed in figure 3 with a non-axisymmetric distribution of active stress in terms of $\zeta_{21}Y_{21}$ with $\zeta_{21} = 1$ and $\zeta_0 = 1$ shown in a). As a consequence, the cortical velocity profile is no longer axisymmetric. Figure 3 b) shows the three-dimensional velocity field for the full system i) and figure 3 c) shows the three-dimensional velocity field for the purely tangential system ii) with normal velocity restricted to zero. Figure b) shows four patches of large normal velocity. Opposite patches show either an outward or an inward pointing normal velocity. In-between, the normal velocity becomes zero. At the sites where in figure b) the normal velocity is maximal, the tangential velocity in c) vanishes. Similar to figure 2 the tangential velocity points from sites with outward

pointing normal velocity in 3 b) towards sites with inward pointing normal velocity in 3 b). Again, we observe very good agreement between numerical and analytical solution as can be seen by the error shown in figure 3 d) and e) for both systems i) and ii), respectively. We again observe a decrease in the error with increasing number of nodes. In total, we obtain numerical solutions for the velocity field on the static cortex in a very good agreement with analytical predictions together with a proper scaling for improving resolution. This validates our developed three-dimensional algorithm for a viscous active cortex in a first step.

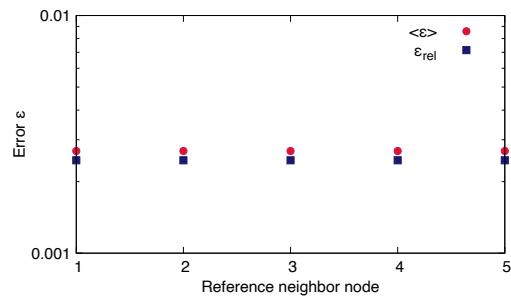


Figure 4: **Variation of the reference neighboring node.** The choice of the reference neighboring node, which serves for the construction of the local coordinate system, does not influence the numerical solution as illustrated by the constant error.

Eventually, we use the full setup with non-axisymmetric active stress distribution in figure 3 with 2562 nodes to systematically study the influence of the reference neighbor node, which serves for the construction of the local coordinate system in simulation, as detailed in section 3.1. We systematically vary the reference neighbor node, run one simulation per reference neighbor node, and quantify the deviation to the analytical solution in terms of the errors in equation (87) and (88). Figure 4 shows a constant error for varying reference neighbor node. Therefore, we are able to conclude that the choice of the reference neighbor node for local coordinate system construction is arbitrary.

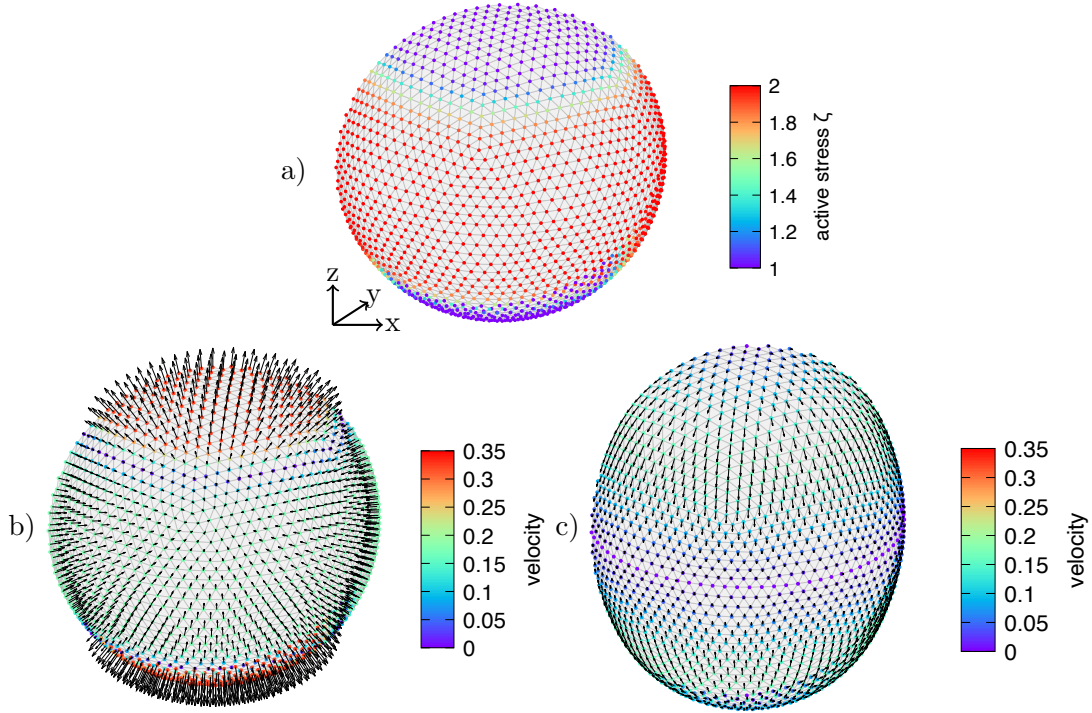


Figure 5: **Dynamically deforming viscous active cortex.** a) The active stress distributed according to equation (89) with exponent $p = 8$, offset $\zeta_0 = 1$, and amplitude $\hat{\zeta} = 1$ is shown color coded on the initially spherical, discrete cortex. Towards the equator the isotropic active stress increases. b) Resulting velocity profile on the initial cortex and c) velocity on the finally deformed cortex. In the finally deformed state the normal velocity vanishes.

4.2. Dynamics of a viscous active cortex

Having tested the algorithm for the static scenario in the previous section, we now want to apply the algorithm to the situation of a dynamically evolving viscous active cortex. We consider an active stress distribution similar to what is known for cytokinesis, i.e., the separation of the two daughter cells during cell division [30, 32, 33, 47]. We consider an isotropic active stress distribution with constant offset ζ_0 at the poles $\theta = 0, \theta = \pi$ and an increasing active stress around the equator $\theta = \frac{\pi}{2}$ similar to an equatorial contractile ring. We therefore apply

$$\zeta_1^1(\theta, \phi) = \zeta_2^2(\theta, \phi) = \zeta(\theta, \phi) = \zeta_0 + \hat{\zeta} \exp\left(-\sigma \left(\theta - \frac{\pi}{2}\right)^p\right), \quad (89)$$

where $\hat{\zeta}$ is the amplitude of active stress increase around the equator, p the exponent, and σ the width of the active stress distribution. We choose for the active stress $\zeta_0 = 1, \sigma = 10$, the planar shear viscosity $\eta_s = 1$, and the bulk viscosity $\eta_b = 1$. We use an initially spherical mesh with 2562 nodes and 5120 triangles.

For the given active stress distribution in equation (89) and for given cortex shape, we solve numerically for the three-dimensional velocity field \mathbf{v} on the discrete cortex. We split up the total velocity field \mathbf{v} into the tangential velocity $\mathbf{v}_t = (\mathbf{1} - \mathbf{n}\mathbf{n}) \cdot \mathbf{v}$ and

the normal velocity $\mathbf{v}_n = \mathbf{n}\mathbf{n} \cdot \mathbf{v}$. Only the normal velocity leads to flows in the cortex that change the overall cortex shape. Therefore, we integrate the cortex evolution by advecting each node ν with its normal velocity \mathbf{v}_n^ν . The latter is done using the Euler algorithm

$$\mathbf{r}_\nu(t + \Delta t) = \mathbf{r}_\nu(t) + \mathbf{v}_n^\nu(t)\Delta t, \quad (90)$$

with a time step Δt , which is typically chosen to be $\Delta t = 5 \times 10^{-4}t_a$ with the time scale $t_a = \frac{\eta_s}{\zeta_0}$. On the evolving cortex, we repeat the procedure. This is done as long as the normal velocity on the whole cortex vanishes, i.e., until the cortex has reached a final, steady state.

We first consider a broad distribution of active stress with exponent $p = 8$ in equation (89) with $\hat{\zeta} = 1$ as shown in figure 5 a). We apply a bending viscosity of $\bar{\eta} = 0.0005\eta_s$ and $\bar{\eta}_b = 0.0025\eta_s$. Figure b) shows the velocity field on the initially spherical cortex. Because of the dominating contractile active stress around the equator, the normal velocity points towards the cell interior around the equator. As a consequence of the incompressibility of the enclosed fluid, the normal velocity points outward at the poles. Therefore, the velocity leads to an expansion of the cortex along the z -axis and a simultaneous contraction around the equator. Integration of the cortex evolution leads to the shape shown in figure c), where we also show the final velocity field on the deformed cortex. Here, no normal velocity remains, but a finite tangential velocity points towards the equator.

For this setup, we compare the three-dimensional dynamics to the one obtained by axisymmetric simulations [60, 61] in detail in figure 6. We compare with simulations of axially symmetric viscous active surfaces, described in detail in [60]. There the boundary value problem describing the force and torque balances is integrated numerically using a fourth-order collocation method, while the surface evolves in time following a Lagrangian description with a re-parametrization to arc length at each time step. For the comparison of the axially symmetric and the three-dimensional method the imposed active tension profile is evolved by attaching the initial profile to a Eulerian grid introduced for this purpose [61]. For comparison between the simulation methods, on the one hand, we track half the distance of the upper and the lower pole of the cortex over time. On the other hand, we analyze the furrow size at the cortex equator by calculating the radius of the equatorial ring. Both quantities are shown over time in figure 6 a). While the pole to pole distance increases over time, the cortex contracts at the equator and thus the furrow radius decreases. Both quantities reach a constant plateau at longer time, which corresponds to the convergence of the simulation. We obtain excellent agreement between three-dimensional and axisymmetric simulation.

To go one step further, we also compare the velocity field on the discrete cortex at different times. On the left hand side of figure 6 we show the absolute value of the tangential velocity \mathbf{v}_t depending on the axial position z . On the right hand side we show the normal velocity v_n . This is done at different times b), c) $t/t_a = 0.01$, d), e) $t/t_a = 1.5$, and f), g) $t/t_a = 3$. The velocity is shown with respect to $v_a = \frac{R_0}{t_a}$. While the tangential velocity increases over time, i.e., with increasing deformation of the cortex, the normal velocity decreases until the cortex reaches its final shape (the latter is shown in figure 5 c)). Overall, our developed three-dimensional algorithm leads to a velocity field on the evolving cortex, which is in very good agreement with the axisymmetric simulation.

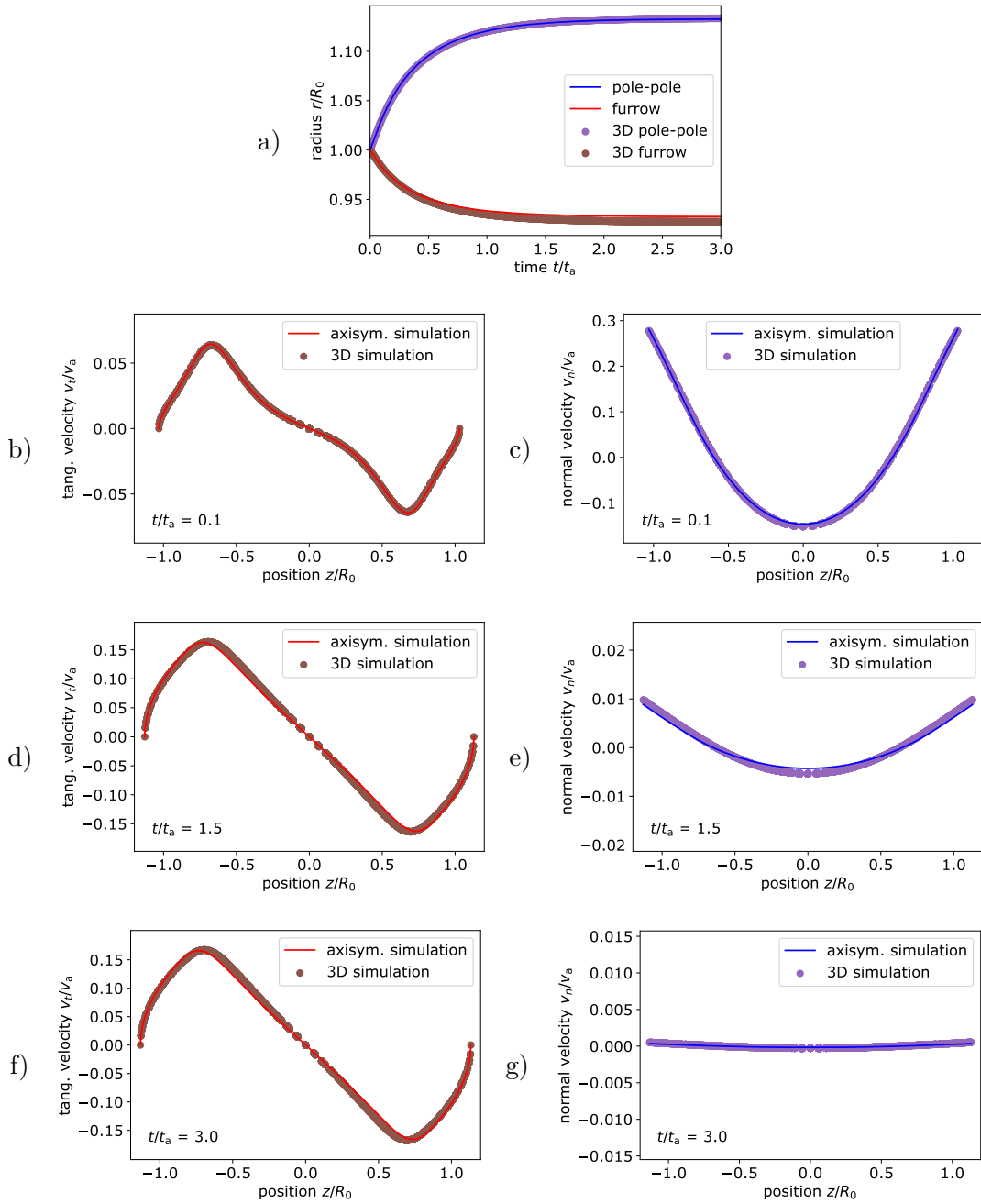


Figure 6: **Comparison of cortex dynamics.** a) Comparison of the pole to pole radius and furrow radius at the equator between axisymmetric (lines) and from three-dimensional simulation (dots) for the setup shown in figure 5 with $p = 8$, $\zeta_0 = 1$, $\hat{\zeta} = 1$. b) - g) The velocity profile obtained from axisymmetric simulation and three-dimensional simulation is compared at different time steps. Tangential (left) and normal (right) velocity depending on the position $\frac{z}{R_0}$ along the axis are shown at time b), c) $t/t_a = 0.1$, d), e) $t/t_a = 1.5$, f), g) $t/t_a = 3$. Both simulation methods are in very good agreement.

In addition, we consider an active stress distribution around the equator, which is narrower with exponent $p = 4$ in equation (89) and systematically vary the amplitude $\hat{\zeta}$. Figure 7 shows the active stress distribution for $\hat{\zeta} = 1$ as illustration in a) together with the corresponding shape and velocity profile in the b) initial and c) final state. Figure 7 d) and e) show the initial and final state for $\hat{\zeta} = 2$ and figure f) and g) for $\hat{\zeta} = 3$. We use $\bar{\eta} = 0.0005\eta_s$ and $\bar{\eta}_b = 0.0025\eta_s$ in a), b), c) and $\bar{\eta}_b = 0.0035$ in d), e), f), g). With increasing amplitude of the active stress the cortex farther extends at the poles and constricts around the equator more strongly. The final tangential velocity increases systematically, which is due to the gradient in the active stress distribution increasing with increasing magnitude and constant offset. We again compare the dynamics based on the pole to pole radius and the furrow size as well as the velocity field at different times to axisymmetric simulations. In figure 8, we show the comparison for the amplitude $\hat{\zeta} = 1$, in figure 9 for $\hat{\zeta} = 2$, and in figure 10 for $\hat{\zeta} = 3$. Again, we show in each figure the temporal comparison of the cortex evolution in a) and the velocity comparison in b) - g). In all cases the results obtained with the developed three-dimensional algorithm agree very well with the results obtained using the axisymmetric simulations. A slight difference occurs for larger $\hat{\zeta}$ due to a small influence of the bending viscosity $\bar{\eta}_b$, which we choose larger in three-dimensional simulations for the reason of stability.

Overall, the comparison to axisymmetric simulations clearly shows the accuracy of the developed algorithm for a viscous active cortex in three dimensions also in case of dynamic cortex evolution.

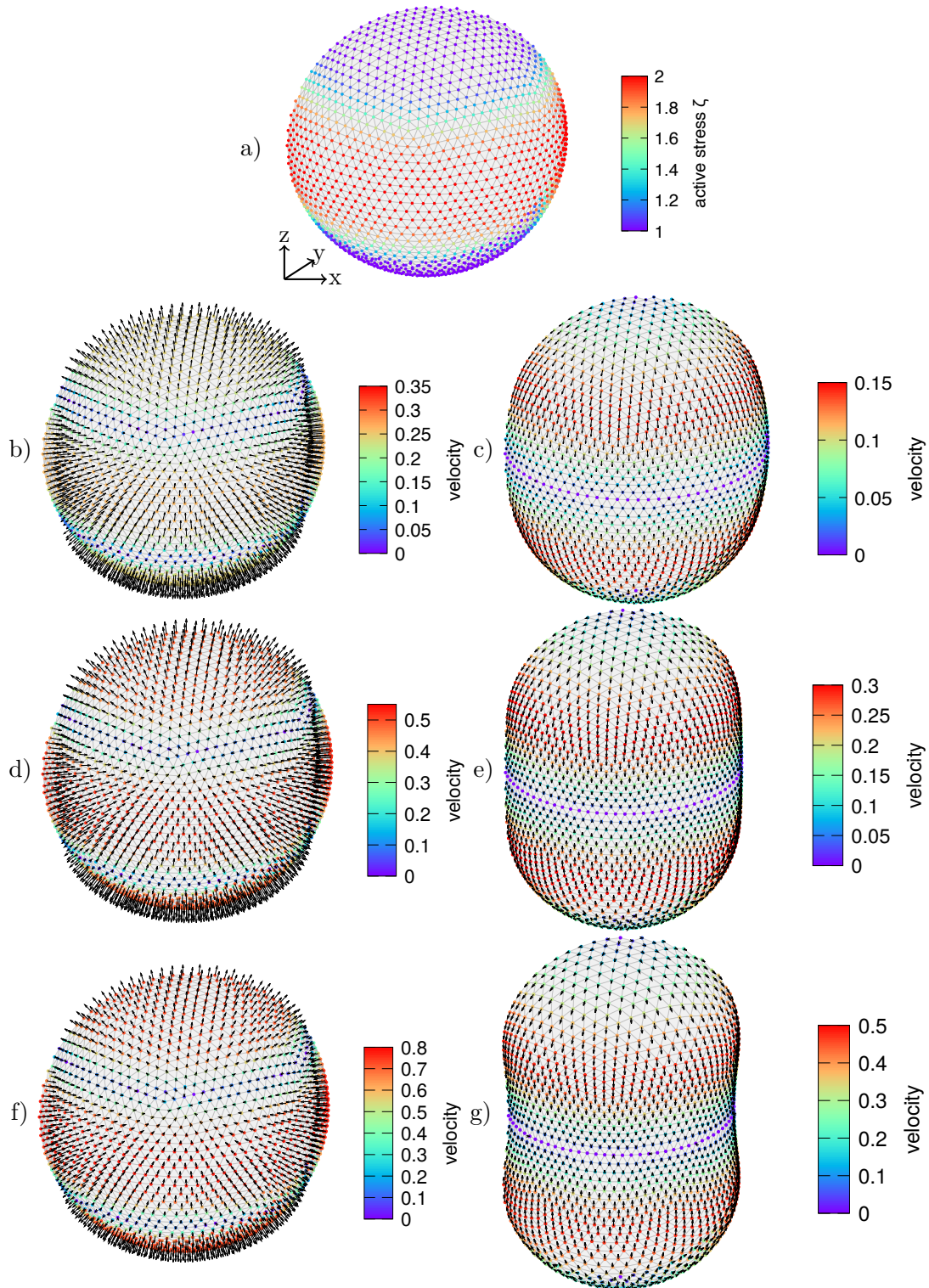


Figure 7: **Varying active stress amplitude.** a) The active stress distribution according to equation (89) with exponent $p = 4$, offset stress $\zeta_0 = 1$, and amplitude $\hat{\zeta} = 1$ is shown color coded on the initially spherical, discrete cortex. b), c) Resulting velocity profile on the initial cortex (left) and on the finally deformed cortex (right) with arrows illustrating the direction and color coded magnitude. d), e) Velocity profile for an active stress magnitude of $\hat{\zeta} = 2$ as well as f), g) for an active stress magnitude $\hat{\zeta} = 3$. In the finally deformed state the normal velocity vanishes.

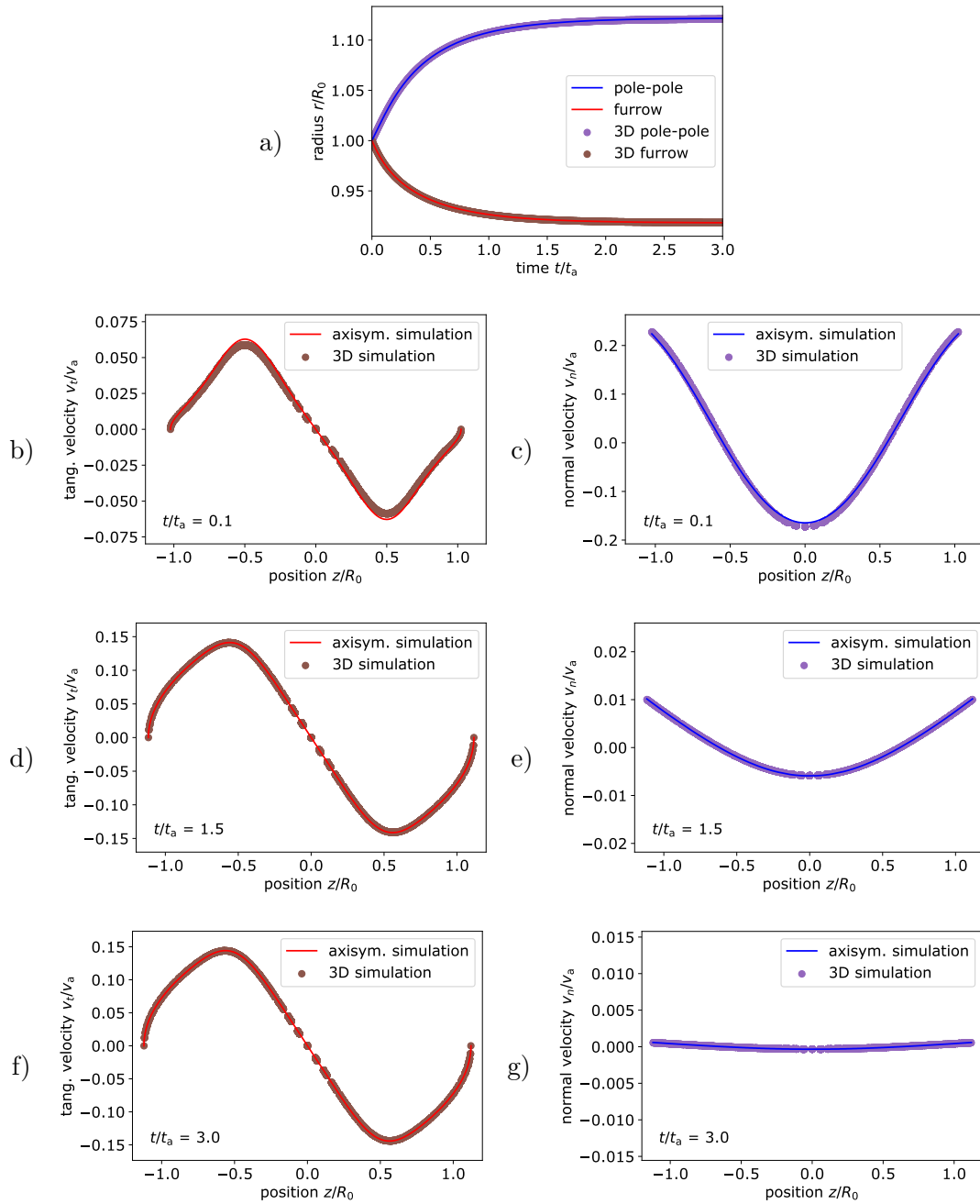


Figure 8: **Comparison of cortex dynamics for $\hat{\zeta} = 1$.** a) Comparison of the pole to pole radius and furrow radius at the equator between axisymmetric (lines) and three-dimensional simulation (dots) for the system shown in figure 7 a), b), c) with $p = 4$, $\zeta_0 = 1$, $\hat{\zeta} = 1$. b) - g) The velocity profile obtained from axisymmetric simulation and three-dimensional simulation is compared at different time steps. Tangential (left) and normal (right) velocity depending on the position $\frac{z}{R_0}$ are shown at time b), c) $t/t_a = 0.1$, d), e) $t/t_a = 1.5$, f), g) $t/t_a = 3$. Both simulation methods are in very good agreement.

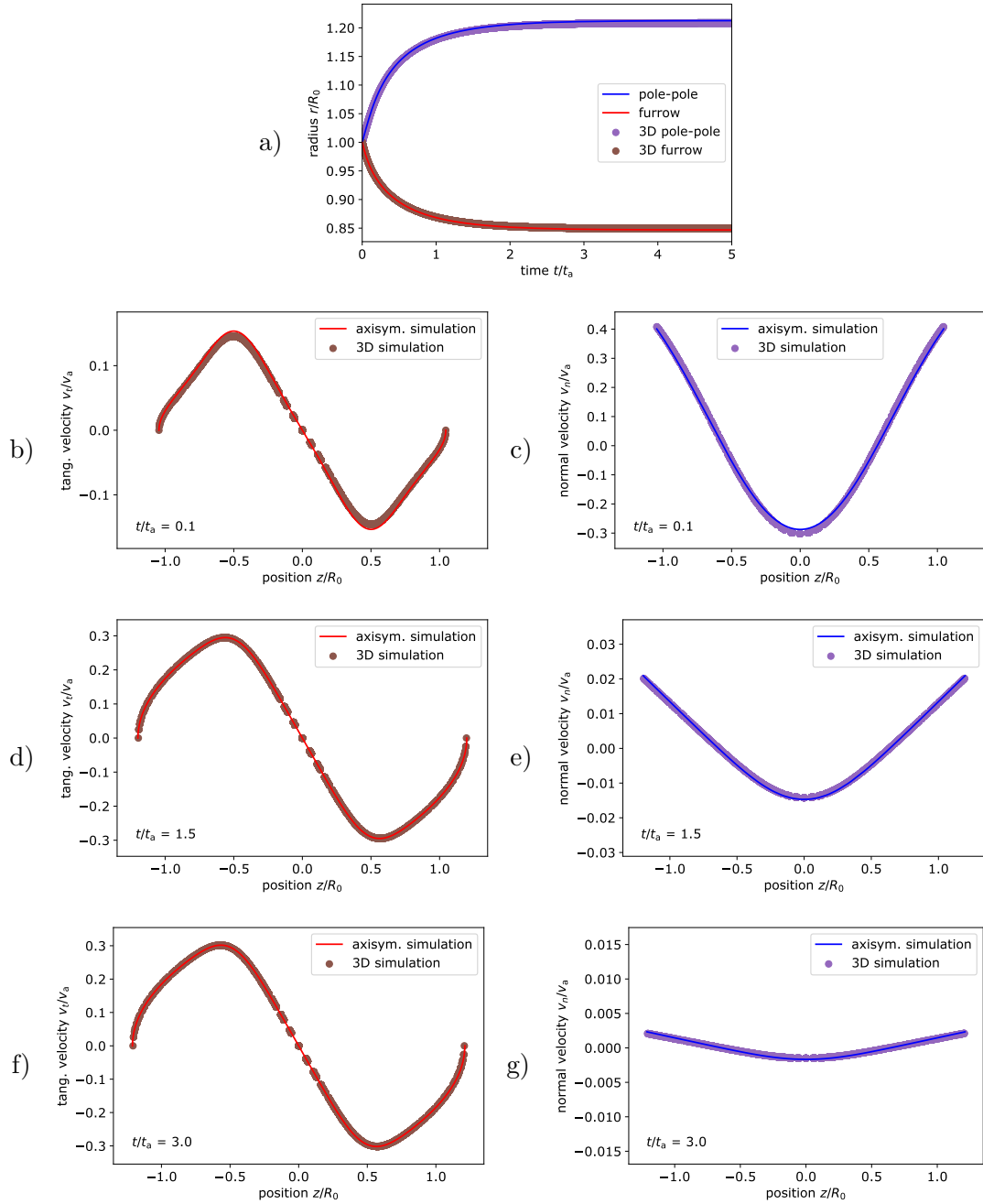


Figure 9: **Comparison of cortex dynamics for $\hat{\zeta} = 2$.** a) Comparison of the pole to pole radius and furrow radius at the equator between axisymmetric (lines) and three-dimensional simulation (dots) for the system shown in figure 7 d), e) with $p = 4, \zeta_0 = 1, \hat{\zeta} = 2$. b) - g) The velocity profile obtained from axisymmetric simulation and three-dimensional simulation is compared at different time steps. Tangential (left) and normal (right) velocity depending on the position $\frac{z}{R_0}$ are shown at time b), c) $t/t_a = 0.1$, d), e) $t/t_a = 1.5$, f), g) $t/t_a = 3$. Both simulation methods are in very good agreement.

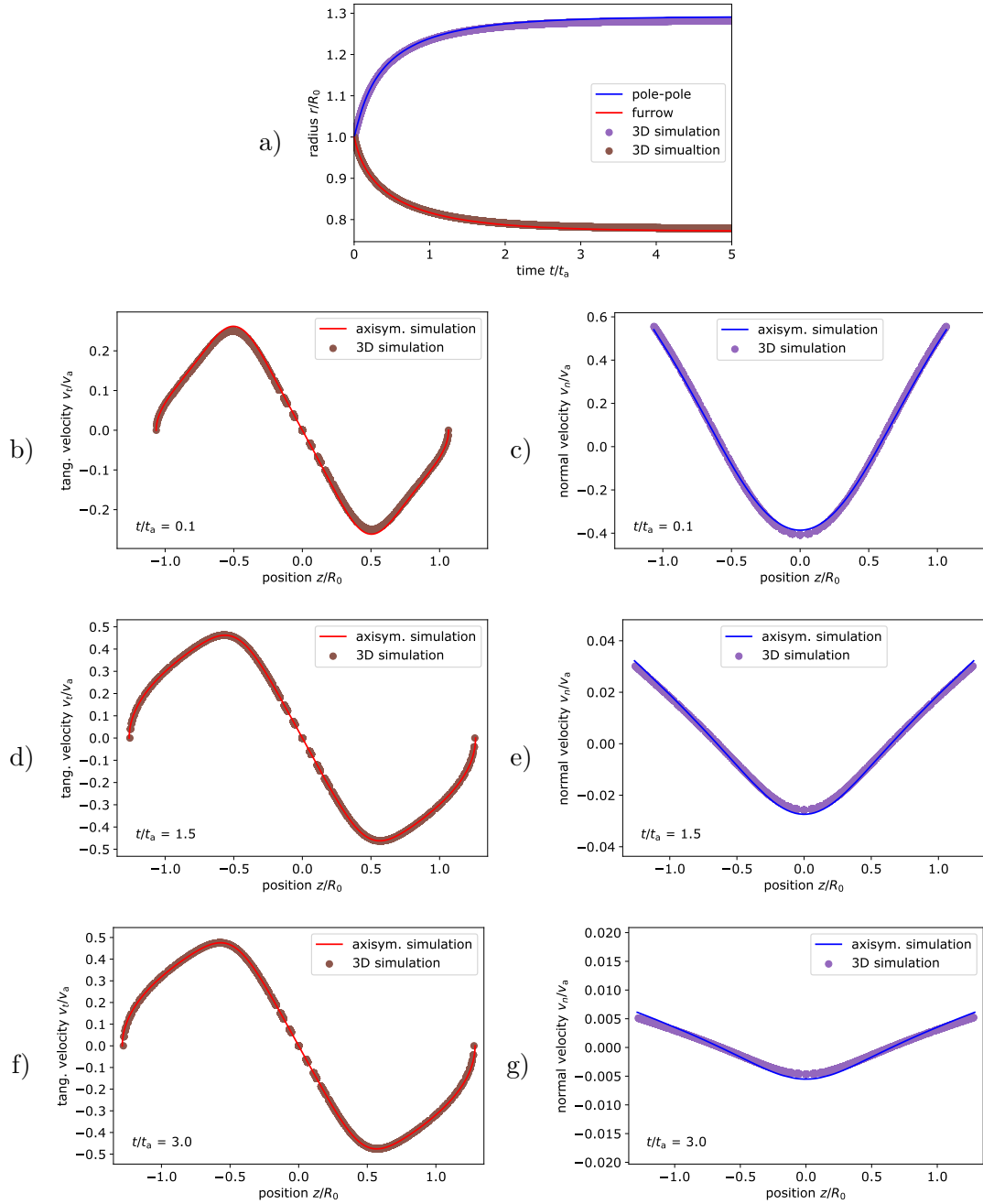


Figure 10: **Comparison of cortex dynamics for $\hat{\zeta} = 3$.** a) Comparison of the pole to pole radius and furrow radius at the equator between axisymmetric (lines) and three-dimensional simulation (dots) for the system shown in figure 7 f), g) with $p = 4$, $\zeta_0 = 1$, $\hat{\zeta} = 3$. b) - g) The velocity profile obtained from axisymmetric simulation and three-dimensional simulation is compared at different time steps. Tangential (left) and normal (right) velocity depending on the position $\frac{z}{R_0}$ are shown at time b), c) $t/t_a = 0.1$, d), e) $t/t_a = 1.5$, f), g) $t/t_a = 3$. Both simulation methods are in very good agreement.

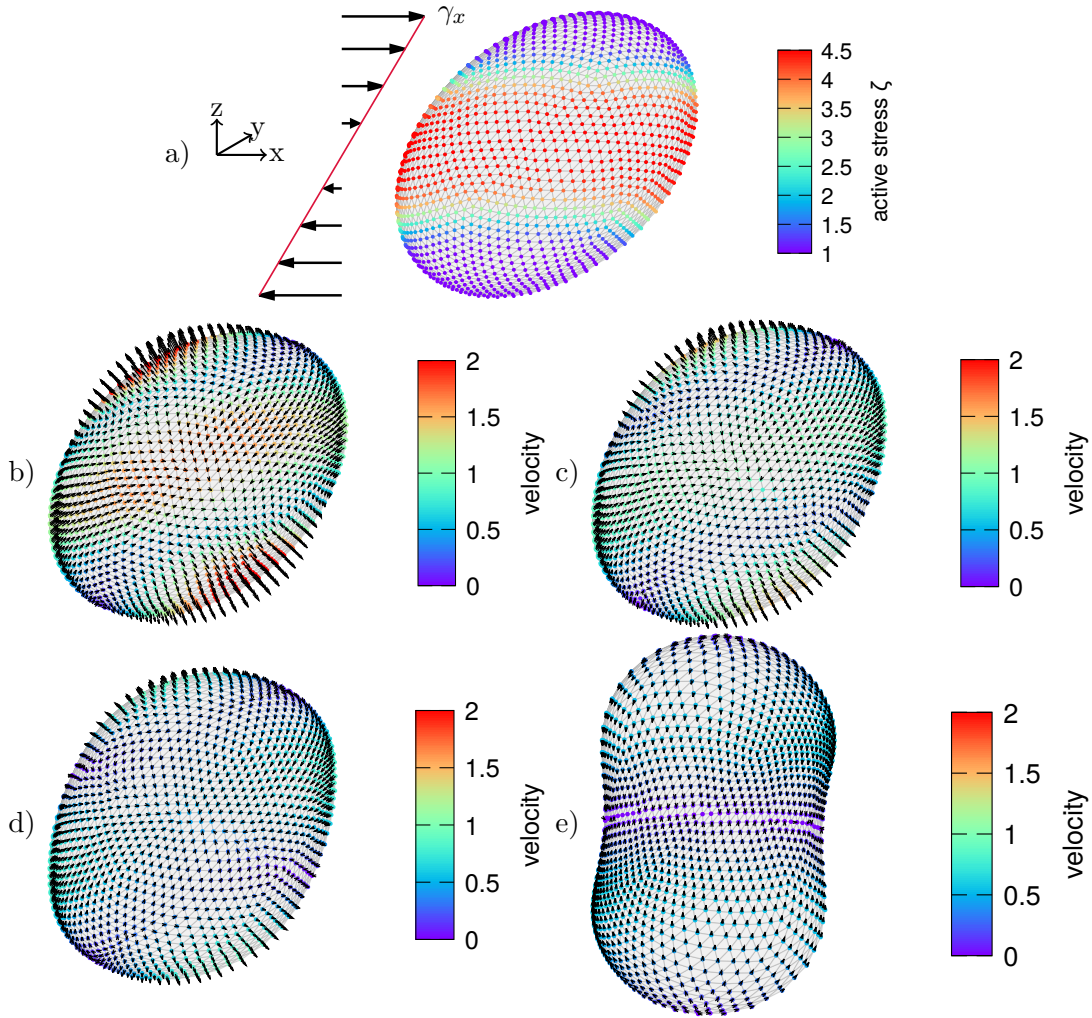


Figure 11: **Sheared cortex.** a) A cortex subject to an initial shear of $\gamma_x = 0.35$ is shown with the active stress distribution according to equation (89) with $\hat{\zeta} = 3.5$ color coded. The velocity field is shown on the evolving cortex over time with arrows indicating the direction and magnitude given by color code for time b) $t/t_a = 3.5 \times 10^{-3}$, c) $t/t_a = 3.5 \times 10^{-2}$, d) $t/t_a = 8.75 \times 10^{-2}$, and e) $t/t_a = 3.5$. While the cortex contracts around the equator and extends at the poles, it relaxes back to a shape nearly oriented as the active stress distribution on the undeformed cortex.

4.3. A first application

In order to provide a first application of an evolving cortex in a non-axisymmetric situation, we consider in the following a cell cortex subjected to an active stress distribution according to equation (89) which is sheared initially. We use the same values for the viscosity as above, i.e., $\eta_s = 1$ and $\eta_b = 1$, an exponent $p = 4$ for the active stress distribution with constant offset $\zeta_0 = 1$ and amplitude $\hat{\zeta} = 3.5$. For the bending viscosity we choose $\bar{\eta} = 1 \times 10^{-4}\eta_s$ and $\bar{\eta}_b = 5 \times 10^{-3}\eta_s$. Initially, we deform the cortex according to a shear strain of $\gamma_x = 0.35$ along the x -axis. On the one hand, we consider the active

stress distribution with gradient along the polar angle θ , i.e., along the z -axis. On the other hand, we rotate the cortex before the deformation such that the gradient of the active stress distribution nearly aligns with the shear.

For the first setup, the active stress distribution is shown in figure 11 a). We show in figure 11 b) - e) the dynamic evolution of the cortex with the velocity magnitude per node color coded and the velocity direction indicated by arrows. Shapes with the velocity profile are shown for time b) $t/t_a = 3.5 \times 10^{-3}$, c) $t/t_a = 3.5 \times 10^{-2}$, d) $t/t_a = 8.75 \times 10^{-2}$, and e) $t/t_a = 3.5$. Initially, a large normal velocity is observed in figure a) with a kind of stripe pattern. More or less along the long axis of the sheared cortex the velocity points inwards the cell cortex. In direction perpendicular to the shear, the velocity points outwards the cell cortex. This illustrates the tendency of the cell cortex to realign with respect to the symmetry of the active stress distribution on the undeformed cortex, which is similar to the one shown in figure 7 a). The reorientation is visible throughout the time evolution as well. Eventually, the cell cortex is nearly aligned with the initial gradient of the active stress distribution. This points to the symmetry of the active stress distribution being the driving mechanism behind this reorientation. From figure d) to e) it can be seen that the cortex also contracts around the equator.

Next, we consider the dynamic evolution of the cortex subject to the same initial shear with rotated active stress distribution as shown in figure 12 a). Again the evolution of the cortex is shown in figure b) - e) at the same time steps. Initially, the flow field shows four patches of large velocity in b). The evolving flow field first leads to a broadening of the cortex and a slight reorientation, presumably with respect to the symmetry of the active stress distribution. Subsequently, the cortex contracts around the equator with the eventual shape shown in figure e). The tangential velocity is directed from the poles to the equator.

Both test applications illustrate the applicability of our algorithm to non-axisymmetric situations with a three-dimensional deformation of the cortex.

5. Conclusion

By directly solving the force balance equations in thin shell formulation taking into account cortical viscosity as well as active stress, we developed a simulation algorithm for a cell cortex in the viscous limit in a fully three-dimensional situation. The cell cortex is represented as thin shell in the framework of active gel theory. Using an inverted parabolic fitting procedure, we were able to express the force balance equations on each node of the discretized cortex in terms of the velocity components. Eventually, the velocity components are obtained by solving the force balance equations on the whole cortex using a minimization ansatz. Extensive validation to presented analytical solutions in the static case as well as to axisymmetric simulations in a dynamic situation showed very good agreement. As a first application in a non-axisymmetric situation, we considered a cortex with differently orientated active stress distribution which is subject to an initial shear deformation.

The generality of the presented algorithm, which directly solves the force balance equations, allows for a straightforward application to different constitutive laws for cortex

behavior and active stress. Furthermore, the active stress distribution on the discrete cortex could be coupled to a concentration field, e.g., taking into account cytoskeleton polymerization and depolymerization. A coupling to an external environment can be also done by adding corresponding external forces to the force balance equations. This would allow a dynamic coupling to a suspending fluid in combination with a fluid solver. All in all, the developed numerical tool can be the basis for future investigations of various three-dimensional scenarios of cell and tissue morphogenesis.

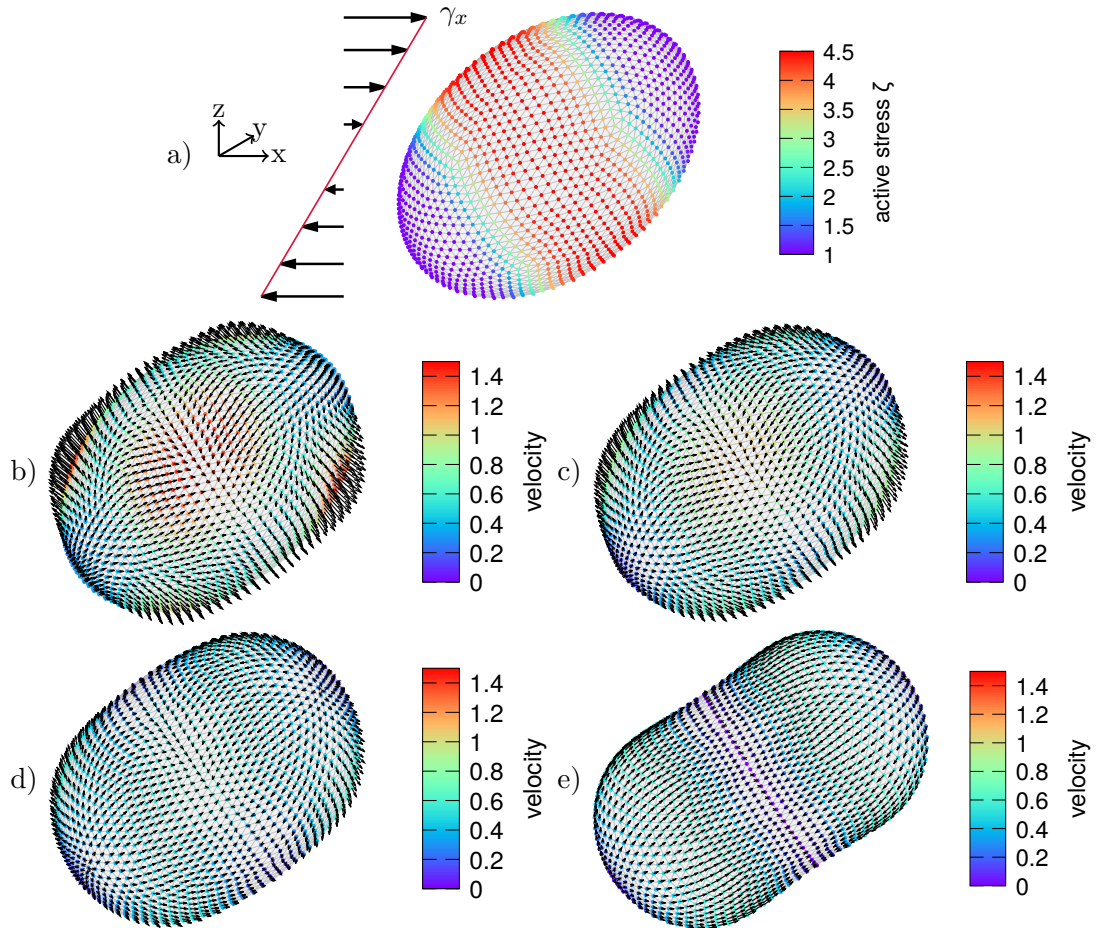


Figure 12: **Tilted sheared cortex.** a) A cortex subject to an initial shear of $\gamma_x = 0.35$ is shown with the active stress distribution according to equation (89) with $\hat{\zeta} = 3.5$ but rotated with an angle of 45° towards the direction of the shear color coded. The velocity field is shown on the evolving cortex over time with arrows indicating the direction and magnitude given by color code for time b) $t/t_a = 3.5 \times 10^{-3}$, c) $t/t_a = 3.5 \times 10^{-2}$, d) $t/t_a = 8.75 \times 10^{-2}$, and e) $t/t_a = 3.5$. While the cortex contracts around the equator and extends at the poles, it retains its overall orientation.

Appendices

A. Analytical solution in terms of spherical harmonics

In the following, we derive an analytical solution for the spherical cortex of radius R with an active stress distribution in terms of spherical harmonics as given by equation (80). According to the expansion of the active stress in terms of spherical harmonics we choose as ansatz an expansion of the normal velocity in spherical harmonics $v^n = \mathbf{v} \cdot \mathbf{n} = \sum_{n,m} N_{nm} Y_{nm}$ together with the in-plane velocity expressed as by vector spherical harmonics [62], such that the velocity becomes

$$\mathbf{v} = \sum_{n,m} \left[A_{nm} \mathbf{s}_{nm}^1 + B_{nm} \mathbf{s}_{nm}^2 + N_{nm} Y_{nm} \mathbf{n} \right], \quad (\text{A.1})$$

with $\mathbf{s}_{nm}^1 = \partial_\alpha Y_{nm} \mathbf{e}^\alpha$ and $\mathbf{s}_{nm}^2 = \mathbf{n} \times \mathbf{s}_{nm}^1$. The azimuthal velocity vanishes and we therefore directly use $B_{nm} = 0$. We further express the pressure in terms of spherical harmonics

$$P = P_0 + \sum_{n,m} P_{nm} Y_{nm}, \quad (\text{A.2})$$

where P_0 is a constant uniform pressure difference, which accounts for the Laplace pressure due to the offset active stress $\langle \zeta \rangle$. In the following, we consider a constant uniform pressure in the cell's interior and therefore the spherical harmonics in the pressure have to vanish, i.e., $P_{nm} = 0$.

With the velocity gradient and its trace in the form

$$v_{\alpha\beta} = \frac{1}{2} [\nabla_\alpha v_\beta + \nabla_\beta v_\alpha] + C_{\alpha\beta} v^n, \quad v_\gamma^\gamma = \nabla_\gamma v^\gamma + C_\gamma^\gamma v^n,$$

the viscous surface stress (15) becomes

$$\begin{aligned} t_{v,\alpha\beta} &= 2\eta_s \left(\frac{1}{2} [\nabla_\alpha v_\beta + \nabla_\beta v_\alpha] + C_{\alpha\beta} v^n - \frac{1}{2} g_{\alpha\beta} \nabla_\gamma v^\gamma - \frac{1}{2} g_{\alpha\beta} C_\gamma^\gamma v^n \right) \\ &\quad + \eta_b \left(\nabla_\gamma v^\gamma + C_\gamma^\gamma v^n \right) g_{\alpha\beta}. \end{aligned}$$

Inserting the ansatz (A.1), using the identity $\nabla_\gamma \nabla^\gamma Y_{nm} = -n(n+1)Y_{nm}$ for the spherical harmonics, and using further the definition of the trace-less tensorial spherical harmonics $S_1^{(n,m)\alpha\beta} = \nabla^\alpha \nabla^\beta Y_{nm} - \frac{1}{2} g^{\alpha\beta} \nabla_\gamma \nabla^\gamma Y_{nm}$ we can write the viscous surface stress as

$$\begin{aligned} t_v^{\alpha\beta} &= 2\eta_s \sum_{n,m} \left[A_{nm} S_1^{(n,m)\alpha\beta} + N_{nm} C^{\alpha\beta} Y_{nm} - \frac{1}{2} g^{\alpha\beta} C_\gamma^\gamma N_{nm} Y_{nm} \right] \\ &\quad + \eta_b g^{\alpha\beta} \sum_{n,m} \left(-A_{nm} n(n+1) Y_{nm} + C_\gamma^\gamma N_{nm} Y_{nm} \right). \end{aligned} \quad (\text{A.3})$$

and its trace becomes

$$t_{v,\gamma}^\gamma = 2\eta_b \sum_{n,m} \left(-A_{nm} n(n+1) Y_{nm} + C_\gamma^\gamma N_{nm} Y_{nm} \right). \quad (\text{A.4})$$

We now solve the three force balance equations, where the tangential ones translate into two separate scalar equations

$$\nabla_\alpha \nabla_\beta t^{\alpha\beta} = 0 \quad (\text{A.5})$$

$$\epsilon_\beta^\gamma \nabla_\gamma \nabla_\alpha t^{\alpha\beta} = 0 \quad (\text{A.6})$$

$$t^{\alpha\beta} C_{\alpha\beta} = \Delta P. \quad (\text{A.7})$$

First, we re-write the normal force balance equation (A.7) using $C_\alpha^\beta = \frac{1}{R} \delta_\alpha^\beta$ and the trace of the viscous stress (A.4) and of the active stress (80) such that the normal force balance becomes

$$2\eta_b \frac{1}{R} \sum_{n,m} \left[-A_{nm} n(n+1) Y_{nm} + C_\gamma^\gamma N_{nm} Y_{nm} \right] + \frac{2}{R} \sum_{n,m} \zeta_{nm} Y_{nm} + \frac{2}{R} \zeta_0 = P_0,$$

which has to be fulfilled for the linear independent spherical harmonics separately and we thus obtain the relation

$$-2\eta_b A_{nm} n(n+1) + \eta_b \frac{4}{R} N_{nm} + 2\zeta_{nm} = 0,$$

where we have identified $P_0 = \frac{2}{R} \zeta_0$, the Laplace pressure. Next, we consider the first in-plane force balance equation (A.5). We calculate the second derivative of the in-plane surface stress tensor using the identity for the tensorial spherical harmonics $\nabla_\alpha \nabla_\beta S_1^{(n,m)\alpha\beta} = \frac{n(n+1)}{2} [n(n+1) - 2] Y_{nm}$ and obtain for the separate spherical harmonics coefficients the relation

$$(\eta_s + \eta_b) A_{nm} n^2 (n+1)^2 - 2\eta_s A_{nm} n(n+1) - \frac{2\eta_b}{R} N_{nm} n(n+1) - n(n+1) \zeta_{nm} = 0. \quad (\text{A.8})$$

Eventually, we note that the second in-plane force balance equation (A.6) is automatically fulfilled due to the relation $\epsilon_\beta^\gamma \nabla_\gamma \nabla_\alpha S_1^{(n,m)\alpha\beta} = 0$. The two conditions for the spherical harmonics coefficients following from the force balance equations can be rearranged into the following form

$$(\eta_s + \eta_b) A_{nm} n(n+1) - 2\eta_s A_{nm} - \frac{2\eta_b}{R} N_{nm} - \zeta_{nm} = 0 \quad (\text{A.9})$$

$$-\eta_b A_{nm} n(n+1) + \frac{2\eta_b}{R} N_{nm} + \zeta_{nm} = 0, \quad (\text{A.10})$$

which determine the solution for the velocity field.

References

- [1] B. Alberts, A. Johnson, J. Lewis, M. Raff, K. Roberts, and P. Walter. *Molecular Biology of the Cell*. Garland Science, New York, fifth edition, 2007.
- [2] M. C. Marchetti, J. F. Joanny, S. Ramaswamy, T. B. Liverpool, J. Prost, M. Rao, and R. A. Simha. Hydrodynamics of soft active matter. *Reviews of Modern Physics*, 85(3):1143–1189, July 2013.

- [3] E. Fodor, C. Nardini, M. E. Cates, J. Tailleur, P. Visco, and F. van Wijland. How Far from Equilibrium Is Active Matter? *Physical Review Letters*, 117(3):038103, July 2016.
- [4] T. Hiraiwa and G. Salbreux. Role of Turnover in Active Stress Generation in a Filament Network. *Physical Review Letters*, 116(18):188101, May 2016.
- [5] A. Ravichandran, G. A. Vliegenthart, G. Saggiorato, T. Auth, and G. Gompper. Enhanced Dynamics of Confined Cytoskeletal Filaments Driven by Asymmetric Motors. *Biophysical Journal*, 113(5):1121–1132, Sept. 2017.
- [6] E. Hannezo, B. Dong, P. Recho, J.-F. Joanny, and S. Hayashi. Cortical instability drives periodic supracellular actin pattern formation in epithelial tubes. *Proceedings of the National Academy of Sciences*, 112(28):8620–8625, July 2015.
- [7] K. Gowrishankar and M. Rao. Nonequilibrium phase transitions, fluctuations and correlations in an active contractile polar fluid. *Soft Matter*, 12(7):2040–2046, 2016.
- [8] A. Mietke, V. Jemseena, K. V. Kumar, I. F. Sbalzarini, and F. Jülicher. Minimal Model of Cellular Symmetry Breaking. *Physical Review Letters*, 123(18):188101, Oct. 2019.
- [9] A. Mietke, F. Jülicher, and I. F. Sbalzarini. Self-organized shape dynamics of active surfaces. *Proceedings of the National Academy of Sciences*, 116(1):29–34, Jan. 2019.
- [10] S. Ramaswamy, J. Toner, and J. Prost. Nonequilibrium Fluctuations, Traveling Waves, and Instabilities in Active Membranes. *Physical Review Letters*, 84(15):3494–3497, Apr. 2000.
- [11] R. Voituriez, J. F. Joanny, and J. Prost. Spontaneous flow transition in active polar gels. *Europhysics Letters*, 70(3):404–410, May 2005.
- [12] D. Marenduzzo, E. Orlandini, M. E. Cates, and J. M. Yeomans. Steady-state hydrodynamic instabilities of active liquid crystals: Hybrid lattice Boltzmann simulations. *Physical Review E*, 76(3), Sept. 2007.
- [13] M. Ravnik and J. M. Yeomans. Confined Active Nematic Flow in Cylindrical Capillaries. *Physical Review Letters*, 110(2), Jan. 2013.
- [14] K. V. Kumar, J. S. Bois, F. Jülicher, and S. W. Grill. Pulsatory Patterns in Active Fluids. *Physical Review Letters*, 112(20), May 2014.
- [15] D. Khoromskaia and G. P. Alexander. Motility of active fluid drops on surfaces. *Physical Review E*, 92(6), Dec. 2015.
- [16] R. Ramaswamy and F. Jülicher. Activity induces traveling waves, vortices and spatiotemporal chaos in a model actomyosin layer. *Scientific Reports*, 6:20838, Feb. 2016.

- [17] F. Bonelli, G. Gonnella, A. Tiribocchi, and D. Marenduzzo. Spontaneous flow in polar active fluids: The effect of a phenomenological self propulsion-like term. *The European Physical Journal E*, 39(1):1, Jan. 2016.
- [18] K.-T. Wu, J. B. Hishamunda, D. T. N. Chen, S. J. DeCamp, Y.-W. Chang, A. Fernández-Nieves, S. Fraden, and Z. Dogic. Transition from turbulent to coherent flows in confined three-dimensional active fluids. *Science*, 355(6331):eaal1979, Mar. 2017.
- [19] S. W. Grill. Growing up is stressful: Biophysical laws of morphogenesis. *Current Opinion in Genetics and Development*, 21(5):647–652, Oct. 2011.
- [20] G. Salbreux, G. Charras, and E. Paluch. Actin cortex mechanics and cellular morphogenesis. *Trends in Cell Biology*, 22(10):536–545, Oct. 2012.
- [21] A. C. Callan-Jones, V. Ruprecht, S. Wieser, C. P. Heisenberg, and R. Voituriez. Cortical Flow-Driven Shapes of Nonadherent Cells. *Physical Review Letters*, 116(2):028102, Jan. 2016.
- [22] E. Fischer-Friedrich, Y. Toyoda, C. J. Cattin, D. J. Müller, A. A. Hyman, and F. Jülicher. Rheology of the Active Cell Cortex in Mitosis. *Biophysical Journal*, 111(3):589–600, Aug. 2016.
- [23] E. Fischer-Friedrich. Active Prestress Leads to an Apparent Stiffening of Cells through Geometrical Effects. *Biophysical Journal*, 114(2):419–424, Jan. 2018.
- [24] R. J. Hawkins, R. Poincloux, O. Bénichou, M. Piel, P. Chavrier, and R. Voituriez. Spontaneous Contractility-Mediated Cortical Flow Generates Cell Migration in Three-Dimensional Environments. *Biophysical Journal*, 101(5):1041–1045, Sept. 2011.
- [25] A. E. Carlsson. Mechanisms of cell propulsion by active stresses. *New Journal of Physics*, 13(7):073009, July 2011.
- [26] D. Shao, H. Levine, and W.-J. Rappel. Coupling actin flow, adhesion, and morphology in a computational cell motility model. *Proceedings of the National Academy of Sciences*, 109(18):6851–6856, 2012.
- [27] W. Marth, S. Praetorius, and A. Voigt. A mechanism for cell motility by active polar gels. *Journal of The Royal Society Interface*, 12(107):20150161, 2015.
- [28] A. C. Callan-Jones and R. Voituriez. Actin flows in cell migration: From locomotion and polarity to trajectories. *Current Opinion in Cell Biology*, 38:12–17, Feb. 2016.
- [29] E. J. Campbell and P. Bagchi. A computational model of amoeboid cell swimming. *Physics of Fluids*, 29(10):101902, Oct. 2017.
- [30] G. Salbreux, J. Prost, and J. F. Joanny. Hydrodynamics of Cellular Cortical Flows and the Formation of Contractile Rings. *Physical Review Letters*, 103(5):058102, July 2009.

- [31] J. Sedzinski, M. Biro, A. Oswald, J.-Y. Tinevez, G. Salbreux, and E. Paluch. Polar actomyosin contractility destabilizes the position of the cytokinetic furrow. *Nature*, 476(7361):462–466, Aug. 2011.
- [32] I. Mendes Pinto, B. Rubinstein, and R. Li. Force to Divide: Structural and Mechanical Requirements for Actomyosin Ring Contraction. *Biophysical Journal*, 105(3):547–554, Aug. 2013.
- [33] H. Turlier, B. Audoly, J. Prost, and J.-F. Joanny. Furrow Constriction in Animal Cell Cytokinesis. *Biophysical Journal*, 106(1):114–123, Jan. 2014.
- [34] A. Sain, M. M. Inamdar, and F. Jülicher. Dynamic Force Balances and Cell Shape Changes during Cytokinesis. *Physical Review Letters*, 114(4):048102, Jan. 2015.
- [35] K. Kruse, J. F. Joanny, F. Jülicher, J. Prost, and K. Sekimoto. Generic theory of active polar gels: A paradigm for cytoskeletal dynamics. *The European Physical Journal E*, 16(1):5–16, Jan. 2005.
- [36] J. Prost, F. Jülicher, and J.-F. Joanny. Active gel physics. *Nature Physics*, 11(2):111–117, Feb. 2015.
- [37] F. Jülicher, S. W. Grill, and G. Salbreux. Hydrodynamic theory of active matter. *Reports on Progress in Physics*, 81(7):076601, July 2018.
- [38] Y. Hatwalne, S. Ramaswamy, M. Rao, and R. A. Simha. Rheology of Active-Particle Suspensions. *Physical Review Letters*, 92(11):118101, Mar. 2004.
- [39] K. Kruse, J. F. Joanny, F. Jülicher, J. Prost, and K. Sekimoto. Asters, Vortices, and Rotating Spirals in Active Gels of Polar Filaments. *Physical Review Letters*, 92(7):078101, Feb. 2004.
- [40] G. Salbreux and F. Jülicher. Mechanics of active surfaces. *Physical Review E*, 96(3):032404, Sept. 2017.
- [41] H. Berthoumieux, J.-L. Maître, C.-P. Heisenberg, E. K. Paluch, F. Jülicher, and G. Salbreux. Active elastic thin shell theory for cellular deformations. *New Journal of Physics*, 16(6):065005, June 2014.
- [42] C. Bächer and S. Gekle. Computational modeling of active deformable membranes embedded in three-dimensional flows. *Physical Review E*, 99(6):062418, June 2019.
- [43] C. Bächer, M. Bender, and S. Gekle. Flow-accelerated platelet biogenesis is due to an elasto-hydrodynamic instability. *Proceedings of the National Academy of Sciences*, 117(32):18969–18976, Aug. 2020.
- [44] A.-C. Reymann, F. Staniscia, A. Erzberger, G. Salbreux, and S. W. Grill. Cortical flow aligns actin filaments to form a furrow. *eLife*, 5:e17807, Oct. 2016.
- [45] A. Torres-Sánchez, D. Millán, and M. Arroyo. Modelling fluid deformable surfaces with an emphasis on biological interfaces. *Journal of Fluid Mechanics*, 872:218–271, Aug. 2019.

- [46] A. Farutin, J. Étienne, C. Misbah, and P. Recho. Crawling in a Fluid. *Physical Review Letters*, 123(11):118101, Sept. 2019.
- [47] R. A. Green, E. Paluch, and K. Oegema. Cytokinesis in Animal Cells. *Annual Review of Cell and Developmental Biology*, 28(1):29–58, Nov. 2012.
- [48] M. Mayer, M. Depken, J. S. Bois, F. Jülicher, and S. W. Grill. Anisotropies in cortical tension reveal the physical basis of polarizing cortical flows. *Nature*, 467(7315):617–621, Sept. 2010.
- [49] R. Etournay, M. Popović, M. Merkel, A. Nandi, C. Blasse, B. Aigouy, H. Brandl, G. Myers, G. Salbreux, F. Jülicher, and S. Eaton. Interplay of cell dynamics and epithelial tension during morphogenesis of the *Drosophila* pupal wing. *eLife*, 4, June 2015.
- [50] N. C. Heer, P. W. Miller, S. Chanet, N. Stoop, J. Dunkel, and A. C. Martin. Actomyosin-based tissue folding requires a multicellular myosin gradient. *Development*, 144(10):1876–1886, May 2017.
- [51] A. Torres-Sánchez, D. Santos-Oliván, and M. Arroyo. Approximation of tensor fields on surfaces of arbitrary topology based on local Monge parametrizations. *Journal of Computational Physics*, 405:109168, Mar. 2020.
- [52] A. E. Green and W. Zerna. *Theoretical Elasticity*. Clarendon Press, Oxford, 1954.
- [53] E. Kreyszig. *Introduction to Differential Geometry and Riemannian Geometry*. University of Toronto Press, 1968.
- [54] D. Chandrasekharaiah and L. Debnath. *Continuum Mechanics*. Elsevier, 2014.
- [55] A. Farutin, T. Biben, and C. Misbah. 3D numerical simulations of vesicle and inextensible capsule dynamics. *Journal of Computational Physics*, 275:539–568, Oct. 2014.
- [56] C. Pozrikidis. Interfacial Dynamics for Stokes Flow. *Journal of Computational Physics*, 169(2):250–301, May 2001.
- [57] Y. Seol, W.-F. Hu, Y. Kim, and M.-C. Lai. An immersed boundary method for simulating vesicle dynamics in three dimensions. *Journal of Computational Physics*, 322:125–141, Oct. 2016.
- [58] A. Guckenberger and S. Gekle. Theory and algorithms to compute Helfrich bending forces: A review. *Journal of Physics: Condensed Matter*, 29(20):203001, May 2017.
- [59] M. Meyer, M. Desbrun, P. Schröder, and A. H. Barr. Discrete differential-geometry operators for triangulated 2-manifolds. In *Visualization and Mathematics III*, pages 35–57. Springer, 2003.
- [60] D. Khoromskaia and G. Salbreux. Active morphogenesis of epithelial shells. *in preparation*, 2020.

- [61] D. Khoromskaia and G. Salbreux. (private communication).
- [62] R. G. Barrera, G. A. Estevez, and J. Giraldo. Vector spherical harmonics and their application to magnetostatics. *European Journal of Physics*, 6(4):287–294, Oct. 1985.

Publication 3

RAYLEIGH–PLATEAU INSTABILITY OF
ANISOTROPIC INTERFACES. PART 1.
AN ANALYTICAL AND NUMERICAL
STUDY OF FLUID INTERFACES

K. Graessel, C. Bächer, and S. Gekle

Journal of Fluid Mechanics **910** (A46), 2021

Copyright by Cambridge University Press. Reprinted
with permission.

Rayleigh–Plateau instability of anisotropic interfaces. Part 1. An analytical and numerical study of fluid interfaces

Katharina Graessel¹, Christian Bächer¹ and Stephan Gekle^{1,†}

¹Biofluid Simulation and Modeling, Theoretische Physik VI, University of Bayreuth, Universitätsstraße 30, 95447 Bayreuth, Germany

(Received 24 March 2020; revised 20 October 2020; accepted 23 October 2020)

Numerous experiments and theoretical calculations have shown that cylindrical vesicles can undergo a pearling instability similar to the Rayleigh–Plateau instability of a liquid jet when they are subjected to external tension. In a living cell, a Rayleigh–Plateau-like instability could be triggered by internal tension generated in the cell cortex. This mechanism has been suggested to play an essential role in biological processes such as cell morphogenesis. In contrast to the simple, passive and isotropic membrane of vesicles, the cortical tensions generated by biological cells are often strongly anisotropic. Here, we theoretically investigate how this anisotropy affects the Rayleigh–Plateau instability mechanism. We do so in the limit of both low and high Reynolds numbers and accordingly cover cell behaviour under anisotropic cortical tension as well as fast liquid jets with anisotropic surface tension. Combining analytical linear stability analysis with numerical simulations we report a strong influence of the anisotropy on the dominant wavelength of the instability: increasing azimuthal with respect to axial tension leads to destabilisation and to a shorter break-up wavelength. In addition, compared to the classical isotropic Rayleigh–Plateau situation, the range of unstable modes grows or shrinks when the azimuthal tension is higher or lower than the axial tension, respectively. We explore nonlinear effects like an altered break-up time and formation of satellite droplets under anisotropic tension. In Part 2 (Bächer *et al.* *J. Fluid Mech.*, vol. xxx, 2021, Ax) of this series we continue our analysis by analytically investigating the influence of bending and shear elasticity, usually present in vesicles and cells, on this anisotropic Rayleigh–Plateau instability.

Key words: instability, capsule/cell dynamics, membranes

1. Introduction

The break-up of liquid jets into droplets, triggered by surface tension, was already investigated intensively by Plateau in the second half of the 19th century (Plateau 1873). Based on the concept of the fastest growing perturbation, Rayleigh derived a relation

† Email address for correspondence: stephan.gekle@uni-bayreuth.de

between the radius of the liquid jet and the dominant wavelength which determines the size of the droplets for an ideal fluid in the absence of an outer medium (Rayleigh 1878). Later, he extended the theoretical description of this Rayleigh–Plateau instability to viscous jets in the inertialess Stokes limit (Rayleigh 1892). Again in the Stokes limit, the presence of an outer medium with arbitrary viscosity ratio between inner and outer fluid has been investigated by Tomotika (1935). A simplified version for the important case of equal viscosities has been presented by Stone & Brenner (1996). The Rayleigh–Plateau instability is a prime example of the beauty of fluid mechanics and possesses great relevance in various applications. We refer to the review article by Eggers & Villermaux (2008) for further details.

However, pearling and break-up due to the Rayleigh–Plateau mechanism are not restricted to liquid jets. In 1994, Bar-Ziv & Moses (1994) reported a pearling instability for a tubular vesicle. A vesicle consists of a lipid bilayer membrane confining an interior fluid and is often considered as a model system for a biological cell (Seifert 1997). Under local application of laser tweezers the vesicle formed pearls (Bar-Ziv & Moses 1994). Using a hydrodynamic theory Nelson, Powers & Seifert (1995) and Goldstein *et al.* (1996) explained the pearling of the vesicle by a laser induced tension, which in turn triggers a Rayleigh–Plateau-like instability. Pearl formation starts at the site of application of the laser and the instability then propagates along the cylindrical vesicle (Goldstein *et al.* 1996; Bar-Ziv, Tlusty & Moses 1997). Later, several experimental studies demonstrated different ways to induce the tension which is required for the pearling instability (Powers 2010). Pulling on membrane tethers with optically trapped particles (Bar-Ziv, Moses & Nelson 1998; Powers, Huber & Goldstein 2002), protein mediated anchoring of membrane tethers to a substrate (Bar-Ziv *et al.* 1999), applying a magnetic field (Ménager *et al.* 2002), electric field (Sinha, Gadkari & Thaokar 2013) or osmotic pressure gradient (Yanagisawa, Imai & Taniguchi 2008; Sanborn *et al.* 2013) can all lead to pearling. Furthermore, Kantsler, Segre & Steinberg (2008) reported the transition of a finite-size, tubular vesicle to a pearling state due to stretching in an extensional flow and noted that the transition is reversible when the external flow stops. In shear flow the instability has also been observed (Pal & Khakhar 2019). Boedec, Jaeger & Leonetti (2014) derived theoretically the growth rate for the instability of a cylindrical vesicle under tension. They treat the fluid surrounding the vesicle in the limit of the Stokes equation and allow for variations of the tension along the vesicle. By means of boundary integral simulations Narsimhan, Spann & Shaqfeh (2015) showed that the initial shape of a closed vesicle in extensional flow influences the number of fragments after pearling.

In contrast to passive vesicles, where the tension triggering the Rayleigh–Plateau instability has to be imposed from the outside, living biological cells are able to internally create active stresses in their cytoskeletal network (Kruse *et al.* 2005; Marchetti *et al.* 2013; Prost, Jülicher & Joanny 2015; Salbreux & Jülicher 2017; Jülicher, Grill & Salbreux 2018). Such cytoskeletal networks can build a thin layer that underlies the plasma membrane, named the cell cortex (Alberts *et al.* 2007; Köster & Mayor 2016; Chugh & Paluch 2018), in which the action of motor proteins leads to active tension at the cell's interface (Chugh *et al.* 2017). A positive constant active tension caused by a homogeneous (Pleines *et al.* 2013) actomyosin distribution in the cortex describes the internal tendency of the cytoskeleton to contract (Needleman & Dogic 2017). Alternatively, proteins which anchor at the plasma membrane can trigger a pearling instability (Tsafrir *et al.* 2001) by bending the membrane and thus inducing a non-zero curvature (Campelo & Hernández-Machado 2007; Jelerčič & Gov 2015). For a viscous active surface Mietke *et al.* (2019a) and Mietke, Jülicher & Sbalzarini (2019b) report a Rayleigh–Plateau instability with mechano-chemical regulation. For a biological

tissue composed of multiple cells Hannezo, Prost & Joanny (2012) provide an energy argument based on an effective surface tension. Berthoumieux *et al.* (2014) considered the Green's function for an elastic cell membrane subjected to active tension, which again leads to the prediction of a Rayleigh–Plateau instability. Bächer & Gekle (2019) confirmed the instability threshold predicted by Berthoumieux *et al.* (2014) and presented the shape of a membrane undergoing Rayleigh–Plateau instability in three-dimensional simulations of active membranes. For soft materials the Rayleigh–Plateau instability is an important mechanism in beaded object formation (Mora *et al.* 2010) and the production of synthetic vesicles (Anna 2016; Pal & Khakhar 2019). Especially in the biological context, Rayleigh–Plateau-like instabilities have been proposed to play an important role in microtubuli-driven cell deformation (Emsellem, Cardoso & Tabeling 1998), as a driving mechanism behind mitochondrial fission (Gonzalez-Rodriguez *et al.* 2015) as well as for pathological shapes of blood vessels during vasoconstriction (Alstrøm *et al.* 1999).

All the above mentioned studies on the Rayleigh–Plateau instability in different contexts have in common that they consider an isotropic tension. However, in reality, cytoskeletal systems often exhibit strong anisotropy (Reymann *et al.* 2012; Murrell *et al.* 2015; Blackwell *et al.* 2016; Zhang *et al.* 2018), e.g. due to the formation of stress fibres (Tojkander, Gateva & Lappalainen 2012). Accordingly, the tension in the cell cortex can be anisotropic (Rauzi *et al.* 2008; Mayer *et al.* 2010; Behrndt *et al.* 2012; Callan-Jones *et al.* 2016), which is important for many biological phenomena such as cell-shape regulation (Callan-Jones *et al.* 2016), cell polarisation (Mayer *et al.* 2010), ingression formation (Reymann *et al.* 2016), the formation of a furrow during cell division (White & Borisy 1983; Salbreux, Prost & Joanny 2009) and the production of blood platelets (Bächer, Bender & Gekle 2020). For a solid rod in the absence of any kind of fluid, Gurski & McFadden (2003) proposed an instability mechanism based on the bulk anisotropy of the underlying crystal lattice for the growing of nanowires. How anisotropic surface tension affects the Rayleigh–Plateau instability of vesicles, cells or even liquid jets, however, remains an open question.

In this work, we analytically extend the framework of the Rayleigh–Plateau instability to include anisotropic interfacial tension for low (Stokes fluid) and high (ideal fluid) Reynolds numbers. In both situations, we derive the dispersion relation depending on the tension anisotropy and report a striking influence on the dominant wavelength and maximum growth rate of the instability. Compared to the classical Rayleigh–Plateau criterion for isotropic surface tension, we observe a decrease in wavelength for dominating azimuthal tension and an increase for dominating axial tension. The analytical predictions agree very well with numerical simulations using a boundary integral method (BIM) and a lattice-Boltzmann/immersed boundary method (LBM/IBM). From these simulations we also compute the nonlinear correction to the linear break-up time. Including interface viscosity in the stability analysis for the Stokes regime also influences the dominant wavelength and growth rate of the instability albeit less pronounced than the tension anisotropy. Finally, we use a long-wavelength expansion to investigate the formation of satellite droplets (Ashgriz & Mashayek 1995; Martínez-Calvo *et al.* 2020) under anisotropic interfacial tension. In Part 2 (Bächer, Graessel & Gekle 2021) we consider the anisotropic Rayleigh–Plateau instability of vesicles or capsules endowed with bending and shear elasticity.

We start by introducing our theoretical model for an anisotropic interface, the coupling to the surrounding fluid as well as the numerical methods used in the simulations in § 2. We then present the dispersion relation for the Rayleigh–Plateau instability of an anisotropic interface obtained by analytical linear stability analysis in § 3 first for a Stokes fluid in § 3.1 and then for an ideal fluid in § 3.2. In § 4.1 we discuss the effect of anisotropic

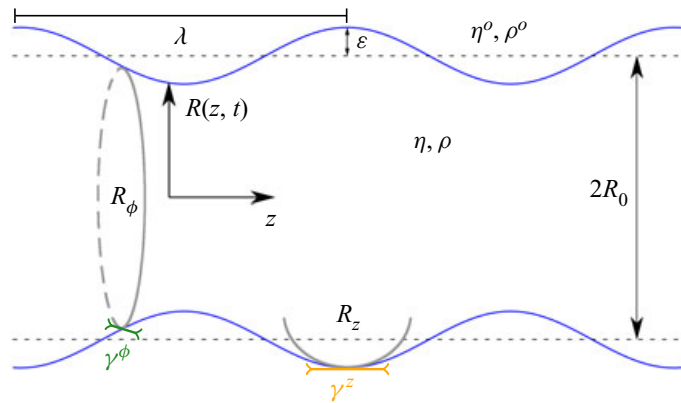


FIGURE 1. Illustration of the set-up. We consider a complex interface which can be either a liquid jet of Newtonian fluid in the limit of vanishing viscosity η or the membrane of a vesicle or cell immersed in a fluid in the limit of the Stokes equation, i.e. density $\rho = 0$. The fluid jet is immersed in an ambient fluid with η^0, ρ^0 . The cylindrical interface of initial radius R_0 (dashed line) is subjected to a periodic perturbation with amplitude ϵ (solid blue line). The interface is parametrised by the position along the cylinder axis z and the radius $R(z, t)$. We consider the interfacial tension in the axial direction γ^z (orange) different from that in the azimuthal direction γ^ϕ (green), both of which contribute to the membrane force acting onto the fluid with different curvature components (grey circles).

interfacial tension on the dominant wavelength of the instability by comparing analytical and simulation results and show a transition between Stokes fluid and ideal fluid in § 4.2. In § 4.3 we discuss the dominant growth rate in comparison to numerical results. Nonlinear corrections of the linear break-up time are investigated in § 4.4. In § 5 we discuss the combination of anisotropic tension and interface viscosity and finally present the formation of satellite droplets under the influence of tension anisotropy for an ideal fluid jet without ambient fluid in § 6. We conclude in § 7.

2. Description of an anisotropic interface

2.1. Problem illustration

We consider a general complex interface, as sketched in figure 1, which is surrounded by a fluid on both sides. This can either represent the interface of a liquid jet in the co-moving frame or the membrane of a vesicle or biological cell. As usual (Eggers & Villermaux 2008; Boedec *et al.* 2014), we assume that the interface is infinitely long. In the analytical stability analysis we consider an axisymmetric interface, which is parametrised by the axial position z and the local radius $R(z, t)$. Initially, the interface is cylindrical with radius $R(z, 0) = R_0$. At arbitrary time t the interface is subjected to a perturbation $\delta R(z, t)$, such that the local radius is given by $R(z, t) = R_0 + \delta R(z, t)$.

In order to perform a linear stability analysis of the complex interface in the presence of anisotropic interfacial tension, we apply a periodic perturbation to its shape (Drazin & Reid 2004). The perturbation of the interface is illustrated in figure 1: it modulates the radius in z -direction along the cylinder axis with amplitude $\epsilon(t) = \epsilon_0 e^{\omega t}$, a wavelength λ and a corresponding wavenumber $k = 2\pi/\lambda$ of the wave vector pointing along the cylinder axis. The perturbation with initial amplitude ϵ_0 grows in time with growth rate ω . Accordingly, the interface of the jet can be described by its radius as

$$R(z, t) = R_0 + \epsilon_0 \exp(\omega t + ikz). \quad (2.1)$$

Throughout this work, we consider an anisotropic interfacial tension, i.e. the value of the axial tension differs from the value of the azimuthal tension. This anisotropic tension accounts for two fundamentally different situations. First, in a liquid jet anisotropy can arise, e.g. from covering the interface with passive anisotropic surfactant molecules, thus extending the classical concept of liquid–liquid surface tension to an anisotropic situation. Second, in biological cells or tissue, an active biological machinery, cytoskeletal filaments with motor proteins underlining the plasma membrane, can produce anisotropic tensions at the interface as described in more detail in the Introduction. Due to their usually contractile nature, these active tensions enter the physical equations in the same way as the classical surface tension, despite their fundamentally different origin. In the following, we therefore use the same symbol and refer to both scenarios with the general term interfacial tension.

2.2. Interface coupled to a surrounding fluid

Interfacial tension leads to internal forces being transmitted from the interface to the fluid (Green & Zerna 1954; Barthès-Biesel 2016; Salbreux & Jülicher 2017). In contrast to the classical isotropic Rayleigh–Plateau scenario, we assign anisotropic tension to the interface, i.e. we distinguish between the azimuthal γ^ϕ and the axial interfacial tension γ^z . As sketched in figure 1 the periodic perturbation along the axis changes the curvature of the interface both in the azimuthal and in the axial direction. In azimuthal direction the curvature $1/R_\phi$ is the inverse of the local radius of the interface $R_\phi = R(z, t)$, where we follow the convention that the curvature of a cylinder is positive. Accordingly, the curvature along the axis is given by the negative second derivative of the radius, $1/R_z = -R''$ such that the curvature is negative at a neck and positive at a bulge (compare figure 1). The derivative R'' follows directly from (2.1).

The anisotropic tension does not depend on the position along the interface, therefore its derivative vanishes and for a liquid–liquid interface no internal forces tangential to the interface arise (Green & Zerna 1954; Salbreux & Jülicher 2017). The internal force normal to the interface is given by the interfacial tension components weighted by the corresponding principal curvature. Balance of forces requires that this normal force is in equilibrium with the difference in tractions exerted by the fluids on either side of the interface. Thus, the normal traction jump across the interface Δf^n reads

$$\frac{\gamma^\phi}{R_\phi} + \frac{\gamma^z}{R_z} = \Delta f^n. \quad (2.2)$$

The traction jump is given by the projection of the three-dimensional viscous stress tensor of the outer and inner fluid onto the interface normal vector (Chandrasekharaiah & Debnath 1994). For an incompressible interface or for negligible viscous effects, i.e. for an ideal fluid, the traction jump is determined by the pressure p of the fluid. With the normal vector pointing outwards from the interface and considering the outer and inner fluid as incompressible, the traction jump in normal direction is thus given by

$$\Delta f^n = -p^{out} + p^{in} = p(r = R), \quad (2.3)$$

with pressures p^{out} and p^{in} of the outer and inner fluid, respectively, and $p(r = R)$ denoting the pressure difference at the interface. Together (2.2) and (2.3) lead to

$$\frac{\gamma^\phi}{R_\phi} + \frac{\gamma^z}{R_z} = p(r = R), \quad (2.4)$$

for an incompressible interface or an ideal fluid interface. The relation in (2.4) reduces to the classical Young–Laplace equation $\gamma/R = p$ in the limit of isotropic surface tension $\gamma = \gamma^\phi = \gamma^z$ and vanishing curvature along z , i.e. $R_z \rightarrow \infty$. The anisotropic interfacial tension thus leads to a pressure disturbance of the inner fluid, where the two contributions of the interfacial tension are weighted with their respective radii of curvature.

2.3. Fluid dynamics

The motion of the fluid inside and outside the jet is in general described by the Navier–Stokes equation

$$\frac{\partial \mathbf{v}}{\partial t} + (\mathbf{v} \cdot \nabla) \mathbf{v} = -\frac{1}{\rho} \nabla p + \nu \Delta \mathbf{v}, \quad (2.5)$$

with the velocity field \mathbf{v} , fluid density ρ , kinematic viscosity $\nu = \eta/\rho$ and shear viscosity η . Density and viscosity of the outer fluid are denoted by ρ^o and η^o , respectively. The fact that the liquid is incompressible, which is true for both the liquid of a jet and the liquid encapsulated in a vesicle, leads furthermore to the continuity equation for the incompressible liquid

$$\nabla \cdot \mathbf{v} = 0. \quad (2.6)$$

The Navier–Stokes and continuity equations together govern the motion of the fluid.

Besides the well-known Reynolds number $Re = \rho R_0 V_0 / \eta$ with a typical velocity V_0 and the unperturbed interface radius R_0 as the typical length, we use the Ohnesorge number (Eggers & Villermaux 2008), which relates characteristic scales of the interface and the surrounding fluid

$$Oh = \frac{\eta}{\sqrt{\rho R_0 \gamma}}. \quad (2.7)$$

In our anisotropic scenario with $\gamma^z \neq \gamma^\phi$ we define two distinct Ohnesorge numbers Oh_z and Oh_ϕ for the respective interfacial tensions.

In the limit of small velocities or large viscosity, i.e. the Stokes regime, the Reynolds number approaches zero while the Ohnesorge number becomes large. In this regime, the Navier–Stokes equation can be replaced by the linear Stokes equation

$$0 = -\nabla p + \eta \Delta \mathbf{v}. \quad (2.8)$$

In the limit of large velocities or small viscosity, i.e. for an ideal fluid, the Reynolds number is larger than one and the Ohnesorge number becomes small. Here, the Euler equation applies

$$\frac{\partial \mathbf{v}}{\partial t} + (\mathbf{v} \cdot \nabla) \mathbf{v} = -\frac{1}{\rho} \nabla p. \quad (2.9)$$

2.4. Numerical simulations

We aim for a comparison of our main analytical results, the dominant wavelength of the instability and its growth rate presented in §§ 4.1 and 4.3, respectively, with numerical simulations solving the coupled fluid and interface dynamics. The simulations further provide us a glimpse on the nonlinear aspects of the instability dynamics. For a Stokes fluid and an ideal fluid with an outer fluid with the same properties, we perform three-dimensional boundary integral method and lattice-Boltzmann/immersed boundary method simulations, respectively.

2.4.1. Three-dimensional numerical investigation of the instability

We consider a fluid column, the liquid jet, immersed in an ambient fluid. We use fully three-dimensional simulations, thus testing also for non-axisymmetric instabilities triggered by anisotropic interfacial tension (which we did not observe).

The interface encapsulates a Newtonian fluid and is surrounded by another Newtonian fluid of the same density $\rho^0 = \rho$ or viscosity $\eta^0 = \eta$. For the fluid, periodic boundary conditions are chosen in each of the three spatial directions together with a kinematic boundary condition at the interface. Fluid dynamics is either solved by the BIM or the LBM/IBM, as detailed below.

Following the set-up sketched in [figure 1](#), we consider an initially cylindrical interface which is modelled as a thin shell and which we discretise by nodes connected to triangles. Anisotropic tension of the interface is realised using the recently developed and validated computational method for active membranes in flows (Bächer & Gekle 2019). This approach can treat both the anisotropic surface tension of a liquid jet in the co-moving frame and the anisotropic active tension of a biological cell cortex on the same footing. To investigate the instability dynamics, we initially apply a small periodic perturbation to the cylindrical interface, as shown in [figure 1](#). From this initial configuration the temporal evolution of the interface and the suspending fluid is solved including a dynamical two way coupling of interface and fluid. The method to determine the dominant wavelength and growth rate is described in [appendix A](#).

2.4.2. Boundary integral method

As the simulation method at zero Reynolds number we use the BIM to solve the fluid dynamics (Pozrikidis 2001; Zhao *et al.* 2010). The BIM solves the Stokes equation in the presence of discretised boundaries based on hydrodynamic Green's functions. It directly solves for the fluid velocity at the nodes of the discretised interface for given interface shape and interfacial force density. As a consequence of using the Stokes equation, in BIM simulations inertial effects are excluded. Neglecting inertial effects corresponds to $Re = 0$ and an Ohnesorge number $Oh \rightarrow \infty$. Membrane forces due to interfacial tension are calculated as detailed in Bächer & Gekle (2019). As the interfacial tension in the simulation we use $\gamma^\phi \approx 10 \text{ pN } \mu\text{m}^{-1}$, a typical tension expected for blood cells (Dmitrieff *et al.* 2017). For details on the implementation of the BIM we refer to Guckenberger & Gekle (2018).

As the box size, we consider the length of the cylindrical tube, which is typically 80 times the tube radius, along the axis and ten times the tube radius in lateral directions. A typical discretisation of the interface consists of approximately 17 000 nodes and 32 500 triangles. We do not use periodic boundary conditions for the membrane due to technical issues of the implementation used for BIM simulations. We rather place the outer rings of nodes exactly at the beginning and end of the box, respectively, and fix the nodes by elastic springs. Due to an insufficient number of neighbouring nodes, at the boundary nodes the force from the interfacial tension is not calculated. We note that using this set-up, the fluid encapsulated by the membrane remains inside. For the initial small deformation of the interface we choose the amplitude $\epsilon_0 = 0.02$. The fluid viscosity is chosen as $\eta \approx 1.2 \times 10^{-3} \text{ Pa s}$. We simulate for approximately 100 time steps with adaptive step size and a total simulation time of approximately 20 ms.

2.4.3. Lattice-Boltzmann/immersed boundary method

As a method to solve fluid dynamics at large/finite Reynolds number, we use the LBM (Aidun & Clausen 2010; Krüger *et al.* 2016) together with the IBM (Peskin 2002;

Mittal & Iaccarino 2005; Bächer, Schrack & Gekle 2017; Mountrakis, Lorenz & Hoekstra 2017; Bächer *et al.* 2018). Our LBM/IBM is implemented in the software package ESPResSo (Limbach *et al.* 2006; Roehm & Arnold 2012; Arnold *et al.* 2013; Weik *et al.* 2019) and has been extensively validated (Gekle 2016; Guckenberger *et al.* 2016; Bächer *et al.* 2018; Bächer & Gekle 2019).

The LBM solves the fluid dynamics on the basis of the mesoscopic Boltzmann equation and accounts for the fluid dynamics according to the full Navier–Stokes equation. The fluid thus has a finite density, a finite viscosity and, therefore, a finite Ohnesorge number. The fluid is discretised by an Eulerian grid and populations representing the distribution functions for the different velocities are assigned to each fluid node. We here use the D3Q19 velocity set and a typical fluid mesh with dimensions of approximately $650 \times 40 \times 40$ with some simulation lattices extending up to $800 \times 40 \times 40$. A typical simulation runs for 500 000 steps. In the limit of an ideal fluid we choose Ohnesorge numbers in the range of 10^{-3} – 10^{-4} . Initially, the fluid has zero velocity.

The discretised interface is coupled to the background fluid using the IBM. A typical interface contains 18 240 nodes and 36 480 triangles, has a radius of 6 LBM grid cells and is periodic along the axial direction with an initial perturbation amplitude $\epsilon_0 = 0.02$ in simulations to determine the dominant wavelength. An additional refined simulation set-up is used for determination of the dominant growth rate, where we simulate one period of the dominant mode with initial perturbation $\epsilon_0 = 0.002$ and increased resolution with a radius of 13 LBM grid cells. Here, a typical fluid lattice consists of $180 \times 70 \times 70$ nodes and a membrane mesh of 15 416 nodes and 30 832 triangles. We again note that axisymmetry is not imposed and that the simulations are fully three-dimensional. The average distance between two interface nodes is approximately the length of one LBM grid cell. An interface node moves with the local fluid velocity which is interpolated at the node position from the surrounding fluid nodes by an eight-point stencil. The force stemming from the interfacial tension and acting from the membrane onto the fluid at the site of each interface node is transmitted to the fluid by the same eight-point stencil interpolation scheme. Thus, the IBM provides a dynamic two way coupling of membrane and fluid.

3. Dispersion relation for anisotropic interfacial tension

3.1. Anisotropic Rayleigh–Plateau instability for a Stokes fluid

Biological cells as well as their synthetic counterpart (vesicles) are typically a few tens micrometres in size. Therefore, we consider the limit of small Reynolds numbers, i.e. $Re \ll 1$, where the Navier–Stokes equation (2.5), reduces to the linear Stokes equation (2.8) which together with the continuity equation (2.6) describes the fluid behaviour. In the following, we consider identical fluid viscosity inside and outside the vesicle, i.e. $\eta^o = \eta$. Our aim is to obtain the dispersion relation in the case of anisotropic interfacial tension, which gives the growth rate depending on the wavenumber of the perturbation (2.1). As detailed in appendix B.1 we perform a linear stability analysis and obtain the dispersion relation for a Stokes fluid

$$\omega(k) = \frac{\gamma^\phi}{R_0 \eta} \left(1 - \frac{\gamma^z}{\gamma^\phi} (R_0 k)^2 \right) \left[I_1(kR_0) K_1(kR_0) + \frac{kR_0}{2} (I_1(kR_0) K_0(kR_0) - I_0(kR_0) K_1(kR_0)) \right], \quad (3.1)$$

with $I_\nu(x)$, $K_\nu(x)$ being the modified Bessel functions of the first and second kind, respectively, and of order ν .

Positive values of ω correspond to growing perturbations (2.1), whereas perturbation modes with negative growth rate are dampened. Because of the positive prefactor $\omega_0^S = \gamma^\phi / (R_0 \eta)$, which is the inverse of the viscocapillary time based on the azimuthal tension γ^ϕ , and the positive modified Bessel functions for positive kR_0 , the tension anisotropy determines the range of growing, i.e. unstable, modes. We obtain from (3.1) the range of growing modes for values of kR_0 between $-\sqrt{\gamma^\phi / \gamma^z}$ and $\sqrt{\gamma^\phi / \gamma^z}$. This range depends on the square root of the anisotropy of the interfacial tension. We recover for isotropic tension $\gamma^z = \gamma^\phi = \gamma$ the range of growing wavelengths between $-\sqrt{\gamma^\phi / \gamma^z} = -1$ and $\sqrt{\gamma^\phi / \gamma^z} = 1$ as found by Plateau (1873). So in the case of the classical Rayleigh–Plateau instability, the growing wavelengths do not depend on the interfacial tension γ but only on the undisturbed radius R_0 of the jet (Drazin & Reid 2004). Here, in addition the anisotropy of interfacial tension enters as a factor.

We show in figure 2(a) the dispersion relation of the classical Rayleigh–Plateau instability, i.e. for isotropic interfacial tension. The growth rate ω is plotted only against positive kR_0 due to symmetry. We further distinguish the individual contributions from γ^ϕ , the first term in (3.1), and from γ^z , the second term in (3.1), and plot them in orange and green, respectively, together with the total dispersion relation in blue. It is the interplay of the two contributions of the interfacial tension γ^z and γ^ϕ that determines the dispersion relation. The azimuthal tension γ^ϕ , i.e. the first term in (3.1), is positive and thus the system would be unstable against any perturbation with arbitrary wavenumber. However, this is not the case, because this term is balanced by the damping contribution from γ^z . Both contributions together determine a finite maximum of the dispersion relation, which corresponds to the dominant mode that grows fastest.

We now consider an anisotropic interface where the contributions γ^ϕ and γ^z are no longer identical. Their changing ratio leads to a different weighting of the contributions to the dispersion relation (3.1). If the destabilising contribution from γ^ϕ rises compared to γ^z as shown in figure 2(b), the range of growing wavelengths increases. On the other hand, if γ^ϕ decreases relative to γ^z , the range becomes smaller (see figure 2c). Because the destabilising γ^ϕ contribution reaches a maximum at $kR_0 = 1.59$ and tends to zero for $kR_0 \rightarrow \infty$, independent of the anisotropy ratio, also for vanishing $\gamma^z \rightarrow 0$ a well-defined mode at finite kR_0 has the largest growth rate. This is shown by figure 2(d) in the case of $\gamma^z = 0$ with an extended kR_0 -range on the horizontal axis. In the limit $\gamma^\phi = 0$ all modes are stable. Furthermore, changes in the anisotropy ratio shift the position of the maximum of the dispersion relation. If $\gamma^\phi > \gamma^z$ (figure 2b), the position of the maximum of ω shifts to larger values of kR_0 , if $\gamma^\phi < \gamma^z$ the maximum is found at smaller kR_0 as shown in figure 2(c). This means for dominating axial tension γ^z the instability wavelength increases.

3.2. Anisotropic Rayleigh–Plateau instability for an ideal fluid

Performing again a linear stability analysis using the same solution procedure as before, we calculate the dispersion relation for an ideal fluid jet with same density inside and outside the jet as detailed in appendix B.2. We obtain the dispersion relation

$$\omega^2 = \frac{\gamma^\phi}{\rho R_0^3} (kR_0)^2 \left(1 - \frac{\gamma^z}{\gamma^\phi} (kR_0)^2 \right) I_1(kR_0) K_1(kR_0). \quad (3.2)$$

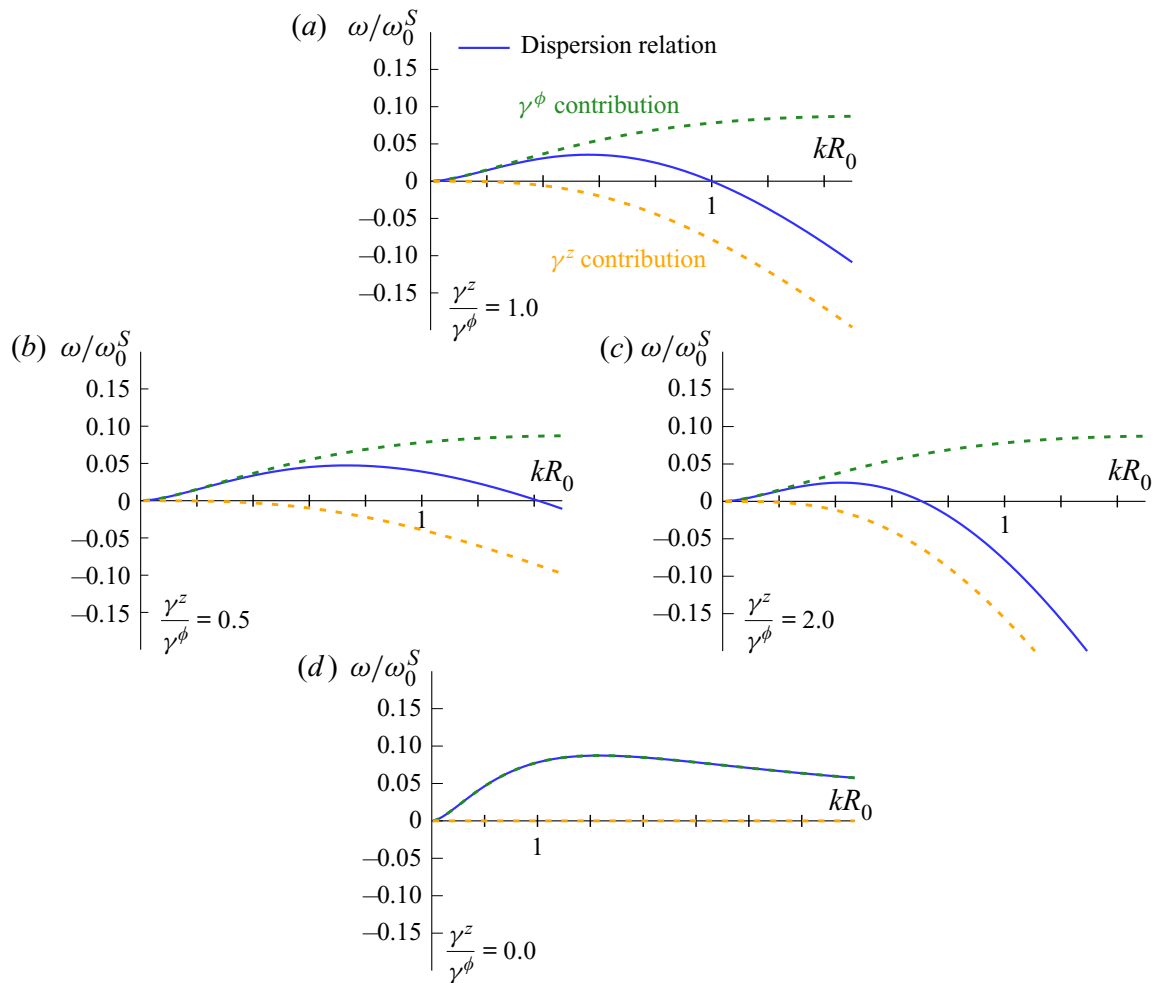


FIGURE 2. Dispersion relation in the Stokes regime for $\eta = \eta^o$. Curves are shown for (a) isotropic interfacial tension $\gamma^z/\gamma^\phi = 1.0$ and for anisotropic interfacial tension with (b) $\gamma^z/\gamma^\phi = 0.5$ and (c) $\gamma^z/\gamma^\phi = 2.0$. We distinguish the contributions from γ^ϕ (green) and γ^z (orange). An anisotropic tension strongly alters the range of growing modes and shifts the maximum towards larger kR_0 in (b) or smaller kR_0 in (c). (d) Dispersion relation for vanishing axial interfacial tension, i.e. $\gamma^z = 0$. The γ^ϕ contribution (green) has its maximum at $kR_0 = 1.59$ in each of the panels, because γ^ϕ is kept constant. Thus, although all modes are unstable in (d), in principle, there still exists a well-defined finite dominant wavelength for a Stokes fluid due to fluid stresses.

Compared to the dispersion relation for a Stokes fluid in (3.1), we here obtain an equation for the squared growth rate ω^2 . According to the ansatz for the perturbed interface in (2.1), perturbations with real and positive ω will grow. Imaginary ω describe oscillatory perturbations of the surface which do not grow in time. Imaginary ω correspond to negative values of ω^2 . Each positive ω^2 has a positive and negative solution ω . The positive solution will grow while the negative is damped. Thus, we are interested in non-negative values of ω^2 which are obtained from (3.2). This leads to the same expression for the range of growing wavelengths as for the Stokes fluid in § 3.1 because the relevant factor in the dispersion relation is identical, i.e. the anisotropy ratio γ^z/γ^ϕ enters the equation in the same way. However, the prefactor of the growth rate changes $\omega_0^2 = \gamma^\phi/(\rho R_0^3)$, it now depends on the density rather than on the viscosity and is the squared inverse of the capillary time based on the azimuthal tension γ^ϕ . Furthermore, the geometrical factor containing the Bessel functions is remarkably different.

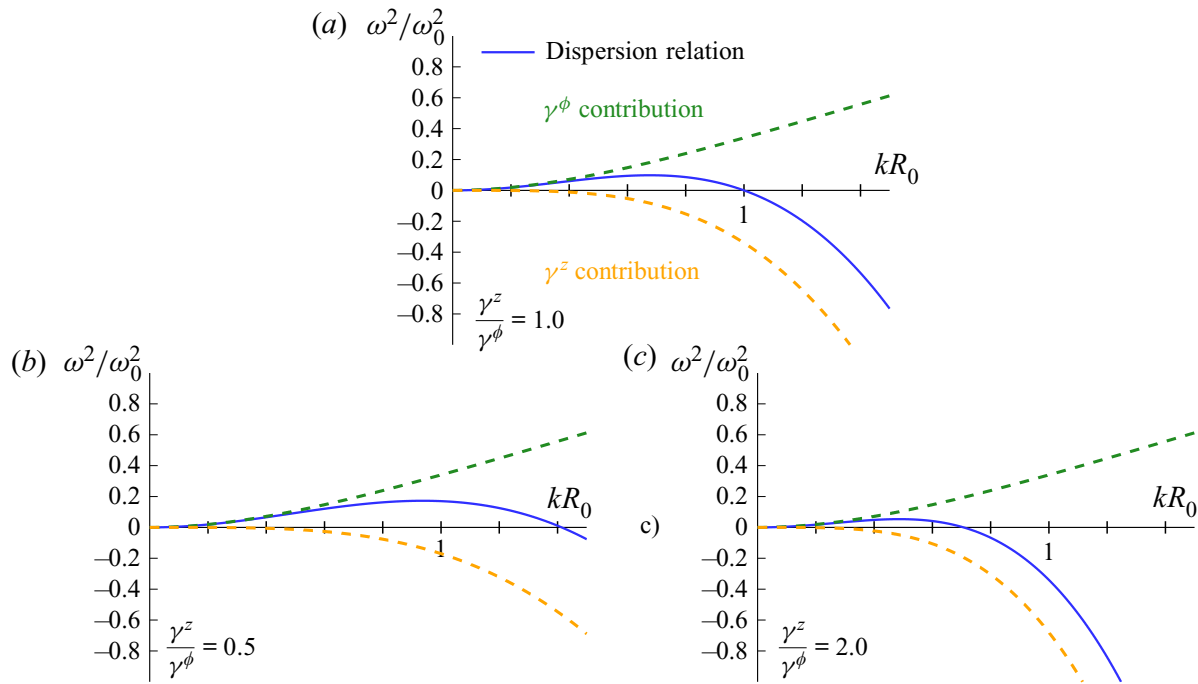


FIGURE 3. Dispersion relation for an ideal fluid with $\rho = \rho^o$. Curves are shown for (a) isotropic interfacial tension $\gamma^z/\gamma^\phi = 1.0$ and for anisotropic interfacial tension with (b) $\gamma^z/\gamma^\phi = 0.5$ and (c) $\gamma^z/\gamma^\phi = 2.0$. We distinguish the contributions from γ^ϕ (green) and γ^z (orange). While γ^z is purely damping, γ^ϕ is destabilising. An anisotropic tension strongly alters the range of growing modes and shifts the maximum towards larger kR_0 in (b) or smaller kR_0 in (c).

The dispersion relation (3.2) for the ideal fluid is shown in figure 3(a–c) for same values of the anisotropy ratio as in figure 2(a–c). We again observe a strong variation of the maximum position and range of unstable modes with changing anisotropy ratio. A remarkable difference to the Stokes fluid is the shape of the γ^ϕ contribution. Here for an ideal fluid the destabilising γ^ϕ contribution no longer reaches a maximum at finite kR_0 but instead increases indefinitely. Thus, in the limit $\gamma^z = 0$ all modes are unstable with steadily increasing growth rate. Compared to the Stokes fluid, the total dispersion relation is furthermore more asymmetric between $kR_0 = 0$ and $\sqrt{\gamma^\phi/\gamma^z}$ and the maximum shifts towards larger wavenumbers (compare e.g. figure 2b to figure 3b).

In appendix E we further generalise our results to the dispersion relation including a general density and viscosity contrast as derived by Tomotika (1935).

4. Quantitative analysis of the effects due to tension anisotropy

4.1. Dominant wavelength

Having determined the range of (un)stable wavenumbers in the previous section, we now explicitly investigate how tension anisotropy affects the value of the dominant, i.e. fastest growing, wavelength λ_m . This quantity is of practical interest as it determines the size of the fragmented vesicles/droplets and provides an intrinsic length scale of the instability. For arbitrary ratios γ^z/γ^ϕ , we use *Mathematica* to determine numerically the maximum of the dispersion relation (3.1) and (3.2). We further perform fully three-dimensional simulations of a membrane endowed with interfacial tension using BIM and LBM/IBM, as detailed in § 2.4. While BIM intrinsically solves the fluid dynamics in the Stokes limit, LBM/IBM simulations are run for $Oh \approx 0.00025$, i.e. very close to the ideal fluid limit.

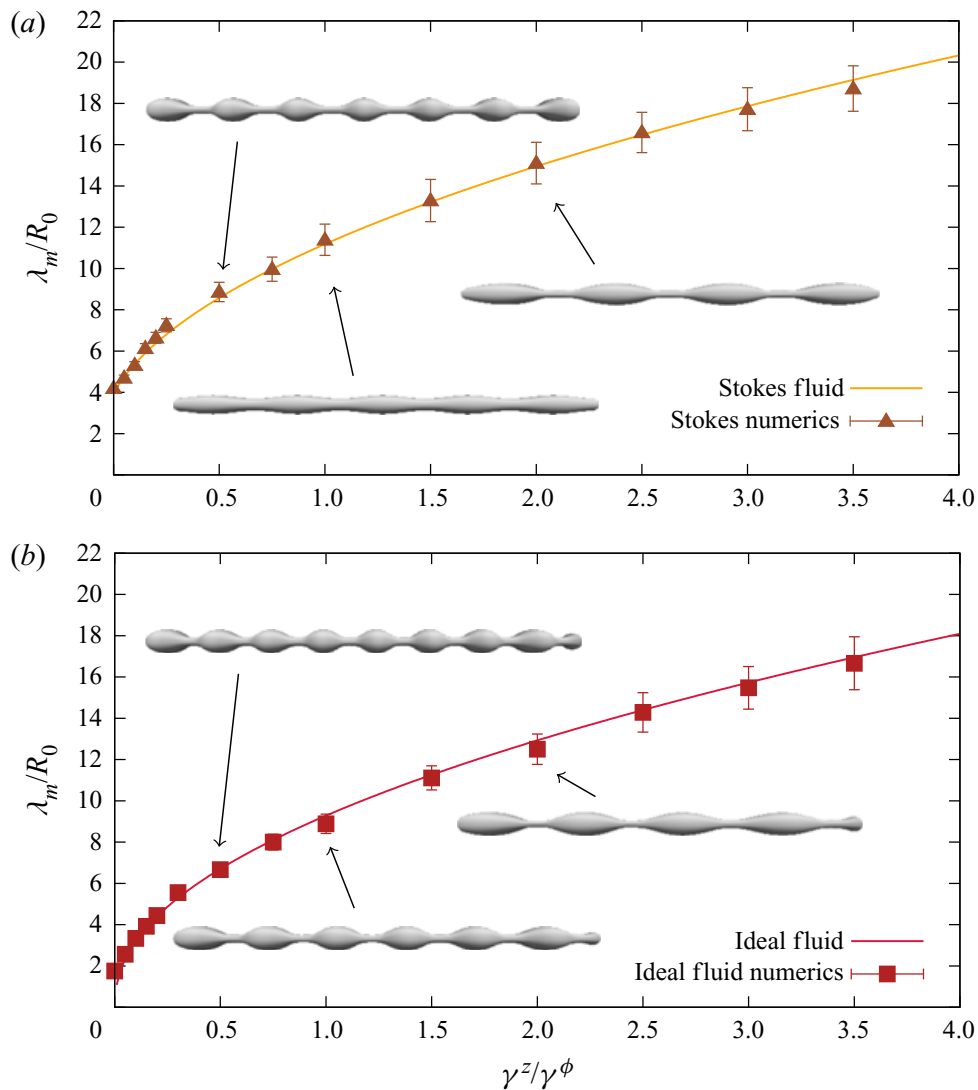


FIGURE 4. Dominant wavelength as function of the anisotropy in interfacial tension. (a) Simulation results from BIM for the Stokes fluid are in very good agreement with the analytical results obtained from the dispersion relation (3.1). (b) Results for the ideal fluid from LBM/IBM agree very well with dominant wavelength obtained from the analytical dispersion relation (3.2). While the whole curve is at larger values in the Stokes limit, in both cases the dominant wavelength increases steadily with increasing γ^z/γ^ϕ . Simulation snapshots of the interface are shown for different ratios γ^z/γ^ϕ over a length of about $55R_0$ as insets.

The result of the linear stability analysis is compared to the simulation results in figure 4. The solid lines show how the position of the maximum of the dispersion relations (3.1) (orange line in figure 4a) and (3.2) (red line in figure 4b), i.e. the dominant wavelength λ_m , changes with the ratio γ^z/γ^ϕ . The simulation results for the Stokes fluid using BIM are drawn as triangles, those for the ideal fluid using LBM/IBM as squares. Both are in very good agreement with the respective theoretical predictions. For the Stokes fluid the obtained value $k_m R_0 \approx 0.562$ (i.e. $\lambda_m/R_0 \approx 11.18$) for isotropic tension $\gamma^z/\gamma^\phi = 1$ is in good agreement with Tomotika (1935) and Stone & Brenner (1996). For the ideal fluid the dominant wavelength is smaller compared to the Stokes limit, which is true for all values of kR_0 . For both Stokes fluid and ideal fluid increasing the ratio γ^z/γ^ϕ leads to an increase in the wavelength compared to its value at isotropic tension (illustrated by the insets from simulations on the right-hand sides of figures 4a and 4b). For decreasing ratio the opposite happens, the wavelength decreases (see inset from simulations at the

top of figures 4*a* and 4*b*). Over the entire range of interfacial tension ratios we observe a nonlinear dependence of the wavelength on the anisotropy ratio. In the Stokes regime at an anisotropy ratio of zero a finite wavelength dominates. This is due to the fact that the γ^ϕ -contribution to the dispersion relation, as shown in figure 2(*d*), does not diverge for large wavenumbers but rather has a maximum at $k_m R_0 = 1.59$ which corresponds to a wavelength of $\lambda_m = 3.96 R_0$. This value matches the y -axis intercept of the dominant wavelength in figure 4(*b*). For the ideal fluid, however, for vanishing anisotropy ratio the wavelength goes to zero. In the limit of infinite ratio the wavelengths tend to infinity for both Stokes and ideal fluid.

In order to explain the effect of anisotropic interfacial tension, we first recall the classical Rayleigh–Plateau mechanism where two opposing effects influence the break-up. Since the radius in the region of a constriction is smaller than in a peak region, a pressure gradient develops pushing fluid out of the constriction and thus amplifying the disturbance. At the same time, however, due to the perturbation of the surface, the radius of curvature along the z -direction is negative in the region of the constriction and positive in the region of a peak. As can be seen from the Young–Laplace equation (2.4) this introduces another pressure gradient dragging the liquid back from the peak regions thus counteracting the pressure difference due to variations of the radius. The instability is a result of the interplay of both effects. An anisotropic interfacial tension weights these effects by either the azimuthal tension γ^ϕ or axial tension γ^z . Thus, a change in the ratio of the interfacial tension leads to a change in the weighting, shifting the region of growing wavelength and also altering the most unstable wavelength. This argument is illustrated by the three cases of the dispersion relation with its different contributions shown in figures 2 and 3.

The limit $\lambda_m \rightarrow \infty$ for $\gamma^z \rightarrow \infty$ can be understood on the basis of the Young–Laplace equation for anisotropic interfacial tension in (2.4), as well. For infinite γ^z a finite curvature along z would result in an infinite pressure difference. Thus, the interfacial tension must be balanced by a vanishing curvature, i.e. by an infinite curvature radius, which is equivalent to an infinite wavelength.

Finally, we discuss the limit $\gamma^z \rightarrow 0$. We start with considering the ideal fluid. Due to finite γ^ϕ every circular segment of the interface along the cylinder axis tends to contract. The incompressibility of the liquid inside prevents this homogeneous contraction. This means that a volume conserving neck–tail perturbation between two neighbouring thin circular segments, thus with very small wavelength and very large curvature in the z -direction, can in principle be established. Since $\gamma^z \rightarrow 0$ there is no counteracting contribution which balances this tendency. The monotonic increase of the growth rate for the γ^ϕ -contribution with increasing k , as shown by the course of the dispersion relation in figure 3, suggests that such a perturbation grows fastest. This, in total, results in $\lambda_m \rightarrow 0$ for the ideal fluid. In the Stokes limit, however, the γ^ϕ -contribution is finite for large kR_0 , possibly due to viscous stresses from the fluid which have a damping effect on the perturbation.

4.2. Transition between the two regimes

In the following, we will show that the border between the Stokes regime and the ideal fluid limit is not necessarily clear cut. In fact, by varying nothing more than the anisotropy ratio, the system can undergo a transition from one regime to the other. To demonstrate this transition, we present simulations using the LBM/IBM for typical parameters of biological cells/vesicles. We choose an interfacial tension of $\gamma^\phi = 10^{-4} \text{ N m}^{-1}$, which is the cortical tension reported for neutrophils (Tinevez *et al.* 2009) and in the middle of the range of typical tensions reported by Winklbauer (2015). As typical diameter of the tubular

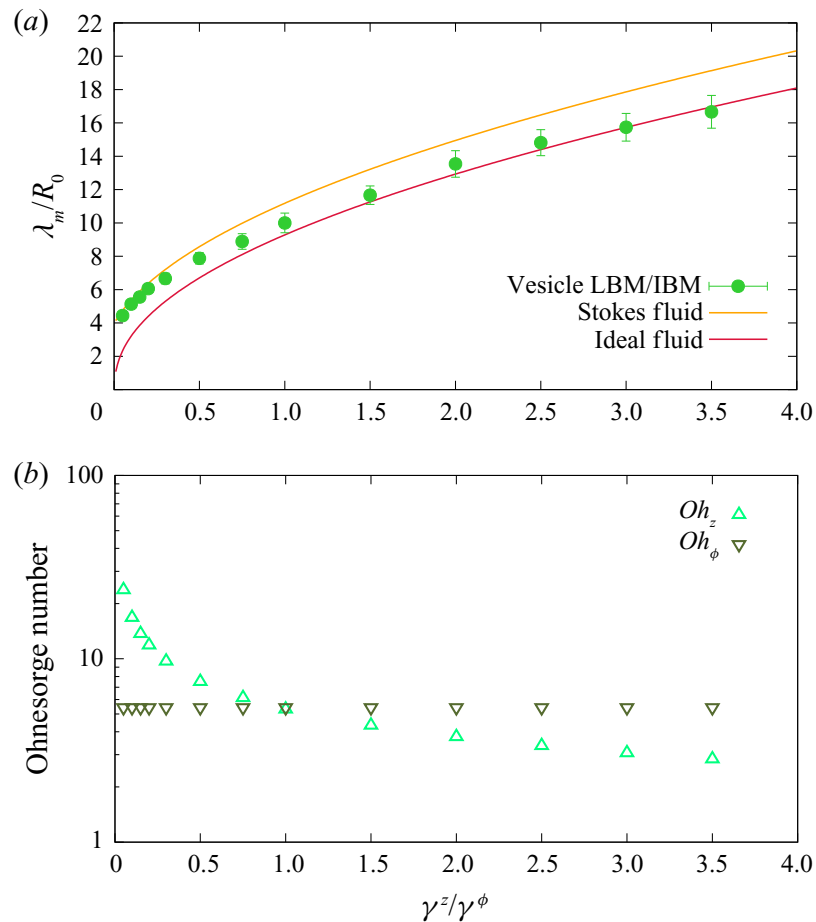


FIGURE 5. Transition between both regimes. (a) LBM/IBM simulations with typical vesicle and cell parameters (green dots) show dominant wavelengths between the two curves obtained in the limit of a Stokes fluid (orange) and an ideal fluid (red). (b) The transition between the two regimes in the wavelength is accompanied by a strong variation in the Ohnesorge number with respect to the tension along the axis z , i.e. Oh_z .

vesicle we choose $2R_0 = 1 \mu\text{m}$ and for the surrounding fluid density $\rho = 1000 \text{ kg m}^{-3}$ and viscosity $\eta = 1.2 \times 10^{-3} \text{ Pa s}$.

The dominant wavelength is shown in figure 5(a) as a function of the anisotropy ratio with green dots. For a clear comparison we also show the Stokes fluid dispersion relation in orange and the relation for the ideal fluid in red. The numerical simulations exhibit a transition between the two curves. For a small anisotropy ratio we obtain a finite wavelength, which nearly matches the result in the Stokes regime. In the case of isotropic tension we obtain a dominant wavelength of $k_m R_0 \approx 0.628$ (i.e. $\lambda_m/R_0 \approx 10.005$), a value in between the one for the ideal fluid and the Stokes regime. For larger values of the anisotropy ratio we end up close to the curve for an ideal fluid.

We explain the transition between both regimes by the varying Ohnesorge number, which is shown in figure 5(b). By varying the anisotropy ratio, either the Ohnesorge number Oh_ϕ or Oh_z varies, while the other can be kept constant. Here, we keep $Oh_\phi \approx 5.5$ shown by the dark-green downwards-pointing triangles in figure 5(b). Consequently, Oh_z changes from 30 to approximately 2.5, as shown by the light-green upwards-pointing triangles. The transition in the Ohnesorge number Oh_z is matched by the transition in the wavelength. At small anisotropy ratios with large Ohnesorge number, the wavelength is close to the analytical prediction for the Stokes equation. This is in good agreement with the Stokes equation having $Oh \rightarrow \infty$. Towards larger anisotropy ratios the Ohnesorge

number becomes smaller and the wavelength approaches the predictions for an ideal fluid. We thus conclude that finite inertia effects trigger the transition, even though the Ohnesorge number is still larger than one. Our results clearly show that finite inertia effects can alter the Rayleigh–Plateau instability of tubular vesicles, even though their micrometric dimensions may at first sight suggest the opposite.

4.3. Dominant growth rate

We now investigate the growth rate of the most unstable mode ω_m , i.e. the value of the maximum of the dispersion relation, in a quantitative manner. Using *Mathematica* we determine the maximum growth rate for varying tension anisotropy from the analytical dispersion relation. In addition, we perform simulations as described in § 2.4, where we extract the growth rate as described in appendix A.

The results in the limit of a Stokes fluid are shown in figure 6(a) and the limit of an ideal fluid is shown in figure 6(b). With increasing tension anisotropy the dominant growth rate decreases strongly. This can again be explained by the stabilising nature of the axial tension γ^z which slows down the instability. For tension anisotropy approaching infinity the growth rate approaches zero. At tension anisotropy equal zero we observe a finite growth rate of $\omega_m \approx 0.087$ for the Stokes fluid in (a), which results from viscous stresses in the Stokes fluid. In stark contrast, for an ideal fluid in (b) the maximum growth rate increases more strongly and even diverges for tension anisotropy to zero due to the destabilising nature of the azimuthal tension γ^ϕ . Simulation results for the Stokes fluid with BIM (triangles) and for the ideal fluid with LBM/IBM (squares) are in very good agreement with the corresponding analytical results. From the inverse of the growth rate the linear break-up time can be estimated, which is the time it takes until a droplet or vesicle pinches off. From figure 6 we can conclude that with decreasing tension anisotropy the break-up of the interface is strongly accelerated.

4.4. Nonlinear correction to the linear break-up time

After discussing dispersion relation, growth rate and dominant wavelength obtained by linear stability analysis, we now proceed to investigate the nonlinear behaviour of the Rayleigh–Plateau instability. This is covered by the simulations presented above using BIM for a Stokes fluid and LBM/IBM for an ideal fluid. In the following, we extract the nonlinear correction of the linear break-up time (Ashgriz & Mashayek 1995; Martínez-Calvo *et al.* 2020), which we define based on (A 1) by

$$\Delta t_{nl} = t_b - \frac{\ln(\epsilon_0^{-1})}{\omega_m}, \quad (4.1)$$

from simulations with initial perturbation amplitude ϵ_0 as described in appendix A. This correction compares the break-up time obtained from simulations t_b to the linear break-up time obtained from the maximum growth rate of the dispersion relation ω_m and is shown in figure 7 in relation to t_b . In the limit of a Stokes fluid the nonlinear correction varies strongly: we observe a change of sign above an anisotropy ratio of about $\gamma^z/\gamma^\phi = 0.5$ where the correction becomes strongly negative. The nonlinear correction for the ideal fluid for the LBM/IBM is smaller, positive, and slightly increases with increasing tension anisotropy. For isotropic tension but varying Marangoni number of a surfactant-covered fluid jet Martínez-Calvo *et al.* (2020) report effects going in the same direction with a more pronounced variation of the nonlinear correction of the linear break-up time towards the Stokes limit and less variation towards the ideal fluid limit.

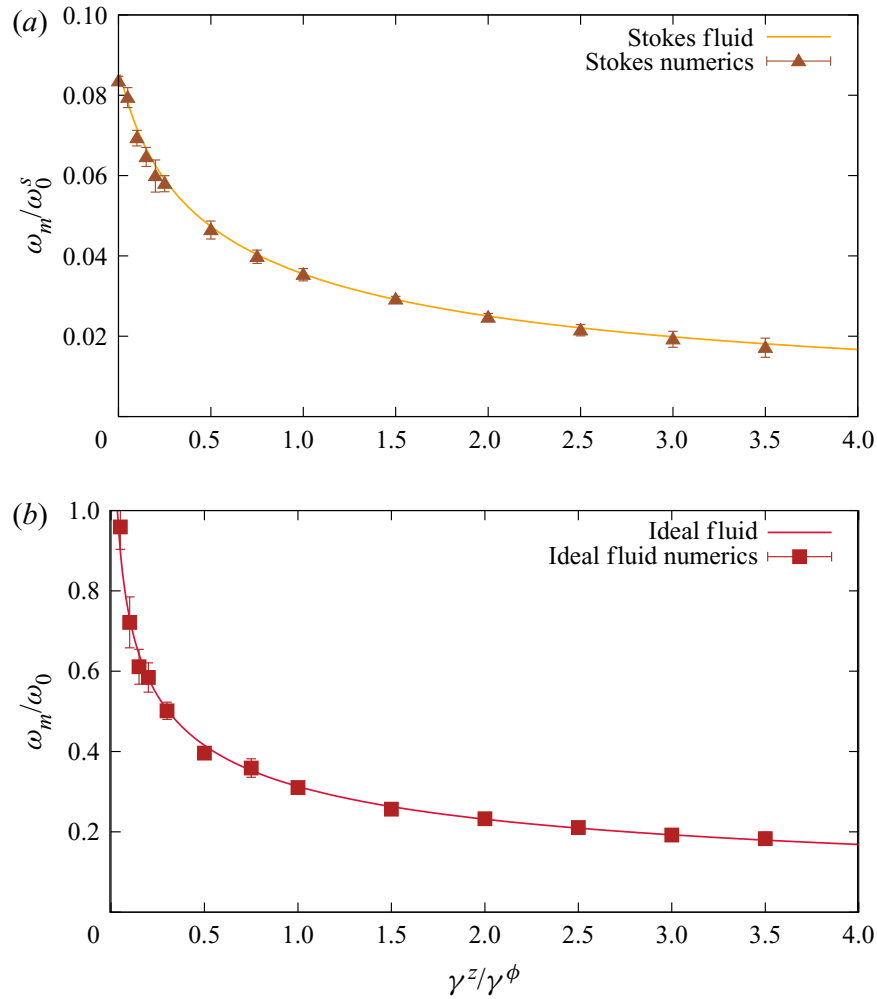


FIGURE 6. Growth rate of the dominant mode as a function of the anisotropy in interfacial tension. The dominant growth rate according to the dispersion relation (a) for a Stokes fluid (3.1) (orange line) and (b) for an ideal fluid (3.2) (red line) is shown with corresponding BIM simulations (triangles) and LBM/IBM simulations (squares), respectively, depending on the tension anisotropy γ^z/γ^ϕ . The dominant growth rate decreases steadily and strongly with increasing tension anisotropy. While the decrease with increasing anisotropy is similar, the growth rate is one order of magnitude larger for the ideal fluid and it does not remain finite at zero anisotropy in contrast to the Stokes fluid in (a). In both cases simulation results are in perfect agreement with the theory.

5. Influence of interface viscosity

We now investigate how anisotropic interfacial tension influences the instability wavelength and growth rate in the Stokes regime if the interface in addition possesses interface viscosity (Boussinesq 1913; Scriven 1960; Whitaker 1976; Hajiloo, Ramamohan & Slattery 1987; Powers 2010; Yazdani & Bagchi 2013; Narsimhan *et al.* 2015; Martínez-Calvo & Sevilla 2018; Guglietta *et al.* 2020). The dispersion relation in presence of interface viscosity and tension anisotropy is derived in appendix B.3 and reads

$$\omega = \frac{\gamma^\phi}{\eta R_0} \left(1 - \frac{\gamma^z}{\gamma^\phi} (kR_0)^2 \right) \left(1 + \frac{2\eta_S}{\eta R_0} kR_0 \xi \right)^{-1} \left[I_1(kR_0) K_1(kR_0) + \frac{kR_0}{2} (I_1(kR_0) K_0(kR_0) - I_0(kR_0) K_1(kR_0)) \right] \quad (5.1)$$

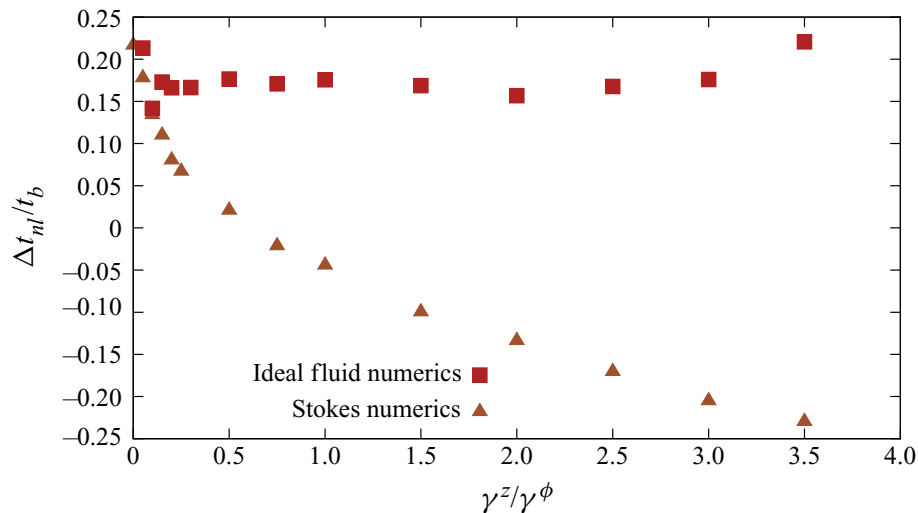


FIGURE 7. Nonlinear correction of the linear break-up time for varying tension anisotropy. The nonlinear correction of the linear break-up time is shown relative to the break-up time t_b obtained from simulations. In the limit of an ideal fluid the LBM/IBM simulations show a slightly increasing nonlinear correction to the linear break-up time with increasing tension anisotropy. In contrast, BIM simulations show the reversed behaviour for a Stokes fluid, where in addition the sign changes and the amplitude variations are more pronounced.

with the abbreviation

$$\xi = -\frac{1}{2} [kR_0 I_1(kR_0) K_1(kR_0) - kR_0 I_0(kR_0) K_0(kR_0)]. \quad (5.2)$$

For vanishing interface viscosity η_S the dispersion relation correctly reduces to (3.1).

From the dispersion relation we numerically calculate the dominant wavelength λ_m and the corresponding growth rate ω_m for varying anisotropy ratio γ^z/γ^ϕ and interface viscosity η_S , which we measure relative to fluid viscosity η . Phase diagrams of the dominant wavelength and the corresponding growth rate are shown in figures 8(a) and 8(b), respectively. Typical values for the interface viscosity of vesicles and red blood cells reported in the literature vary from 10^{-10} Pa s m to 10^{-7} Pa s m (Dimova *et al.* 2006; den Otter & Shkulipa 2007; Guglietta *et al.* 2020). In combination with typical fluid viscosities (§ 2.4) and sizes of the order of $R_0 = 1$ μm for vesicles and $R_0 = 4$ μm for red blood cells this leads to typical viscosity ratios $2\eta_S/(\eta R_0) = 0.1\text{--}40$. In figure 8 these values correspond to the range from approximately -1 to approximately 1.6 on the ordinate. For fixed values of the viscosity ratio, an increase in the anisotropy ratio leads to a larger dominant wavelength and smaller maximum growth rate. This is in line with the results discussed above for zero interface viscosity in §§ 4.1 and 4.3. Especially in the region of small interface viscosities, changes in η_S have little effect on dominant wavelength and growth rate, but also around a fraction of 1 the anisotropy dominates. If the interface viscosity η_S becomes very large compared to the fluid viscosity, the growth rate tends to zero, as a more viscous interface leads to a slower dynamics of the perturbation. The latter is consistent with the results of Narsimhan *et al.* (2015) for isotropic interfaces. We also note that the maximum wavenumber of the instability, beyond which perturbations do not grow, is influenced only by the anisotropy ratio and not the viscosity ratio, because the root of the dispersion relation (5.1) is determined by the first term in brackets.

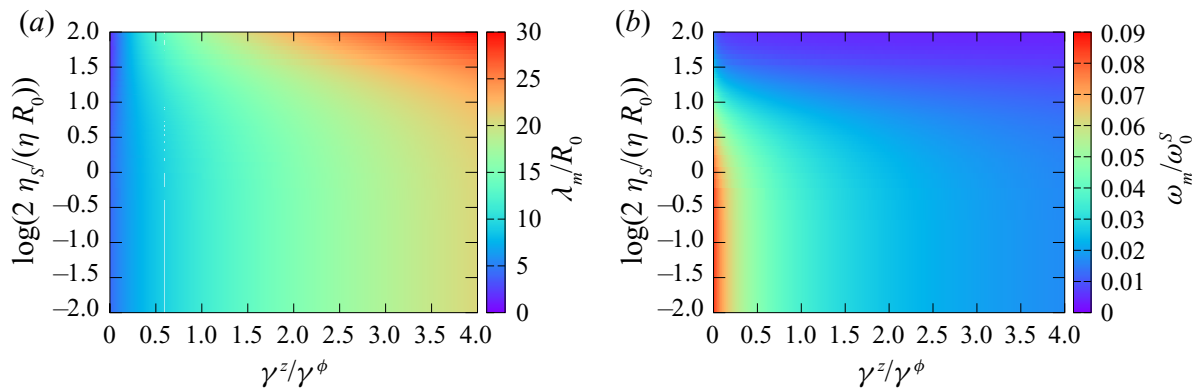


FIGURE 8. Influence of interface viscosity on the anisotropic Rayleigh–Plateau instability. Phase diagrams for (a) the dominant wavelength and (b) the corresponding growth rate. The dominant wavelength increases both with increasing anisotropy ratio and increasing interface viscosity η_s . The growth rate of the dominant perturbation decreases with increasing anisotropy ratio and interface viscosity. Despite the increase in the wavelength and the slowing down of the instability for very large values of the interface viscosity, the tension anisotropy is the dominating parameter.

6. Formation of satellite droplets for an ideal fluid jet without ambient fluid under influence of tension anisotropy

We eventually consider an ideal fluid jet without ambient fluid, i.e. $\eta^0 = 0$ and $\rho^0 \ll \rho$. In [appendix C](#) we derive the dispersion relation including anisotropic interfacial tension and show that for the ideal fluid jet without ambient fluid similar results hold as for the ideal fluid discussed in §§ 3.2 and 4. To compare our analytical results to simulations of an ideal fluid jet without ambient fluid we develop an axisymmetric simulation method based on a long-wavelength (or small- k) approximation as detailed in [appendix D](#). We consider the Navier–Stokes equation (D 9) together with the kinematic boundary condition (D 10) in the small- k approximation and solve them numerically. From the dynamic evolution the dominant growth rate and wavelength can be calculated, similarly to the procedure for the three-dimensional simulations detailed in [appendix A](#). They are in good agreement with the theory as detailed in [appendix C](#). We further obtain the jet shape over time.

With this, we are able to study the formation of satellite droplets under anisotropic interfacial tension. Satellite droplets are typically much smaller than and form in between the main drops during break-up of a liquid jet for certain parameter combinations (Eggers & Dupont 1994; Eggers 1997; Martínez-Calvo *et al.* 2020). In the presence of an ambient fluid (BIM and LBM/IBM simulations) we do not observe satellite droplet formation, which may be related to limitations in the resolution of our simulation and the fact that we do not simulate the actual pinch-off. In the following, we therefore investigate satellite droplet formation using the small- k simulations for a liquid jet without ambient fluid at varying tension anisotropy and viscosity. Starting with the zero-viscosity, ideal fluid jet ($Oh = 0$), we observe satellite droplets as shown at the bottom of [figure 9](#). As the dominant wavelength increases with increasing anisotropy, the satellite droplet at the bottom right of [figure 9](#) is more elongated compared to the left one. However, both satellites possess the same relative volume of approximately $\mathcal{E} = 3\%$ (Rutland & Jameson 1970; Lafrance 1975; Mansour & Lundgren 1990; Ashgriz & Mashayek 1995; Eggers 1997), which is defined as the volume integral over the satellite droplet divided by the volume integral over one period of the perturbation (Martínez-Calvo *et al.* 2020). For the ideal fluid jet, \mathcal{E} is independent of the tension anisotropy.

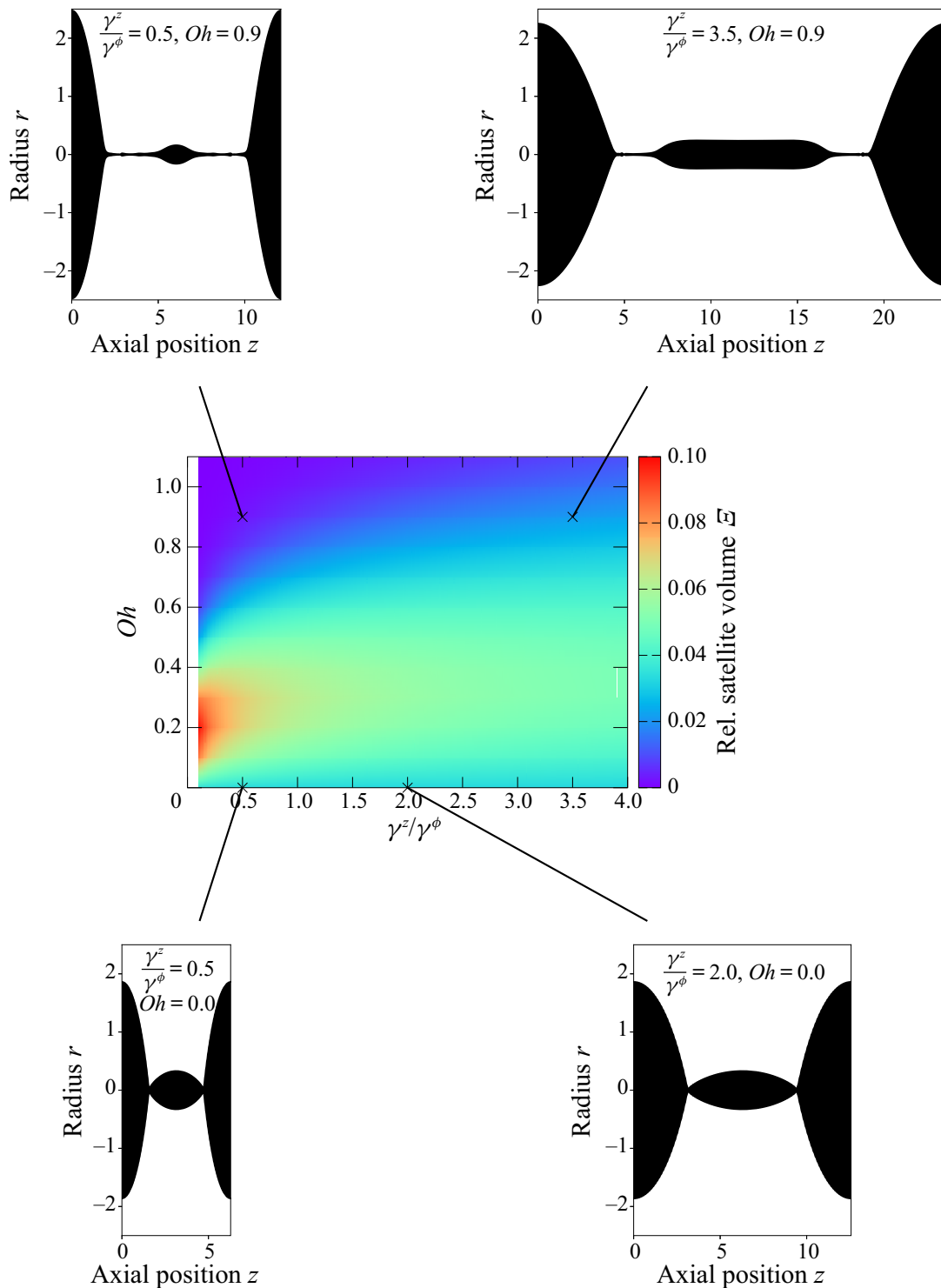


FIGURE 9. Formation of satellite droplets under the influence of tension anisotropy in the absence of an ambient fluid $\rho^o = 0$, $\eta^o = 0$. Relative volume \mathcal{E} of the satellite droplet for varying tension anisotropy γ^z/γ^ϕ and varying Ohnesorge number Oh . Parameter combinations for the shapes shown around the colour map are indicated in the phase diagram by black crosses. For the ideal fluid jet without ambient fluid with $\rho^o = 0$ ($Oh = 0$) the relative volume of 3% remains constant while for the Stokes fluid without ambient fluid $\eta^o = 0$ (large Oh) no satellites appear. In the intermediate range, a significant influence of tension anisotropy on the relative volume is observed. Especially, the satellite droplet becomes cylindrical for large tension anisotropy, as shown in the top right image.

As our small- k simulations are based on the full Navier–Stokes equation, they allow us to explore the effect of fluid viscosity measured in terms of the Ohnesorge number Oh on the satellite droplet. In the centre of figure 9 we show the relative volume \mathcal{E} in a colour map. For isotropic interfacial tension, we observe a decrease in the satellite volume, which is in agreement with results reported by Martínez-Calvo *et al.* (2020) in the absence of surfactants. With increasing Ohnesorge number the phase diagram in figure 9 shows a growing influence of the anisotropy. For a small but non-zero $Oh \approx 0.2$, the volume assumes its maximum at $\gamma^z/\gamma^\phi = 0$ and decreases with increasing anisotropy. At higher Oh , the effect is reversed and the volume strongly increases with increasing tension anisotropy. In contrast to $Oh = 0$, at larger Ohnesorge number $Oh = 0.9$ the shape of the satellite droplet is strongly influenced by an increase in tension anisotropy from $\gamma^z/\gamma^\phi = 0.5$ to $\gamma^z/\gamma^\phi = 3.5$ as illustrated by the images at the top of figure 9. For small anisotropy (upper left shape) the satellite droplet is small and spherical but most remarkably for larger tension anisotropy (upper right) it develops a more cylindrical shape, it is longer and larger. In both cases the satellite droplet is connected to the main droplets by a thin fluid string. At very large Ohnesorge number beyond one, i.e. towards the Stokes regime, the satellite volume decreases to zero over the whole range of anisotropy. All in all, over a broad range of intermediate Ohnesorge numbers we observe a striking influence of tension anisotropy on the satellite droplet, where at larger Oh larger tension anisotropy stabilises the satellite droplet.

7. Conclusion

Using linear stability analysis supported by numerical simulations we generalised the Rayleigh–Plateau mechanism for the break-up of a liquid cylinder to situations where the interfacial tension is anisotropic. Two physically relevant situations were studied: a vesicle/biological cell in the limit of small Reynolds number (Stokes equation) and an ideal fluid in the limit of large Reynolds number (Euler equation). We found that anisotropic interfacial tension alters not only the range of growing perturbations but also strongly affects the dominant wavelength of the instability. If the axial tension is inferior/superior to the azimuthal tension, the dominant wavelength becomes smaller/larger than the wavelength of the classical isotropic Rayleigh–Plateau instability. For strong anisotropy, the dominant wavelength can even lie outside the instability range of the classical isotropic Rayleigh–Plateau instability. The predictions of our linear stability analysis were found to be in excellent agreement with numerical simulations using a boundary integral method at low and a lattice-Boltzmann/immersed boundary method at high Reynolds number. LBM/IBM simulations with typical vesicle/cell parameters, which include finite inertia effects, show a transition in the wavelength for decreasing Ohnesorge number from the Stokes regime to the ideal fluid. Using simulations, we found the nonlinear correction to the linear break-up time to decrease/increase with the anisotropy ratio in the Stokes/Euler limits, respectively. We found that including viscosity of the interface surrounded by Stokes fluid leads to an increase in the dominant wavelength and a slower dynamics of the perturbation. However, except at very large interface viscosity, changes are small compared to the effects of varying tension anisotropy. Finally, we showed that the satellite droplet volume of 3% is not affected by varying tension anisotropy in the limit of an ideal fluid. For Ohnesorge numbers just below one, the satellite volume decreases with increasing anisotropy.

In Part 2 we investigate the alteration of the anisotropic Rayleigh–Plateau instability due to the bending and shear elasticity present in a typical cell. Besides biological cells, our results apply to synthetic interfaces with anisotropic properties such as nematic liquid

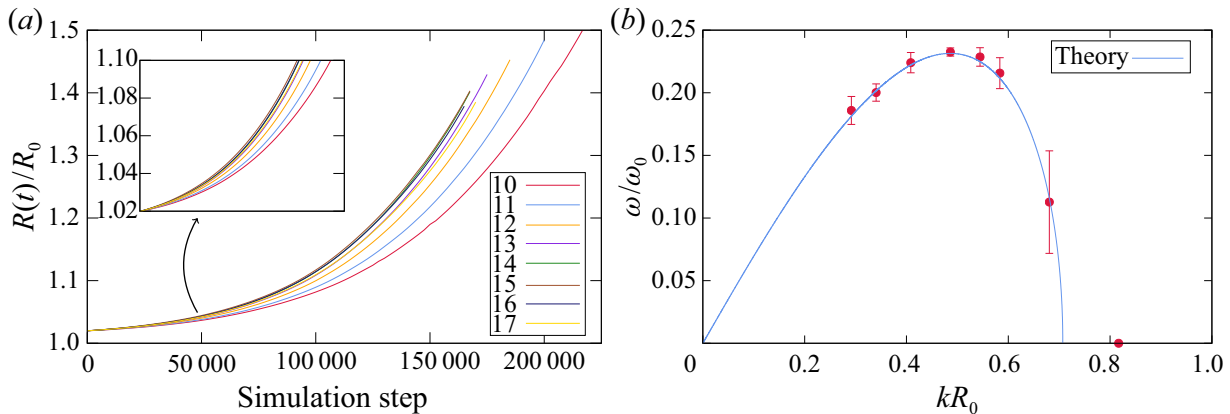


FIGURE 10. Illustration of the analysis of the numerical simulations. (a) For fixed values of the anisotropic interfacial tension, in this case $\gamma^z/\gamma^\phi = 0.4$, we run multiple simulations with varying wavelengths of the interface perturbation. One simulation corresponds to one wavelength, which is determined by the number of maxima (different curves) per box length. The radius averaged over all maxima divided by the unperturbed radius R_0 is shown over time. The inset shows the growth up to a radius of 110 % of R_0 . The first simulation to reach this threshold is considered as the fastest growing mode. (b) LBM/IBM simulations of a single period of the perturbation with increasing resolution and smaller initial perturbation amplitude $\epsilon_0 = 0.002$ allow us to determine the growth rate (here shown for different perturbation wavelengths with $\gamma^z/\gamma^\phi = 2$ in comparison to the analytical solution (3.2)) and the nonlinear correction of the linear break-up time.

crystals confined to interfaces (Keber *et al.* 2014) or cell-laden hydrogels extruded from a nozzle during bioprinting applications (Snyder *et al.* 2015; Mandrycky *et al.* 2016).

Acknowledgements

C.B. and K.G. thank the Studienstiftung des deutschen Volkes for financial support. C.B. acknowledges support by the study programme ‘Biological Physics’ of the Elite Network of Bavaria. We acknowledge funding from Deutsche Forschungsgemeinschaft in the framework of FOR 2688 ‘Instabilities, Bifurcations and Migration in Pulsating Flow’, Project B3. We gratefully acknowledge computing time provided by the SuperMUC system of the Leibniz Rechenzentrum, Garching, as well as by the Bavarian Polymer Institute, and financial support from the Volkswagen Foundation.

Declaration of interests

The authors report no conflict of interest.

Appendix A. Simulation analysis

In the following we explain in detail the analysis procedure of the BIM and LBM/IBM simulations. In order to analyse in simulations both the wavelength of the dominant mode and its growth rate we consider the interface shape over time for a given perturbation and track a local maximum corresponding to a later droplet/vesicle as shown in figure 10(a). In order to obtain the most unstable mode for given anisotropic interfacial tension in the simulations, we consider a cylindrical interface of fixed anisotropic interfacial tension immersed in a fluid of fixed properties and apply a series of perturbations with varying wavelength. One simulation corresponds to one perturbation with fixed

wavelength. The initial amplitude of the perturbation is chosen as $\epsilon(t=0) = 0.02R_0$ in all simulations. Note that a multiple of the wavelength has to fit in the simulation box and we thus vary the wavelength in discrete steps. Figure 10(a) shows an example of a series of simulations for given anisotropic interfacial tension $\gamma^z/\gamma^\phi = 0.4$ using the LBM/IBM. In this example we force a perturbation with 10–17 maxima onto a cylindrical interface in a box of length 650 grid cells. Each curve corresponds to a simulation with different wavelength of the perturbation. In each of the simulations the radius at the position of the different maxima is tracked over time. The curves show the local radius at the position of the maxima, averaged over all maxima, varying in time. From the initial amplitude $\epsilon(t=0) = 0.02R_0$ all modes grow with a different speed. In order to determine the fastest growing wavelength, we define a threshold for the amplitude $\epsilon_{crit} = 0.1R_0$, which can be considered as an upper limit of small deformations. The inset of figure 10 shows the growth of all modes up to the radius $R_0 + \epsilon_{crit}$. The mode which first reaches this threshold, is considered as the fastest growing mode and its corresponding wavelength as the most unstable wavelength. This procedure can be applied to different values of the anisotropy ratio γ^z/γ^ϕ and allows us to numerically determine the most unstable wavelength depending on tension anisotropy. With increasing wavelength we increase the box length in order to ensure a good resolution for this procedure. Nevertheless, the finite box size and the resulting discrete variation of the wavelength result in discretisation effects. In order to account for these discretisation effects we compute the range in wavelength which cannot be distinguished due to the discrete variation: adding/subtracting half the wavelength is not possible for a given box length, because we necessarily enforce an integral number of wavelengths in the simulation box. This range is given in the figures as error bars of the simulation results.

The growth rate is calculated as the quotient of the derivative of the maximum radius over time and the maximum radius itself, in a regime of linear growth. In BIM simulations we use the series of perturbations as detailed above, for the LBM/IBM simulations we consider one period of the dominant perturbation with increased resolution and initial perturbation amplitude $\epsilon_0 = 0.002$. Figure 10(b) shows the growth rate determined from simulations for varying wavenumber in comparison to the analytically obtained dispersion relation (3.2) for LBM/IBM simulations. An error is estimated from the average value of the quotient which determines the growth rate.

As a measure of the nonlinear behaviour covered by the simulations, we further extract the nonlinear correction to the linear break-up time Δt_{nl} defined in (4.1). To do so we determine the break-up time in the simulation t_b by tracking a minimum of the interface shape over time and extrapolating the last time steps towards a radius of zero. From the analytical evolution of a perturbation based on the linear stability analysis as given in (B 1) the linear break-up time can be calculated at the position of a minimum by

$$R_{min} = R_0 - R_0\epsilon_0 e^{\omega t} \stackrel{!}{=} 0. \quad (\text{A } 1)$$

The difference between t_b and the linear break-up time determines the nonlinear correction as given by (4.1).

Appendix B. Analytical derivation of the dispersion relations

B.1. Dispersion relation for a Stokes fluid

In the following we consider the inner and outer fluid in the Stokes limit with same viscosity, i.e. $\eta^o = \eta$. The following calculations are based on the method introduced by

Stone & Brenner (1996). We use an ansatz of a cylindrical interface which is slightly perturbed in a periodic fashion with time dependent amplitude $\epsilon(t) \ll 1$. For later convenience we write the equation describing the shape as

$$R = R_0 (1 + \epsilon(t) \cos(kz)), \quad (\text{B } 1)$$

which is a slightly different notation but equivalent to the ansatz in (2.1). We calculate the traction jump at the interface Δf_n in (2.2), which is equal to the negative membrane force, using (B 1) and assuming that the magnitude of the interface perturbation is small, i.e. $\epsilon \ll 1$,

$$\frac{\gamma^\phi}{R(z, t)} + \frac{\gamma^z}{R_z(z, t)} \approx \frac{\gamma^\phi}{R_0} (1 - \epsilon \cos(kz)) - \gamma^z \frac{\partial^2 R}{\partial z^2} = \frac{\gamma^\phi}{R_0} \left(1 - \left[1 - \frac{\gamma^z}{\gamma^\phi} (kR_0)^2 \right] \epsilon \cos(kz) \right). \quad (\text{B } 2)$$

The traction jump can be decomposed into a constant pressure contribution $p_0 = \gamma^\phi/R_0$ and a perturbation in the traction jump

$$- \frac{\gamma^\phi}{R_0} \epsilon \left(1 - \frac{\gamma^z}{\gamma^\phi} (R_0 k)^2 \right) \cos(kz), \quad (\text{B } 3)$$

which is evaluated at the position of the unperturbed interface due to linearisation (Tomotika 1935; Stone & Brenner 1996). The goal now is to solve the Stokes equation (2.8) in the presence of the traction jump perturbation (B 3). This is done by considering a ring force representing the traction jump (Stone & Brenner 1996) such that the Stokes equation becomes

$$- \nabla p + \eta \nabla^2 \mathbf{v} + \hat{\mathbf{e}}_r \delta(r - R_0) \frac{\gamma^\phi \epsilon}{R_0} \left(1 - \frac{\gamma^z}{\gamma^\phi} (R_0 k)^2 \right) \cos(kz) = \mathbf{0}. \quad (\text{B } 4)$$

The ring force in the radial direction (third term entering in (B 4) with the radial unit vector $\hat{\mathbf{e}}_r$) accounts for the presence of the membrane, from which a force due to interfacial tension is acting on the fluid. The interfacial force is evaluated at the undeformed radial position of the infinitely thin interface. As a consequence the ring force enters with a delta distribution $\delta(r - R_0)$.

In line with the periodic perturbation of the radius of the interface in (B 1), a periodic ansatz for the velocity components and the pressure field is chosen (Stone & Brenner 1996)

$$v_r(r, z) = \frac{\gamma^\phi \epsilon}{\eta} \bar{v}_r(r) \cos(kz), \quad (\text{B } 5)$$

$$v_z(r, z) = \frac{\gamma^\phi \epsilon}{\eta} \bar{v}_z(r) \sin(kz), \quad (\text{B } 6)$$

$$p(r, z) = \frac{\gamma^\phi \epsilon}{R_0} \bar{p}(r) \cos(kz), \quad (\text{B } 7)$$

where, due to the perturbation of the interface (B 1) and kinematic boundary conditions, the radial velocity is written with a cosine while the axial velocity due to continuity equation (2.6), which involves a derivative with respect to z , is written with a sine. The prefactor of the velocities γ^ϕ/η is chosen such that \bar{v}_r and \bar{v}_z become dimensionless, where the same applies for the pressure prefactor. The velocity prefactor γ^ϕ/η is identical to the viscocapillary velocity based on the azimuthal tension γ^ϕ . The amplitude of the

perturbation varies in time, i.e. $\epsilon = \epsilon(t)$. For solving the Stokes equation we introduce the Hankel transforms (Poularikas 2000) of the velocity amplitudes $V_r(s)$, $V_z(s)$ and the pressure $P(s)$

$$V_r(s) = \mathcal{H}_1[\bar{v}_r] = \int_0^\infty \bar{v}_r(r)rJ_1(sr) dr, \quad (\text{B } 8)$$

$$V_z(s) = \mathcal{H}_0[\bar{v}_z] = \int_0^\infty \bar{v}_z(r)rJ_0(sr) dr, \quad (\text{B } 9)$$

$$P(s) = \mathcal{H}_0[\bar{p}] = \int_0^\infty \bar{p}(r)rJ_0(sr) dr, \quad (\text{B } 10)$$

together with their inverse transforms

$$\bar{v}_r(r) = \mathcal{H}_1^{-1}[V_r] = \int_0^\infty V_r(s)sJ_1(sr) ds, \quad (\text{B } 11)$$

$$\bar{v}_z(r) = \mathcal{H}_0^{-1}[V_z] = \int_0^\infty V_z(s)sJ_0(sr) ds, \quad (\text{B } 12)$$

$$\bar{p}(r) = \mathcal{H}_0^{-1}[P] = \int_0^\infty P(s)sJ_0(sr) ds, \quad (\text{B } 13)$$

where J_ν is the Bessel function of the first kind and order ν .

For the transformation of the Stokes equation (B 4) and continuity equation (2.6) into Hankel space we use the following identities for the Bessel differential operators (Poularikas 2000):

$$\mathcal{H}_1\left[\frac{\partial^2}{\partial r^2}f + \frac{1}{r}\frac{\partial}{\partial r}f - \frac{1}{r^2}f\right] = -s^2\mathcal{H}_1[f] \quad (\text{B } 14)$$

and

$$\mathcal{H}_0\left[\frac{\partial^2}{\partial r^2}f + \frac{1}{r}\frac{\partial}{\partial r}f\right] = -s^2\mathcal{H}_0[f]. \quad (\text{B } 15)$$

Together with the Hankel transform of the ring force

$$\mathcal{H}_1\left[\delta(r - R_0)\frac{\gamma^\phi\epsilon}{R_0}\left(1 - \frac{\gamma^z}{\gamma^\phi}(R_0k)^2\right)\cos(kz)\right] = J_1(sR_0)\gamma^\phi\epsilon\left(1 - \frac{\gamma^z}{\gamma^\phi}(R_0k)^2\right)\cos(kz), \quad (\text{B } 16)$$

we are able to write down the continuity equation together with the two components of the Stokes equation in Hankel space

$$sV_r + kV_z = 0, \quad (\text{B } 17)$$

$$\frac{s}{R_0}P - (s^2 + k^2)V_r + \left(1 - \frac{\gamma^z}{\gamma^\phi}(R_0k)^2\right)J_1(sR_0) = 0, \quad (\text{B } 18)$$

$$\frac{k}{R_0}P - (s^2 + k^2)V_z = 0. \quad (\text{B } 19)$$

We can solve this system of equations for the radial velocity in Hankel space and obtain

$$V_r = \left(1 - \frac{\gamma^z}{\gamma^\phi}(R_0k)^2\right)k^2\frac{1}{(s^2 + k^2)^2}J_1(sR_0), \quad (\text{B } 20)$$

which leads to the radial velocity in real space using the inverse Hankel transform

$$v_r = \frac{\gamma^\phi \epsilon}{\eta} \cos(kz) \left(1 - \frac{\gamma^z}{\gamma^\phi} (R_0 k)^2 \right) k^2 \int_0^\infty \frac{s J_1(s R_0) J_1(sr)}{(s^2 + k^2)^2} ds. \quad (\text{B } 21)$$

As done in the case of the ideal fluid jet without ambient fluid, we consider a perturbation of the interface growing with rate ω , i.e.

$$\epsilon(t) = \epsilon_0 e^{\omega t}. \quad (\text{B } 22)$$

The kinematic boundary condition at the interface leads to

$$v_r(r = R_0, z) = R_0 \partial_t \epsilon \cos(kz) = R_0 \omega \epsilon \cos(kz), \quad (\text{B } 23)$$

and using (B 21) we obtain the growth rate

$$\omega = \frac{\gamma^\phi}{R_0 \eta} \left(1 - \frac{\gamma^z}{\gamma^\phi} (R_0 k)^2 \right) \int_0^\infty \frac{k^2 s J_1(s R_0)^2}{(s^2 + k^2)^2} ds. \quad (\text{B } 24)$$

The integral can be evaluated (Gradshteyn, Ryzhik & Jeffrey 2007, 6.535), taking the derivative with respect to variable k in the denominator) and we obtain the dispersion relation for a Stokes fluid in (3.1).

B.2. Dispersion relation for an ideal fluid

Below we perform a linear stability analysis in the ideal fluid limit. Since the perturbation of the interface between both fluids is small, also the perturbation of the velocity is small. Because we consider a co-moving frame, the velocity vector contains only the perturbation and thus is small, $v_i \ll 1$, as well. As a consequence, the nonlinear term in the Euler equation is of second order and can be neglected, leading to the linear Euler equation

$$\frac{\partial \mathbf{v}}{\partial t} = -\frac{1}{\rho} \nabla p. \quad (\text{B } 25)$$

We here solve the linearised Euler equation (B 25) which is valid for each position (r, z) both in the inner and in the outer fluid of same density $\rho^o = \rho$. Note that the continuity equation does not change compared to the previous section.

In the linearised Euler equation we add the traction jump that here equals a pressure disturbance occurring at the interface due to interfacial tension according to (2.4), which is expanded as done in (B 1) and enters in terms of a ring force. In turn we have to solve

$$\frac{\partial}{\partial t} \mathbf{v} = -\frac{1}{\rho} \nabla p + \hat{\mathbf{e}}_r \delta(r - R_0) \frac{1}{\rho} \frac{\gamma^\phi \epsilon}{R_0} \left(1 - \frac{\gamma^z}{\gamma^\phi} (k R_0)^2 \right) \cos(kz). \quad (\text{B } 26)$$

In the linearised Euler equation (B 25) the density appears rather than the viscosity. In the perturbation ansatz for the velocity (B 5) and (B 6) the prefactor changes accordingly to $\sqrt{\gamma^\phi / (\rho R_0)}$. The prefactors are chosen such that $\bar{v}_r(r)$, $\bar{v}_z(r)$ are again dimensionless.

In total, after transformation into the Hankel space, we obtain the analytical equations

$$sV_r = -kV_z, \quad (\text{B } 27)$$

$$\omega V_z = \sqrt{\frac{\gamma^\phi}{\rho R_0}} kP, \quad (\text{B } 28)$$

$$\omega V_r = \sqrt{\frac{\gamma^\phi}{\rho R_0}} sP + R_0 \sqrt{\frac{\gamma^\phi}{\rho R_0}} J_1(sR_0) \left(1 - \frac{\gamma^z}{\gamma^\phi} (kR_0)^2\right), \quad (\text{B } 29)$$

which are solved for the radial component of the velocity, as done in the case of the Stokes equation in § 3.1. We obtain for the velocity

$$v_r(r, z) = \frac{k^2 R_0}{\omega} \frac{\gamma^\phi}{\rho R_0} \epsilon \cos(kz) \left(1 - \frac{\gamma^z}{\gamma^\phi} (kR_0)^2\right) \int_0^\infty \frac{sJ_1(sR_0)J_1(sr)}{k^2 + s^2} ds \quad (\text{B } 30)$$

and using the kinematic boundary condition we obtain the squared growth rate

$$\omega^2 = k^2 \frac{\gamma^\phi}{\rho R_0} \left(1 - \frac{\gamma^z}{\gamma^\phi} (kR_0)^2\right) \int_0^\infty \frac{sJ_1^2(sR_0)}{k^2 + s^2} ds. \quad (\text{B } 31)$$

We can again evaluate the integral (Gradshteyn *et al.* 2007, 6.535) and the resulting dispersion relation for an ideal fluid is given in (3.2).

B.3. Dispersion relation taking interface viscosity into account

We now derive a dispersion relation for a system where, in addition to the fluid viscosity η , a viscosity of the interface η_S is considered. The solution method starts from the Stokes equation and is again based on the previous B.1. Here, the interface viscosity results in an additional force acting from the interface onto the fluid (Scriven 1960; Narsimhan *et al.* 2015; Sprenger *et al.* 2020). The component normal to the interface is given by

$$f_{i.v.}^n = \frac{2\eta_S}{R_0} \partial_z v_z = \frac{2\eta_S}{R_0} \frac{\gamma^\phi}{\eta} \epsilon \bar{v}_z(R_0) k \cos(kz), \quad (\text{B } 32)$$

where surface incompressibility and for the second identity the velocity ansatz from (B 6) is used. Similar to Powers (2010) we do not consider any tangential component of the viscous force. This additional normal force contribution appears as an additional term in the ring force in (B 4) such that (B 18) in the Hankel space becomes

$$\frac{s}{R_0} P - (s^2 + k^2) V_r + \left(1 - \frac{\gamma^z}{\gamma^\phi} (kR_0)^2 + \frac{2\eta_S}{\eta R_0} \bar{v}_z(R_0) kR_0\right) J_1(sR_0) = 0. \quad (\text{B } 33)$$

Analogously, the radial velocity in Hankel space from (B 20) becomes

$$V_r = \left(1 - \frac{\gamma^z}{\gamma^\phi} (R_0 k)^2 + \frac{2\eta_S}{\eta R_0} \bar{v}_z(R_0) kR_0\right) k^2 \frac{1}{(s^2 + k^2)^2} J_1(sR_0), \quad (\text{B } 34)$$

which is then transformed back to obtain v_r , which still depends on $\bar{v}_z(R_0)$. In order to obtain $\bar{v}_z(R_0)$, we use the continuity equation (B 17) to relate V_z to V_r and insert (B 34),

then transform V_z back from Hankel space and thus identify

$$\bar{v}_z(R_0) = - \left(1 - \frac{\gamma^z}{\gamma^\phi} (R_0 k)^2 + \frac{2\eta_S}{\eta R_0} \bar{v}_z(R_0) k R_0 \right) \int_0^\infty \frac{s^2 k J_1(s R_0) J_0(s R_0)}{(s^2 + k^2)^2} ds, \quad (\text{B } 35)$$

which is then solved for $\bar{v}_z(R_0)$. Following the same steps as in [appendix B.1](#) we then calculate the growth rate ω :

$$\omega = \frac{\gamma^\phi}{\eta R_0} \left(1 - \frac{\gamma^z}{\gamma^\phi} (R_0 k)^2 + \frac{2\eta_S}{\eta R_0} \bar{v}_z(R_0) k R_0 \right) k^2 \int_0^\infty \frac{s J_1(s R_0)^2}{(s^2 + k^2)^2} ds. \quad (\text{B } 36)$$

The integral in this equation has already been solved in [appendix B.1](#). Combining [\(B 36\)](#) and the solution for $\bar{v}_z(R_0)$ and solving the integral in [\(B 35\)](#) (based on 49(13) and 49(14) of Erdelyi *et al.* 1954) leads to the dispersion relation in [\(5.1\)](#).

Appendix C. Dispersion relation for an ideal fluid jet without ambient fluid

In deriving the dispersion relation for an ideal fluid jet without ambient fluid we follow the ansatz by Eggers & Villermaux (2008). Here, we consider the outer fluid to have no influence, i.e. $\eta^o = 0$ and $\rho^o \ll \rho$. As we perform a linear stability analysis, we again use the linearised version of the Euler equation [\(B 25\)](#). By the linearised Euler equation [\(B 25\)](#) and the continuity equation [\(2.6\)](#) the pressure p must fulfil a Laplace equation

$$\nabla^2 p = 0. \quad (\text{C } 1)$$

Corresponding to the interface perturbation, a perturbation ansatz for the pressure distribution in the jet is chosen (Eggers & Villermaux 2008)

$$p(z, r, t) = p_0 + \delta p(z, r, t), \quad (\text{C } 2)$$

with constant pressure p_0 and a general perturbation δp . At the interface, the pressure is determined by the modified Young–Laplace equation which according to [\(2.4\)](#) is

$$p_0 + \delta p(r = R) = \frac{\gamma^\phi}{R(z, t)} + \frac{\gamma^z}{R_z(z, t)}. \quad (\text{C } 3)$$

The pressure perturbation can be separated into the periodic perturbation in the z -direction, its magnitude $F(r)$ depending on the radial position and the constant prefactor $\delta \bar{p}$

$$\delta p(z, r, t) = \delta \bar{p} F(r) \exp(\omega t + ikz). \quad (\text{C } 4)$$

The pressure obeys the Laplace equation [\(C 1\)](#), which in cylindrical coordinates and using that p does not depend on the angular coordinate ϕ , reads

$$\frac{\partial^2 p}{\partial r^2} + \frac{1}{r} \frac{\partial p}{\partial r} + \frac{\partial^2 p}{\partial z^2} = 0. \quad (\text{C } 5)$$

Now, using [\(C 2\)](#) for the pressure and inserting [\(C 4\)](#) leads to a partial differential equation for the function $F(r)$

$$\frac{\partial^2 F}{\partial r^2} + \frac{1}{r} \frac{\partial F}{\partial r} - k^2 F(r) = 0. \quad (\text{C } 6)$$

This equation is solved by the modified Bessel function of the first kind and of order zero

$$F(r) = I_0(kr). \quad (\text{C } 7)$$

Using the perturbation ansatz (2.1) for the interface and considering anisotropic interfacial tension, the perturbation in the pressure in (C 3) is in analogy to (B 3) given by

$$\delta p(r = R) = -\frac{\epsilon_0}{R_0^2} (\gamma^\phi - \gamma^z R_0^2 k^2) \exp(\omega t + ikz). \quad (\text{C } 8)$$

From (C 4) and (C 7) we have the relation $\delta p = \delta \bar{p} I_0(kr) \exp(\omega t + ikz)$, which together with (C 8) leads to the magnitude of the pressure perturbation

$$\delta \bar{p} = -\frac{\epsilon_0}{R_0^2} (\gamma^\phi - \gamma^z R_0^2 k^2) \frac{1}{I_0(kR_0)}. \quad (\text{C } 9)$$

Since $\epsilon_0 \ll R_0$ we can evaluate the modified Bessel functions at the position of the unperturbed interface R_0 .

In line with the ansatz for the pressure a perturbation ansatz for the velocity is chosen,

$$\mathbf{v} = \mathbf{v}_0 + \delta \mathbf{v}, \quad (\text{C } 10)$$

with \mathbf{v}_0 the velocity of the unperturbed jet, which vanishes in the co-moving frame. The motion of the interface is governed by the kinematic boundary condition

$$\frac{\partial R}{\partial t} + v_z \frac{\partial R}{\partial z} = \delta v_r(r = R). \quad (\text{C } 11)$$

The velocity perturbation is linked to the pressure by the linearised Euler equation (B 25), its r -component in cylindrical coordinates reads

$$\frac{\partial \delta v_r}{\partial t} = -\frac{1}{\rho} \frac{\partial p}{\partial r}. \quad (\text{C } 12)$$

Combination of the derivative with respect to time t of (C 11), where in linearised form the second term on the left-hand side vanishes, and (C 12) gives

$$\frac{\partial^2 R}{\partial t^2} = -\frac{1}{\rho} \frac{\partial p}{\partial r} \Big|_{r=R}. \quad (\text{C } 13)$$

Inserting the ansatz for the interface radius (2.1) on the left and the one for the pressure (C 2) on the right-hand side of (C 13) and using the fact that $I_0'(x) = I_1(x)$ leads to

$$\omega^2 = -\frac{k}{\rho \epsilon_0} \delta \bar{p} I_1(kr) \Big|_{r=R}. \quad (\text{C } 14)$$

Evaluating the modified Bessel functions at R_0 and inserting (C 9) finally yields the dispersion relation for an ideal fluid jet without ambient fluid

$$\omega^2 = \frac{\gamma^\phi}{\rho R_0^3} k R_0 \left[1 - \frac{\gamma^z}{\gamma^\phi} (k R_0)^2 \right] \frac{I_1(k R_0)}{I_0(k R_0)}. \quad (\text{C } 15)$$

This dispersion relation is shown in figures 11(a)–11(c) for different values of the anisotropy ratio. The general shape of the dispersion relation and the changes due to variation of the anisotropy ratio are similar to that discussed in § 3.2.

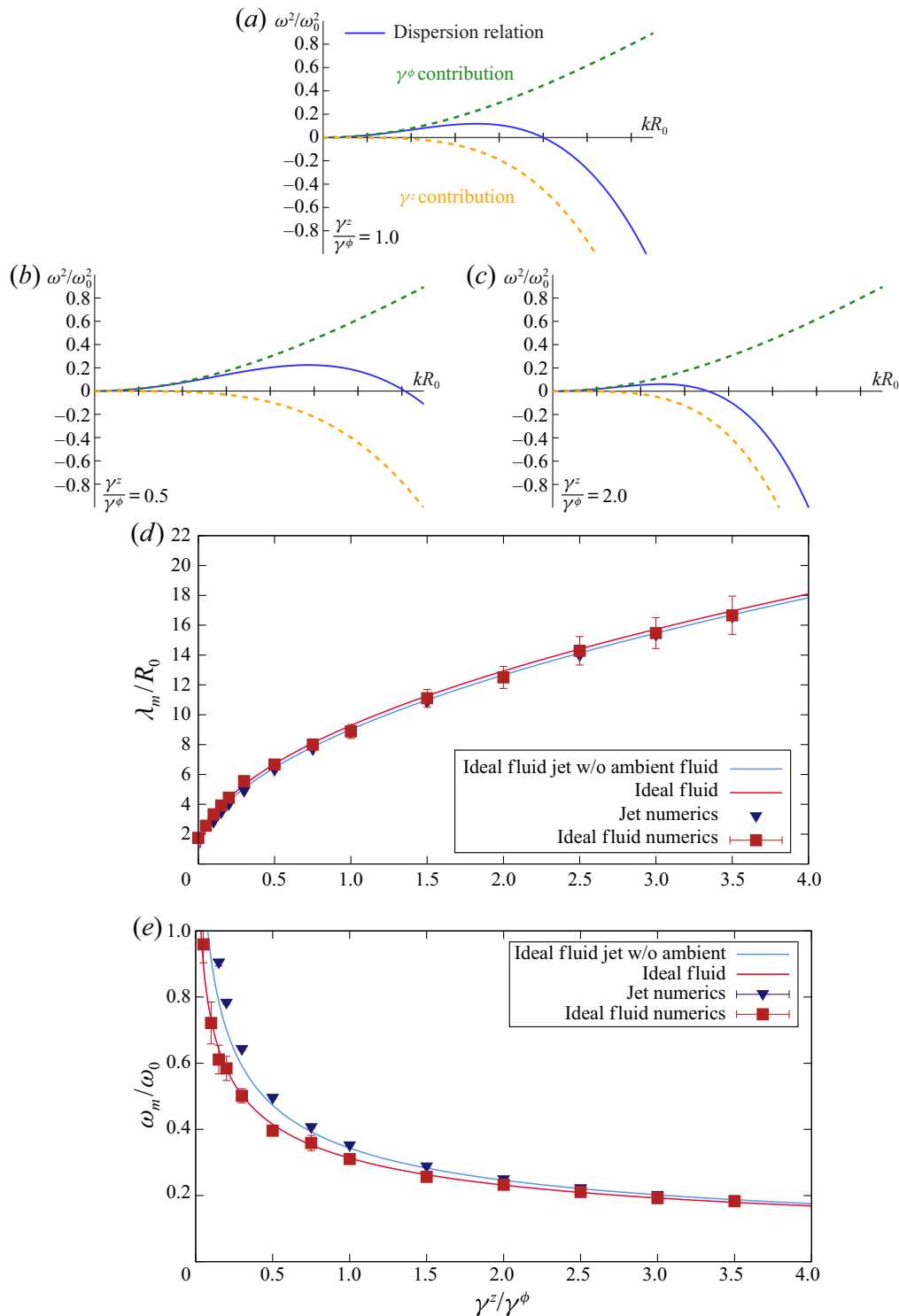


FIGURE 11. Results for an ideal fluid jet without ambient fluid. The dispersion relation for an ideal fluid jet without ambient fluid with $\rho^o = 0$ is shown for (a) isotropic interfacial tension $\gamma^z/\gamma^\phi = 1.0$ and for anisotropic interfacial tension with (b) $\gamma^z/\gamma^\phi = 0.5$ and (c) $\gamma^z/\gamma^\phi = 2.0$. We distinguish the contributions from γ^ϕ (green) and γ^z (orange). Depending on the tension anisotropy (d) wavelength and (e) growth rate (blue curves) are shown in comparison with the results presented above in figures 4(b) and 6(b) for an ideal fluid (red curves). While the wavelength is similar to the case of an ideal fluid, for small and intermediate anisotropy ratios the growth rate is visibly larger.

In figures 11(d) and 11(e) dominant wavelength and corresponding maximal growth rate for the ideal fluid jet without ambient fluid are drawn as blue lines. For isotropic tension $\gamma^z/\gamma^\phi = 1$ we recover the well-known result (Rayleigh 1878; Drazin & Reid 2004; Eggers & Villermaux 2008) for the dominant wavelength of $k_m R_0 \approx 0.697$ (i.e. $\lambda_m/R_0 \approx 9.015$). Simulations for the ideal fluid jet without ambient fluid based on the small- k approximation are included as blue triangles. They agree well with the analytical results. For comparison the curves and simulations for the ideal fluid from 4(b) and 6(b) are shown as red lines/squares. In figure 11(d) we see that the curves are quite similar, i.e. the dominant wavelength changes only slightly when there is no ambient fluid. The corresponding growth rate is significantly influenced by an additional ambient ideal fluid at small and intermediate tension anisotropy, while the influence vanishes for large anisotropy as we can observe in figure 11(e).

Appendix D. Long-wavelength description

D.1. Dynamic equations for jet simulations

In the following, we derive the fluid equations of motion in long-wavelength (or small- k) approximation (Weber 1931; Eggers & Dupont 1994; García & Castellanos 1994; Eggers 1997) for a fluid jet without ambient fluid, i.e. $\eta^o = \rho^o = 0$. The final equations are then solved numerically as detailed below to obtain the dynamic nonlinear evolution of an ideal jet interface in absence of an ambient fluid. The perturbation of the interface is considered to have a wavelength considerably longer than the radius of the liquid jet. Therefore, a typical radial length is small compared to a typical axial length, i.e. terms with a dependency on the radial position enter with a factor $\hat{\epsilon} \ll 1$ (Eggers & Villermaux 2008). The axial velocity is expanded in radial direction using a Taylor series and considering axisymmetry

$$v_z(z, r) = v_0(z) + v_2(z)\hat{\epsilon}^2 r^2 + O(r^4). \quad (\text{D } 1)$$

From the continuity equation (2.6) one can obtain the radial velocity

$$v_r = -\frac{1}{2}v_0'\hat{\epsilon}r - \frac{1}{4}v_2'\hat{\epsilon}^3 r^3 + O(r^5), \quad (\text{D } 2)$$

where a prime denotes the partial derivative with respect to z . Similarly, we consider an expansion of the pressure with respect to the radial position

$$p(z, r) = p_0(z) + p_2\hat{\epsilon}^2 r^2 + O(r^4). \quad (\text{D } 3)$$

We further calculate the force from the inner fluid of the jet onto the interface using the outward unit normal vector on the interface given by

$$\mathbf{n} = \frac{1}{\sqrt{1 + R^2}} (\hat{\mathbf{e}}_r - R'\hat{\mathbf{e}}_z), \quad (\text{D } 4)$$

with $\hat{\mathbf{e}}_z$ the unit vector along the jet axis. The normal component of the force is given by the projection of the three-dimensional fluid stress twice onto the normal vector

(Chandrasekharaiah & Debnath 2014)

$$-\mathbf{n} \cdot \boldsymbol{\sigma} \cdot \mathbf{n} \simeq +p_0 + \eta v_0' \quad (\text{D } 5)$$

and the tangential force evaluated at the interface $r = R$ is

$$-\mathbf{t} \cdot \boldsymbol{\sigma} \cdot \mathbf{n} \simeq -\eta \left(2Rv_2 - \frac{1}{2}Rv_0'' - 3v_0'R' \right), \quad (\text{D } 6)$$

with \mathbf{t} pointing along the interface which is perpendicular to \mathbf{n} in the plane. Combining the force from the internal fluid and the force due to anisotropic interfacial tension the pressure at the interface follows

$$p_0 = \gamma^\phi \left(\frac{1}{R} - \frac{\gamma^z}{\gamma^\phi} R'' \right) - \eta v_0'. \quad (\text{D } 7)$$

In addition, we obtain from the tangential force across the interface

$$v_2 = \frac{1}{4}v_0'' + \frac{3}{2}\frac{1}{R}v_0'R'. \quad (\text{D } 8)$$

The Navier–Stokes equation determining the fluid dynamics finally becomes

$$\partial_t v_0 + v_0 v_0' = -\frac{1}{\rho} \gamma^\phi \left(\frac{1}{R} - \frac{\gamma^z}{\gamma^\phi} R'' \right)' + \frac{1}{\rho} \eta v_0'' + \nu (4v_2 + v_0'). \quad (\text{D } 9)$$

The kinematic boundary condition is also considered up to terms in lowest order with respect to $\hat{\epsilon}$, which gives the dynamics of the interface

$$\partial_t R = -v_0 R' - \frac{1}{2} R v_0'. \quad (\text{D } 10)$$

The closed system of coupled equations (D 9) and (D 10) can then be solved numerically. We consider a one-dimensional interface which is discretised by 220 points. We initially perturb the interface according to (D 11) with $\epsilon_0 = 0.001$ and initialise the velocity profile $v_0(z)$ with zero. Derivatives of the radius and velocity profile are calculated at each time step using quintic splines. This allows us to calculate (D 8) and the right-hand side of (D 9) and (D 10). For solving the equations a three step Runge–Kutta algorithm is used with a typical time step of $\Delta t = 0.00025$.

D.2. Dispersion relation in the long-wavelength description

The aim of the following discussion is to derive a simple, analytical equation for the wavenumber and growth rate of the most unstable perturbation mode. This we use to prescribe the dominant mode in small- k simulations of a fluid jet with varying Ohnesorge

number. As ansatz for the periodic interface perturbation growing in time we use

$$R(z, t) = R_0 + R_0 \epsilon_0 \cos(kz) \exp(\omega t) \quad (\text{D } 11)$$

and for the velocity

$$v_0 = \hat{v} \epsilon_0 \sin(kz) \exp(\omega t). \quad (\text{D } 12)$$

Inserting the ansatz into the kinematic boundary condition (D 10) leads to

$$\hat{v} = -2 \frac{\omega}{k} \quad (\text{D } 13)$$

in linear order in ϵ_0 . The Navier–Stokes equation leads to

$$\omega \hat{v} = -\frac{\gamma^\phi}{\rho} \left(\frac{k}{R_0} - \frac{\gamma^z}{\gamma^\phi} k^3 R_0 \right) - 3 \frac{\eta}{\rho} k^2 \hat{v}. \quad (\text{D } 14)$$

Combining both equations results in the dispersion relation for a fluid jet without ambient fluid in the small- k approximation

$$\omega^2 = \frac{1}{2} \frac{\gamma^\phi}{\rho R_0^3} \left((kR_0)^2 - \frac{\gamma^z}{\gamma^\phi} (kR_0)^4 \right) - 3 \frac{\eta}{\rho R_0^2} (kR_0)^2 \omega, \quad (\text{D } 15)$$

which now depends on tension anisotropy, fluid density and viscosity.

The dispersion relation in the small- k approximation (D 15) can be solved analytically for the position of the maximum, i.e. the dominant mode

$$(kR_0)_{max} = \frac{1}{\sqrt{2 \frac{\gamma^z}{\gamma^\phi} \mp 3 \sqrt{2 \frac{\gamma^z}{\gamma^\phi} Oh}}} \quad (\text{D } 16)$$

and the dominant growth rate is determined by

$$\omega_m^2 = \frac{1}{2} \frac{\gamma^\phi}{\rho R_0^3} \left(\frac{1}{2 \frac{\gamma^z}{\gamma^\phi} \mp 3 \sqrt{2 \frac{\gamma^z}{\gamma^\phi} Oh}} - \frac{\frac{\gamma^z}{\gamma^\phi}}{\left(2 \frac{\gamma^z}{\gamma^\phi} \mp 3 \sqrt{2 \frac{\gamma^z}{\gamma^\phi} Oh} \right)^2} \right) - 3 \frac{\eta}{\rho R_0^2} \frac{\omega_m}{2 \frac{\gamma^z}{\gamma^\phi} \mp 3 \sqrt{2 \frac{\gamma^z}{\gamma^\phi} Oh}}. \quad (\text{D } 17)$$

In the limit of an ideal fluid jet, i.e. for vanishing viscosity and vanishing Ohnesorge number we obtain for the maximum growth rate

$$\omega_m^2 = \frac{1}{8} \frac{\gamma^\phi}{\rho R_0^3} \frac{1}{\gamma^z}, \quad (\text{D } 18)$$

which approximates the blue curve in figure 11(e). We observe that in the framework of the small- k approximation the dominant growth rate scales with the tension anisotropy to

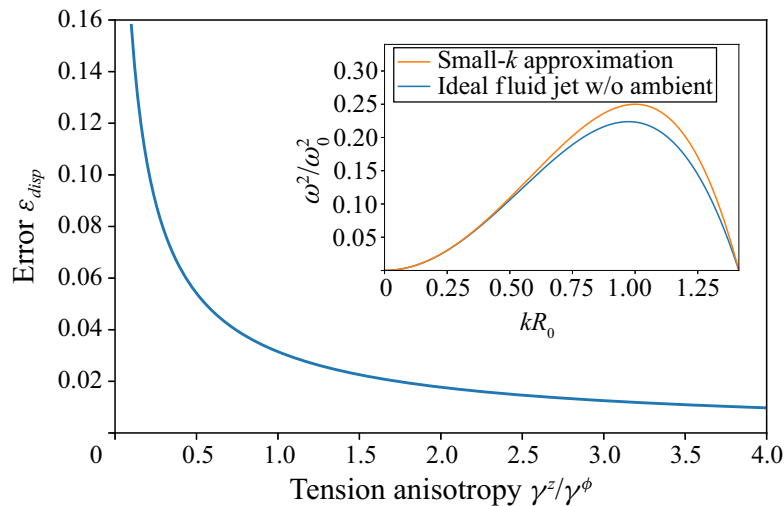


FIGURE 12. Comparison of the small- k approximation with the analytical results. The inset shows the dispersion relation obtained by the small- k approximation (orange line) compared to the analytically obtained accurate dispersion relation (C 15) for an ideal fluid jet without ambient fluid (blue line) for a tension anisotropy of $\gamma^z/\gamma^\phi = 0.5$. Systematically varying the tension anisotropy shows that the error (D 19) between exact theory and approximation strongly decreases towards large tension anisotropy. Therefore, the small- k approximation is less accurate for small anisotropy, but becomes a very accurate approximation for large anisotropy.

the power of minus one half. Analogously, the dominant wavelength in the limit of an ideal fluid jet scales with the square root of the tension anisotropy, as can be seen from (D 16). We note that the full dispersion relation with contributions of the Bessel functions leads to deviations from this scaling behaviour.

In figure 12 we compare the full dispersion relation obtained analytically for an ideal fluid jet without ambient fluid (C 15) to the one obtained in the small- k limit (D 15) for vanishing viscosity. The inset shows the two dispersion relations for an anisotropy ratio of $\gamma^z/\gamma^\phi = 0.5$. We analyse the deviation of the approximation quantitatively by calculating the squared difference averaged over all sample points relative to the maximum of the dispersion relation

$$\epsilon_{disp} = \sqrt{\frac{\langle (\omega^2 - \omega_{ska}^2)^2 \rangle}{\omega_{max}^4}} \quad (\text{D } 19)$$

as the error. We observe a strong increase of the error towards small anisotropy. Nevertheless, the deviation for $\gamma^z/\gamma^\phi = 0.1$ is approximately 15% and thus the approximation still reasonable accurate. Increasing the anisotropy results in the deviation approaching zero, i.e. the approximation becomes perfectly accurate towards large tension anisotropy.

Appendix E. General dispersion relation

We use the insights from the detailed derivations of the dispersion relations in the appendices B and C to obtain the modifications due to anisotropic interfacial tension of more general dispersion relations. From the dispersion relation in presence of an ambient Stokes fluid (3.1) or an ambient ideal fluid (3.2) we follow Tomotika (1935) and introduce a general density $N_\rho = \rho/\rho^o$ and viscosity contrast $N_\eta = \eta/\eta^o$ between inner and outer fluid. We use the following abbreviations concerning the wavenumber and the modified

Bessel functions

$$y^2 = (kR_0)^2 + \omega \frac{\rho}{\eta} R_0^2 \quad F(x) = x \frac{I_0(x)}{I_1(x)} \quad G(x) = x \frac{K_0(x)}{K_1(x)}, \quad (\text{E } 1a-c)$$

where an additional superscript o indicates definition with the corresponding parameters of the outer fluid. The dispersion relation in presence of an ambient medium with a density and viscosity contrast (Tomotika 1935) including anisotropic interfacial tension then takes the form

$$\begin{aligned} & \frac{\rho^{o2} R_0^4}{\eta^{o2}} \omega^2 N_\rho [F(kR_0)F(y^o R_0) + G(kR_0)G(yR_0)] - 4(kR_0)^4 (1 - N_\eta)^2 F(y^o R_0)G(yR_0) \\ & + \left(2(kR_0)^2 (N_\eta - 1) + \omega N_\rho \frac{\rho R_0^2}{\eta^o} \right)^2 F(kR_0)G(yR_0) \\ & + \left(2(kR_0)^2 (N_\eta - 1) - \omega \frac{\rho^o R_0^2}{\eta^o} \right)^2 F(y^o R_0)G(kR_0) \\ & - \left(2(kR_0)^2 (N_\eta - 1) + \omega \frac{\rho^o R_0^2}{\eta^o} (N_\rho - 1) \right)^2 F(kR_0)G(kR_0) \\ & + (kR_0)^2 \left(\frac{\gamma^\phi \rho^o R_0}{\eta^{o2}} \left(1 - \frac{\gamma^z}{\gamma^\phi} k^2 R_0^2 \right) + 2\omega \frac{\rho^o R_0^2}{\eta^o} (N_\eta - 1) \right) \\ & \quad [F(kR_0) - F(y^o R_0) + N_\rho G(kR_0) - N_\rho G(yR_0)] \\ & = 0. \end{aligned} \quad (\text{E } 2)$$

This general dispersion relation includes the Stokes fluid in (3.1) as well as the dispersion relation for an ideal fluid (3.2) in the corresponding limits. These are obtained by first considering identical fluids inside and outside, i.e. $N_\rho = 1$ and $N_\eta = 1$. Second, for the Stokes fluid an expansion of the Bessel functions in the limit of small density is necessary, while for the ideal fluid the viscosity is set to zero and identities for the Bessel functions are used to rewrite the remaining terms.

Starting from the dispersion relation for an ideal fluid jet without ambient fluid (C 15) we follow Chandrasekhar (1961) to obtain the general dispersion relation for a jet in a passive ambient medium. The general dispersion relation including tension anisotropy in this case has the form

$$\begin{aligned} & 2(kR_0)^2 \omega \frac{\rho}{\eta} R_0^2 (2F(kR_0) - 1) + 4(kR_0)^4 (F(kR_0) - F(y)) + \omega^2 \frac{\rho^2}{\eta^2} R_0^4 F(kR_0) \\ & - \frac{\gamma^\phi \rho R_0}{\eta^2} (kR_0)^2 \left(1 - \frac{\gamma^z}{\gamma^\phi} (kR_0)^2 \right) = 0. \end{aligned} \quad (\text{E } 3)$$

This contains the dispersion relation of an ideal fluid jet in (C 15) in the limit of negligible viscosity.

REFERENCES

- AIDUN, C. K. & CLAUSEN, J. R. 2010 Lattice-Boltzmann method for complex flows. *Annu. Rev. Fluid Mech.* **42** (1), 439–472.

- ALBERTS, B., JOHNSON, A., LEWIS, J., RAFF, M., ROBERTS, K. & WALTER, P. 2007 *Molecular Biology of the Cell with CD*, 5th edn. Garland Science.
- ALSTRØM, P., EGUÍLUZ, V. M., COLDING-JØRGENSEN, M., GUSTAFSSON, F. & HOLSTEIN-RATHLOU, N.-H. 1999 Instability and ‘sausage-string’ appearance in blood vessels during high blood pressure. *Phys. Rev. Lett.* **82** (9), 1995.
- ANNA, S. L. 2016 Droplets and bubbles in microfluidic devices. *Annu. Rev. Fluid Mech.* **48** (1), 285–309.
- ARNOLD, A., LENZ, O., KESSELHEIM, S., WEEBER, R., FAHRENBERGER, F., ROEHM, D., KOŠOVAN, P. & HOLM, C. 2013 ESPResSo 3.1: molecular dynamics software for coarse-grained models. In *Meshfree Methods for Partial Differential Equations VI*, pp. 1–23. Springer.
- ASHGRIZ, N. & MASHAYEK, F. 1995 Temporal analysis of capillary jet breakup. *J. Fluid Mech.* **291**, 163–190.
- BÄCHER, C., BENDER, M. & GEKLE, S. 2020 Flow-accelerated platelet biogenesis is due to an elasto-hydrodynamic instability. *Proc. Natl Acad. Sci. USA* **117** (32), 18969–18976.
- BÄCHER, C. & GEKLE, S. 2019 Computational modeling of active deformable membranes embedded in three-dimensional flows. *Phys. Rev. E* **99** (6), 062418.
- BÄCHER, C., GRAESSEL, K. & GEKLE, S. 2021 Rayleigh–Plateau instability of anisotropic interfaces. Part 2. Limited instability of elastic interfaces. *J. Fluid Mech.* **xxx**, Ax.
- BÄCHER, C., KIHM, A., SCHRACK, L., KAESTNER, L., LASCHKE, M. W., WAGNER, C. & GEKLE, S. 2018 Antimargination of microparticles and platelets in the vicinity of branching vessels. *Biophys. J.* **115** (2), 411–425.
- BÄCHER, C., SCHRACK, L. & GEKLE, S. 2017 Clustering of microscopic particles in constricted blood flow. *Phys. Rev. Fluids* **2** (1), 013102.
- BAR-ZIV, R. & MOSES, E. 1994 Instability and ‘pearling’ states produced in tubular membranes by competition of curvature and tension. *Phys. Rev. Lett.* **73** (10), 1392–1395.
- BAR-ZIV, R., MOSES, E. & NELSON, P. 1998 Dynamic excitations in membranes induced by optical tweezers. *Biophys. J.* **75** (1), 294–320.
- BAR-ZIV, R., TLUSTY, T. & MOSES, E. 1997 Critical dynamics in the pearling instability of membranes. *Phys. Rev. Lett.* **79** (6), 1158–1161.
- BAR-ZIV, R., TLUSTY, T., MOSES, E., SAFRAN, S. A. & BERSHADSKY, A. 1999 Pearling in cells: a clue to understanding cell shape. *Proc. Natl Acad. Sci. USA* **96** (18), 10140–10145.
- BARTHÈS-BIESEL, D. 2016 Motion and deformation of elastic capsules and vesicles in flow. *Annu. Rev. Fluid Mech.* **48** (1), 25–52.
- BEHRNDT, M., SALBREUX, G., CAMPINHO, P., HAUSCHILD, R., OSWALD, F., ROENSCH, J., GRILL, S. W. & HEISENBERG, C.-P. 2012 Forces driving epithelial spreading in zebrafish gastrulation. *Science* **338** (6104), 257–260.
- BERTHOUMIEUX, H., MAÎTRE, J.-L., HEISENBERG, C.-P., PALUCH, E. K., JÜLICHER, F. & SALBREUX, G. 2014 Active elastic thin shell theory for cellular deformations. *New J. Phys.* **16** (6), 065005.
- BLACKWELL, R., SWEEZY-SCHINDLER, O., BALDWIN, C., HOUGH, L. E., GLASER, M. A. & BETTERTON, M. D. 2016 Microscopic origins of anisotropic active stress in motor-driven nematic liquid crystals. *Soft Matt.* **12** (10), 2676–2687.
- BOEDEC, G., JAEGER, M. & LEONETTI, M. 2014 Pearling instability of a cylindrical vesicle. *J. Fluid Mech.* **743**, 262–279.
- BOUSSINESQ, M. J. 1913 The application of the formula for surface viscosity to the surface of a slowly falling droplet in the midst of a large unlimited amount of fluid which is at rest and possesses a smaller specific gravity. *Ann. Chim. Phys.* **29** (349), 357–364.
- CALLAN-JONES, A. C., RUPRECHT, V., WIESER, S., HEISENBERG, C. P. & VOITURIEZ, R. 2016 Cortical flow-driven shapes of nonadherent cells. *Phys. Rev. Lett.* **116** (2), 028102.
- CAMPELO, F. & HERNÁNDEZ-MACHADO, A. 2007 Model for curvature-driven pearling instability in membranes. *Phys. Rev. Lett.* **99** (8), 088101.
- CHANDRASEKHAR, S. 1961 *Hydrodynamic and Hydromagnetic Stability*. Dover Publications.
- CHANDRASEKHARIAH, D. S. & DEBNATH, L. 2014 *Continuum Mechanics*. Elsevier.
- CHANDRASEKHARIAH, D. S. & DEBNATH, L. 1994 *Continuum Mechanics*. Academic Press.

- CHUGH, P., CLARK, A. G., SMITH, M. B., CASSANI, D. A. D., DIERKES, K., RAGAB, A., ROUX, P. P., CHARRAS, G., SALBREUX, G. & PALUCH, E. K. 2017 Actin cortex architecture regulates cell surface tension. *Nat. Cell Biol.* **19** (6), 689–697.
- CHUGH, P. & PALUCH, E. K. 2018 The actin cortex at a glance. *J. Cell Sci.* **131** (14), jcs186254.
- DIMOVA, R., ARANDA, S., BEZLYEPKINA, N., NIKOLOV, V., RISKE, K. A. & LIPOWSKY, R. 2006 A practical guide to giant vesicles. Probing the membrane nanoregime via optical microscopy. *J. Phys.: Condens. Matter* **18** (28), S1151–S1176.
- DMITRIEFF, S., ALSINA, A., MATHUR, A. & NÉDÉLEC, F. J. 2017 Balance of microtubule stiffness and cortical tension determines the size of blood cells with marginal band across species. *Proc. Natl Acad. Sci. USA* **114**, 4418–4423.
- DRAZIN, P. G. & REID, W. H. 2004 *Hydrodynamic Stability*. Cambridge University Press.
- EGGERS, J. 1997 Nonlinear dynamics and breakup of free-surface flows. *Rev. Mod. Phys.* **69**, 865–930.
- EGGERS, J. & DUPONT, T. F. 1994 Drop formation in a one-dimensional approximation of the Navier–Stokes equation. *J. Fluid Mech.* **262**, 205–221.
- EGGERS, J. & VILLERMAUX, E. 2008 Physics of liquid jets. *Rep. Prog. Phys.* **71** (3), 036601.
- EMSELLEM, V., CARDOSO, O. & TABELING, P. 1998 Vesicle deformation by microtubules: a phase diagram. *Phys. Rev. E* **58** (4), 4807–4810.
- ERDELYI, A., MAGNUS, W., OBERHETTINGER, F. & TRICOMI, F. 1954 *Tables of Integral Transforms*, vol. 2. McGraw Hill.
- GARCÍA, F. J. & CASTELLANOS, A. 1994 One-dimensional models for slender axisymmetric viscous liquid jets. *Phys. Fluids* **6** (8), 2676–2689.
- GEKLE, S. 2016 Strongly accelerated margination of active particles in blood flow. *Biophys. J.* **110** (2), 514–520.
- GOLDSTEIN, R. E., NELSON, P., POWERS, T. & SEIFERT, U. 1996 Front propagation in the pearling instability of tubular vesicles. *J. Phys. II* **6** (5), 767–796.
- GONZALEZ-RODRIGUEZ, D., SART, S., BABATAHERI, A., TARESTE, D., BARAKAT, A. I., CLANET, C. & HUSSON, J. 2015 Elastocapillary instability in mitochondrial fission. *Phys. Rev. Lett.* **115** (8), 088102.
- GRADSHTEĪN, I. S., RYZHIK, I. M. & JEFFREY, A. 2007 *Table of Integrals, Series, and Products*, 7th edn. Academic Press.
- GREEN, A. E. & ZERNA, W. 1954 *Theoretical Elasticity*. Clarendon.
- GUCKENBERGER, A. & GEKLE, S. 2018 A boundary integral method with volume-changing objects for ultrasound-triggered margination of microbubbles. *J. Fluid Mech.* **836**, 952–997.
- GUCKENBERGER, A., SCHRAML, M. P., CHEN, P. G., LEONETTI, M. & GEKLE, S. 2016 On the bending algorithms for soft objects in flows. *Comput. Phys. Commun.* **207**, 1–23.
- GUGLIETTA, F., BEHR, M., BIFERALE, L., FALCUCCI, G. & SBRAGAGLIA, M. 2020 On the effects of membrane viscosity on transient red blood cell dynamics. [arXiv:2004.04109](https://arxiv.org/abs/2004.04109).
- GURSKI, K. F. & MCFADDEN, G. B. 2003 The effect of anisotropic surface energy on the Rayleigh instability. *Proc. R. Soc. Lond. A* **459** (2038), 2575–2598.
- HAIJLOO, A., RAMAMOHAN, T. R. & SLATTERY, J. C. 1987 Effect of interfacial viscosities on the stability of a liquid thread. *J. Colloid Interface Sci.* **117** (2), 384–393.
- HANNEZO, E., PROST, J. & JOANNY, J.-F. 2012 Mechanical instabilities of biological tubes. *Phys. Rev. Lett.* **109** (1), 018101.
- JELERČIČ, U. & GOV, N. S. 2015 Pearling instability of membrane tubes driven by curved proteins and actin polymerization. *Phys. Biol.* **12** (6), 066022.
- JÜLICHER, F., GRILL, S. W. & SALBREUX, G. 2018 Hydrodynamic theory of active matter. *Rep. Prog. Phys.* **81** (7), 076601.
- KANTSLER, V., SEGRE, E. & STEINBERG, V. 2008 Critical dynamics of vesicle stretching transition in elongational flow. *Phys. Rev. Lett.* **101** (4), 048101.
- KEBER, F. C., LOISEAU, E., SANCHEZ, T., DECAMP, S. J., GIOMI, L., BOWICK, M. J., MARCHETTI, M. C., DOGIC, Z. & BAUSCH, A. R. 2014 Topology and dynamics of active nematic vesicles. *Science* **345**, 1135–1139.
- KÖSTER, D. V. & MAYOR, S. 2016 Cortical actin and the plasma membrane: inextricably intertwined. *Curr. Opin. Cell Biol.* **38**, 81–89.

- KRÜGER, T., KUSUMAATMAJA, H., KUZMIN, A., SHARDT, O., SILVA, G. & VIGGEN, E. M. 2016 *The Lattice Boltzmann Method: Principles and Practice*. Springer.
- KRUSE, K., JOANNY, J. F., JÜLICHER, F., PROST, J. & SEKIMOTO, K. 2005 Generic theory of active polar gels: a paradigm for cytoskeletal dynamics. *Eur. Phys. J. E* **16** (1), 5–16.
- LAFRANCE, P. 1975 Nonlinear breakup of a laminar liquid jet. *Phys. Fluids* **18** (4), 428–432.
- LIMBACH, H. J., ARNOLD, A., MANN, B. A. & HOLM, C. 2006 ESPResSo—an extensible simulation package for research on soft matter systems. *Comput. Phys. Commun.* **174** (9), 704–727.
- MANDRYCKY, C., WANG, Z., KIM, K. & KIM, D.-H. 2016 3D bioprinting for engineering complex tissues. *Biotechnol. Adv.* **34**, 422–434.
- MANSOUR, N. N. & LUNDGREN, T. S. 1990 Satellite formation in capillary jet breakup. *Phys. Fluids A* **2** (7), 1141–1144.
- MARCHETTI, M. C., JOANNY, J. F., RAMASWAMY, S., LIVERPOOL, T. B., PROST, J., RAO, M. & SIMHA, R. A. 2013 Hydrodynamics of soft active matter. *Rev. Mod. Phys.* **85** (3), 1143–1189.
- MARTÍNEZ-CALVO, A., RIVERO-RODRÍGUEZ, J., SCHEID, B. & SEVILLA, A. 2020 Natural break-up and satellite formation regimes of surfactant-laden liquid threads. *J. Fluid Mech.* **883**, A35.
- MARTÍNEZ-CALVO, A. & SEVILLA, A. 2018 Temporal stability of free liquid threads with surface viscoelasticity. *J. Fluid Mech.* **846**, 877–901.
- MAYER, M., DEPKEN, M., BOIS, J. S., JÜLICHER, F. & GRILL, S. W. 2010 Anisotropies in cortical tension reveal the physical basis of polarizing cortical flows. *Nature* **467** (7315), 617–621.
- MÉNAGER, C., MEYER, M., CABUIL, V., CEBERS, A., BACRI, J.-C. & PERZYNSKI, R. 2002 Magnetic phospholipid tubes connected to magnetoliposomes: pearling instability induced by a magnetic field. *Eur. Phys. J. E* **7** (4), 325–337.
- MIETKE, A., JEMSEENA, V., KUMAR, K. V., SBALZARINI, I. F. & JÜLICHER, F. 2019a Minimal model of cellular symmetry breaking. *Phys. Rev. Lett.* **123**, 188101.
- MIETKE, A., JÜLICHER, F. & SBALZARINI, I. F. 2019b Self-organized shape dynamics of active surfaces. *Proc. Natl Acad. Sci. USA* **116** (1), 29–34.
- MITTAL, R. & IACCARINO, G. 2005 Immersed boundary methods. *Annu. Rev. Fluid Mech.* **37** (1), 239–261.
- MORA, S., PHOU, T., FROMENTAL, J.-M., PISMEN, L. M. & POMEAU, Y. 2010 Capillarity driven instability of a soft solid. *Phys. Rev. Lett.* **105** (21), 214301.
- MOUNTRAKIS, L., LORENZ, E. & HOEKSTRA, A. G. 2017 Revisiting the use of the immersed-boundary lattice-Boltzmann method for simulations of suspended particles. *Phys. Rev. E* **96** (1), 013302.
- MURRELL, M., OAKES, P. W., LENZ, M. & GARDEL, M. L. 2015 Forcing cells into shape: the mechanics of actomyosin contractility. *Nat. Rev. Mol. Cell Biol.* **16** (8), 486–498.
- NARSIMHAN, V., SPANN, A. P. & SHAQFEH, E. S. G. 2015 Pearling, wrinkling, and buckling of vesicles in elongational flows. *J. Fluid Mech.* **777**, 1–26.
- NEEDLEMAN, D. & DOGIC, Z. 2017 Active matter at the interface between materials science and cell biology. *Nat. Rev. Mater.* **2** (9), 17048.
- NELSON, P., POWERS, T. & SEIFERT, U. 1995 Dynamical theory of the pearling instability in cylindrical vesicles. *Phys. Rev. Lett.* **74** (17), 3384–3387.
- DEN OTTER, W. K. & SHKULIPA, S. A. 2007 Intermonolayer friction and surface shear viscosity of lipid bilayer membranes. *Biophys. J.* **93** (2), 423–433.
- PAL, A. & KHAKHAR, D. V. 2019 Breakage of vesicles in a simple shear flow. *Soft Matt.* **15** (9), 1979–1987.
- PESKIN, C. S. 2002 The immersed boundary method. *Acta Numerica* **11**, 479–517.
- PLATEAU, J. A. F. 1873 *Statique Expérimentale et Théorique Des Liquides Soumis Aux Seules Forces Moléculaires*, vol. 2. Gauthier-Villars.
- PLEINES, I., DUTTING, S., CHERPOKOVA, D., ECKLY, A., MEYER, I., MOROWSKI, M., KROHNE, G., SCHULZE, H., GACHET, C., DEBILI, N., *et al.* 2013 Defective tubulin organization and proplatelet formation in murine megakaryocytes lacking Rac1 and Cdc42. *Blood* **122** (18), 3178–3187.
- POULARIKAS, A. D. (Ed.) 2000 *The Transforms and Applications Handbook*, 2nd edn. The Electrical Engineering Handbook Series. CRC Press.
- POWERS, T. R. 2010 Dynamics of filaments and membranes in a viscous fluid. *Rev. Mod. Phys.* **82** (2), 1607–1631.

- POWERS, T. R., HUBER, G. & GOLDSTEIN, R. E. 2002 Fluid-membrane tethers: minimal surfaces and elastic boundary layers. *Phys. Rev. E* **65** (4), 041901.
- POZRIKIDIS, C. 2001 Interfacial dynamics for stokes flow. *J. Comput. Phys.* **169** (2), 250–301.
- PROST, J., JÜLICHER, F. & JOANNY, J.-F. 2015 Active gel physics. *Nat. Phys.* **11** (2), 111–117.
- RAUZI, M., VERANT, P., LECUIT, T. & LENNE, P.-F. 2008 Nature and anisotropy of cortical forces orienting *Drosophila* tissue morphogenesis. *Nat. Cell Biol.* **10** (12), 1401–1410.
- RAYLEIGH, LORD 1878 On the instability of jets. *Proc. Lond. Math. Soc.* **1** (1), 4–13.
- RAYLEIGH, LORD 1892 XVI. On the instability of a cylinder of viscous liquid under capillary force. *London Edinburgh Philos. Mag. J. Sci.* **34** (207), 145–154.
- REYMANN, A.-C., BOUJEMAA-PATERSKI, R., MARTIEL, J.-L., GUERIN, C., CAO, W., CHIN, H. F., DE LA CRUZ, E. M., THERY, M. & BLANCHOIN, L. 2012 Actin network architecture can determine myosin motor activity. *Science* **336** (6086), 1310–1314.
- REYMANN, A.-C., STANISCIJA, F., ERZBERGER, A., SALBREUX, G. & GRILL, S. W. 2016 Cortical flow aligns actin filaments to form a furrow. *eLife* **5**, e17807.
- ROEHM, D. & ARNOLD, A. 2012 Lattice Boltzmann simulations on GPUs with ESPResSo. *Eur. Phys. J.: Spec. Top.* **210** (1), 89–100.
- RUTLAND, D. F. & JAMESON, G. J. 1970 Theoretical prediction of the sizes of drops formed in the breakup of capillary jets. *Chem. Engng Sci.* **25** (11), 1689–1698.
- SALBREUX, G. & JÜLICHER, F. 2017 Mechanics of active surfaces. *Phys. Rev. E* **96** (3), 032404.
- SALBREUX, G., PROST, J. & JOANNY, J. F. 2009 Hydrodynamics of cellular cortical flows and the formation of contractile rings. *Phys. Rev. Lett.* **103** (5), 058102.
- SANBORN, J., OGLECKA, K., KRAUT, R. S. & PARIKH, A. N. 2013 Transient pearling and vesiculation of membrane tubes under osmotic gradients. *Faraday Discuss.* **161**, 167–176.
- SCRIVEN, L. E. 1960 Dynamics of a fluid interface equation of motion for Newtonian surface fluids. *Chem. Engng Sci.* **12** (2), 98–108.
- SEIFERT, U. 1997 Configurations of fluid membranes and vesicles. *Adv. Phys.* **46**, 13–137.
- SINHA, K. P., GADKARI, S. & THAOKAR, R. M. 2013 Electric field induced pearling instability in cylindrical vesicles. *Soft Matt.* **9** (30), 7274–7293.
- SNYDER, J., RIN SON, A. E., HAMID, Q., WANG, C., LUI, Y. & SUN, W. 2015 Mesenchymal stem cell printing and process regulated cell properties. *Biofabrication* **7**, 044106.
- SPRENGER, A. R., SHAIK, V. A., ARDEKANI, A. M., LISICKI, M., MATHIJSSSEN, A. J. T. M., GUZMÁN-LASTRA, F., LÖWEN, H., MENZEL, A. M. & DADDI-MOUSSA-IDER, A. 2020 Towards an analytical description of active microswimmers in clean and in surfactant-covered drops. [arXiv:2005.14661](https://arxiv.org/abs/2005.14661).
- STONE, H. A. & BRENNER, M. P. 1996 Note on the capillary thread instability for fluids of equal viscosities. *J. Fluid Mech.* **318** (1), 373–374.
- TINEVEZ, J.-Y., SCHULZE, U., SALBREUX, G., ROENSCH, J., JOANNY, J.-F. & PALUCH, E. 2009 Role of cortical tension in bleb growth. *Proc. Natl Acad. Sci. USA* **106** (44), 18581–18586.
- TOJKANDER, S., GATEVA, G. & LAPPALAINEN, P. 2012 Actin stress fibers – assembly, dynamics and biological roles. *J. Cell Sci.* **125** (8), 1855–1864.
- TOMOTIKA, S. 1935 On the instability of a cylindrical thread of a viscous liquid surrounded by another viscous fluid. *Proc. R. Soc. Lond. A* **150** (870), 322–337.
- TSAFRIR, I., SAGI, D., ARZI, T., GUEDEAU-BOUDEVILLE, M.-A., FRETTE, V., KANDEL, D. & STAVANS, J. 2001 Pearling instabilities of membrane tubes with anchored polymers. *Phys. Rev. Lett.* **86** (6), 1138–1141.
- WEBER, C. 1931 Zum Zerfall eines Flüssigkeitsstrahles. *Z. Angew. Math. Mech.* **11** (2), 136–154.
- WEIK, F., WEEBER, R., SZUTTOR, K., BREITSPRECHER, K., DE GRAAF, J., KURON, M., LANDSGESELL, J., MENKE, H., SEAN, D. & HOLM, C. 2019 ESPResSo 4.0 – an extensible software package for simulating soft matter systems. *Eur. Phys. J.: Spec. Top.* **227** (14), 1789–1816.
- WHITAKER, S. 1976 Studies of the drop-weight method for surfactant solutions III. Drop stability, the effect of surfactants on the stability of a column of liquid. *J. Colloid Interface Sci.* **54**, 231–248.
- WHITE, J. G. & BORISY, G. G. 1983 On the mechanisms of cytokinesis in animal cells. *J. Theor. Biol.* **101** (2), 289–316.

- WINKLBAUER, R. 2015 Cell adhesion strength from cortical tension – an integration of concepts. *J. Cell Sci.* **128** (20), 3687–3693.
- YANAGISAWA, M., IMAI, M. & TANIGUCHI, T. 2008 Shape deformation of ternary vesicles coupled with phase separation. *Phys. Rev. Lett.* **100** (14), 148102.
- YAZDANI, A. & BAGCHI, P. 2013 Influence of membrane viscosity on capsule dynamics in shear flow. *J. Fluid Mech.* **718**, 569–595.
- ZHANG, R., KUMAR, N., ROSS, J. L., GARDEL, M. L. & DE PABLO, J. J. 2018 Interplay of structure, elasticity, and dynamics in actin-based nematic materials. *Proc. Natl Acad. Sci. USA* **115** (2), E124–E133.
- ZHAO, H., ISFAHANI, A. H. G., OLSON, L. N. & FREUND, J. B. 2010 A spectral boundary integral method for flowing blood cells. *J. Comput. Phys.* **229** (10), 3726–3744.

Publication 4

RAYLEIGH–PLATEAU INSTABILITY OF
ANISOTROPIC INTERFACES. PART 2.
LIMITED INSTABILITY OF ELASTIC
INTERFACES

C. Bächer, K. Graessel, and S. Gekle

Journal of Fluid Mechanics **910** (A47), 2021

Copyright by Cambridge University Press. Reprinted
with permission.

Rayleigh–Plateau instability of anisotropic interfaces. Part 2. Limited instability of elastic interfaces

Christian Bächer¹, Katharina Graessel¹ and Stephan Gekle^{1,†}

¹Biofluid Simulation and Modeling, Theoretische Physik VI, University of Bayreuth, Universitätsstraße 30, 95447 Bayreuth, Germany

(Received 24 March 2020; revised 20 October 2020; accepted 23 October 2020)

Cylindrical vesicle and cell membranes under tension can undergo a Rayleigh–Plateau instability leading to break-up. In Part 1 (Graessel *et al.*, *J. Fluid Mech.*, vol. xxx, 2021, Ax) we showed that anisotropic tension, created by active biological processes underneath the cell membrane, can significantly influence this process for a liquid–liquid interface. Here, we study the combined influence of anisotropic tension and membrane elasticity on the Rayleigh–Plateau instability. We analytically derive the dispersion relation for an interface endowed with bending and/or shear elasticity considering explicitly the dynamics of the suspending fluid. We find that the combination of bending elasticity and tension anisotropy leads to three qualitatively different regimes for the Rayleigh–Plateau scenario: (i) the classical regime in which short wavelengths are stable and long wavelengths are unstable, (ii) the suppressed regime in which the system is stable against all perturbation wavelengths and (iii) the restricted regime, in which a stable region at short and another one at long wavelengths are separated by a range of unstable modes centred around the dimensionless wavenumber $kR_0 = 1$. The width of this unstable range as well as the dominant wavelength of the instability depend on the bending modulus and tension anisotropy. For shear elasticity and area dilatation, on the other hand, only the classical and the suppressed regimes are observed, with the transition between them being independent of the tension anisotropy.

Key words: capsule/cell dynamics, membranes, instability

1. Introduction

The break-up of cylindrical vesicles under external tension has been successfully described by a Rayleigh–Plateau mechanism in direct analogy to the break-up of a liquid jet due to surface tension (Bar-Ziv & Moses 1994; Goldstein *et al.* 1996; Kantsler, Segre & Steinberg 2008; Powers 2010; Sanborn *et al.* 2013; Boedec, Jaeger & Leonetti 2014; Narsimhan, Spann & Shaqfeh 2015; Pal & Khakhar 2019). In living cells, a Rayleigh–Plateau instability has further been proposed for fission of mitochondria

† Email address for correspondence: stephan.gekle@uni-bayreuth.de

(Gonzalez-Rodriguez *et al.* 2015) and for blood platelet formation (Bächer, Bender & Gekle 2020).

In contrast to passive systems such as vesicles or liquid jets, living cells can actively produce tensions within their cell membrane (Prost, Jülicher & Joanny 2015; Salbreux & Jülicher 2017; Jülicher, Grill & Salbreux 2018). These tensions, in turn, are often anisotropic (Rauzi *et al.* 2008; Salbreux, Prost & Joanny 2009; Mayer *et al.* 2010; Behrndt *et al.* 2012; Reymann *et al.* 2012; Murrell *et al.* 2015; Blackwell *et al.* 2016; Callan-Jones *et al.* 2016; Reymann *et al.* 2016; Zhang *et al.* 2018), which has substantial consequences for the Rayleigh–Plateau scenario as we have demonstrated by linear stability analysis and numerical simulations for a fluid interface in Part 1 of this series (Graessel, Bächer & Gekle 2021): if azimuthal tensions are stronger than axial tensions, the range of unstable wavelengths grows and the most unstable mode shifts towards a shorter wavelength.

Another crucial difference between liquid jets and cell or vesicle membranes is the elastic response of the latter. The elastic response typically consists of independent contributions which can be related to different structural components of the membrane. First, the lipid bilayer induces a resistance to bending as well as area dilatation. Second, biological cells possess a cellular cortex, located directly beneath the lipid bilayer (Alberts *et al.* 2007), in which cross-linked polymers such as spectrin form an elastic network which adds a resistance to shear deformation. Over the last decades, a series of semi-empirical constitutive laws have been shown to fairly accurately describe these resistances. For bending, the Helfrich Hamiltonian (Helfrich 1973; Guckenberger & Gekle 2017) is the most widely used description, while for shear and area dilatation the Skalak (Skalak *et al.* 1973) as well as neo-Hookean laws (Barthès-Biesel, Diaz & Dhenin 2002; Barthès-Biesel 2016; Jaensson & Vermant 2018) have been established. The elasticity is not only important for the regulation of vesicle or cell shape (Fischer 2004; Barthès-Biesel 2016; Jelerčič 2017), it is further known to drive wrinkling on the vesicle surface (Finken & Seifert 2006; Li & Sarkar 2008; Finken, Kessler & Seifert 2011; Dupont *et al.* 2015; Narsimhan *et al.* 2015) and can lead to budding of vesicles (Seifert, Berndl & Lipowsky 1991; Seifert & Lipowsky 1995).

A small number of theoretical studies have so far investigated the influence of these elastic properties on the Rayleigh–Plateau instability of vesicles and cells. Bending elasticity has been shown to set a threshold for the tension required to trigger the instability (Nelson, Powers & Seifert 1995; Goldstein *et al.* 1996; Powers 2010; Patrascu & Balan 2020). Furthermore, Campelo & Hernández-Machado (2007) show by simulations that a non-zero curvature in the Helfrich Hamiltonian due to membrane anchoring proteins (Tsafirir *et al.* 2001) is capable of triggering a Rayleigh–Plateau instability. Boedec *et al.* (2014) investigate the growth rate and the most unstable wavelength for a general tension with respect to bending elasticity. They show that increasing the bending modulus leads to a smaller range of unstable modes compared to the classical Rayleigh–Plateau regime, where modes grow up to a wavenumber equal to the undeformed tube radius (Rayleigh 1878; Drazin & Reid 2004). Beyond a threshold bending modulus, they find that the instability is suppressed (Boedec *et al.* 2014). Considering shear elasticity, Hannezo, Prost & Joanny (2012) use an energy argument to predict a Rayleigh–Plateau instability of a tissue tube above a critical active tension depending on the Young's modulus of the tissue. Going in the same direction, Berthoumieux *et al.* (2014) derive the Green's function of an elastic membrane subjected to active tension. Both approaches, however, do not lead to the full dispersion relation for the growth of perturbations. To the best of our knowledge, a full linear stability analysis including shear elasticity has so far not been carried out. Furthermore, and most importantly, all the above studies on the

Rayleigh–Plateau instability under the influence of bending and shear elasticity consider isotropic tension.

In this paper, motivated by the frequent observation of anisotropic active tensions in cell membranes, we explore the diversity of the Rayleigh–Plateau instability which results from the interplay of tension anisotropy and interface elasticity. We first consider bending elasticity in the framework of the Helfrich model and analytically derive the dispersion relation in the Stokes limit by a linear stability analysis. In addition to the classical scenario with a single wavenumber separating stable from unstable modes, we find that bending elasticity introduces a new restricted regime in which an intermediate range of unstable modes is bounded from above and below by two separate stable ranges. Bending resistance can also lead to a regime where the interface is stable against all perturbations, the onset of which strongly depends on the tension anisotropy. We also provide a detailed investigation of the influence of the reference curvature. We show that the scenario remains qualitatively unchanged when replacing the Stokes by the Euler equation for the fluid dynamics. Next, we consider shear elasticity and area dilatation based on the Skalak law and calculate the corresponding dispersion relation in the Stokes limit. The dominant wavelength is found to increase due to the damping nature of the shear elasticity. Above a critical shear modulus only a stable phase exists, the critical value decreases when strengthening the resistance to area dilatation. While the threshold to the stable phase is independent of tension anisotropy, increasing the latter systematically increases the instability wavelength. Investigating the interplay of bending and shear elasticity, we analyse the resulting dispersion relation and observe a combination of the characteristic features of both effects with strong influence of the tension anisotropy.

We start by introducing the description of a deformable, elastic interface in § 2 which requires a different theoretical basis than the purely viscous interfaces in Part 1. In § 3 we proceed with the interfacial forces due to bending elasticity based on the Helfrich model and in § 3.1 perform a linear stability analysis which leads to the dispersion relation. Next, we analyse the growing modes and the different regimes induced by the bending elasticity (§ 3.2), followed by the dominant wavelength in § 3.3. In § 3.4 we systematically vary the reference curvature. As a next step we derive the dispersion relation for shear resistance and area dilatation based on the Skalak law and investigate the stability and dominant wavelength under the influence of both Skalak elasticity and tension anisotropy in § 4. Eventually, we combine bending and shear resistance in § 5. We conclude in § 6.

2. Problem set-up: a deformable elastic interface surrounded by fluid

2.1. Differential geometry of a deformable interface

We consider an initially cylindrical elastic interface subjected to an axisymmetric periodic perturbation along its axis, as illustrated in figure 1. In contrast to Part 1, the elasticity of the interface now requires us to consider the total deformation \mathbf{u} of an interface point from its initial location, and not only the local curvature and velocity. For this we employ the differential geometry (Kreyszig 1968) of thin shells as detailed in Green & Zerna (1954), Deserno (2015), Salbreux & Jülicher (2017) and Bächer & Gekle (2019), whose notation we follow. In the following, we introduce all quantities used in the linear stability analysis.

The undeformed state of the interface is a cylinder with radius R_0 in the radial direction r , which is parametrised in cylindrical coordinates by azimuthal angle ϕ and axial position z

$$\mathbf{X}_0 = \mathbf{X}_0(\phi, z) = R_0 \hat{\mathbf{e}}_r + z \hat{\mathbf{e}}_z \quad (2.1)$$

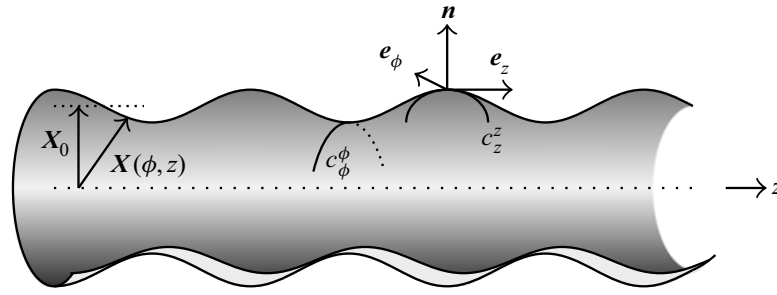


FIGURE 1. Cylindrical, elastic interface under periodic perturbation. We consider an axisymmetric interface between an inner, enclosed and an outer, surrounding fluid. The surface of the complex interface is parametrised by $\mathbf{X}(\phi, z)$, the undeformed reference state (dotted line) is described by \mathbf{X}_0 . The in-plane coordinate vectors which point along the interface are \mathbf{e}_ϕ and \mathbf{e}_z , the unit normal vector on the interface \mathbf{n} points outwards. In addition to the azimuthal curvature c_ϕ^ϕ along \mathbf{e}_ϕ the perturbation leads to an axial curvature c_z^z along \mathbf{e}_z .

with the normalised radial $\hat{\mathbf{e}}_r = (\cos \phi, \sin \phi, 0)$ and axial coordinate vector $\hat{\mathbf{e}}_z = (0, 0, 1)$. A periodic perturbation along the axis leads to a deformation \mathbf{u} of the interface

$$\mathbf{u} = \mathbf{X} - \mathbf{X}_0 = u_r \hat{\mathbf{e}}_r + u_z \hat{\mathbf{e}}_z, \quad (2.2)$$

where we parametrise the deformed interface with varying radius $R(z) = R_0 + u_r(z)$ by

$$\mathbf{X} = \mathbf{X}(\phi, z) = \begin{pmatrix} R(z) \cos \phi \\ R(z) \sin \phi \\ z + u_z(z) \end{pmatrix}. \quad (2.3)$$

In the following, we consider small amplitude perturbations and therefore keep only terms up to linear order in the deformation (Berthoumieux *et al.* 2014; Daddi-Moussa-Ider, Lisicki & Gekle 2017). The in-plane coordinate vectors, i.e. the coordinate vectors along the deformed interface, are

$$\mathbf{e}_\phi = \frac{\partial}{\partial \phi} \mathbf{X} = \begin{pmatrix} -R \sin \phi \\ R \cos \phi \\ 0 \end{pmatrix}, \quad \mathbf{e}_z = \frac{\partial}{\partial z} \mathbf{X} = \begin{pmatrix} R' \cos \phi \\ R' \sin \phi \\ 1 + u'_z \end{pmatrix}, \quad (2.4a,b)$$

with the prime denoting a derivative with respect to z . From the in-plane coordinate vectors the metric on the deformed interface can be calculated (Kreyszig 1968) and linearised

$$g_{\alpha\beta} = \mathbf{e}_\alpha \cdot \mathbf{e}_\beta = \begin{pmatrix} R^2 & 0 \\ 0 & (1 + u'_z)^2 + R^2 \end{pmatrix} \approx \begin{pmatrix} R_0^2 + 2R_0 u_r & 0 \\ 0 & 1 + 2u'_z \end{pmatrix}, \quad (2.5)$$

with $\alpha, \beta = \phi, z$. The inverse metric defined by $g_{\alpha\gamma} g^{\gamma\beta} = \delta_\alpha^\beta$ takes the form

$$g^{\alpha\beta} = \begin{pmatrix} \frac{1}{R^2} & 0 \\ 0 & \frac{1}{(1 + u'_z)^2 + R^2} \end{pmatrix} \approx \begin{pmatrix} \frac{1}{R_0^2} - 2\frac{u_r}{R_0^3} & 0 \\ 0 & 1 - 2u'_z \end{pmatrix}. \quad (2.6)$$

We obtain the metric on the undeformed interface $G_{\alpha\beta}$ by setting the deformation to zero

$$G_{\alpha\beta} = \begin{pmatrix} R_0^2 & 0 \\ 0 & 1 \end{pmatrix}, \quad G^{\alpha\beta} = \begin{pmatrix} \frac{1}{R_0^2} & 0 \\ 0 & 1 \end{pmatrix}. \quad (2.7a,b)$$

From the metric the Christoffel symbols can be calculated by

$$\Gamma_{\alpha\beta}^{\gamma} = \frac{1}{2}g^{\gamma\delta} (\partial_{\beta}g_{\alpha\delta} + \partial_{\alpha}g_{\beta\delta} - \partial_{\delta}g_{\alpha\beta}), \quad (2.8)$$

where indices occurring twice are summed over according to the Einstein notation. By the use of the Christoffel symbols the covariant derivative of an arbitrary tensor $t^{\alpha\beta}$ is defined by

$$\nabla_{\alpha}t^{\beta\gamma} = \partial_{\alpha}t^{\beta\gamma} + \Gamma_{\alpha\delta}^{\beta}t^{\delta\gamma} + \Gamma_{\alpha\delta}^{\gamma}t^{\beta\delta}. \quad (2.9)$$

The unit normal vector on the interface, which points outwards, can be calculated in linearised form as

$$\mathbf{n} = \frac{\mathbf{e}_{\phi} \times \mathbf{e}_z}{|\mathbf{e}_{\phi} \times \mathbf{e}_z|} \approx \begin{pmatrix} \cos \phi \\ \sin \phi \\ -R' \end{pmatrix}. \quad (2.10)$$

The curvature tensor, which is defined by $c_{\alpha\beta} = -(\partial_{\alpha}\mathbf{e}_{\beta}) \cdot \mathbf{n}$, becomes on the deformed interface

$$c_{\alpha}^{\beta} \approx \begin{pmatrix} \frac{1}{R(z)} & 0 \\ 0 & -R'' \end{pmatrix}. \quad (2.11)$$

On the undeformed surface the curvature tensor is

$$C_{\alpha}^{\beta} = \begin{pmatrix} \frac{1}{R_0} & 0 \\ 0 & 0 \end{pmatrix}. \quad (2.12)$$

2.2. Mechanical properties of the interface

The mechanical properties of the interface are (i) the anisotropic interfacial tension and (ii) the resistance to elastic deformations. If in addition interface viscosity is included, we would expect effects similar to those discussed in [Part 1](#). In general, mechanical properties of the interface are described by the surface stress (Green & Zerna 1954; Barthès-Biesel 2016; Guckenberger & Gekle 2017; Salbreux & Jülicher 2017; Bächer & Gekle 2019), which can be expressed in vector notation as

$$\mathbf{t}^{\beta} = t_{\alpha}^{\beta}\mathbf{e}^{\alpha} + t_n^{\beta}\mathbf{n}, \quad (2.13)$$

with its in-plane components t_{α}^{β} and the normal component t_n^{β} . As introduced above, we split the surface stress into an (i) anisotropic and an (ii) elastic contribution

$$\mathbf{t}^{\beta} = \mathbf{t}_{aniso}^{\beta} + \mathbf{t}_{el}^{\beta}. \quad (2.14)$$

As discussed in [Part 1](#), anisotropic interfacial tension can have different origins. In this paper, we focus on biological cells where proteins in the cell cortex produce an

active tension, which enters the anisotropic contribution of the surface stress (2.14). A positive active tension accounts for the internal tendency of the cortical protein network to contract. Similar to surface tension triggering the Rayleigh–Plateau instability of a liquid jet (Eggers & Villermaux 2008), such a contractile active tension in the cell cortex can lead to a Rayleigh–Plateau instability of a cell or tissue tube (Hannezo *et al.* 2012; Berthoumieux *et al.* 2014; Bächer & Gekle 2019; Bächer *et al.* 2020). In contrast to the classical surface tension, however, here, a constitutive law directly prescribes the active, thus interfacial, tension (rather than deriving it from an interfacial energy) (Salbreux & Jülicher 2017; Bächer & Gekle 2019). In analogy to Part 1, the anisotropic interfacial tension is denoted by γ^ϕ and γ^z , distinguishing azimuthal and axial directions, respectively, and it contributes to the surface stress as

$$t_{aniso,\alpha}^\beta = \begin{pmatrix} \gamma^\phi & 0 \\ 0 & \gamma^z \end{pmatrix}. \quad (2.15)$$

The normal component of the anisotropic surface stress vanishes, i.e. $t_{aniso,n}^\beta = 0$. We assume that the anisotropic tension is constant along the interface and therefore derivatives of the anisotropic tension vanish, i.e. $\nabla_\alpha t_{aniso}^{\beta\gamma} = 0$.

In addition to Part 1, we here consider a resistance to elastic deformations, which splits into the three different contributions due to bending deformation, shear deformation and area dilatation. The surface stress due to elasticity t_{el}^α can be derived from constitutive laws typically defining an energy functional, which covers the elastic properties (Green & Zerna 1954). In the present paper we use the Helfrich law for bending elasticity with the bending modulus κ_B and the Skalak law for shear elasticity with modulus κ_S and area dilatation with modulus $C\kappa_S$. The corresponding contributions to the surface stress t_{el}^α are derived in §§ 3.1 and 4.1, respectively.

We end this section with a discussion of typical values for vesicles and cells. For the active cortical stress values in the range of 10^{-5} – 10^{-3} N m⁻¹ have been reported depending on the cell type (Lomakina *et al.* 2004; Krieg *et al.* 2008; Tinevez *et al.* 2009; Bergert *et al.* 2012; Fischer-Friedrich *et al.* 2014; Chugh *et al.* 2017; Dmitrieff *et al.* 2017). Exact values for the anisotropy of the active stress are scattered as well. Mayer *et al.* (2010) report a polar tension half the angular tension for an ellipsoidal embryo, Behrndt *et al.* (2012) report a factor of 4 in the case of epiboly. Reymann *et al.* (2016) report anisotropy in terms of a nematic order parameter which takes values from -0.04 to 0.12 . Rauzi *et al.* (2008) consider planar anisotropy from 1 to 4. Typical values for the bending modulus are in a range from 10^{-20} – 10^{-18} Nm (Goldstein *et al.* 1996; Freund 2014; Guckenberger & Gekle 2017). The shear elasticity of a red blood cell is in the range 10^{-6} – 10^{-5} N m⁻¹ (Freund 2014) and the Young's modulus of a tissue tube is approximately 10^4 – 10^6 Pa (Laurent *et al.* 1994; Hannezo *et al.* 2012). Eventually, the typical radii from vesicles to tissue tubes varies from approximately half a micrometre (Bar-Ziv & Moses 1994; Goldstein *et al.* 1996) to several micrometres (Freund 2014) to a millimetre. All in all, this leads to a wide parameter space, which we cover by presenting phase diagrams for a broad range of dimensionless parameters in the following sections.

2.3. Coupling to the surrounding fluid

Due to the presence of the surrounding fluid, in addition to the surface stress, forces from the fluid act on the interface, which are described by the traction jump across the

membrane (Pozrikidis 2001; Daddi-Moussa-Ider & Gekle 2018)

$$\Delta \mathbf{f} = \Delta f^\alpha \mathbf{e}_\alpha + \Delta f^n \mathbf{n}, \quad (2.16)$$

with components parallel to the interface denoted by Δf^α and components along the outward pointing normal vector by Δf^n . The traction jump is given by the difference of the three-dimensional ($i, j = x, y, z$) stress tensors σ_{ij}^{out} , σ_{ij}^{in} of the outer and inner fluid, respectively, projected onto the normal vector of the interface (Chandrasekharaiah & Debnath 2014)

$$\Delta f_j = (\sigma_{ij}^{out} - \sigma_{ij}^{in}) n_i. \quad (2.17)$$

For a Newtonian and incompressible fluid with shear viscosity η the stress tensor is (Chandrasekharaiah & Debnath 2014)

$$\boldsymbol{\sigma} = -p\mathbf{I} + \eta [(\nabla \mathbf{v} + (\nabla \mathbf{v})^T)], \quad (2.18)$$

where $\mathbf{v}(\mathbf{r}, t)$ is the velocity field and $p(\mathbf{r}, t)$ the pressure of the fluid.

The interface is considered in mechanical equilibrium with the fluid enclosed by the interface and the surrounding fluid. Therefore, interfacial forces derived from the surface stress (2.14) together with the traction jump (2.16) fulfil the force balance equation (Green & Zerna 1954; Barthès-Biesel 2016; Salbreux & Jülicher 2017)

$$\nabla_\beta \mathbf{t}^\beta + \Delta \mathbf{f} = 0. \quad (2.19)$$

The interfacial forces acting from the interface onto the fluid are thus given by either the derivative of the surface stress or the negative traction jump and denoted by

$$\mathbf{f} \equiv \nabla_\beta \mathbf{t}^\beta = -\Delta \mathbf{f}. \quad (2.20)$$

Decomposing the force balance into components parallel and normal to the interface and using (2.14), (2.15) and (2.16) leads to the force balance equations in the form

$$\nabla_\alpha \mathbf{t}_{el}^{\alpha\beta} + c_\alpha^\beta \mathbf{t}_{el,n}^\alpha = -\Delta f^\beta, \quad (2.21)$$

$$\nabla_\alpha \mathbf{t}_{el,n}^\alpha - c_{\alpha\beta} \mathbf{t}_{el}^{\alpha\beta} - c_{\alpha\beta} \mathbf{t}_{aniso}^{\alpha\beta} = -\Delta f^n. \quad (2.22)$$

In contrast to Part 1, the interface elasticity causes a traction jump in the tangential component Δf^β along the interface and, in addition, modifies the normal force balance. For the exact form of the elastic surface stresses we again refer to §§ 3.1 and 4.1. According to the normal component of the force balance equation (2.22) the anisotropic interfacial tension leads to a contribution

$$c_{\alpha\beta} \mathbf{t}_{aniso}^{\alpha\beta} = \frac{\gamma^z}{R_z} + \frac{\gamma^\phi}{R_\phi}, \quad (2.23)$$

which balances the normal component of the traction jump. In the present paper we consider an interior fluid which has the same viscosity as the surrounding fluid.

3. Bending elasticity restricts anisotropic Rayleigh–Plateau instability

3.1. Dispersion relation from the Helfrich Hamiltonian

We now investigate the influence of bending elasticity on the anisotropic Rayleigh–Plateau instability of an interface specifically aiming at the description of vesicle and cell

membranes composed of a lipid bilayer. This bilayer resists bending deformations, i.e. changes of the mean curvature H , which is given by half the trace of the curvature tensor (2.11) (Deserno 2015; Daddi-Moussa-Ider *et al.* 2017)

$$H = \frac{1}{2}c_\gamma^\gamma = \frac{1}{2} \left(c_z^z + c_\phi^\phi \right). \quad (3.1)$$

Deformations which lead to a mean curvature H different from the reference curvature H_0 trigger elastic forces. Due to the Gauss–Bonnet theorem the Gaussian curvature does not affect the interface elasticity (Deserno 2015; Daddi-Moussa-Ider *et al.* 2017). The resistance to bending is described by the Helfrich Hamiltonian (Helfrich 1973; Guckenberger & Gekle 2017) with the elastic bending modulus κ_B as a measure of the bending elasticity

$$W^{HF} = 2\kappa_B(H - H_0)^2. \quad (3.2)$$

As detailed above, the bending elasticity contributes to the elastic surface stress t_{el}^α in (2.14). This contribution can be derived from the Helfrich Hamiltonian (3.2) using thin shell theory (Capovilla & Guven 2002; Guven 2004; Powers 2010; Deserno 2015; Guckenberger & Gekle 2017), which leads to the general form

$$t_{el,B}^\alpha = 2\kappa_B(H - H_0)^2 g^{\alpha\beta} e_\beta - 2\kappa_B(H - H_0) c^{\alpha\beta} e_\beta + 2\kappa_B \nabla_\beta (H - H_0) g^{\alpha\beta} \mathbf{n}. \quad (3.3)$$

In the following, we explicitly consider the initially cylindrical interface, subjected to a deformation as given by (2.2) and shown in figure 1. Using the curvature tensor (2.11) the mean curvature of the interface in linearised form is

$$H \approx \frac{1}{2} \left(\frac{1}{R_0} - \frac{u_r}{R_0^2} - u_r'' \right). \quad (3.4)$$

In contrast to previous works (Powers 2010; Boedec *et al.* 2014) we first choose as reference curvature the curvature of the unperturbed cylindrical interface that can be obtained from the curvature tensor of the undeformed interface (2.12)

$$H_0 = \frac{1}{2R_0}. \quad (3.5)$$

In § 3.4, we investigate the influence of different values for the reference curvature. Linearising the surface stress (3.3) and splitting it into tangential and normal components gives

$$t_{el,B\alpha}^\beta = 2\kappa_B(H - H_0)^2 \delta_\alpha^\beta - 2\kappa_B(H - H_0) c_\alpha^\beta \approx \kappa_B \left(\frac{u_r}{R_0^2} + u_r'' \right) c_\alpha^\beta \quad (3.6)$$

$$t_{el,B,n}^\alpha = 2\kappa_B \nabla_\beta (H - H_0) g^{\alpha\beta} \approx -\kappa_B \nabla_\beta \left(\frac{u_r}{R_0^2} + u_r'' \right) g^{\alpha\beta}. \quad (3.7)$$

Using (2.6) to explicitly write out the z -component of the last equation gives

$$t_{el,B,n}^z = -\kappa_B \left(\frac{u_r'}{R_0^2} + u_r''' \right) g^{zz} \approx -\kappa_B \left(\frac{u_r'}{R_0^2} + u_r''' \right) = -\kappa_B \left(\frac{u_r'}{R_0^2} + u_r''' \right), \quad (3.8)$$

and for the ϕ -component $t_{el,B,n}^\phi = 0$. The tangential component of the force balance (2.21) results in a vanishing tangential bending force $f_B^\alpha = 0$ consistent with the general case

(Guckenberger & Gekle 2017). The normal component of the force balance (2.22) has two contributions from the bending elasticity

$$-c_{\alpha\beta} t_{el,B}^{\alpha\beta} = -c_{\phi}^{\phi} t_{el,B\phi}^{\phi} - c_z^z t_{el,Bz}^z \approx -\kappa_B \left(\frac{u_r}{R_0^4} + \frac{u_r''}{R_0^2} \right), \quad (3.9)$$

$$\nabla_{\alpha} t_{el,B,n}^{\alpha} = \nabla_z t_{el,B,n}^z \approx -\kappa_B \left(\frac{u_r''}{R_0^2} + u_r'''' \right). \quad (3.10)$$

Eventually, the linearised form of the normal component of the elastic force due to bending is obtained as

$$f_B^n = -\kappa_B \left[\frac{u_r}{R_0^4} + \frac{2u_r''}{R_0^2} + u_r'''' \right]. \quad (3.11)$$

This is consistent with the result given in Daddi-Moussa-Ider *et al.* (2017).

In a next step, we perform an analytical linear stability analysis of the interface. The goal is to derive the dispersion relation, which relates the growth rate ω of a perturbation to its wavenumber $k = 2\pi/\lambda$ with wavelength λ . We use a perturbation ansatz for the interface depicted in figure 1 of the form

$$R(z, t) = R_0 (1 + \epsilon \cos(kz)), \quad \epsilon = \epsilon_0 e^{\omega t}, \quad (3.12)$$

with amplitude ϵ growing in time. Due to the bending force (3.11) and the anisotropic interfacial tension (2.15) the normal force balance (2.22) leads to the traction jump at the interface of the form

$$\Delta f^n = \frac{\gamma^{\phi}}{R_0} + \left[-\frac{\gamma^{\phi}}{R_0} + \gamma^z k^2 R_0 + \kappa_B \left(\frac{1}{R_0^3} - \frac{2k^2}{R_0} + k^4 R_0 \right) \right] \epsilon \cos(kz). \quad (3.13)$$

As can be seen from (2.17) and (2.18) the traction jump includes the pressure at the interface $p_0 + \delta p(r = R)$, where p_0 denotes the pressure difference of the undeformed interface and $\delta p(r = R)$ the pressure perturbation as a consequence of the interface perturbation (3.12). By comparing the constant terms, which do not arise from the perturbation, on both sides of (3.13) we identify the Laplace pressure for the unperturbed interface as

$$p_0 = \frac{\gamma^{\phi}}{R_0}. \quad (3.14)$$

The perturbation in the traction jump in (3.13) due to the disturbance of the interface is now balanced not only by the contribution from anisotropic interfacial tension as in (B 3) of Part 1 but also by contributions from the resistance to bending.

The motion of inner and outer fluid with same density ρ and viscosity η are in general governed by the Navier–Stokes equation and continuity equation, the solution of which is the velocity \mathbf{v} and pressure field p of the fluid. In the following, we consider a fluid in the limit of small Reynolds number, which is usually a very good approximation for vesicles and cells (Freund 2014; Barthès-Biesel 2016). Thus, for the inner and outer fluid the Stokes equation holds, which we solve in presence of the interface using the same approach as in Part 1. Compared to Part 1 the traction jump (3.13) includes a fourth-order polynomial in the wavenumber stemming from bending, which behaves in the same way with respect to the variables r, z as the anisotropic tension does in (B 3) of Part 1. We thus can continue as described in appendix B.1 of Part 1 to derive the dispersion relation: we choose a periodic

ansatz also for the velocities in the r - and z -directions and for the pressure p , then transform their amplitudes to Hankel space, where we solve the Stokes and continuity equation for the velocity components. Transformation back to real space and inserting the results into the kinematic boundary condition at the interface finally leads to the dispersion relation in the Stokes regime including bending elasticity

$$\omega(k) = \omega_0^S \left(1 - \frac{\gamma^z}{\gamma^\phi} (kR_0)^2 - \mathcal{B} (1 - 2(kR_0)^2 + (kR_0)^4) \right) \times \left[\text{I}_1(kR_0)\text{K}_1(kR_0) + \frac{kR_0}{2} (\text{I}_1(kR_0)\text{K}_0(kR_0) - \text{I}_0(kR_0)\text{K}_1(kR_0)) \right], \quad (3.15)$$

with the relative bending modulus $\mathcal{B} = \kappa_B / (\gamma^\phi R_0^2)$. The dispersion relation consists of a constant prefactor $\omega_0^S = \gamma^\phi / (R_0 \eta)$ fixing the dimensions of the growth rate, the factor accounting for membrane forces

$$\mathcal{F}(k) = \left[1 - \frac{\gamma^z}{\gamma^\phi} (kR_0)^2 - \mathcal{B} (1 - 2(kR_0)^2 + (kR_0)^4) \right] \quad (3.16)$$

and a factor of Bessel functions, which is positive for positive argument kR_0 and stems from the fluid dynamics. For a similar setting but with isotropic tension, Boedec *et al.* (2014) and Powers (2010) derive dispersion relations including in addition tension gradients and surface viscosity, respectively. These derivations also differ in the choice of reference curvature, as mentioned above, which leads to different factors in the bending contribution.

In appendix A we in addition show the result for an ideal fluid described by the Euler equation, which is derived from the Navier–Stokes equation in the limit of vanishing viscosity, where we solve the Laplace equation for the pressure.

3.2. Bending elasticity introduces stability

3.2.1. Qualitative description

The dispersion relation (3.15) of an anisotropic interface including bending elasticity, which gives the growth rate ω for each mode with wavenumber kR_0 , is shown in figure 2 as a blue line. Additionally, we show the γ^z -contribution from the anisotropic interfacial tension in orange, the γ^ϕ -contribution in green and the bending contribution as a red, dashed line. From the left to the right column we increase the anisotropy ratio from $\gamma^z/\gamma^\phi = 0.5$ to the isotropic case $\gamma^z/\gamma^\phi = 1.0$ in the middle and up to $\gamma^z/\gamma^\phi = 2.0$ on the right. From top to bottom the bending resistance increases from $\mathcal{B} = 0$ in the first line 2(a) to $\mathcal{B} = 2.0$ in the last line (e). Where the dispersion relation takes positive values, modes with corresponding wavenumber kR_0 will grow, i.e. the interface is unstable to these modes. In contrast, modes with negative growth rate are damped, correspondingly the interface is stable to these modes. The maximum of the dispersion relation determines the dominant, i.e. fastest growing, wavelength, which eventually defines the size of the fragments (Drazin & Reid 2004). The γ^ϕ -contribution is purely positive, thus destabilises the interface, whereas the γ^z -contribution is purely negative and dampens the instability. We observe that the bending part dampens the growth rate for all wavenumbers except $kR_0 = 1$, where the bending energy (3.2) and thus the force (3.11) vanish since the mean curvature equals the reference curvature. This further illustrates that the initial cylindrical interface remains stable if solely bending elasticity is considered.

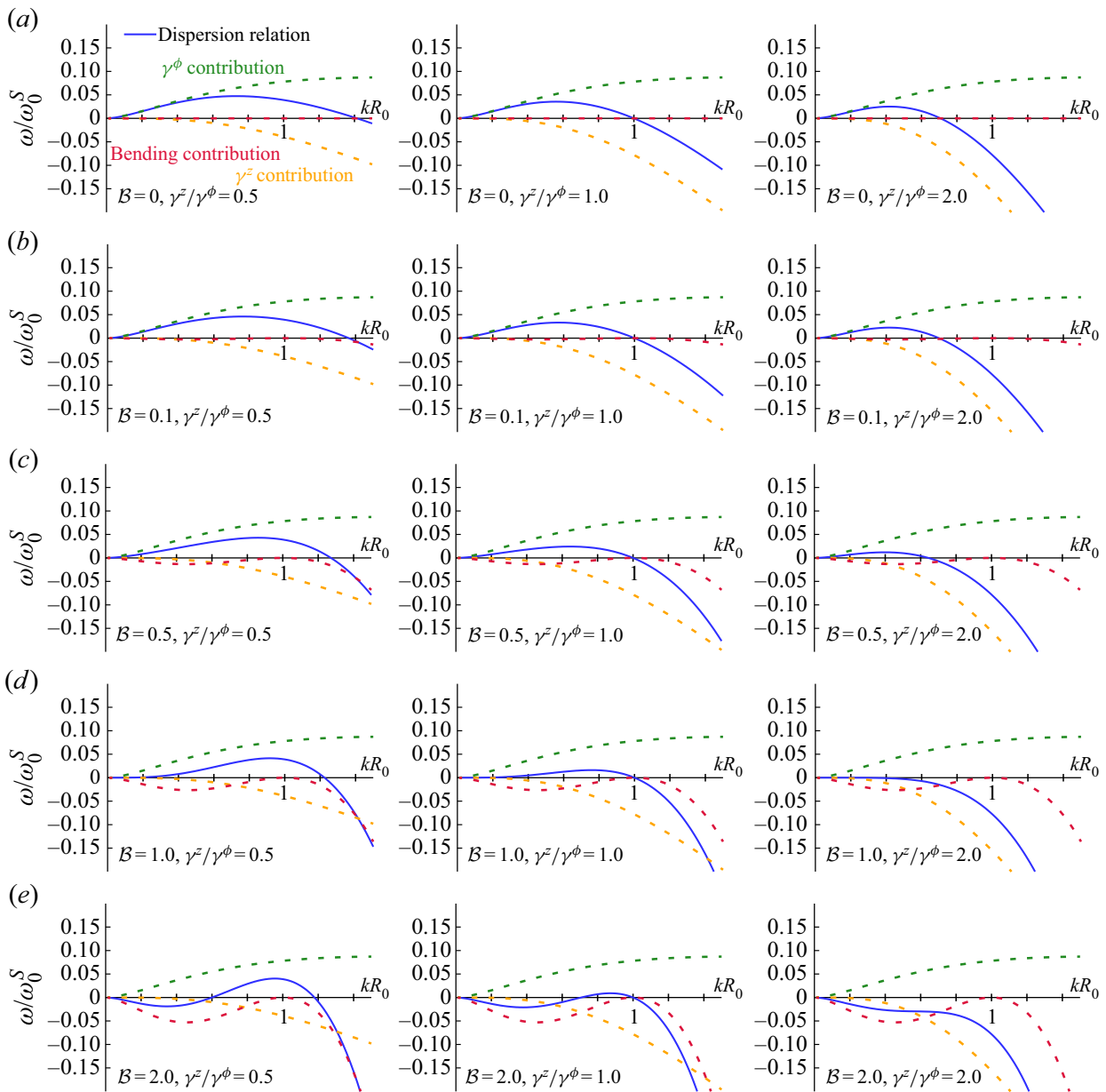


FIGURE 2. Dispersion relations for bending resistance and anisotropic interfacial tension. We distinguish the contributions from bending resistance \mathcal{B} (red), γ^ϕ (green) and γ^z (orange). From left to right the anisotropy ratio increases, whereas from top to bottom the bending resistance increases, with values given as labels. The bending and γ^z contributions are stabilising for all wavenumbers, while the γ^ϕ -contribution destabilises the interface. Bending either reduces the unstable range from its right, large kR_0 , boundary (classical regime) and/or restricts the range of growing modes by the appearance of another positive root to its left, small kR_0 , boundary (restricted regime). The maximum of the dispersion relation shifts depending on bending resistance. Large bending and anisotropy in (d,e) on the right can even lead to a purely negative dispersion relation, thus completely suppressing the Rayleigh–Plateau instability (suppressed regime).

For $\gamma^z/\gamma^\phi = 0.5$ (left column), increasing the bending modulus leads to a shift of the right-most root towards smaller values and thus entails a shrinking of the range of unstable modes. The position of the maximum shifts towards larger wavenumbers. For the isotropic case $\gamma^z/\gamma^\phi = 1.0$ (middle column), however, shrinkage of the range is not observed: the right stability boundary remains at the Rayleigh–Plateau value $kR_0 = 1$ and is not affected

by bending as the bending contribution is identically zero at $kR_0 = 1$. Yet, also in the isotropic case, we observe a shift of the maximum to larger wavenumbers. In the right column, where $\gamma^z/\gamma^\phi = 2.0$, once again a shrinking range is observed. Interestingly, the variation in the position of the maximum is now reversed and it shifts towards smaller wavenumbers. Most remarkably, for $\mathcal{B} \geq 1$ the total dispersion relation is purely negative.

From [figure 2](#), we can identify three different regimes occurring at certain combinations of tension anisotropy and bending modulus. The first case, resembling what is known from the classical Rayleigh–Plateau scenario (Rayleigh 1878), we term the classical regime. Here, the dispersion relation has one root at wavenumber zero and another at a larger wavenumber $k_{max}R_0$. Thus, modes in the range $]0; k_{max}R_0[$ are growing. The classical regime is located at low to moderate values of the bending modulus and persists for all anisotropy ratios. The second case, which we term the restricted regime appears at moderate anisotropy ratio and large enough bending contribution (first two columns in row *e*). Here, the dispersion relation develops another root at a finite wavenumber $k_{min}R_0 < k_{max}R_0$. Therefore, modes with small enough wavenumber become stable while modes with intermediate wavenumber $]k_{min}R_0; k_{max}R_0[$ still grow. Thus, bending elasticity restricts the range of growing modes from above and from below. Finally, for large bending modulus (rows *d*) and *e*) an anisotropy of $\gamma^z/\gamma^\phi = 2.0$ can lead to a completely negative dispersion relation: no modes are growing and the cylindrical interface remains stable. We call this stable phase the suppressed regime. The fact that bending can, in principle, suppress the instability has also been reported by Boedec *et al.* (2014) for isotropic tension if the reference curvature vanishes ($H_0 = 0$). Our results in [figure 2](#) show that the combination of anisotropic tension and bending elasticity can lead to suppression of the instability also for the natural case of a cylindrical reference curvature $H_0 = 1/(2R_0)$.

In [appendix A](#) we show in [figure 12](#) that for an ideal fluid the destabilising γ^ϕ -contribution does not possess a maximum and the maximum of the dispersion relation shifts towards larger kR_0 . In this work, we explicitly consider only positive interfacial tension for which the Rayleigh–Plateau instability occurs. We note briefly that for negative axial tension γ^z , independent of the sign of γ^ϕ , the dispersion relation still shows a maximum at a finite wavenumber, as it does in [figure 2](#). This corresponds to a buckling instability with finite wavelength due to the extensile nature of the axial tension (Berthoumieux *et al.* 2014; Bächer & Gekle 2019).

3.2.2. Quantitative discussion

We now turn to a quantitative analysis of the range of unstable modes. As discussed based on [figure 2](#), the unstable range is either (i) bounded on the left by $kR_0 = 0$ and on the right by the single positive root of the dispersion relation (classical regime), (ii) bounded on the left and right by the two positive roots of the dispersion relation (restricted regime) or (iii) completely absent (suppressed regime). The roots of the dispersion relation in turn are given by the roots of $\mathcal{F}(k)$ in (3.16). For vanishing bending resistance the single root obeys

$$\left. \frac{\gamma^z}{\gamma^\phi} \right|_{root, \mathcal{B}=0} = \frac{1}{(kR_0)^2}, \quad (3.17)$$

whereas for finite bending resistance the roots obey

$$\left. \frac{\gamma^z}{\gamma^\phi} \right|_{root, \mathcal{B} \neq 0} = \frac{1}{(kR_0)^2} - \mathcal{B} \frac{1}{(kR_0)^2} + 2\mathcal{B} - \mathcal{B}(kR_0)^2. \quad (3.18)$$

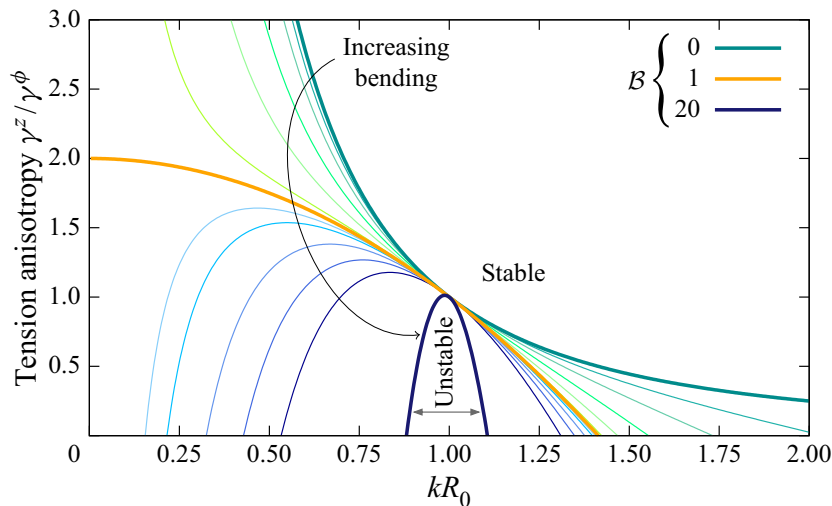


FIGURE 3. Range of unstable modes as a function of tension anisotropy and bending modulus. The curves show the roots of the dispersion relation such that regions above the curves are stable, while regions below are unstable. For bending moduli between 0 and 1 the single root shifts to the left. Bending moduli above 1 in addition lead to a second root at finite wavenumber, which determines the left border of the unstable domain. Thus, bending elasticity restricts the range of unstable modes and for large bending modulus a critical tension anisotropy exists, above which the cylinder remains stable. For a three-dimensional illustration we refer to the supplementary gnuplot script, supplementary material available at <https://doi.org/10.1017/jfm.2020.946>.

Figure 3 shows the range of unstable modes with increasing bending modulus \mathcal{B} coded by colours and with tension anisotropy on the ordinate. Each curve represents the strictly positive root(s) ($kR_0 > 0$) of the dispersion relation. The area underneath a curve thus corresponds to unstable modes and the area above a curve to stable modes.

At vanishing bending (dark green curve), for each tension anisotropy there exists only a single root marking the right boundary of the unstable range. The unstable range shrinks when tension anisotropy increases. However, the right boundary goes to infinity for infinitesimal small anisotropy, thus for the anisotropy being zero all modes are unstable. When adding a small bending contribution (lighter green curves), the right boundary shifts to the left and the unstable range shrinks, qualitatively independent of the anisotropy. All green curves correspond to the classical regime with the left root of the dispersion relation being at $kR_0 = 0$ (not shown in figure 3) and a finite root on the right. Increasing bending resistance further, at $\mathcal{B} = 1$ (orange) the factor \mathcal{F} in (3.16) becomes zero at $kR_0 = 0$, so the orange curve is the only one which intersects the ordinate. It is also the first to exhibit an upper bound at $\gamma^z/\gamma^\phi = 2.0$ indicating the appearance of the suppressed regime for all $\gamma^z/\gamma^\phi \geq 2$. Further increasing the bending modulus (blue curves) leads to another root at finite wavenumbers and a corridor of unstable modes develops as seen in figure 2(e) in the first two columns. All blue curves correspond to the restricted regime. The corridor of unstable modes narrows for increasingly larger bending modulus and is centred around $kR_0 = 1$. In addition, the instability threshold (maximum of the curves), which indicates the transition from the restricted to the suppressed regime, shifts to smaller values of the tension anisotropy. Interestingly, for isotropic tension, the right root is pinned at $kR_0 = 1$ and is not affected by bending contributions.

3.2.3. Phase diagram

The goal now is to derive a relation for the instability threshold as a function of \mathcal{B} and γ^z/γ^ϕ . For this, we again consider the factor $\mathcal{F}(k)$ in (3.16). For positive k the sign of the

growth rate is determined by $\mathcal{F}(k)$. If $\mathcal{F}(k) < 0 \forall k > 0$, all perturbations decay and the interface is stable indicating the suppressed regime

$$\frac{\gamma^z}{\gamma^\phi} > \frac{1 - \mathcal{B}}{(kR_0)^2} + 2\mathcal{B} - \mathcal{B} (kR_0)^2. \quad (3.19)$$

If $\mathcal{B} < 1$, the right-hand side tends to infinity for small kR_0 (see first term) and thus the condition (3.19) is violated, i.e. growing perturbations do exist for any γ^z/γ^ϕ . This is the classical regime. For $\mathcal{B} \geq 1$, a suppressed regime exists whenever condition (3.19) is fulfilled for all values of kR_0 , especially for the maximal value of the right-hand side. Determining the position $kR_0|_{max}$ of this maximal value and inserting it into (3.19) we can determine a critical value above which the suppressed regime appears

$$\left. \frac{\gamma^z}{\gamma^\phi} \right|_{crit} = -2 [\mathcal{B} (\mathcal{B} - 1)]^{1/2} + 2\mathcal{B}. \quad (3.20)$$

For γ^z/γ^ϕ larger than this critical value, no perturbation grows. For $\mathcal{B} = 1$ (3.20) yields the critical value $\gamma^z/\gamma^\phi|_{crit} = 2$. This corresponds to the intersection of the orange line with the ordinate in figure 3, where the two roots which determine the unstable range collapse. For large bending energy the critical value (3.20) approaches one. This manifests itself in the maximum of the dark blue line in figure 3.

The detailed variation of the threshold determined by (3.20) is illustrated by the phase diagrams in figure 4(a,b). In the region where unstable modes exist, (a) dominant wavelength λ_m and (b) maximum growth rate ω_m are colour coded. We obtain the dominant wavelength, i.e. the position of the positive maximum of the dispersion relation, by calculating the root of its derivative using *Mathematica*, and in turn the maximum growth rate from the dispersion relation. At the top of the phase diagram, i.e. at large bending modulus, a corridor exists at small anisotropy ratios, which broadens with decreasing bending modulus. In this corridor the range of unstable modes is bounded by two roots of the dispersion relation, this is the restricted regime. For $\mathcal{B} < 1$ unstable modes always exist and the instability wavelength increases with increasing tension anisotropy, we termed this the classical regime.

In total, our results show that bending resistance can suppress the Rayleigh–Plateau instability in a certain parameter space: the bending force is another damping factor in the dispersion relation as is γ^z , which explains why this strong increase happens for large bending elasticity and large γ^z . However, at anisotropy ratios smaller than one, there always exists a corridor of unstable modes where the destabilising γ^ϕ -contribution dominates the stabilising γ^z -contribution and in total the dispersion relation becomes positive.

3.3. Bending elasticity affects dominant wavelength and growth rate

We now discuss the dominant wavelength of the instability in more detail. Figure 4(c) shows the dominant wavelength depending on the anisotropy ratio for different values of the bending modulus. We note that curves in figure 4(c) are horizontal lines in the phase diagram 4(a), i.e. drawn for constant bending modulus at the same values as used in figure 2. In general, the wavelength decreases towards small anisotropy and *vice versa*, which means that smaller fragments form for $\gamma^z/\gamma^\phi \leq 1$ and larger ones for larger anisotropy. The red curve without bending elasticity recovers the result shown in figure 4(a) of Part 1. Next, the blue and orange curves for $\mathcal{B} = 0.1$ and $\mathcal{B} = 0.5$ show that small

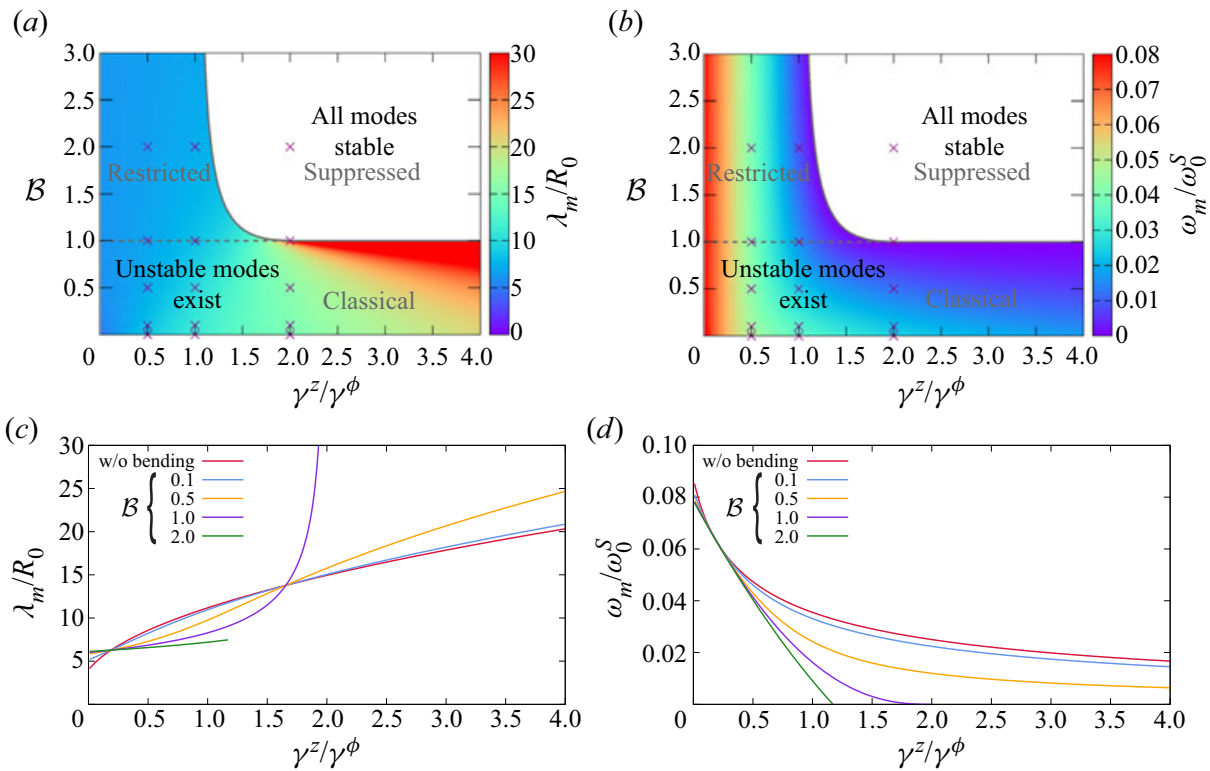


FIGURE 4. (a,b) Phase diagrams with bending resistance and anisotropic tension. The solid grey line indicates the instability threshold below which the interface undergoes a Rayleigh–Plateau instability. For bending moduli above 1, the range of unstable modes is restricted. The border to the classical regime is independent of the tension anisotropy. Strong bending elasticity $B \geq 1$ together with $\gamma^z/\gamma^\phi > 1$ can suppress the instability (white region). In the unstable phase (a) the dominant wavelength λ_m and (b) the maximum growth rate ω_m are given by colour code. Crosses correspond to the dispersion relations in figure 2. (c,d) Dominant wavelength and growth rate for different values of the bending modulus. Increasing bending resistance (from red to green) changes the wavelength strongly, especially at very large anisotropy ratio. For large enough bending contribution and larger anisotropy ratios, the instability is suppressed (lilac and green curve) with the growth rate decreasing towards zero at the threshold. Curves correspond to horizontal lines in the phase diagrams (a,b).

and moderate bending resistances do not significantly affect the dominant wavelength. Especially for anisotropy values around the isotropic case $\gamma^z/\gamma^\phi = 1.0$, the bending resistance only slightly lowers the wavelength. Increasing bending further, however, the lilac curve for $B = 1.0$ shows a qualitatively different behaviour: the wavelength strongly bends upwards and tends to infinity for $\gamma^z/\gamma^\phi \rightarrow 2.0$. This corresponds to the tension anisotropy approaching the instability threshold in figure 4(a). Finally, the green curve for $B = 2.0$ abruptly ends at an anisotropy ratio slightly larger than 1. This corresponds to figure 2(e) where in the last column the maximum is negative and therefore no instability wavelength exists and this is again due to the threshold in the phase diagram 4(a). Before this abrupt end is reached, the wavelength is nearly the same for all values of γ^z/γ^ϕ .

We further investigate the influence of anisotropy on the dominant growth rate in the phase diagram 4(b) and specifically for certain values of the bending modulus in 4(d). Most remarkably, the growth rate is not significantly affected by the bending modulus at small anisotropy. In contrast, at large anisotropy increasing the bending modulus reduces the growth rate. For the lilac and green curve, where bending suppresses the instability at large anisotropy the growth rate goes to zero with the anisotropy reaching the threshold.

3.4. Influence of reference curvature

Up to now, we assumed $H_0 = 1/(2R_0)$. However, in real systems, such as cell membranes, the bending reference shape (where bending forces vanish) can be different from the equilibrium shape (where the sum of all forces vanishes) leading to $H_0 \neq 1/(2R_0)$ for a cylindrical equilibrium shape. The limits $H_0 = 0$ and $H_0 = 1/R_0$ refer to a flat or spherical reference shape, respectively. For a membrane made of lipid molecules both the shape and the mixture of the lipids determines the reference curvature (Burger 2000; Fuller & Rand 2001; Dimova 2019). The effect of the reference curvature on the shape of vesicles and cells has been intensively studied (Seifert *et al.* 1991; Fischer 2017). Especially, for the Rayleigh–Plateau instability a non-zero reference curvature has been used to explain the effect of anchoring proteins (Tsafrir *et al.* 2001; Campelo & Hernández-Machado 2007). To complete our discussion, we therefore vary in the following the reference curvature and investigate its effect on the dispersion relation and the phase diagram. For a general value of H_0 , the normal component of the interfacial force due to the bending elasticity (3.11) takes the form

$$f_B^n = -\frac{(4H_0^2R_0^2 - 1)\kappa_B}{2R_0^3} - u_r(z) \left(\frac{3\kappa_B}{2R_0^4} - \frac{2H_0^2\kappa_B}{R_0^2} \right) - \left(-2H_0^2\kappa_B + \frac{4H_0\kappa_B}{R_0} + \frac{\kappa_B}{2R_0^2} \right) \partial_z^2 u_r - \kappa_B \partial_z^4 u_r. \quad (3.21)$$

Considering both the anisotropic tension and bending elasticity with general reference curvature, we can identify the constant part of the pressure analogously to (3.14) as

$$p_0 = \frac{\gamma^\phi}{R_0} + \frac{(4H_0^2R_0^2 - 1)\kappa_B}{2R_0^3}. \quad (3.22)$$

For a reference curvature smaller than that of a cylinder the second term becomes negative and the corresponding contribution to p_0 counteracts the tendency of the interface to increase the radius in order to minimise the curvature (Goldstein *et al.* 1996). For $H_0 = 0$ the reference pressure p_0 equals the one obtained by Powers (2010) and Boedec *et al.* (2014).

Omitting details, we derive the dispersion relation in the Stokes regime starting from (3.21) in the same manner as above. The result is shown in figure 5 for systematically increasing reference curvature. We choose (a) the value of a flat membrane $H_0 = 0$, (b) $H_0 = 1/(4R_0)$ a value smaller, (c) $H_0 = 3/(4R_0)$ a value larger than $H_0 = 1/(2R_0)$ – which is used in figure 2 – and eventually (d) $H_0 = 1/R_0$, corresponding to a spherical reference shape. In figure 5 we show in the left column results for $\gamma^z/\gamma^\phi = 0.5$, in the middle for $\gamma^z/\gamma^\phi = 1.0$ and in the right column for $\gamma^z/\gamma^\phi = 2.0$. The value of the bending coefficient is fixed at $\mathcal{B} = 1.0$, thus the curves can be directly compared to figure 2(d) where $H_0 = 1/(2R_0)$. For vanishing reference curvature in figure 5(a) we observe a strongly damping bending contribution such that the dispersion relation is purely negative and no mode is unstable. Increasing the reference curvature to $H_0 = 1/(4R_0)$ in 5(b) reduces damping, but does not qualitatively change the picture. For $H_0 = 1/(2R_0)$ (which was already shown in figure 2(d)) the sign for some wavenumbers changes, leading to unstable modes. Most remarkably, a further increase in the reference curvature to $H_0 = 3/(4R_0)$ in figure 5(c) even leads to positive values of the bending contribution to the dispersion relation. This trend continues for the spherical reference shape $H_0 = 1/R_0$ in figure 5(d). Therefore, the larger the reference curvature the larger the maximum of the

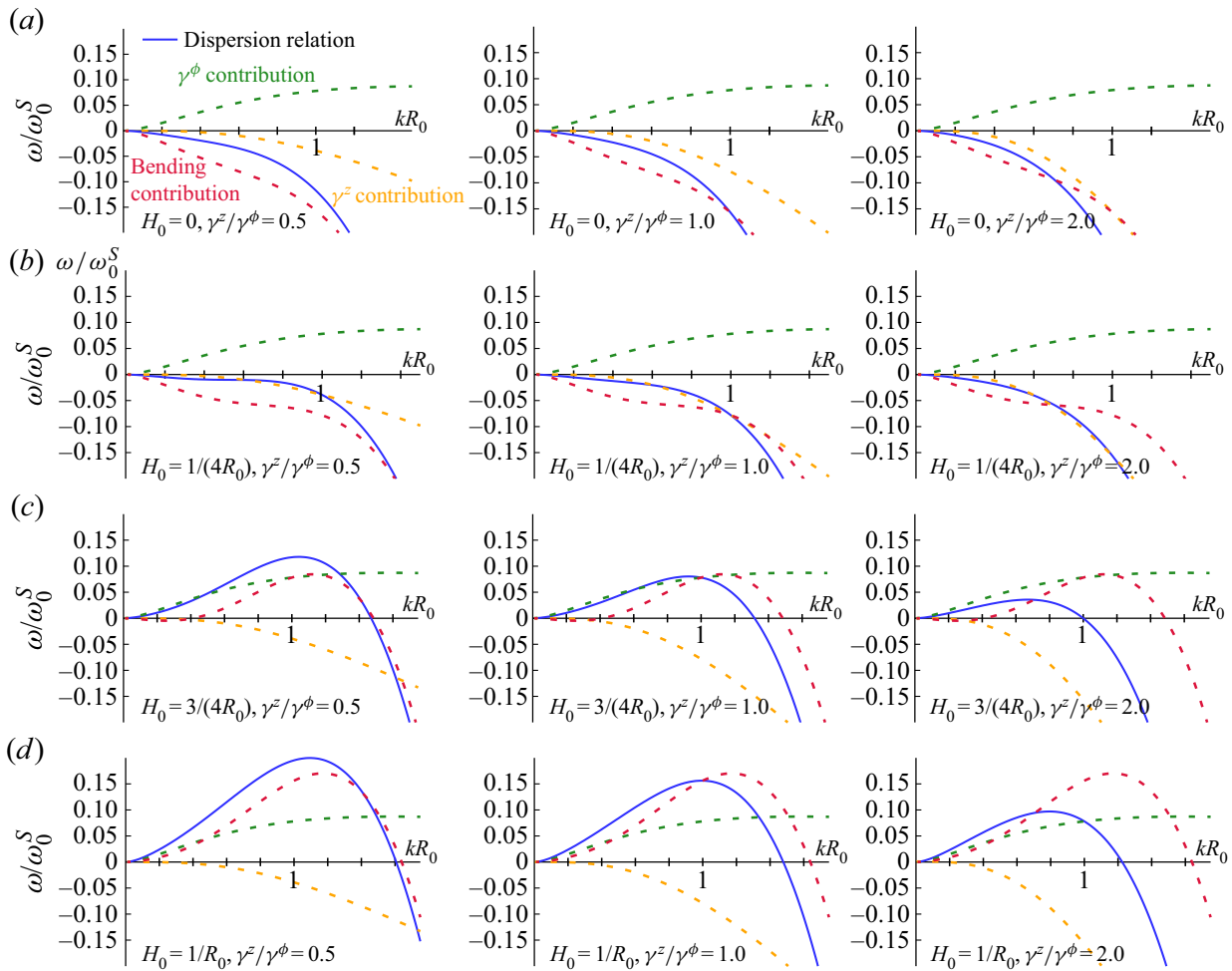


FIGURE 5. Influence of the reference curvature on the dispersion relation. Curves are shown for different reference curvatures in the different rows and from the left column to the right column the anisotropy ratio increases while the bending modulus $\mathcal{B} = 1.0$ remains fixed. In (a) the flat reference curvature leads to strong damping, which suppresses the instability. Increasing the reference curvature weakens this damping nature in (b) and eventually in (c,d) leads to positive values even of the bending contribution itself. Thus, a reference curvature beyond that of a cylinder can destabilise the interface.

dispersion relation becomes and the broader the range of unstable modes is. Variation of the anisotropy ratio which increases from left to right leads to damping of the dispersion relation and thus shifts the maximum to smaller wavenumbers. We note that the linear stability analysis considers small deformations and thus describes the initial behaviour of the interface after the onset of the instability. Therefore, for reference curvatures larger than that of a cylinder, despite the (initially) positive growth rates the tube might not break up completely but assume an undulated final shape, which minimises the total surface energy (Goldstein *et al.* 1996).

To further clarify the effect of different reference curvatures on the instability we show phase diagrams in figure 6. For vanishing reference curvature in figure (a), we observe an instability threshold which is nearly independent of the tension anisotropy γ^z/γ^ϕ . Only at very small anisotropy the threshold slightly shifts towards larger bending modulus. The nearly constant threshold of $\mathcal{B} = 2/3$ matches the critical value obtained for isotropic tension by Boedec *et al.* (2014). Increasing the reference curvature to $H_0 = 1/(4R_0)$ in 6(b) the threshold shifts towards a larger bending modulus for all anisotropy values. Moreover, the threshold bends upwards towards smaller anisotropy in a more pronounced

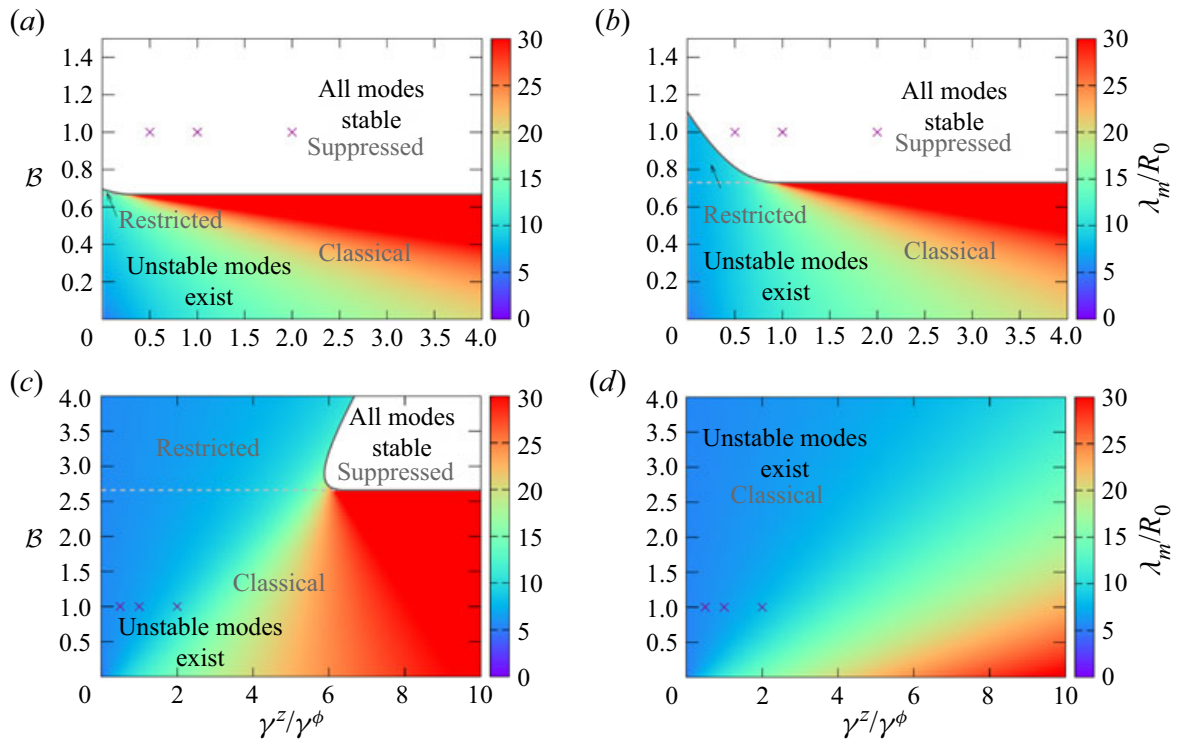


FIGURE 6. Phase diagrams for varying reference curvature. Instability threshold (grey line) and dominant wavelength (colour code) are shown for different reference curvatures (a) $H_0 = 0$, (b) $H_0 = 1/(4R_0)$, (c) $H_0 = 3/(4R_0)$ and (d) $H_0 = 1/R_0$. With increasing reference curvature the dominant wavelength decreases and the area of stable interface in the phase space becomes smaller. For the largest reference curvature no stable phase exists at all, thus a larger reference curvature facilitates the instability. Crosses refer to the dispersion relations in figure 5.

fashion and over a broader range of the anisotropy ratio. Thus, with increasing reference curvature the unstable phase is larger. For $H_0 = 1/(2R_0)$, figure 4(a) has already shown that at anisotropy ratios $\gamma^z/\gamma^\phi \in [0; 1]$ no stable phase exists. Further increasing the reference curvature to $H_0 = 3/(4R_0)$ in 6(c), on the one hand, increases the bending modulus of the threshold and the instability phase even further. On the other hand, the shape of the threshold curve changes strongly: at large anisotropy a vertical line, i.e. increasing the bending modulus for fixed anisotropy, intersects the threshold twice. Thus, increasing the bending modulus first leads to a transition from instability to the stable phase, but further increasing the bending modulus leads to another transition from the stable phase to the instability. Eventually, for the reference curvature of a sphere $H_0 = 1/R_0$ in figure 6(d) unstable modes exist for any combination of anisotropy and bending.

The complex behaviour with respect to the reference curvature can be understood by considering the limit of a flat and that of a spherical membrane. For a reference curvature of zero, the preferred shape of the interface is flat. As a consequence, the curvature due to the perturbation along the axis in addition to the azimuthal curvature is penalised more strongly by the bending energy. Thus, the instability threshold shifts towards smaller bending moduli. However, at very small anisotropy the destabilising γ^ϕ contribution strongly dominates and the instability sets in up to a larger bending modulus. If the reference curvature takes the value of a sphere, it favours the additional curvature of the developing fragments (after instability onset). Therefore, large reference curvature not only renders the interface unstable for all anisotropy values, a large reference curvature can lead to a dominant bending contribution such that bending alone can trigger an instability.

4. Shear elasticity can render the interface stable

4.1. Dispersion relation from the Skalak Hamiltonian

Apart from the resistance to bending deformations, very often the resistance to shear deformation and area dilatation is of great importance (Hannezo *et al.* 2012; Berthoumieux *et al.* 2014; Freund 2014; Bächer *et al.* 2020). In the following, we study the Rayleigh–Plateau instability of a membrane endowed with resistance to shear measured by the shear modulus κ_S and resistance to area dilatation measured by the modulus $\kappa_A = C\kappa_S$, which is expressed as a multiple of κ_S . In stark contrast to the bending forces above, here, forces tangential to the interface arise. Therefore, the hydrodynamic approach used in Part 1 and for the bending elastic interface above has to be modified. In the following, we first derive the tangential and normal elastic forces from the constitutive law and then present the changes required for including the tangential force. Eventually we obtain the dispersion relation for a shear elastic interface.

As the constitutive equation for the shear elasticity including area dilatation we use the energy functional introduced by Skalak *et al.* (1973),

$$W^{SK} = \frac{\kappa_S}{12} [(I_1^2 + 2I_1 - 2I_2) + CI_2^2], \quad (4.1)$$

with the invariants of the deformation (Green & Zerna 1954; Skalak *et al.* 1973; Barthès-Biesel 2016; Daddi-Moussa-Ider *et al.* 2017)

$$I_1 = G^{\alpha\beta} g_{\alpha\beta} - 2, \quad (4.2)$$

$$I_2 = \det(G^{\alpha\beta}) \det(g_{\alpha\beta}) - 1 \quad (4.3)$$

and the additional parameter

$$J = \sqrt{1 + I_2}. \quad (4.4)$$

The Skalak Hamiltonian (4.1) represents a nonlinear constitutive law empirically proposed for elastic cell membranes (Skalak *et al.* 1973). It describes a strain hardening behaviour of the membrane (Barthès-Biesel *et al.* 2002). The first term of (4.1) describes the shear elasticity of the elastic membrane. The second term proportional to C is related to area incompressibility, where the value of C is chosen much larger than one for a completely area incompressible membrane (Barthès-Biesel *et al.* 2002; Freund 2014). A typical value used for simulations of red blood cells is $C = 100$ (Gekle 2016; Bächer, Schrack & Gekle 2017; Bächer *et al.* 2018; Guckenberger *et al.* 2018). The invariants (4.2), (4.3) and (4.4) can be calculated using (2.5) and (2.7a,b). We perform a linearisation of the invariants with respect to small perturbations ϵ using that the actual radius is $R = R_0 + u_r(z)$ with the deformation $u_r = O(\epsilon)$ and in turn $R' = O(\epsilon)$, $R'^2 = O(\epsilon^2)$, $u_r^2 = O(\epsilon^2)$ and thus $R^2/R_0^2 = (1/R_0^2)(R_0^2 + 2u_r R_0 + u_r^2) \approx 1 + 2(u_r/R_0)$. The invariants in leading order of ϵ therefore are

$$I_1 \approx 2 \frac{u_r}{R_0} + 2u'_z, \quad (4.5)$$

$$I_2 \approx 2 \frac{u_r}{R_0} + 2u'_z, \quad (4.6)$$

$$J \approx 1 + \frac{u_r}{R_0} + u'_z. \quad (4.7)$$

From the given strain energy functional (4.1) the in-plane components of the elastic surface stress t_{el}^α in (2.14) are deduced as

$$t_{el,SK}^{\alpha\beta} = \frac{2}{J} \frac{\partial W^{SK}}{\partial I_1} G^{\alpha\beta} + 2J \frac{\partial W^{SK}}{\partial I_2} g^{\alpha\beta}, \quad (4.8)$$

where we obtain using (2.6), (2.7a,b), (4.1), (4.5)–(4.7)

$$t_{el,SK}^{\phi\phi} = \frac{2\kappa_S}{3R_0^2} \left((1+C) \frac{u_r}{R_0} + C u'_z \right), \quad (4.9)$$

$$t_{el,SK}^{zz} = \frac{2\kappa_S}{3} \left(C \frac{u_r}{R_0} + (1+C) u'_z \right). \quad (4.10)$$

Due to the in-plane and normal force balances (2.21) and (2.22), respectively, the elastic interfacial forces are calculated by (Green & Zerna 1954; Barthès-Biesel 2016; Salbreux & Jülicher 2017)

$$\nabla_\alpha t_{el,SK}^{\alpha\beta} = f_{SK}^\beta, \quad (4.11)$$

$$-c_{\alpha\beta} t_{el,SK}^{\alpha\beta} = f_{SK}^n, \quad (4.12)$$

with $t_{el,n}^\alpha = 0$ (Daddi-Moussa-Ider, Guckenberger & Gekle 2016; Daddi-Moussa-Ider *et al.* 2017; Daddi-Moussa-Ider & Gekle 2018). Due to the derivatives of the metric in its definition (2.8) the Christoffel symbols only possess terms linear or of higher order in ϵ . In the covariant derivative of the in-plane surface stress a multiplication occurs with the in-plane surface stress components and the resulting terms are of higher order, thus negligible. Therefore, the covariant derivative (2.9) equals the partial derivative in linear order. Calculating the derivatives and using the curvature tensor (2.11), we obtain the elastic interfacial forces

$$f_{SK}^z = \frac{2\kappa_S}{3} \left(C \frac{u'_r}{R_0} + (1+C) u''_z \right), \quad (4.13)$$

$$f_{SK}^n = -\frac{2\kappa_S}{3R_0} \left((1+C) \frac{u_r}{R_0} + C u'_z \right), \quad (4.14)$$

in the limit of small deformations. Due to axisymmetry the force in azimuthal direction vanishes, i.e. $f^\phi = 0$.

We then perform a linear stability analysis for the elastic interface endowed with anisotropic tension in the limit of small Reynolds numbers, i.e. for the Stokes equation covering the dynamics of the suspending fluid. Using the perturbation ansatz for the interface (3.12) we obtain for the radial deformation $u_r = \epsilon R_0 \cos(kz)$. Furthermore, the deformation fulfils the kinematic boundary conditions (Daddi-Moussa-Ider *et al.* 2016, 2018)

$$\frac{\partial u_r}{\partial t} = v_r|_{r=R_0}, \quad (4.15)$$

$$\frac{\partial u_z}{\partial t} = v_z|_{r=R_0}, \quad (4.16)$$

which allow us to couple the deformation and the fluid velocity. Starting from the kinematic boundary conditions we use $\partial_t \epsilon = \omega \epsilon$. For the velocity components we choose

a perturbation ansatz $v_r(r, z) = (\gamma^\phi \epsilon / \eta) \bar{v}_r(r) \cos(kz)$ and $v_z(r, z) = (\gamma^\phi \epsilon / \eta) \bar{v}_z(r) \sin(kz)$ as done in the case of bending elasticity and as in (B 5), (B 6) of Part 1. Doing so, we obtain the growth rate and further the axial deformation

$$\omega \epsilon R_0 \cos(kz) = \frac{\gamma^\phi \epsilon}{\eta} \bar{v}_r(R_0) \cos(kz), \quad (4.17)$$

$$u_z = \frac{\gamma^\phi \epsilon}{\eta} \frac{1}{\omega} \bar{v}_z(R_0) \sin(kz). \quad (4.18)$$

The elastic forces from (4.13) and (4.14) become

$$f_{SK}^z = -\frac{2\kappa_S}{3} \left(Ck + (1 + C) \frac{\gamma^\phi}{\eta} \frac{1}{\omega} \bar{v}_z(R_0) k^2 \right) \epsilon \sin(kz), \quad (4.19)$$

$$f_{SK}^n = -\frac{2\kappa_S}{3R_0} \left((1 + C) + C \frac{\gamma^\phi}{\eta} \frac{1}{\omega} \bar{v}_z(R_0) k \right) \epsilon \cos(kz). \quad (4.20)$$

Using again the separation ansatz for the velocities, the perturbation ansatz of the interface (3.12), the elastic forces and utilising the ring forcing concept, we obtain the fluid equations of motion in the Hankel space

$$\begin{aligned} & \frac{s}{R_0} P(s) - (s^2 + k^2) V_r(s) \\ & + \left(\underbrace{1 - \frac{\gamma^z}{\gamma^\phi} (kR_0)^2 - \frac{2\kappa_S}{3\gamma^\phi} \left((1 + C) + C \frac{\gamma^\phi}{\eta} \frac{1}{\omega} \bar{v}_z(R_0) k \right)}_{=\chi} \right) J_1(sR_0) = 0, \end{aligned} \quad (4.21)$$

$$\begin{aligned} & \frac{k}{R_0} P(s) - (s^2 + k^2) V_z(s) \\ & + \left(\underbrace{-\frac{2\kappa_S}{3\gamma^\phi} \left(CkR_0 + (1 + C) \frac{\gamma^\phi}{\eta} \frac{1}{\omega} \bar{v}_z(R_0) k^2 R_0 \right)}_{=\psi} \right) J_0(sR_0) = 0, \end{aligned} \quad (4.22)$$

$$sV_r(s) + kV_z(s) = 0, \quad (4.23)$$

where we introduce the abbreviations χ and ψ and with $V_r(s)$, $V_z(s)$, $P(s)$ being the Hankel transforms of the r -dependent parts of the velocity and the pressure. As in the previous part, the anisotropy of the interfacial tension is given by the fraction γ^z/γ^ϕ . The influence of shear elasticity is determined by the dimensionless factor $\mathcal{S} = 2\kappa_S/(3\gamma^\phi)$, which appears in both χ and ψ . The influence of area dilatation compared to shear elasticity is tuned by the factor C according to the Skalak law (4.1).

We solve the fluid equations of motion in Hankel space (4.21)–(4.23) for the velocities

$$V_r = -ks\psi \frac{J_0(sR_0)}{(s^2 + k^2)^2} + \chi \frac{k^2 J_1(sR_0)}{(s^2 + k^2)^2}, \quad (4.24)$$

$$V_z = s^2\psi \frac{J_0(sR_0)}{(s^2 + k^2)^2} - \chi \frac{ksJ_1(sR_0)}{(s^2 + k^2)^2} \quad (4.25)$$

and we obtain in real space, evaluated at the interface

$$\bar{v}_z(R_0) = \psi \underbrace{\int_0^\infty ds \frac{s^3 J_0(sR_0) J_0(sR_0)}{(s^2 + k^2)^2}}_{=\xi_1} - \chi \underbrace{\int_0^\infty ds \frac{s^2 k J_1(sR_0) J_0(sR_0)}{(s^2 + k^2)^2}}_{=\xi_2}, \quad (4.26)$$

$$\bar{v}_r(R_0) = -\psi \underbrace{\int_0^\infty ds \frac{ks^2 J_0(sR_0) J_1(sR_0)}{(s^2 + k^2)^2}}_{=\xi_2} + \chi \underbrace{\int_0^\infty ds \frac{k^2 s J_1(sR_0) J_1(sR_0)}{(s^2 + k^2)^2}}_{=\xi_3}, \quad (4.27)$$

where ξ_1 – ξ_3 abbreviate the corresponding integrals, which can be calculated e.g. using *Mathematica*. Plugging the definitions of χ and ψ into the expression (4.26) leads to an equation which can be solved for \bar{v}_z :

$$\bar{v}_z(R_0) = \frac{-\xi_1 \mathcal{S} C k R_0 - \xi_2 + \xi_2 \frac{\gamma^z}{\gamma^\phi} (k R_0)^2 + \xi_2 \mathcal{S} (1 + C)}{1 + \xi_1 \mathcal{S} (1 + C) \frac{\gamma^\phi}{\eta} \frac{1}{\omega} k^2 R_0 - \xi_2 \mathcal{S} C \frac{\gamma^\phi}{\eta} \frac{1}{\omega} k}, \quad (4.28)$$

which still contains the growth rate. Using furthermore the relation following from (4.17) for the growth rate $\omega = (\gamma^\phi / (\eta R_0)) \bar{v}_r(R_0) = -(\gamma^\phi / (\eta R_0)) \psi \xi_2 + (\gamma^\phi / (\eta R_0)) \chi \xi_3$ and inserting all definitions above, leads to a final expression, which we solve with *Mathematica* for the growth rate. This procedure results in the dispersion relation for the interface endowed with shear elasticity and area dilatation

$$\begin{aligned} \omega_{1,2} = & \mp \frac{1}{2} \omega_0^{\mathcal{S}} \mathcal{S} (k R_0 ((C + 1) k \xi_1 R_0 - 2C \xi_2) + C \xi_3 + \xi_3) + \frac{1}{2} \omega_0^{\mathcal{S}} \xi_3 \left(\frac{\gamma^z}{\gamma^\phi} k^2 R_0^2 - 1 \right) \\ & \mp \omega_0^{\mathcal{S}} \left[k^2 R_0^2 \mathcal{S} (\xi_2^2 - \xi_1 \xi_3) \left((C + 1) \left(\frac{\gamma^z}{\gamma^\phi} k^2 R_0^2 - 1 \right) + 2CS + \mathcal{S} \right) \right. \\ & \left. + \frac{1}{4} \left(\xi_3 \left(CS + \frac{\gamma^z}{\gamma^\phi} k^2 R_0^2 + \mathcal{S} - 1 \right) + k R_0 \mathcal{S} ((C + 1) k \xi_1 R_0 - 2C \xi_2) \right)^2 \right]^{1/2}. \end{aligned} \quad (4.29)$$

Because the Skalak law equals the neo-Hookean constitutive law in the limit of small deformations and $C = 1$ (Barthès-Biesel *et al.* 2002) all of the above results for $C = 1$ apply also to interfaces with neo-Hookean elasticity.

4.2. Shear elasticity introduces stability

Figure 7 shows the dispersion relation (blue line) for different relative shear moduli \mathcal{S} and different area dilatation coefficients C as given by (4.29). One of its two solutions is

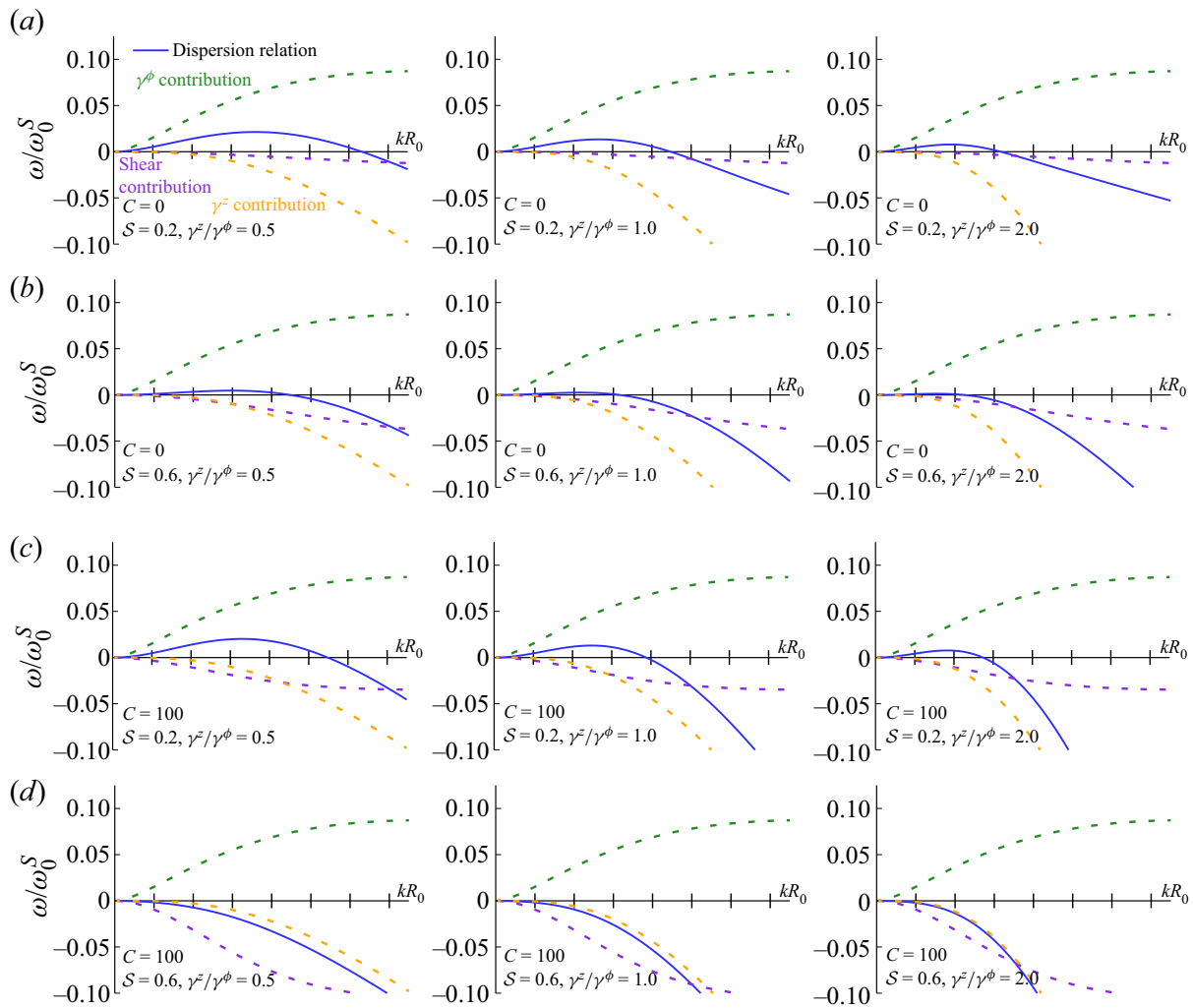


FIGURE 7. Dispersion relation for shear elasticity and anisotropic interfacial tension. Contributions from the shear elasticity \mathcal{S} (purple), γ^ϕ (green) and γ^z (orange) are distinguished (dashed lines). Dispersion relations are shown for two different area dilatation moduli in the upper two and the lower two rows, respectively, and in each case for two different shear moduli (first and second row of each case). The anisotropy ratio is varied column-wise. The shear contribution is always negative and thus damping. Increasing the shear modulus strongly lowers the maximum of the dispersion relation. A similar effect is obtained for increasing area dilatation to the extent that both together can lead to a purely negative dispersion relation and thus a stable interface.

always negative and thus not shown in the figure. Tension anisotropy γ^z/γ^ϕ is increased from the left to the right column using the same values 0.5, 1.0 and 2.0 as before. The shear contribution depicted by the purple, dashed curve is purely damping. Therefore, the initial state would be stable when interfacial tension $t_{aniso,\alpha}^\beta$ is absent. While the bending contribution in figure 2 has a root at $kR_0 = 1$, the shear contribution does not show any positive root. The negative shear contribution alters the range of growing wavenumbers.

From 7(a) to (b) and from (c) to (d) the shear modulus \mathcal{S} is increased while the resistance to area dilatation C is held constant. From (a) to (c) and from (b) to (d) the resistance to area dilatation increases but the shear modulus does not change. Both an increase in the shear modulus and in the area dilatation coefficient strengthens the damping shear contribution. In (b) the increase in shear modulus strongly dampens the dispersion relation, but it still retains a positive maximum and thus an unstable range exists for all γ^z/γ^ϕ .

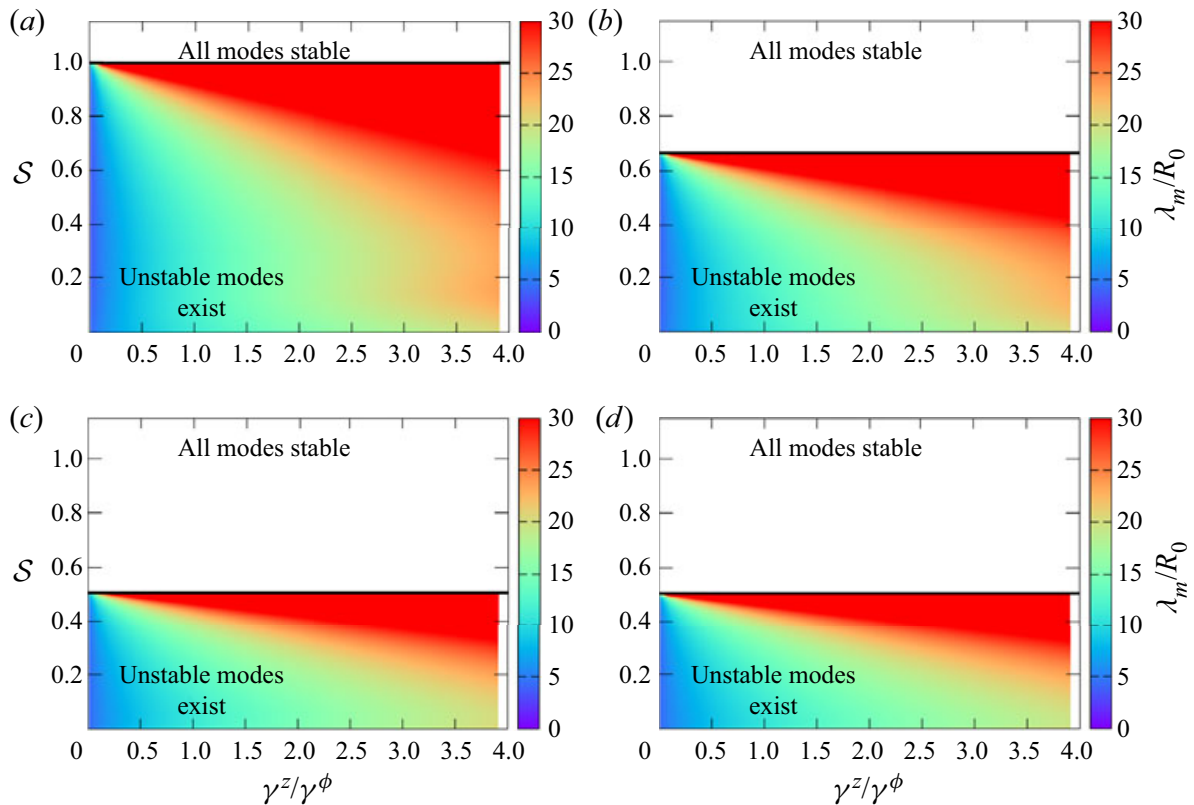


FIGURE 8. Phase diagram for anisotropic tension and shear elasticity. We vary the resistance to area dilatation from (a) $C = 0$ to (b) $C = 1$, (c) $C = 25$ and (d) $C = 100$. Above a critical shear modulus \mathcal{S} the shear elasticity renders the interface stable, where the critical value decreases from (a) to (d), but never depends on γ^z/γ^ϕ .

In (d), due to an additional increase in C the total dispersion relation eventually becomes negative such that the cylindrical interface remains stable.

In order to investigate the transition to a stable phase for shear elasticity in more detail, we show the corresponding phase diagrams for several area dilatation coefficients in figure 8. The colour in the phase diagrams encodes the dominant wavelength. We find that above a critical shear modulus \mathcal{S}_{crit} a region of stable interfaces develops in all cases. Most remarkably, this threshold is independent of the tension anisotropy. Compared to the phase diagrams including bending elasticity (figure 4a), the unstable corridor for $\gamma^z/\gamma^\phi \leq 1$ no longer exists. Besides the increase in wavelength for stronger area dilatation, in figure (b) to (d) we observe that increasing the value of C lowers the critical shear modulus.

The change of the critical shear modulus with increasing area dilatation coefficient C is quantified in figure 9. For $C = 0$ the critical shear modulus \mathcal{S}_{crit} is one, towards larger C values the critical value saturates around 0.5. Thus, increasing area dilatation can render the interface stable, just as the shear elasticity can. The curve is the same for different values of the tension anisotropy. The predicted threshold for an axisymmetric, isotropic active membrane without surrounding fluid by Berthoumieux *et al.* (2014), which has been confirmed in simulations by Bächer & Gekle (2019), agrees very well with our findings for $C = 1$ (blue triangle in figure 9).

4.3. Shear elasticity affects dominant wavelength

In figure 10 we systematically investigate the change in dominant wavelength λ_m due to changes in the anisotropy ratio and the shear modulus. Figure 10(a) shows an increase

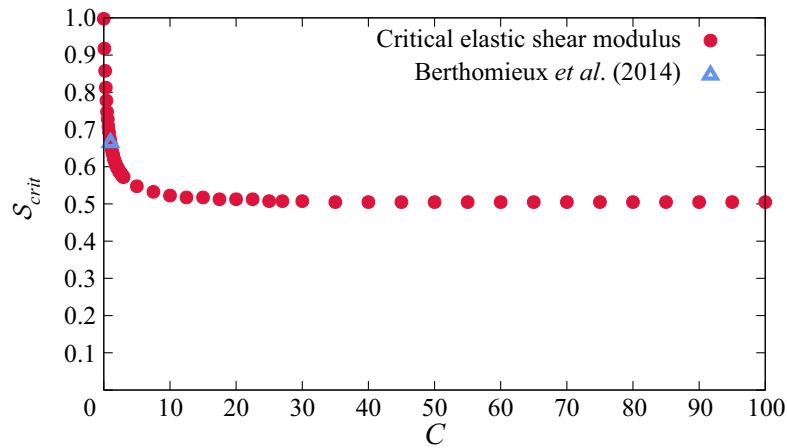


FIGURE 9. Critical shear modulus. The critical elastic shear modulus, \mathcal{S}_{crit} , above which the interface remains stable, decreases with increasing area dilatation coefficient C and towards larger C saturates at approximately 0.5. Findings of Berthoumieux *et al.* (2014) for isotropic tension in absence of any fluid agree very well with our data (blue triangle).

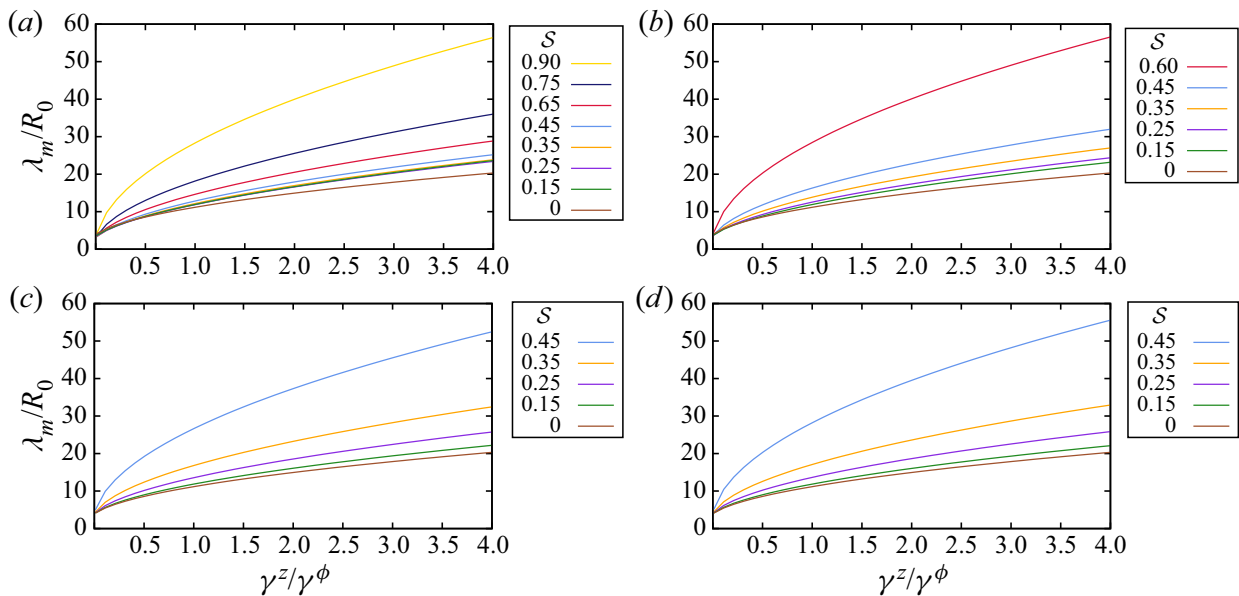


FIGURE 10. Dominant wavelength for shear elasticity. The resistance to area dilatation is varied from (a) $C = 0$ to (b) $C = 1$, (c) $C = 25$ and (d) $C = 100$. Increasing shear modulus \mathcal{S} (differently coloured curves) increases the most unstable wavelength λ_m as does increasing anisotropy of the interface tension γ^z/γ^ϕ as well as increasing C . Curves for large shear modulus such as the yellow or dark blue curve in (a) vanish in (b), because the interface becomes stable by increasing C for large shear modulus. Curves correspond to horizontal lines in the phase diagram 8.

in wavelength with increasing anisotropy γ^z/γ^ϕ for fixed C and varying shear modulus. A larger shear modulus for fixed tension anisotropy leads to an increase in the dominant wavelength of the instability. Furthermore, increasing the area dilatation coefficient C from figures 10(a) to 10(d) increases the wavelength: all curves shift towards larger values of the wavelength, while the shape of the curves remains similar. For a large shear modulus, the increase in C renders the dispersion relation negative, the cylinder is stable and therefore curves for large shear elasticity gradually disappear when going from figures 10(a) to 10(d). As seen based on the dispersion relation in figure 7, the transition

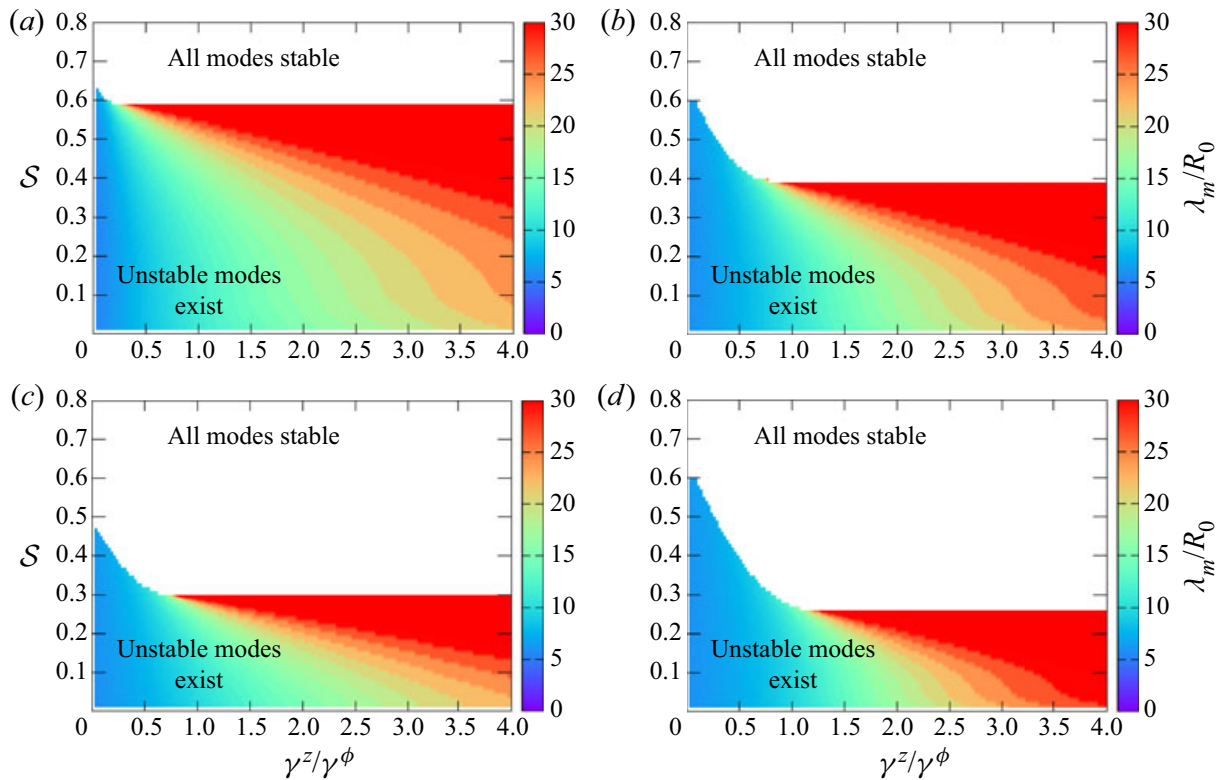


FIGURE 11. Phase diagram combining bending and shear elasticity. We vary the shear elasticity S for fixed (a) $B = 0.1$, $C = 1$, (b) $B = 0.4$, $C = 1$, (c) $B = 0.4$, $C = 100$ and (d) $B = 0.6$, $C = 1$. The interplay of resistance to bending and shearing leads to a phase diagram which combines the corresponding effects from figures 4(a) and 8. In particular, the instability threshold shifts to smaller values of the shear modulus for fixed bending elasticity and increasing anisotropy.

to the stable phase is independent of γ^z/γ^ϕ , which is in stark contrast to the bending elasticity. For larger C values in figures (c) and (d), changes are less pronounced, which reflects the saturation of the effects for strong area dilatation as observed in figure 9. As a consequence, we do not expect any distinct effects for even larger area dilatation modulus.

5. Interplay of bending and shear elasticity

Finally, in this section we combine both bending and shear elasticity. We perform a linear stability analysis in the same way as detailed in § 4.1, but modify the normal component of the ring force, expression χ in (4.21): bending elasticity leads to contributions to the normal force and thus the terms in (3.13) which are proportional to the bending modulus are added to χ . In figure 11 we show the resulting phase diagram for different combinations of the elastic parameters: while we vary the tension anisotropy and the relative shear modulus S , each diagram belongs to a fixed bending elasticity and area dilatation coefficient.

Small bending elasticity in (a) leads to results which are similar to those of a pure shear elastic interface with $C = 1$ in figure 8(b): except the small increase around zero, we have an instability threshold that is constant for varying tension anisotropy. Compared to pure shear elasticity in figure 8(b) the threshold decreases despite the rather small value of the bending resistance. Increasing the bending elasticity in figure 11(b) shows an overlap of effects due to shear elasticity and due to bending elasticity: while shear elasticity alone leads to a constant threshold for all γ^z/γ^ϕ , bending elasticity alone leads

to a range of unstable anisotropy values and a threshold towards larger anisotropy as shown in [figure 4\(a\)](#). Together these result in a peak and a decrease of the threshold at smaller anisotropy. At larger anisotropy the threshold is at lower shear modulus due to the finite bending elasticity and interplay of both. An additional increase in the area dilatation coefficient in [11\(c\)](#) leads to an overall shift of the threshold towards smaller shear modulus, but the corridor extension over $\gamma^z/\gamma^\phi \leq 0.7$ remains. Further increasing the bending modulus in [11\(d\)](#) compared to [\(b\)](#) for $C = 1$ keeps the peak in the threshold at small anisotropy but further decreases the plateau at larger anisotropy. The transition of the threshold is therefore more pronounced. For finite shear elasticity a corridor of unstable modes towards bending modulus to infinity does not exist. In all cases, the instability wavelength increases in the whole parameter space compared to pure bending and pure shear elasticity.

6. Conclusion

In this series of two papers we provided a detailed study of the Rayleigh–Plateau instability driven by anisotropic tension. The common starting point of all studied scenarios is the linear stability analysis of an infinitely long cylindrical interface subjected to an azimuthal and an axial contractile tension, the ratio of the two representing our main control parameter. We consider the full dynamics of the interior and the exterior fluid and perform a separate analysis for the high Reynolds number (Euler) and low Reynolds number (Stokes) regime. Physically, this includes fluid jets with a liquid–liquid or liquid–air interface in the Euler regime as well as tubular vesicles and biological cells in the Stokes regime. While anisotropy in the surface tension of fluid jets may be considered a somewhat special case, anisotropic tension is a common feature in cell cortices. An anisotropic tension can arise, e.g. due to alignment of actin stress fibres, and represents the core motivation of our work. In [Part 1](#) we studied the general mechanism of anisotropic Rayleigh–Plateau instability for fluid–fluid interfaces. The present paper extends these studies by including elastic forces due to bending, shearing and area dilatation in order to properly account for the mechanical characteristics of membranes. Our main findings can be summarised as follows:

- (i) Increasing azimuthal with respect to axial tension leads to destabilisation of the interface. Destabilisation expresses itself in an extension of the range of unstable wavenumbers beyond the classical Rayleigh–Plateau threshold $kR_0 = 1$. It furthermore leads to a shift in the dominant, most unstable mode towards shorter wavelengths.
- (ii) Bending forces have only a small influence if the driving tension is isotropic. If axial tension dominates, however, they exert a strongly stabilising effect up to a complete suppression of the Rayleigh–Plateau instability.
- (iii) The interplay of bending forces and anisotropy leads to the creation of a novel regime, in which the interface is stable against both very large and very small wavelengths. Only at intermediate wavelengths does an unstable range appear.
- (iv) Increasing bending forces and/or varying tension anisotropy can completely suppress the instability.
- (v) Shear elasticity always leads to stabilisation of the interface.

An important future research direction will be to investigate the coupling of anisotropic tensions with anisotropic elastic properties of the interface, where a modified elastic constitutive law including anisotropy must be derived or proposed.

Acknowledgements

C.B. and K.G. thank the Studienstiftung des deutschen Volkes for financial support. C.B. acknowledges support by the study programme ‘Biological Physics’ of the Elite Network of Bavaria. We acknowledge funding by the Deutsche Forschungsgemeinschaft (DFG, German Research Foundation) – project number 326998133 – TRR 225 ‘Biofabrication’ (subproject B07). We gratefully acknowledge computing time provided by the SuperMUC system of the Leibniz Rechenzentrum, Garching, as well as by the Bavarian Polymer Institute, and financial support from the Volkswagen Foundation.

Declaration of interests

The authors report no conflict of interest.

Supplementary material

Supplementary material are available at <https://doi.org/10.1017/jfm.2020.946>.

Appendix A. Anisotropic Rayleigh–Plateau instability of an ideal fluid jet with bending elasticity

We derive the dispersion relation of a liquid jet filled with an ideal fluid (Rayleigh 1878; Eggers & Villermaux 2008) including the bending elasticity of a possible surfactant. We here consider vanishing influence of an ambient fluid, but according to appendix C of Part 1 including an ambient fluid leads to results which look similar. The interfacial force due to bending in (3.11) together with the anisotropic interfacial tension (2.14) contributes to the traction jump at the interface given in (3.13). If we rewrite the radius $R(z)$ with the perturbation ansatz $R_0 + u_r(z)$ and consider a perturbation of the interface of the form

$$u_r = \epsilon_0 \exp(\omega t + ikz), \quad (\text{A } 1)$$

with a small amplitude ϵ_0 , growth rate ω and wavenumber k , we can calculate the linear traction jump at the interface. For an ideal fluid the traction jump in normal direction Δf^n is identical to the pressure $p_0 + \delta p(r = R)$ at the interface and we thus can write

$$\begin{aligned} p_0 + \delta p(r = R) &= \frac{\gamma^\phi}{R_0} \left(1 - \frac{\epsilon_0}{R_0} \exp(\omega t + ikz) \right) + \gamma^z \epsilon_0 k^2 \exp(\omega t + ikz) \\ &+ \kappa_B \left(\frac{1}{R_0^4} - \frac{2k^2}{R_0^2} + k^4 \right) \epsilon_0 \exp(\omega t + ikz). \end{aligned} \quad (\text{A } 2)$$

Starting from this pressure disturbance at the interface, we derive the dispersion relation as detailed in appendix C of Part 1: we identify p_0 as the constant Laplace pressure of the unperturbed interface as given in (3.14), solve the Laplace equation for the pressure and the linearised Euler equation for the velocity contribution in radial direction and use the kinematic boundary condition (Eggers & Villermaux 2008). We neglect the density of the outer fluid and thus consider a liquid jet in air (Eggers & Villermaux 2008). This procedure leads to the dispersion relation for an ideal fluid including bending elasticity

$$\omega^2 = \omega_0^2 k R_0 \left[1 - \frac{\gamma^z}{\gamma^\phi} (k R_0)^2 - \mathcal{B} (1 - 2 (k R_0)^2 + (k R_0)^4) \right] \frac{I_1(k R_0)}{I_0(k R_0)}, \quad (\text{A } 3)$$

with the prefactor $\omega_0^2 = \gamma^\phi / (\rho R_0^3)$. We obtain the same geometrical factor $k R_0 (I_1(k R_0) / I_0(k R_0))$ as Rayleigh (1892) and Patrascu & Balan (2020) for isotropic tension without

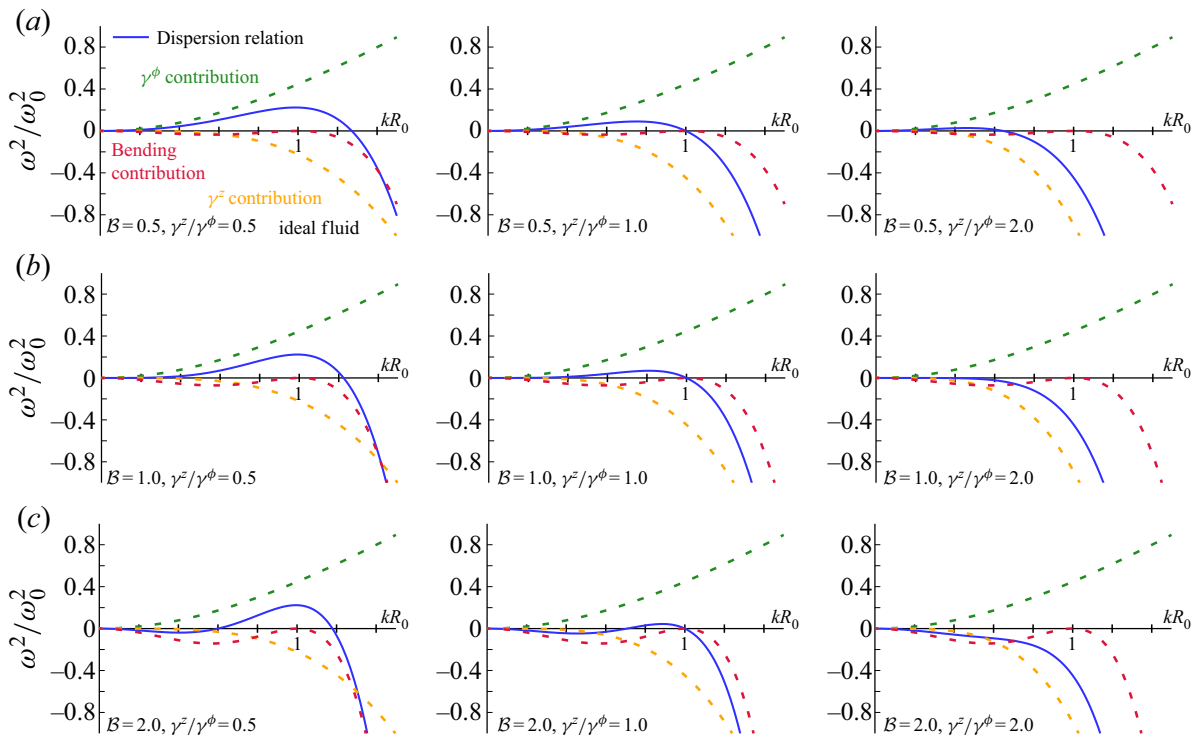


FIGURE 12. Dispersion relation for bending resistance and anisotropic interfacial tension for the ideal fluid. From left to right the anisotropy ratio increases. From top to bottom the bending resistance is increased, the values are given by the labels. The bending contribution is purely damping for all wavenumbers, except at the position of its root. It alters the range of growing modes and shifts the maximum of the dispersion relation. For the ideal the γ^ϕ -contribution tends to infinity.

and with bending elasticity, respectively. However, the prefactor including bending forces deviates from the one obtained by Patrascu & Balan (2020) for isotropic tension. The latter uses a bending tension expanded around zero curvature, which significantly differs from the one obtained from the full Helfrich Hamiltonian (Guckenberger & Gekle 2017). In contrast to the Stokes dispersion relation (3.15), we here obtain the square of the growth rate. If ω^2 is negative, the growth rate is imaginary and corresponding small perturbations are oscillatory but do not grow in time. However, $\omega^2 > 0$ results in a positive ω leading to growth of the perturbation, while the negative solution for ω will decay and is of no interest. Thus, wavenumbers where $\omega^2 > 0$ are unstable. Analogously to the calculation in the Stokes regime in § 3.1, the bending elasticity makes a contribution proportional to the dimensionless prefactor \mathcal{B} in addition to the contributions of the anisotropic tension, already appearing in (C 15) in Part 1. The factor due to bending and anisotropy in the dispersion relation (A 3) is identical to \mathcal{F} in (3.16), thus the discussion of the unstable range and the instability threshold is the same for the ideal fluid as for the Stokes fluid in § 3.

However, the dispersion relation and its maximum, the dominant wavelength, change strongly. The dispersion relation (A 3) of an anisotropic interface including bending elasticity for the ideal fluid is shown in figure 12 as blue line. Analogously to figure 2 for the Stokes limit, we also draw the bending contribution as red dashed line and the γ^z - and γ^ϕ -contribution from the anisotropic interfacial tension in orange and green, respectively. From the left to right columns in figure 12 the anisotropy ratio increases and from top to bottom the bending resistance is increased from 0.5 to 1.0 and 2.0. As already observed for

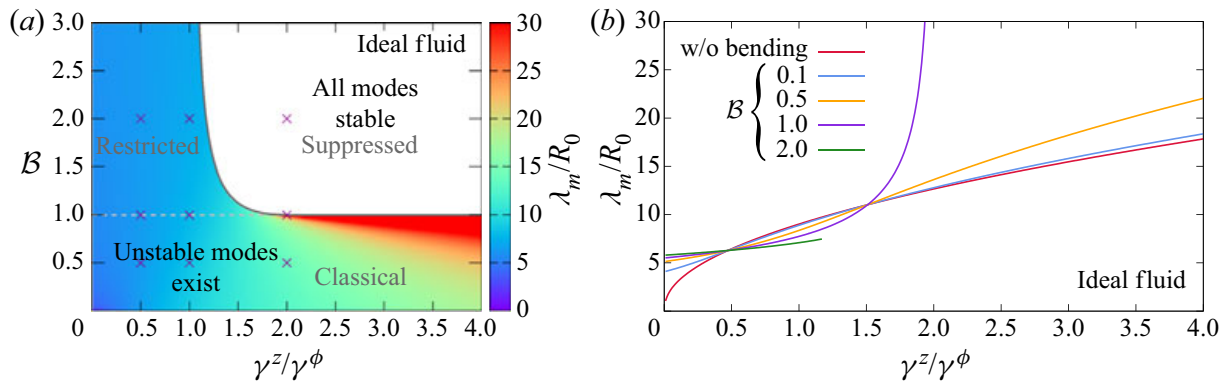


FIGURE 13. Stability of an ideal fluid jet with bending elasticity. (a) Phase diagram depending on tension anisotropy and bending elasticity. Strong bending elasticity $B \geq 1$ with $\gamma^z/\gamma^\phi > 1$ can render the interface stable (suppressed regime), whereas for smaller tension anisotropy unstable modes always exist but are restricted. (b) The instability wavelength for different bending moduli, where each curve corresponds to a horizontal line through (a). Increasing bending resistance (from orange to red) changes the wavelength strongly, especially at very small and very large anisotropy ratio and can even suppress the instability (red curve). Around the classical Rayleigh–Plateau instability, i.e. for anisotropy ratio of one, the wavelength changes only slightly.

the dispersion relations in the Stokes limit in figure 2, the bending resistance is a damping contribution for nearly all wavenumbers and becomes zero only at $kR_0 = 1$, which is a consequence of the reference curvature. Also in the case of the ideal fluid, an increase in the anisotropy ratio (from left column to right column) as well as an increase in the bending modulus (from top row 12(a) to bottom row (c)) strengthens the damping contributions which eventually leads to a negative dispersion relation and therefore a stable cylindrical interface (suppressed regime). We again observe that a large enough bending contribution in 12(c) and moderate anisotropy ratios (first two columns) lead to another root of the dispersion relation at finite wavenumbers and therefore stable modes at small wavenumber (restricted regime). However, comparison with the dispersion relations in the Stokes regime also shows that the different contributions and thus the shapes of the dispersion relation differ visibly. In contrast to the Stokes regime the destabilising γ^ϕ -contribution for the ideal fluid tends to infinity, instead of bending downwards after having reached its maximum. Thus the positive part of the dispersion relation is more asymmetric. As a consequence the maximum shifts towards larger wavenumbers. However, the right root, which determines the right border of the growing modes, is the same for both fluid limits.

In figure 13 we show the (a) phase diagram and (b) dominant wavelength λ_m for the ideal fluid jet with bending elasticity. The threshold and the border between the classical and restricted regime are the same as in the Stokes limit (figure 4a), because the factor \mathcal{F} (3.16) in the dispersion relation is the same. Each curve in 13(b) corresponds to a horizontal line through the phase diagram in (a), where the value of the most unstable wavelength is given by colour code. The curves without the influence of bending elasticity (orange) recover the result shown in figure 4(b) of Part 1. Interestingly, around the anisotropy ratio $\gamma^z/\gamma^\phi = 1$ even very large bending contributions hardly affect the wavelength. However, for strongly anisotropic interfacial tension, with a ratio close to zero or much larger than one, the dominant wavelength changes distinctly. Strikingly, a finite wavelength for $\gamma^z/\gamma^\phi \rightarrow 0$ is predicted if bending elasticity is included, whereas without bending for an ideal fluid the wavelength approaches zero, as discussed in Part 1. This can also be seen at the bottom left corner of the phase diagram. If the anisotropy ratio becomes larger for

smaller bending resistance the wavelength strongly increases and tends to infinity. The red curve for $\mathcal{B} = 2.0$ shows that for larger anisotropy ratios no unstable wavelength exists, which is reflected in figure 12(c): in the last column the dispersion relation does not assume a positive value for any wavenumber. In the phase diagram this corresponds to the region above the value $\mathcal{B} = 1.0$ where on the right all modes are stable (white region). As discussed above, for large enough bending (in the blue region in 13(a) and the red curve in 13(b) the wavelength, which correlates with the maximum of the bending contribution due to reference curvature, stays nearly constant, independently of the tension anisotropy.

REFERENCES

- ALBERTS, B., JOHNSON, A., LEWIS, J., RAFF, M., ROBERTS, K. & WALTER, P. 2007 *Molecular Biology of the Cell with CD*, 5th edn. Garland Science.
- BÄCHER, C., BENDER, M. & GEKLE, S. 2020 Flow-accelerated platelet biogenesis is due to an elasto-hydrodynamic instability. *Proc. Natl Acad. Sci. USA* **117** (32), 18969–18976.
- BÄCHER, C. & GEKLE, S. 2019 Computational modeling of active deformable membranes embedded in three-dimensional flows. *Phys. Rev. E* **99** (6), 062418.
- BÄCHER, C., KIHM, A., SCHRACK, L., KAESTNER, L., LASCHKE, M. W., WAGNER, C. & GEKLE, S. 2018 Antimargination of microparticles and platelets in the vicinity of branching vessels. *Biophys. J.* **115** (2), 411–425.
- BÄCHER, C., SCHRACK, L. & GEKLE, S. 2017 Clustering of microscopic particles in constricted blood flow. *Phys. Rev. Fluids* **2** (1), 013102.
- BAR-ZIV, R. & MOSES, E. 1994 Instability and ‘Pearling’ states produced in tubular membranes by competition of curvature and tension. *Phys. Rev. Lett.* **73** (10), 1392–1395.
- BARTHÈS-BIESEL, D. 2016 Motion and deformation of elastic capsules and vesicles in flow. *Annu. Rev. Fluid Mech.* **48** (1), 25–52.
- BARTHÈS-BIESEL, D., DIAZ, A. & DHENIN, E. 2002 Effect of constitutive laws for two-dimensional membranes on flow-induced capsule deformation. *J. Fluid Mech.* **460**, 211–222.
- BEHRNDT, M., SALBREUX, G., CAMPINHO, P., HAUSCHILD, R., OSWALD, F., ROENSCH, J., GRILL, S. W. & HEISENBERG, C.-P. 2012 Forces driving epithelial spreading in zebrafish gastrulation. *Science* **338** (6104), 257–260.
- BERGERT, M., CHANDRADOSS, S. D., DESAI, R. A. & PALUCH, E. 2012 Cell mechanics control rapid transitions between blebs and lamellipodia during migration. *Proc. Natl Acad. Sci. USA* **109** (36), 14434–14439.
- BERTHOUMIEUX, H., MAÎTRE, J.-L., HEISENBERG, C.-P., PALUCH, E. K., JÜLICHER, F. & SALBREUX, G. 2014 Active elastic thin shell theory for cellular deformations. *New J. Phys.* **16** (6), 065005.
- BLACKWELL, R., SWEETZ-SCHINDLER, O., BALDWIN, C., HOUGH, L. E., GLASER, M. A. & BETTERTON, M. D. 2016 Microscopic origins of anisotropic active stress in motor-driven nematic liquid crystals. *Soft Matt.* **12** (10), 2676–2687.
- BOEDEC, G., JAEGER, M. & LEONETTI, M. 2014 Pearling instability of a cylindrical vesicle. *J. Fluid Mech.* **743**, 262–279.
- BURGER, K. N. J. 2000 Greasing membrane fusion and fission machineries. *Traffic* **1** (8), 605–613.
- CALLAN-JONES, A. C., RUPRECHT, V., WIESER, S., HEISENBERG, C. P. & VOITURIEZ, R. 2016 Cortical flow-driven shapes of nonadherent cells. *Phys. Rev. Lett.* **116** (2), 028102.
- CAMPELO, F. & HERNÁNDEZ-MACHADO, A. 2007 Model for curvature-driven pearling instability in membranes. *Phys. Rev. Lett.* **99** (8), 088101.
- CAPOVILLA, R. & GUVEN, J. 2002 Stresses in lipid membranes. *J. Phys. A* **35** (30), 6233–6247.
- CHANDRASEKHARAI, D. S. & DEBNATH, L. 2014 *Continuum Mechanics*. Elsevier.
- CHUGH, P., CLARK, A. G., SMITH, M. B., CASSANI, D. A. D., DIERKES, K., RAGAB, A., ROUX, P. P., CHARRAS, G., SALBREUX, G. & PALUCH, E. K. 2017 Actin cortex architecture regulates cell surface tension. *Nat. Cell Biol.* **19** (6), 689–697.

- DADDI-MOUSSA-IDER, A. & GEKLE, S. 2018 Brownian motion near an elastic cell membrane: a theoretical study. *Eur. Phys. J. E* **41** (2), 19.
- DADDI-MOUSSA-IDER, A., GUCKENBERGER, A. & GEKLE, S. 2016 Long-lived anomalous thermal diffusion induced by elastic cell membranes on nearby particles. *Phys. Rev. E* **93** (1), 012612.
- DADDI-MOUSSA-IDER, A., LISICKI, M. & GEKLE, S. 2017 Hydrodynamic mobility of a sphere moving on the centerline of an elastic tube. *Phys. Fluids* **29** (11), 111901.
- DADDI-MOUSSA-IDER, A., RALLABANDI, B., GEKLE, S. & STONE, H. A. 2018 Reciprocal theorem for the prediction of the normal force induced on a particle translating parallel to an elastic membrane. *Phys. Rev. Fluids* **3** (8), 084101.
- DESERNO, M. 2015 Fluid lipid membranes: from differential geometry to curvature stresses. *Chem. Phys. Lipids* **185**, 11–45.
- DIMOVA, R. 2019 Giant vesicles and their use in assays for assessing membrane phase state, curvature, mechanics, and electrical properties. *Annu. Rev. Biophys.* **48** (1), 93–119.
- DMITRIEFF, S., ALSINA, A., MATHUR, A. & NÉDÉLEC, F. J. 2017 Balance of microtubule stiffness and cortical tension determines the size of blood cells with marginal band across species. *Proc. Natl Acad. Sci.* **114**, 201618041.
- DRAZIN, P. G. & REID, W. H. 2004 *Hydrodynamic Stability*. Cambridge University Press.
- DUPONT, C., SALSAC, A.-V., BARTHÈS-BIESEL, D., VIDRASCU, M. & LE TALLEC, P. 2015 Influence of bending resistance on the dynamics of a spherical capsule in shear flow. *Phys. Fluids* **27** (5), 051902.
- EGGERS, J. & VILLERMAUX, E. 2008 Physics of liquid jets. *Rep. Prog. Phys.* **71** (3), 036601.
- FINKEN, R., KESSLER, S. & SEIFERT, U. 2011 Micro-capsules in shear flow. *J. Phys.: Condens. Matter* **23** (18), 184113.
- FINKEN, R. & SEIFERT, U. 2006 Wrinkling of microcapsules in shear flow. *J. Phys.: Condens. Matter* **18** (15), L185–L191.
- FISCHER, T. M. 2004 Shape memory of human red blood cells. *Biophys. J.* **86** (5), 3304–3313.
- FISCHER, T. M. 2017 Creep and stress relaxation of human red cell membrane. *Biomech. Model. Mechanobiol.* **16** (1), 239–247.
- FISCHER-FRIEDRICH, E., HYMAN, A. A., JÜLICHER, F., MÜLLER, D. J. & HELENIUS, J. 2014 Quantification of surface tension and internal pressure generated by single mitotic cells. *Sci. Rep.* **4**, 6213.
- FREUND, J. B. 2014 Numerical simulation of flowing blood cells. *Annu. Rev. Fluid Mech.* **46** (1), 67–95.
- FULLER, N. & RAND, R. P. 2001 The influence of lysolipids on the spontaneous curvature and bending elasticity of phospholipid membranes. *Biophys. J.* **81** (1), 243–254.
- GEKLE, S. 2016 Strongly accelerated margination of active particles in blood flow. *Biophys. J.* **110** (2), 514–520.
- GOLDSTEIN, R. E., NELSON, P., POWERS, T. & SEIFERT, U. 1996 Front propagation in the pearling instability of tubular vesicles. *J. Phys. II* **6** (5), 767–796.
- GONZALEZ-RODRIGUEZ, D., SART, S., BABATAHERI, A., TARESTE, D., BARAKAT, A. I., CLANET, C. & HUSSON, J. 2015 Elastocapillary instability in mitochondrial fission. *Phys. Rev. Lett.* **115** (8), 088102.
- GRAESSEL, K., BÄCHER, C. & GEKLE, S. 2021 Rayleigh–Plateau instability of anisotropic interfaces. Part 1. An analytical and numerical study. *J. Fluid Mech.* **xxx**, Ax.
- GREEN, A. E. & ZERNA, W. 1954 *Theoretical Elasticity*. Clarendon Press.
- GUCKENBERGER, A. & GEKLE, S. 2017 Theory and algorithms to compute Helfrich bending forces: a review. *J. Phys.: Condens. Matter* **29** (20), 203001.
- GUCKENBERGER, A., KIHM, A., JOHN, T., WAGNER, C. & GEKLE, S. 2018 Numerical–experimental observation of shape bistability of red blood cells flowing in a microchannel. *Soft Matt.* **14** (11), 2032–2043.
- GUVEN, J. 2004 Membrane geometry with auxiliary variables and quadratic constraints. *J. Phys. A: Math. Gen.* **37** (28), L313–L319.
- HANNEZO, E., PROST, J. & JOANNY, J.-F. 2012 Mechanical instabilities of biological tubes. *Phys. Rev. Lett.* **109** (1), 018101.

- HELFRICH, W. 1973 Elastic properties of lipid bilayers: theory and possible experiments. *Z. Naturforsch. C* **28** (11–12), 693–703.
- JAENSSON, N. & VERMANT, J. 2018 Tensiometry and rheology of complex interfaces. *Curr. Opin. Colloid Interface Sci.* **37**, 136–150.
- JELERČIČ, U. 2017 Equilibrium shapes of tubular lipid membranes. *Soft Matt.* **13** (16), 3048–3052.
- JÜLICHER, F., GRILL, S. W & SALBREUX, G. 2018 Hydrodynamic theory of active matter. *Rep. Prog. Phys.* **81** (7), 076601.
- KANTSLEER, V., SEGRE, E. & STEINBERG, V. 2008 Critical dynamics of vesicle stretching transition in elongational flow. *Phys. Rev. Lett.* **101** (4), 048101.
- KREYSZIG, E. 1968 *Introduction to Differential Geometry and Riemannian Geometry*. University of Toronto Press.
- KRIEG, M., ARBOLEDA-ESTUDILLO, Y., PUECH, P.-H., KÄFER, J., GRANER, F., MÜLLER, D. J. & HEISENBERG, C.-P. 2008 Tensile forces govern germ-layer organization in zebrafish. *Nat. Cell Biol.* **10** (4), 429–436.
- LAURENT, S., GIRERD, X., MOURAD, J. J., LACOLLEY, P., BECK, L., BOUTOUYRIE, P., MIGNOT, J. P. & SAFAR, M. 1994 Elastic modulus of the radial artery wall material is not increased in patients with essential hypertension. *Arterioscler. Thromb.* **14** (7), 1223–1231.
- LI, X. & SARKAR, K. 2008 Front tracking simulation of deformation and buckling instability of a liquid capsule enclosed by an elastic membrane. *J. Comput. Phys.* **227** (10), 4998–5018.
- LOMAKINA, E. B., SPILLMANN, C. M., KING, M. R. & WAUGH, R. E. 2004 Rheological analysis and measurement of neutrophil indentation. *Biophys. J.* **87** (6), 4246–4258.
- MAYER, M., DEPKEN, M., BOIS, J. S., JÜLICHER, F. & GRILL, S. W. 2010 Anisotropies in cortical tension reveal the physical basis of polarizing cortical flows. *Nature* **467** (7315), 617–621.
- MURRELL, M., OAKES, P. W., LENZ, M. & GARDEL, M. L. 2015 Forcing cells into shape: the mechanics of actomyosin contractility. *Nat. Rev. Mol. Cell Biol.* **16** (8), 486–498.
- NARSIMHAN, V., SPANN, A. P. & SHAQFEH, E. S. G. 2015 Pearling, wrinkling, and buckling of vesicles in elongational flows. *J. Fluid Mech.* **777**, 1–26.
- NELSON, P., POWERS, T. & SEIFERT, U. 1995 Dynamical theory of the pearling instability in cylindrical vesicles. *Phys. Rev. Lett.* **74** (17), 3384–3387.
- PAL, A. & KHAKHAR, D. V. 2019 Breakage of vesicles in a simple shear flow. *Soft Matt.* **15** (9), 1979–1987.
- PATRASCU, C. & BALAN, C. 2020 The effect of curvature elasticity on Rayleigh–Plateau instability. *Eur. J. Mech. B/Fluids* **80**, 167–173.
- POWERS, T. R. 2010 Dynamics of filaments and membranes in a viscous fluid. *Rev. Mod. Phys.* **82** (2), 1607–1631.
- POZRIKIDIS, C. 2001 Interfacial dynamics for Stokes flow. *J. Comput. Phys.* **169** (2), 250–301.
- PROST, J., JÜLICHER, F. & JOANNY, J.-F. 2015 Active gel physics. *Nat. Phys.* **11** (2), 111–117.
- RAUZI, M., VERANT, P., LECUIT, T. & LENNE, P.-F. 2008 Nature and anisotropy of cortical forces orienting *Drosophila* tissue morphogenesis. *Nat. Cell Biol.* **10** (12), 1401–1410.
- RAYLEIGH, LORD 1878 On the instability of jets. *Proc. Lond. Math. Soc.* **1** (1), 4–13.
- RAYLEIGH, LORD 1892 XVI. On the instability of a cylinder of viscous liquid under capillary force. *Lond. Edinb. Dubl. Philos. Mag. J. Sci.* **34** (207), 145–154.
- REYMANN, A.-C., BOUJEMAA-PATERSKI, R., MARTIEL, J.-L., GUERIN, C., CAO, W., CHIN, H. F., DE LA CRUZ, E. M., THERY, M. & BLANCHOIN, L. 2012 Actin network architecture can determine myosin motor activity. *Science* **336** (6086), 1310–1314.
- REYMANN, A.-C., STANISCIJA, F., ERZBERGER, A., SALBREUX, G. & GRILL, S. W. 2016 Cortical flow aligns actin filaments to form a furrow. *eLife* **5**, e17807.
- SALBREUX, G. & JÜLICHER, F. 2017 Mechanics of active surfaces. *Phys. Rev. E* **96** (3), 032404.
- SALBREUX, G., PROST, J. & JOANNY, J. F. 2009 Hydrodynamics of cellular cortical flows and the formation of contractile rings. *Phys. Rev. Lett.* **103** (5), 058102.
- SANBORN, J., OGLECKA, K., KRAUT, R. S. & PARIKH, A. N. 2013 Transient pearling and vesiculation of membrane tubes under osmotic gradients. *Faraday Discuss.* **161**, 167–176.
- SEIFERT, U., BERNDL, K. & LIPOWSKY, R. 1991 Shape transformations of vesicles: phase diagram for spontaneous-curvature and bilayer-coupling models. *Phys. Rev. A* **44** (2), 1182.

- SEIFERT, U. & LIPOWSKY, R. 1995 Morphology of vesicles. In *Handbook of Biological Physics* (ed. R. Lipowsky & E. Sackmann), vol. 1, pp. 403–464. Elsevier Science B.V.
- SKALAK, R., TOZEREN, A., ZARDA, R. P. & CHIEN, S. 1973 Strain energy function of red blood cell membranes. *Biophys. J.* **13** (3), 245.
- TINEVEZ, J.-Y., SCHULZE, U., SALBREUX, G., ROENSCH, J., JOANNY, J.-F. & PALUCH, E. 2009 Role of cortical tension in bleb growth. *Proc. Natl Acad. Sci.* **106** (44), 18581–18586.
- TSAFRIR, I., SAGI, D., ARZI, T., GUEDEAU-BOUDEVILLE, M.-A., FRETTE, V., KANDEL, D. & STAVANS, J. 2001 Pearling instabilities of membrane tubes with anchored polymers. *Phys. Rev. Lett.* **86** (6), 1138–1141.
- ZHANG, R., KUMAR, N., ROSS, J. L., GARDEL, M. L. & DE PABLO, J. J. 2018 Interplay of structure, elasticity, and dynamics in actin-based nematic materials. *Proc. Natl Acad. Sci.* **115** (2), E124–E133.

Publication 5

FLOW-ACCELERATED PLATELET BIOGENESIS IS DUE TO AN ELASTO-HYDRODYNAMIC INSTABILITY

C. Bächer, M. Bender, and S. Gekle

Proceedings of the National Academy of Sciences
117 (32), 2020

Copyright by the National Academy of Sciences.

DOI: [10.1073/pnas.2002985117](https://doi.org/10.1073/pnas.2002985117)



Flow-accelerated platelet biogenesis is due to an elasto-hydrodynamic instability

Christian Bächer^{a,1} , Markus Bender^b , and Stephan Gekle^{a,1}

^aBiofluid Simulation and Modeling, Theoretische Physik VI, University of Bayreuth, 95447 Bayreuth, Germany; and ^bInstitute of Experimental Biomedicine I, University Hospital and Rudolf Virchow Center, 97080 Würzburg, Germany

Edited by Michael D. Graham, University of Wisconsin-Madison, Madison, WI, and accepted by Editorial Board Member Pablo G. Debenedetti June 30, 2020 (received for review February 19, 2020)

Blood platelets are formed by fragmentation of long membrane extensions from bone marrow megakaryocytes in the blood flow. Using lattice-Boltzmann/immersed boundary simulations we propose a biological Rayleigh–Plateau instability as the biophysical mechanism behind this fragmentation process. This instability is akin to the surface tension-induced breakup of a liquid jet but is driven by active cortical processes including actomyosin contractility and microtubule sliding. Our fully three-dimensional simulations highlight the crucial role of actomyosin contractility, which is required to trigger the instability, and illustrate how the wavelength of the instability determines the size of the final platelets. The elasto-hydrodynamic origin of the fragmentation explains the strong acceleration of platelet biogenesis in the presence of an external flow, which we observe in agreement with experiments. Our simulations then allow us to disentangle the influence of specific flow conditions: While a homogeneous flow with uniform velocity leads to the strongest acceleration, a shear flow with a linear velocity gradient can cause fusion events of two developing platelet-sized swellings during fragmentation. A fusion event may lead to the release of larger structures which are observable as preplatelets in experiments. Together, our findings strongly indicate a mainly physical origin of fragmentation and regulation of platelet size in flow-accelerated platelet biogenesis.

biophysics | blood platelet biogenesis | actomyosin contractility | Rayleigh–Plateau instability | blood flow

Blood platelets are the second most abundant cell type in blood and are responsible for a quick stop of bleeding after an injury (1). Due to their short life span of only 7 to 10 d, platelets need to be constantly produced and global platelet number kinetics have been studied using mathematical models for quite some time (2–6). On a single-cell level, the highly efficient process of platelet biogenesis starts from megakaryocytes (MKs) residing extravascularly in the bone marrow. Mature MKs first grow long tubular extensions, termed proplatelets, which reach into the adjacent sinusoidal blood vessels. The extended proplatelets then form periodic swellings and fragment into smaller pieces that eventually mature into functional platelets (7, 8). Recently, intensive efforts have been under way toward the *in vitro* production of platelets (9–19) in various kinds of bioreactors. In those microfluidic devices, MKs are either attached to pillars (17) and exposed to an approximately homogeneous flow or trapped in structures resembling the vascular endothelium (15, 16) and exposed to parabolic Poiseuille flow during the process of proplatelet growth and fragmentation. In both cases, the flow strength to which proplatelets are subjected can easily be tuned externally. Interestingly, a dramatic acceleration of platelet biogenesis up to 20 times caused by fluid flow has been consistently reported in various bioreactor geometries (7, 12, 15–17, 19). The mechanisms behind this fascinating example of an active biological process directly interacting with its surrounding hydrodynamic environment have so far not been elucidated.

Here, to explain these findings, we propose an elasto-hydrodynamic instability akin to the Rayleigh–Plateau instability of a water jet leading to breakup into droplets as the key biophysical mechanism behind platelet biogenesis. To back up this hypothesis, we use our recently developed simulation method (20) which computes the forces created by the cortical actomyosin system and microtubules and the resulting dynamic deformation of the proplatelet membrane as well as the important two-way coupling to the flowing hydrodynamic environment in a fully three-dimensional (3D) situation. Motivated by experimental observations on the importance of actomyosin (9, 21–29), we show how cortical actomyosin contractility creates periodic swellings along the proplatelet in a similar, yet not identical, way as surface tension triggers the breakup of a water jet exiting from a faucet into a series of droplets in the classic Rayleigh–Plateau scenario. Indeed, we find that experimentally observed platelet sizes are in good agreement with predictions for this mechanism. That such a “biological Rayleigh–Plateau instability” may exist different from platelet biogenesis has been hypothesized before in axisymmetric situations for active (30, 31) as well as passive (32–34) vesicles and membranes. Here, specifically focusing on cell biogenesis in fully 3D, hydrodynamic flows, we go one step farther and fully take into account the flowing environment present both in sinusoidal blood vessels *in vivo* and in microfluidic devices *in vitro*. Consistent with experimental findings, we report a strong acceleration of the fragmentation process in the presence of hydrodynamic flow. We then uncover the specific

Significance

To maintain the high number of blood platelets in mammalian blood, an exceptionally efficient process for platelet biogenesis is required. While recent *in vitro* experiments demonstrate blood flow as a key factor accelerating biogenesis, the biophysical mechanism behind this acceleration remains unclear. Here we use computer simulations to show how fluid flow can indeed strongly increase biogenesis. The key aspect of our work is that we introduce a physical mechanism, akin to the well-known Rayleigh–Plateau instability of a liquid jet, as the likely origin of accelerated platelet production. Our findings can lead to a more efficient design of microfluidic bioreactors for platelet production, but also explain the exceptionally strong coupling of fluid flow and platelet biogenesis *in vivo*.

Author contributions: C.B., M.B., and S.G. designed research; C.B. and M.B. performed research; C.B. analyzed data; and C.B., M.B., and S.G. wrote the paper.

The authors declare no competing interest.

This article is a PNAS Direct Submission. M.D.G. is a guest editor invited by the Editorial Board.

Published under the [PNAS license](#).

See [online](#) for related content such as Commentaries.

¹To whom correspondence may be addressed. Email: christian.baecher@uni-bayreuth.de or stephan.gekle@uni-bayreuth.de.

This article contains supporting information online at <https://www.pnas.org/lookup/suppl/doi:10.1073/pnas.2002985117/-DCSupplemental>.

First published July 27, 2020.

effects of different flow patterns: Shear, i.e., velocity gradients, as present in parabolic Poiseuille flow through microchannels or blood vessels leads to the fusion of neighboring swellings. We hypothesize this to be the mechanism behind the formation of larger structures, called proplatelets, frequently observed in the bloodstream (35). In contrast, homogeneous flow with constant velocity, as approximately present in some bioreactor systems (17), leads to a systematic and strong acceleration without fusion events, which highlights its potential role for efficient *in vitro* production of monodisperse platelets. We report a robust size of the released platelets which is determined by the dominant wavelength of the instability and is largely independent of fluid flow in agreement with experimental findings. Our model thus strongly indicates that a simple physical mechanism determines both platelet size and accelerated platelet biogenesis in flow without the need of specific biochemical regulation. Furthermore, our findings highlight in general the strong influence of external flow on activity-driven cell deformation and thus may be relevant for other processes such as cell division and *in vitro* cell reproduction.

Computational Model for Platelet Biogenesis

In the following, we introduce our computational model for platelet biogenesis. Platelet biogenesis can be divided into two key steps: proplatelet extension and proplatelet fragmentation, which itself consists of formation of platelet-like swellings and their release as premature platelets. The first step, proplatelet extension, has been shown to rely on sliding of microtubule filaments driven by dynein (16). In the second step, once the proplatelet is extended, characteristic swellings form along the proplatelet shaft as we show in Fig. 1 *A–C* by experiments using a bioreactor, which are described in *Materials and Methods*. After swelling formation, the proplatelet ruptures, releasing the swellings as separate premature platelets into the bloodstream. In this work we focus specifically on the second step, i.e., the fragmentation mechanism of already extended proplatelets. Key ingredients of our model are the proplatelet's active cell cortex including actomyosin and microtubules, its elastic membrane, and external fluid flow.

A sketch of our simulation setup is shown in Fig. 1*D*. We model the extended proplatelet as a cylindrical membrane of finite length and radius $R_0 = 1.5 \mu\text{m}$ (17) terminated by a spherical cap on the right and attached to a solid wall on the left. Attachment is achieved by an overlap of the proplatelet end with the wall and mimics the large and spatially fixed MK as seen in experiments, e.g., in Fig. 1*A*. In our simulations we use 90 times the radius as typical length of a proplatelet. The proplatelet is immersed in blood plasma.

The overall picture that has emerged from a series of recent studies (9, 21–29) highlights the key role of the cortical actomyosin system for swelling formation. Actin filaments have been shown by electron micrographs to be confined mostly to the thin cell cortex of the proplatelet (36, 37) where they form a disordered but homogeneous network (38). Such actomyosin networks are known to be contractile (39–47) in an isotropic fashion (39). In addition to the actomyosin, microtubule sliding has been shown to extend the proplatelet (16), which we therefore consider as being extensible mainly along the axis. These observations motivate us to use an active thin shell formulation; i.e., we treat the cortex together with the plasma membrane as an infinitely thin two-dimensional shell. The theoretical framework for active membranes has recently been established (48) based on active gel theory, which is a well-established tool for the continuum description of active dynamics in cytoskeletal assemblies (49, 50) and has been successfully utilized for the investigation of mechanisms regulating the cell shape in general (51, 52), in cell division (53, 54), and for cell motility (55). For the computational realization, we use our recently developed method for

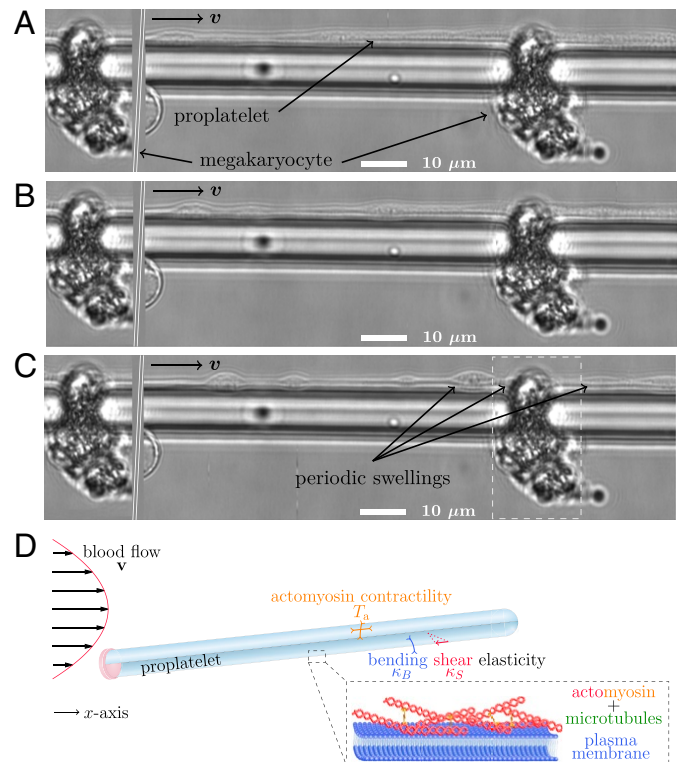


Fig. 1. Experiments and setup illustration. (A) MKs imaged *in vitro* grow long tubular extensions (proplatelets) which after some time form periodic swellings along their shaft as shown in *B* and *C*. MKs are trapped in the bottom part of a microfluidic bioreactor by small gaps (15, 16) and remain fixed during proplatelet extension and fragmentation. To illustrate the periodic arrangement of MKs as shown in *SI Appendix, Fig. S21*, the marked area on the right-hand side has been copied and reinserted on the left of the image. Fluid flows with a maximum velocity of 2.2 mm/s and the complete width of the experimental image is 137.5 μm . (D) Illustration of the computational model for the proplatelet membrane. Plasma membrane and cortex (*Inset*) are treated together as an active, elastic thin shell. The shell is endowed with bending and shear elasticity as well as actomyosin contractility in concert with microtubule sliding. We model the proplatelet as an initially cylindrical membrane with one fixed end and one free end according to the experimental situation. The proplatelet is subject to external flow.

active membranes in 3D fluid flows (20), which is based on the lattice-Boltzmann/immersed boundary method (56) and is further detailed in *SI Appendix, section S1*. This method covers both the influence of the cell on the surrounding fluid flow and the forces acting on the cell due to external flow. Taken together, we consider an anisotropic active stress which accounts for the combination of microtubule extension and actomyosin contractility. The active part of the in-plane surface stress tensor (20) therefore takes the form

$$t_{a\alpha}^{\beta} = \begin{pmatrix} T_a^z & 0 \\ 0 & T_a^{\phi} \end{pmatrix} \quad [1]$$

with $T_a^z < T_a^{\phi}$ due to microtubule extension acting against actomyosin contractility in the axial direction. We choose a ratio of $T_a^z/T_a^{\phi} = 0.75$ and the value $T_a^{\phi} = 2.5 \times 10^{-5} \text{ N/m}$, which is close to what has been predicted as the cortical tension of human blood platelets (36). This value is somewhat below, but in the same range as, the contractile stress of activated platelets where 3D stresses of $\sigma_0 = 150 \text{ kPa}$ have been reported in adhered platelets with a thickness of $h = 10$ to 100 nm (57, 58) leading to a membrane stress of around $\sigma_0 h = 1.5 \cdot 10^{-3} \text{ N/m}$. Direct measurements of the active stress in MKs or extended proplatelets

have thus far not been carried out. We show in *SI Appendix, Fig. S11*, however, that our results do not critically depend on the precise value of the active stress. Similarly, *SI Appendix, section S3* shows that our results are not qualitatively altered if an isotropic contractility ($T_a^z / T_a^\phi = 1$) is assumed.

To cover the passive elasticity of the plasma membrane and cortical cytoskeletal network, we furthermore assign shear and bending resistance to the proplatelet membrane. Shear elasticity stems from the continuous spectrin network in the proplatelet (59) and is considered using the common Skalak model which has been established for numerical simulations of red blood cells (60). Bending elasticity stems from the properties of the plasma membrane and is modeled using the Helfrich model (60, 61). We use a resistance to shear of $\kappa_S = 5 \times 10^{-6}$ N/m and a resistance to bending of $\kappa_B = 2 \times 10^{-19}$ Nm as they are reported for red blood cells (60). Proplatelets are immersed into a flowing liquid with the properties of blood plasma having a density $\rho = 1,000$ g/L and a viscosity $\eta = 1.2 \times 10^{-3}$ Pa·s. The proplatelet interior is filled with a liquid of the same properties, except in *SI Appendix, Fig. S13* where we increase the viscosity contrast. The channel diameter is chosen to be about eight times the proplatelet diameter. Our simulations in general do not consider thermal fluctuations. Including them, however, does not significantly affect the results as shown in *SI Appendix, Fig. S12*.

Results

In the following three subsections, we investigate proplatelet fragmentation first in a quiescent fluid such as a petri dish followed by fragmentation in parabolic Poiseuille flow for two different geometries. In the first geometry, the flow is loosely confined between two parallel plates with a channel height of 23.5 μm corresponding to microchannel bioreactors as well as to typical sinusoidal capillaries in the bone marrow (62). The second geometry is a narrow cylinder with a diameter of 9 μm and thus only slightly larger than the proplatelet itself corresponding to small and intermediate capillaries in the bone marrow (62). Finally, we consider a homogeneous flow with constant velocity, which can be utilized for efficient platelet biogenesis in micropillar bioreactors.

Proplatelet Fragmentation without Flow by a Biological Rayleigh–Plateau Instability. We start by considering a proplatelet immersed in a quiescent fluid subject to actomyosin contractility in concert with microtubule sliding. Fig. 2 *A–C* shows the dynamic evolution of the proplatelet shape for different times. Initially, in Fig. 2*A* the proplatelet is attached to a pillar on the left-hand side. As the simulation starts, the free end of the proplatelet on the right starts contracting and a spherical tip forms as seen in Fig. 2*B*. The initially cylindrical shaft starts to deform and a periodic, equidistant arrangement of platelet-sized swellings develops. These swellings are connected by small mem-

brane strings, as shown in Fig. 2*C*. Once the membrane strings become too thin to be properly resolved numerically, the simulation is stopped and fragmentation is considered complete. The entire process is shown in *Movie S1*.

The numerically obtained proplatelet dynamics in Fig. 2 *A–C* can be compared to our experimental images in Fig. 1 *A–C* and *SI Appendix, Fig. S21*. For the complete, experimental time series we refer to *SI Appendix, Fig. S20*. The simulations resemble the experimental proplatelet shapes very well: The initially cylindrical proplatelet (shown in Fig. 2*A*) first exhibits small undulations (shown in Fig. 2*B*) which eventually grow to swellings connected by membrane strings in Fig. 2*C*. This agreement demonstrates that our computational model is able to reproduce well the experimentally observed proplatelet fragmentation process.

A complete illustration of proplatelet fragmentation is given by the kymograph in Fig. 2*D*. Here, the color code corresponds to the local proplatelet radius shown with respect to position along the proplatelet axis and time. At the beginning of the simulation, contraction at the proplatelet's free tip is visible by the dark blue band developing at the top right. With increasing time a periodic pattern of vertical stripes develops. These stripes correspond to the swellings visible in Fig. 2 *B* and *C*. We note that fragmentation in our simulations happens on shorter time scales than in corresponding in vitro experiments (e.g., figure S3 of ref. 17) which we attribute to the low viscosity that we use and the omitted viscoelasticity for the proplatelet interior. Indeed, simulations presented in *SI Appendix, Fig. S13* indicate a strong increase in fragmentation time with an increase in internal viscosity. After the swellings are established, the periodic pattern along the shaft remains without any movement of the individual swellings.

The observed fragmentation in Fig. 2 is visually strikingly similar to the fragmentation of a liquid jet, e.g., water issuing from a tap, by the classic Rayleigh–Plateau instability (63) as shown in figure 2 of ref. 64. To further quantify our hypothesis that indeed a biological equivalent of the Rayleigh–Plateau instability is the key mechanism behind proplatelet fragmentation we investigate the wavelength of the periodic swellings along the proplatelet. To ensure a one-to-one correspondence of the two mechanisms, we consider first the results for isotropic actomyosin contractility in *SI Appendix, Fig. S7*, where we observe a wavelength of about $\lambda = 14.3$ μm . Taken relative to the cylinder radius this leads to $\frac{2\pi}{\lambda} R_0 \approx 0.66$ which is very close to the classic Rayleigh–Plateau value of 0.69 for the most unstable wavelength. The value for anisotropic contractility of 0.74 is close to the theory, as well. Furthermore, from experimentally measured proplatelet diameters of 2 to 4 μm (8) we can estimate, based on the classic Rayleigh–Plateau criterion, a range for the platelet-sized swelling volume of about 28.6 to 229 μm^3 . This compares well with observations in refs. 65 and 66 who found volumes of matured platelets in the range 8.377 to 50 μm^3 [for volume calculation we use

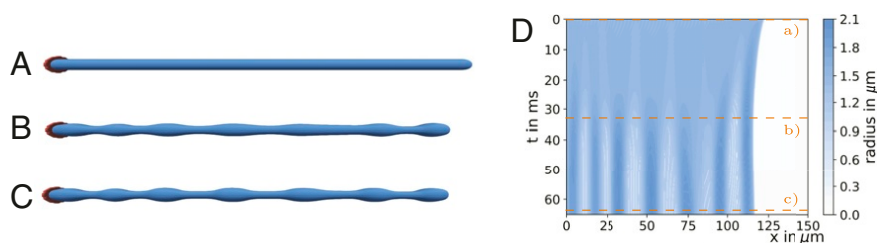


Fig. 2. Proplatelet fragmentation by a biological Rayleigh–Plateau instability without flow. (A) The initially cylindrical proplatelet is subject to microtubule sliding and actomyosin contractility. (B) The proplatelet starts contracting and periodic swellings develop. (C) Eventually the proplatelet consists of a series of platelet-sized swellings. (D) A kymograph illustrates the dynamics of swelling formation with the color coding for the local proplatelet radius. Time steps for the corresponding proplatelet shapes in *A–C* are indicated by the orange lines.

diameter and height reported for platelets (65, 66) assuming an oblate ellipsoid].

The Rayleigh–Plateau instability of a liquid jet is driven by the surface tension γ of a liquid–gas interface. At the interface the surface tension enters as an in-plane surface stress

$$t_{\alpha}^{\text{Jet } \beta} = \begin{pmatrix} \gamma & 0 \\ 0 & \gamma \end{pmatrix} \quad [2]$$

in mathematically the same way as the actomyosin/microtubule system in terms of an active stress T_a given in Eq. 1 does in the case of the proplatelet membrane. An important difference is that the proplatelet membrane is subject to anisotropic stresses due to microtubule extension along the axis. Thus, it becomes clear that the actomyosin contractility during proplatelet fragmentation plays essentially the same role as surface tension in the case of a liquid jet. The contractility triggers a biological Rayleigh–Plateau instability with a wavelength not depending on the absolute value of the contractility (*SI Appendix, Fig. S11*), in a similar way as the dominant wavelength of the classic Rayleigh–Plateau instability does not depend on the value of the surface tension coefficient (63). The biological Rayleigh–Plateau instability directly sets in with tip contraction and does not depend on thermal fluctuations (as shown in *SI Appendix, Fig. S12*). Our simulations thus suggest a physical mechanism regulating platelet size during the formation process: The dominant wavelength of the biological Rayleigh–Plateau instability determines platelet size.

Platelet Biogenesis In Vivo and in Microchannels: Parabolic Poiseuille Flow. Motivated by the fact that in vivo platelet biogenesis occurs in the flowing bloodstream and that in vitro experiments have demonstrated a massive acceleration of platelet biogenesis due to flow in bioreactors (7, 12, 15–17, 19), we now go one step farther and investigate the role of various nonaxisymmetric flow fields. We first consider a channel bounded on top and bottom by a flat wall mimicking a typical bioreactor geometry or an in vivo sinusoidal blood vessel. Below we compare this to a narrow cylindrical channel corresponding closely to the geometry of a narrow capillary. The geometry in Fig. 3 leads to the well-known parabolic Poiseuille velocity profile far away from the cell. The simulations include the realistic alteration of the

flow field due to the presence of the proplatelet by the two-way coupling between fluid and membrane (20). The channel height of 23.5 μm and the flow velocities are chosen in the range reported by experiments (62) on sinusoidal blood vessels. The bioreactor used in Fig. 1 A–C and used in refs. 15 and 16 with approximately twice the diameter has the same order of magnitude. As shown in Fig. 3A, we then attach a proplatelet to one of the walls which, corresponding to proplatelet extension into sinusoidal blood vessels in the bone marrow and in the bioreactor as shown in *SI Appendix, Fig. S21*, is tilted in the flow direction (in *SI Appendix, Fig. S15* we show a minor influence of a change in the tilting angle). Due to actomyosin contractility the proplatelet undergoes a biological Rayleigh–Plateau instability and platelet-sized swellings develop along its shaft similar to that in a quiescent fluid in *Proplatelet Fragmentation without Flow by a Biological Rayleigh–Plateau Instability* above. Proplatelet shapes after swelling formation are shown in Fig. 3 B and C for a flow velocity of $v = 3.33 \text{ mm/s}$. In contrast to a quiescent fluid, the action of the flow suppresses the contraction at the proplatelet free tip and the proplatelet undergoes a net extension. Furthermore, the proplatelet is tilted downward by the flow and eventually the proplatelet tip nearly aligns in the flow direction. Again, a close similarity between the predicted proplatelet shape in Fig. 3C and the experimental image in Fig. 1C is observed. The complete simulation is shown in *Movie S2*.

To investigate the dynamics of the fragmentation process in Poiseuille flow in more detail, we show in Fig. 3D the temporal evolution of the membrane shape in the corresponding kymograph. At the top, i.e., at very short times, membrane dynamics directly set in and the proplatelet swelling at the tip forms; however, it does not contract. The fluid flow rather leads to proplatelet extension. After 5 ms formation of the three leftmost platelet-sized swellings sets in. The other swellings form after 6 to 11 ms. In contrast to the quiescent fluid, the Poiseuille flow leads to nonsimultaneous formation, which may be triggered by locally different forces on the membrane caused by fluid flow. The nonsimultaneous formation is in good agreement with the experimental observations in Fig. 1A where the leftmost swelling is visible before the others form.

In contrast to Fig. 2D, the presence of flow disturbs the periodic arrangement of swellings with uniform distance. The

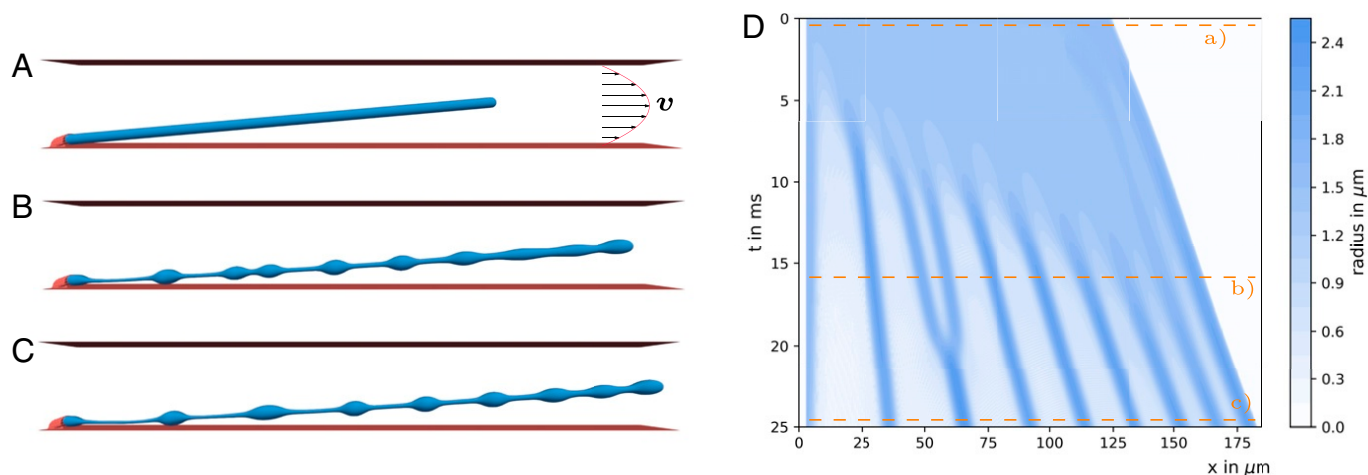


Fig. 3. Blood platelet biogenesis in Poiseuille flow. Shown is blood platelet biogenesis in a parabolic Poiseuille flow with maximum velocity of $v = 3.33 \text{ mm/s}$. (A) A proplatelet is subject to Poiseuille flow with a parabolic velocity profile far away from the cell confined between two walls. (B) Due to the action of the flow the proplatelet extends and swellings form. (C) The final platelet-sized swellings move at nonuniform distance along the proplatelet shaft. (D) The corresponding kymograph shows the dynamics of swelling formation and the motion of the final swellings. Compared to the case without external flow in Fig. 2, swellings form at earlier times. Furthermore, swellings move along the proplatelet shaft with different velocity, resulting in nonuniform distances between neighboring swellings. Two initially separated platelet-sized swellings fuse at around 20 ms.

negative slope of the bands in the kymograph clearly demonstrates the movement of the swellings with different velocities along the extending proplatelet. The different velocity of the individual swellings is due to the different location relative to the curved velocity profile of the external flow: Swellings close to the channel center are advected faster than swellings near the wall. While the swellings move in the flow direction, the contraction at the tip opposes the flow and leads to slower tip movement. Most remarkably, swellings two and three from the left first form and are clearly separate, but fuse afterward at around 20 ms. While the two swellings at first move with nearly constant velocity (according to the slope of the corresponding band in the kymograph in Fig. 3D), swelling three slows down. As a consequence both swellings approach each other, come into contact, and due to contractility eventually fuse. This points to a realignment in flow direction due to external shear through velocity gradients as the origin of swelling fusion. As the swelling shapes in Fig. 3 B and C illustrate, the fusion of two swellings leads to larger spherical structures, which eventually can be released into the bloodstream.

To bring out more clearly this apparent connection between fluid shear and swelling fusion, we consider a proplatelet immersed in pure shear flow as shown in *SI Appendix, Fig. S2A* and *Movie S3*. The channel geometry is the same as in Fig. 3A, but the flow now possesses a linear shear rather than a parabolic profile. Proplatelet fragmentation and swelling dynamics are shown in *SI Appendix, Fig. S2 A–C*. Comparing the simulation snapshots in *SI Appendix, Fig. S2 B and C* shows clear fusion events: one between swellings two and three and two more events for swellings farther to the right. These rich dynamics, swelling movement and fusion, are also reflected in the corresponding kymograph in *SI Appendix, Fig. S2D*, where a heterogeneous movement of the individual swellings, the fusions of swellings two and three and the neighboring ones at around 20 ms, and another at around 27 ms are clearly visible. Such fusion events could explain the release of larger structures called preplatelets into the circulatory system (35), as discussed in more detail in *Discussion*. In summary, we conclude that swelling fusion is triggered by fluid shear via a realignment of the proplatelet during swelling formation.

As a next step we investigate the influence of the external flow more systematically by varying the flow velocity. For this, we track the formation of the individual swellings over time as described in *SI Appendix, section S1*. We do so for the first to the fourth swellings, which are clearly separated in Fig. 3B. In Fig. 4 A–D we show the local proplatelet radius following the position of an individual swelling while forming. Starting from the initially homogeneous proplatelet radius, the radius at the position of a swelling increases and finally reaches a plateau, which indicates completion of swelling formation. Color coding of the curves indicates the systematic variation of the external flow velocity. With increasing external flow velocity the formation process takes place at earlier times (*SI Appendix, Fig. S17*) and the slope between the initial and the final plateau becomes steeper. This clearly demonstrates an acceleration of swelling formation with increasing velocity.

Despite the acceleration of swelling formation by flow, the final swelling radius varies only by about 10% and swelling volume (shown in Fig. 4E) stays nearly constant over the entire range of velocities. The small variation can be understood by the fact that the proplatelet extends with larger velocity and thus also the swellings and the membrane strings in between are stretched. To quantify the acceleration, we analyze the duration of swelling formation. We fix the time when the local proplatelet deformation reaches 2% as the beginning and the time when the plateau is reached as the end; the time difference serves as a measure for formation duration. Remarkably, for all swellings a significant acceleration occurs, demonstrating that fluid flow strongly influ-

ences the dynamics of proplatelet fragmentation. *SI Appendix, Fig. S3* confirms that an acceleration of proplatelet fragmentation is also present in pure shear flow, but less pronounced compared to Poiseuille flow.

The above results correspond to the flow situation occurring in typical platelet bioreactor geometries (15, 16) as well as sinusoidal blood vessels in vivo (62). We now modify the geometry and consider a proplatelet in cylindrical confinement mimicking a narrow capillary of the bone marrow (62). The proplatelet undergoes a biological Rayleigh–Plateau instability as illustrated in *SI Appendix, Fig. S4*. Importantly, we again observe a strong acceleration of the swelling formation in *SI Appendix, Fig. S5D* with increasing flow speed. No fusion events are observed. This indicates that the biological Rayleigh–Plateau instability is the key mechanism behind accelerated platelet biogenesis also under narrowly confined in vivo flow conditions.

All in all, the predictions from our model are in full agreement with experimental observations where the size distribution of the produced platelets was largely independent of the applied flow velocity, but the production rate increased dramatically (16, 17). Our modeling efforts allow us to trace back this remarkable observation to the elasto-hydrodynamic origin of platelet biogenesis by a biological Rayleigh–Plateau instability.

Efficient Acceleration in Bioreactors with Homogeneous Flow. As a next step we consider a homogeneous flow with uniform velocity approximating the flow pattern in microfluidic bioreactors, where megakaryocytes are attached to pillars (17). Studying the simple homogeneous flow geometry will further clarify the role of pulling (as opposed to shearing) by fluid forces as the origin of the accelerated swelling formation.

In Fig. 5A we show a proplatelet immersed in a homogeneous flow. The complete simulation is shown in *Movie S4*. Under the action of the homogeneous flow the proplatelet strongly extends in Fig. 5B while three swellings form. Fig. 5C shows the formation of additional swellings. In Fig. 5D, we show that homogeneous flow leads to a strong acceleration of proplatelet fragmentation with increasing flow velocity.

By comparing the kymograph for Poiseuille flow in Fig. 3D and that for homogeneous flow in *SI Appendix, Fig. S6A*, we discover a more pronounced successive formation of swellings in homogeneous flow. We further observe that, in contrast to Poiseuille and shear flow, in homogeneous flow no swelling fusion events occur. All swellings move with the same velocity as seen by the same slope of the bands in the kymograph, because they all experience the same external flow. Consequently, swellings show a more uniform distribution. In accordance with the argument above, fusion does not occur due to the absence of flow-induced realignment.

In *SI Appendix, Fig. S6 B–E* we again trace the swelling radius during formation. Here, for all three completely separated swellings we observe a shift of the curves toward shorter times and a strong change in slope when increasing the flow velocity. The final swelling radius does not vary for the first swelling. Swellings two and three show a certain variation in the final radius which is due to a pronounced stretching against proplatelet tip contraction at large velocities. In *SI Appendix, Fig. S6F* we show that swelling volume hardly varies with flow velocity despite the accelerated fragmentation in agreement with experimental observations.

Discussion

In this work, we provide a physical computational model for platelet biogenesis. We explicitly consider a single proplatelet and focus on its mechanical behavior under the influence of an external flow. Previous mathematical models (2, 3) account for

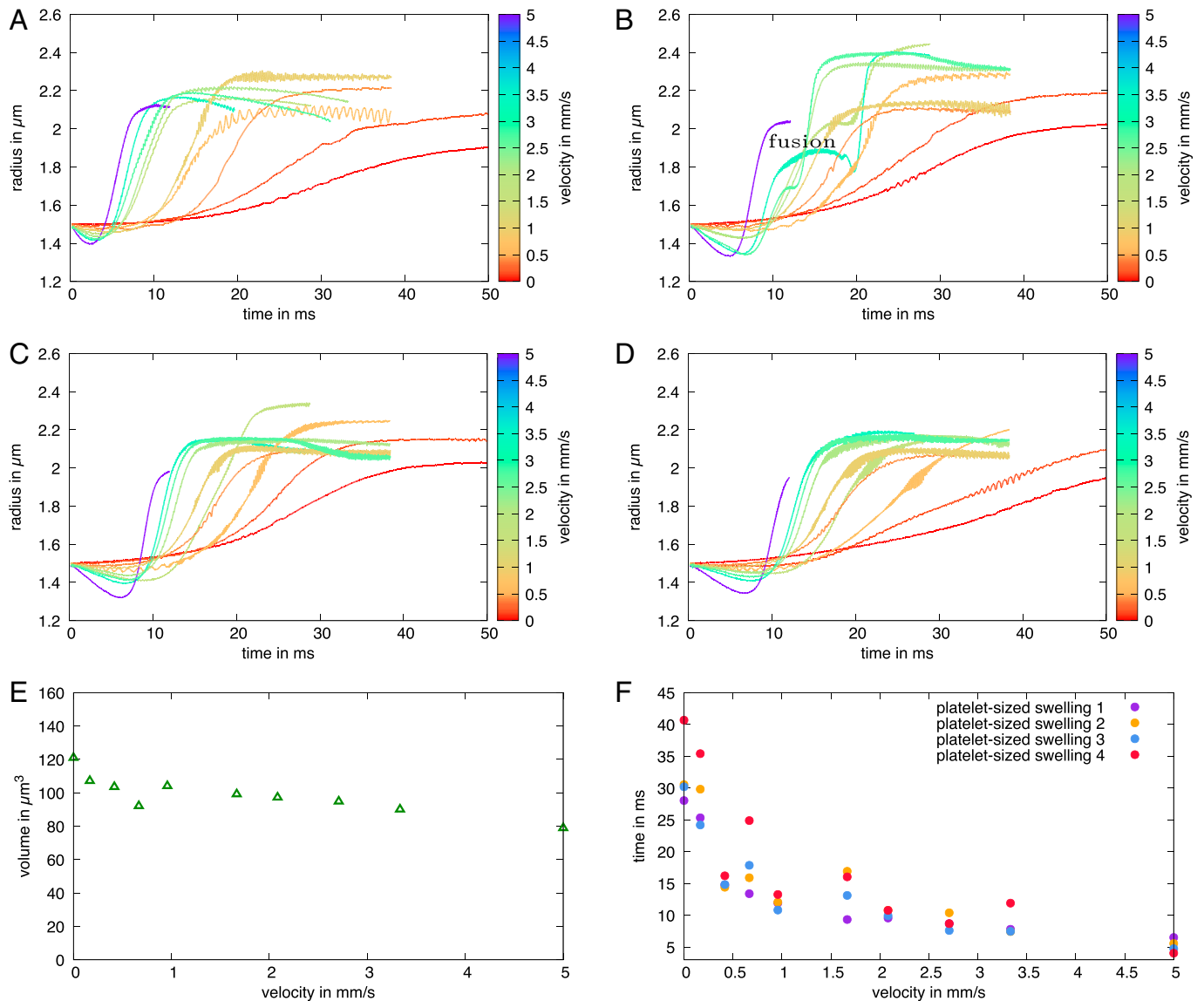


Fig. 4. Acceleration of swelling formation in flow. (A–D) Time course of platelet-sized swelling formation in Poiseuille flow for (A) first, (B) second, (C) third, and (D) fourth swelling at varying external flow velocity. With increasing velocity, swelling formation shifts toward earlier times and the slope in the profile becomes steeper, which indicates acceleration of proplatelet fragmentation. At large velocity the second swelling shows a fusion event, which manifests itself in an additional transient plateau (fusion). (E) Swelling volume stays nearly constant over the whole range of velocities. (F) With increasing flow velocity the duration time of the biological Rayleigh–Plateau instability / of swelling formation strongly accelerates.

the regulation of global platelet counts and are based on empirical differential equations describing macroscopic platelet number kinetics. Such an approach has been utilized to investigate pathological cyclic oscillations in platelet number (4) and the

influence of chemotherapy (5, 6). In contrast to these empirical kinetic models, our computational model provides a mechanistic insight and unravels the biophysical mechanism of platelet biogenesis in external flows on the single-cell level.

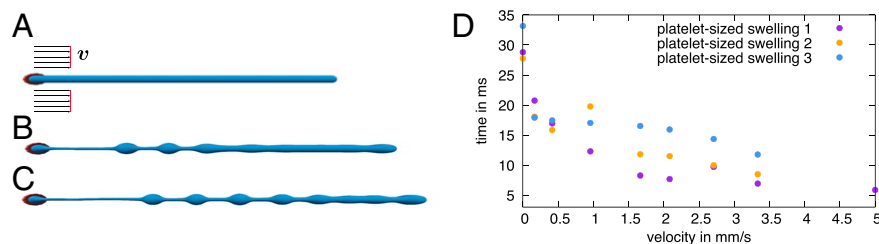


Fig. 5. Blood platelet biogenesis in homogeneous flow. (A) A proplatelet is immersed in a homogeneous flow with constant velocity $v = 2.0$ mm/s and attached to a wall on the left-hand side. (B and C) The proplatelet undergoes a biological Rayleigh–Plateau instability while being extended by the homogeneous flow. (D) Systematic variation of the external flow velocity shows a strong and systematic acceleration of the duration of swelling formation.

The key ingredient of our proposed mechanism and trigger of the instability is actomyosin contractility. Indeed, it has been shown that extended proplatelets lack formed swellings when actin activity is disturbed (9, 22, 28, 29), e.g., by usage of drugs (9) or gene knockout (22, 28, 29). Our findings propose an explanation for these observations: If filamentous actin is absent (22), no contractility can arise in the proplatelet cortex and thus in turn no biological Rayleigh–Plateau instability occurs; i.e., the proplatelet does not fragment. Microtubule extension along the axis reduces the importance of the (stabilizing) axial contractility relative to the (destabilizing) actomyosin-induced azimuthal contractility and thus further amplifies the instability. Our findings suggest that the biological Rayleigh–Plateau instability may be a generic mechanism and that a similar instability may play a role also for other cells subject to actomyosin contractility such as axons of neurons. We note that our model does not incorporate biochemical effects such as the reported up-regulation of myosin contractility by induced stresses (27). Most likely an additional up-regulation would even enhance the acceleration in presence of flow. Our model can be the basis to include these biochemical regulation effects in the future, which would require a refined constitutive law for the active stress based on future experimental insights into proplatelet mechanics. Our simulations nevertheless show that biochemical regulation per se is not required for accelerated proplatelet fragmentation in flow.

In Poiseuille as well as in pure shear flow we report motion of swellings along the proplatelet shaft. Most importantly, this motion leads to fusion events of adjacent swellings as can be seen, e.g., in Fig. 3D. This is in agreement with observations in the experimental videos of ref. 17 (video S2 of ref. 17 at 6:44 min left above the pillar and at 12:36 min right above the pillar). Leading to considerably larger fragments, fusion events can explain the release of preplatelets. These fragments, which typically are about twice as large as an individual platelet, are frequently observed in the circulatory system (35) and have been demonstrated to represent an intermediate stage of platelet biogenesis (8). In the circulatory system these preplatelets undergo a transition to barbell-shaped proplatelets, which eventually fission into two platelets (35). In line with the reported failure of preplatelet to barbell-shaped proplatelet transition for inhibited myosin (27), an interplay of microtubule extension and actomyosin contractility is argued to drive the transition of preplatelets to barbell-shaped proplatelets (23). Our findings suggest a more precise physical role of actomyosin similar to proplatelet fragmentation: After extension of the spherical preplatelet by microtubules the actomyosin triggers a biological Rayleigh–Plateau instability. This in turn leads to the conversion to barbell-shaped proplatelets that eventually fission into platelets (as shown in *SI Appendix*, Fig. S19). Based on our simulations, we predict that preplatelets should to a much lesser extent occur in quiescent or homogeneous flow situations. Indeed, this prediction is supported by a reduced occurrence of preplatelets during platelet biogenesis in quiescent situations (16). Thus, a homogeneous flow velocity *in vitro* not only should lead to efficient, accelerated platelet production but also is expected to show a more monodisperse distribution of platelet size. In contrast, shear gradients in microfluidic devices would favor the fusion of swellings and thus the release of larger structures.

The teardrop-like structure of the free end of the proplatelet in Fig. 3C resembles the tip shape of proplatelets quite remarkably, as can be seen by comparing figures 3C and 4B of ref. 15. In our simulations, the proplatelet tip contracts due to actomyosin contractility in line with the so-called retraction phases (16, 17). As in our simulations, tip retraction has been found to

be suppressed at higher flow velocities (16, 17). Thus, our simulations explain the transition between retraction phase (16) for no flow and pure extension in presence of flow (16, 17) by the hydrodynamic drag acting against actomyosin contractility.

Different from platelet biogenesis, theoretical studies predicted the existence of a Rayleigh–Plateau instability for membranes by an energy argument with an incorporated surface tension term (30) or by considering the force balance of an axisymmetric membrane including isotropic active stresses (31). For passive vesicle membranes, lacking the actomyosin, a Rayleigh–Plateau instability can occur due to external stimuli, as shown in the experiments (32) due to laser-induced tension, in a theoretical study (33), or in simulations for vesicles in extensional flow (34). An elastocapillary instability has also been suggested for mitochondrial fission (67).

In summary, our simulations reproduce the experimentally observed acceleration of platelet biogenesis in external flows. Our work strongly indicates that flow-accelerated proplatelet fragmentation into (pre)platelets can be understood as a mainly physical, accelerated elasto-hydrodynamic instability which is not triggered by biochemical sensing of external flow. We have identified actomyosin contractility in the cortex of an extended proplatelet as the essential ingredient required for this instability. Going further, the 3D simulations allow us to disentangle the different roles played by the different flow patterns. The observation that proplatelet fragmentation is strongly accelerated in homogeneous and parabolic flows, but to a much lesser extent in shear flows, leads us to conclude that the pulling of the flow at the proplatelet, rather than shear forces, is chiefly responsible for the accelerated fragmentation. Shear flows, on the other hand, are predicted to lead to more heterogeneous platelet size distributions due to fusion of platelet-sized swellings during the fragmentation process. These findings can serve as guidelines for the design of future bioreactors: It may indeed be desirable to employ geometries that produce relatively homogeneous flow components while at the same time avoiding shear components.

Our present simulations not only strongly indicate a biological Rayleigh–Plateau instability as a mechanism of platelet biogenesis, but also highlight in a general fashion the strong influence of external flow. Accordingly, we speculate that interaction with flow may also significantly affect the dynamics of other activity-driven processes in flowing environments.

Materials and Methods

Experimental Methodology. Fetal liver cells of embryos at days 13.5 to 14.5 were cultured in medium (Dulbecco's Modified Eagle's Medium, 10% fetal calf serum, and 1% penicillin/streptomycin) containing 50 ng/mL thrombopoietin (68). On day 3, MKs were enriched by gradient density filtration with 1.5 and 3% bovine serum albumin. Day 4 MKs were infused at 12.5 μ L/h into a microfluidic bioreactor (15) (only bovine serum albumin coated) and proplatelet formation was observed with a Zeiss Observer Z1 microscope.

Data Availability. All data discussed in this paper are available in the main text and *SI Appendix*.

ACKNOWLEDGMENTS. C.B. thanks the Studienstiftung des Deutschen Volkes for financial support and acknowledges support by the study program Biological Physics of the Elite Network of Bavaria. M.B. is supported by an Emmy Noether (BE5084/3-1) and TR240 (Project 374031971) grant of the Deutsche Forschungsgemeinschaft (DFG). Funding by the DFG (German Research Foundation)–Project 326998133–TRR 225 “Biofabrication” (Subproject B07) is acknowledged. We gratefully acknowledge computing time provided by the SuperMUC system of the Leibniz Rechenzentrum, Garching, Germany, as well as by the Bavarian Polymer Institute and financial support from the Volkswagen Foundation.

1. G. D. Boon, An overview of hemostasis. *Toxicol. Pathol.* **21**, 170–179 (1993).
2. H. E. Wichmann, M. D. Gerhards, H. Spechtmeier, R. Gross, A mathematical model of thrombopoiesis in rats. *Cell Prolif.* **12**, 551–567 (1979).

3. J. Eller, I. Györi, M. Zöllei, F. Krizsa, Modelling thrombopoiesis regulation—I. *Comput. Math. Appl.* **14**, 841–848 (1987).
4. R. Apostu, M. C. Mackey, Understanding cyclical thrombocytopenia: A mathematical modeling approach. *J. Theor. Biol.* **251**, 297–316 (2008).

5. M. Scholz, A. Gross, M. Loeffler, A biomathematical model of human thrombopoiesis under chemotherapy. *J. Theor. Biol.* **264**, 287–300 (2010).
6. Y. Kheifetz, M. Scholz, Modeling individual time courses of thrombopoiesis during multi-cyclic chemotherapy. *PLoS Comput. Biol.* **15**, e1006775 (2019).
7. T. Junt *et al.*, Dynamic visualization of thrombopoiesis within bone marrow. *Science* **317**, 1767–1770 (2007).
8. K. R. Machlus, J. N. Thon, J. E. Italiano, Interpreting the developmental dance of the megakaryocyte: A review of the cellular and molecular processes mediating platelet formation. *Br. J. Haematol.* **165**, 227–236 (2014).
9. J. E. Italiano, P. Lecine, R. A. Shivdasani, J. H. Hartwig, Blood platelets are assembled principally at the ends of proplatelet processes produced by differentiated megakaryocytes. *J. Cell Biol.* **147**, 1299–1312 (1999).
10. S. R. Patel, The biogenesis of platelets from megakaryocyte proplatelets. *J. Clin. Invest.* **115**, 3348–3354 (2005).
11. D. F. Stroncek, P. Rebulla, Platelet transfusions. *Lancet* **370**, 427–438 (2007).
12. C. Dunois-Larde *et al.*, Exposure of human megakaryocytes to high shear rates accelerates platelet production. *Blood* **114**, 1875–1883 (2009).
13. J. N. Thon, J. E. Italiano, Platelet formation. *Semin. Hematol.* **47**, 220–226 (2010).
14. J. N. Thon, J. E. Italiano, "Platelets: Production, morphology and ultrastructure" in *Antiplatelet Agents*, P. Gesele, G. V. R. Born, C. Patrono, C. P. Page, Eds. (Springer Berlin Heidelberg, Berlin/Heidelberg, Germany, 2012) vol. 210, pp. 3–22.
15. J. N. Thon *et al.*, Platelet bioreactor-on-a-chip. *Blood* **124**, 1857–1867 (2014).
16. M. Bender *et al.*, Microtubule sliding drives proplatelet elongation and is dependent on cytoplasmic dynein. *Blood* **125**, 860–868 (2015).
17. A. Blin *et al.*, Microfluidic model of the platelet-generating organ: Beyond bone marrow biomimetics. *Sci. Rep.* **6**, 21700 (2016).
18. J. N. Thon, B. J. Dykstra, L. M. Beaulieu, Platelet bioreactor: Accelerated evolution of design and manufacture. *Platelets* **28**, 472–477 (2017).
19. Y. Ito *et al.*, Turbulence activates platelet biogenesis to enable clinical scale ex vivo production. *Cell* **174**, 636–648.e18 (2018).
20. C. Bächer, S. Gekle, Computational modeling of active deformable membranes embedded in three-dimensional flows. *Phys. Rev. E* **99**, 062418 (2019).
21. A. Eckly *et al.*, Abnormal megakaryocyte morphology and proplatelet formation in mice with megakaryocyte-restricted MYH9 inactivation. *Blood* **113**, 3182–3189 (2009).
22. M. Bender *et al.*, ADF/n-cofilin-dependent actin turnover determines platelet formation and sizing. *Blood* **116**, 1767–1775 (2010).
23. J. N. Thon *et al.*, Microtubule and cortical forces determine platelet size during vascular platelet production. *Nat. Commun.* **3**, 852 (2012).
24. T. Kanaji, J. Ware, T. Okamura, P. J. Newman, GPIb regulates platelet size by controlling the subcellular localization of filamin. *Blood* **119**, 2906–2913 (2012).
25. Y. Chen *et al.*, The abnormal proplatelet formation in MYH9-related macrothrombocytopenia results from an increased actomyosin contractility and is rescued by myosin IIA inhibition. *J. Thromb. Haemostasis* **11**, 2163–2175 (2013).
26. J. Pan *et al.*, The formin DIAPH1 (mDia1) regulates megakaryocyte proplatelet formation by remodeling the actin and microtubule cytoskeletons. *Blood* **124**, 3967–3977 (2014).
27. K. R. Spinler, J. W. Shin, M. P. Lambert, D. E. Discher, Myosin-II repression favors pre/proplatelets but shear activation generates platelets and fails in macrothrombocytopenia. *Blood* **125**, 525–533 (2015).
28. Z. Sui *et al.*, Regulation of actin polymerization by tropomodulin-3 controls megakaryocyte actin organization and platelet biogenesis. *Blood* **126**, 520–530 (2015).
29. I. Pleines *et al.*, Mutations in tropomyosin 4 underlie a rare form of human macrothrombocytopenia. *J. Clin. Invest.* **127**, 814–829 (2017).
30. E. Hannezo, J. Prost, J. F. Joanny, Mechanical instabilities of biological tubes. *Phys. Rev. Lett.* **109**, 018101 (2012).
31. H. Berthoumioux *et al.*, Active elastic thin shell theory for cellular deformations. *New J. Phys.* **16**, 065005 (2014).
32. R. Bar-Ziv, E. Moses, Instability and "pearling" states produced in tubular membranes by competition of curvature and tension. *Phys. Rev. Lett.* **73**, 1392–1395 (1994).
33. G. Boedec, M. Jaeger, M. Leonetti, Pearling instability of a cylindrical vesicle. *J. Fluid Mech.* **743**, 262–279 (2014).
34. V. Narsimhan, A. P. Spann, E. S. G. Shaqfeh, Pearling, wrinkling, and buckling of vesicles in elongational flows. *J. Fluid Mech.* **777**, 1–26 (2015).
35. J. N. Thon *et al.*, Cytoskeletal mechanics of proplatelet maturation and platelet release. *J. Cell Biol.* **191**, 861–874 (2010).
36. S. Dmitrieff, A. Alsina, A. Mathur, F. J. Nédélec, Balance of microtubule stiffness and cortical tension determines the size of blood cells with marginal band across species. *Proc. Natl. Acad. Sci. U.S.A.* **114**, 201618041 (2017).
37. E. Brown, L. M. Carlin, C. Nerlov, C. Lo Celso, A. W. Poole, Multiple membrane extrusion sites drive megakaryocyte migration into bone marrow blood vessels. *Life Science Alliance* **1**, e201800061 (2018).
38. I. Pleines *et al.*, Defective tubulin organization and proplatelet formation in murine megakaryocytes lacking Rac1 and Cdc42. *Blood* **122**, 3178–3187 (2013).
39. G. H. Koenderink *et al.*, An active biopolymer network controlled by molecular motors. *Proc. Natl. Acad. Sci. U.S.A.* **106**, 15192–15197 (2009).
40. M. R. Mofrad, Rheology of the cytoskeleton. *Annu. Rev. Fluid Mech.* **41**, 433–453 (2009).
41. M. Murrell, P. W. Oakes, M. Lenz, M. L. Gardel, Forcing cells into shape: The mechanics of actomyosin contractility. *Nat. Rev. Mol. Cell Biol.* **16**, 486–498 (2015).
42. D. V. Köster, S. Mayor, Cortical actin and the plasma membrane: Inextricably intertwined. *Curr. Opin. Cell Biol.* **38**, 81–89 (2016).
43. P. Chugh *et al.*, Actin cortex architecture regulates cell surface tension. *Nat. Cell Biol.* **19**, 689–697 (2017).
44. C. J. Miller, D. Harris, R. Weaver, G. B. Ermentrout, L. A. Davidson, Emergent mechanics of actomyosin drive punctuated contractions and shape network morphology in the cell cortex. *PLoS Comput. Biol.* **14**, e1006344 (2018).
45. Y. Mulla, A. Aufderhorst-Roberts, G. H. Koenderink, Shaping up synthetic cells. *Phys. Biol.* **15**, 041001 (2018).
46. P. Chugh, E. K. Paluch, The actin cortex at a glance. *J. Cell Sci.* **131**, jcs186254 (2018).
47. G. H. Koenderink, E. K. Paluch, Architecture shapes contractility in actomyosin networks. *Curr. Opin. Cell Biol.* **50**, 79–85 (2018).
48. G. Salbreux, F. Jülicher, Mechanics of active surfaces. *Phys. Rev.* **96**, 032404 (2017).
49. M. C. Marchetti *et al.*, Hydrodynamics of soft active matter. *Rev. Mod. Phys.* **85**, 1143–1189 (2013).
50. F. Jülicher, S. W. Grill, G. Salbreux, Hydrodynamic theory of active matter. *Rep. Prog. Phys.* **81**, 076601 (2018).
51. S. W. Grill, Growing up is stressful: Biophysical laws of morphogenesis. *Curr. Opin. Genet. Dev.* **21**, 647–652 (2011).
52. A. C. Callan-Jones, V. Ruprecht, S. Wieser, C. P. Heisenberg, R. Voituriez, Cortical flow-driven shapes of nonadherent cells. *Phys. Rev. Lett.* **116**, 028102 (2016).
53. H. Turlier, B. Audoly, J. Prost, J. F. Joanny, Furrow constriction in animal cell cytokinesis. *Biophys. J.* **106**, 114–123 (2014).
54. A. C. Reymann, F. Staniscia, A. Erzberger, G. Salbreux, S. W. Grill, Cortical flow aligns actin filaments to form a furrow. *eLife* **5**, e17807 (2016).
55. A. E. Carlsson, Mechanisms of cell propulsion by active stresses. *New J. Phys.* **13**, 073009 (2011).
56. C. Bächer *et al.*, Antimargination of microparticles and platelets in the vicinity of branching vessels. *Biophys. J.* **115**, 411–425 (2018).
57. J. Hanke, D. Probst, A. Zemel, U. S. Schwarz, S. Köster, Dynamics of force generation by spreading platelets. *Soft Matter* **14**, 6571–6581 (2018).
58. J. Hanke, C. Ranke, E. Peregó, S. Köster, Human blood platelets contract in perpendicular direction to shear flow. *Soft Matter* **15**, 2009–2019 (2019).
59. S. Patel-Hett *et al.*, The spectrin-based membrane skeleton stabilizes mouse megakaryocyte membrane systems and is essential for proplatelet and platelet formation. *Blood* **118**, 1641–1652 (2011).
60. J. B. Freund, Numerical simulation of flowing blood cells. *Annu. Rev. Fluid Mech.* **46**, 67–95 (2014).
61. A. Guckenberger, S. Gekle, Theory and algorithms to compute Helfrich bending forces: A review. *J. Phys. Condens. Matter* **29**, 203001 (2017).
62. M. G. Bixel *et al.*, Flow dynamics and HSPC homing in bone marrow microvessels. *Cell Rep.* **18**, 1804–1816 (2017).
63. J. Eggers, E. Villermaux, Physics of liquid jets. *Rep. Prog. Phys.* **71**, 036601 (2008).
64. E. Castro-Hernández, F. Campo-Cortés, J. M. Gordillo, Slender-body theory for the generation of micrometre-sized emulsions through tip streaming. *J. Fluid Mech.* **698**, 423–445 (2012).
65. A. D. Michelson, *Platelets* (Elsevier, Amsterdam, The Netherlands, 2013).
66. A. K. Paknikar, B. Eltzner, S. Köster, Direct characterization of cytoskeletal reorganization during blood platelet spreading. *Prog. Biophys. Mol. Biol.* **144**, 166–176 (2019).
67. D. Gonzalez-Rodriguez *et al.*, Elastocapillary instability in mitochondrial fission. *Phys. Rev. Lett.* **115**, 088102 (2015).
68. J. L. Villeval *et al.*, High thrombopoietin production by hematopoietic cells induces a fatal myeloproliferative syndrome in mice. *Blood* **90**, 4369–4383 (1997).

PNAS

www.pnas.org

1

2 **Supplementary Information for**

3 **Flow-accelerated platelet biogenesis is due to an elasto-hydrodynamic instability**

4 **Christian Bächer, Markus Bender and Stephan Gekle**

5 **Christian Bächer.**

6 **E-mail: christian.baecher@uni-bayreuth.de**

7 **This PDF file includes:**

8 Supplementary text

9 Figs. S1 to S21

10 Legends for Movies S1 to S5

11 SI References

12 **Other supplementary materials for this manuscript include the following:**

13 Movies S1 to S5

14 Supporting Information Text

15 S1. Methods - Details on the simulation method

16 **A. Combined lattice-Boltzmann/immersed boundary method for active membranes.** For the numerical investigation of blood
 17 platelet biogenesis we use a combined lattice-Boltzmann/immersed boundary method for active elastic membranes suspended
 18 in a 3D Newtonian fluid. We refer to our recent publication (3) for a detailed description of the algorithm. For extensive
 19 validation in case of active membranes as well as passive membrane we refer to ref. (3) and refs. (4, 5), respectively.

20 The dynamics of the suspending fluid is calculated on an Eulerian 3D grid by the mesoscopic lattice-Boltzmann method
 21 (6–8). Simulations are performed using the lattice-Boltzmann implementation in the software package ESPResSo (9–12) with
 22 the D3Q19 lattice-Boltzmann velocity set. A typical fluid mesh, as e.g. for the system shown in figure 3 a) of the main
 23 text, has dimensions of $720 \times 100 \times 40$. The time step is about 5×10^{-9} s and a typical total simulation time is 0.04 s. We
 24 assign to the suspending fluid a density of 1×10^3 kg/m³ and a viscosity of 1.2×10^{-3} Pas, values resembling the properties of
 25 the *in vivo* environment of platelet formation, the blood plasma. Our LBM implementation furthermore allows for thermal
 26 fluctuations of the suspending fluid associated with a given temperature. In direction with no wall present, we use periodic
 27 boundary conditions. Walls are realized by the bounce back boundary condition. In the system shown in figure 3 a) we
 28 consider a channel with a height of 98 grid cells and apply a constant body force which corresponds to a pressure gradient
 29 driving Poiseuille flow. Velocities given in the text correspond to the maximum velocity of the corresponding flow profile. In
 30 figure 5 we apply a constant velocity to all fluid nodes surrounding the pillar, which leads to a homogeneous flow field. In figure
 31 S2 we apply a tangential velocity to the upper wall while the bottom remains steady. This leads to a pure linear shear flow.

32 The proplatelet membrane is discretized by nodes, which are separated by about one lattice-Boltzmann grid cell and
 33 connected to triangles. The resulting membrane mesh represents a Lagrangian grid immersed into the Eulerian fluid grid.
 34 Coupling of the membrane nodes to the fluid consists of the transmission of elastic membrane forces to the surrounding fluid
 35 nodes and advection of the membrane nodes with local fluid velocity (immersed boundary method (13–15)). In both cases an
 36 interpolation between membrane and fluid mesh is performed using an eight point stencil. A typical proplatelet membrane
 37 mesh consists of 22741 nodes and 45440 triangles and has a radius of approximately 6.25 LBM grid cells. If not stated explicitly
 38 the viscosity contrast of the fluid inside and outside the proplatelet is one. On its left hand side the proplatelet is fixed to
 39 a solid wall which mimics the fixed megakaryocyte *in vivo* or in experiments as illustrated in figure 1 a) of the main text.
 40 Fixation is done by an overlap of the last ring of the mesh with the solid boundary. As a consequence no fluid can enter/leave
 41 the proplatelet shaft. The terminal ring of nodes thus does not experience fluid forces and remains fixed. For stability reasons,
 42 in the last ring of nodes the calculation of active forces as well as bending forces is omitted.

43 The proplatelet membrane is attributed with different elastic properties. Shear elasticity associated with the cytoskeletal
 44 network underlining the plasma membrane is considered using the Skalak model (16, 17). We use the shear elasticity typical
 45 for red blood cell membranes $\kappa_S = 5 \times 10^{-6}$ N/m with $C = 100$ (18). Bending elasticity is modeled using Helfrich law (18–20)
 46 with a bending elasticity of $\kappa_B = 2 \times 10^{-19}$ Nm and realized by the algorithm denoted B in ref. (19). Activity of motor
 47 proteins walking on the cytoskeletal filaments is incorporated by actomyosin contractility as detailed in ref. (3).

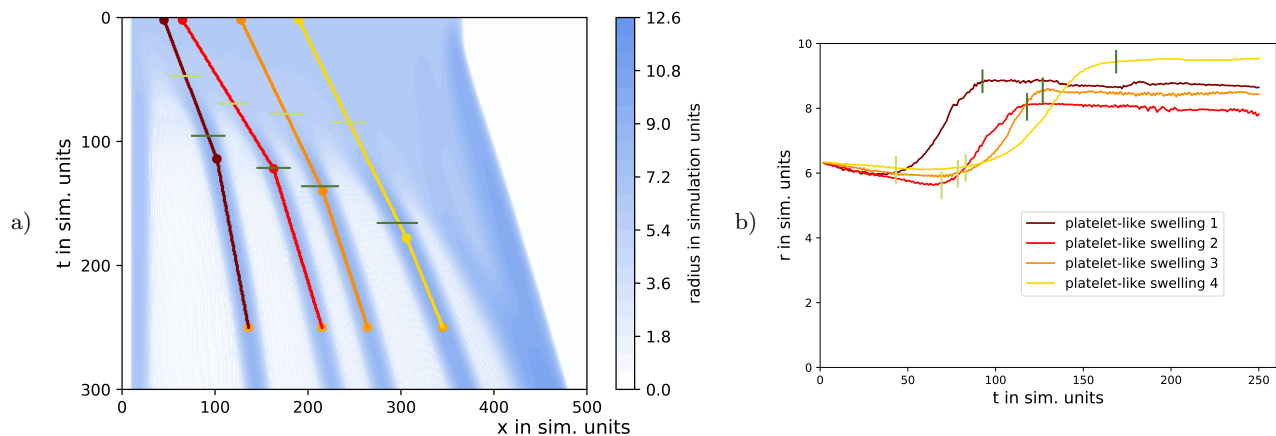


Fig. S1. Analysis of swelling formation. a) Kymograph showing the swelling formation along the shaft of a proplatelet. We track the position of the individual swellings indicated by the red to yellow lines in the kymograph. Out of the kymograph the local proplatelet radius over time is extracted leading to the profiles shown in figure b). Onset and duration of swelling formation are determined by the time step at which the deformation exceeds two percent of the initial radius (light green lines) and the time step at which the radius reaches a plateau (dark green lines).

48 **B. Simulation analysis.** *Kymograph* In order to visualize and analyze the temporal evolution of swelling formation we show
 49 kymographs of the proplatelet as e.g. in figure 2 d) or for an initial phase in figure S1 a). For the kymograph we analyze
 50 the local radius of the proplatelet depending on the position along the proplatelet axis. For this, we divide the nodes of the
 51 proplatelet mesh into bins along the proplatelet axis. In each bin, we first calculate the radial center-of-mass position and then
 52 determine the average radius over all nodes in the bin. With this we determine the radius depending on axial position for

53 each time step. For the kymograph we then plot the axial position on the abscissa and the time on the ordinate with time
54 increasing downwards. Each point in the plot is colored according to the local radius at a given time.

55 *Instability analysis* In order to investigate the dynamics of swelling formation further we analyze the time course of swelling
56 formation based on the kymograph. As shown in figure S1 a) each developing swelling manifests itself in a broad band with
57 increased radius clearly separated from neighboring developing swellings. To analyze these dynamics we follow each developing
58 swelling over time. We start from the initial configuration (dots at the top of figure S1 a)) and follow each maximum developing
59 at the center of each swelling (red to yellow lines). As end point (dots at the bottom of figure S1 a)) we choose the time step
60 when the local radius reaches a constant plateau. Taking the local radius from the kymograph for each point along the lines
61 gives the time course of the local radius as shown in figure S1 b). Figure S1 b) clearly shows that swelling formation starts
62 from a constant radius for all swellings and in the end terminates with a plateau.

63 From figure S1 b) we can furthermore calculate the onset time and the total duration of the instability. As onset we denote
64 the time step at which the radius exceeds a deformation of two percent of the initial radius. Onsets for the different swellings
65 are indicated by lines in light green in figure S1. As the end of the formation, we determine the time when the deformation
66 reaches a plateau, as indicated by the dark green lines in figure S1. The time difference between these two stages gives the
67 duration of the formation.

68 *Platelet-sized swelling volume* For each simulation we first determine the time of completed swelling development, as
69 described above. At this time step, we calculate the volume of each swelling. This is done by considering just the swelling,
70 where we have to close the membrane by triangles perpendicular to the proplatelet shaft. For the now closed platelet-like
71 particle we can calculate the volume as described in reference (21). For each simulation we then filter for larger fragments,
72 preplatelets, which form by swelling fusion. Eventually, we can calculate the average volume of all formed platelet-like particles.

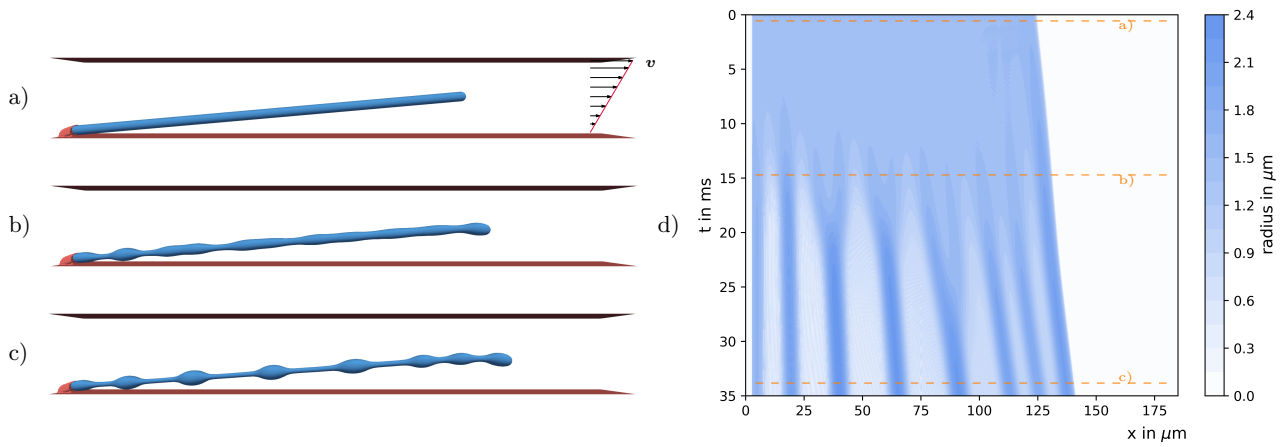
73 **S2. Varying flow geometries**74 **A. Pure shear flow.**

Fig. S2. Swelling fusion in shear flow. a) A proplatelet with the same properties as in the main text is immersed in a shear flow confined between two flat walls with velocity $v = 2 \text{ mm/s}$. b), c) Simulation snapshots show the biological Rayleigh-Plateau instability and swelling fusion. The entire process is shown in Supplemental Video S3. d) Kymograph showing the dynamics of swelling formation and swelling movement along the shaft followed by several fusion events.

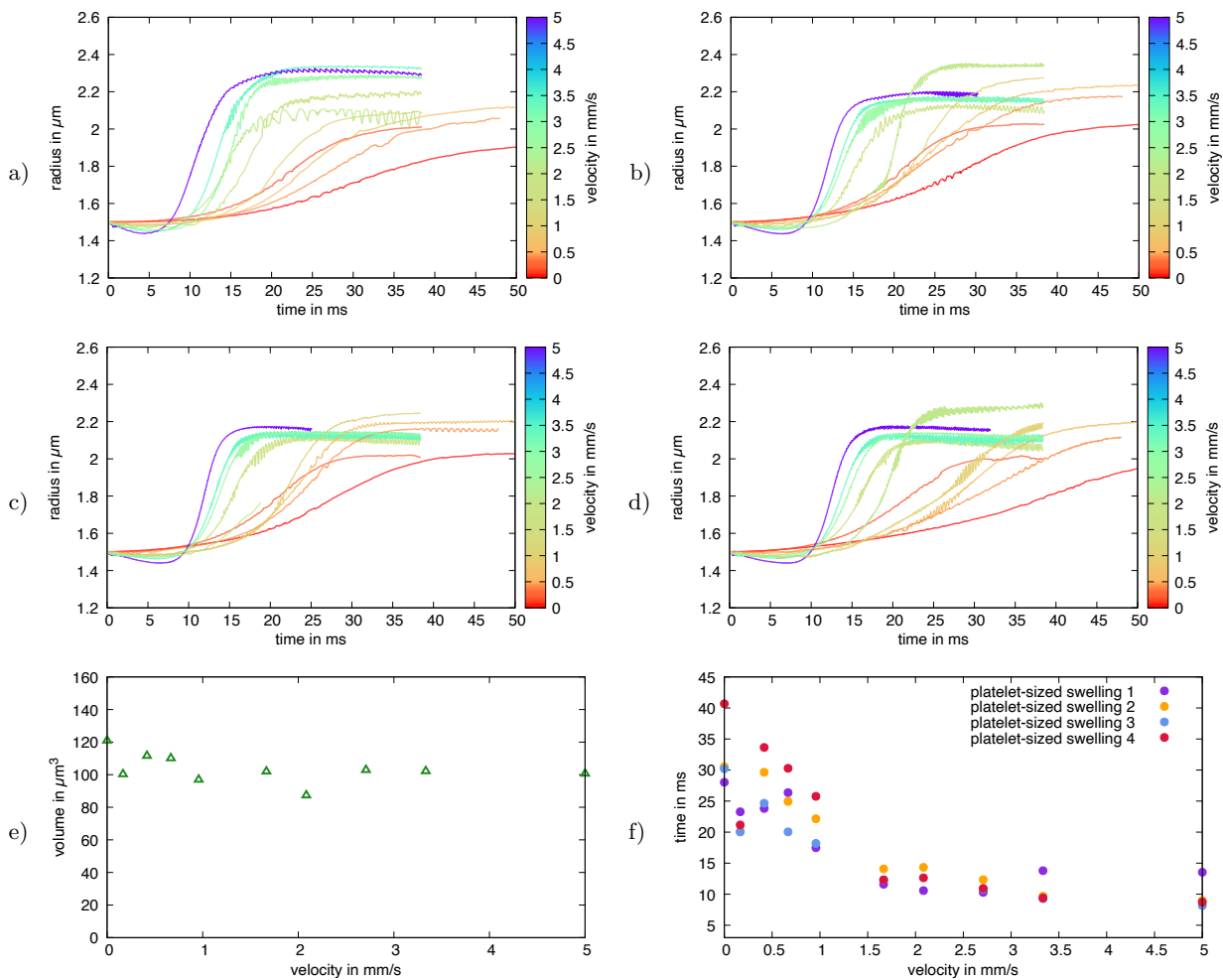


Fig. S3. Platelet biogenesis in shear flow. Time dependent formation process for a) first, b) second, c) third, and d) fourth swelling. The curves for different velocities are less broadly distributed, the formation process does not shift towards earlier times as strongly as it does in homogeneous flow. Systematic variation of the external flow velocity shows a nearly constant volume e) and a non-monotonous, less pronounced acceleration based on duration of swelling formation f).

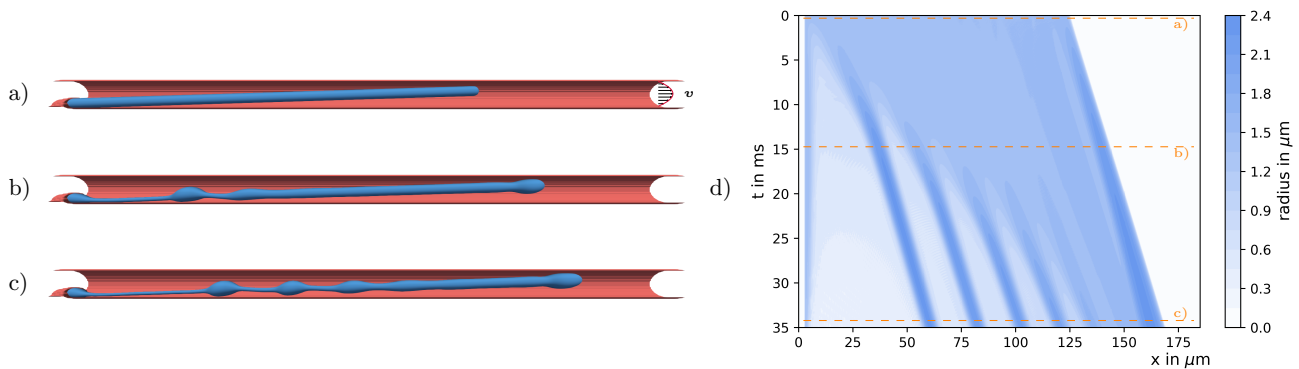
75 **B. Platelet biogenesis in a narrow blood vessel.**

Fig. S4. Platelet biogenesis in a narrow blood vessel. a) A proplatelet with the same properties as in the main text is confined within a cylindrical channel with a diameter of $9 \mu\text{m}$ which corresponds to three times the proplatelet diameter. b) Under the action of the flow the proplatelet is extended and c) forms swellings via a biological Rayleigh-Plateau instability. The entire process is shown in Supplemental Video S5. d) Kymograph showing the dynamics of swelling formation.

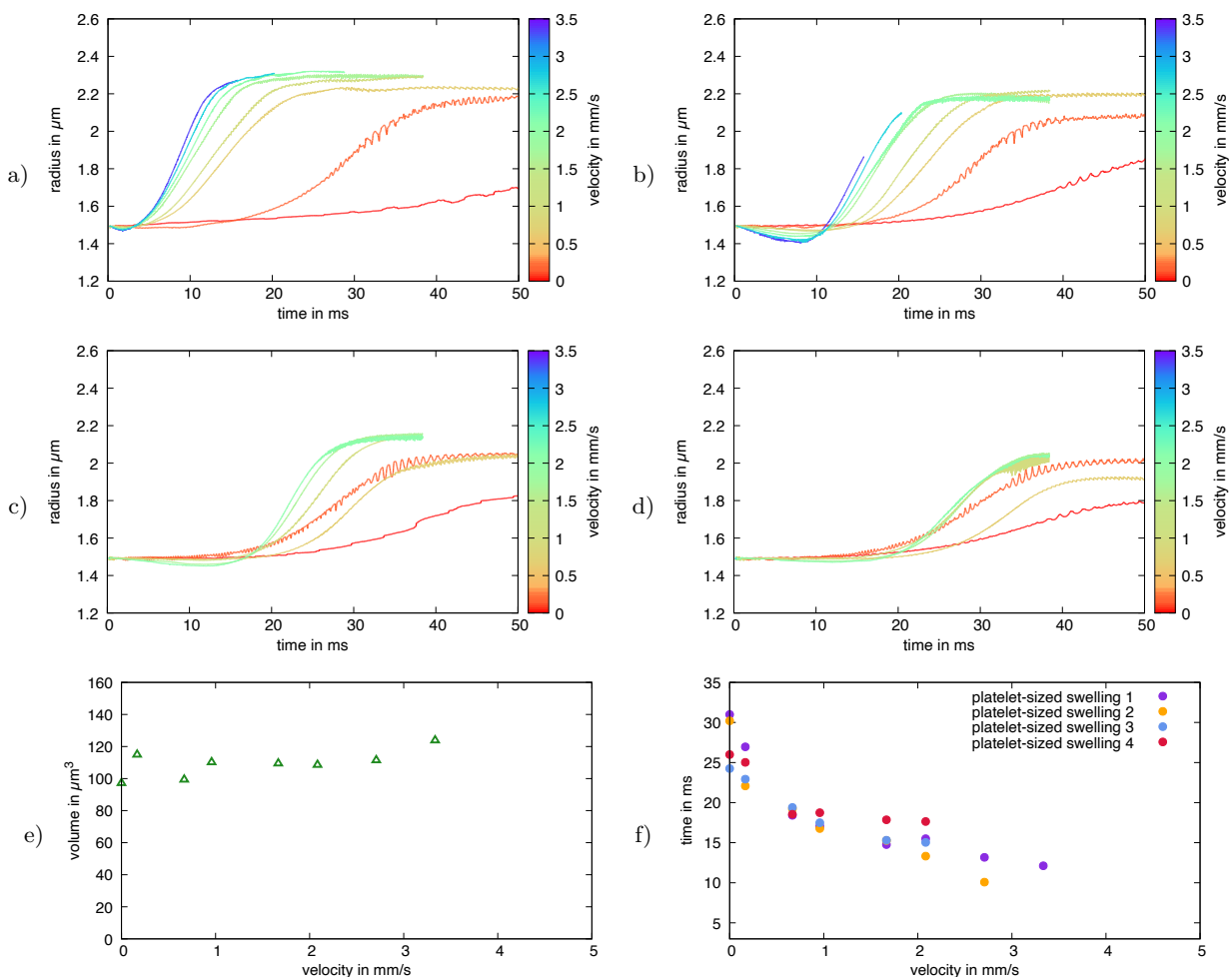


Fig. S5. Acceleration of platelet biogenesis in a narrow blood vessel. Time dependent formation process for a) first, b) second, c) third, and d) fourth swelling. The formation process shifts towards earlier times and time courses become steeper with increasing velocity. Systematic variation of the external flow velocity shows a nearly constant volume e) and systematic acceleration based on the duration of swelling formation f).

76 C. Additional data for homogeneous flow.

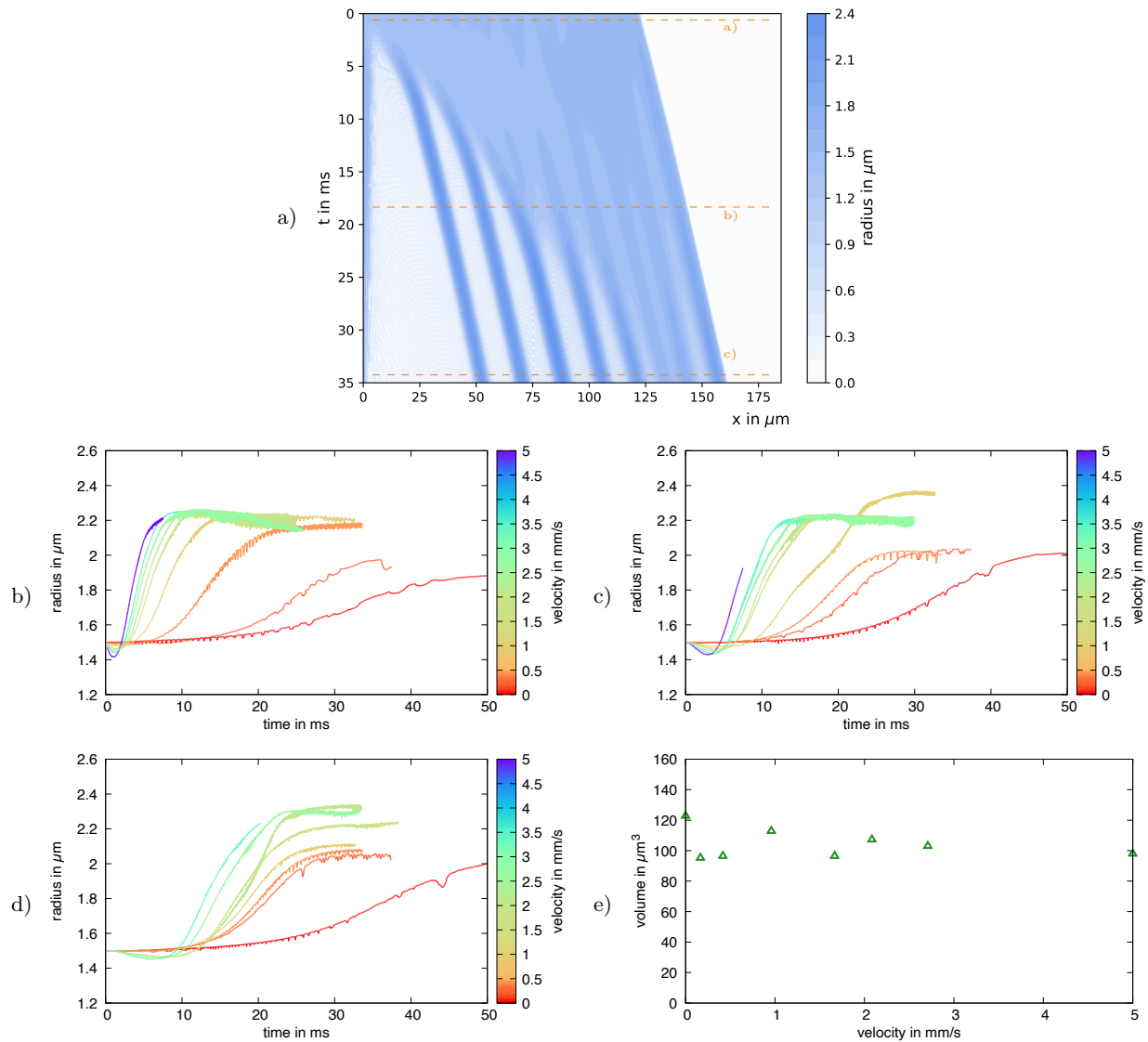


Fig. S6. Swelling formation in homogeneous flow. a) Kymograph corresponding to figure 5 of the manuscript shows the dynamics of swelling formation and swelling movement along the proplatelet shaft at uniform distances. b) - d) Time dependent formation process of the swellings. With increasing velocity the formation shifts towards shorter times and the slope of the curves becomes steeper. e) The volume stays constant over the whole range of velocities.

77 S3. Results for isotropic contractility

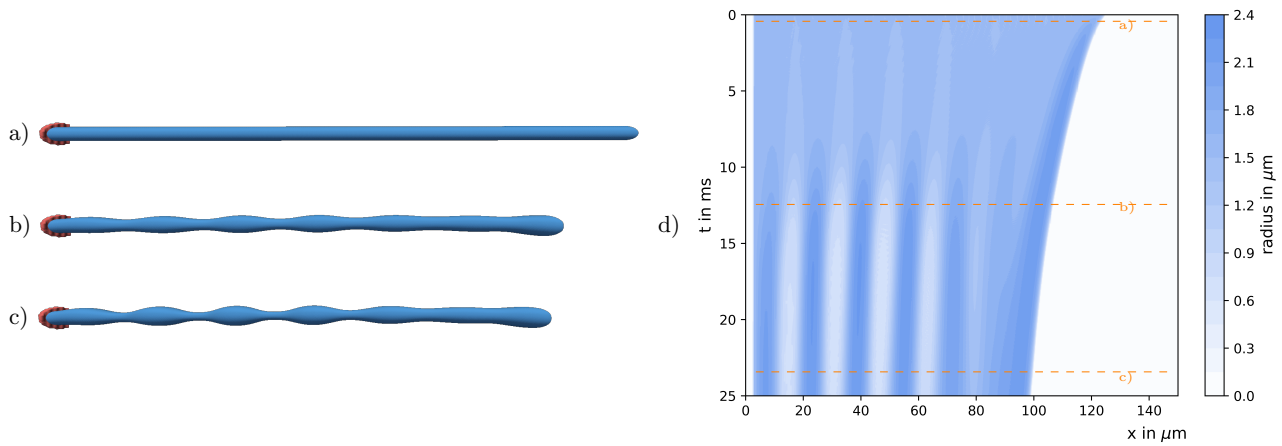


Fig. S7. Proplatelet fragmentation by a biological Rayleigh-Plateau instability for isotropic contractility without flow. a), b), c) the proplatelet undergoes a biological Rayleigh-Plateau instability and develops periodic swellings with a wavelength λ approximately satisfying the classical Rayleigh-Plateau criterion $2\pi R_0/\lambda \approx 0.69$. d) A kymograph illustrates the dynamics of swelling formation with the color coding for the local proplatelet radius. Time steps for the corresponding proplatelet shapes in figures a) - c) are indicated by the orange lines. Corresponding results for anisotropic contractility are shown in figure 2 of the manuscript.

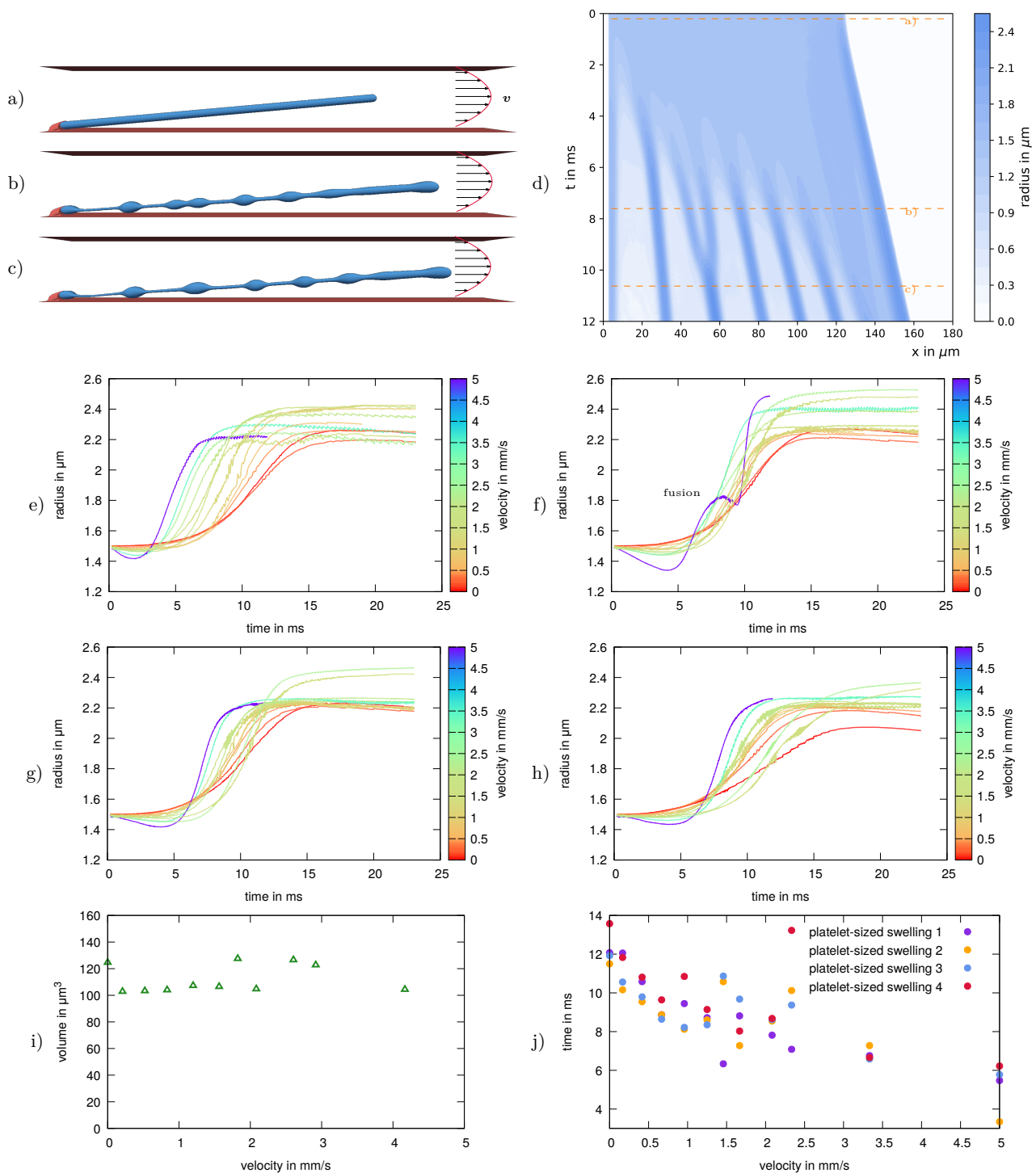


Fig. S8. Blood platelet biogenesis for isotropic contractility in Poiseuille flow. Blood platelet biogenesis in a channel with a parabolic Poiseuille flow with maximum velocity of $v = 5$ mm/s. a) A proplatelet is subject to an external Poiseuille flow confined between two walls. Due to the action of the flow the proplatelet extends b), swellings form, and the final platelet-sized swellings move at non-uniform distance along the proplatelet shaft c). d) The corresponding kymograph shows the dynamics of swelling formation and the motion of the final swellings. Two initially separated platelet-sized swellings fuse at around 10 ms. e), f), g), h) Time course of platelet-sized swelling formation in Poiseuille flow for e) first, f) second, g) third, and h) fourth swelling at varying external flow velocity. i) Swelling volume stays nearly constant over the whole range of velocities. j) With increasing flow velocity the duration time of the biological Rayleigh-Plateau instability / of swelling formation strongly accelerates. Corresponding results for anisotropic contractility are shown in figure 3 and 4 of the manuscript.

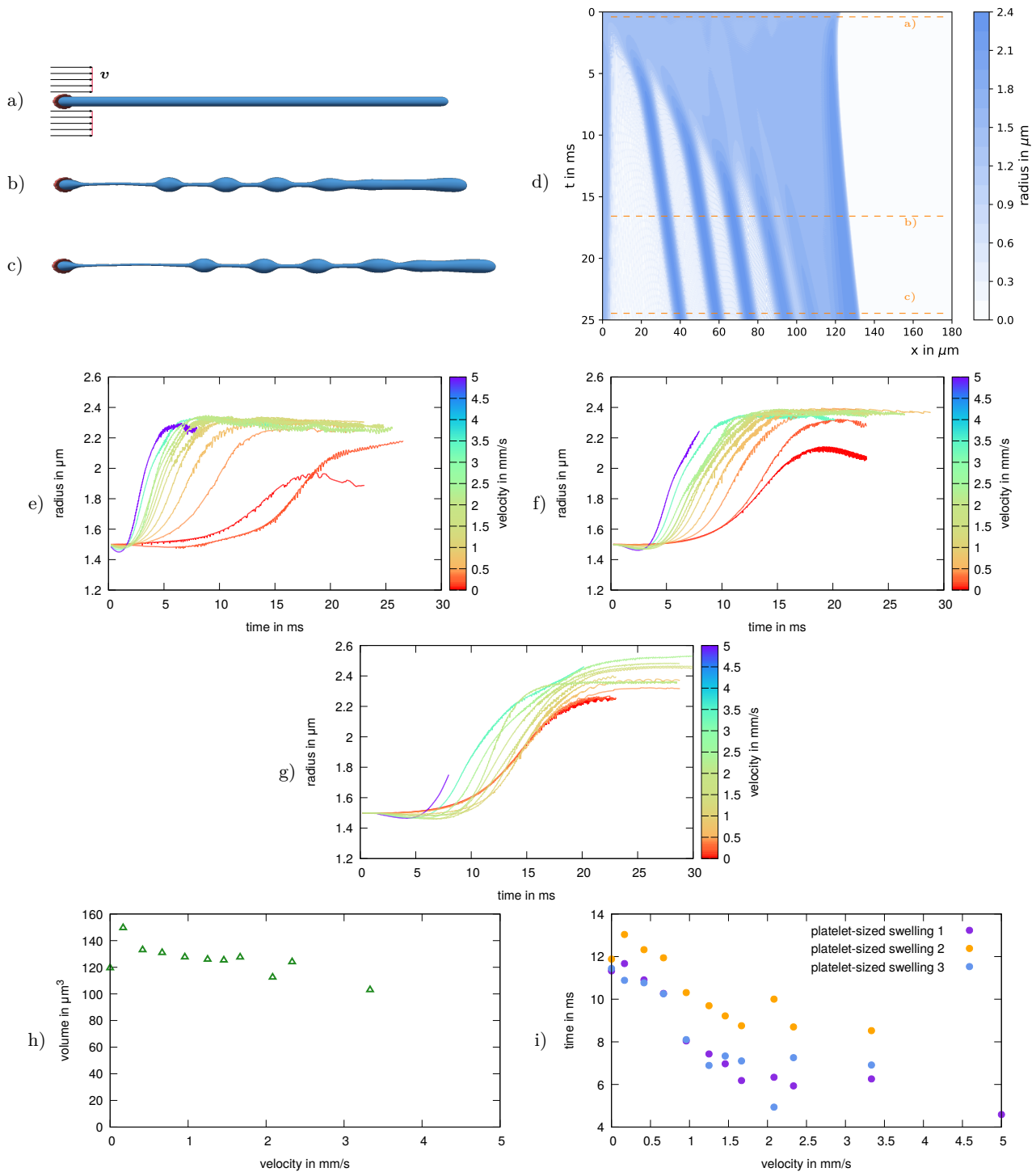


Fig. S9. Blood platelet biogenesis for isotropic contractility in homogeneous flow. Swelling formation in homogeneous flow with $v = 2.0$ mm/s. a) A proplatelet is immersed in a homogeneous flow and attached to a wall on the left hand side. b), c) The proplatelet undergoes a biological Rayleigh-Plateau instability while being extended by the homogeneous flow. d) Kymograph showing the dynamics of swelling formation and swelling movement along the proplatelet shaft at uniform distances. e), f), g) Time dependent formation process for e) first, f) second, and g) third swelling. With increasing velocity the formation shifts towards shorter times and the slope of the curves becomes steeper. No fusion events are visible. Systematic variation of the external flow velocity hardly affects the swelling volume h), but shows a strong acceleration of the duration of swelling formation i). Corresponding results for anisotropic contractility are shown in figure 5 of the manuscript and figure S6.

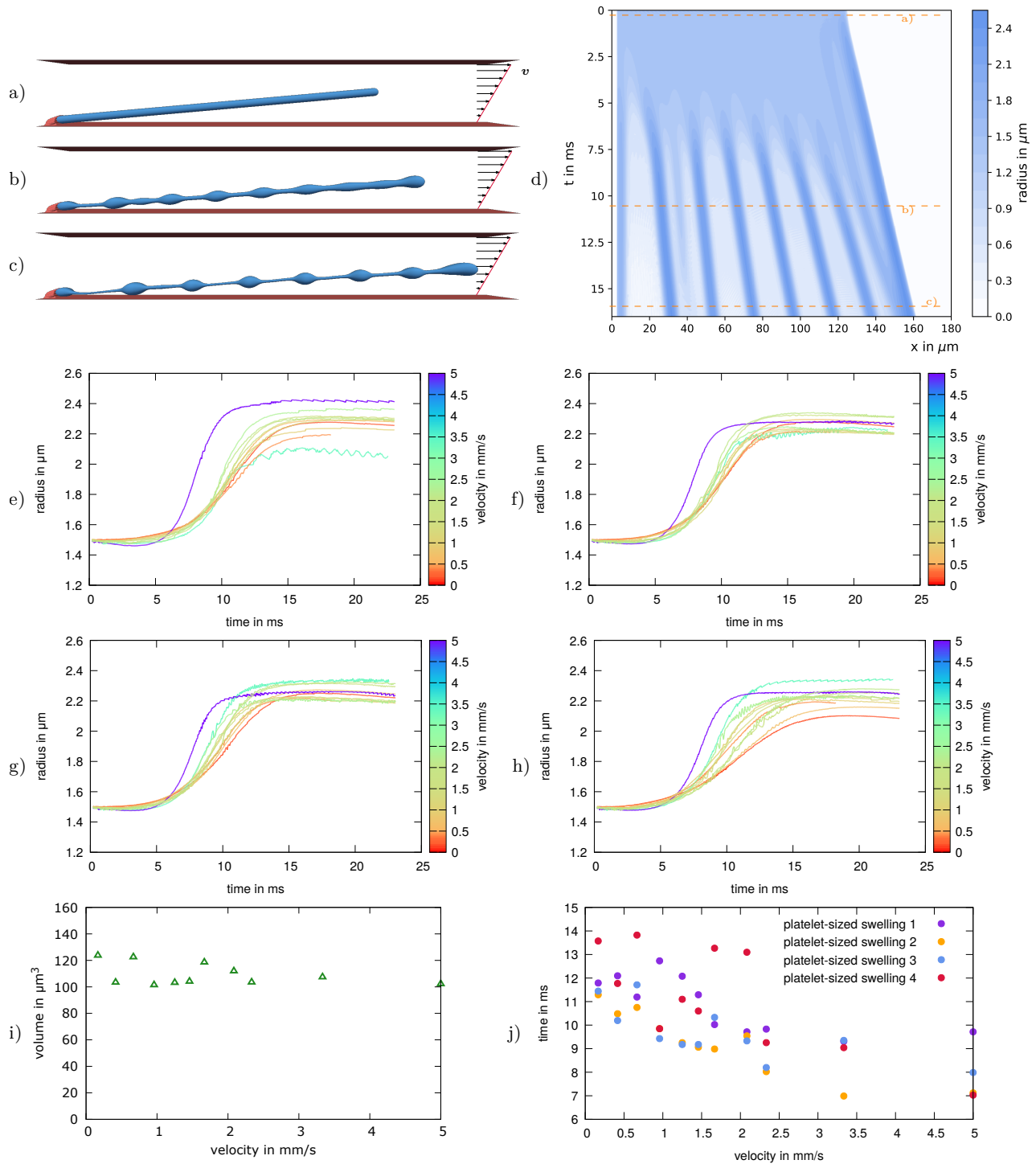


Fig. S10. Platelet biogenesis for isotropic contractility in shear flow. a) A proplatelet is immersed in a shear flow confined between two flat walls with velocity $v = 9 \text{ mm/s}$. b), c) Simulation snapshots show the biological Rayleigh-Plateau instability and swelling fusion. d) Kymograph showing the dynamics of swelling formation and swelling movement along the shaft followed by fusion events at the first swelling and at the tip. e), f), g) h), Time dependent formation process for e) first, f) second, g) third, and h) fourth swelling. The curves for different velocities are less broadly distributed, the formation process does not shift towards earlier times as strongly as it does in homogeneous flow. Systematic variation of the external flow velocity shows a nearly constant volume e) and a non-monotonous, less pronounced acceleration based on duration of swelling formation f). Corresponding results for anisotropic contractility are shown in figure S2 and S3.

78 S4. Robustness against parameter variations

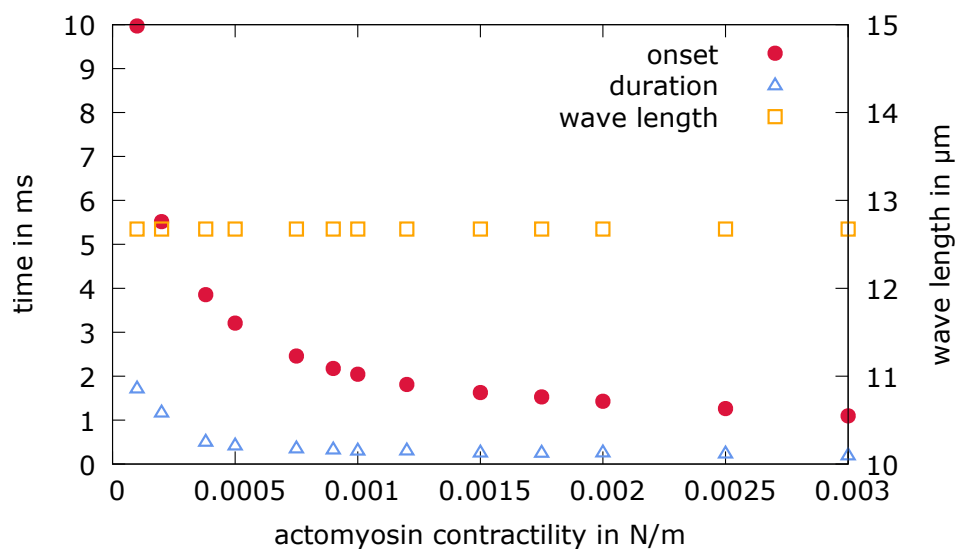


Fig. S11. Magnitude of actomyosin contractility. Towards smaller contractility an exponential increase in onset and duration is observed for a periodic cylindrical membrane. The instability wavelength however does not change with varying contractility.

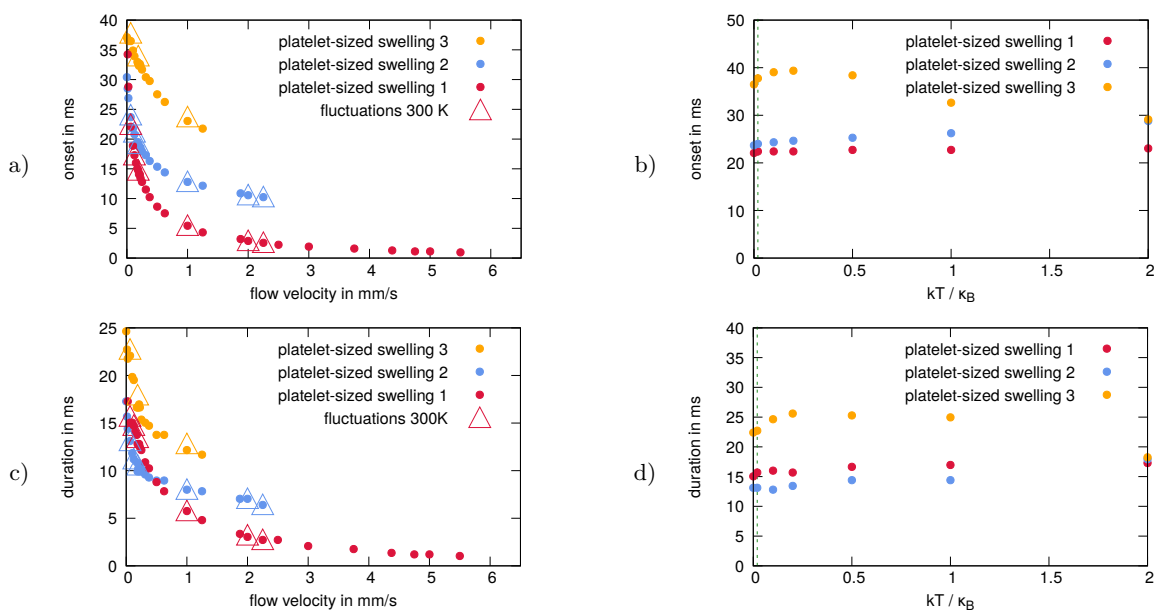


Fig. S12. Fluctuations do not influence instability dynamics. a) Onset time depending on the flow velocity of a homogeneous flow without (dots) and with (triangles) thermal fluctuations. b) For given velocity the temperature is systematically varied. c) Duration time depending on the flow velocity of a homogeneous flow without (dots) and with (triangles) thermal fluctuations. d) For given velocity the temperature is systematically varied. In total, the instability dynamics is not influenced in presence of thermal fluctuations. This can be explained by the initial proplatelet shape not being an unstable fix point, but proplatelet dynamics directly sets in.

a) $\eta_{\text{in}}/\eta_{\text{out}} = 1, v \approx 0.13 \text{ mm/s}$



b) $\eta_{\text{in}}/\eta_{\text{out}} = 5, v \approx 0.13 \text{ mm/s}$



c) $\eta_{\text{in}}/\eta_{\text{out}} = 1, v \approx 0.5 \text{ mm/s}$



d) $\eta_{\text{in}}/\eta_{\text{out}} = 5, v \approx 0.5 \text{ mm/s}$

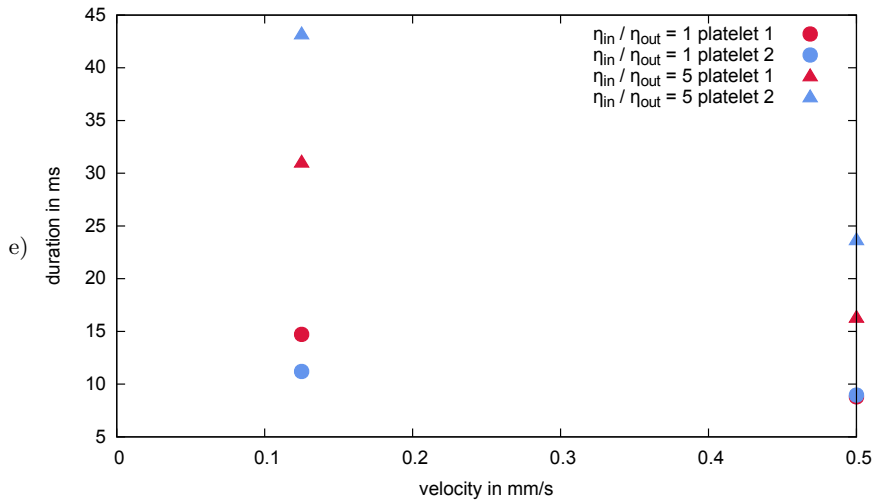
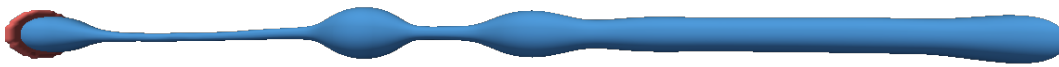


Fig. S13. Viscosity contrast increases instability duration. We compare swelling formation for isotropic actomyosin contractility in homogeneous flow at viscosity contrast of one at intermediate (a) and high (c) velocity to swelling formation at viscosity contrast of five in (b) and (d) for the same two velocities. Snapshots are shown at same time steps and thus comparison shows that swelling formation is slower for increased viscosity contrast. e) Quantitative comparison confirms that duration increases for higher viscosity contrast.

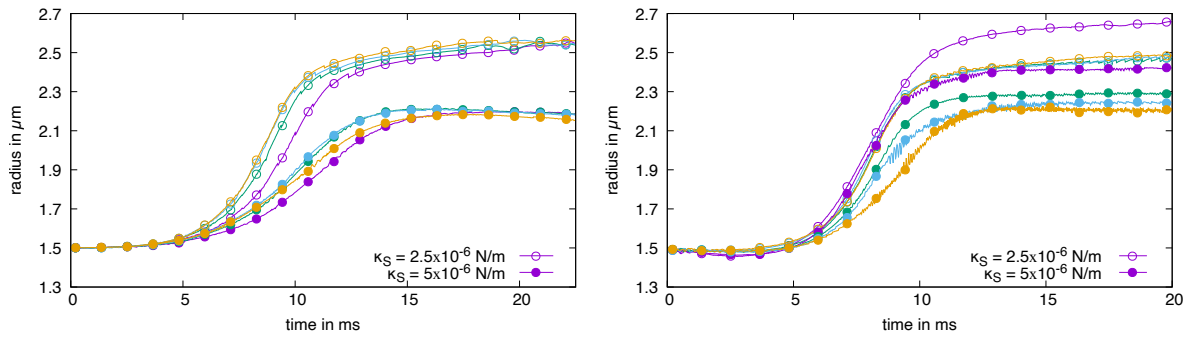


Fig. S14. Influence of shear elasticity. Comparison of simulations with two values of the shear elasticity: $k_S = 5 \cdot 10^{-6} \text{ N/m}$ (as in the main text) and $k_S = 2.5 \cdot 10^{-6} \text{ N/m}$. Curves show the dynamic formation over time of platelet-sized swelling one (violet), two (green), three (blue), four (orange). Simulations are carried out for a) a small velocity $v = 0.167 \text{ mm/s}$ and b) a larger velocity $v = 1.67 \text{ mm/s}$. Except for a slight difference in the proplatelet height, which is due to stronger relative contraction driven by actomyosin contractility, the formation process is not influenced.

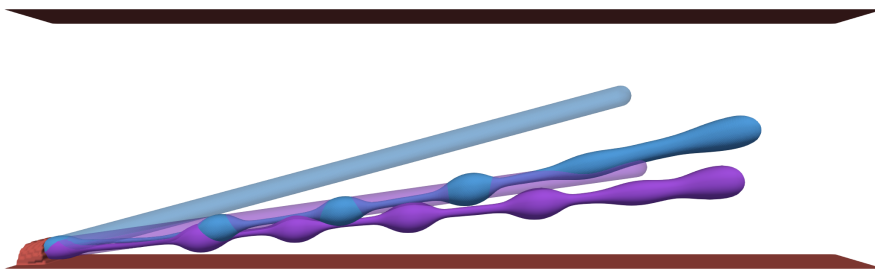


Fig. S15. Influence of the initial proplatelet angle in Poiseuille flow. Corresponding shapes for two different initial angles (different colors) are shown at the beginning and at one fixed time point in transparent and solid color, respectively. The less tilted proplatelet is stretched more strongly, but the overall behavior (number and size of swellings) remains the same.

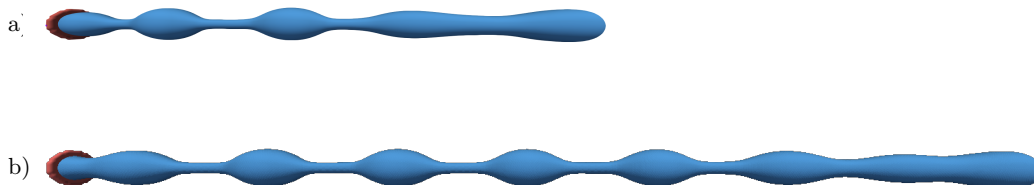


Fig. S16. Varying proplatelet length in simulation. a) A shorter and b) a longer proplatelet undergoing a biological Rayleigh-Plateau instability is simulated with a length 65 and 97 times the radius, respectively. The size of the swellings formed is the same in both simulations, we find a ratio $\frac{2\pi}{\lambda} R_0$ of 0.63 in a) and of 0.65 in b) together with a value of 0.66 for figure S7, which matches the result expected from the classical Rayleigh-Plateau theory 0.69 very well (22).

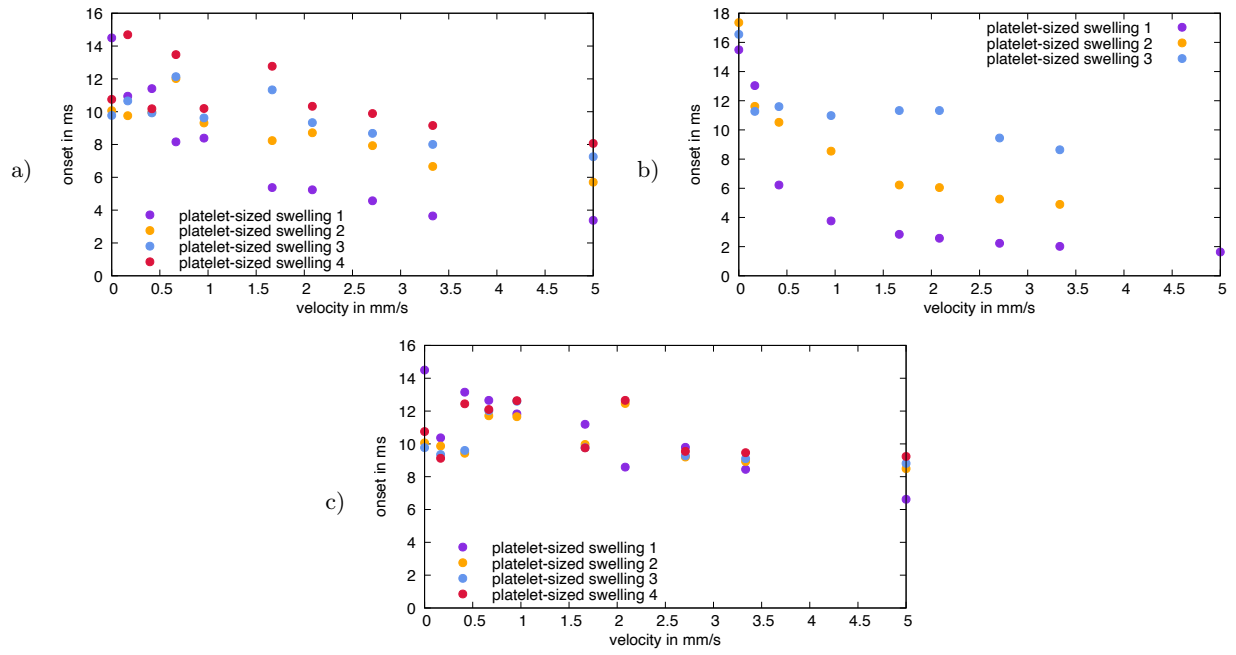


Fig. S17. Instability onset. Onset time of the instability depending on the flow velocity of a) Poiseuille flow, b) homogeneous flow, and c) shear flow. The instability onset can shift to earlier times, which is especially pronounced in the homogeneous flow in b).

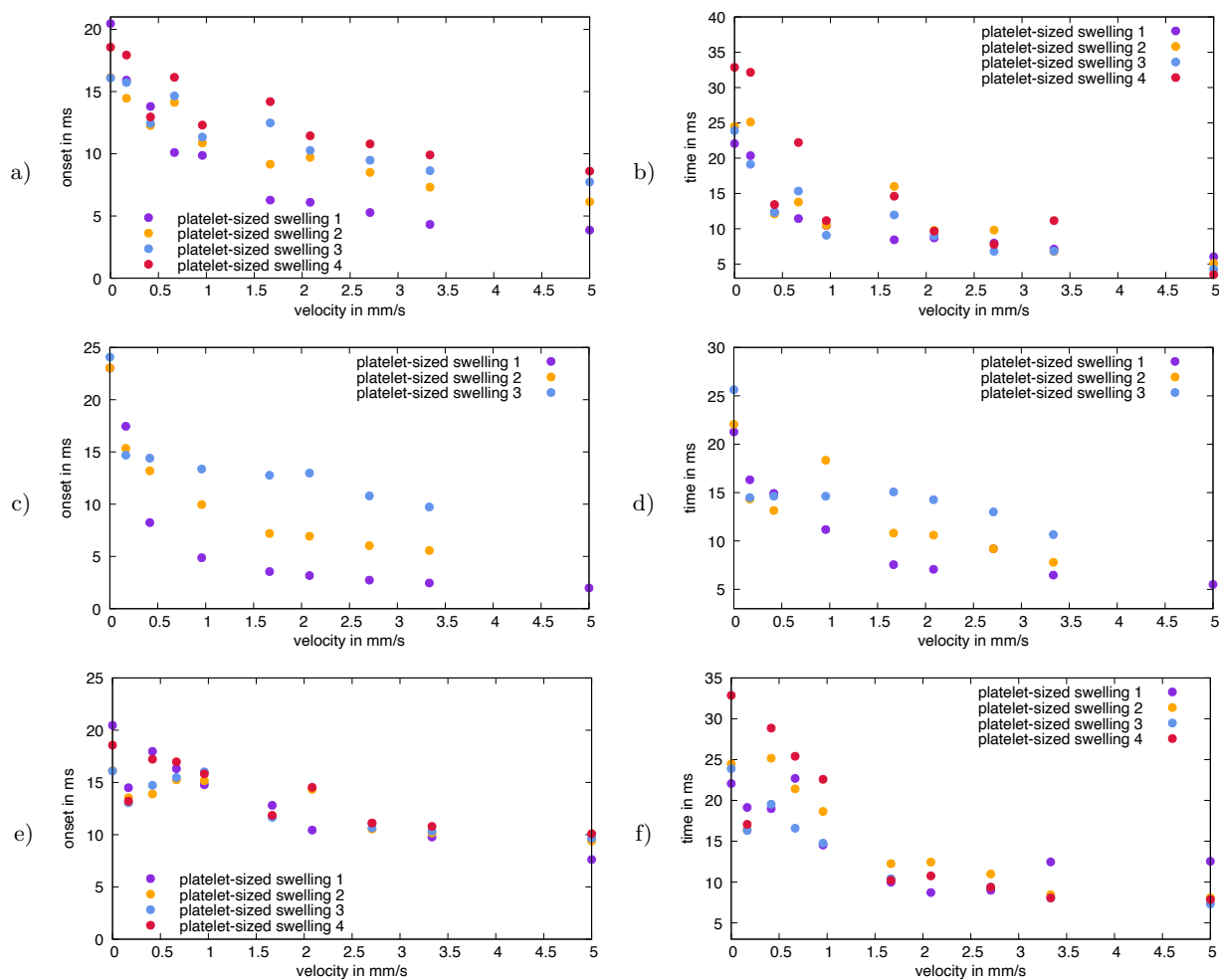


Fig. S18. Onset criterion of 5%. Considering a deformation of 5% of the initial proplatelet radius as criterion for instability onset does not affect the results in the manuscript for a criterion of 2%. In figure a) and b) we show the onset and duration for Poiseuille flow, as done in figure 4 of the manuscript. In figure c) and d) we show the onset and duration for homogeneous flow, as done in figure 5 of the manuscript. In figure e) and f) we show the onset and duration for shear flow, as done in figure S3. Onset shifts to longer times due to the larger deformation to be reached and duration reduces because of the reduced difference in time between onset and reaching a plateau. However, the dependency on flow velocity does not change.

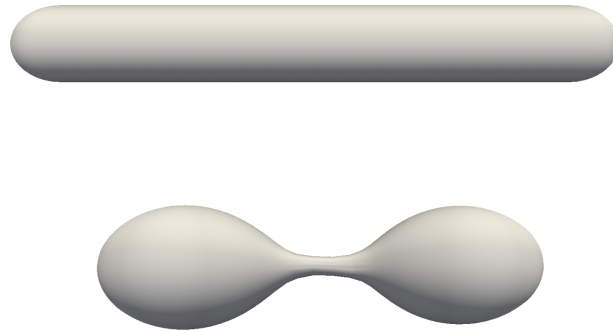
79 **S5. Fragmentation of released proplatelet**

Fig. S19. Transition of a free, extended proplatelet. An already extended proplatelet undergoes a biological Rayleigh-Plateau instability and fragments into two separate platelets.

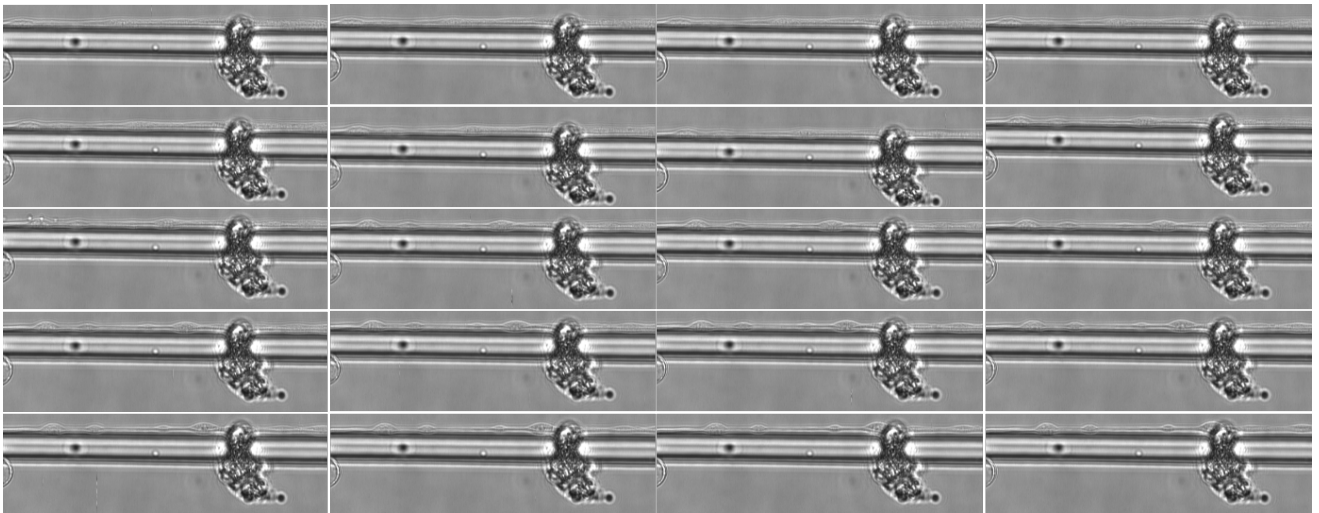
80 **S6. Additional experimental data**

Fig. S20. Detailed time series of swelling formation observed in experiment. Images are taken every every five seconds, shown from left to right and from top to bottom, and image width corresponds to $137.5 \mu\text{m}$. The initial extended proplatelet is shown in the top left corner and the eventual proplatelet with swellings formed in the bottom right corner.

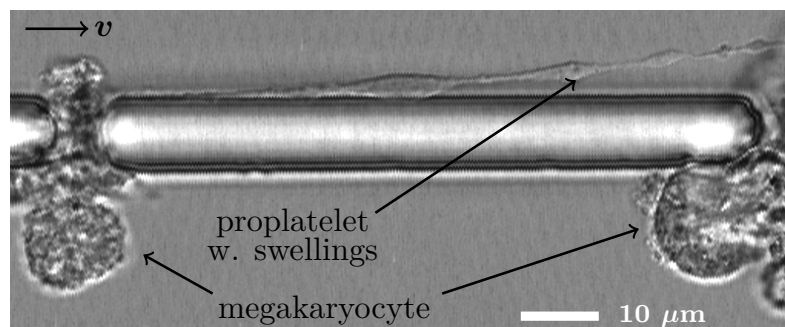


Fig. S21. Periodic arrangement of the Megakaryocytes. Megakaryocytes are trapped in the bottom part of a microfluidic bioreactor in periodically arranged gaps. The left megakaryocyte extends a proplatelet, which forms periodic swellings. Fluid flows with a maximum velocity of 2.2 mm/s and the complete width of the experimental image is $100.81 \mu\text{m}$.

81 **Movie S1.** Proplatelet undergoing a biological Rayleigh-Plateau instability in a quiescent fluid. Movie
82 corresponding to figure 2 of the manuscript.

83 **Movie S2.** Proplatelet undergoing a biological Rayleigh-Plateau instability in a parabolic Poiseuille flow
84 with maximum velocity of $v = 3.33$ mm/s. Movie corresponding to figure 3 of the manuscript.

85 **Movie S3.** Proplatelet undergoing a biological Rayleigh-Plateau instability in a shear flow with velocity
86 $v = 2.0$ mm/s. Movie corresponding to figure S2.

87 **Movie S4.** Proplatelet undergoing a biological Rayleigh-Plateau instability in a homogeneous flow with
88 constant velocity $v = 2.0$ mm/s. Movie corresponding to figure 5 of the manuscript and figure S6.

89 **Movie S5.** Proplatelet undergoing a biological Rayleigh-Plateau instability in a narrow blood vessel with a
90 maximum velocity of $v = 2.0$ mm/s. Movie corresponding to figure S4 and S5.

91 References

- 92 1. JL Villeval, et al., High Thrombopoietin Production by Hematopoietic Cells Induces a Fatal Myeloproliferative Syndrome
93 in Mice. *Blood* **90**, 4369–4383 (1997).
- 94 2. JN Thon, et al., Platelet bioreactor-on-a-chip. *Blood* **124**, 1857–1867 (2014).
- 95 3. C Bächer, S Gekle, Computational modeling of active deformable membranes embedded in three-dimensional flows. *Phys.*
96 *Rev. E* **99**, 062418 (2019).
- 97 4. C Bächer, L Schrack, S Gekle, Clustering of microscopic particles in constricted blood flow. *Phys. Rev. Fluids* **2**, 013102
98 (2017).
- 99 5. C Bächer, et al., Antimargination of Microparticles and Platelets in the Vicinity of Branching Vessels. *Biophys. J.* **115**,
100 411–425 (2018).
- 101 6. B Dünweg, AJ Ladd, Lattice Boltzmann simulations of soft matter systems in *Advanced Computer Simulation Approaches*
102 *for Soft Matter Sciences III*. (Springer), pp. 89–166 (2009).
- 103 7. CK Aidun, JR Clausen, Lattice-Boltzmann Method for Complex Flows. *Annu. Rev. Fluid Mech.* **42**, 439–472 (2010).
- 104 8. T Krüger, et al., *The Lattice Boltzmann Method: Principles and Practice*. (Springer), (2016).
- 105 9. H Limbach, A Arnold, B Mann, C Holm, ESPResSo—an extensible simulation package for research on soft matter systems.
106 *Comput. Phys. Commun.* **174**, 704–727 (2006).
- 107 10. D Roehm, A Arnold, Lattice Boltzmann simulations on GPUs with ESPResSo. *The Eur. Phys. J. Special Top.* **210**,
108 89–100 (2012).
- 109 11. A Arnold, et al., ESPResSo 3.1: Molecular Dynamics Software for Coarse-Grained Models in *Meshfree Methods for Partial*
110 *Differential Equations VI*. (Springer, Berlin, Heidelberg), pp. 1–23 (2013).
- 111 12. F Weik, et al., ESPResSo 4.0 – an extensible software package for simulating soft matter systems. *The Eur. Phys. J.*
112 *Special Top.* **227**, 1789–1816 (2019).
- 113 13. CS Peskin, The immersed boundary method. *Acta Numer.* **11**, 479–517 (2002).
- 114 14. R Mittal, G Iaccarino, Immersed Boundary Methods. *Annu. Rev. Fluid Mech.* **37**, 239–261 (2005).
- 115 15. L Mountrakis, E Lorenz, AG Hoekstra, Revisiting the use of the immersed-boundary lattice-Boltzmann method for
116 simulations of suspended particles. *Phys. Rev. E* **96**, 013302 (2017).
- 117 16. R Skalak, A Tozeren, RP Zarda, S Chien, Strain energy function of red blood cell membranes. *Biophys. J.* **13**, 245 (1973).
- 118 17. D Barthès-Biesel, Motion and Deformation of Elastic Capsules and Vesicles in Flow. *Annu. Rev. Fluid Mech.* **48**, 25–52
119 (2016).
- 120 18. JB Freund, Numerical Simulation of Flowing Blood Cells. *Annu. Rev. Fluid Mech.* **46**, 67–95 (2014).
- 121 19. A Guckenberger, MP Schraml, PG Chen, M Leonetti, S Gekle, On the bending algorithms for soft objects in flows.
122 *Comput. Phys. Commun.* **207**, 1–23 (2016).
- 123 20. A Guckenberger, S Gekle, Theory and algorithms to compute Helfrich bending forces: A review. *J. Physics: Condens.*
124 *Matter* **29**, 203001 (2017).
- 125 21. Cha Zhang, Tsuhan Chen, Efficient feature extraction for 2D/3D objects in mesh representation in *Proceedings 2001*
126 *International Conference on Image Processing (Cat. No.01CH37205)*. (IEEE, Thessaloniki, Greece), Vol. 2, pp. 935–938
127 (2001).
- 128 22. J Eggers, E Villermaux, Physics of liquid jets. *Reports on Prog. Phys.* **71**, 036601 (2008).

Publication 6

ANTIMARGINATION OF MICROPARTICLES AND PLATELETS IN THE VICINITY OF BRANCHING VESSELS

C. Bächer, A. Kihm, L. Schrack, L. Kaestner, M. W.
Laschke, C. Wagner, and S. Gekle

Biophysical Journal **115** (2), 2018

Copyright by CellPress.

DOI: 10.1016/j.bpj.2018.06.013

Antimargination of Microparticles and Platelets in the Vicinity of Branching Vessels

Christian Bächer,^{1,*} Alexander Kihm,² Lukas Schrack,^{1,3} Lars Kaestner,⁴ Matthias W. Laschke,⁵ Christian Wagner,^{2,6} and Stephan Gekle¹

¹Biofluid Simulation and Modeling, Theoretische Physik, Universität Bayreuth, Bayreuth, Germany; ²Experimental Physics, Saarland University, Saarbrücken, Germany; ³Institute for Theoretical Physics, University of Innsbruck, Innsbruck, Austria; ⁴Institute for Molecular Cell Biology, Research Centre for Molecular Imaging and Screening, Center for Molecular Signaling, Medical Faculty, Saarland University, Homburg/Saar, Germany and ⁵Institute for Clinical & Experimental Surgery, Saarland University, Homburg/Saar, Germany; and ⁶Physics and Materials Science Research Unit, University of Luxembourg, Luxembourg City, Luxembourg

ABSTRACT We investigate the margination of microparticles/platelets in blood flow through complex geometries typical for *in vivo* vessel networks: a vessel confluence and a bifurcation. Using three-dimensional lattice Boltzmann simulations, we confirm that behind the confluence of two vessels, a cell-free layer devoid of red blood cells develops in the channel center. Despite its small size of roughly 1 μm , this central cell-free layer persists for up to 100 μm after the confluence. Most importantly, we show from simulations that this layer also contains a significant amount of microparticles/platelets and validate this result by *in vivo* microscopy in mouse venules. At bifurcations, however, a similar effect does not appear, and margination is largely unaffected by the geometry. This antimargination toward the vessel center after a confluence may explain earlier *in vivo* observations, which found that platelet concentrations near the vessel wall are seen to be much higher on the arteriolar side (containing bifurcations) than on the venular side (containing confluences) of the vascular system.

INTRODUCTION

Red blood cells fill up to 45 percent of the volume of human blood (1–5) and thus represent by far the major cellular blood constituent. Because of their high deformability, red blood cells flowing through a cylindrical channel or blood vessel prefer the low-shear-rate region in the center of the channel. By hydrodynamic interactions with the red blood cells, stiffer particles such as platelets, white blood cells, or artificial drug-delivery agents are thus expelled toward the wall. This separation of red blood cells and stiffer particles is known as margination and is essential for the ability of blood platelets to quickly stop bleeding or for drug delivery agents to closely approach the endothelial wall. One of the first observations of margination studied white blood cells *in vivo* as well as an *in vitro* model system containing disks and spheres already in 1980 (6). Interestingly, an *in vivo* study by Woldhuis et al. (7) demonstrated a striking difference between the platelet distribution in arterioles and venules, with significantly more margination occurring on the arteriolar side of the vascular system. Since

then, more detailed insights were gained by experimental studies (8–19), computer simulations (20–41), and theoretical modeling (42–46). These studies all deal with margination in spatially constant geometries such as shear flow, pipes with cylindrical or rectangular cross sections, and plane Couette systems.

In contrast, in living organisms, blood vessels form a hierarchical structure in which large arteries branch all the way down to microcapillaries in a series of bifurcations followed by a reversed series of confluences leading up to larger and larger vessels on the venular side. The typical distance between two bifurcations lies within 0.4 mm up to 1 mm in the microvascular system (2,4). Despite their importance, studies on red blood cell distribution and margination using spatially varying geometries are surprisingly scarce. Platelets have been studied by two-dimensional (2D) simulations in the vicinity of an aneurysm (47,48) and in the recirculation zone behind a sudden expansion of a channel (49). Near a vessel constriction, the locally varying distribution of red blood cells (50–52) and rigid microparticles in suspension with red blood cells have been investigated (53–56). In (56), a local increase in microparticle concentration in front of the constriction has been reported. On a technical side, microchannels including

Submitted November 20, 2017, and accepted for publication June 5, 2018.

*Correspondence: christian.baecher@uni-bayreuth.de

Editor: Jochen Guck.

<https://doi.org/10.1016/j.bpj.2018.06.013>

© 2018 Biophysical Society.



bifurcations are investigated as a possible basis for microdevices separating blood plasma (57,58). In asymmetric branches, the Zweifach-Fung effect (59,60) describes an asymmetric red blood cell distribution, i.e., a larger hematocrit in the large flow rate branch (61,62). Under certain circumstances, even an inversion of the Zweifach-Fung effect may occur (63). Combining experiments and simulations in a rectangular channel with bifurcation (64) and for a diverging and converging bifurcation using 2D simulations (65), a cell-depleted zone right after the confluence has been reported. Downstream a bifurcation asymmetry of red blood cell distribution has been seen (57,64,66,67). Reference (68) reported margination of hardened red blood cells while flowing through branching vessels. Balogh and Bagchi (69) investigated the transient behavior of red blood cell motion in more complex networks (69–71). Besides the red blood cell behavior, it is important to consider suspended particles like blood platelets or synthetic particles because possible influences of bifurcations and confluences may play a major role in medical applications. Nevertheless, systematic studies covering particle blood suspensions in networks are scarce. White blood cell motion in asymmetric bifurcations has been studied experimentally in the context of a branched vessel geometry (72), whereas Sun et al. (73) investigated the interaction of six red blood cells flowing behind a white blood cell in the vicinity of vessel junctions.

In this report, we study the margination of stiff spherical particles suspended among red blood cells in the vicinity of vessel confluences and bifurcations. This allows us first to confirm and investigate quantitatively the previously observed cell-depleted layer of red blood cells after confluences. Second, we provide results on the influence of network geometries on stiff particle margination. Our generic stiff particles are a model for artificial drug delivery agents but also serve as a reasonable approximation for blood platelets. We investigate two cylindrical branches either bifurcating from or forming a confluence into a larger vessel by means of three-dimensional (3D) lattice Boltzmann simulations. To realize simulations of these systems, we implement inflow and outflow boundary conditions to the lattice Boltzmann/immersed boundary algorithm similar to an approach based on dissipative particle dynamics by Lykov et al. (74). Behind a vessel confluence, we observe a red blood cell-free layer in the center of the channel persisting for up to 100 μm after the confluence. Importantly, this central cell-free layer is not only devoid of red blood cells but also contains a significant amount of antimarginated microparticles/platelets. Using fluorescent microparticles in mouse microvessels, we consistently observe this antimargination also in vivo. At bifurcations, no equivalent effect occurs. Our findings may explain in vivo observations of Woldhuis et al. (7), who found that in the vascular system, platelet margination is strongly present at the arteriolar side with bifurcations but less at the venular side with confluences. Similarly, recent observations show that thrombi

formed in arterioles contain significantly more platelets than thrombi formed in venules (75), which is another indication of increased platelet margination on the arteriolar side. By considering the axial distribution of microparticles along the flow direction, we furthermore reveal the site of confluence as a spot with locally increased concentration. The article is organized as follows: we first introduce the simulation and experimental methods and then report 2D and one-dimensional (1D) concentration profiles first in the system with vessel confluence, including the experimental results, then in the system with a bifurcation. Finally, we investigate the influence of larger hematocrit and microparticle distribution in an asymmetric bifurcation.

METHODS

Lattice Boltzmann/immersed boundary method

Fluid flow in the confluence/bifurcation geometry is modeled using the 3D lattice Boltzmann method (LBM), which calculates fluid behavior by a mesoscopic description (76–78). We use the implementation of LBM in the framework of the simulation package ESPResSo (79–81). Red blood cells and particles are modeled using the immersed boundary method (IBM) (37,56,82,83).

To mimic realistic conditions of blood flow, we assign the blood plasma density $\rho_{\text{plasma}} = 1000 \text{ kg/m}^3$ and viscosity $\mu_{\text{plasma}} = 1.2 \times 10^{-3} \text{ Pas}$. Due to the large size of the red blood cells and microparticles, we expect the temperature to hardly affect collective flow behavior of cells and particles and thus neglect the effect of thermal fluctuations. A typical fluid grid of these simulations contains $170 \times 110 \times 58$ nodes for a bifurcation and $288 \times 110 \times 58$ nodes for a confluence. The time step is chosen as $0.09 \mu\text{s}$, with the time of a typical simulation being about 2.5 s.

Red blood cells and microparticles are realized by an infinitely thin elastic membrane interacting with the fluid. For the calculation of elastic forces imposed on the fluid, the membrane is discretized by nodes that are connected by triangles. A red blood cell possesses 1280 triangles and 642 nodes and has a diameter of $7.82 \mu\text{m}$. The averaged distance between neighboring nodes is about one LBM grid cell. Nodes transfer forces to the fluid and are themselves convected with the local fluid velocity. Interpolation between membrane nodes and fluid nodes is done using an eight-point stencil. The viscosity contrast of the cells is $\lambda = \eta_{\text{in}}/\eta_{\text{out}} = 1$, i.e., the fluid inside and outside the cells has the same viscosity. The elastic properties of a red blood cell are achieved by applying the Skalak model (5,84,85) with a shear modulus $k_S = 5 \times 10^{-6} \text{ N/m}$ and an area dilatation modulus $k_A = 100k_S$. Additional bending forces are computed on the basis of the Helfrich model using a bending modulus $k_B = 2 \times 10^{-19} \text{ Nm}$ (5,86,87). For the calculation, the algorithm denoted method A in (86) is used with the bending energy being proportional to the angle of adjacent triangles and the actual forces being computed by analytically differentiating the energy with respect to node position. This somewhat simplistic approach is appropriate for this work, in which we focus on collective rather than detailed single-cell behavior and in which especially the behavior of the microparticles is of interest.

Microparticles are modeled in a similar fashion as the red blood cells with 320 triangles and 162 nodes. The microparticles are chosen to have half the size of red blood cells ($a = 3.2 \mu\text{m}$), which has been reported to show strong margination (32). In contrast to the red blood cells, the microparticles contain an additional inner grid to ensure the stiffness and (approximate) nondeformability of the microparticles (37). The inner grid is linked to the membrane nodes by a harmonic potential. Elastic properties of microparticles are chosen 1000 times larger than for red blood cells. For the purpose of numerical stability, we apply an empirical volume conservation potential (38) as well as a short-ranged soft-sphere repulsion, which decays

with the inverse fourth power of the distance and with a cutoff radius equal to one grid cell. The latter potential acts between all particles and between the particles and the channel wall.

The stability and accuracy of our simulation method have been extensively validated in (37,86). In addition, as detailed in [Supporting Materials and Methods](#), the shapes of isolated red blood cells in cylindrical and rectangular channels have been validated to agree with methodically very different dissipative particle dynamics (88) and boundary integral (89) simulations. The behavior of stiff particles is validated by considering the drag force on a sphere as well as the tumbling of a spheroid in shear flow (90). We also demonstrate that the numerically motivated short-range repulsive force does not affect our results. Finally, we validate our simulation method by comparing the asymmetric red blood cell distribution in bifurcations with recent computational results by Balogh and Bagchi (70) as well as experimental data (61,91).

Channel geometry

The systems of interest, a confluence and a bifurcation, are shown in [Fig. 1 a](#). Both geometries are constructed in the same way: a main cylindrical channel of radius R_{ch} branches into two symmetric daughter channels of radius R_{br} . To obtain a smooth boundary, i.e., the boundary itself and the first derivative is continuous, the transition between main channel and the branches is modeled by third-order polynomials: one polynomial, $y_c(x)$, describes the bifurcating centerline, whereas another, $y_{up}(x)$, describes the upper/lower boundary. By rotation around the centerline with radius $y_{up}(x) - y_c(x)$, we obtain a circular cross section for each x forming the bifurcation along the flow direction. Where the cross sections of the two branches overlap, the boundary is left out.

Inflow/outflow boundary condition for IBM-LBM

To investigate a confluence and a bifurcation as displayed in [Fig. 1 a](#), periodic boundary conditions cannot be employed. Joining both geometries into one very large system would be computationally far too expensive because of the very long-range influence of bifurcations/confluences, as will be detailed in the course of this work. At the same time, at the entrance of the branches in [Fig. 1 a \(left\)](#) as well as at the entrance of the main channel in [Fig. 1 a \(right\)](#), we do not want the microparticles and red blood cells to enter in a randomly distributed fashion but instead obey a margined configuration to match with the well-known behavior in a long tube. The purpose behind this inflow condition is to bring out clearly how the behavior of the margined fraction of microparticles is influenced by the confluence/bifurcation.

To meet these requirements, we implemented inflow and outflow boundary conditions to our IBM-LBM algorithm similar to a recent work using dissipative particle dynamics (74). We start by simulating straight cylinders with periodic boundaries and a body force driving the flow, as depicted at the top of [Fig. 1 b](#). These feeding simulations yield a time-dependent sequence, which then serves for particle inflow in the complex system of interest. During the simulation of the complex system, we check a frame of the feeding sequence for cells and particles crossing a certain (arbitrary) plane. Particles crossing this plane are then inserted at the same radial position with the same shape into the complex system, as illustrated also in [Fig. 1 b](#). For crossing of the plane, the center-of-mass serves as a criterion similar to (74). The inflow velocity is chosen to match the flow rate prescribed in the straight cylinder. To prevent overlap of cells during inflow, we sometimes increase the flow rate slightly ($\sim 10\%$). As a result, we obtain a margined pattern at the entrance of our complex systems, as proven by the cross-sectional concentration profiles shown in [Supporting Materials and Methods](#).

Because azimuthal motion of the dilute microparticles in the feeding channels is extremely slow, even a very long feeding simulation would lead to a biased distribution of microparticles upon entering the complex channel. This is prevented by applying a small angular random force to the microparticles in the feeding channel, thus guaranteeing an azimuthally homogenous, yet well margined distribution of microparticles. We furthermore show in [Supporting Materials and Methods](#) that after a first filling of the system, the cell and particle number in the system reaches a plateau and slightly fluctuates around a constant value.

For the fluid, to prescribe a distinct flow rate, we assign a constant velocity to all fluid LBM nodes at the beginning of the simulation box. The same is done at the end of the box, taking into account the different cross sections of the main channel and branches, thus matching fluid inflow and outflow. About 15 grid cells behind the inflow, the flow profile matches tube flow. This region with evolving flow profile is skipped for particle inflow and in data analysis.

Analysis

In our work, we employ different concentration profiles at given positions along the channel. First, we compute cross-sectionally averaged concentrations, leading to 1D concentration profiles as a function of position along the flow direction x . Some of these profiles consider only a certain fraction of cells or particles entering the channel in specific regions, which are labeled as a function of their lateral (r, ϕ) position in polar coordinates at the entrance of the system. Corresponding concentrations are calculated, taking into account only this particular fraction of cells or particles. The

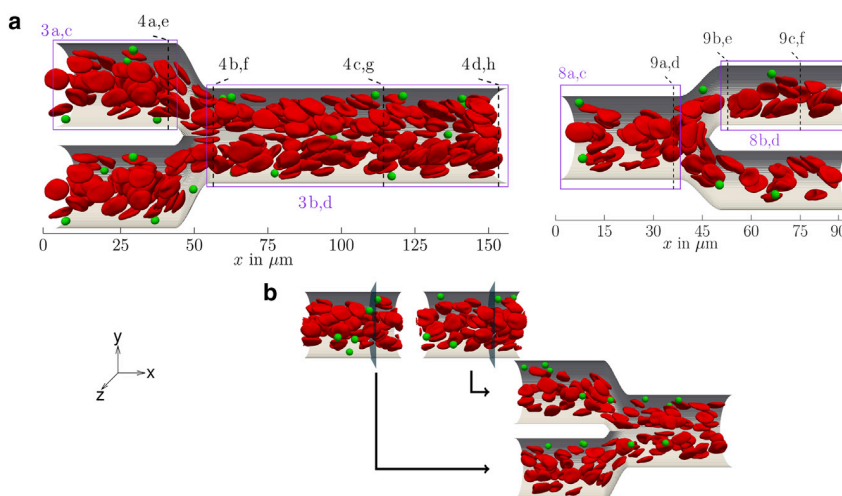


FIGURE 1 (a) Systems of interest: a suspension of red blood cells and microparticles flowing either through a confluence (*left*) or a bifurcation (*right*). Rectangles with numbers refer to figures containing corresponding 2D radial/planar projections, whereas dashed lines refer to figures containing cross-sectional profiles. (b) Inflow is realized using straight cylinders as feeding systems: whenever a cell/particle crosses the indicated plane, it is fed into one of the branches of the confluence system. To see this figure in color, go online.

labeling is illustrated by the color code in Fig. 2 a and by the criteria for r and ϕ in Fig. 2 b.

Second, we use three types of 2D concentration profiles. For microparticle concentrations, 2D radial projections in the r, x plane are calculated, which reflect the radial symmetry of the main and the branch channels. Such projections, however, are not appropriate to understand nonradially symmetric effects occurring near confluences or bifurcations. We thus employ in addition, mainly for red blood cell concentrations, planar projections of the 3D concentrations on the y, x plane by integrating the concentration over the z direction perpendicular to the plane of the paper. Finally, to get further insight into cell and particle distributions perpendicular to the flow direction, we calculate cross-sectional profiles within the y, z plane.

All concentration profiles are averaged over the whole simulation time, starting from the moment at which the number of cells and particles does not vary significantly.

Preparation of dorsal skinfold chamber and in vivo imaging

Animals

The in vivo experiments were performed in 10–12 week old male C57BL/6 mice ($n = 3$) with a body weight of 23–26 g. The animals were bred and housed in open cages in the conventional animal husbandry of the Institute for Clinical & Experimental Surgery (Saarland University, Saarbrücken, Germany) in a temperature-controlled environment under a 12 h/12 h light-dark cycle and had free access to drinking water and standard pellet food (Altromin, Lage, Germany). The experiment was approved by the local governmental animal care committee (approval number 06/2015) and was conducted in accordance with the German legislation on protection of animals and the National Institutes of Health Guidelines for the Care and Use of Laboratory Animals (Institute of Laboratory Animal Resources, National Research Council, Washington).

Dorsal skinfold chamber model

Microvessels were analyzed in the dorsal skinfold chamber model, which provides continuous microscopic access to the microcirculation of the striated skin muscle and the underlying subcutaneous tissue (92). For the implantation of the chamber, the mice were anesthetized by i.p. injection of ketamine (75 mg/kg body weight; Ursotamin; Serumwerke Bernburg, Bernburg, Germany) and xylazine (15 mg/kg body weight, Rompun; Bayer, Leverkusen, Germany). Subsequently, two symmetrical titanium frames (Irola Industriekomponenten KG, Schonach, Germany) were implanted on the extended dorsal skinfold of the animals, as described previously in detail (93). Within the area of the observation window, one layer of skin was completely removed in a circular area of ~ 15 mm in diameter. The remaining layers (striated skin muscle, subcutaneous tissue, and skin) were finally covered with a removable cover glass. To exclude alterations of the microcirculation due to the surgical intervention, the mice were allowed to recover for 48 h.

In vivo microscopy

In vivo microscopic analysis was performed, as previously described (94). In detail, the mice were anesthetized, and a fine polyethylene cath-

eter (PE10, 0.28 mm internal diameter) was inserted into the carotid artery for application of the plasma marker 5% fluorescein-isothiocyanate-labeled dextran 150,000 (Sigma-Aldrich, Taufkirchen, Germany) and microspheres (Fluoresbrite Plain YG 1.0 μm ; Polysciences, Warrington, PA). Then, the animals were put in lateral decubital position on a plexiglass stage, and the dorsal skinfold chamber was attached to the microscopic stage of an upright microscope (Axiotech; Zeiss, Jena, Germany) equipped with an LD EC Epiplan-Neofluar $50\times/0.55$ long-distance objective (Zeiss) and a 100 W mercury lamp attached to a filterset (excitation 450–490 nm, emission > 520 nm). The microscopic images were recorded using a complementary metal-oxide semiconductor video camera (Prime 95B; Photometrics, Tucson, AZ) at an acquisition speed of 415 images per second controlled by a personal-computer-based acquisition software (NIS-Elements; Nikon, Tokyo, Japan).

Trajectory analysis

The recorded video sequence was analyzed using a single-particle tracking algorithm. Hereby, the intensity profile of each frame was adjusted to have both the top and bottom 1% of all pixels saturated, correcting for changes in illumination and exposure time. With the aid of a tailored MATLAB (The MathWorks, Natick, MA) script, all spherical (round) objects were detected and interconnected among all frames by cross correlating consecutive images. To only detect microspheres (and not red blood cells), we set a threshold of 0.9 as a lower limit in normalized intensity values because they are fluorescent. Further, we defined a minimal diameter for the detected particles (0.7 μm), causing a trajectory to end if the measured value falls below this value. Combining the coordinates of all classified microspheres in this way over the whole video sequence, we derived the respective trajectories.

RESULTS AND DISCUSSION

Channel confluence

We first investigate the system with two branches of radius 16 μm merging into one main channel of radius 17.5 μm , as depicted in Fig. 1 a (left) and shown in Video S1. Results for a larger/smaller main channel are qualitatively similar and shown in the Supporting Materials and Methods. The centerlines of the two branches are separated by 39 μm , and the transition zone from the end of the branches to the beginning of the main channel is about 13 μm . We choose the mean velocity at the entrance of our system to be about $v = 2.5$ mm/s. Simulations are first performed for a physiologically realistic hematocrit (red blood cell volume fraction) of $Ht = 12\%$. Results for a higher $Ht = 20\%$ are qualitatively similar and are presented at the end of this contribution. The Reynolds

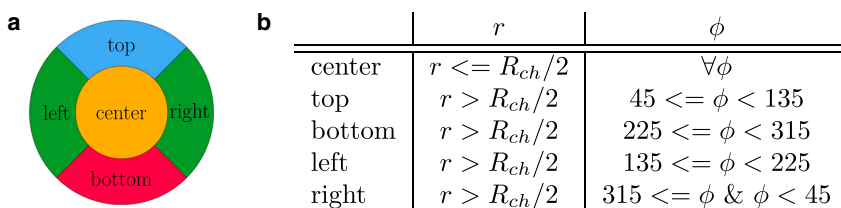


FIGURE 2 (a) Color labeling and (b) labeling criteria for red blood cells and microparticles at the entrance of the system with respect to the in-plane position in the cross section. Because of symmetry, the particles at left and right can be treated equally. To see this figure in color, go online.

number calculated from the centerline velocity, the red blood cell radius R_{RBC} , and the kinematic viscosity of the fluid ν_{plasma} is $Re = \frac{(R_{RBC} \cdot v)}{\nu} = \mathcal{O}(10^{-2})$.

Cell and particle distribution

We start by considering 2D concentration profiles along the flow direction in Fig. 3. In the two small branches and far away from the confluence, we observe a homogeneous distribution of red blood cells around the center and the cell-free layer with vanishing concentration (95–97) near the wall, as can be seen by Fig. 3 a. The microparticle concentration in Fig. 3 c exhibits the typical margination peak near the wall. The state of full and azimuthally homogeneous margination is confirmed by the cross sections at channel entrance shown in Supporting Materials and Methods. This behavior is the same as in a straight channel.

Approaching the confluence, we observe an asymmetric cell-free layer; near the inner boundary of the branch, the cell-free layer decreases, whereas near the outer boundary, it increases. The asymmetry becomes more pronounced toward the end of the branches ($x \approx 40 \mu m$) stemming from cells flowing toward the main channel. However, the motion of red blood cells toward the main channel already initiates at $x \approx 30 \mu m$, i.e., about $10 \mu m$ before the end of the branches. This also affects microparticle behavior, as can be seen by the two separate peaks in the radially projected concentration in Fig. 3 c. These two peaks stem from the particles near the inner and the outer boundary, respectively; the microparticles near the inner boundary remain close to the wall, whereas the particles near the outer boundary migrate away from the wall because of the flow profile toward the main channel and the increased cell-free layer.

Entering the main channel, we observe a decreased cell-free layer near the upper and lower boundary in Fig. 3 b (right) at the beginning. An interesting feature of the red

blood cell concentration is the additional cell-free layer that develops in the channel center after the confluence. This agrees well with the findings of (64), which showed that a cell-depleted zone behind the apex of a confluence develops. We confirm that finding by considering the concentration and also highlight the long-range stability of the central cell-free layer.

Most remarkably, this central cell-free layer contains, just like its classical near-wall counterpart, a significant amount of microparticles, as can clearly be seen in the radially projected microparticle concentration of Fig. 3 d.

Before investigating further this central cell-free layer, we consider cross-sectional concentration profiles in Fig. 4. In Fig. 4 a, we observe how the circular pattern of red blood cells is shifted toward the inner boundary at the end of the branches. This corresponds to the asymmetric cell-free layer in Fig. 3 a. Entering the main channel, the pattern of red blood cell concentration possesses two flattened and asymmetric spots (Fig. 4 b) clearly separated by the central cell-free layer, which shows vanishing concentration. At the left and right of the main channel, an additional large cell-free spot is obtained. This central-cell-free layer stems from the cells flowing out of the upper and lower branch competing for the channel center.

Microparticles in the two branches remain well margined until the end of the branches, as shown in Fig. 4 e. After the confluence, however, Fig. 4 f shows how a notable fraction of microparticles is now located very near the channel center. This can be understood by the original location of the microparticles inside the branches; those microparticles that are located near the inner boundary of the branch enter the main channel in the center. This location is favorable because of the additional central cell-free layer observed in Fig. 4 b. In Supporting Materials and Methods, we show the antimargination also for platelet-shaped microparticles. Thus, this geometry leads to a redistribution of

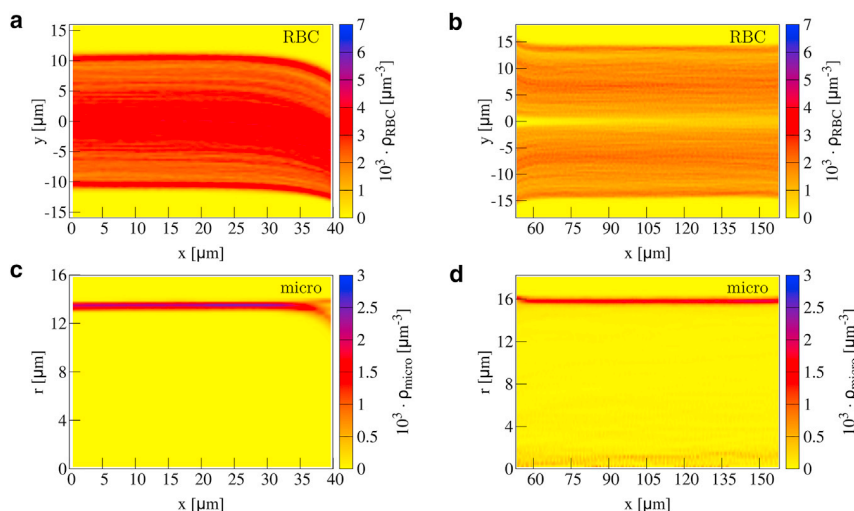


FIGURE 3 Concentration of red blood cells in a confluence in 2D planar projection (a) along the upper branch and (b) along the main channel. Microparticle concentration in 2D radial projection is shown (c) along the upper branch and (d) along the main channel. The cell-free layer near the inner boundary decreases at the end of the branches, whereas it increases near the outer boundary. Inside the main channel, an additional cell-free layer in the center develops. To see this figure in color, go online.

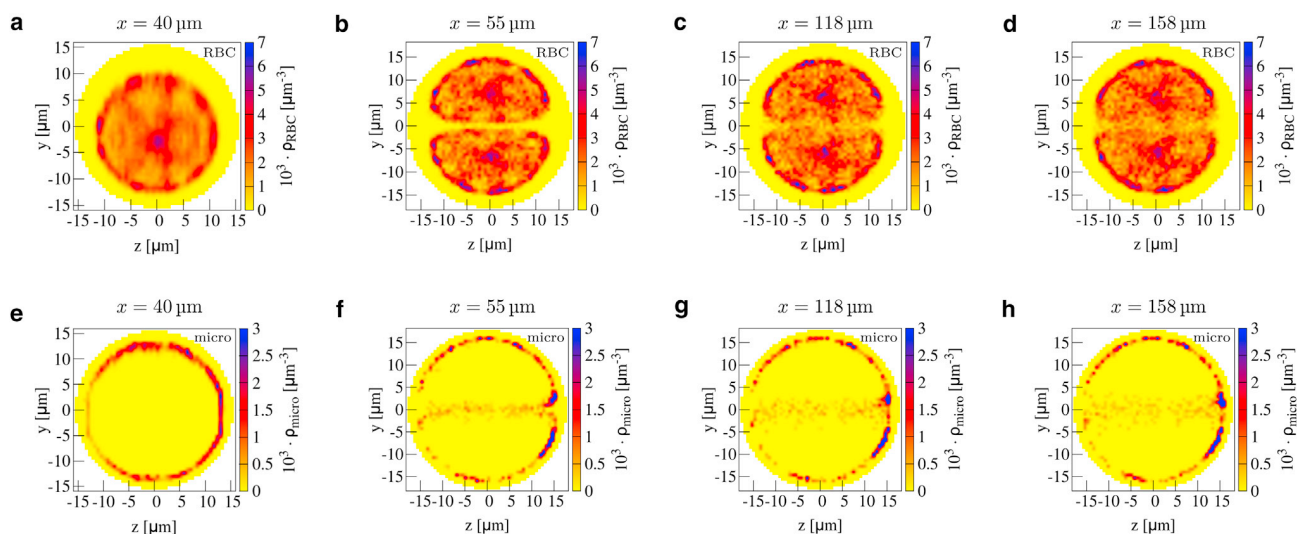


FIGURE 4 2D cross-sectional concentration in a confluence for red blood cells (*a–d*) and microparticles (*e–h*) at the end of the branches (*a* and *e*), at the beginning of the main channel (*b* and *f*), at the middle of the main channel (*c* and *g*), and at the end of the main channel (*d* and *h*). Positions are also indicated by the dashed black lines in Fig. 1 *a*. In the main channel, a clear cell-free layer in the center together with microparticle antimargination is present. To see this figure in color, go online.

microparticles from a near-wall margined position before the confluence to a near-center antimargined position after the confluence.

Lifetime of the central cell-free layer, antimargination, and physiological consequences

An interesting question is the stability of the red blood cell-depleted central cell-free layer and the corresponding antimargined microparticles as the flow continues away from the confluence location along the main channel. Fig. 3 *b* shows that the central cell-free layer is surprisingly stable, being visible all along the main channel and only becoming slightly blurred toward the end. The same trend can be observed in the cross-sectional concentration at three sites along the main channel in Fig. 4, *b–d*. Although it starts to become blurred after 60 μm in Fig. 4 *c*, the central cell-free layer and especially the cell-free spot left and right is visibly present until at least 100 μm behind the confluence, as shown in Fig. 4 *d*. Similarly, the corresponding microparticle concentration in Fig. 4, *f–h* shows that microparticles are located in the center all along the main channel. Thus, a confluence of two channels influences microparticle behavior over distances that are much longer than the channel diameter.

To gain a more mechanistic insight into this long-time stability of the central cell-free layer, we calculate the (shear-induced) diffusion coefficient (23,25,97–101) of red blood cells in the center. For this, we compute the time-dependent mean-square displacement, which is shown in Supporting Materials and Methods. By modeling the increase in mean-square displacement with time by the theoretical expectation for normal diffusion $\langle \Delta y(t)^2 \rangle = 2Dt$, we extract a diffusion coefficient for the red blood cells of

$D_{RBC} \approx 28 \mu\text{m}^2/\text{s}$ in the case of $Ht = 12\%$. This value is of the same order as that of previous results in experiments with red blood cells (98,99,101) and simulations of spheres and platelets (23,25). By assuming a thickness of 1.5 μm and a flow speed of 2.5 mm/s, we calculate a distance of 100 μm required to bridge the central cell-free layer. This length scale agrees well with the observation in the concentration profiles that the central cell-free layer starts to become blurred after 100 μm . We calculate in the same way the shear-induced diffusion coefficient of the microparticles $D_{micro} \approx 25 \mu\text{m}^2/\text{s}$. Reference (98) reports for platelets in a perfusion chamber 34 $\mu\text{m}^2/\text{s}$ for a shear rate of 8321/s and unknown hematocrit. References (23,25) obtain a diffusivity of a factor 2 smaller in simulations of plane Couette flow with $Ht = 0.2$. Considering not only the gap of the central cell-free layer to be closed but also the larger spot left/right (assuming a distance of 5 μm to be bridged), we can estimate a distance of 1.1 mm for red blood cell redistribution, which is comparable to the estimation of 25 times the channel diameter by Katanov et al. (97). When we estimate the length scale required for microparticles to migrate toward the channel wall, i.e., to marginate, we get ~ 5 mm. Comparing this to the typical distance between successive confluences of ~ 0.4 –1 mm (2,4), we conclude that full margination cannot be regained. This in turn may explain the in vivo observations that on the venular side of the vascular system, margination is much less pronounced than on the arteriolar side (7,75).

Furthermore, we want to address the question of how strong the effect of antimargination is. Therefore, we calculate the fraction of particles that are not located directly next to the wall, i.e., we consider particles that are more than one particle radius away from the vessel wall. For the

concentration profiles in Fig. 4, we obtain the fractions 0 at $x = 40 \mu\text{m}$, 0.158 at $x = 55 \mu\text{m}$, 0.138 at $x = 118 \mu\text{m}$, and 0.135 at $x = 158 \mu\text{m}$. We find that the fraction decreases very slowly with increasing distance from the confluence because of marginating microparticles (most likely those located *left/right*).

Axial concentration

Further insight can be gained by considering 1D axial cell and particle concentration profiles in Fig. 5. The overall red blood cell concentration exhibits two plateaus inside the main channel and inside the branches, respectively. Inside the branches, the concentration is lower than in the main channel, which is in agreement with the Fahraeus effect (102). Right at the confluence, we observe a zone in which the red blood cells become slightly depleted. The microparticle concentration along the branches first increases slightly, and right at the confluence, a strong peak develops. In the main channel, the microparticles have a nearly constant concentration.

To elucidate red blood cell behavior further and especially to explain the peak in microparticle concentration, we label the cells/particles while entering the branches, as explained in Methods. The concentrations for the labeled cells and particles are shown in Fig. 6.

The red blood cells in the center, those *left/right*, and those at the bottom of the branches behave in a similar fashion: at the end of the branches, they are accelerated and thus have a decreased concentration. After a small peak, they quickly reach a constant concentration in the main channel. Only the cells arriving at the top exhibit a slightly increasing concentration at the end of the branches but are depleted as well at the site of the confluence. Microparticles arriving *left/right* or at the bottom show a similar concentration profile as that of the corresponding red blood cells and thus do not cause the peak in overall concentration in Fig. 5. We note that these concentration profiles can be understood by passive tracer particles similar to those in

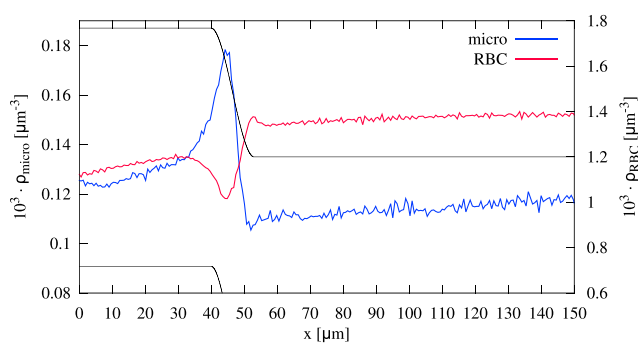


FIGURE 5 1D axial profile of red blood cells and microparticles flowing through a vessel confluence. Whereas the red blood cells are depleted at the site of the confluence, the microparticles exhibit a concentration increase of $\sim 50\%$ compared to the branches and the main channel. To see this figure in color, go online.

constricted channels (56) and as detailed in Supporting Materials and Methods. From Fig. 6 *b*, we are thus able to conclude that the peak stems from the microparticles flowing at the top of the branches. The concentration of these microparticles increases more than twofold compared to the branches and the main channel. Because of the margination, the microparticles are located right beside the wall. Also, the concentration profile of the microparticles at the top can be reproduced by passive tracer particles, as done in Supporting Materials and Methods. Thus, the local increase in microparticle concentration can be understood by the underlying flow profile.

In vivo observation of microparticle antimargination

To demonstrate the relevance of the antimargination observed in our simulations, we inject fluorescent beads into living mice and image their behavior when flowing through a microvessel confluence. In Fig. 7, we show a set of trajectories obtained from the video of microscopy images (corresponding Video S2). In agreement with the predictions of our numerical simulations, beads that are initially marginated at the outer walls (*blue lines* in Fig. 7) remain marginated, whereas beads located initially at the inner walls (*red lines* in Fig. 7) undergo antimargination and end up near the channel center after passing through the confluence.

Channel bifurcation

Next, a bifurcation is investigated, as depicted in Fig. 1 *a* (*right*) and shown in Video S3. The suspension of red blood cells and microparticles flows through a straight channel of radius $16 \mu\text{m}$, branching into two daughter channels of radius $11.5 \mu\text{m}$. The main channel and the combined branches have the same cross-sectional area, and the centerlines of the two branches are separated by $34 \mu\text{m}$. The transition zone from the end of the main channel to the beginning of the branches is about $13 \mu\text{m}$.

Cell and particle distribution

In Fig. 8, we first investigate the 2D concentration of red blood cells and microparticles along the flow direction. At the very beginning, around $x \approx 0$, we again observe a homogeneous red blood cell distribution (Fig. 8 *a*) around the center and the cell-free layer with vanishing red blood cell concentration near the wall. Approaching the bifurcation, the cell-free layer decreases. The decrease in cell-free layer is of the same amount at both locations near the upper boundary and near the lower boundary. It can be straightforwardly explained by the bifurcating geometry, which causes the red blood cells to flow upwards/downwards into the daughter channels. This motion into the daughter channels starts already $\sim 10 \mu\text{m}$ before the end of the main channel and makes the cells migrate toward the outer wall.

An asymmetry in the cell-free layer occurs inside the daughter channels (Fig. 8 *b*), as also observed in recent

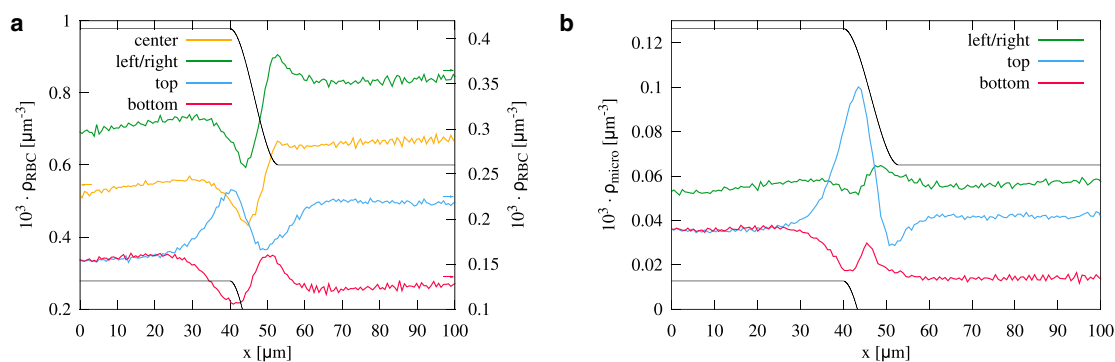


FIGURE 6 Axial concentration of (a) red blood cells and (b) microparticles distinguished regarding their position inside the cross section of the branches, as illustrated in Fig. 2. The microparticles entering at the top of the upper branch (or equivalently, the bottom of the lower branch) exhibit a pronounced peak. To see this figure in color, go online.

work (57,67). The asymmetry is especially pronounced at the beginning of the branches, stemming from cells flowing in the center of the main channel, which enter either the upper or lower branch near the inner wall. We observe a strongly decreased cell-free layer near the inner boundary right at the beginning of the daughter branches. The thickness of the cell-free layer near the outer boundary increases correspondingly. After $\sim 10 \mu\text{m}$, the inner and outer cell-free layers both reach a constant value, which is similar to the length scale for the re-establishment of the outer cell-free layer after the confluence. Interestingly, the inner and outer cell-free layers do remain asymmetric and retain this asymmetry until the very end of our channel, $\sim 50 \mu\text{m}$ behind the bifurcation.

Although the cell-free layer decreases at the end of the main channel, hardly an effect is observed on microparticle behavior. Entering the branches, the microparticle concentration peak only becomes more blurred because of the microparticles located near the upper boundary entering the larger cell-free layer inside the branch.

The asymmetries in cell and particle distribution can be seen in more detail in the 2D cross-sectional profiles in Fig. 9. At the end of the main channel in Fig. 9 a, the red blood cell distribution is still circular, with only small devi-

ations corresponding to the decrease in cell-free layer seen in Fig. 8 a. At the beginning of the branch, the circular red blood cell concentration is strongly shifted toward the inner boundary in Fig. 9 b, and a less pronounced but still clearly visible asymmetry is still present at the end of the branch in Fig. 9 c. Furthermore, a local spot with increased red blood cell concentration is observed near the inner boundary.

Whereas the microparticles are hardly affected at the end of the main channel (Fig. 9 d), a notable effect is the vanishing concentration of microparticles near the inner boundary of the branches in Fig. 9, e and f. Over an angle range of $\sim 90^\circ$ at the bottom of Fig. 9, e and f, the microparticle concentration vanishes completely. The vanishing microparticle concentration can be understood by the radial distribution in the main channel because of margination: to reach positions near the lower boundary of the branch, the microparticles would have to be located near the center of the main channel, which is not the case because of margination. Thus, we report a region within the branches that possesses a vanishing microparticle concentration in comparison to a simple straight channel.

Axial concentration

As for the confluence, we now investigate the behavior of cells and particles along the varying geometry by 1D axial concentration profiles in Fig. 10. After a constant plateau inside the main channel, both red blood cell and microparticles show a clear peak ahead of the apex of the bifurcation. Inside the branches, the red blood cell take the same concentration as in the main channel, whereas the microparticle concentration decreases. The latter can be explained by the intrinsic velocity profile; flowing beside the boundary, the stiff microparticles cover a certain ring of tube diameter along the boundary. Because of the fixed particle size, this ring has the same diameter in the main channel and within the branches. Assuming a Poiseuille flow and averaging over such a ring around the boundary leads to a higher

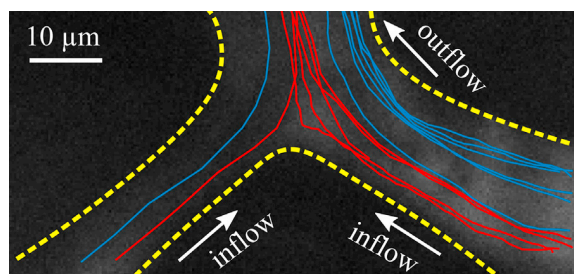


FIGURE 7 In vivo measurement of tracked fluorescent beads in mouse microvessels. Blue lines show trajectories of beads that remain margined after the bifurcation, whereas red lines show beads undergoing antimargination. Yellow dashed lines denote the vessel boundaries. To see this figure in color, go online.

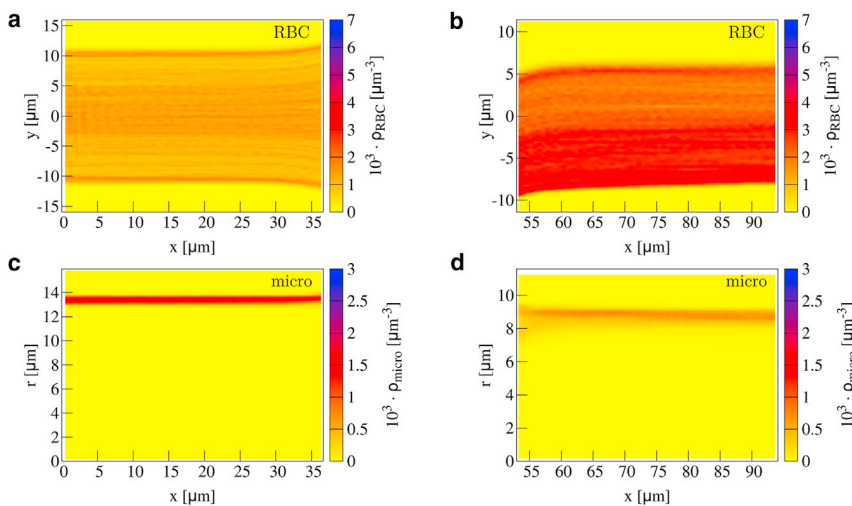


FIGURE 8 2D planar projection within the bifurcation for red blood cells (*a*) along the main channel and (*b*) along the upper branch. 2D radial projection shows microparticle concentration (*c*) along the main channel and (*d*) along the branches. The cell-free layer decreases at the end of the main channel, and we observe an asymmetric cell distribution inside the branches. The margination peak of microparticles is somewhat blurred after the bifurcation but is otherwise unaffected. To see this figure in color, go online.

flow rate inside the branches because they cover a larger part of the steep velocity profile. Thus, within the branch, the microparticles experience a larger velocity, leading to lower residence time, thereby causing a decreasing concentration.

We furthermore distinguish the cells and particles regarding their position inside the main channel and calculate the axial concentration profiles for each cell/particle fraction in Fig. 11, *a* and *b*. All fractions of red blood cells behave in a similar manner with a small peak at the apex. This peak stems from cells being trapped at the apex of the bifurcation; arriving in the center of the main channel, red blood cells have to break symmetry and decide for one branch. As visible in Fig. 1 *a* (right), some cells flow

directly onto the apex and are trapped there before flowing in one of both branches, a phenomenon called “lingering” in (69). We note that also the red blood cells at the top/bottom show a peak because they are still located close enough to the center to be influenced by more central cells getting trapped at the apex.

In full analogy, a similar peak is observed for microparticles located left/right in Fig. 1 *b*. Also, these microparticles flow onto the apex and become trapped for a short period of time. In contrast, the microparticles located top/bottom are diluted at the bifurcation. After a subsequent little dip in concentration, microparticles from both regions quickly reach a constant concentration inside the branches.

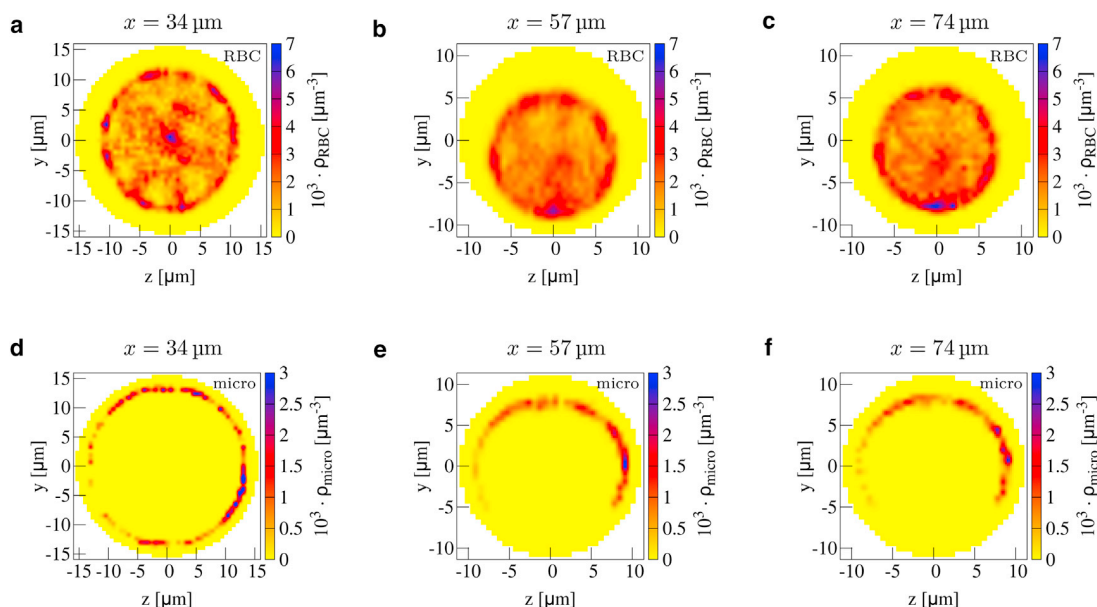


FIGURE 9 2D cross-sectional concentration of red blood cells (*a–c*) and microparticles (*d–f*) at the end of the main channel (*a* and *d*), at the beginning of the branches (*b* and *e*), and at the end of the branches (*c* and *f*). See Fig. 1 *a* for indications of the respective positions along the channel. Inside the branches, an asymmetric cell-free layer develops, and microparticles suffer a loss of concentration directly beside the inner wall. To see this figure in color, go online.

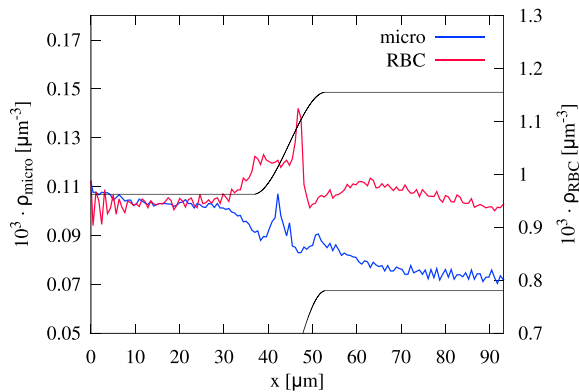


FIGURE 10 Axial concentration of red blood cells and microparticles flowing through a bifurcating channel. Both red blood cells and microparticles exhibit a peak in front of the bifurcation apex. The microparticle concentration increases directly in front of the apex, whereas the red blood cell concentration exhibits a second small peak because of a second cell flowing onto a cell already being stuck at the apex. To see this figure in color, go online.

The concentration profile of both cells and particles can be understood again by considering tracer particles (see [Supporting Materials and Methods](#)).

Influence of hematocrit

In the following section, we present simulations that have the same geometrical properties as the channels in [Fig. 1](#) but with a hematocrit of $Ht = 20\%$ for the inflow.

[Fig. 12](#) shows that behind the confluence of two branches, the red blood cell distribution behaves qualitatively similarly to the lower hematocrit. Although the cell-free layer near the vessel wall is reduced compared to [Fig. 3 b](#), the cell-free layer in the center of the main channel in [Fig. 12 a](#) is of about the same size. Only at the left and right of the cross section, the cell-free space clearly reduces compared to the lower hematocrit ([Fig. 12 b](#)). The central cell-free layer is very pronounced up to $40 \mu\text{m}$ behind the confluence but becomes blurred slightly faster toward the

end of the channel when compared to the low hematocrit case. This faster decay can be explained by the larger shear-induced diffusion coefficient of $D_{RBC} = 38 \mu\text{m}^2/\text{s}$. This agrees with the theoretical expectation that the shear-induced diffusion coefficient depends on the number of cell-cell collisions and thus on the cell concentration ([101,103](#)). The microparticles are still located in the cell-free layer in the center all along the main channel, as can be seen in [Fig. 12, c and d](#). We can again calculate the fraction of antimarginated microparticles and obtain the fractions 0.145 at $x = 55 \mu\text{m}$ and 0.137 at $x = 158 \mu\text{m}$. Also, when we compare the axial concentration of labeled red blood cells and microparticles in [Fig. 13, a and b](#)) to the case of lower hematocrit in [Fig. 6](#), we see similar behavior in both cases.

When we investigate the influence of larger hematocrit on the system with bifurcation, we find that each cell-free layer in the system decreases with increasing hematocrit (results shown in [Supporting Materials and Methods](#)). At the end of the main channel, the cell-free layer still decreases, and the pronounced asymmetry of cell-free layers within the branches is present. The increase in concentration due to the apex of the bifurcation remains unaffected by larger hematocrit, as seen in [Fig. 13, c and d](#). Because a certain number of cells or microparticles stacks at the apex of the bifurcation, the effect is not modified when more cells are added to the system. Especially, the absolute number of cells in the center region stays approximately the same for larger hematocrit.

Asymmetric bifurcations

We finally touch briefly on the subject of asymmetric bifurcations. For this, we keep the main channel radius $R_{ch} = 16 \mu\text{m}$ and the upper branch $R_{br} = 11.5 \mu\text{m}$, as in [Fig. 1 \(right\)](#), and only vary the diameter of the lower branch. Two different simulations are done with radius $R^{low} = 8$ and $5.5 \mu\text{m}$. Here, we focus on the total

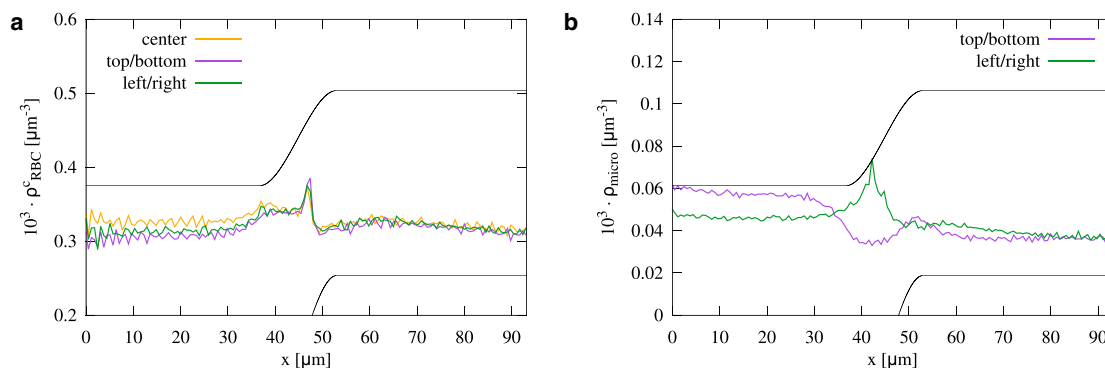


FIGURE 11 Axial concentration of (a) red blood cells and (b) microparticles distinguished regarding their initial position inside the cross section of the main channel. The peak in red blood cell concentration stems from the cells trapped at the apex of the bifurcation. The microparticles exhibit a similar peak when arriving left/right. However, for microparticles entering top/bottom, no peak occurs. To see this figure in color, go online.

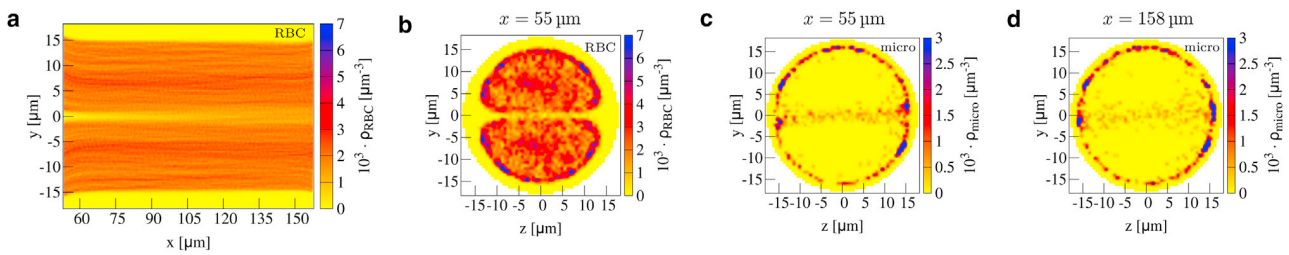


FIGURE 12 (a) 2D planar projection within the confluence for red blood cells along the main channel behind a confluence as in Fig. 3, but with larger hematocrit $Ht = 20\%$. (b–d) 2D cross-sectional profiles for (b) red blood cells and (c and d) microparticles in the main channel as in Fig. 4, but for larger hematocrit $Ht = 20\%$. To see this figure in color, go online.

concentration of red blood cells and microparticles within the two branches, as listed in Table 1.

The red blood cell concentration clearly differs between the upper and lower branch. The upper branch, being the one with the larger flow rate, receives clearly more cells than the lower branch. This effect is enhanced when the diameter and correspondingly the flow rate further decrease, as in the case of $R^{low} = 5.5 \mu\text{m}$. The fraction of concentration between lower and upper branch ρ^{low}/ρ^{up} changes from 0.77 to 0.67 when R^{low} is changed from 8 to $5.5 \mu\text{m}$. We note that the total flow rate at the outflow of the system is the same in both simulations to match the flow rate at the entrance. As a consequence, the flow rate in the upper branch slightly differs in both simulations (the fractions of flow rates are 0.5 and 0.26, respectively). The asymmetric

distribution of red blood cells qualitatively matches the Zweifach-Fung effect observed earlier (61,70,74,102) and can be attributed to the cell-free layer (102) combined with red blood cell deformability.

In contrast to the asymmetric red blood cell distribution, the microparticles are nearly evenly distributed to the daughter channels. Furthermore, the distribution is not affected by decreasing the diameter of the lower branch, the fraction in both cases being ~ 1.11 . Because the stiff microparticles are located within the cell-free layer, the different flow rate does not affect their distribution. Although the lower branch is significantly smaller, the apex of the bifurcation and thus the separation line between the two branches are located near the center of the main channel by construction of the geometry. Thus,

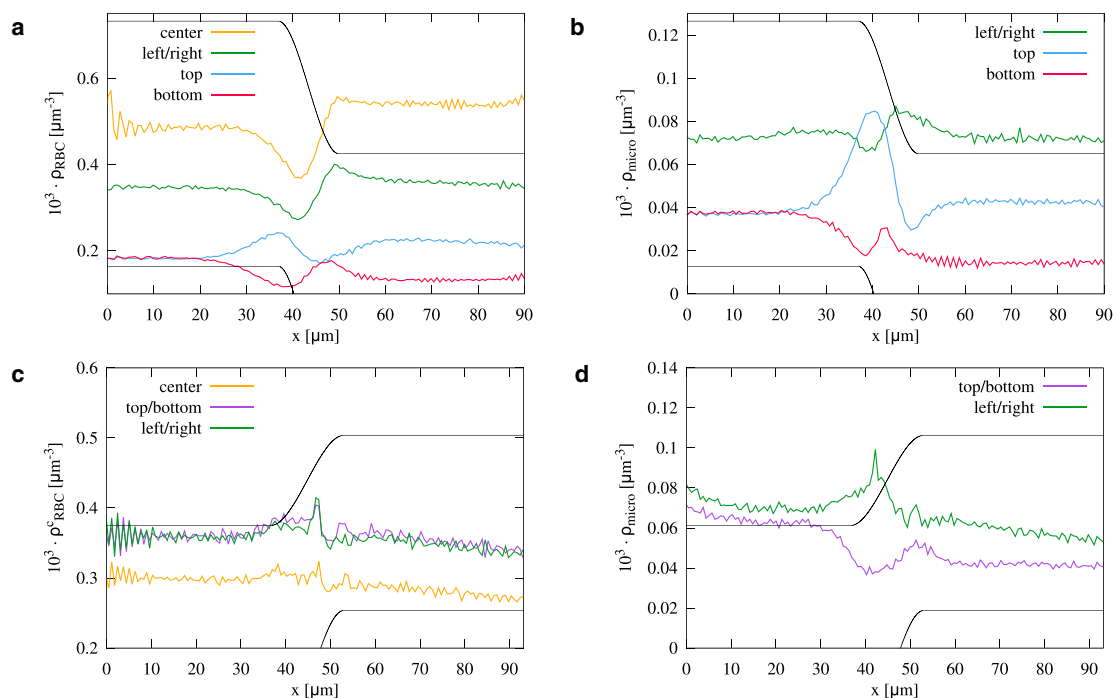


FIGURE 13 1D axial concentration of (a and c) red blood cells and (b and d) microparticles flowing through a (a and b) confluence or (c and d) bifurcation with larger hematocrit $Ht = 20\%$ labeled by their radial position at the entrance. The larger hematocrit hardly affects the behavior of red blood cells and microparticles. To see this figure in color, go online.

TABLE 1 Concentration of Red Blood Cells and Microparticles in the Upper and Lower Channel of an Asymmetric Bifurcation with Radius $11\ \mu\text{m}$ of the Upper Branch and R^{low} of the Lower Branch

R^{low}	$\rho_{\text{RBC}}^{\text{up}}$	$\rho_{\text{RBC}}^{\text{low}}$	$\rho_{\text{micro}}^{\text{up}}$	$\rho_{\text{micro}}^{\text{low}}$
$8\ \mu\text{m}$	1.027	0.794	0.0711	0.0792
$5.5\ \mu\text{m}$	1.005	0.674	0.0722	0.0806

Concentrations are given in $10^3\ \mu\text{m}^{-3}$.

arriving near the wall, only the microparticles located around the equator are drawn into the upper branch by the flow, whereas all other microparticles may be distributed equally into the branches. All in all, the microparticles exhibit a very similar concentration in both branches.

CONCLUSIONS

We used 3D IBM-LBM simulations with inflow/outflow boundary conditions to investigate a mixed suspension of red blood cells and stiff particles flowing through a vessel confluence as well as a vessel bifurcation. The stiff particles can be regarded as models for synthetic drug delivery agents or naturally occurring stiff cells such as platelets. In agreement with earlier studies, we observe and quantify the formation of a pronounced central cell-free layer behind the confluence of two vessels. We find that the central cell-free layer is very stable, being still observable even $100\ \mu\text{m}$ after the confluence. As a consequence, we show that stiff particles at the confluence are strongly redistributed. Although all stiff particles arrive on a margined position inside the well-known near-wall cell-free layer, while transversing the confluence, a significant fraction of them undergo antimargination, ending up trapped in the central cell-free layer near the channel center. This position is retained even longer than the $100\ \mu\text{m}$ lifetime of the central cell-free layer itself. Calculating the fraction of antimargined microparticles, we found that more than 13% of the particles are located around the center $100\ \mu\text{m}$ behind a confluence. Under the assumption that at the succeeding confluence, this fraction of microparticles is still antimargined, we estimate that after five confluences half of the initially completely margined particles are now evenly distributed across the cross section of the channel. In contrast, a bifurcating geometry is found to not significantly influence the margination propensity of stiff particles. For the confluence, we also conducted in vivo measurements, which proved the relevance of antimargination of stiff microparticles in living mice.

In previous in vivo studies, platelets have been observed to be mainly located near the wall in arterioles (7,104) but not in venules, where the platelet concentration was rather continuous across vessel diameters. In a similar direction, the recent work of Casa et al. (75) found that thrombi were platelet-rich on the arterial but not on the venous

side of the blood vessel network. Our findings may provide an explanation for these observations. On the arterial side, the microvascular network consists mainly of bifurcations from larger into smaller and smaller vessels, which according to our findings, do not significantly disturb the margination propensity of platelets. On the venous side, however, small channels frequently merge into larger ones. At such confluences, our results clearly demonstrated antimargination, i.e., the tendency of platelets to be forced into the center of the vessel. In a network with a cascade of confluences being only $400\text{--}1000\ \mu\text{m}$ apart (2,4) the platelet margination near the channel wall will be further and further disturbed, ending up finally in a rather continuous concentration profile and thus explaining the experimental observations of (7,75).

SUPPORTING MATERIAL

Supporting Materials and Methods, thirteen figures, and three videos are available at [http://www.biophysj.org/biophysj/supplemental/S0006-3495\(18\)30689-1](http://www.biophysj.org/biophysj/supplemental/S0006-3495(18)30689-1).

AUTHOR CONTRIBUTIONS

C.B. performed the research, analyzed the data, and wrote the article. L.S. contributed to simulation tools. S.G. designed the research and wrote the article. A.K. performed image treatment and data analysis. C.W. designed and interpreted the research. L.K. and M.W.L. designed and performed the in vivo experiments.

ACKNOWLEDGMENTS

The authors thank the Gauss Centre for Supercomputing e.V. for providing computing time on the GCS Supercomputer SuperMUC at the Leibniz Supercomputing Centre. We gratefully acknowledge the Elite Study Program Biological Physics and the *Studienstiftung des deutschen Volkes*.

This work was supported by the Volkswagen Foundation.

REFERENCES

1. Popel, A. S., and P. C. Johnson. 2005. Microcirculation and Hemorheology. *Annu. Rev. Fluid Mech.* 37:43–69.
2. Pries, A. R., and T. W. Secomb. 2008. Chapter 1 blood flow in microvascular networks. In *Microcirculation*. Elsevier, pp. 3–36.
3. Misbah, C., and C. Wagner. 2013. Living fluids. *C. R. Phys.* 14:447–450.
4. Gompper, G., and D. A. Fedosov. 2016. Modeling microcirculatory blood flow: current state and future perspectives. *Wiley Interdiscip. Rev. Syst. Biol. Med.* 8:157–168.
5. Freund, J. B. 2014. Numerical simulation of flowing blood cells. *Annu. Rev. Fluid Mech.* 46:67–95.
6. Schmid-Schönbein, G. W., S. Usami, ..., S. Chien. 1980. The interaction of leukocytes and erythrocytes in capillary and postcapillary vessels. *Microvasc. Res.* 19:45–70.
7. Woldhuis, B., G. J. Tangelder, ..., R. S. Reneman. 1992. Concentration profile of blood platelets differs in arterioles and venules. *Am. J. Physiol.* 262:H1217–H1223.

8. Eckstein, E. C., A. W. Tilles, and F. J. Millero, III. 1988. Conditions for the occurrence of large near-wall excesses of small particles during blood flow. *Microvasc. Res.* 36:31–39.
9. Jain, A., and L. L. Munn. 2009. Determinants of leukocyte margination in rectangular microchannels. *PLoS One.* 4:e7104.
10. Charoenphol, P., R. B. Huang, and O. Eniola-Adefeso. 2010. Potential role of size and hemodynamics in the efficacy of vascular-targeted spherical drug carriers. *Biomaterials.* 31:1392–1402.
11. Chen, H., J. I. Angerer, ..., A. Alexander-Katz. 2013. Hematocrit and flow rate regulate the adhesion of platelets to von Willebrand factor. *Biomicrofluidics.* 7:64113.
12. Namdee, K., A. J. Thompson, ..., O. Eniola-Adefeso. 2013. Margination propensity of vascular-targeted spheres from blood flow in a microfluidic model of human microvessels. *Langmuir.* 29:2530–2535.
13. Wang, G., W. Mao, ..., T. Sulchek. 2013. Stiffness dependent separation of cells in a microfluidic device. *PLoS One.* 8:e75901.
14. Lee, T. R., M. Choi, ..., P. Decuzzi. 2013. On the near-wall accumulation of injectable particles in the microcirculation: smaller is not better. *Sci. Rep.* 3:2079.
15. Fitzgibbon, S., A. P. Spann, ..., E. S. G. Shaqfeh. 2015. In vitro measurement of particle margination in the microchannel flow: effect of varying hematocrit. *Biophys. J.* 108:2601–2608.
16. D'Apolito, R., F. Taraballi, ..., S. Guido. 2016. Microfluidic interactions between red blood cells and drug carriers by image analysis techniques. *Med. Eng. Phys.* 38:17–23.
17. D'Apolito, R., G. Tomaiuolo, ..., S. Guido. 2015. Red blood cells affect the margination of microparticles in synthetic microcapillaries and intravital microcirculation as a function of their size and shape. *J. Control. Release.* 217:263–272.
18. Carboni, E. J., B. H. Bognet, ..., A. W. K. Ma. 2016. Direct tracking of particles and quantification of margination in blood flow. *Biophys. J.* 111:1487–1495.
19. Fay, M. E., D. R. Myers, ..., W. A. Lam. 2016. Cellular softening mediates leukocyte demargination and trafficking, thereby increasing clinical blood counts. *Proc. Natl. Acad. Sci. USA.* 113:1987–1992.
20. Migliorini, C., Y. Qian, ..., L. L. Munn. 2002. Red blood cells augment leukocyte rolling in a virtual blood vessel. *Biophys. J.* 83:1834–1841.
21. Freund, J. B. 2007. Leukocyte margination in a model microvessel. *Phys. Fluids.* 19:023301.
22. Kumar, A., and M. D. Graham. 2011. Segregation by membrane rigidity in flowing binary suspensions of elastic capsules. *Phys. Rev. E Stat. Nonlin. Soft Matter Phys.* 84:066316.
23. Zhao, H., and E. S. G. Shaqfeh. 2011. Shear-induced platelet margination in a microchannel. *Phys. Rev. E Stat. Nonlin. Soft Matter Phys.* 83:061924.
24. Tan, J., A. Thomas, and Y. Liu. 2011. Influence of red blood cells on nanoparticle targeted delivery in microcirculation. *Soft Matter.* 8:1934–1946.
25. Zhao, H., E. S. G. Shaqfeh, and V. Narsimhan. 2012. Shear-induced particle migration and margination in a cellular suspension. *Phys. Fluids.* 24:011902.
26. Kumar, A., and M. D. Graham. 2012. Mechanism of margination in confined flows of blood and other multicomponent suspensions. *Phys. Rev. Lett.* 109:108102.
27. Fedosov, D. A., J. Fornleitner, and G. Gompper. 2012. Margination of white blood cells in microcapillary flow. *Phys. Rev. Lett.* 108:028104.
28. Freund, J. B., and B. Shapiro. 2012. Transport of particles by magnetic forces and cellular blood flow in a model microvessel. *Phys. Fluids.* 24:051904–051912.
29. Reasor, D. A., Jr., M. Mehrabadi, ..., C. K. Aidun. 2013. Determination of critical parameters in platelet margination. *Ann. Biomed. Eng.* 41:238–249.
30. Kumar, A., R. G. H. Rivera, and M. D. Graham. 2014. Flow-induced segregation in confined multicomponent suspensions: effects of particle size and rigidity. *J. Fluid Mech.* 738:423–462.
31. Fedosov, D. A., and G. Gompper. 2014. White blood cell margination in microcirculation. *Soft Matter.* 10:2961–2970.
32. Müller, K., D. A. Fedosov, and G. Gompper. 2014. Margination of micro- and nano-particles in blood flow and its effect on drug delivery. *Sci. Rep.* 4:4871.
33. Vahidkhal, K., S. L. Diamond, and P. Bagchi. 2014. Platelet dynamics in three-dimensional simulation of whole blood. *Biophys. J.* 106:2529–2540.
34. Vahidkhal, K., and P. Bagchi. 2015. Microparticle shape effects on margination, near-wall dynamics and adhesion in a three-dimensional simulation of red blood cell suspension. *Soft Matter.* 11:2097–2109.
35. Henríquez Rivera, R. G., K. Sinha, and M. D. Graham. 2015. Margination regimes and drainage transition in confined multicomponent suspensions. *Phys. Rev. Lett.* 114:188101.
36. Müller, K., D. A. Fedosov, and G. Gompper. 2016. Understanding particle margination in blood flow: a step toward optimized drug delivery systems. *Med. Eng. Phys.* 38:2–10.
37. Gekle, S. 2016. Strongly accelerated margination of active particles in blood flow. *Biophys. J.* 110:514–520.
38. Krüger, T. 2016. Effect of tube diameter and capillary number on platelet margination and near-wall dynamics. *Rheol. Acta.* 55:511–526.
39. Mehrabadi, M., D. N. Ku, and C. K. Aidun. 2016. Effects of shear rate, confinement, and particle parameters on margination in blood flow. *Phys. Rev. E.* 93:023109.
40. Spann, A. P., J. E. Campbell, ..., E. S. G. Shaqfeh. 2016. The effect of hematocrit on platelet adhesion: experiments and simulations. *Biophys. J.* 111:577–588.
41. Guckenberger, A., and S. Gekle. 2018. A boundary integral method with volume-changing objects for ultrasound-triggered margination of microbubbles. *J. Fluid Mech.* 836:952–997.
42. Tokarev, A. A., A. A. Butylin, ..., F. I. Ataullakhanov. 2011. Finite platelet size could be responsible for platelet margination effect. *Biophys. J.* 101:1835–1843.
43. Crowl, L., and A. L. Fogelson. 2011. Analysis of mechanisms for platelet near-wall excess under arterial blood flow conditions. *J. Fluid Mech.* 676:348–375.
44. Henríquez Rivera, R. G., X. Zhang, and M. D. Graham. 2016. Mechanistic theory of margination and flow-induced segregation in confined multicomponent suspensions: simple shear and poiseuille flows. *Phys. Rev. Fluids.* 1:060501.
45. Qi, Q. M., and E. S. G. Shaqfeh. 2017. Theory to predict particle migration and margination in the pressure-driven channel flow of blood. *Phys. Rev. Fluids.* 2:093102.
46. Qi, Q. M., and E. S. G. Shaqfeh. 2018. Time-dependent particle migration and margination in the pressure-driven channel flow of blood. *Phys. Rev. Fluids.* 3:034302.
47. Mountrakis, L., E. Lorenz, and A. G. Hoekstra. 2013. Where do the platelets go? A simulation study of fully resolved blood flow through aneurysmal vessels. *Interface Focus.* 3:20120089.
48. Wu, W.-T., Y. Li, ..., J. F. Antaki. 2017. Numerical simulation of red blood cell-induced platelet transport in saccular aneurysms. *Appl. Sci. (Basel).* 7:484.
49. Zhao, R., J. N. Marhefka, ..., J. F. Antaki. 2008. Micro-flow visualization of red blood cell-enhanced platelet concentration at sudden expansion. *Ann. Biomed. Eng.* 36:1130–1141.
50. Faivre, M., M. Abkarian, ..., H. A. Stone. 2006. Geometrical focusing of cells in a microfluidic device: an approach to separate blood plasma. *Biorheology.* 43:147–159.
51. Fujiwara, H., T. Ishikawa, ..., T. Yamaguchi. 2009. Red blood cell motions in high-hematocrit blood flowing through a stenosed microchannel. *J. Biomech.* 42:838–843.

52. Vahidkhan, K., P. Balogh, and P. Bagchi. 2016. Flow of red blood cells in stenosed microvessels. *Sci. Rep.* 6:28194.
53. Wang, W., T. G. Diacovo, ..., M. R. King. 2013. Simulation of platelet, thrombus and erythrocyte hydrodynamic interactions in a 3D arteriole with in vivo comparison. *PLoS One.* 8:e76949.
54. Skorczewski, T., L. C. Erickson, and A. L. Fogelson. 2013. Platelet motion near a vessel wall or thrombus surface in two-dimensional whole blood simulations. *Biophys. J.* 104:1764–1772.
55. Yazdani, A., and G. E. Karniadakis. 2016. Sub-cellular modeling of platelet transport in blood flow through microchannels with constriction. *Soft Matter.* 12:4339–4351.
56. Bächer, C., L. Schrack, and S. Gekle. 2017. Clustering of microscopic particles in constricted blood flow. *Phys. Rev. Fluids.* 2:013102.
57. Li, X., A. S. Popel, and G. E. Karniadakis. 2012. Blood-plasma separation in Y-shaped bifurcating microfluidic channels: a dissipative particle dynamics simulation study. *Phys. Biol.* 9:026010.
58. Tripathi, S., Y. B. V. Kumar, ..., A. Agrawal. 2015. Passive blood plasma separation at the microscale: a review of design principles and microdevices. *J. Micromech. Microeng.* 25:083001.
59. Svanes, K., and B. Zweifach. 1968. Variations in small blood vessel hematocrits produced in hypothermic rats by micro-occlusion. *Microvasc. Res.* 1:210–220.
60. Fung, Y. C. 1973. Stochastic flow in capillary blood vessels. *Microvasc. Res.* 5:34–48.
61. Pries, A. R., K. Ley, ..., P. Gaehtgens. 1989. Red cell distribution at microvascular bifurcations. *Microvasc. Res.* 38:81–101.
62. Pries, A. R., T. W. Secomb, and P. Gaehtgens. 1996. Biophysical aspects of blood flow in the microvasculature. *Cardiovasc. Res.* 32:654–667.
63. Shen, Z., G. Coupier, ..., T. Podgorski. 2016. Inversion of hematocrit partition at microfluidic bifurcations. *Microvasc. Res.* 105:40–46.
64. Leble, V., R. Lima, ..., T. Yamaguchi. 2011. Asymmetry of red blood cell motions in a microchannel with a diverging and converging bifurcation. *Biomicrofluidics.* 5:44120–4412015.
65. Wang, T., U. Rongin, and Z. Xing. 2016. A micro-scale simulation of red blood cell passage through symmetric and asymmetric bifurcated vessels. *Sci. Rep.* 6:20262.
66. Barber, J. O., J. M. Restrepo, and T. W. Secomb. 2011. Simulated red blood cell motion in microvessel bifurcations: effects of cell-cell interactions on cell partitioning. *Cardiovasc. Eng. Technol.* 2:349–360.
67. Ng, Y. C., B. Namgung, ..., S. Kim. 2016. Symmetry recovery of cell-free layer after bifurcations of small arterioles in reduced flow conditions: effect of RBC aggregation. *Am. J. Physiol. Heart Circ. Physiol.* 311:H487–H497.
68. Namgung, B., Y. C. Ng, ..., S. Kim. 2017. Near-wall migration dynamics of erythrocytes in vivo: effects of cell deformability and arteriolar bifurcation. *Front. Physiol.* 8:963.
69. Balogh, P., and P. Bagchi. 2017. Direct numerical simulation of cellular-scale blood flow in 3D microvascular networks. *Biophys. J.* 113:2815–2826.
70. Balogh, P., and P. Bagchi. 2017. A computational approach to modeling cellular-scale blood flow in complex geometry. *J. Comput. Phys.* 334:280–307.
71. Balogh, P., and P. Bagchi. 2018. Analysis of red blood cell partitioning at bifurcations in simulated microvascular networks. *Phys. Fluids.* 30:051902–051917.
72. Yang, X., O. Forouzan, ..., S. S. Shevkoplyas. 2011. Traffic of leukocytes in microfluidic channels with rectangular and rounded cross-sections. *Lab Chip.* 11:3231–3240.
73. Sun, C., and L. L. Munn. 2008. Lattice Boltzmann simulation of blood flow in digitized vessel networks. *Comput. Math. Appl.* 55:1594–1600.
74. Lykov, K., X. Li, ..., G. E. Karniadakis. 2015. Inflow/outflow boundary conditions for particle-based blood flow simulations: application to arterial bifurcations and trees. *PLoS Comput. Biol.* 11:e1004410.
75. Casa, L. D., D. H. Deaton, and D. N. Ku. 2015. Role of high shear rate in thrombosis. *J. Vasc. Surg.* 61:1068–1080.
76. Succi, S. 2001. *The Lattice Boltzmann Equation: For Fluid Dynamics and Beyond.* Oxford university press, Oxford, UK.
77. Dünweg, B., and A. J. Ladd. 2008. Lattice Boltzmann simulations of soft matter systems. In *Advanced Computer Simulation Approaches for Soft Matter Sciences III.* Springer, pp. 89–166.
78. Aidun, C. K., and J. R. Clausen. 2010. Lattice-Boltzmann method for complex flows. *Annu. Rev. Fluid Mech.* 42:439–472.
79. Limbach, H., A. Arnold, ..., C. Holm. 2006. ESPResSo—an extensible simulation package for research on soft matter systems. *Comput. Phys. Commun.* 174:704–727.
80. Roehm, D., and A. Arnold. 2012. Lattice Boltzmann simulations on GPUs with ESPResSo. *Eur. Phys. J. Spec. Top.* 210:89–100.
81. Arnold, A., O. Lenz, ..., C. Holm. 2013. Espresso 3.1: Molecular dynamics software for coarse-grained models. In *Meshfree methods for partial differential equations VI.* Springer, pp. 1–23.
82. Peskin, C. S. 2002. The immersed boundary method. *Acta Numer.* 11:479–517.
83. Mittal, R., and G. Iaccarino. 2005. Immersed boundary methods. *Annu. Rev. Fluid Mech.* 37:239–261.
84. Barthès-Biesel, D. 2011. Modeling the motion of capsules in flow. *Curr. Opin. Colloid Interface Sci.* 16:3–12.
85. Daddi-Moussa-Ider, A., A. Guckenberger, and S. Gekle. 2016. Long-lived anomalous thermal diffusion induced by elastic cell membranes on nearby particles. *Phys. Rev. E.* 93:012612.
86. Guckenberger, A., M. P. Schraml, ..., S. Gekle. 2016. On the bending algorithms for soft objects in flows. *Comput. Phys. Commun.* 207:1–23.
87. Guckenberger, A., and S. Gekle. 2017. Theory and algorithms to compute Helfrich bending forces: a review. *J. Phys. Condens. Matter.* 29:203001.
88. Fedosov, D. A., M. Peltomäki, and G. Gompper. 2014. Deformation and dynamics of red blood cells in flow through cylindrical microchannels. *Soft Matter.* 10:4258–4267.
89. Guckenberger, A., A. Kihm, ..., S. Gekle. 2018. Numerical-experimental observation of shape bistability of red blood cells flowing in a microchannel. *Soft Matter.* 14:2032–2043.
90. Jeffery, G. B. 1922. The motion of ellipsoidal particles immersed in a viscous fluid. *Proc. R. Soc. Lond., A Contain. Pap. Math. Phys. Character.* 102:161–179.
91. Yang, S., A. Ündar, and J. D. Zahn. 2006. A microfluidic device for continuous, real time blood plasma separation. *Lab Chip.* 6:871–880.
92. Laschke, M. W., and M. D. Menger. 2016. The dorsal skinfold chamber: a versatile tool for preclinical research in tissue engineering and regenerative medicine. *Eur. Cell. Mater.* 32:202–215.
93. Laschke, M. W., B. Vollmar, and M. D. Menger. 2011. The dorsal skinfold chamber: window into the dynamic interaction of biomaterials with their surrounding host tissue. *Eur. Cell. Mater.* 22:147–164, discussion 164–167.
94. Brust, M., O. Aouane, ..., C. Wagner. 2014. The plasma protein fibrinogen stabilizes clusters of red blood cells in microcapillary flows. *Sci. Rep.* 4:4348.
95. Fedosov, D. A., B. Caswell, ..., G. E. Karniadakis. 2010. Blood flow and cell-free layer in microvessels. *Microcirculation.* 17:615–628.
96. Freund, J. B., and M. M. Orescanin. 2011. Cellular flow in a small blood vessel. *J. Fluid Mech.* 671:466–490.
97. Katanov, D., G. Gompper, and D. A. Fedosov. 2015. Microvascular blood flow resistance: role of red blood cell migration and dispersion. *Microvasc. Res.* 99:57–66.
98. Turitto, V. T., and H. R. Baumgartner. 1975. Platelet deposition on sub-endothelium exposed to flowing blood: mathematical analysis of physical parameters. *Trans. Am. Soc. Artif. Intern. Organs.* 21:593–601.

Antimargination in Branching Vessels

99. Goldsmith, H., and J. Marlow. 1979. Flow behavior of erythrocytes. II. Particle motions in concentrated suspensions of ghost cells. *J. Colloid Interface Sci.* 71:383–407.
100. Kumar, A., and M. D. Graham. 2012. Margination and segregation in confined flows of blood and other multicomponent suspensions. *Soft Matter*. 8:10536–10548.
101. Grandchamp, X., G. Coupier, ..., T. Podgorski. 2013. Lift and down-gradient shear-induced diffusion in red blood cell suspensions. *Phys. Rev. Lett.* 110:108101.
102. Secomb, T. W. 1995. Mechanics of blood flow in the microcirculation. *Symp. Soc. Exp. Biol.* 49:305–321.
103. Da Cunha, F. R., and E. J. Hinch. 1996. Shear-induced dispersion in a dilute suspension of rough spheres. *J. Fluid Mech.* 309:211–223.
104. Tangelder, G. J., H. C. Teirlinck, ..., R. S. Reneman. 1985. Distribution of blood platelets flowing in arterioles. *Am. J. Physiol.* 248:H318–H323.

Supplemental Information - Anti-margination of microparticles and platelets in the vicinity of branching vessels

Christian Bächer¹, A. Kihm², L. Schrack^{1,3}, L. Kaestner⁴, M.W. Laschke⁵, C. Wagner², and S. Gekle¹

¹Biofluid Simulation and Modeling, Theoretische Physik, Universität Bayreuth, Bayreuth, Germany

²Experimental Physics, Saarland University, Saarbrücken, Germany

³Institute for Theoretical Physics, University of Innsbruck, Innsbruck, Austria

⁴Institute for Molecular Cell Biology, Research Centre for Molecular Imaging and Screening, Center for Molecular Signaling (PZMS), Medical Faculty, Saarland University, Homburg/Saar, Germany

⁵Institute for Clinical & Experimental Surgery, Saarland University, Homburg/Saar, Germany

Inflow: full margination and constant particle number

In figure S1 we show the state of complete margination at the entrance of a bifurcating channel and a confluence, respectively. The cross-sectional concentrations show the red blood cells accumulated around the channel center and the microparticles close to the wall.

Figure S2 shows that after a short transient time the implemented particle inflow/outflow leads to a constant number of red blood cells and microparticles in the system.

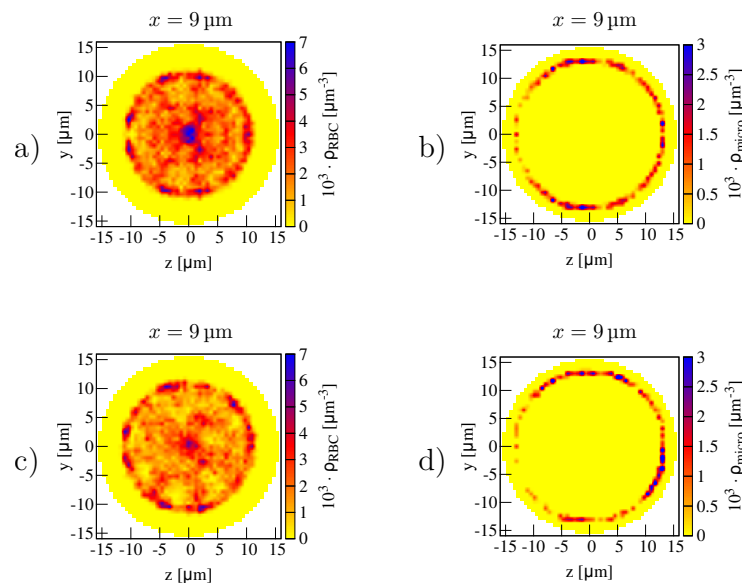


Figure S1: At the entrance of the confluence system a),b) and the bifurcation system c),d) we have a state of full margination: the red blood cells a),c) are located in the channel center, the microparticles b),d) near the wall.

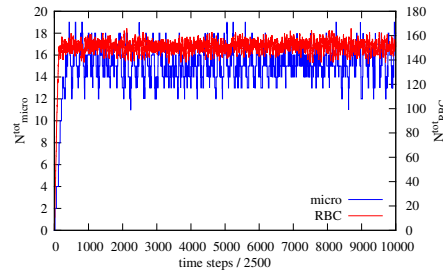


Figure S2: Total number of RBCs and microparticles within the confluence system depending on the simulation time. Both numbers fluctuate around a constant value after initial filling of the system.

Concentration profiles of tracer particles

In order to model the behavior of red blood cells and microparticles we use passive point particles as tracers flowing with the intrinsic velocity profile (1). We first start with the confluence. Homogeneously distributed particles exhibit a similar concentration profile as the red blood cells. As a consequence, red blood cell behavior can be explained by the intrinsic velocity profile. Doing the same calculations for tracers in the different regions resemble the labeled red blood cells. It also fits the concentration profiles for the microparticles.

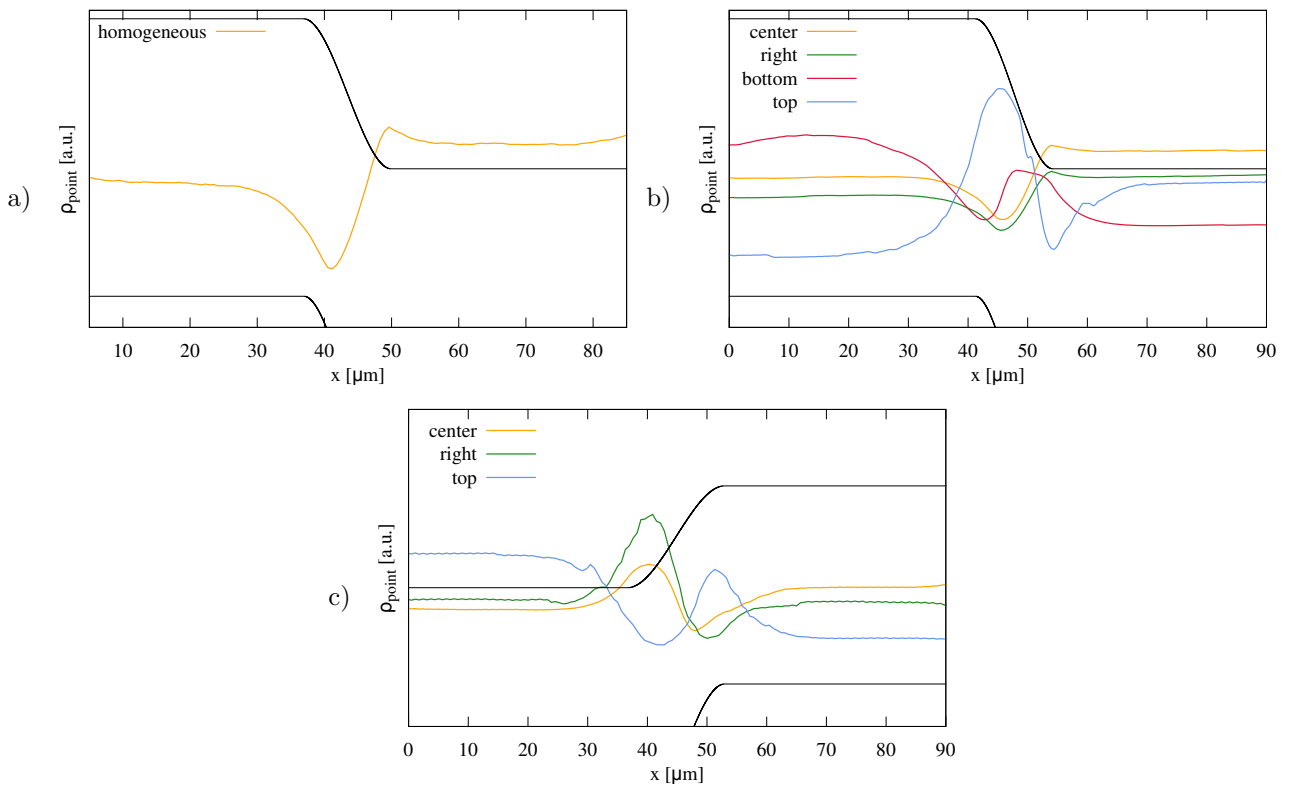


Figure S3: Concentration of a) homogeneously distributed tracer particles and b) tracer particles flowing in the distinct regions at system entrance within the confluence. c) Tracer particles flowing in the distinct regions at system entrance within the diverging bifurcation. These figures are compared to cell and particle concentration in figure 6, 11 and 13 in the main text.

In the diverging bifurcation starting at top the concentration profile of the point particles matches that of the microparticles quite well. Also the point particles located right reproduce microparticle behavior. We note that starting point particles top or bottom and left or right results in the same concentration due to symmetry. Red

blood cell behavior is also similar to that of point particles, except the peak at the bifurcation apex. The differences are effects due to the finite size and deformability of red blood cells.

Shear-induced diffusion

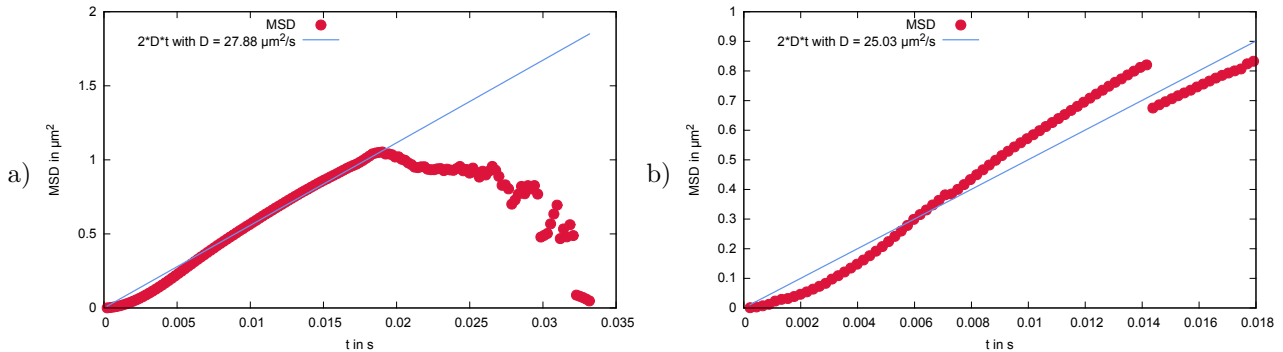


Figure S4: Mean square displacement over time for a) red blood cells and b) microparticles located near the center behind a confluence. By modeling the theoretical expectation we can extract a shear-induced diffusion coefficient.

Larger hematocrit

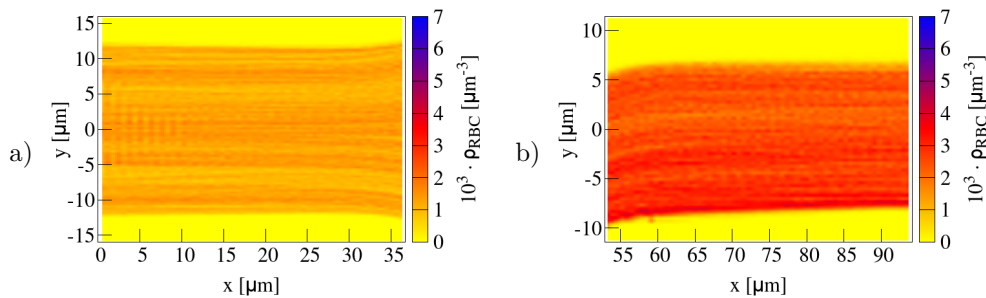


Figure S5: 2D planar projection for red blood cells along the a) main channel and b) branches of the bifurcation with larger hematocrit $Ht = 20\%$. The cell-free layer decreases, but the behavior is qualitatively unchanged.

Anti-margination of platelet-shaped microparticles

In the main text we focus on spherical microparticles. Here, we show additional results for oblate spheroids – a geometry that mimicks more closely that of real platelets. The platelets have a diameter of $3.9 \mu\text{m}$ along the two long axes and $2.3 \mu\text{m}$ along the small axis and are illustrated in figure S6. Similar to the spherical particles of the main text, about 14% of the spheroidal microparticles are anti-marginated directly behind the confluence.

Narrow confluence

In figure S7 we investigate the influence of the main vessel diameter. We perform simulations with radius $22.8 \mu\text{m}$ and $14.3 \mu\text{m}$ of the main vessel, but with the same branch properties as in figure 1 a) of the main text. In figure S7 a) the red blood cell concentration shows a more stable central cell-free layer for a wider vessel. In case of a narrow vessel the central cell-free layer vanishes more quickly (figure S7 b). Correspondingly, the microparticles stay close

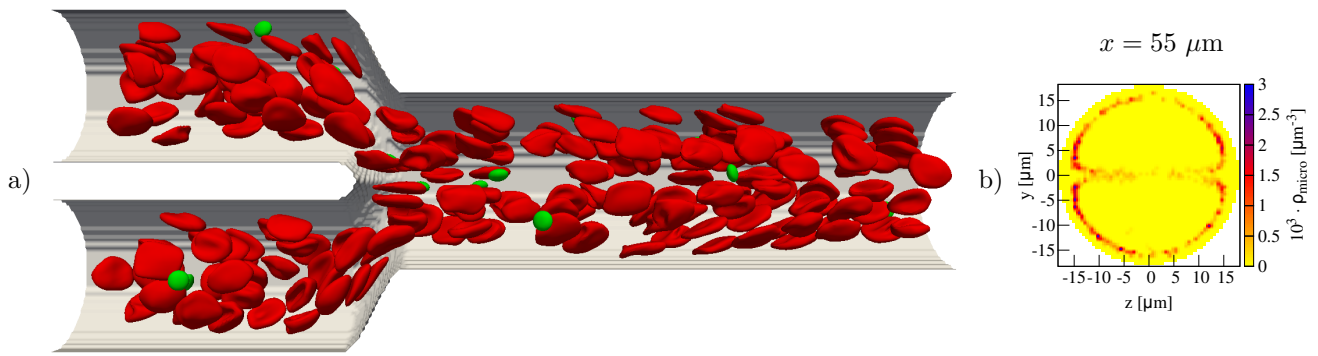


Figure S6: (a) Simulation of microparticles with a platelet-like oblate shape flowing through a confluence. (b) Similar to the spherical microparticles of the main text, these particles also undergo anti-margination.

to the center in the wider vessel (figure S7 c) and marginate faster within the narrow main vessel (figure S7 d). Both observations can be explained by the shear-induced diffusion coefficient depending on the local cell concentration, which increases with narrowing main vessel for the same inflow. Indeed, the red blood cell shear-induced diffusion coefficient decreases in figure S7 a) to $15.5 \mu\text{m}^2/\text{s}$ and increases in figure S7 b) to $45.4 \mu\text{m}^2/\text{s}$.

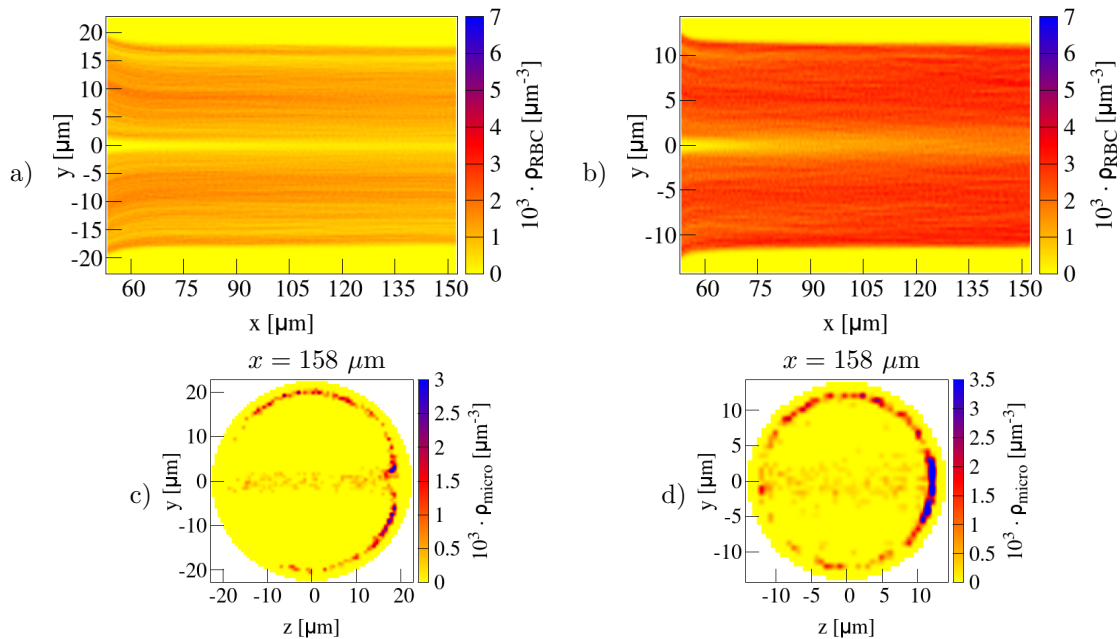


Figure S7: a),b) Red blood cell distribution and c),d) cross-sectional microparticle concentration $100 \mu\text{m}$ behind a confluence with main vessel radius of a),c) $22.8 \mu\text{m}$ and b),d) $14.3 \mu\text{m}$. While a wider vessel leads to a more stable central cell-free layer a narrower vessel causes the cell-free layer to smear out faster. Correspondingly, in case of a narrower main channel margination of microparticles takes place faster.

Validation of the used IBM-LBM algorithm

In the following, we summarize and extend the validation for our Immersed Boundary method (IBM) and Lattice-Boltzmann method (LBM). In ref. (2) the calculation of shear and bending forces has been validated for a capsule in shear flow. In ref. (3) the hematocrit profile for tube flow and plane-Poiseuille flow has been shown to agree with previous, established studies. Furthermore, the stability of the stiff spherical particles used has been demonstrated and the flow profile past a sphere has been compared favorably to the analytical solution.

In addition, we here calculate the Stokes drag $1/(6\pi\eta a)$ that relates the force on a sphere of radius a to its velocity in a suspending fluid of viscosity η for a sphere with two different particle resolutions in figure S8. We performed simulations with the resolution used in the main text (81 nodes of the inner stiff grid) and an increased resolution (485 nodes of the inner grid). We note that for the former the number of fluid nodes per particle does not change compared to the main text. Both resolutions show good agreement with the theoretical prediction and convergence to the theory for increasing grid resolution.

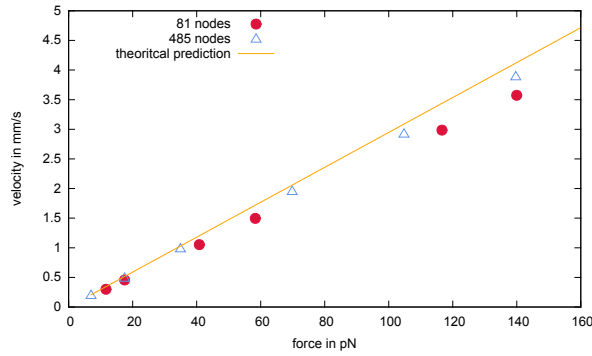


Figure S8: Velocity of a spherical particle pulled through a fluid with a given force. Simulations with two different particle resolutions are compared to the theoretical prediction given by the Stokes drag. The resolution given in the legend denotes the node number of the stiff inner grid.

In order to provide another quantitative validation of stiff particle behavior we simulate a spheroid with aspect ratio $\epsilon = 3$ subjected to shear flow, as sketched in figure S9 a). Ref. (4) provides an analytical solution for the spheroid inclination angle θ over time t

$$\theta(t) = \tan^{-1} \left(\epsilon \tan \left(\frac{t\dot{\gamma}}{\epsilon + \frac{1}{\epsilon}} \right) \right), \quad (\text{S1})$$

with $\dot{\gamma}$ being the shear rate. In figure S9 b) we compare our numerical results (2562 nodes and 5120 triangles for the outer membrane of the spheroid) to the theoretical prediction and find very good agreement.

In order to validate the red blood cell behavior, we present a detailed investigation of a single red blood cell flowing through a cylindrical channel. In figure S10 we show the red blood cell shape obtained for a confinement - effective red blood cell diameter divided by the channel diameter - of 0.55, which can directly be compared to literature data in figure 1 of Fedosov et al. (5). From left to right we increased the dimensionless shear $\dot{\gamma}^* = \bar{\gamma}\tau$ with the averaged shear rate $\bar{\gamma}$ defined by the averaged velocity over the channel diameter and τ the relaxation time of a red blood cell. Since in this setup the focus is on the single cell behavior we performed our simulations with a membrane mesh resolution of 5120 triangles. With increasing velocity we first observe a tumbling discocyte, a tank-treading slipper, and eventually a croissant. The shapes are in very good agreement with the shapes shown in figure 1 of ref. (5).

Furthermore, we compare the single cell behavior for different resolutions of the red blood cell mesh with simulations using the Boundary Integral method (BIM) in a rectangular channel of cross-section $10 \mu\text{m} \times 12 \mu\text{m}$ in figure S11. The BIM simulations are part of an extensive study on single cell behavior in rectangular channels which demonstrated quantitative agreement with detailed experiments (6). The presently used LBM-IBM method leads to the same shapes as the more sophisticated BIM simulations.

We further validate our method considering the red blood cell behavior in a setup strongly related to those of the main text: we investigate the Zweifach-Fung effect and compare the results with literature data for a bifurcation

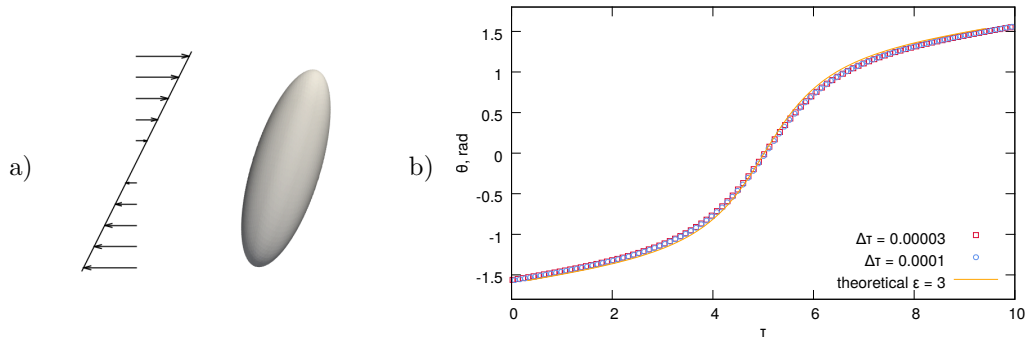


Figure S9: a) A rigid spheroid subjected to a shear flow. b) The orientation angle of the spheroid $\theta(\tau)$ over time $\tau = \dot{\gamma}t$ for simulations with different time steps compared to the analytical solution of ref. (4).

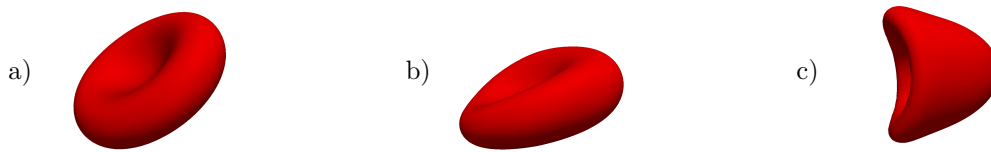


Figure S10: Red blood cell shapes in a cylinder for different flow rates obtained with LBM-IBM simulations. The confinement is 0.55. We observe a) a tumbling discocyte for a shear rate $\dot{\gamma}^* = 5$, b) a slipper for $\dot{\gamma}^* = 22.5$ and c) a croissant for $\dot{\gamma}^* = 60$. These shapes are in very good agreement with the shapes shown in figure 1 of ref. (5) for a confinement of 0.58 and $\dot{\gamma}^* = 5$, $\dot{\gamma}^* = 24.8$, and $\dot{\gamma}^* = 59.6$, respectively, that are obtained using Dissipative Particle Dynamics (5).

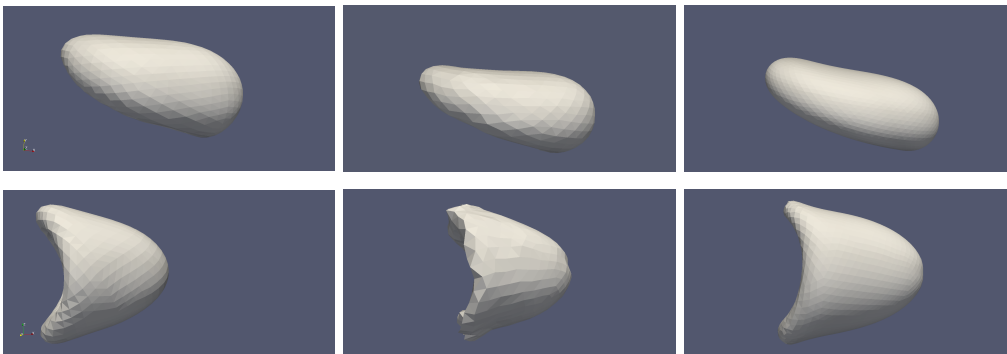


Figure S11: Single red blood cell in a rectangular channel with cross-section $10 \mu\text{m} \times 12 \mu\text{m}$ simulated with the Boundary Integral method from (6), LBM-IBM with 1280 triangles and LBM-IBM 5120 triangles (from left to right). For a centroid velocity of 0.5 mm/s (top) a tank-treading slipper shape is observed and for 1.5 mm/s (bottom) a croissant shape.

of a vessel into two daughter vessels followed by a confluence, as sketched in figure S12 a). In contrast to the main text, here we use periodic boundary conditions. We construct our setup in a way that the cross-sections of the cylindrical branches match with the setup consisting of rectangular vessels of ref. (7), namely the main branch with radius $6.84 \mu\text{m}$, the bottom branch with $5.86 \mu\text{m}$, and the top branch varied in the range of $3.26 \mu\text{m}$ to $5.35 \mu\text{m}$. We simulate a suspension of 50 red blood cells with a membrane mesh consisting of 642 nodes and 1280 triangles being the same as in the main text. The fluid grid is chosen such that the number of fluid nodes per cell is also the same as in the main text. With varying flow rate ratio between the bottom branch and the main branch (achieved by varying the diameter of the top branch) a disproportional partitioning of the red blood cells takes place, known as the Zweifach-Fung effect (7–9). In order to quantify this behavior in simulations we calculate the fraction of

the flow rate in the bottom branch Q_{bot} and in the main branch Q_m without any cells present. This is done by integrating the axial velocity v_x over the cross-section C of the branch

$$Q_m = \int_C v_x^m dA, \quad Q_{\text{bot}} = \int_C v_x^{\text{bot}} dA. \quad (\text{S2})$$

As a measure for the red blood cell flux we calculate the number of red blood cells per time $\dot{N}(t)$ passing through the mid-plane of main branch and bottom branch, respectively, and average over all T time steps

$$n = \langle \dot{N}(t) \rangle_t = \frac{\sum_{i=1}^T \dot{N}(t_i) \Delta t}{\sum_{i=1}^T \Delta t}. \quad (\text{S3})$$

We compare the fraction of red blood cell flux in bottom and main branch n_{bot}/n_m to data from the literature in figure S12 b). As done in ref. (7) we compare our results with experimental values from Pries et al. (8) and Yang et al. (10) as well as with the numerical values from Balogh and Bagchi (7). Overall, we find very good agreement and our simulations show the expected half-sigmoidal variation collapsing with literature data over a wide range of flow rate fractions. We note that varying the overall velocity does not affect the results in figure S12.

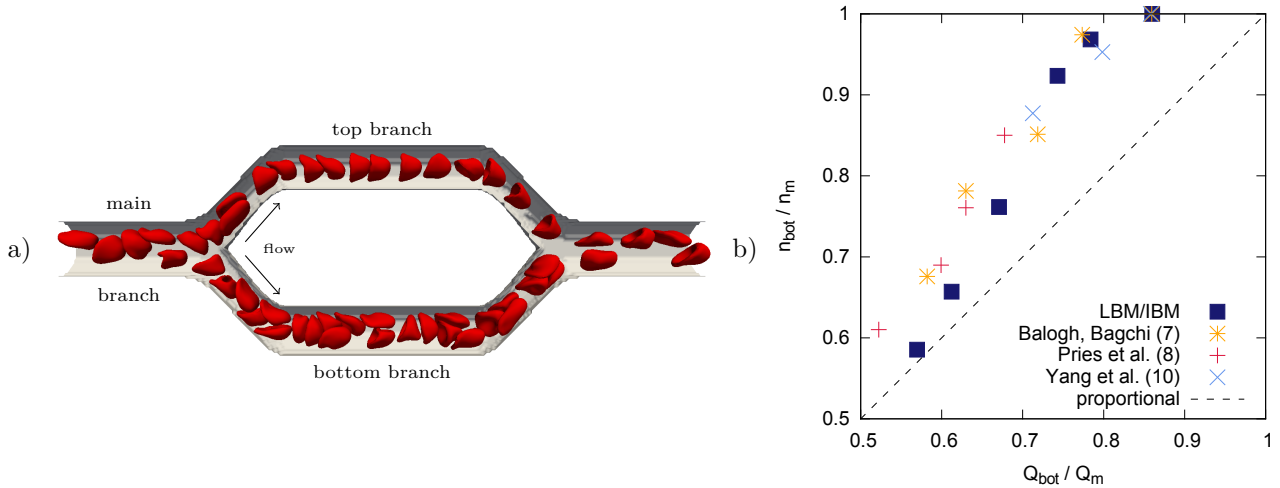


Figure S12: Red blood cells flowing through a bifurcation followed by a confluence. a) Simulation snapshot of one setup: main branch with radius $6.84 \mu\text{m}$, bottom branch with radius $5.86 \mu\text{m}$, and top branch with radius $5.35 \mu\text{m}$. b) Fraction of cells flowing through the bottom branch n_{bot} and the main branch n_m depending on the fraction of flow rate in bottom Q_{bot} and main branch Q_m . Despite some deviations at low flow rate fraction our simulations lead to the expected half-sigmoidal dependency and match literature data at large fractions.

Next, in order to prove mesh insensitivity we reduced the resolution of the membrane mesh of the red blood cells to 258 nodes and 512 triangles and the resolution of the stiff particles to 66 nodes and 128 triangles. In the same way the fluid mesh changes from $288 \times 110 \times 58$ to $200 \times 82 \times 42$. The red blood cell distribution behind a confluence and the cross-sectional microparticle concentration are compared to the results of the manuscript in figure S13 a), b) and d), e), respectively. The results are in very good agreement. Small discrepancies may be caused by slightly different inflow concentrations.

Finally, in figure S13 c), f) we provide evidence that the repulsion force among the cells and particles does not affect our results. For this, we show the red blood cell distribution behind a confluence (corresponding to figure S13 b) and the cross-sectional microparticle concentration (corresponding to figure S13 e) for a simulation without repulsion force. We observe very similar behavior and are thus able to conclude that our main results are robust with respect to the repulsion force.

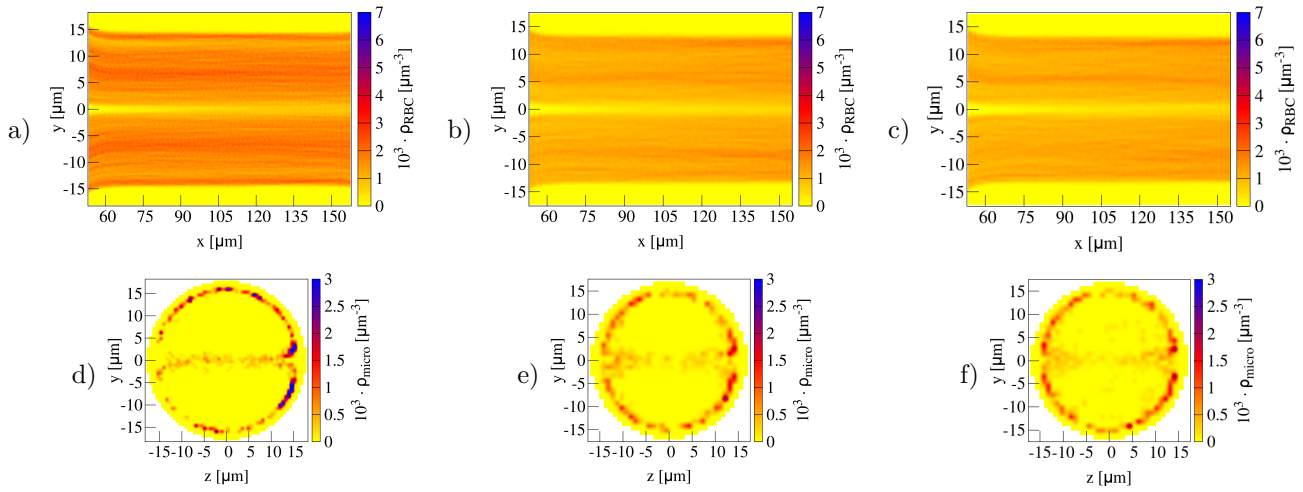


Figure S13: The main results for different mesh resolutions: The cell free-layer in a), b), c) and the microparticle anti-margination in d), e), f). a),d) resolution used in the main text (RBC: 1280, microparticle: 320, fluid: 288x110x58) and b), c), e), f) decreased resolution (RBC: 512, microparticle: 128, fluid: 200x82x42). Both resolutions lead to similar results for central cell free layer stability (in a) and b)) and fraction of anti-marginated microparticles (d) 15.8% and e) 16.2%). In figure c) and f) we provide evidence that without any repulsive force between cells, particles, and the vessel wall our main results do not change (16.7% antimarginated microparticles in f). Figures a) and d) are from the main text.

Taken together, our LBM-IBM method gives accurate results for stiff particles and red blood cells in simple tube flow, but also within a more complex system such as a bifurcation followed by a confluence. We provided evidence that neither the resolution of cell membrane mesh nor the fluid mesh nor the introduced repulsive force for additional stability affect our main results and conclusions.

References

- [1] Bächer, C., L. Schrack, and S. Gekle, 2017. Clustering of Microscopic Particles in Constricted Blood Flow. Physical Review Fluids 2:013102.
- [2] Guckenberger, A., M. P. Schraml, P. G. Chen, M. Leonetti, and S. Gekle, 2016. On the bending algorithms for soft objects in flows. Computer Physics Communications 207:1–23.
- [3] Gekle, S., 2016. Strongly Accelerated Margination of Active Particles in Blood Flow. Biophysical Journal 110:514 – 520.
- [4] Jeffery, G. B., 1922. The motion of ellipsoidal particles immersed in a viscous fluid. Proc. R. Soc. Lond. A 102:161–179.
- [5] Fedosov, D. A., M. Peltomäki, and G. Gompper, 2014. Deformation and dynamics of red blood cells in flow through cylindrical microchannels. Soft matter 10:4258–4267.
- [6] Guckenberger, A., A. Kihm, T. John, C. Wagner, and S. Gekle, 2018. Numerical-experimental observation of shape bistability of red blood cells flowing in a microchannel. Soft Matter 14:2032–2043.
- [7] Balogh, P., and P. Bagchi, 2017. A Computational Approach to Modeling Cellular-Scale Blood Flow in Complex Geometry. Journal of Computational Physics 334:280–307.
- [8] Pries, A., K. Ley, M. Claassen, and P. Gaetgens, 1989. Red cell distribution at microvascular bifurcations. Microvascular research 38:81–101.
- [9] Secomb, T. W., 2017. Blood Flow in the Microcirculation. Annual Review of Fluid Mechanics 49:443–461.
- [10] Yang, S., A. Ündar, and J. D. Zahn, 2006. A microfluidic device for continuous, real time blood plasma separation. Lab on a Chip 6:871–880.

About the author

Christian Bächer was born on April 30, 1992 in Marktredwitz in the state of Bavaria in Germany. He went to the high school Otto-Hahn-Gymnasium in Marktredwitz, where he graduated in 2011. Afterwards he spent three months on further education and internships in the hospital and rescue service. He started studying physics at the University of Bayreuth in October 2011. During his Bachelor studies, which he finished 2014, he worked on binary glass formers investigated by means of ^{31}P nuclear magnetic resonance spectroscopy during his Bachelor thesis. In 2016, he finished his Master studies with a thesis on particle and red blood cell dynamics in microcirculatory blood flow.



After his Master studies Christian Bächer joined the newly founded study program Biological Physics of the Elite Network Bavaria, which he finished parallel to his doctorate in 2019. His doctorate at the group Biofluid Simulation and Modeling at the University of Bayreuth started in December 2016. For his doctorate, Christian Bächer received a grant from the Studienstiftung des deutschen Volkes.

Acknowledgments

First of all, I would like to express my gratitude to my supervisor, Prof. Stephan Gekle, for supporting me during the entire thesis including various very interesting topics with close relation to biology. I enjoyed working with him and being part of his group every day and I am especially thankful for learning a lot during this whole period. His calm manner, his way of thinking about physical problems and his great motivation have been very pleasant. Furthermore, he was always willing to listen to all uprising issues and provided very good counsel.

For hosting me during my external research stay abroad and for all the appealing discussions on the very interesting topic of active membranes, I thank Dr. Guillaume Salbreux from the Francis-Crick Institute in London. I also thank Dr. Diana Khoromskaia for her help during my stay abroad, the discussions, and the collaboration.

Furthermore, I want to thank all members of the Biofluid Modeling and Simulation group for advises, the work together, and a really good time. I am very grateful to my office members, Rebecca Benelli, Lukas Schrack, Carina Bezold, and Katharina Grassel for a great working atmosphere and appealing discussions. Special thanks go to Rebecca for the numerous discussions on biological physics and on a better world. Especially, I want to say "thank you" for intensive, constructive, and detailed trial talks on various occasions. One of the most important institution during both my studies and the work on this thesis has been the coffee break with Lukas, to whom I deliver my great gratitude. Whether in Bayreuth, in the Fichtelgebirge, on the annual DPG meeting or virtually, the coffee breaks with Lukas Schrack have been a perfect platform to discuss physics, good coffee, and life. For the very interesting collaboration and for ample discussion concerning physics, mathematics, and the English language accompanied by black tea, I thank Katharina Graessel. For his advises, the remaining contact, and discussions on conferences I thank Dr. Abdallah Daddi-Moussa-Ider. For his help on creating good-looking images and for working together my thanks go to Sebastian Müller. In particular, I express my gratitude to Markus Hilt and Claudia Brandt for constant support on technical and organizational issues.

My special and greatest thanks go to Carolin Barth. Without your support, without the great time I could share with you, and without you as my partner during all the time, the thesis in this form would not have been possible.

For financial support during this thesis I thank the Studienstiftung des deutschen Volkes. Furthermore, I acknowledge the study program Biological Physics of the University of Bayreuth for support and a very interesting and interdisciplinary education on biology.

For the proofreading of this thesis I thank again Rebecca, Lukas, and Caro.

Extensive gratitude goes to my parents, Sigrid and Harald, and my grandparents to provide me the basis for studying physics and supporting me in all parts of my life. I

would like to thank also the rest of my kinship and all my friends, especially my godmother Sabine with Rainer, Marie, Amelie, and Luca. For their continuous support in the daily life I further thank Elisabeth and Ernst. For a great daily feel-good-environment during the past two years I thank Margitta and Leon.

Eidesstattliche Versicherung

Hiermit versichere ich an Eides statt, dass ich die vorliegende Arbeit selbstständig verfasst und keine anderen als die von mir angegebenen Quellen und Hilfsmittel verwendet habe.

Weiterhin erkläre ich, dass ich die Hilfe von gewerblichen Promotionsberatern bzw. -vermittlern oder ähnlichen Dienstleistern weder bisher in Anspruch genommen habe, noch künftig in Anspruch nehmen werde.

Zusätzlich erkläre ich hiermit, dass ich keinerlei frühere Promotionsversuche unternommen habe. Die Arbeit wurde nicht bereits in gleicher oder vergleichbarer Form zur Erlangung eines akademischen Grades eingereicht.

Bayreuth, den

Christian Bächer